An Investigation of

Microstructure and Sliding Wear in

Thermally Sprayed WC-Co Coatings

by Tippaban Sudaprasert, MEng

Thesis submitted to the University of Nottingham for

the degree of Doctor of Philosophy

November 2002

Abstract

Four types of WC-Co cermet powders (conventional WC-12 wt% Co, two different types of conventional WC-17 wt% Co and nanoscale WC-12 wt% Co powders), which have differences in terms of Co content, powder manufacturing process and WC grain size, have been sprayed to form coatings with both the high velocity oxygen-gas fuel (HVOGF) and the high velocity oxygen-liquid fuel (HVOLF) processes. The carbide grain size, powder particle size distribution and phase volume fraction of the starting powders were measured. The as-sprayed coatings were characterised by optical microscopy (OM), scanning electron microscopy (SEM), x-ray diffraction (XRD), transmission electron microscopy (TEM) and microhardness and surface roughness measurements.

The HVOGF coatings all displayed a lamellar splat structure characteristic of thermal spraying. HVOLF coatings had less well defined splat structures which suggested lower degrees of particle melting. A number of phases (WC, W_2C, W and amorphous) were observed in the coatings by XRD, SEM and TEM analysis indicating phase decomposition and oxidation during spraying. The degree of decomposition was increased by higher gas temperatures, longer particle residence times in the jet, small carbide grain size in the powder particles and an open powder structure. By suitable selection of the spraying system, spraying parameters and powder feedstock, particle decomposition during spraying could be minimised.

All coatings obtained were subjected to sliding wear against an alumina ball; a sintered WC-11 wt% Co solid disc was also tested for comparison. The decomposition of the original WC-Co powder structure in the coatings was found to be deleterious to wear resistance since the tungsten rich binder phase that now existed was significantly more brittle than the pure cobalt binder in the feedstock powder from which it was derived. However, optimisation of the conditions to reduce decomposition did not result in an increase in wear resistance. Instead, deposition of powder particles that had a significant portion of solid phase resulted in fragmentation and debonding of the carbides resulting from deformation during impact and causing increased wear. The sintered WC-Co exhibited the highest wear resistance of all materials examined, whilst the HVOGF sprayed WC-12 wt% Co coating, which exhibited significant decomposition, was the most wear resistant of all the coatings examined.

Contents

Abbreviations/Nomenclature

Abbreviations

BCC	body-centered cubic
BF	bright field
BOD	ball-on-disc
BSE	backscattered electron
DF	dark field
EDX	energy dispersive x-ray
FCC	face-centered cubic
FG	fine grinding
HVOF	high velocity oxygen-fuel
HVOGF	high velocity oxygen-gaseous fuel
HVOLF	high velocity oxygen-liquid fuel
JCPDS	Joint Committee on Powder Diffraction Standard
LVDT	linearly variable differential transformer
PG	plane grinding
SAD	selected area diffraction
SE	secondary electron
SEI	secondary electron image
SEM	scanning electron microscopy
TEM	transmission electron microscopy
XRD	x-ray diffraction

Nomenclature

Al	alminium
Al_2O_3	alminium oxide (alumina)
°C	degree Celsius
C	carbon

CO	carbon monoxide
CO_2	carbon dioxide
Co	cobalt
Co_3W_3C	cobalt tungsten carbide
Co_6W_6C	cobalt tungsten carbide
Cr	chromium
CrC	chromium carbide
HV	Vickers hardness
Ni	nickel
Ra	mean roughness (μm)
SiO_2	silicon oxide
vol%	volume percent
wt%	weight percent
W	tungsten
WC	tungsten carbide
W_2C	di-tungsten carbide
WO_3	tungsten tri-oxide

Chapter 1

Introduction

Sintered WC-Co materials, consisting of hard phase WC grains embedded in a ductile Co metal binder, have been used extensively in wear resistant applications in a variety of industries. A typical sintered WC-Co can be produced by a powder metallurgical method, namely compacting and sintering. The properties of sintered WC-Co depend primarily on the Co content and WC grain size. To achieve high wear resistance and high hardness, reduced Co content and finer WC grain sizes are required whilst retaining sufficient toughness (O'Quigley et al., 1996). Since a reduction in WC grain size results in an increase of hardness (Scussel, 1992), there have been attempts to produce nanostructured sintered WC-Co. Sintered WC-Co with nanoscale WC grain size (100 - 600 nm) has been produced by the spray conversion process (McCandlish et al., 1990; 1994). The materials obtained from this process are in the form of powder which can be compacted and sintered. The nanostructured sintered WC-Co exhibits substantially higher hardness than the microstructured sintered WC-Co (McCandlish et al., 1994). Also, nanostructured sintered WC-Co shows an increase of abrasive and sliding wear resistance compared to conventional materials (Jia and Fischer, 1996; 1997). The production of sintered WC-Co by powder metallurgical methods is limited to production of relatively small and simple components, and is a high cost production route (Voyer and Marple, 1997). However, failure of a component from wear only

involves surface degradation. For this reason, thermally sprayed coatings of WC-Co may be employed to resist wear.

WC-Co coatings can be sprayed by air plasma spraying (APS) and more recently high velocity oxy-fuel (HVOF) spraying. However, HVOF spraying has emerged as a better process than APS in achieving coatings which are well bonded to the substrate with minimal porosity and a reduced quantity of undesirable reaction products (Sobolev et al., 1996; Smith and Knight, 1995). This is widely attributed to the higher particle impact velocities and lower peak particle temperatures in HVOF compared to APS. After the inception of the HVOF process in the early 1980s, it has been continuously developed into several versions of spray gun (Sturgeon, 1992). However, all of the guns still retain the same characteristics, i.e., high powder particle velocities and relatively low powder temperatures (Li et al., 1996). Systems which employ a gaseous fuel such as hydrogen often yield comparatively higher particle temperatures and lower velocities than systems which employ a liquid fuel such as kerosene.

During spraying, WC-Co powders are exposed to the hot flame and reaction causing decomposition of powder particles occurs. This leads to dissolution of WC into the liquid Co-binder, loss of carbon by oxidation and the formation of an amorphous/nanocrystalline binder phase on resolidification. The parameters playing an important role in microstructure formation are types of fuel (causing a difference in flame temperature), fuel and oxygen flow rates (affecting the particle velocity), gun design, and type and structure of starting powder (Li et al., 1996). Moreover, within any HVOF process, there is a wide variety of conditions available such as powder

feed rate, gun to substrate stand-off distance, fuel and oxygen flow and powder injection position.

WC-Co coatings show complex, multiple-phase microstructures (WC, W_2C, W, complex carbides and Co(W,C) amorphous/nanocrystalline phase), with a significantly lower volume fraction of primary carbide than the starting powders (Stewart, 1998). The degree of decomposition of the powders during spraying, depends primarily on particle temperature, particle velocity and characteristics of the powder (such as surface morphology and WC grain sizes within particle). Decomposition is favoured by high temperature and low velocity (leading to a long residence time of the particle in the hot flame temperature) and by small carbide grain sizes. A high degree of decomposition is generally observed leading to a detrimental effect on the sliding wear performance of WC-Co coatings resulting from the presence of the brittle W_2C phase (Voyer and Marple, 1997). However, when spraying with a system which reduces the degree of particle heating, the coatings may exhibit poor bonding between the splats and again this results in high rates of wear (Qiao et al., 2001).

In this study, the effect of Co content, WC grain size, powder manufacturing process and spray conditions on the WC-Co coatings produced by a liquid-fuelled gun (HVOLF) and a gas-fuelled gun (HVOGF) will be examined. Following characterisation of the WC-Co coatings, the mechanisms of microstructure formation will be explained and related to differences in spraying conditions and powder characteristics. Furthermore, the sliding wear behaviour of the WC-Co coatings

(compared to sintered WC-Co) will be examined and related to the coating microstructure.

Chapter 2

Literature Review

2.1 Thermal Spray Technology

Thermal spraying is a group of processes in surface engineering, which is employed for enhancement of the surface properties of a component. Fig. 2.1 summarises the development of thermal spray technology (Smith and Novak, 1991). Thermal spray coating, named as a metallizing process, was invented by Dr. M.U. Schoop in the early 1900s (US Patent No 28001, 1912). This process used an oxy-acetylene flame as the heat source to spray low melting point materials such as tin and lead (Tucker, 1994; Fauchais et al., 2001). Due to its limitation to low melting point materials, new techniques of thermal spraying emerged. Plasma spraying, which can spray any material which does not decompose before melting, was invented by Thermal Dynamic Corp. (Lebanon, NH) in 1957 (Fauchais et al., 2001). This process uses a plasma as a heat source generating temperatures of up to 15000 °C (Herman, 1988). Vacuum plasma spraying or low pressure plasma spraying was developed in the 1970's by Muehlberger (Pawlowski, 1995). Vacuum plasma spraying controls the environment to achieve less oxidation in the coating. Further developments of the process include high gas velocity direct current (d.c.) arc spraying, radio frequency (R.F.) induction plasma spraying, twin wire arc spraying and underwater plasma

spraying (Fauchais et al., 2001; Pawlowski, 1995). At almost the same time as plasma spraying, detonation-gun spraying was developed by Poorman et al. (1955) and a spray gun with a tradename 'D-gun' was produced by Union Carbide (now Praxair Surface Technology, Inc.) (Fauchais et al., 2001; Pawlowski, 1995). At the beginning of the 1980s, a high velocity oxy-fuel spraying (HVOF) process was developed. The emergence of HVOF systems provided competition to D-gun and plasma systems for depositing cermet coatings, such as WC-Co and Cr_3C_2/NiCr, as it was able to achieve high coating densities, high bond strengths with the substrate and less reaction (Sturgeon, 1992; McIntyre, 1996). As can be seen in Fig. 2.1, the materials used for spraying have originally evolved from metals (such as zinc and aluminium), to composite materials (fibre-reinforced materials). Thermal spraying is used extensively to enhance the properties of many engineering components in a variety of industrial applications, ranging from agricultural to aerospace parts. Thermal spray processes can be categorized by the heat source, feedstock materials and the surrounding environment. Basically, they can be classified into three main categories: combustion spraying, plasma spraying and electric/wire arc spraying, as shown in Fig. 2.2 (Smith and Knight, 1995). A comparison of characteristics of thermal spray processes is listed in Table 2.1. The present research considers in detail only the high velocity oxy-fuel spraying process.

2.2 High Velocity Oxy-Fuel (HVOF) Spraying

HVOF spraying was developed from conventional flame spraying by an increase of the gas flow rates and the generation of high pressure in a combustion chamber. This results in a supersonic flame with the appearance of shock diamonds in the free jet. A

schematic of an HVOF gun is shown in Fig. 2.3. A fuel, frequently a gas, (such as propane, propylene, methyl-acetylene-propadiene (MAPP) or hydrogen), and oxygen are fed into the combustion chamber where they are premixed and burnt. Powder transported by a carrier gas (nitrogen or argon) is usually introduced axially into the combustion chamber (although some systems employ a radial feed into the nozzle). The powder is heated and propelled along the nozzle by the rapidly expanding gases. The gas velocity is typically about 1800 m s^{-1} resulting from the pressure in the combustion chamber of over 4 bar and gas flow rates of several hundred l min^{-1} (Sturgeon, 1992). Powder is normally fully or partially melted with a temperature between 1500 - 2500 °C. The flame temperature depends mainly on the type of fuel gas used, the oxygen to fuel gas ratio and the pressure inside the combustion chamber and barrel (Tucker, 1994; Clare and Crawmer, 1982).

2.2.1 Types of HVOF Spray Gun

The Browning Engineering Co. invented HVOF spray system, known as Jet-Kote HVOF system, in the early 1980s (Sturgeon, 1992). Later on, several types of HVOF spray systems were commercialised: Jet-Kote II (Thermadyne Deloro Stellite), Top-Gun (UTP), HV-2000 (Miller Thermal), Diamond Jet (Sulzer Metco), Continuous Detonation Spraying (CDS) (Plasma Technik), JP-5000 (Hobert Tafa), and Met-Jet II (Metallisation) (Sturgeon, 1992; Harvey, 1996). Each HVOF process is based on the same fundamental principles but each has different internal gun designs. HVOF gun designs can be classified by the position of ignition and the position of powder feed (Thrope and Richter, 1992). Fig. 2.4 shows a schematic diagram of a variety of HVOF spray guns.

Type A

In this type, fuel gas and oxygen are mixed and burnt in a combustion chamber. The hot gas jet is turned 90 degree into a nozzle. In that area, the hot gas jet is constricted and accelerated. Powder in a carrier gas (Ar, He or N_2) is injected axially via the back of the gun into the hot gas jet (Thrope and Richter, 1992). An example of this type of system in the Jet-Kote II spray gun (Fig. 2.4a).

Type B

An example of this type is the Diamond Jet (DJ) spray gun (Fig. 2.4b). With this system, fuel gas, oxygen and compressed air are introduced into the gun. Both fuel and oxygen are thoroughly mixed in a proprietary siphon system in the front part of the gun. Powder is fed axially into the gun using carrier gas. Therefore, the powder is heated when it exits the gun (Berz et al., 1991).

Type C

With this type, fuel gas and oxygen are injected axially into the mixing chamber and the mixed gases are burnt in the combustion chamber. The hot gas jet is accelerated along the nozzle. Powder is fed axially and directly into the combustion chamber, where the powder can gain highest temperature. Examples of a spray gun of this type are the Top-Gun (Fig. 2.4c), HV 2000 (Fig. 2.4d) and CDS systems.

Type D

In this type, liquid fuel (kerosene) is used instead of a gas fuel. Kerosene and oxygen are premixed and injected axially into a combustion chamber where they are burnt. The hot gas jet passes through a converging-diverging throat which imparts high

velocity into the gas stream entering the nozzle. Powder is fed in downstream of the throat into the hot gas jet. Examples of spray guns in this system are the Met-Jet II (Fig. 2.4e), the JP 5000 and the JP 8000 (Fig. 2.4f).

Thrope and Richter (1992) classified burner designs into throat combustion burner types and chamber burner types. The chamber burner generates higher particle velocities and higher levels of particle heating than that for the throat combustion burner. Higher particle velocities result from a larger diameter combustion burner leading to higher chamber pressure. Using a longer nozzle length causes a higher degree of heating of the powder. In addition, they concluded that the Jet-Kote spray gun exhibits heat losses associated with turning of the hot gas 90° into the nozzle. Potential cracking of the gun system due to high differential heat flux and reduced gas temperature due to cooling of the chamber before the introduction of the powder are also possible. The in-line Top-Gun spray system improves thermal efficiency by axially feeding the powder into the combustion chamber. This design produces more uniform heating of the powder. In spray guns with a converging-diverging nozzle (Met-Jet II or JP-5000), the powder is introduced into the reduced pressure region downstream of the throat. This results in higher powder spray rates (mass feed rates) per unit of energy input and has a more uniform powder distribution within the exit jet leading to a flatter spray area footprint profile when compared with axial injection.

In general, cermet coatings sprayed by HVOF systems exhibit lower porosity, higher bond strength and higher hardness than coatings deposited by plasma spraying. Within HVOF spraying, some of the coating properties can be improved by using the JP-5000, DJ-2600 and DJ-2700 systems due to the higher kinetic energy and lower

thermal energy associated with these. Kreye et al. (1996) studied characteristics of WC-Co coatings sprayed with various HVOF spray guns (i.e. Jet-Kote, Top-Gun, CDS, JP-5000, DJ-2600 and DJ-2700). They found that powders receive the least thermal energy input from the JP-5000, the DJ-2600 and the DJ-2700 spray guns, whereas the highest thermal energy is transferred to particles in the Top-Gun spray gun. In spraying agglomerated and sintered WC-17 wt% Co powder, they reported that powder sprayed with the JP-5000, the DJ-2600 and the DJ-2700 resulted in lower coating porosity with a higher volume fraction of retained carbides. Also, less phase transformation was found in coatings sprayed by the JP-5000, the DJ-2600 and the DJ-2700 systems (Kreye et al., 1999).

Recently, Irving (2000) stated that a new HVOF spray process, known as high velocity impact forging (HVIF), reduced the flame temperature in the hottest zone by water cooling. With this spray gun, fuel oil and compressed air are used. Powder particles impact on the substrate to form a coating by forge welding. In general, coatings with low porosity and oxide content can be achieved when the velocity of powder particles is over 1219 m s^{-1}, temperatures are below 1093 °C and a combustion pressure above 1378 Pa. WC-Co coatings were also sprayed by the HVIF process at a combustion pressure slightly above 6890 Pa. The WC-Co coating showed fully dense microstructure with no decomposition of WC particles, which was confirmed by XRD.

2.2.2 Advantages of HVOF Process

As mentioned previously in the section 2.2.1, HVOF spraying was invented to compete with D-gun spraying and plasma spraying. Table 2.2 shows a comparison of the quality of WC-Co coatings which were sprayed with different thermal spray processes (Sturgeon, 1992). In HVOF spraying, particles have a higher kinetic energy than in plasma spraying, this produces WC-Co coatings with low porosity (0.1-2 %) and reduces the amount of oxidation of particles during their residence in the hot gas jet. With higher particle velocities, HVOF spraying generates more plastic deformation leading to a lower coating porosity and achieves adhesive strength between coating and substrate of approximately 70 MN m^{-2} (Sturgeon, 1992; McIntyre, 1996). Cermet coatings (such as WC-Co and Cr_3C_2/NiCr) have commonly been sprayed with the D-gun, HVOF and plasma. There are many published papers addressing the microstructural characterisation of WC-Co coatings deposited with HVOF and plasma spray systems and report the mechanical properties of the coatings. It is generally reported that HVOF sprayed WC-Co coating has a higher bond strength, hardness and density than a plasma sprayed WC-Co coating. Plasma sprayed WC-Co coatings are usually highly degraded (i.e. decarburised and oxidised) and contain complex carbides such as W_2C, $Co_xW_yC_z$ and metallic tungsten (Fincke et al., 1994; Ramnath and Jayaraman, 1989). Dorfman et al. (1989) and De Villiers Lovelock et al. (1998) have reported that a higher degree of decarburisation reduces wear resistance. Therefore, HVOF spraying has been used increasingly to spray WC-Co coatings to achieve desirable engineering properties.

2.3 WC-Co Powder Production

Commercial WC-Co spray powders generally contain between 8 wt% Co and 20 wt% Co. Other systems involving WC are employed to improve the corrosion resistance; for instance WC-Ni, WC-Co-Cr and WC-Cr_xC_y-Ni are typical compositions. A variety of manufacturing processes are used to produce WC-Co powder which result in differences in morphology, carbide phases present and microstructure. The main manufacturing processes for WC-Co powder used in industrial applications are outlined below.

2.3.1 Agglomerated and Sintered Process (or Agglomerated and Furnaced, or Agglomerated and Densified)

The manufacturing process starts with very fine WC and Co powders, < 5 μm in size, which is obtained by milling, pelletizing, pressing or spray drying. An organic binder is used to agglomerate the powders. The agglomerated powder is heated in a furnace. The organic binder is vaporised and the fine powder particles bond to form larger solid particles (Huddleston, 1990). In general, agglomerated and sintered WC-Co powder shows near spherical morphology with high levels of porosity (Schwetzke and Kreye, 1998).

2.3.2 Fused and Crushed Process (or Cast and Crushed)

The certain compositions of WC-Co material are cast and crushed into a small particle size. The resulting powder has a blocky and angular morphology with a low porosity.

2.3.3 Sintered and Crushed Process

The constituents of the powder are mixed together and heated, resulting in sintering by diffusion. Then, the product is crushed to obtain the particle size required. A sintered-crushed powder has blocky morphology with a relatively low porosity.

2.3.4 Agglomerated and Plasma Densified Process

Agglomerated particles are formed as in the agglomerate and sintered process (section 2.3.1). They are then heated by a thermal plasma jet to melt the metallic binder phase. This process produces dense powders with a spherical morphology.

2.3.5 Spray Dried Process

Either particles of WC and Co or particles of WC-Co are suspended in a binder solution to form a slurry. This is then used to produce spray dried powder granules, which are joined together by an organic binder. These powders are densified by sintering using plasma or flame treatments. Spray dried powder has a spherical morphology with high levels of porosity (Keller et al., 2001; Kim and Suhr, 2001).

In addition, WC-Co HVOF feedstock powder can be produced by other processes, such as carbide activation technology (CAT), cast-crushed and fused and multimodal agglomeration processes (Skandan et al., 2001; Ajdelsztajn et al., 2001). The multimodal powder is produced by blending conventional WC-Co powder with

nanoscale WC-Co powder, followed by a heat treatment to form an agglomerated particle.

Table 2.3 shows examples of WC-Co powder types described above and referred to in the literature. Different manufacturing processes result in different morphology, density, initial phases, particle size distribution and carbide grain size within the powders. Li et al. (1996) stated that the degree of decarburisation during HVOF spraying mainly depends on the type of powder, in particular, the presence of complex carbides (such as W_2C and Co_3W_3C) in the powder. De Villiers Lovelock et al. (1998) also reported that a high amount of W_2C in the starting powder generates a larger amount of complex carbide phases in the thermally sprayed coating leading to lower wear resistant coatings. The particle surface to volume ratio also affects the degree of decomposition, with porous particles being prone to overheating. Finer carbide sizes in these powders result in a lower surface roughness of the coating (Jorosinski et al., 1993). Powder with a spherical morphology has excellent flowability and feedability through the system. Hwang et al. (1996) stated that the fused and crushed WC-Co powder, which has an angular shape, did not flow continuously when sprayed with HVOF (JP-5000). The shape of powder affects the flow rate; as a result, very low deposition rates for angular powders are commonly observed.

Nanostructured materials, which have grain sizes in the order of several tens of nanometres, have been produced in the last decade. Nanostructured WC-Co powder is produced by spray conversion and mechanical milling as follows:

2.3.6 Spray Conversion Processing

Kear and McCandlish (1994) discovered a new method to produce nanostructured WC-Co powder, which have powder particles sizes (of about 75 μm) and WC grain sizes of 20-50 nm. Powders are produced by a thermochemical method, called spray conversion process. At an industrial scale this process consists of 3 steps as follows (Kear et al., 1990):

1. The starting solution using precursor powder is prepared with $(NH_4)_6(H_2W_{12}O_{40}) \cdot 4H_2O$ (ammonium metatungstate) and $CoCl_2$, $Co(NO_3)_2$ or $Co(CH_3COO)_2$. The solution is then homogeneously mixed.

2. The solution is then spray-dried, where the solvent mixture is rapidly evaporated in hot gas stream, and as a result, the solute mixture is precipitated at a sufficiently high rate without phase separation.

3. The resulting precursor powder is thermochemically processed in a fluidised bed reactor with a gas mixture to deposit carbon on the surface of powder. The carbon is diffused into the particles and reacts with W to form WC.

The nanocomposite WC-Co powder produced by the spray conversion process exhibits a hollow spherical morphology. The WC grains, with an average grain size reported to be 20-50 nm, are embedded in the Co matrix. Mohan and Strutt (1996 a, b) observed the microstructure of nanocomposite powder consolidated by liquid phase sintering and hot deformation processing. They reported that the ultrafine Co rich

precipitates were found inside WC. The Co precipitates were analysed to be face-centered cubic (FCC) Co with the size ranging from 20-30 nm. Apart from Co (FCC), they stated that Co (HCP) was also detected.

2.3.7 Mechanical Milling

In this process, conventional WC-Co powder is placed together with a number of WC balls in hexane in a sealed container. He et al. (2000) stated that initially the powders are a mixture of crystalline Co binder with polycrystalline carbides. During milling, the carbide particles are fractured and then embedded into the binder phase to form polycrystalline nanocomposite powders. He et al. (2000) reported that longer milling times (14 hour) reduced the powder particle size and also resulted in a finer carbide grain size (6 ± 3 nm). However, fine powder particles were re-agglomerated to form particles in the range of 30 - 50 μm for HVOF spraying. WC-Co powder produced by mechanical milling is rarely used as a commercial product.

2.4 Previous Studies on WC-Co Coatings

Thermally sprayed WC-Co coatings have been deposited under a wide range of process conditions such as spray type (plasma spraying, HVOF spraying and D-gun spraying), spray parameters, WC-Co powder properties and post-treatment. WC-Co powders produced by a range of methods have been sprayed with different HVOF spray systems and compared in this literature review.

2.4.1 Microstructures of WC-Co Coatings

A schematic image indicates that a coating (Fig. 2.5) generally consists of several splats (droplets of semi-molten or molten powders), unmelted particles, voids and oxidised particles. The microstructure of thermally sprayed WC-Co coatings is reported by several investigators to contain retained WC, W_2C, W, complex carbides (such as Co_3W_3C and Co_6W_6C), amorphous/nanocrystalline binder phase and micropores. Phases and microstructures of thermally sprayed WC-Co coatings are examined by means of X-ray diffraction, optical microscopy, scanning electron microscopy, transmission electron microscopy and energy dispersive spectroscopy.

2.4.1.1 X-Ray Diffraction (XRD)

XRD has been used to identify phases present and shows the changes in phase content between the powder and coatings. XRD spectra also reveals the differences of the degree of dissolution in coatings through showing amorphous phase formation.

Many workers have analysed the phases of the powders and coatings of WC-Co sprayed with various techniques. For example, Khan et al. (1997) have reported the phase analysis of WC-17 wt% Co spray-dried powder, WC-17 wt% Co, WC-12 wt% Co and WC-9 wt% Co sintered and crushed powders. All of them were sprayed with the Top-Gun using 90% and 70% stoichiometric mixtures. Two fuel gases (hydrogen and propylene) were used. The XRD spectra of all starting powders contained significant peaks of WC and a small amount of Co; however, Co_3W_3C (η phase) peaks were found in the sintered and crushed WC-9 wt% Co powder. The XRD

spectra of coatings generally contained WC, W_2C, W peaks and a broad diffraction peak of an amorphous phase. In similar work, a WC-17 wt% Co sintered and crushed powder with WC grain sizes about 2-5 μm was sprayed with the UTP Top-Gun using a 75% stoichiometric gas mixture of hydrogen and oxygen. The XRD spectrum of the coating consisted of WC, W_2C and an amorphous/nanocrystalline phase but the W peak was not observed (Stewart et al., 2000).

Coulson and Harris (1997) have characterised the phases present in a WC-17 wt% Co sintered and crushed powder with WC grains, approximately 1-2 μm in size, in a coating sprayed with the Met-Jet HVOF system using kerosene and oxygen. It was reported that the powder consisted of WC and Co phases whereas in the coating WC, W_2C, W and an amorphous/nanocrystalline phase were formed.

2.4.1.2 Optical Microscopy (OM)

Optical microscopy has been used to attain basic information on cross sections of coatings such as the fraction of unmelted and melted areas, distribution of carbide particles in the coating, voids and microstructure at the interface between coating and substrate. Also, plan view optical imaging of coatings has been employed.

To observe the microstructure of thermally sprayed WC-Co coatings, Murakami's reagent has been used, as applied into sintered carbide (Haller, 1985; Blann, 1991). Haller (1985) has stated that various phases in sintered carbide (such as Co or Ni, WC, (Ta, Ti, Nb, W)C, $(Co_3W_3)C$, $(Co_6W_6)C$ and W_2C) reacted with Murakami's

reagent with different reaction rates. However, the reaction rate with an amorphous or nanocrystalline binder phase was not reported.

A few authors have used Murakami's reagent to etch microstructures of coatings because the carbide grains were outlined and darkened slightly (Vander Voort, 1999). However, they have not clearly stated how Murakami's reagent reacted with the coating. Korpiola and Vuoristo (1996) have characterised the WC-17 wt% Co coating etched with Murakami's reagent. The relative reaction rates of sintered carbide quoted by Haller (1985) were also mentioned in their work. In addition, they believed that the amorphous or nanocrystalline binder phase was etched at the same rate as the eta phase (Co_3W_3C and Co_6W_6C). Microstructures of WC-Co coating etched with Murakami's reagent, characterised by optical microscopy, showed unetched areas and etched areas, which appeared black. They stated that the etched areas were probably the W_2C, eta phase and amorphous or nanocrystalline binder phase. WC grains and non-reacted Co were unetched. Moreover, Tomita et al. (1993) have stated that coatings containing higher amounts of Co_3W_3C and Co_6W_6C were rapidly attacked with Murakami's reagent.

Many workers (e.g. Guilemany and De Paco (1996)) employed optical microscopy of coating cross sections to observe the homogeneity of coating, to determine the thickness and to measure the level of porosity.

2.4.1.3 Scanning Electron Microscopy (SEM)

The appearance of the morphology of powders and the microstructure of thermally sprayed coatings are observed by SEM utilising secondary and backscattered electron imaging modes (SEI and BEI, respectively). The SEI mode is generally used to view surfaces whereas BEI mode (showing contrast based on the mean atomic number) is used to investigate the microstructure of coatings and the degree of reaction in the coatings. The compositions at different areas in the coatings have been analysed with an EDS. Also, quantitative image analysis has been performed on microimages to measure the WC grain sizes and volume fraction of the WC grains.

Most workers have used SEM to observed the powder and cross sections of coatings, for example, Verdon et al. (1998) have examined the morphology of WC-12 wt% Co powder produced by agglomerated and densified method and subsequent coatings sprayed by HVOF using two types of fuel gases, namely, hydrogen and propane. SEM observations of the powder showed near spherical morphology. A cross sectional image revealed a fairly dense structure with an average carbide grain size of about 1 μm. In general, the cross section of the coatings showed splat-like structures which are parallel to the substrate. The matrix showed a range of grey shades. In the bright grey shaded regions, carbide particles showed round edges, as compared with the dark grey shade which has sharp edges. The bright grey shaded regions have higher amount of W present when analysed with EDS-SEM. Also, the volume fraction of the binder phase in the coating is increased, when compared with the powder.

Coulson and Harris (1997) have characterised WC-17 wt% Co powder and coatings sprayed with the Met-Jet using kerosene as a fuel liquid. The WC-17 wt% Co powder examined by SEM had blocky and angular shape. A cross section of the powder showed a fairly dense structure with carbide grain sizes approximately 1 - 2 μm. Cross sectional microstructures of the coating showed a binder matrix phase containing dark and bright binder shades. In the dark binder shade, WC particles with an angular shape corresponding to unreacted areas were found, whereas WC particles with round edges corresponding to reacted areas were observed in the bright binder shaded regions. Moreover, the coating etched with Murakami's reagent showed the reacted areas were related to the bright binder shade.

WC-17 wt% Co powders and coatings were characterised by Stewart et al. (2000). The morphology of the sintered and crushed WC-17 wt% Co powder had angular shape. A cross sectional image showed angular WC grains about 2 - 5 μm in size. Microstructures of the coating sprayed with the UTP Top-Gun using hydrogen as fuel gas had basic structures as reported by Verdon et al. (1998) and Coulson and Harris (1997). The investigators have analysed the volume fraction of carbide in the dark and bright binder shaded regions and reported 38% and 9%, respectively. A range of shade levels in the binder phase resulted from different W levels. In the bright binder shaded regions, WC particles with round edges and some carbide particles surrounded with partially or wholly with bright layer, presumably W_2C, were reported.

2.4.1.4 Transmission Electron Microscopy (TEM)

For higher resolution observation, TEM is applied to examine thermally sprayed WC-Co coatings. Also, an EDS microanalysis is used for local phase identification.

Many researchers examined microstructures of HVOF sprayed WC-12 wt% Co coatings. Much less work is reported on WC-17 wt% Co using TEM. An early characterisation of a WC-12 wt% Co coating sprayed with HVOF was reported that some hexagonal WC particles, containing a high density of dislocations and stacking faults, and hexagonal W_2C particles embedded in an amorphous binder (Nerz et al., 1991). However, they stated that small grains of W were nucleated and grown on the WC surface. Karimi et al. (1993) examined the WC-12 wt% Co coating sprayed with a CDS spray gun. They also stated that the coating consisted of a reacted carbide corresponding to WC with a high density of defects and a nanocrystalline binder matrix of Co-W-C with grains 4 - 8 nm in size. Non-reacted WC particles with sharp edges were also found. W_2C structures surrounding WC particles were observed. Similar work by Guilemany and De Paco (1996) involved WC-12 wt% Co coatings sprayed with the CDS-100 gun. It was reported that WC particles with rounded edges were embedded in a matrix which was confirmed by the diffraction patterns to be amorphous/nanocrystalline were observed. Also Guilemany and De Paco (1999 a), argued that the high density of defects in the carbide particles were produced from higher impact velocities with the substrate. W_2C phase showing globular structures was detected on WC grains. In further work (Guilemany and De Paco, 1999 b), they examined a WC-12 wt% Co coating. They stated that WC particles passing through the hot gas without reaching a high temperature exhibited faceted structures with

sharp edges. Some carbide particles showed defect structures generated from the very high velocity impact onto the substrate. Some carbide particles reaching high temperatures revealed rounded edges. They were also dissolved in the matrix. Some carbide particles exhibited a high density of defects at its outer areas which diffraction confirmed was W_2C. The inner areas of those particles were still WC. Globular structures of W_2C were found on the surface of WC. The W_2C structures were formed by precipitation from the liquid phase on cooling. The matrix structures were amorphous and nanocrystalline having a grain size about 1 - 10 nm. Moreover, small equiaxed grains were observed at the interface of the binder phase and WC particles.

Verdon et al. (1998) characterised WC-12 wt% Co coatings sprayed by HVOF using different fuels gases: hydrogen and propane. The matrix of the coating sprayed with hydrogen was shown to be nanocrystalline with a grain size of 2-8 nm. WC cores epitaxially surrounded by W_2C were detected. WC grains contained dislocations whereas the W_2C phase did not contain dislocations. The interface between W_2C and the nanocrystalline matrix phase was rather sharp and curved shape. The investigators have stated that carbide dissolution and decarburisation took place at the same time at the surface of WC grains. W_2C formed from carbon diffusing back to the WC grains. In addition, tungsten precipitates, about 100 nm in size, were found. Dendritic structures of Co were also observed in the areas where carbide density was high. Chemical analysis of the binder matrix showed that it contained a large amount of tungsten and carbon when compared to the Co binder matrix in the powder.

Stewart et al. (2000) sprayed WC-17 wt% Co powder by the UTP Top-Gun and examined WC-17 wt% Co coatings by TEM. Faceted crystals, indexed to WC, with

high density of dislocations were observed. W_2C particles (confirmed by SAD) were found at the interface between WC and the amorphous/nanocrystalline binder phase. Dislocations did not appear in W_2C particles. Moreover, a TEM image showed a WC core surrounded by a W_2C shell in an amorphous/nanocrystalline binder matrix.

In summary of microstructural observations, there are generally four main techniques (i.e. XRD, OM, SEM and TEM) used to analyse the microstructure of WC-Co coatings. Each method provides a variety of information. XRD has been used to analyse phases present in the coating compared with the feedstock powder. The changes in phases present exhibit the reactions occurring during spraying. XRD patterns also show the differences in the degree of decomposition by the intensity of an amorphous phase formation. Optical microscopy has been used to observe a general microstructure of the coating including the fraction of unmelted and molten areas in an etched coating, the distribution of carbide particles, the pores and the coating/substrate interface. Due to low resolution of optical microscopy, SEM has been used to examine the coatings and general morphology of powder using SE imaging mode. Microstructural observation using BSE imaging mode shows atomic number differences present in the SE image and aids identification of compositional variation. Also the EDS analysis is used to differentiate compositions in different areas associated with the BSE image. Thus, the results from XRD analysis and microstructures examined by SEM can explain how phases form in the coating. TEM observations at high resolution have been used to characterise the details of microstructure of the coating. Also, selected-area diffraction can be used to identify phases formed.

2.4.2 Mechanism of Phase Transformations

Many authors have examined the structures and properties of WC-Co coatings sprayed with various techniques, and have attempted to propose a model of phase transformations that occurs during spraying. In this section, the mechanisms of phase transformation in thermally sprayed WC-Co coatings are discussed.

Guilemany and De Paco (1999 a) have proposed two mechanisms of degradation for powder particles exposed to the hot gas jet.

Mechanism I

1. Carbide particles on the free surface of powder react directly with oxygen. This results in decarburisation of the original WC particles to form W_2C. The reactions are given in (1) and (2) (Guilemany et al., 1999 b).

$$2WC + O_2 \Leftrightarrow W_2C + CO_2 \qquad (1)$$

$$W_2C + \frac{1}{2} O_2 \Leftrightarrow W_2(CO) \qquad (2)$$

These reactions take place when WC particles react with high level of oxygen in the hot gas jet. The carbon is eliminated to form CO_2 and CO.

Mechanism II

1. The binder phase melts when it reaches its melting point.

2. The carbide particles dissolve in the molten binder leading to an increase of C and W in the binder matrix. Equations (3) through (5) support the evidence of significant variations of W and C in the binder matrix.

$$4Co + 4WC + O_2 \rightarrow 2Co_2W_4C + 2CO \quad (3)$$

$$3Co + 3WC + O_2 \rightarrow Co_3W_3C + 2CO \quad (4)$$

$$12Co + 12WC + 5O_2 \rightarrow 2Co_6W_6C + 10CO \quad (5)$$

3. Oxygen diffuses quickly into the molten phase and reactes with carbon to form CO(g) and CO_2(g).
4. When the temperature decreases, a new binder matrix (W,C)Co is formed. With the small amount of carbon remaining in the coating, W and W_2C are formed.
5. WC particles act as nuclei for growth of W_2C, partly as a result of high amount of C and W in the matrix near those WC particles.

Khan and Clyne (1996) proposed a different thermodynamic for WC decarburisation leading to CO_2 and CO formations. They stated that at high temperatures WC grains reacting with plentiful oxygen resulted in W and CO_2 formation.

$$WC + O_2 = W + CO_2 \quad (6)$$

However, if the oxygen was decreased, W_2C and Co were formed.

$$4WC + O_2 = 2W_2C + 2CO \quad (7)$$

In their work, WC-Co coatings sprayed with air and vacuum plasma spraying showed different phase formation in each spray process, resulting from a role of oxygen. The air plasma coating contained W_2C, whilst the vacuum plasma coating did not contain W_2C. This confirms the role of oxygen in decarburisation.

Schwetzke and Kreye (1999) have agreed with Guilemany et al. (1999 a, b) that WC particles were dissolved in the molten Co binder leading to different grey shades in BSE images of sprayed coatings corresponding to different amount of W and C. The Co binder formed an amorphous or nanocrystalline supersaturated solid cobalt (tungsten, carbon) solution or η-phase depending on the solidification conditions. They have pointed out that the precipitation of W and W_2C from the supersaturated solid solution can occur.

Verdon et al. (1998) have stated that when WC-Co powders were heated, the Co-binder phase melted. Higher temperatures produced higher dissolution of WC in the molten Co binder matrix to form a nanocrystalline structure containing Co, W and C. Some non-dissolved WC grains were still retained in the coating. W_2C surrounding a WC core was commonly found. Dislocations were observed in WC grains. Since dislocations (associated with impact) were not observed in W_2C, they argued that W_2C precipitates were formed from the melt after impact with the substrate. W precipitation in the Co binder matrix also resulted from carbon loss. The main mechanism for the carbon loss was the oxidation reaction at the surface of particles; another mechanism was the dissolution of WC in the molten Co binder matrix.

Stewart et al. (2000) agreed with Verdon et al. (1998) about W_2C precipitates being produced directly from the liquid state after cooling. In addition, they have described the decarburisation of WC to W_2C transformation and a formation of W generated by the direct oxidation of solid WC. This mechanism occurs on WC grains at the interface between gas/particle only. They suggested that the melting of the Co binder matrix prevents the direct oxidation of solid WC. Therefore, they have proposed that carbon loss results from the reaction with oxygen at the interface of molten Co/gas or oxygen diffusing into the edge of molten Co. They argue that the formation of W_2C, W and Co(W,C) nanocrystalline/amorphous phase takes place during rapid solidification depending on the degree of decarburisation.

2.4.3 Effect of Powder Type on Microstructure

WC-Co powders have been produced by different manufacturing processes, e.g. cast-crushed, sintered-crushed and agglomerated-sintered, resulting in different morphologies, tungsten carbide grain sizes in a powder particle, powder grain sizes and distributions, and initial phases of powder (Li et al., 1996). Powder morphology plays a role on powder transport of the powder feeder and gun. The spherical agglomerated powder has been shown to flow and feed better. A powder size distribution, of 10 - 45 μm, is generally used when spraying with HVOF process. Large differences in powder size leads to the greater differences in degree of melting achieved. The effects of different powders produced by the various methods have been reported by many researchers.

Tomita et al. (1993) have examined the influence of powder type (WC-12 wt% Co powders from two different manufacturing processes (i.e. sintered and crushed process and spray dried process) on coatings sprayed with the Jet-Kote gun. The XRD spectra of the starting powders exhibited large WC peaks in both powders. In the spray dried powder, small Co peaks were observed. However, in the sintered and crushed powder, Co_3W_3C and Co_6W_6C phases were found and peaks from the Co phase were not observed. The XRD patterns of both coatings showed high levels of retained WC and small amounts of W_2C. Also, significant peaks of Co_3W_3C and Co_6W_6C were found in the coating sprayed with the sintered and crushed powder. Their work indicates that not only powder manufacturing process but also initial phases in the starting powder affect the microstructures of the coatings.

Jacobs et al. (1999) have identified the phases present in two WC-12 wt% Co powders produced by sintering and crushing, and agglomeration. The XRD spectra of these powders showed only WC and Co peaks. The sintered and crushed powder has a smaller carbide grain size than the agglomerated powder. The powders were sprayed with different spray guns, namely, the Jetstar, DJ-2600, DJ-2700 and HV-2000. It was reported that the ratios of W_2C/W in the coatings sprayed with the sintered and crushed powder were higher than those in the coatings sprayed with the agglomerated powder. This indicated that more decarburisation had occurred in the coating sprayed with the sintered and crushed powder. This is an unusual result for a coating sprayed with the agglomerated powder, which has a porous structure. The porous powders, which have high ratios of particle surface to volume, could be melted rapidly (in particular the Co-binder). However, in their investigation, it might be an effect of small carbide grain size in the sintered and crushed powder.

De Villiers Lovelock et al. (1998) have examined fifteen WC-12 wt% Co powders selected from commercial suppliers. These powders were classified into three groups: cast and crushed powders, sintered and crushed powders, and agglomerated densified powders. It was reported that cast and crushed powders generally contained WC, W_2C and ternary W-Co-C phases. The XRD spectra of the sintered and crushed powders generally exhibited WC and Co phases without W_2C and other phases. The agglomerated and densified powders exhibited different phase compositions: the WC-616 and Amperit 518.074 contained WC and Co whilst the 1371P and JK 7112 showed WC with smaller amounts of W_2C and CoC_x. This again shows that powders produced by different processes contain different phases.

Furthermore, Li et al.(1996) have indentified the phases present in five WC-Co powders, which had different Co binder contents and were produced by different manufacturing processes. It was reported that aggregated powder (manufactured through sintering and crushing), agglomerated powder and cladded powder contained only WC and metallic Co, whereas, sintered and crushed powder, and cast-crushed and fused powder contained WC and complex carbides (W_2C, Co_3W_3C and Co_6W_6C). These powders were sprayed with the Jet-Kote using acetylene and 30% propylene as a fuel gas. The XRD spectrum of all coatings showed a peak of free carbon. All coatings, except the coating sprayed with sintered and crushed powder, contained a large amount of WC. The coatings sprayed with the aggregated powder and the agglomerated powder showed a small amount of W_2C and W peaks. However, the XRD spectrum of the coating sprayed with clad powder showed substantial retained WC peaks and a large broad diffuse peak. The XRD trace of the coating sprayed with cast-crushed and fused powder revealed that Co_2W_4C was formed along with WC,

W_2C and W. It was noted that the formation of Co_2W_4C phase was related to the disappearance of Co_3W_3C and Co_6W_6C phases. In their work, they stated that the decomposition of WC in the powder particles depended mainly on the initial phases in the starting powder, in particular containing complex carbides such as Co_3W_3C and W_2C.

Usmani et al. (1997) have examined the microstructure of an HVOF sprayed WC-17 wt% Co coating sprayed with powders with different median carbide size, i.e., fine (1.2 μm), medium (3.8 μm) and coarse (7.9 μm). The microstructure of the coatings showed a more rounded shape of carbide particles, compared with carbide particles in starting powder. The XRD spectra exhibited a higher percentage (68%) of W_2C phase in the coating containing fine carbide particles than those containing medium (48%) and coarse carbide particles (48%). It was further shown that mean carbide size in the coatings was significantly smaller than that of the starting powder, causing an increase in the mean free path of binder in the coating and a decrease of the average number of carbide grains per unit area.

2.4.4 Effect of Fuel Gas on Microstructures

Different fuel gases are applied to the HVOF spraying method. Each fuel gas generates different flame temperatures. It is reported that acetylene generates higher flame temperature (3087 °C) than other fuel gases such as propane, hydrogen and propylene (Tucker, 1994). Thus, coatings sprayed with different fuel gases result in different degrees of melting of the powder particles.

Verdon et al. (1998) have examined an agglomerated and densified WC-12 wt% Co powder and the coating sprayed from it. XRD analysis of the powder showed WC, Co and a small amount of Co_6W_6C phases. Two fuel gases (i.e. hydrogen and propane) were used. The XRD spectra of those coatings showed similar phases (i.e. WC, W_2C, W and two broad diffusion peaks). The difference between these coatings was examined quantitatively by Rietveld analysis and revealed that the amount of W_2C, W and the fraction of the amorphous or nanocrystalline binder phase were higher in the coating using hydrogen as the fuel gas. This is attributed to a higher flame temperature leading to a larger degree of decomposition. Furthermore, the coating sprayed using hydrogen showed a higher volume fraction of matrix phase (65 vol%) than the coating sprayed using propane (40 vol%) indicating WC particles had dissolved to a greater extent with hydrogen fuel

Nerz et al. (1991) have characterised a fused and crushed WC-12 wt% Co powder and coating. XRD showed that the powder consisted of WC, W_2C, W, Co_3W_3C and Co. The XRD spectrum of the coating sprayed with a Metco Diamond Jet using propylene as the fuel gas showed that the amount of W_2C and W were substantially increased while Co_3W_3C, Co_6W_6C or Co_2W_4C were not observed.

2.4.5 Effect of Spray Distance on Microstructures

As the powder particles are exposed in the hot gas jet. The Co-binder melts. A longer spray distance increases the degree of melting and exposure time to O_2 leading to higher degree of decomposition of powders during spraying resulting in complex microstructures. Guilemany et al. (1999) sprayed plasma densified WC-12 wt% Co

powder with the CDS 100 system with spraying distances of 200, 300 and 400 mm. The XRD results showed that the fraction of WC decreased and the fraction of W_2C and W increased with an increase in the spraying distance. This result from an increase in the residence time of powder in the hot gas and allowing further oxidation and decarburisation. The ratios of WC/W_2C phases in the coatings was less than in the powders due to decarburisation reactions (Guilemany and De Paco, 1996). The absence of the Co peak in the coating was also explained by appearance of an amorphous or nanocrystalline phase leading to distortion of the Co peak.

2.4.6 Effect of Gun Type on Microstructures

Each HVOF process utilises different gun designs, i.e. differences mixing of the fuel and oxygen and combustion burners, convergent-divergent nozzle sections and the position of powder entry. All of these play an important role on the residence time of the powder particles in the hot flame temperature and result in differences in the degree of melting of powder.

Jacobs et al. (1999) have stated that the gun type used for spraying affected the phase formation. All coatings sprayed with a sintered and crushed powder showed the highest ratio of W_2C/W when sprayed with the HV-2000, DJ-2600 and DJ-2700, compared to the coatings sprayed with an agglomerated powder. This was a result of a smaller carbide grain size of a sintered and crushed powder. Moreover, a coating sprayed with a sintered and crushed powder showed the highest ratio of W_2C/W when sprayed with the HV-2000 using propylene as fuel gas, indicating the highest level of

decarburisation. Coatings sprayed with the DJ-2600 using hydrogen as fuel gas showed lower levels of decarburisation.

Schwetzke and Kreye (1998) sprayed a range of WC-Co powders with the Jet-Kote, Top-Gun, DJ standard, DJ 2600, DJ 2700 and JP-5000 systems. EDS-SEM analysis of all coatings indicated that the amount of carbon loss in the coating resulting from oxidation reaction relied on the spray gun used and increased with higher flame temperatures.

2.5 Sintered WC-Co Materials

Sintered WC-Co is a highly wear resistant material and it is used in a variety of applications requiring wear resistance. It was developed in 1923 under the trade name "Widia" (Schwarzkopf et al., 1960). Sintered WC-Co cermets, typically containing hard WC grains in a ductile cobalt binder, in the range of 5 to 30 wt%, are well established as materials highly resistance to wear in a variety of situations (Exner and Gurland, 1970). Sintered WC-Co is produced by a powder metallurgical process consisting of three steps (Scussel, 1992) as follows:

1. Raw materials of WC and Co are mixed, and milled to reduce the particle size and provide a uniform mixture.

2. The mixture is pressed, at pressures of 50 - 150 MPa, into an ingot or a billet. The ingot or billet is preformed or machined to a near net shape. The mixture can be extruded to form a long component.

3. The consolidated powder is sintered in a furnace under vacuum, or in a hydrogen or inert atmosphere. It is preheated at 400 - 500 °C to eliminate wax and lubricant used in the milling step and in the pressing step, respectively. After that, the consolidated powder is heated up to 1300 - 1600 °C (above the eutectic temperature of the cobalt binder system) depending on the cobalt content, as shown in Table 2.4. The Co binder partially melts and generates a liquid phase sintering process leading to a fully dense microstructure.

The microstructure of the sintered WC-Co consists of WC grains with angular shapes and a Co metal binder. Its structure and the other parameters (such as binder and carbide alloy contents) influence the mechanical properties. Table 2.5 summarises the mechanical properties of sintered WC-Co depending on Co content and carbide grain size.

2.5.1 Effect of Co Content

Co content plays an important role on the density and hardness of the sintered WC-Co (Table 2.5). An increase in the Co content results in a decrease of the density and the hardness value. However, it is noted that sintering temperature and time are of influence on the density of the sintered WC-Co (Schwarzkopf et al., 1960). Microporosity has some effects on the hardness, whereas grain size, purity and composition of carbide phases, and degree of dispersion of carbide phases and the Co binder all strongly affect the hardness (Schwarzkopf et al., 1960).

2.5.2 Effect of WC Grain Size

WC grain size is one of the main factors which affects the hardness and toughness. An excellent combination of hardness and toughness is attained with an average WC grain size below 1 μm (Smithells, 1983). WC grain sizes ranging from 1 - 3.5 μm result in hardness values between 800 - 1850 HV (Table 2.5). A decrease in the WC grain size leads to an increase in the hardness. Therefore, some researchers have attempted to produce sintered WC-Co with very fine WC grains in nanoscale-sizes. It is reported that sintered WC-Co with WC grain sizes of less than 50 nm results in a hardness value more than 2200 HV (Seegopaul et al., 1997).

The hardness of sintered WC-Co is associated with the mean free path (λ). The mean free path is defined as an average distance between carbide grains. The mean free path decreases with decreasing WC grain size (Liu et al., 2000). This results in an increase of the hardness of sintered WC-Co (Jia et al. 1998).

2.6 Nanoscale WC-Co Materials

Nanoscale or nanocrystalline materials generally have structural dimensions in the range of 1 nm to 100 nm (Gell, 1994). Material scientists and engineers have attempted to develop nanoscale materials (i.e. ceramic, metallic and composite nanoscale materials) with enhanced physical and mechanical properties. Table 2.6 lists the effect on typical properties for nanostructured materials (Gell, 1994; Brook and Mackenzie, 1993).

2.6.1 Nanoscale WC-Co Sintered Material

Sintered WC-Co is normally produced from micrometre-sized powders of WC and Co, as mentioned in section 2.5. In order to enhance combinations of mechanical properties, in particular hardness and toughness, sintered WC-Co have been developed from submicrometre-sized powders with particle size of up to 0.6 μm, ultra-fine powders with a particle size of up to 0.3 μm and nanometre grain size powders (Berger et al., 1997). The major difference between nano-sized and micro-sized structures is the grain/grain boundary volume fraction. Nanoscale structures in sintered WC-Co can be produced by a spray conversion process (McCandlish et al., 1991), chemical synthesis (Zhu and Manthiram (1994) and mechanical milling (He et al., 2000).

A number of researchers have studied the microstructure, sintering behaviour and mechanical and physical properties of such materials. Berger et al. (1997) have reported that the hardness and fracture toughness of sintered WC-Co mainly depended on the initial powder grain size before sintering. The sample with nano-sized grains showed high hardness with low fracture toughness. In contrast, Jia and Fischer (1997 a) have studied the correlation of hardness and toughness of conventional and nanophase WC-Co composites. They have stated that hardness of both types of materials increased with decreasing binder mean free path. The rate of an increase of hardness with a decrease of binder mean free path has greater effects in the nanophase composite. In the conventional composite, the toughness decreased with increasing hardness. However, the toughness increased with increasing hardness in the nanophase composite.

2.6.2 Nanoscale WC-Co Coating

Nanocomposite thermally sprayed WC-Co coatings have been increasingly studied by many research groups. In particular, WC-12 wt% Co and WC-15 wt% Co powders produced by Nanodyne have been sprayed with the JP-5000, the Diamond Jet, the Jet-Kote and the High Energy Plasma guns. Dense coatings with hardness values about 1000 -1200 HV and good bonding between coating and substrate have been achieved (Kear and Skandan, 1997). Thermal spraying of nanocomposite powders results in a finely dispersed and homogeneous composite microstructure with less porosities leading to higher hardnesses and good corrosion resistance. However, nanocomposite coatings have a limitation for wear resistance resulting from coarsening and oxidation during spraying (Gärtner et al., 2000).

Nanoscale WC-Co powder is generally produced by either the spray conversion process or mechanical milling. Spray-conversion-processed powder (trade name Nanocarb) typically has a carbide grain size in the order of 100 - 600 nm (McCandlish et al., 1990) whereas ball-milled powder has an average carbide grain size of 3 - 9 nm (He et al., 2000). To be sprayable, nanoscale powder should have an average particle size in the range of 10 - 50 μm (Gärtner et al., 2000; He et al., 2000). If the average powder particle sizes are not suitable for spraying, powders are consolidated and agglomerated into larger size particles.

There are many researchers studying and characterising nanoscale WC-Co coatings and comparing them with conventional coatings. He et al. (2000) have characterised a coating when spraying a mechanically milled WC-12 wt% Co powder with HVOF (a

Metco Diamond Jet) using propylene as fuel gas. Milled powder, which had particle sizes less than 10 μm, was consolidated into a suitable spray powder. The XRD pattern of the milled powder showed the existence of WC, some W_2C and a small amount of Co. The milled powder had an irregular shape with a rough surface. TEM analysis proved that the Co binder phase was crystalline. The nanoscale coating was also observed by TEM. The average carbide particle size was 35 nm; the Co-binder was observed to be amorphous. In addition, it was found that the volume fraction of carbide particles in the nanoscale coating was less than that in the conventional WC-12 wt% Co coating. Due to high surface areas per unit volume of nanoscale powder, it produced more severe decarburisation/decomposition of carbide particles. This is agreement with the work of Stewart et al. (2000), who also proposed that the large surface areas of the carbides within the nanoscale powder favours dissolution and reaction during spraying.

Marple et al. (2001) have characterised and compared nanoscale WC-12 wt% Co powder sprayed with the HVOF DJ-2600 and the HVOF DJ-2700 using hydrogen and propylene as fuel gases, respectively. They have stated that the spraying conditions had an important role in determining the properties of the nanoscale coatings. The different fuel gases produced different particle temperatures and velocities and consequently, they affected the degree of carbide dissolution. In addition, Voyer and Marple (2000) have characterised nanoscale WC-Co powders with different Co contents, i.e. 8 wt% Co and 12 wt% Co. Both powders were sprayed with the DJ-2700 using propylene as the fuel gas and the JP-5000 using kerosene as the fuel. A comparison of the coatings sprayed with both guns showed that the coatings produced with the JP-5000 gun tended to have lower porosity than the coatings produced with

the DJ-2700 gun, as a result of the higher velocity of the combustion gases in the JP-5000. They argued that the degree of decomposition depended on the composition of the powder, type of spraying gun and spraying parameters.

In order to study the effect of powder manufacturing process, four nanoscale powders and one microscale powder were sprayed with the Metco DJ-2700 (Dent et al., 2001). They stated that powders produced by the spray conversion process with the same size distribution but with different Co contents and WC grain sizes did not show significantly different degrees of WC decomposition. However, one of the nanoscale powders was modified from a spray-conversion-processed nanoscale WC-8 wt% Co powder and showed greater degradation characteristics. They believed that the powder processing route for the nanoscale powder had the most significant effect on the phase formation within the coating.

Strutt (1998) have discussed the hardnesses of nanoscale WC-Co coatings. Initially, nanoscale coatings sprayed with the Metco Diamond Jet, with hardnesses in the range of 1050 - 1350 HV, were shown to have WC, W_2C and W phases present. Higher hardnesses were observed in the nanoscale coating sprayed with HVIF. A hardness of about 1600 HV was observed without any phase change in the coating. The highest hardness observed in the nanoscale coatings was achieved by spraying with a dc plasma arc system; in such coatings, containing WC, W_2C and W phases, the hardness was 1650 - 1900 HV. Therefore, he suggested that hardness was reduced not only by phase decomposition but also by microporosity in the coating.

Karthikeyan et al. (2001) have used the cold gas dynamic spray method (CGSM) or cold spraying with spraying nanoscale WC-Co powder. This method provides no particle melting due to low temperatures (not exceeding 600 °C) and high particle velocities in the range of 600 - 1000 m s^{-1}. The cold-sprayed nanoscale WC-12 wt% Co coating showed a very low porosity, good adhesion between the coating and substrate and no significant differences in carbide grain size before and after spraying. The XRD spectrum of this coating revealed no appearance of degradation phases, except WC and Co peaks.

Kear et al. (2000) have investigated nanoscale WC-12 wt% Co powder sprayed to form coatings by HVOF and plasma spraying methods. The nanoscale powder was produced by a spray conversion process. Following HVOF spraying, it was found that the coating contained a nonuniform structure and a significant amount of microporosities leading to a hardness reduction. The XRD pattern of the nanoscale coating showed significant peaks associated with W_2C and W, as compared with the conventional WC-12 wt% Co sprayed with HVOF. This resulted from the high surface areas per unit volume of nanoscale powder. Following plasma spraying, the XRD spectrum of a nanoscale coating, sprayed with N_2/H_2 system, showed a higher degree of decarburisation than the coating sprayed with a Ar/He system. It was also found that a considerable amount of Co and C were lost in plasma spraying with N_2/H_2 system. The investigators proposed a similar decarburisation reaction to that proposed by Guilemany and De Paco (1991 a), Verdon et al., (1998) and Stewart et al. (2000). They have also reported that the higher temperatures in plasma spraying evaporated Co from the particle surface.

Other workers have examined the role of particle size on the formation of coatings. Nanoscale WC-18 wt% Co powder, which had carbide grain sizes in the order of 200 - 500 nm, was separated into 3 sizes, i.e., small, medium and large sizes with an average diameter of 20 μm, 32 μm and 38 μm, respectively. The powder was sprayed with a Metco Diamond Jet HVOF gun using hydrogen and propylene as fuel gases. He et al. (2002) have stated that the flame temperature depends mainly on fuel chemistry and fuel/oxygen ratio, which controlled the degree of melting of the powder particle. Also, fuel chemistry and powder particle size have a significant influence on particle temperature. The WC-Co powder particles sprayed using the lowest temperatures resulted in the highest roughness of the external surface of the coating. As the spraying temperature increased, the roughness of the external surface reduced. At the same spraying temperature, the powder particles with the small sizes gave a smoother external surface of the coating, resulting from a larger proportion of Co-binder melting during spraying. Microstructural observations of the coating sprayed using low particle temperatures showed rounded splats and high levels of porosity in the coating due to reduced melting of binder phase during spraying. At higher particle temperatures reduced porosity is observed in the coating but leads to more WC decomposition.

2.7 Wear

A general definition of wear is gradual damage when two surfaces in contact move relative to each other. Damage may occur to one or both surfaces. Although the amount of material removed is relatively small, the failure of large and complex machines may result.

2.7.1 Types of Wear

Owing to the complexity of wear mechanisms, types of wear may be classified. However, wear can occur by two or more mechanisms operating together. Sometimes it can be misleading to identify the type of wear because there may be interactions between the wear modes. Wear has been broadly classified according to the operating mechanisms. The most commonly observed types of wear, namely, sliding and adhesive wear, and abrasive wear, are described below.

2.7.1.1 Sliding and Adhesive Wear

Sliding wear is generally defined as the wear resulting from two solid surfaces in contact sliding over each other. One or both of the surfaces will suffer wear. During sliding (with high enough pressure), asperities on one or both of the surfaces suffer local plastic deformation and adhesion. Fracture occurs at the weakest point and fragments may break off from one surface to adhere to the other. Then, these fragments may either detach from that surface to adhere to the original surface or form loose wear debris. An illustration of the processes occurring in adhesive wear is shown in Fig. 2.6. Therefore, adhesive wear is included as part of the sliding wear process because it can play an important role (Hutchings, 1992).

2.7.1.2 Abrasive Wear

In abrasive wear, sometimes called abrasion, hard particles or hard protuberances on a counterface, which slide across a smooth surface, penetrate the surface and displace

material. This results in a rough surface with grooves. The damage is described as scratching, scoring or gouging, depending on the severity of the damage (Eyre, 1978). Abrasive wear may occur by plastic flow or brittle fracture. Abrasive wear can be further subdivided into two-body abrasive wear (Fig. 2.7a) and three-body abrasive wear (Fig. 2.7b).

Two-body abrasive wear results from hard protuberances on the counterface sliding on the surface, whereas, hard particles which are trapped between two sliding surfaces and are free to rotate and abrade one or both surfaces induce three-body abrasion.

2.7.2 Theory of Sliding Wear

2.7.2.1 Asperity

An asperity is defined as a protuberance at the scale of topographical irregularities of a solid surface. When two plane and parallel surfaces are brought together, a large number of asperities on two surfaces come into contact and support the applied load.

2.7.2.2 Wear Theory

The wear of a metal is a complex phenomenon. A simple mechanism of sliding wear has been proposed by Archard (Archard, 1953; Hutchings, 1992). The assumptions of this theory are that:

1. the true area of contact where the asperities from two surfaces touch will be equal to the sum of each asperity contact area,
2. this area is proportional to the normal load,
3. local plastic deformation of asperities, for a metal at least, will take place under most conditions.

The Archard wear equation is given by

$$Q = \frac{KW}{H}$$

where : Q = overall wear rate (volume per unit sliding distance)

K = constant value called dimensionless wear coefficient

W = normal load

H = hardness or yield strength of the softer-surface

Suh (1973) has, however, pointed out that the theory was weak in that

1. the physics and physical metallurgy of the metal were disregarded,
2. many of the assumptions for the mathematical derivation are unreasonable and arbitrary,
3. in case of different sliding conditions, the equation cannot be used to support the results obtained for wear of metals.

Suh (1973), therefore, proposed a new theory for wear of metals, called the delamination theory of wear. The theory was based on the behaviour of dislocations at

the surface, sub-surface crack and void formation, and subsequent joining of cracks by shear deformation of the surface. However, this theory cannot resolve many questions concerning the formation and joining of voids and the relation of the surface traction to the shear deformation of the surface layer.

2.7.3 Types of Sliding Wear Test

In general, wear tests are performed either to study the mechanism by which wear occurs or to imitate a service application to obtain useful data on wear rate and friction coefficient. There are many different basic geometries of test machines for sliding wear. Fig 2.8 shows the geometries for sliding wear tests which can be classified into symmetrical and asymmetrical arrangements (Hutchings, 1992; Rigney, 1981). In symmetrical arrangements (a, b and g in Fig. 2.8), the wear rate of the same materials of two bodies should be equal. In asymmetrical sliding wear geometries (c, d, e, and f in Fig. 2.8) even bodies of the same material will have different rates of wear.

Sliding wear test rigs usually comprise pin-on-disc (c), pin-on-flat (f), pin-on-rim (d) and block-on-ring (e) geometries where a pin or block presses against a disc, flat surface or on the rim. In general, the pin or block is the specimen material of interest, whereas, the disc, flat or ring are referred to as the counterface.

The sliding wear test rigs shown in Fig. 2.8 have a simple specimen-shape. The counterfaces, disc or ring, are in the range of several tens of millimetres in diameter. In addition, pins and blocks are generally smaller than 25 millimetres in size

(Hutchings, 1992). The advantages of these rigs are to cover wide load ranges from fractions of a Newton to several kiloNewtons and to cover wide speed ranges from fractions of a millimetre per second to several metres per second. Wear is usually measured by weighing the specimen at intervals during testing or continuously recording its displacement and friction force with an electrical or mechanical transducer. The coefficient of friction data (μ) can be recorded continually during the wear test and allows variations in sliding behaviour to be monitored (Hutchings, 1992).

2.7.4 Factors Influencing Sliding Wear

The selection of a suitable sliding wear test for laboratory use must consider the orientation aspect (Gee, 1993). For instance, in pin-on-rim geometry, the pin presses against the disc. The orientation of the pin with respect to the rim may effect debris entrapment which then influences the wear and friction. There are many factors which may contribute to sliding wear behaviour. As shown in Fig. 2.9, wear behaviour depends on three main factors, namely, a nature of counterface, specimen and sliding condition. Counterfaces and specimens depend on the material composition and microstructure. Also, surface finish is important. Wear behaviour depends on contact pressure and test environment, resulting in a wide range of wear rates and mechanisms in all types of materials. Wear also depends on sliding distance, contact area, test duration and sliding velocity; the latter influences the rate of frictional energy generation and thus the temperature at the interface. In addition, the test temperature affects the mechanical properties of materials and can cause thermally activated chemical processes.

2.7.5 Sliding Wear of Ductile and Brittle Materials

2.7.5.1 Sliding Wear of Ductile Materials

In the sliding wear of metals (for example, wear of a leaded α/β brass), wear can be divided into 2 regimes (Hutchings, 1992), as shown in Fig. 2.10. At a low load, the regime of wear is generally called mild wear. The sizes of the wear debris in this regime are about 0.01 μm to 1 μm in particle size. The majority of wear debris formed in the mild wear regime is oxide and the worn surface is relatively smooth. The regime of wear at high loads is called severe wear. Wear debris formed in severe wear is in the form of large particles (20 - 200 μm) of metallic debris and the worn surface is relatively rough.

Lim et al. (1987) have divided wear of steel into seven mechanisms of material removal. A wear-mode map is shown in Fig. 2.11. It shows that the wear mechanism depends on pressure and velocity. The two main mechanisms of wear, as mentioned above, are mild and severe wear. Transitions between mild wear and severe wear are indicated by the dotted regions.

Another model of ductile wear is proposed by Kayaba and Kato (1979). Wear relates to an adhesive transfer consisting of two modes, namely, transfer of a slip-tongue by shear rupture and transfer of wedge by shear rupture, as shown in Fig. 2.12. A metal-to-metal junction is formed in static contact when load is applied (Fig. 2.12a). As a friction force is applied, the junction grows plastically (Fig. 2.12b). Area ABC is the plastic zone with slip line AC. Slip is formed at slip line 'AC' and slip tongue is

produced at ABCC' (Fig. 2.12c). As a result of the shearing force, the second plastic zone AC'CE is formed leading to a second slip tongue (Fig. 2.12d). The shear crack occurs and propagates through the slip tongue (Fig. 2.12e). This generates the removal of a transferred fragment. This model predicts plate-like debris.

Sasada et al. (1979) have proposed another model for the formation of debris fragments, as shown in Fig. 2.13. Fig. 2.13a shows an asperity in metal-to-metal contact. When a shearing force is supplied, a small fragment of each rubbing surface will be sheared off and adhered to the opposite surface to form a new asperity (Figs. 2.13b-c). The small fragment is called the transfer element. In further sliding, the new asperity may generate a new junction (Fig. 2.14d). A small fragment is transferred from upper surface to lower surface and vice versa, and as a result, it grows by degrees during repeat sliding (Figs. 2.13e-f). The transferred element is formed by the accumulation of two asperities and is removed from the surface to form a wear particle which has a roughly equiaxed shape. During further sliding, the transferred particle between the two surfaces is compressed by a normal load (Fig. 2.13g). Due to compression and shear forces, the debris particle will be flattened and elongated in the direction of sliding (Fig. 2.13h-i). Therefore, this model predicts composite plate-like debris.

2.7.5.2 Sliding Wear of Brittle Materials

Ceramics are generally more brittle than metals and have limited capability for plastic deformation at room temperature. Therefore, brittle fracture plays an important role in the wear of ceramics. Environmental or chemical effects can influence wear

mechanism. Wang and Hsu (1996) have reviewed the literature concerning wear mechanisms of ceramics. They have stated that the main mechanism of wear was fracture. Some researchers have reported that plastic deformation is found in brittle materials at high temperature. In addition, fatigue induced wear, chemical reaction induced wear and adhesive wear can be observed in brittle materials.

The wear of ceramics is classified into mild wear and severe wear, as for metals (Hutchings, 1992). Mild wear results in smooth surfaces, low wear rates and a steady frictional force. Wear is associated with plastic deformation or tribochemical reactions. On the other hand, severe wear produces rougher surfaces, high wear rates and a fluctuating frictional force. Wear is basically associated with brittle fracture. Many authors have attempted to understand the wear mechanisms in different operating conditions and the occurrence of wear transitions.

Wang and Hsu (1996) have proposed a wear mechanism for ceramics. They have observed wear mechanisms in sintered α-alumina, hot-pressed silicon nitride and hot-pressed silicon carbide following sliding wear tests (four-ball wear tester). It was found that when the asperities of both surfaces contact under very low loads, only elastic deformation occurs. At higher contact stress, asperities plastically deform with dislocation movement and twin formation. The dislocations and twins generate sub-micro cracking. The sub-micro cracks intersect with each other, with grain boundaries or with free surfaces, producing small particles which are removed as wear debris. When higher stress is applied, microcracks, which are the main mechanism of material removal, are formed.

2.7.6 Previous Studies on Sliding Wear Behaviour and Microstructures of Sintered WC-Co Materials

Sintered WC-Co cermets are used in various applications because of high wear resistance. As mentioned before in section 2.5, Table 2.5 shows the properties of sintered WC-Co cermets relating to Co content and carbide grain size.

Lassen-Basse (1985) has characterised the wear behaviour of sintered WC-Co with 8 wt% Co and 15 wt% Co slid against hardened steel balls. The average carbide grain size of WC-8 wt% Co and WC-15 wt% Co was 1.6 and 1.5 μm, respectively. The wear surface of the sintered WC-8 wt% Co showed cracks in the wear track, a large number of fragmented carbide particles, the removal of whole carbide particles and an accumulation of binder material at the rim of the wear track. For the sintered WC-15wt% Co, fragmented carbide particles and the removal of carbide grains were also observed in the wear track. In addition, smearing of Co over the surface was observed. It was concluded that the binder material was extruded from binder regions below the surface. Fig. 2.14 shows a schematic of binder extrusion. Two WC grains with binder regions perpendicular to the stress axis are strained permanently by axial compression; the binder is then constrained to flow only in one direction, i.e. out of the surface. This resulted in Co smearing. Moreover, micro-fractures on the WC grains were found, and as a result, WC grains were broken into small fragments and then gradually removed.

Jia and Fischer (1996) have observed sintered WC-20 wt% Co with an average carbide grain size of 2.5 μm following a scratch test using a Vickers diamond

indenter. It was clearly seen that WC grains and the binder were extruded from the wear track. Cracks and slip steps caused by plastic deformation were also observed either on the displaced carbide grains or carbide grains in the wear track. When the load was increased, more cracks on the carbide grains were observed, leading to severe fracture; more extruded material was also visible. In the case of repeated scratching, it was found that more material was extruded from the wear track and then removed as wear debris. The carbide grains in the wear track showed severe fracture. This generated fragmented carbide particles which were removed from the wear track. In addition, the investigators have reported the wear behaviour of sintered WC-6 wt% Co with an average carbide grain size of 0.8 μm. It was seen that carbide grains and the binder were extruded from the wear track. Fragmented carbide grains and plastic deformation were also found. Compared with sintered WC-10 wt% Co, less material was extruded and a smaller fraction of carbide grains were fragmented. In repeated scratching, a small amount of material was removed. The investigators also performed scratching tests on sintered WC-13 wt% Co with an average grain size of 0.07 μm. Little damage occurred, with a smaller wear track and small amount of extruded material, even following repeated scratching. At low loads it showed no microcracking. However, cracks perpendicular to the sliding direction were found at the high loads.

Further work by Jia and Fischer (1997 b), reported the unlubricated sliding wear behaviour of pins of sintered WC-Co against silicon nitride (Si_3N_4) discs. They stated that the sliding wear resistance of conventional sintered WC-Co relied on the Co content, the grain size and the hardness of the material. Smaller carbide grain sizes resulted in an increase in hardness; however, the sliding wear resistance also

decreased. Citing Masuda et al. (1996), they argued that larger WC grain sizes resulted in higher sliding wear resistance. When the WC grains wore, they could not be firmly held by the matrix leading to their removal. However, they did observe an increase in wear resistance when the carbides became nanosized. They concluded that the increase in the sliding wear resistance of nanoscale sintered carbide resulted from their increased hardness.

Sheikh-Ahmad and Bailey (1999) have characterised sintered carbide tools (WC-Co) with different grain sizes and Co contents. It was stated that the wear resistance of sintered carbide tools relied on the bulk hardness of tool material. In contrast to the work of Jia and Fischer (1997 b), they showed that a smaller grain size and lower Co content gave an increase in hardness resulting in a decrease in tool wear. The investigators agreed with Jia and Fischer (1996) about the wear mechanism of WC-Co composite. They have stated that the wear of WC-Co composite resulted from the removal of Co binder by plastic deformation, microabrasion and probably oxidation. After this, carbide grains were fractured by transgranular cracks and the fragmented particles removed from the surface.

The wear mechanism is also strongly dependent on the counterface material. Golden and Rowe (1957) have investigated the sliding mechanism of a sintered WC-6 wt% Co on copper and steel. It was found that transferred carbide was firmly embedded in the copper and steel plates. Also, they have suggested that the sliding wear of different materials can generate consequent abrasive wear. Also, Bhaget et al. (1996) have examined cemented WC-Co blocks following sliding against circular steel rings. The wear track showed fragmented WC particles dragged across the steel transferred

layer leading to an appearance of grooving. A small amount of steel debris was transferred and adhered to the cemented WC-Co. Also, cracks were found on the transferred layer leading to its removal. Therefore, it could be stated that the main wear mechanism of sintered carbide block-on-steel ring was adhesive and delamination wear.

2.7.7 Previous Studies on Sliding Wear Behaviour and Microstructures of WC-Co Coatings

The microstructure of a WC-Co thermally sprayed coating is built up from individual splats which are relatively less well bonded when compared to a sintered WC-Co composite. The fact is that a WC-Co coating generally consists of WC, W_2C and W particles embedded in Co-based binder matrix (which may have significantly reduced ductility) with some porosity, as mentioned before in section 2.4.1. Therefore, WC-Co coatings will have a more complicated wear behaviour. These characteristics have limited the use of coatings to low-stress applications (Ahmed and Hadfield, 1997).

In this section, the wear behaviour of WC-Co coatings, sprayed with different methods, are discussed. Wear failure of WC-Co coatings in sliding mode are investigated generally using ball-on-disc, ball-on-flat, pin-on-disc and block-on-ring apparatuses. A few papers examine rolling contact fatigue (RCF) behaviour or use specially designed apparatus to simulate working situations.

Wear behaviour of HVAF (high velocity air fuel) sprayed WC-12 wt% Co coating and HVAF and HVOF WC-10 wt% Co-4 wt% Cr coatings were evaluated using a

ball-on-flat geometry (a corundum ball) under velocity of 0.46 m s^{-1}, a load of 49 N and 20,000 revolutions. Jacobs et al. (1998) have stated that the presence of W_2C reduced the coating performance. Therefore, the absence of W_2C in the HVAF coating promoted the best wear resistance. Also, the microstructure contained a good distribution of hard WC particles in the binder matrix assisting wear resistance. Wear failure of HVAF sprayed WC-12 wt% Co coatings exhibited a smooth surface with material extrusion at the edges of the wear track. Also, material smearing and carbide pullout was observed. The investigators have stated that the predominant mechanism was adhesive wear leading to particle pullout. The softness of the binder matrix prevented three-body abrasive wear.

Qiau et al. (2000) have studied the correlation between microstructure and wear behaviour. They provided evidence that decarburisation produced a brittle phase, and as a result, the hardness of the coating increased. Si_3N_4 balls were slid against WC-Co coatings under a sliding speed of 30 mm s^{-1}, a load of 9.8 N and sliding distance of 10,000 - 12,000 m. The investigations showed that the wear resistance of the coatings was restricted by their hardness, namely, the highest wear resistance achieved results from an increase of hardness. The coatings with severe decarburisation or high porosity had low wear resistance. Worn surfaces of the coatings showed smooth surface areas and cracks causing the removal of material.

Due to the negative effect of porosity on wear resistance, hot isostatic pressing (HIP) was used to improve the microstructure of HVOF sprayed WC-12 wt% Co coating (Stoica and Ahmed, 2002). Sliding wear tests (ball-on-plate) were conducted using steel and silicon nitride (Si_3N_4) ceramic balls under a load of 6 kg and sliding speed

0.012 m s^{-1}. The HIPing process produced densification leading to harder and tougher coatings and thus, greater wear resistance. The investigators claimed that wear of the coating with low porosity proceeded by the extrusion of the binder matrix followed by three-body abrasion.

Voyer and Marple (1999) have characterised the wear behaviour of WC-10 wt% Ni and WC-12 wt% Co coatings sprayed with HVOF and high pressure plasma (HPPS) spraying methods. All coatings were slid against stationary carbon discs under a load of 66.7 N, a rotational speed of 1500 rpm, pressure of 250 kPa and duration 24 h. Microstructural observations showed that the porosity level in HPPS coatings (> 5%) was higher than in HVOF coatings (< 1%). However, the wear tests revealed that the HVOF coatings had a higher mass loss than the HPPS coatings. In general, the presence of porosity at surfaces generates increasing contact stresses and an increase of wear of coatings. In contrast, in this work, pores in the HPPS coating acted as reservoirs to trap both hard debris from the coatings and soft debris from the carbon discs. Soft debris (graphite) acted as a lubricant and reduced wear.

Some reviews have reported a comparison of the wear behaviour of WC-Co coatings sprayed with both the HVOF process and high energy plasma (HEP) spraying processes. Wear behaviour was examined on a pin-on-disc sliding wear apparatus using a ruby-sapphire ball with a sliding velocity 3 m s^{-1} and loads of 4.45 N and 44.5 N. Slavin and Nerz (1990) have reported that no significant differences were observed in the microstructure of HVOF coatings and HEP coatings. Therefore, both coatings showed similar excellent wear resistance at the test conditions. Worn surface observations revealed local material spalling and glazed regions in the wear track.

Also, microcracks propagating through the matrix and along the interface of the matrix and carbide particles were found. It was clearly seen that the Co binder matrix was deformed during sliding.

In similar work by Akasawa and Ai (1998), a plate-on-ring apparatus was used to examine the wear behaviour of WC-17 wt% Co coatings sprayed by plasma (F4-MB) and HVOF (JP-5000) systems. It was found that the HVOF coating showed no appearance of porosity, whilst plasma sprayed coatings revealed some porosity. Both coatings had lower wear resistance compared to sintered WC-Co material. They also showed that the wear rate increases with increasing sliding speed.

Sundararajan et al. (1998) have investigated wear behaviour of WC-12 wt% Co coatings deposited by plasma spraying and the D-gun processes. A pin-on-disc sliding wear test was carried out using self-mated coatings (both the pin and the disc being made from the same material). The microstructure of the D-gun coating was denser and contained a finer carbide distribution than the plasma sprayed coating. It was reported that the plasma sprayed coating had a higher wear rate than the D-gun coating.

Nicoletto et al. (1993) have studied wear behaviour of an HVOF-sprayed (a Metco Diamond Jet) WC-12 wt% Co coating. The coating was worn in a pin-on-disc tester using steel pins. The worn surface of the coating showed evidence of plastic deformation. It was also argued that the wear mechanism was mild abrasive wear resulting from compacted debris of iron oxide.

WC-17 wt% Co powder with different sizes of carbide particles was deposited by HVOF spraying. Usmani et al. (1997) investigated their wear behaviour with a ball-on-flat geometry. The wear tests using Al_2O_3 balls were performed under test loads of 10 N and 50 N, sliding speed of 0.015 m s^{-1} and sliding distance of 27 m. In general, the worn surfaces of the coatings showed that cracks propagated through the Co binder, indicating its loss of ductility, or around the carbide particles. Also, fragmented carbide particles and splat delamination were observed. Cracks originated at pores or at the interface of carbide and binder and propagated perpendicular to the sliding direction. As the test load increased, the length and intensity of cracking increased. Further observations in the coatings with fine carbide grain size showed that material loss occurred by delamination of entire splats and that most cracks propagated through the binder and around the fine carbide particles. The coatings with a medium carbide grain size exhibited splat delamination, especially in the areas of fine carbide concentration. For the coating with the coarse carbide grain size, it was seen that cracks propagated through the carbide particles.

WC-12 wt% Co powders produced via a number of routes, namely, fused and crushed (WC1), sintered and crushed (WC2) and agglomerated and sintered (WC3) were deposited by plasma spraying using N_2/H_2 system. Pin-on-disc sliding wear tests were carried out using high speed tool steel as a pin under a load of 6.4 kg and a rotation speed of 300 rpm (Ahn and Lee, 1998). Coating 'WC2' presented the best wear resistance followed by the coatings 'WC3' and 'WC1'. This is because 'WC2' had the highest hardness and lowest porosity of the three coatings. They concluded that the main wear mechanisms of WC-Co coatings were adhesion, transfer material formation, fatigue cracking, splat fracture and delamination of coating layers.

WC-15%Co coatings deposited with a high velocity plasma spraying were examined in a rolling contact fatigue (RCF) test using a modified four ball machine (Ahmed and Hadfield, 1999). It was found there were two modes of failure, i.e., surface wear and coating delamination. Surface wear was initiated by micro-fracture or plastic deformation of asperities. Asperity contact in the presence of the slip within the contact area, caused micro-pitting of the surface. Furthermore, an additional mechanism of three-body abrasion operated in the latter stages of RCF in the presence of wear debris. Coating delamination was related to the initiation/propagation of subsurface cracks. These cracks initiated from various defects within the coating structure and/or at the coating-substrate interface. These cracks propagated at the depths of maximum shear stress under the surface of the wear track.

Su and Lin (1993) studied the wear behaviour of WC-12 wt% Co coatings sprayed with continuous detonation gun (CDS). A sliding-screw system was used to perform a wear test of coatings sliding against heat-treated steel balls. The investigators proposed a wear model of the WC-Co coatings as follows: 1) transferred layer formation, 2) the removal of transferred layer by spalling, 3) shallow pit formation, 4) linkage of shallow pits, 5) new transferred layer formation in combined-pit, 6) crack propagation in the transferred layer due to fatigue wear and 7) the removal of fragmented transferred layer.

A comparison of the wear behaviour of WC-12 wt% Co coatings and WC-17 wt% Co coatings which were sprayed with HVOF (CDS-100) spraying was reported by Guilemany and De Paco (1998). A ball-on-disc test was employed using sintered WC-6 wt% Co balls and a sliding speed of 0.11 m s^{-1}, sliding distance of 1000 m and

a load of 15 N. A high friction coefficient observed for the WC-17 wt% Co coatings was associated with severe damage. Wear behaviour of the WC-12 wt% Co coating showed material loss by spalling resulting from repeated sliding, pores and cracks. A small amount of debris containing W, Co and O was also found. Moreover, pores and cracks were filled with debris. The WC-17 wt% Co coatings exhibited more material loss and carbide particle pullout. The WC-12 wt% Co and WC-17 %Co coatings showed the same wear mechanism, i.e., Co binder was removed and carbide particles were removed by pullout. This resulted in the formation of cracks and pores. Also, fragmented particles and other debris filled in the pores. However, Marple et al. (1997) have stated that many factors, i.e., metallic binder content and type, size and morphology of WC grains also affected the sliding wear behaviour of WC-Co coatings.

A self-mated plasma-sprayed WC-12%Co coating was worn under dry oscillating sliding conditions (Jin and Yang,. 1996). Two wear mechanisms were observed, i.e., plastic smearing and adhesive tearing. Plastic smearing resulted in a lower friction coefficient and a lower wear rate. Adhesive tearing corresponded to higher friction regimes. Plastic smearing was the dominant mechanism.

A WC-14 wt% Co-3 wt% C coating sprayed by D-gun was worn against a tool steel in a block-on-ring sliding wear apparatus under a velocity of 4 m s^{-1} and a load of 4.9 N. Delamination, cracks and plastic deformation of a transferred layer were seen in the wear track. The transferred layer contained Fe and some traces of W and Co. The tool steel ring showed no transferred layer from the coating to the tool steel. However, iron oxide was found in the worn surface of tool steel.

The findings about nanoscale WC-Co coatings have been mentioned in the previous section 2.6.2. Qiao et al. (2001) showed that nanoscale WC-Co coatings exhibited more decomposition during spraying than conventional WC-Co coatings which resulted in severe wear in nanoscale WC-Co coatings. Nanoscale WC-12 wt% Co powders were sprayed with different fuel gases, namely, propylene and hydrogen (Marple et al., 2001). The abrasive wear rate of the coatings produced using hydrogen were significantly lower than those produced using propylene. The coatings sprayed using hydrogen showed higher hardness and a lower degree of reaction. A nanoscale WC-23 wt% Co coating deposited by low pressure plasma spraying was examined in a sliding wear test using a sapphire ball. McCandlish et al. (1990) have reported that the friction coefficient of the nanoscale coating for loads up to 1 kg was half that of the conventional coatings.

Liu et al. (2002) have investigated the nanoscale WC-18 wt% Co sprayed with HVOF using hydrogen and propylene as fuel gases. The coatings were examined in a ball-on-disc sliding wear test. Higher sliding wear resistance was achieved as the hardness of the coatings increased. In general, the worn surface exhibited pits and cracks parallel to the surface. The investigators stated that the fracture predominantly occurred at the splat boundaries. Large cracks in the worn surface were not generated by the sliding wear but they existed in the as-received coatings. Cracks caused the removal of the large splats after long sliding distances leading to a decrease in wear resistance. Therefore, the investigators have proposed the form of wear to be fatigue dominated.

In summary, wear behaviour of WC-Co coating depends mainly on its microstructure, which differs significantly from sintered WC-Co. The best wear resistance for WC-Co

coatings may be obtained from less WC decomposition, an absence of W_2C, a good distribution of WC particles in the Co-binder, low porosity and/or high hardness. Wear behaviour of WC-Co coatings generally occurs by Co-binder extrusion, carbide cracking, carbide pullout and material removal.

Table 2.1 Comparison of characteristics of thermal spray processes.

Deposition technique	Heat Source	Feed material	Propellant	Typical Temparature (°C)	Typical powder velocity (m s^{-1})	Average spray rate (kg h^{-1})
Powder flame spraying	Oxy-acetylene Oxy-hydrogen	Powder	Air	~3000	24 - 40	2 - 6
Wire flame spraying	Oxy-acetylene Oxy-hydrogen	Wire	Air	~3000	240	2 - 30
Ceramic rod spraying	NI	Rod	Air	~3000	240	0.45 - 0.9
Electric arc spraying	Arc between consumable electrodes	Wire	Air	~6000	100 - 240	12
Detonation flame spraying	Oxygen-acetylene-nitrogen gas detonation	Powder	Detonation waves	~4500	800	0.5
Air plasma spraying	Plasma arc	Powder	Inert gas	~12000	200 - 400	3 - 9
Low pressure plasma spraying	Plasma arc	Powder	Inert gas	~12000	400 - 600	3 - 9
Direct current plasma arc (40 kW unit)	NI	Powder	NI	~12000	490	3 - 9
High velocity oxy-fuel spraying	Oxyfuel combustion	Powder	Exhaust jet	~3000	400 - 600	2 - 4

Adapted from Clare and Crawmer (1982) and Sturgeon (1993)
Note: NI = Not identified

Table 2.2 Comparison of quality of WC-Co coating sprayed with different thermal spray processes (Sturgeon, 1992).

Deposition technique	Heat source	Propellant	Typical gas temperature (°C)	Typical particle velocity (m s^{-1})	Average spray rate (kg h^{-1})	Coating porosity (% by volume)	Relative bond strength
Flame spraying	Oxyacetylene / oxyhydrogen	Air	3000	30 - 120	2 - 6	10 - 20	Fair
Plasma spraying	Plasma arc	Inert gas	16000	120 - 600	4 - 9	2 - 5	Very good to excellent
Low pressure plasma spraying	Plasma arc	Inert gas	16000	Up to 900	NI	< 5	Excellent
Detonation gun spraying	Oxygen/acetylene/ nitrogen gas detonation	Detonation shock waves	4500	800	0.5	0.1 - 1	Excellent
High velocity oxyfuel	Fuel gases	Combustion jet	3000	300 - 600	2 - 4	0.1 - 2	Excellent

Note: NI = Not identified

Table 2.3 Examples of WC-Co powder produced by different manufacturing processes.

Investigator	Composition	Trade name	Manufacturing process	Morphology	Cross section morphology	Initial phase	Nominal particle size (μm)	Average carbide size (μm)
De Villiers Lovelock, Kinds and Young (1998)	WC-12 wt% Co	Diamalloy 2003	C - C	Blocky, angular	Dense	WC, W_2C, Co_3W_3C	5 - 30	1 - 5
		WC-432	C - C	Blocky, angular	Dense	WC, W_2C, Co_3W_3C, $Co_3W_9C_4$	16 - 45	2 - 12
		AI 1101	C - C	Blocky, angular	Dense	WC, Co_3W_3C	16 - 45	2 - 12
		Diamalloy 2004	S - C	Blocky	NI	WC, Co	16 - 38	NM
		WC-489-1	S - C	Blocky and plated-like particle	Fairly dense	WC, Co	16 - 45	0 - 4
		AI 1172	S - C	Blocky and plated-like particle	Dense	WC, Co	16 - 45	1 - 6
		1342V	S - C	Blocky and plated-like particle	Dense	WC, Co	16 - 45	NM
		WC-114	S - C	Blocky and plated-like particle	Dense	WC, Co	11 - 45	0 - 4
		72F NS	S - C	Blocky	Fairly dense	WC, Co	11 - 45	0 - 4
		Amperit 516.3	S - C	Blocky	Dense	WC, Co_3W_3C	11 - 45	0 - 8
		AMDRY 1927	A - D	NI	NI	NI	~ 16 - 45	NM
		WC-616	A - D	Spherical	Porous	WC, Co	22 - 45	0 - 5
		1341P	A - D	Spherical	Porous	WC, W_2C, CoC_x	16 - 53	0 - 6
		Amperit 518.074	A - D	Spherical	Porous	WC, Co	16 - 53	0 - 6
		JK 7112 (JK 112)	A - D	Spherical	Fairly dense	WC, W_2C, CoC_x	16 - 45	0 - 5
Li et al. (1996)	WC-12 wt% Co	Not identified	S - C	Blocky	Dense	WC, Co_3W_3C	10 - 44	NM
	WC-12 wt% Co	Not identified	S - C	Blocky	Dense	WC, Co	15 - 45	NM
	WC-17 wt% Co	Not identified	A - S	Nearly spherical	Porous	WC, Co	5 - 44	NM
	WC-18 wt% Co	Not identified	Clad	Blocky, angular	Dense	WC, Co, α-Co	5 - 44	NM
	WC-12 wt% Co	Not identified	C - C - F	Spherical	Dense	WC, W_2C, Co_3W_3C, Co_6W_6C	45 - 75	NM

Note: 1. C - C = Cast and crushed; S - C = Sintered and crushed; A- D = Agglomerated and densified; C - C - F = Cast, crushed and fused; S = Sintered; F = Fused;
2. NI = Not identified; NM = Not measured

Table 2.3 (cont.)

Investigator	Composition	Trade name	Manufacturing process	Morphology	Cross section morphology	Initial phase	Nominal particle size (μm)	Average carbide size (μm)
Schwetzke and Kreye, (1999)	WC-17 wt% Co	Not identified	A - S	Nearly spherical	Porous	WC, Co	10 - 45	2 - 8
	WC-12 wt% Co	Not identified	A - S	Nearly spherical	Porous	WC, Co	10 - 45	2 - 8
	WC-12 wt% Co	Not identified	S	Blocky, angular	Fairly dense	WC, Co	5.6 - 45	2 - 8
	WC-12 wt% Co	Not identified	F	Blocky, angular	Fairly dense	WC, W_2C, Co_3W_3C	10 - 45	2 - 8
Jarosinski et al., (1993)	WC-12 wt% Co	Not identified	S - C	Blocky	NI	NI	NM	5 - 7
	WC-17 wt% Co	Not identified	S - C	Blocky	NI	NI	NM	5 - 7
	WC-17 wt% Co	Not identified	A	Nearly spherical	NI	NI	NM	3 - 5
	WC-17 wt% Co	Not identified	A	Nearly spherical	NI	NI	NM	3 - 5
	WC-12 wt% Co	Not identified	C - C	Angular	NI	NI	NM	~ 10
Kim and Suhr (2001)	WC-17 wt% Co	Not identified	SD	Spherical	Porous	WC, hcp-Co, fcc-Co *	21 - 52	NM
Nerz et al., (1999)	WC-12 wt% Co	Not identified	F - C	Angular	Dense	WC, W_2C, Co	~ 13	NM
Guilemany and De Paco (1999)	WC-12 wt% Co	CDS 1927	A - PD	Spherical	Dense	WC, W_2C, Co	24 - 50	1 - 3
Jacobs et al., (1999)	WC-12 wt% Co	WC-616	CAT	Spherical	Porous	WC, Co	NM	NM
Khan et al., (1997)	WC-12 wt% Co	Metco 73F-Ns-2	SD	Agglomerated - sintered	Porous	WC, Co	10 - 53	NM
	WC-17 wt% Co	Plasmalloy AI1173	S - C	Blocky	Fairly dense	WC, Co	15 - 45	NM
	WC-12 wt% Co	Plasmalloy AI1172	S - C	Blocky	Less dense	WC, Co	15 - 45	NM
	WC-9 wt% Co	Plasmalloy AI1109	S - C	Blocky	Fairly dense	WC, Co_3W_3C	15 - 45	NM

Note:

1. C - C = Cast and crushed; S - C = Sintered and crushed; A - D = Agglomerated and densified; C - C - F = Cast, crushed and fused; S = Sintered; F = Fused; SD = Spray dried; F - C = Fused and crushed; A - PD = Agglomerated and plasma densified, CAT = Carbide Activation Technology
2. * : Initial phase without treatment
3. NI = Not identified; NM = Not measured

Table 2.4 Typical sintering temperature for sintered WC-Co.

Composition (wt%)		Sintering Temperature
WC	Co	(°C)
94	6	1540
91	9	1480
89	11	1460
87	13	1450
80	20	1400
75	25	1380
70	30	1350

Adapted from Smithells, 1983.

Table 2.5 Properties of sintered WC-Co with different Co content and carbide grain size.

Composition (wt%)	Grain size (μm)	Density (g cm^{-3})	Hardness (HV)	Transverse rupture strength (MPa)	Compressive properties				Charpy impact value (J)	Abrasion resistance (vol. loss)$^{-1}$
					Ultimate strength (MPa)	Elastic limit (N mm^{-2})	Young modulus (GPa)	Ductility (%)		
97WC/3Co	1	15.3	1850	1600	4300	3500	640	0.6	1.1	100
94WC/6Co	1	15.0	1680	2000	4700	1950	650	0.8	1.4	55
94WC/6Co	2	15.0	1550	2200	4800	1450	640	1.0	1.4	25
91WC/9Co	2	14.7	1380	2350	4150	950	610	1.5	1.4	15
87WC/13Co	3.5	14.2	1250	2700	3650	550	550	1.9	1.9	6
84WC/16Co	3.5	13.8	1100	2900	3800	650	530	2.7	2.8	5
80WC/20Co	3.5	13.4	950	2750	3500	520	500	3.0	3.0	4
75WC/25Co	3.5	13.0	800	2600	3100	380	480	3.5	3.1	3

Adapted from Smithells, 1983.

Table 2.6 Changes of mechanism and physical properties of nanostructured materials

Property	Effect of reducing grain size to nanometre size
Strength and hardness	Increased
Ductility and toughness	Improved
Young's modulus	Increased
Elastic modulus	Decreased
Density	Decreased
Diffusivity	10 - 20 orders of magnitude greater than lattice diffusion, 2 - 4 orders of magnitude greater than grain boundary diffusion
Solubility	Increased (in some case dramatically)
Thermal conductivity	Lower
Thermal expansion coefficient	Increased (controllable between lattice expansion and grain boundary expansion
Magnetic	Each crystallite acts as a single domain

Adapted from Brook and MaCkenzie (1993) and Gell (1994).

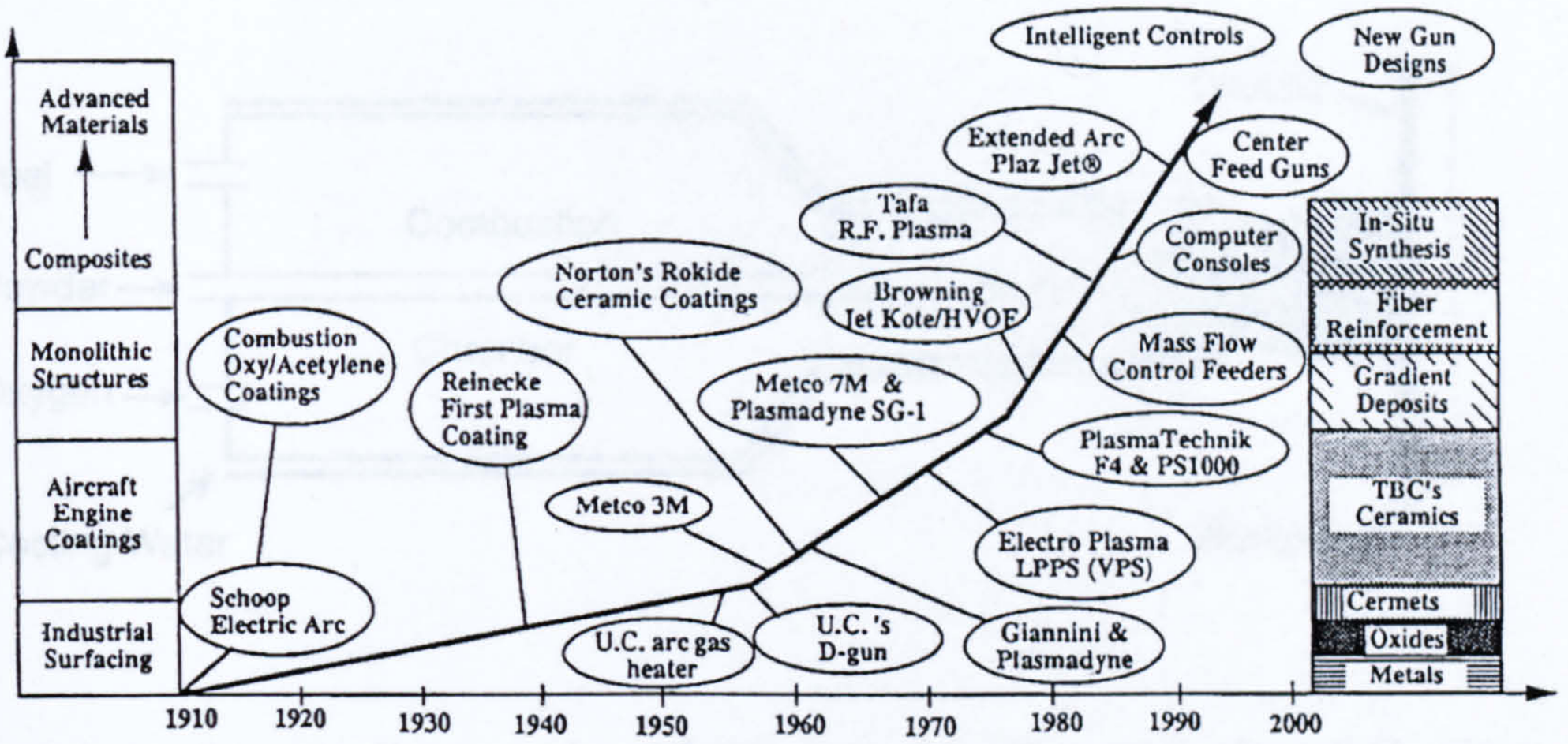

Fig. 2.1 Development with time (year of invention) of thermal spray technology (Smith and Novak, 1991).

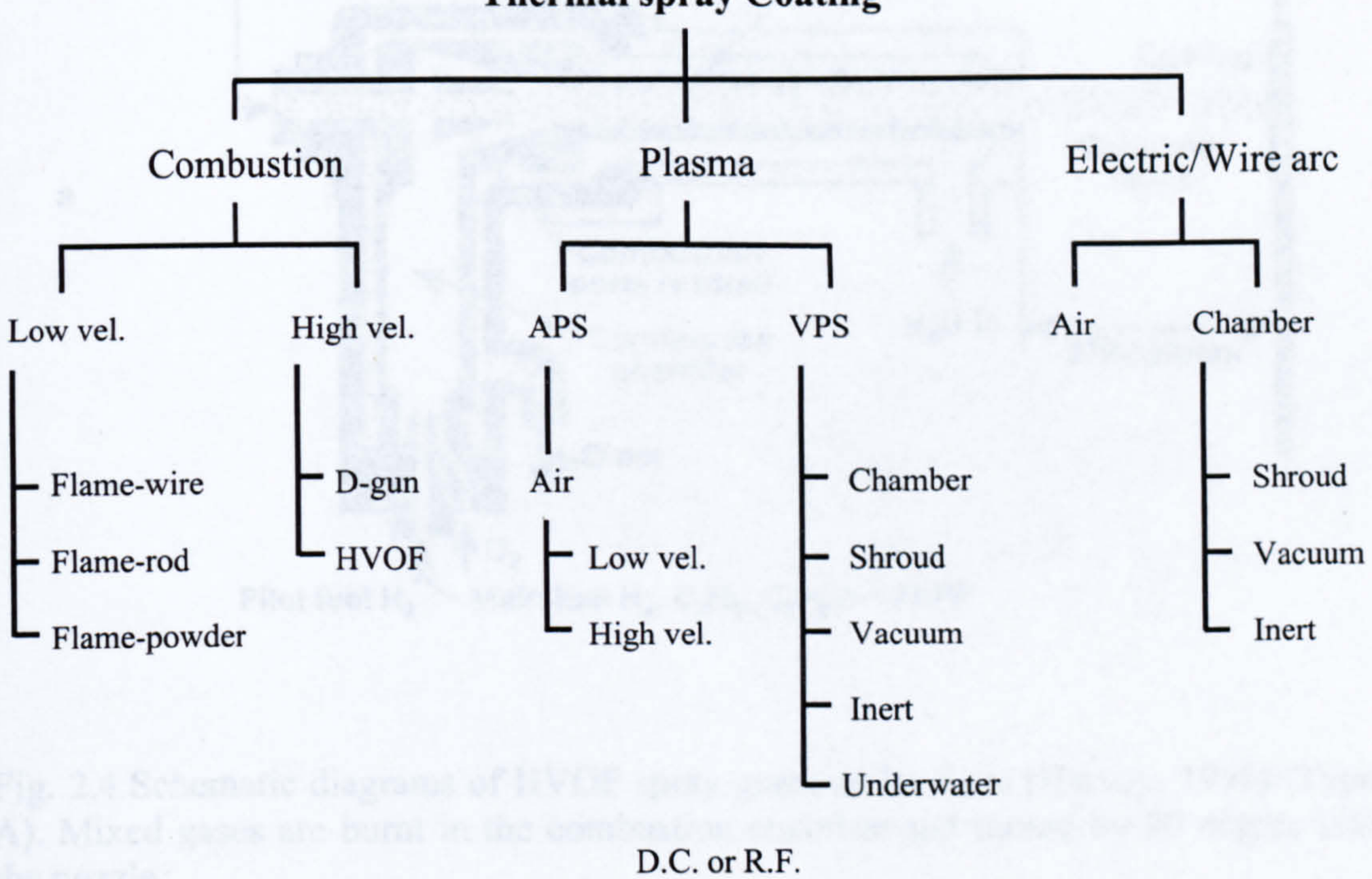

Fig. 2.2 Thermal spray processes classified by heat source, feed material, particle velocity and surrounding environment (Smith and Knight, 1995).

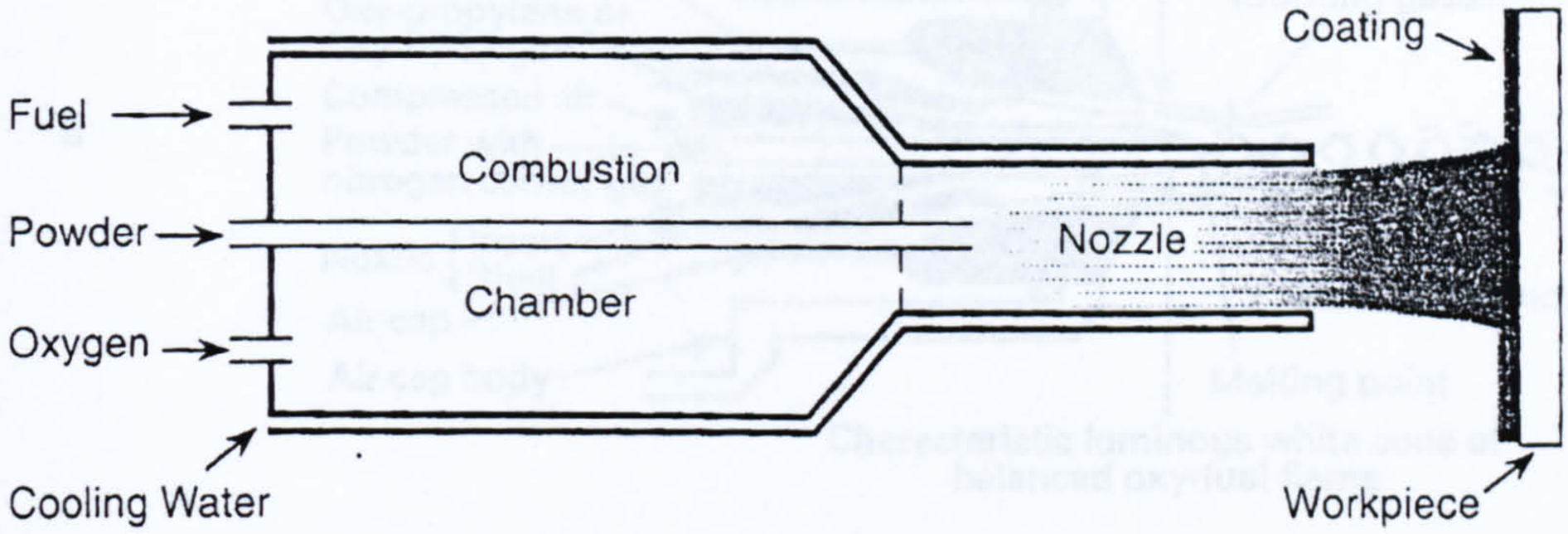

Fig. 2.3 A schematic diagram of an HVOF spray gun (Praxair Surface Technology, Inc.) showing a combustion chamber where gases are mixed and burnt. Powder is injected axially into a nozzle (Tucker. Jr, 1994).

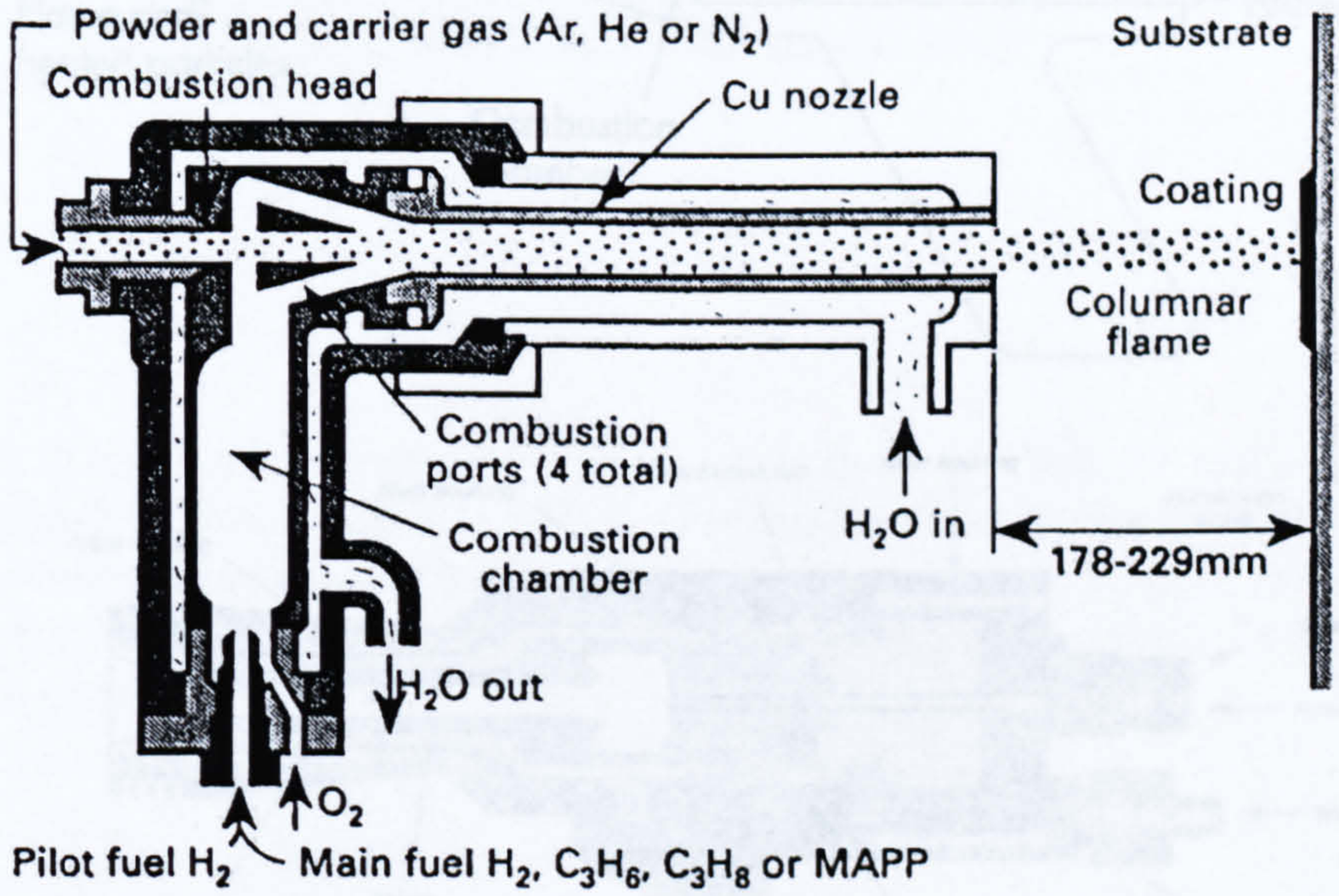

a

Fig. 2.4 Schematic diagrams of HVOF spray guns: a) Jet-Kote (Harvey, 1996) (Type A). Mixed gases are burnt in the combustion chamber and turned by 90 degree into the nozzle.

b

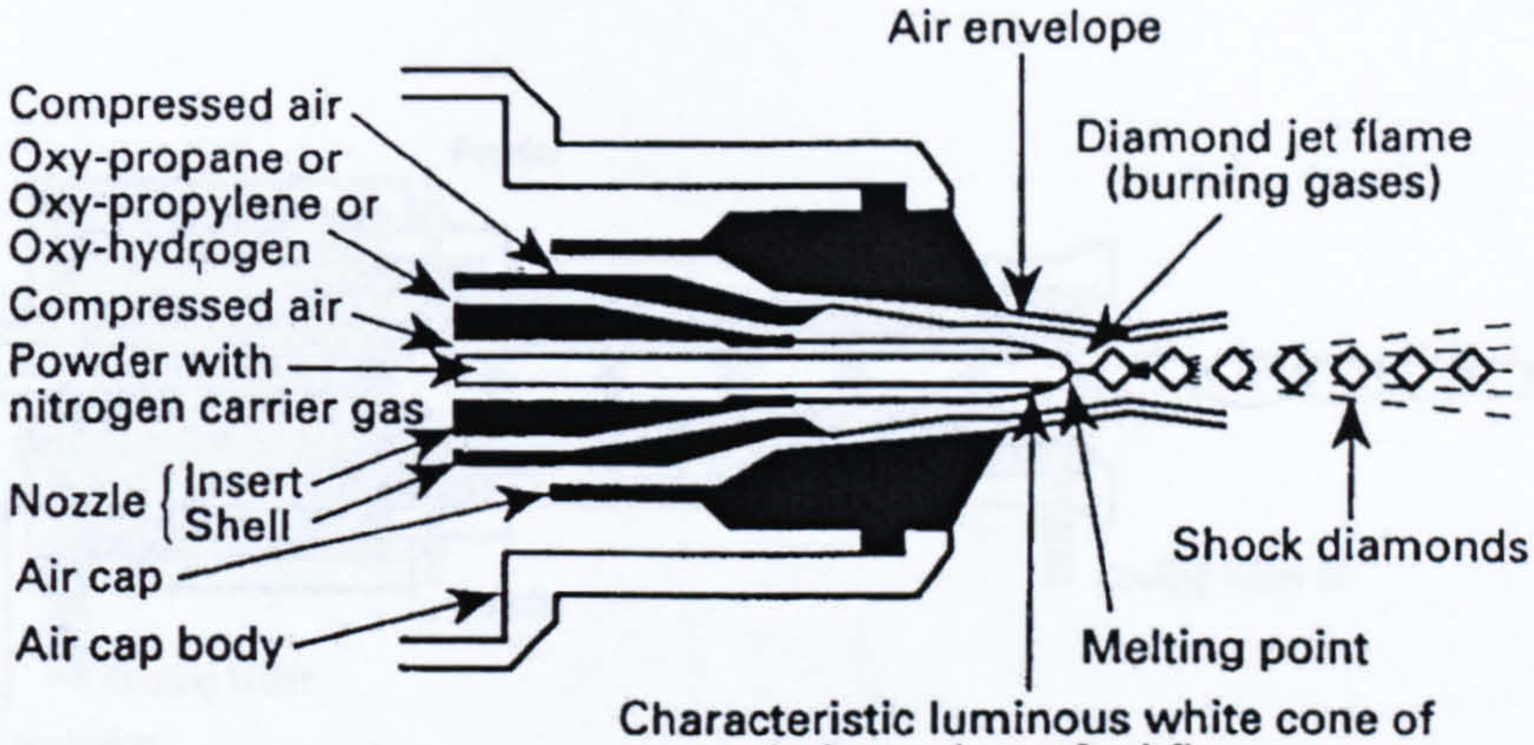

c

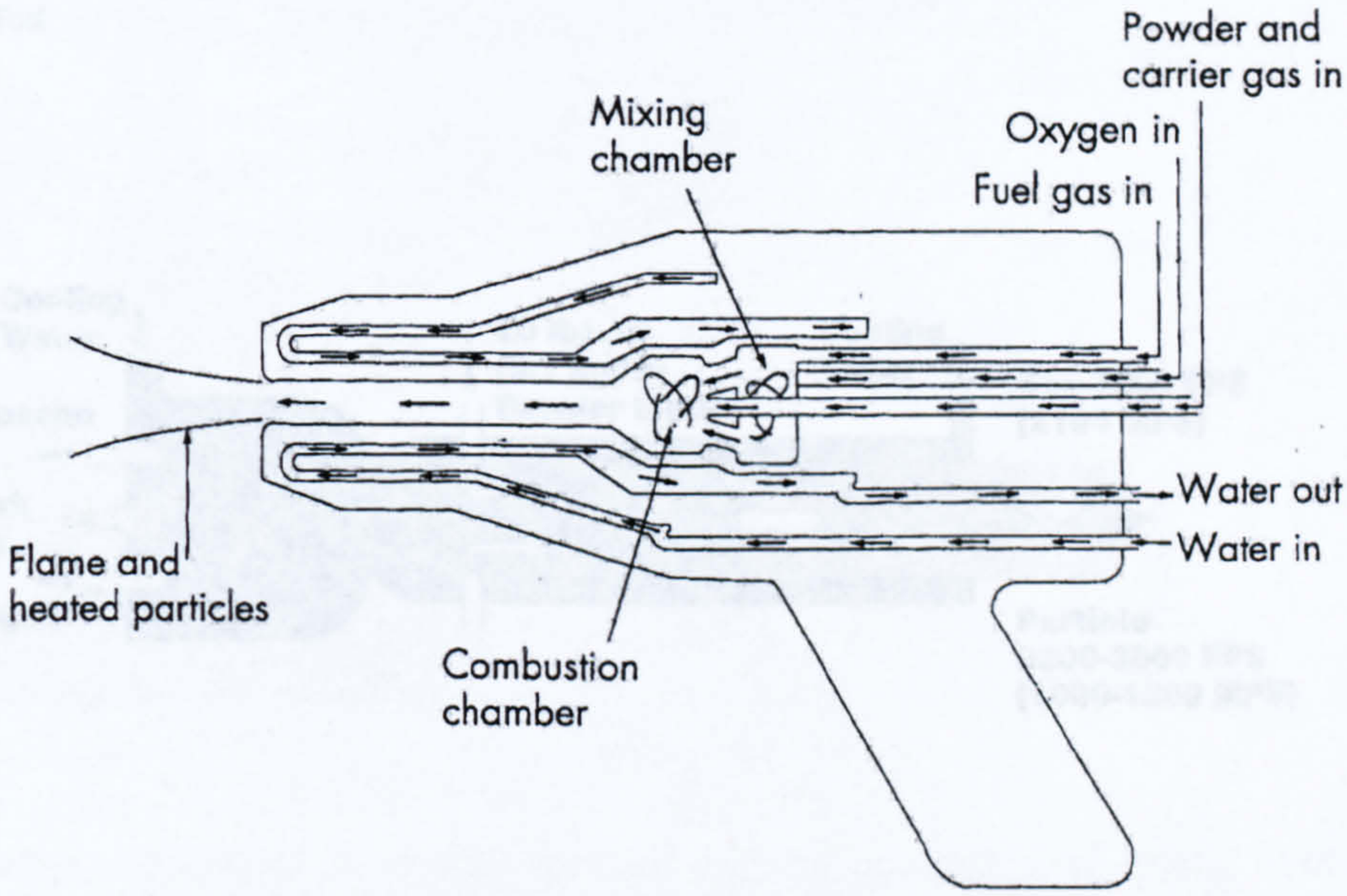

d

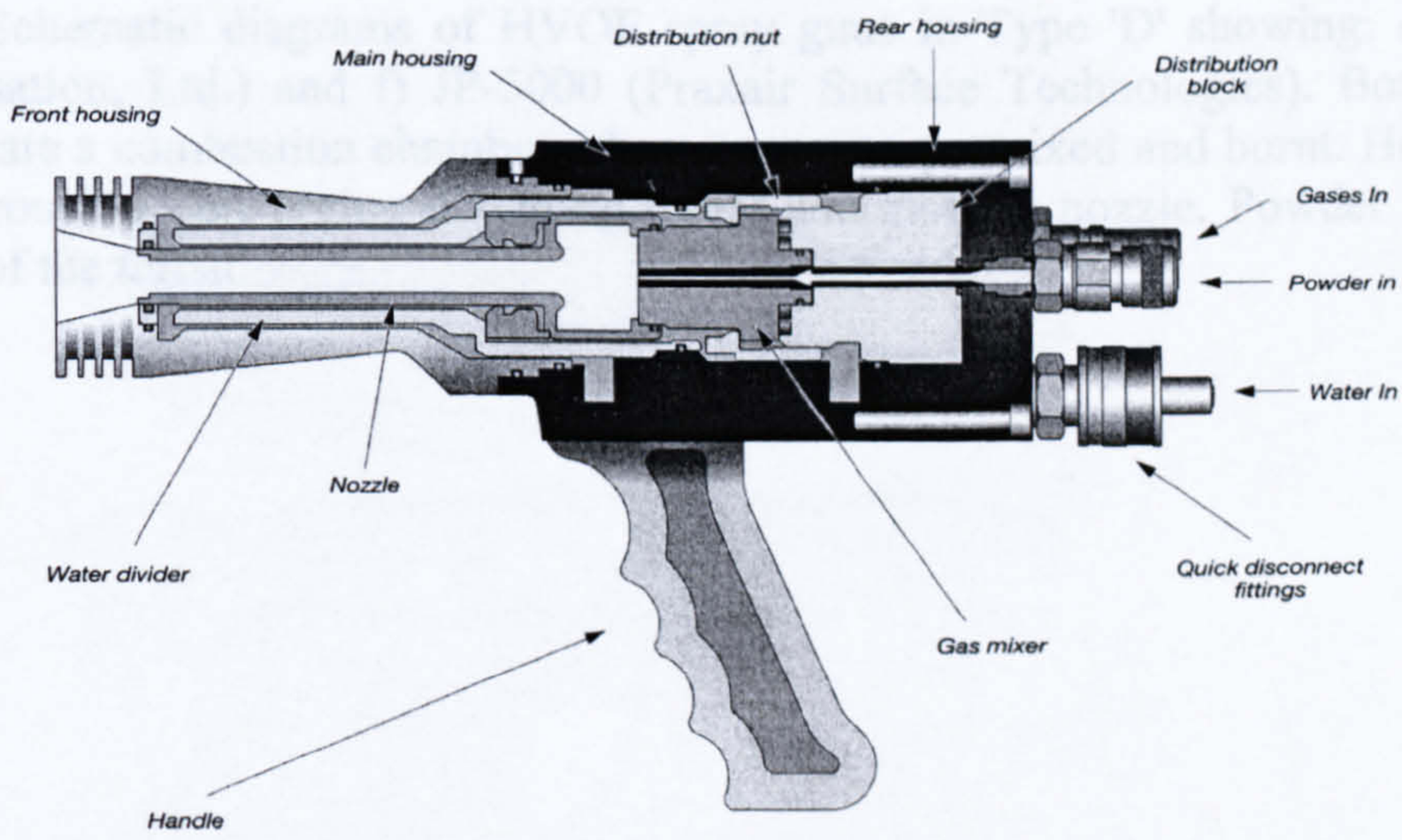

Fig. 2.4 (cont.) Schematic diagrams of HVOF spray guns: b) Diamond Jet (Type 'B') showing fuel gas and oxygen mixed in front of the gun (Harvey, 1996), c) Top-Gun (Harvey, 1996) and d) HV-2000 (Praxair Surface Technologies, Inc., 1997) showing Type 'C' where gases are premixed and burnt in a combustion chamber.

e

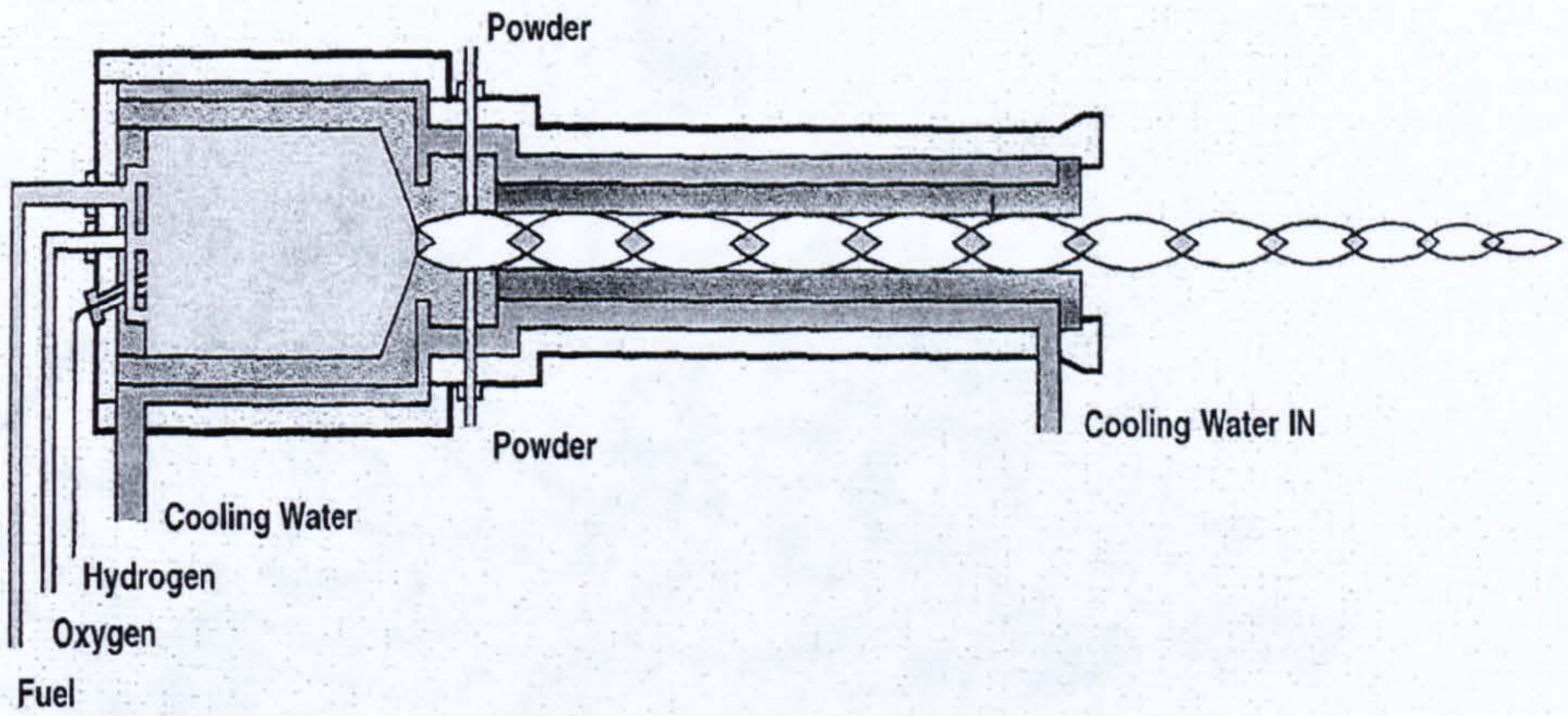

f

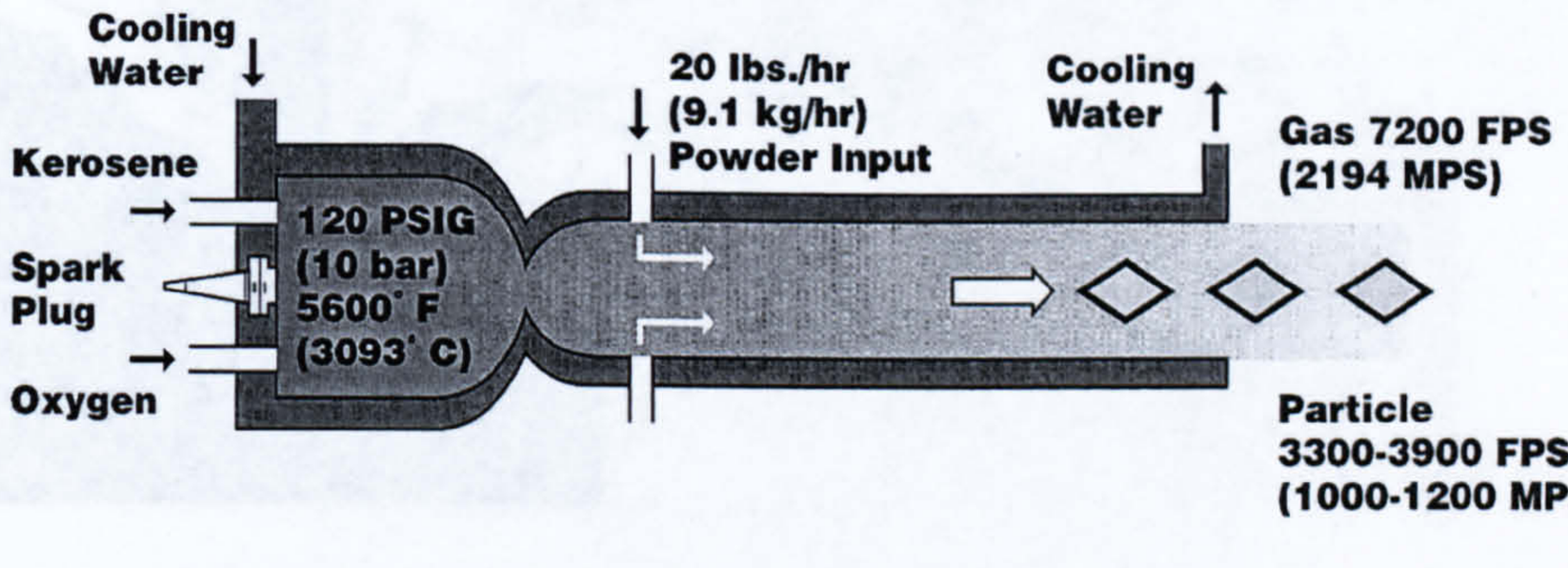

Fig. 2.4 (cont.) Schematic diagrams of HVOF spray guns in Type 'D' showing: e) Met-Jet (Metallisation, Ltd.) and f) JP-5000 (Praxair Surface Technologies). Both spray guns illustrate a combustion chamber where gases are premixed and burnt. Hot gas jet passes through a converging-diverging throat and along a nozzle. Powder is fed downstream of the throat.

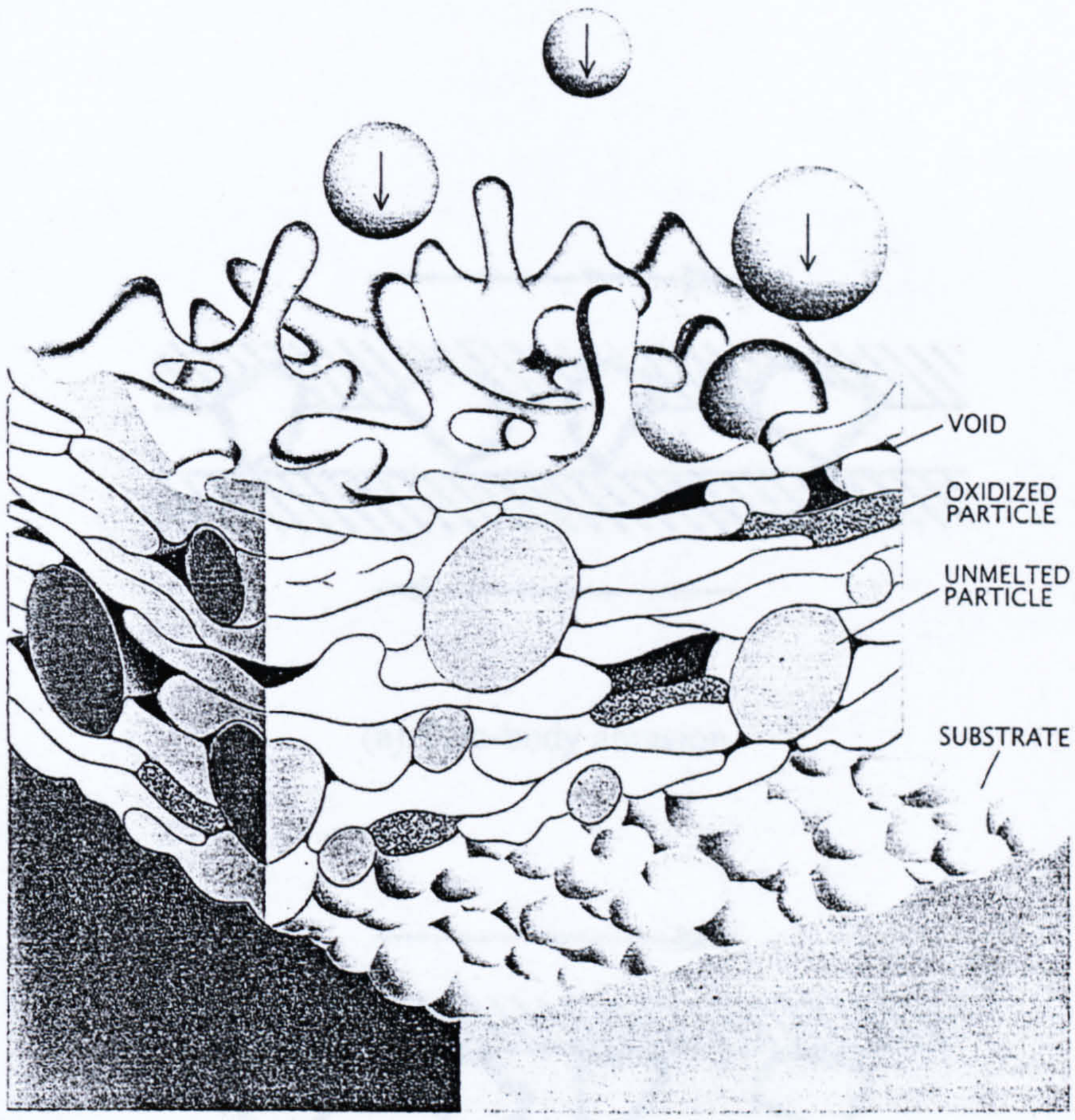

Fig. 2.5 A schematic image of thermally sprayed coating consisting of splats, voids, oxidized particles, unmelted particles (Herman, 1988).

Fig. 2.6 Schematic of adhesive wear showing adhesion between contacting asperities. One or both of the surfaces will suffer wear (Schey, 1987).

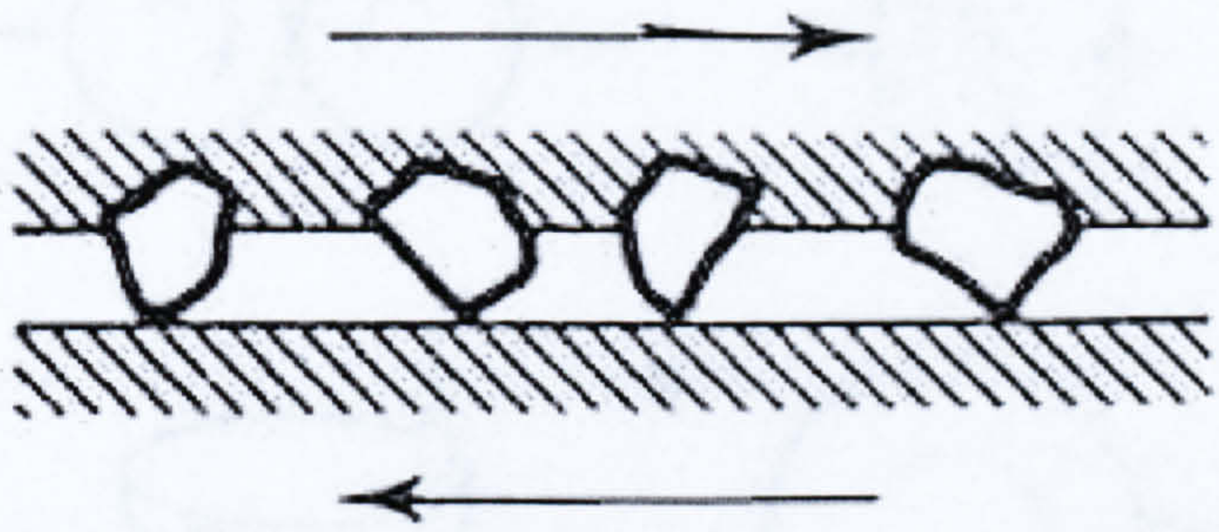

(a) Two-body abrasion

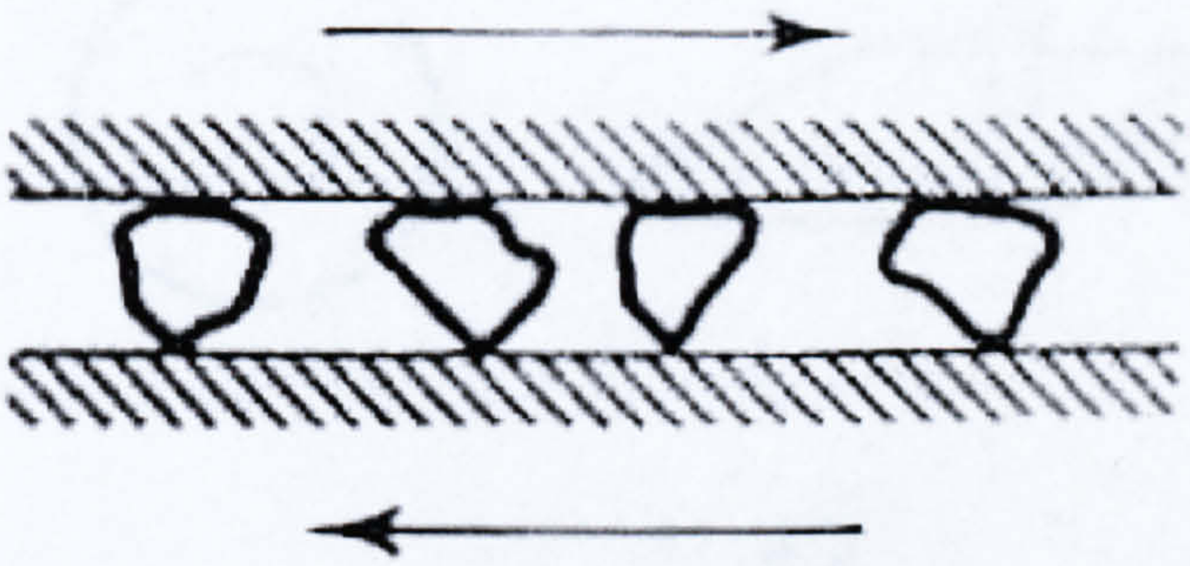

(b) Three-body abrasion

Fig. 2.7 Illustration of the differences of abrasive wear between (a) two-body abrasion (b) three-body abrasion (Hutchings, 1992).

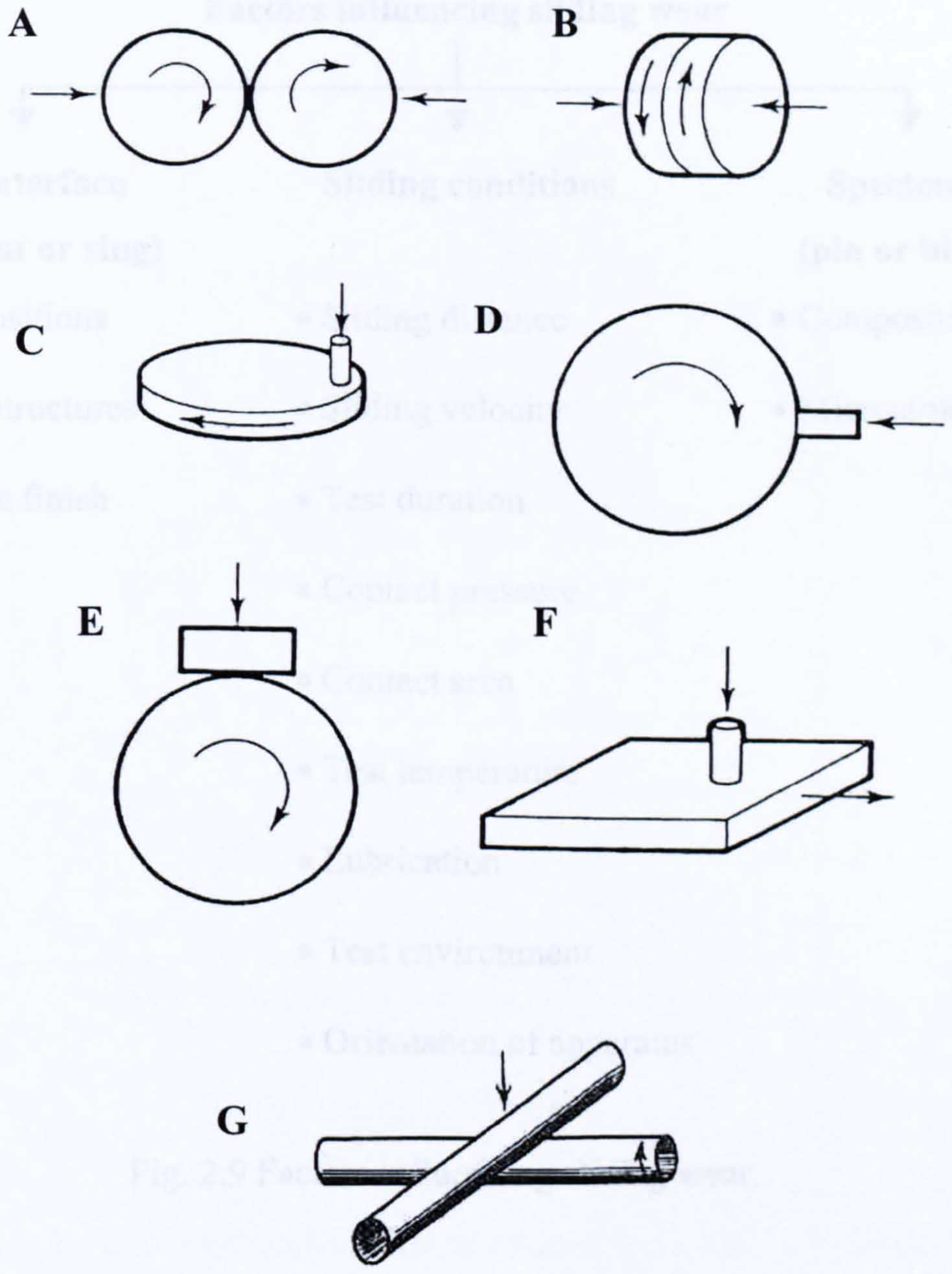

Fig. 2.8 Geometries employed in sliding wear tests (Hutchings, 1992; Rigney, 1981).

(a) Ring-on-ring (b) Face-to-face (c) Pin-on-disc
(d) Pin-on-rim (e) Block-on-ring (f) Pin-on-flat
(g) Crossed cylinders

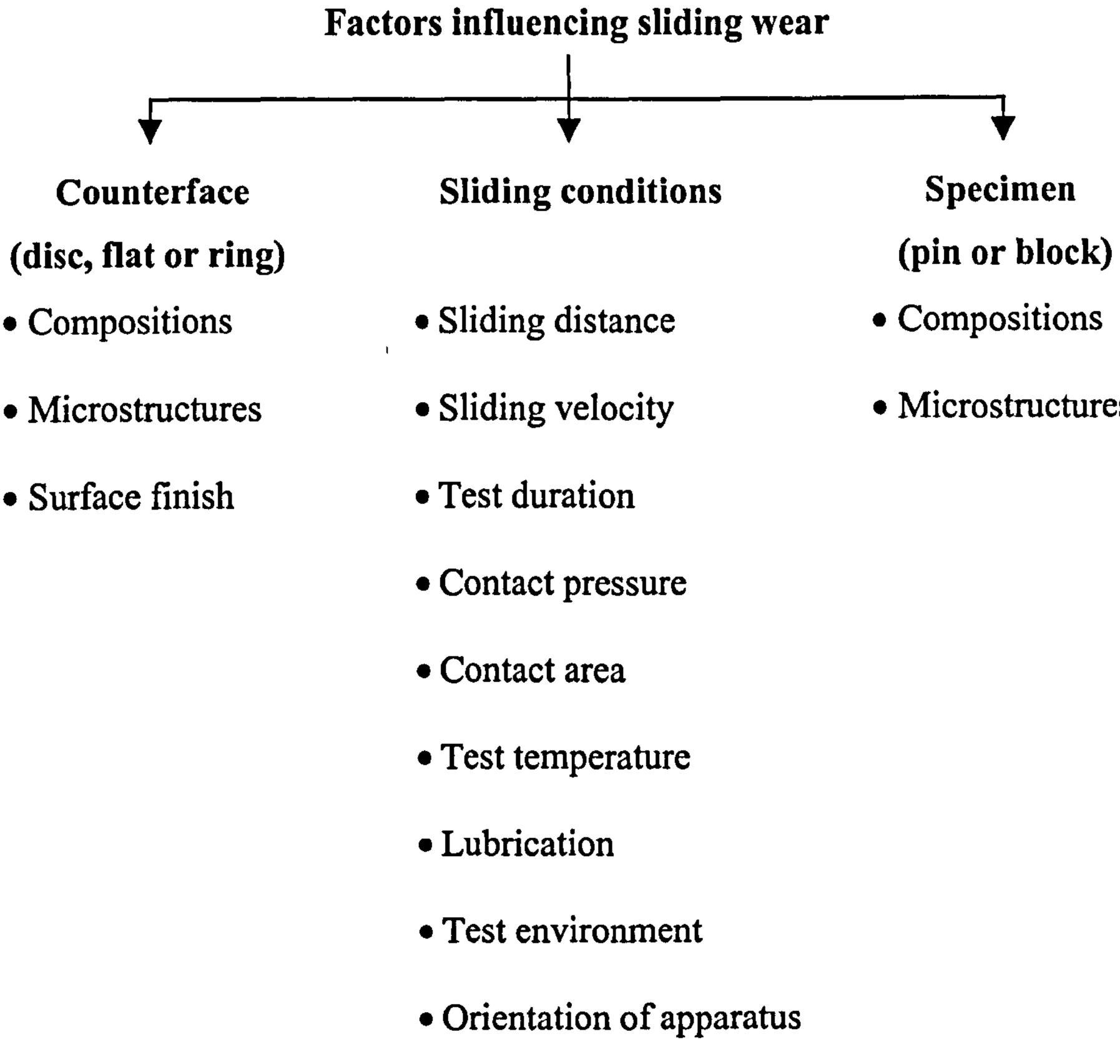

Fig. 2.9 Factors influencing sliding wear.

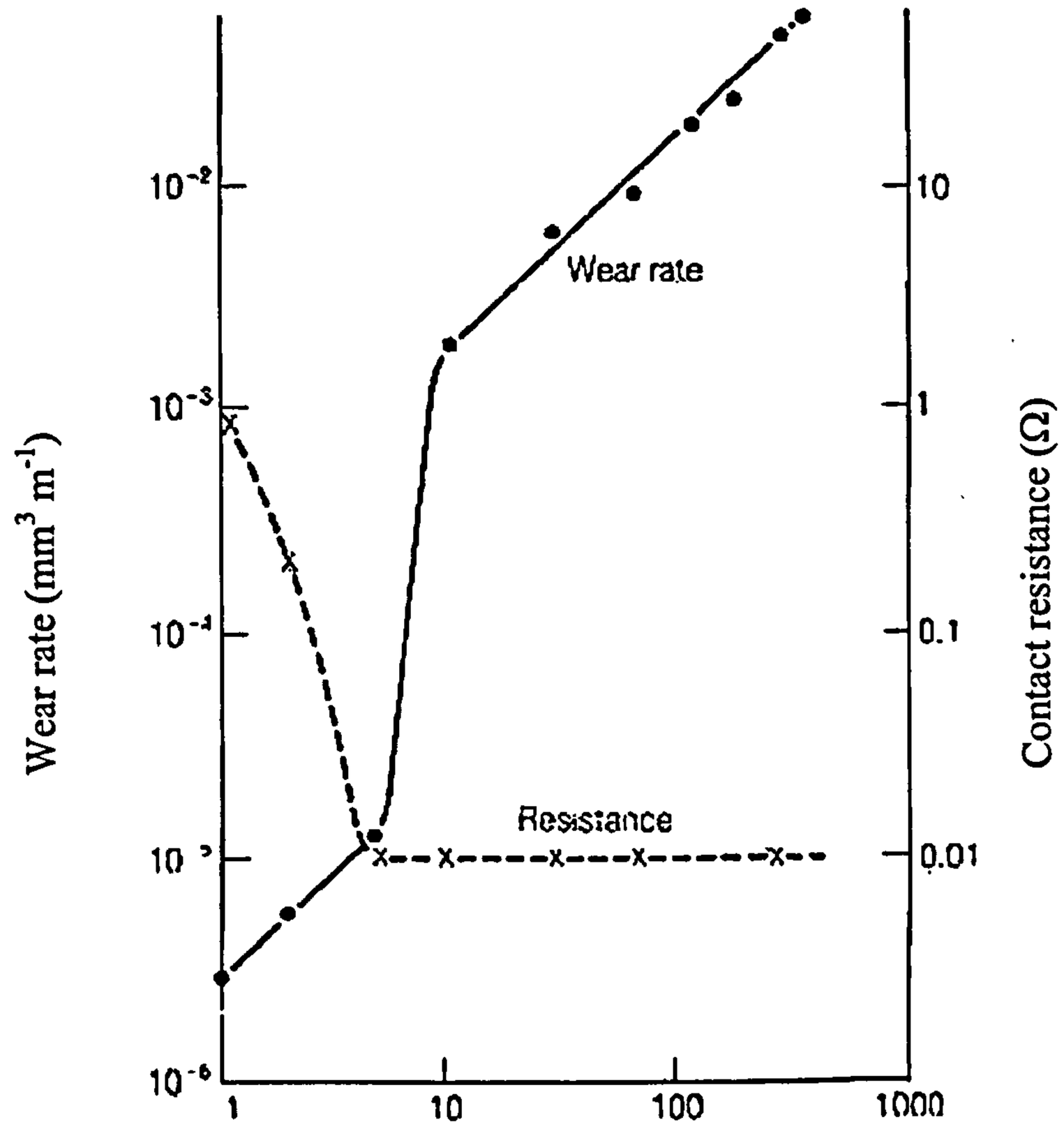

Fig. 2.10 Wear rate and electrical contact resistance for leaded α/β brass pin sliding against a hard stellite ring, as a function of normal load (Hirst and Lancaster, 1956).

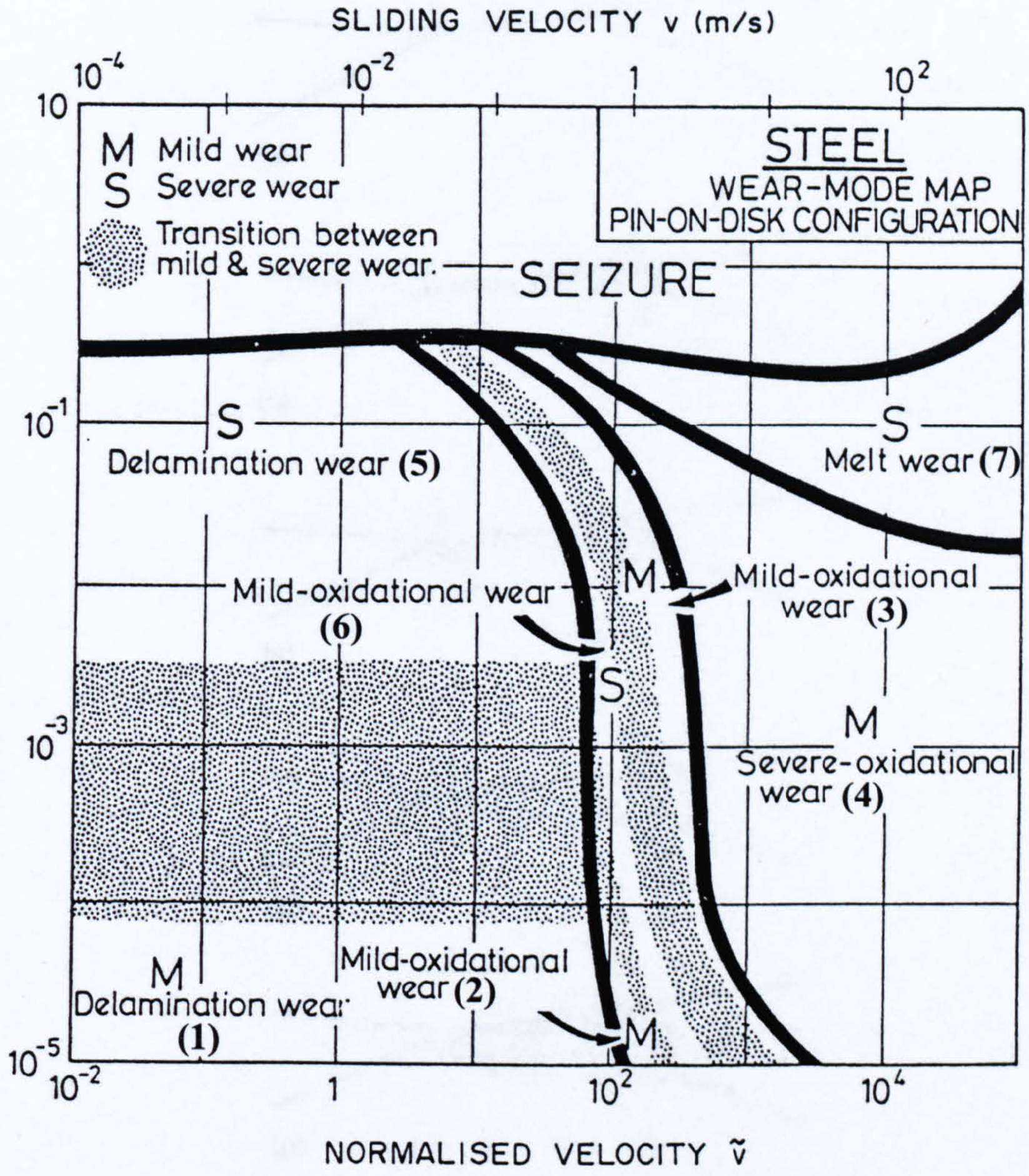

Fig. 2.11 The wear-mode map for unlubricated sliding of steel using pin-on-disc configuration (adapted from Lim et al., 1987).

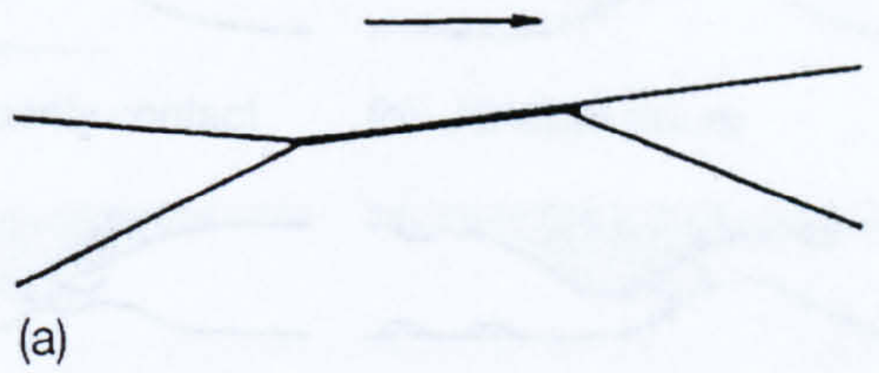

(a)

(b)

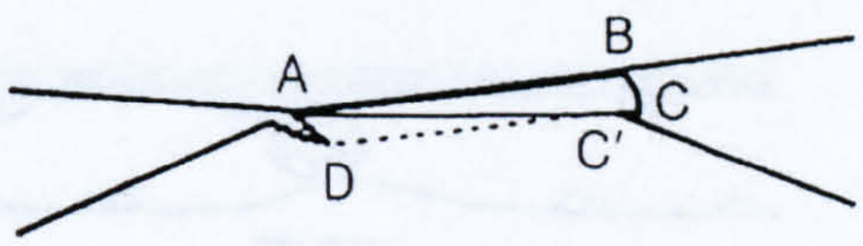

(c)

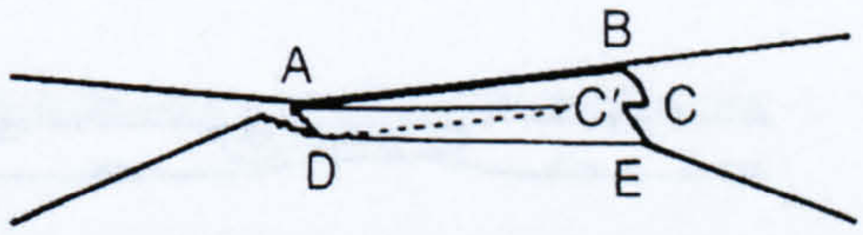

(d)

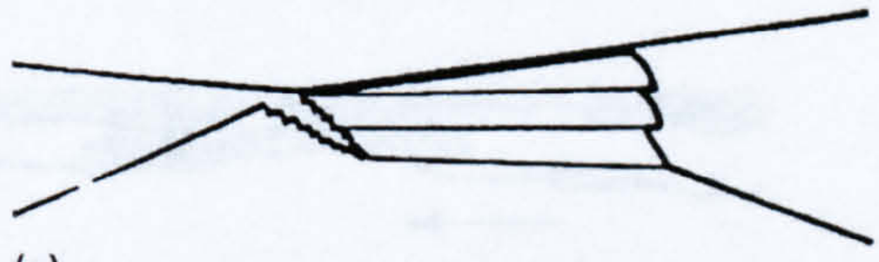

(e)

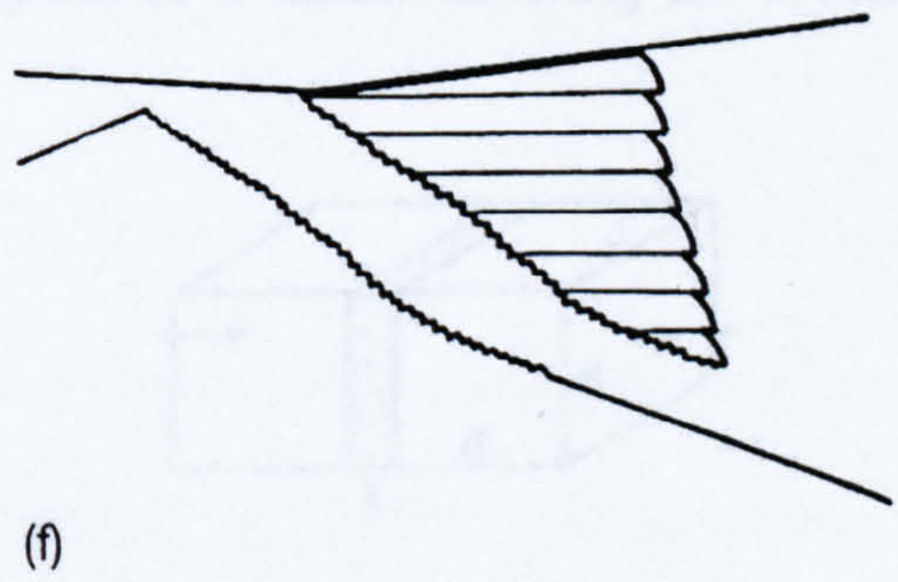

(f)

Fig. 2.12 A schematic diagram of a model showing the wear mechanisms of metal producing a fragmented material (Hutchings, 1992).

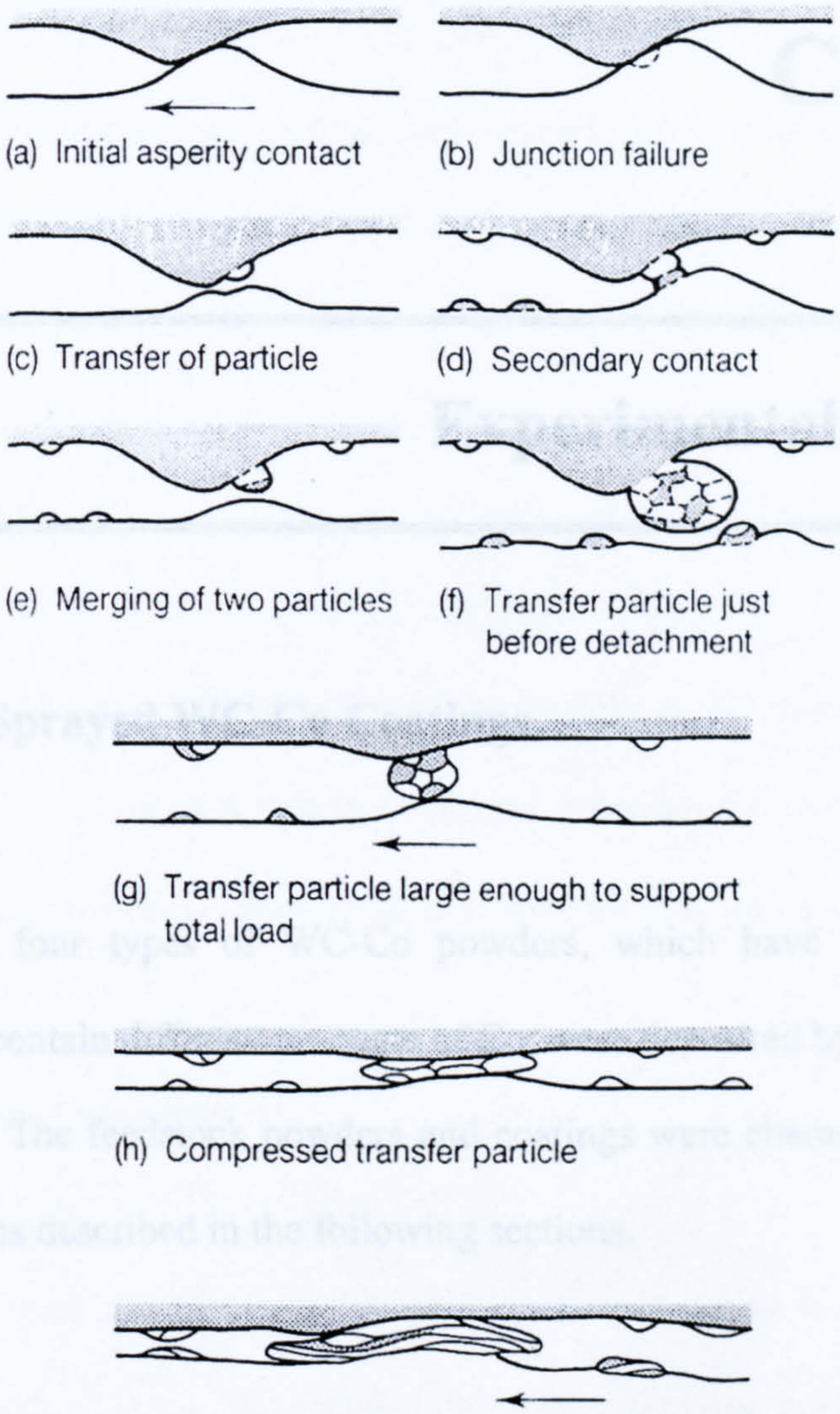

Fig. 2.13 A schematic diagram of a model showing the formation of wear debris (Sasada et al., 1979).

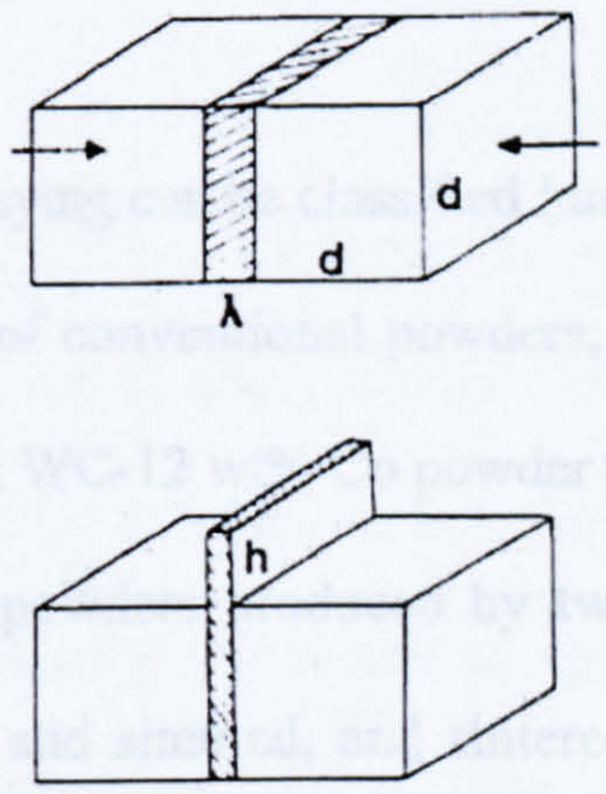

Fig. 2.14 A schematic diagram of Co binder extrusion (Lassen-Basse, 1985).

Chapter 3

Experimental Procedures

3.1 HVOF Sprayed WC-Co Coatings

In this study, four types of WC-Co powders, which have different production processes and contain different amounts of Co, were deposited by two types of HVOF spray systems. The feedstock powders and coatings were characterised by a number of techniques, as described in the following sections.

3.1.1 Materials

3.1.1.1 Powder

The types of powder used for spraying can be classified into conventional powder and nanoscale powder. In the subset of conventional powders, three different types were employed in this work as follows: WC-12 wt% Co powder produced by a sintered and crushed route; WC-17 wt% Co powders produced by two different manufacturing processes, namely agglomerated and sintered, and sintered and crushed. The fourth powder was nanoscale powder, WC-12 wt% Co powder was produced by a spray

conversion process (McCandlish at al., 1990). This powder was reported to have a hollow spherical morphology and uniform carbide grain size of less than 100 nm. Details of the powders are given in Table 3.1 whilst their compositions are given in Table 3.2.

3.1.1.2 Substrate

Substrates of mild steel (BS080A15) rectangular plates (57 mm x 12 mm x 2 mm in size) and discs (ϕ 38 mm x 6 mm in thickness) were used for coating deposition, the coated rectangular plates for microstructural analysis and the discs for wear testing.

3.1.2 Deposition Procedure

The substrates were grit-blasted with Al_2O_3 before spraying to provide a roughened surface on which to spray the coating. The grit size was nominally 250 μm. Grit blasting air pressure was 6 bar, the blasting angle was approximately 90°. The resultant roughness of the substrates was approximately Ra ≅ 1.7 μm.

Coatings were sprayed using two separate HVOF gun systems: a Metallisation Met-Jet II spray system and a Praxair/UTP Top-Gun spray system, shown schematically in Fig. 3.1. The Metallisation Met-Jet II spray system (HVOLF) uses oxygen plus kerosene (liquid fuel) which are burnt in a combustion chamber. The resultant hot gas passes through a converging-diverging throat and along a 200 mm nozzle before emerging as a free jet. Powder is radially injected downstream of the throat. In the Praxair/UTP Top-Gun spray system (HVOGF), hydrogen was employed as the fuel

gas. Here, the powder is introduced axially into the rear of the 22 mm combustion chamber, where gases are pre-mixed and burnt. The powder is propelled along the nozzle, approximately 120 mm in length, to impact with the substrate. The guns were mounted on a unidirectional traverse arm (Pro-Trav 1200, Electro Mechanical Services Ltd., UK.) controlling the vertical movement at the velocity of 5 mm s^{-1}. The specimens were mounted on the circumference of a horizontally rotating turntable with a radius of 120 mm giving a surface velocity of 1 m s^{-1}. The specimens were cooled during and after spraying with compressed air jets. The schematic diagram of the spraying set-up is shown in Fig. 3.2. The operating parameters of the Met-Jet II spray system and the UTP Top Gun spray system are shown in Tables 3.3, 3.4 and 3.5, respectively.

3.1.3 Powder and Coating Characterisation

3.1.3.1 Particle Size Distribution

A Malvern Mastersizer S (Malvern Instruments Ltd, UK) was used to measure the particle size distribution of the powder by laser granulometry. The powders were dispersed and circulated in water. When the powder particles passed through the laser beam, the light was scattered, and collected by annular detectors. The angles and intensity of the scattering of the light beam enabled the equivalent powder diameter to be calculated.

3.1.3.2 Phase Volume Fraction

The random point counting method (DeHoff and Rhines, 1968) was employed to measure phase volume fraction, assuming that the point fraction was equal to the volume fraction. The carbide particles in the conventional powder were estimated by random point counting on SEM images at magnifications of between about 4500 and 13000 times. For estimation of the volume fraction in coatings, SEM images of coatings at magnifications between approximately 6500 and 11500 times were used. A square grid (1 cm x 1 cm and 1.5 cm x 1.5 cm, respectively) drawn on transparent plastic was placed on the images of the powder and coatings, respectively. At each intersection of the grid, the phase present was identified and logged. From these, the number fraction of each phase was calculated; the number fraction was assumed to be equal to the volume fraction. From this data, the weight fraction of carbide in the powder was calculated.

3.1.3.3 Carbide Grain Size Analysis

Line analysis was used to measure the carbide grain size of the conventional powder. A square grid (1 cm x 1 cm) drawn on transparent plastic was placed on the SEM images of the powder. The length of line intersecting each carbide particle was measured. The grain size quoted is the average of such measurements.

3.1.3.4 X-Ray Diffraction (XRD)

X-ray diffraction (XRD) using a Siemens D500 Diffractometer with CuKα (λ = 1.5406 Å) radiation was used to identify the phases present in powders and coatings. The diffractometer was operated at 40 kV and 20 mA with diffraction angles (2θ) ranging from 10° to 140°. A 0.05° step size and a 2 s dwell time per step were employed. Phases present in the spectra were identified with the aid of JCPDS diffraction files. The preparation method for the powders was to sprinkle them on to an adhesive tab mounted on the sample holder. Coatings were prepared by grinding the top surface down to a 1 μm finish.

3.1.3.5 Scanning Electron Microscopy (SEM)

The external morphology and cross section of powders were investigated by scanning electron microscopy (SEM) using a JEOL-6400 instrument. The cross section of the nanoscale powder was observed by environmental scanning electron microscopy - field emission gun (ESEM-FEG, FEI-XL30) with the extra resolution afforded by the FEG source. The morphology of powders was examined by powder sprinkled on a carbon tab (attached to an aluminium stub) which was then sputtered with gold. Cross sections of the powders were prepared by mixing powder in cold-mounting resin. The sample was then ground with SiC paper (240, 400 800 and 1200 grit size), polished with 6 μm and 1 μm diamond paste and followed by gold-coating.

The microstructures of the cross sections of the coatings were also observed by SEM utilizing secondary and backscattered electron imaging (SEI and BEI, respectively).

The compositions were also analyzed with energy dispersive spectroscopy (EDS) (NORAN Series II). All SEM investigations on powders and coatings were performed at 20 kV. The specimens were prepared by sectioning normal to the coating by a precision diamond blade on an automatic precision cut-off machine (Accutom-5) operating at 3000 rpm and a cutting rate of 0.015-0.02 mm s^{-1}. After cutting, the specimens were cleaned with acetone and then mounted in cold-mounting resin. The specimens were cured in air at 25 °C for 8-12 h. The mounted specimens were ground and polished by a lapping procedure (Bjerregaard et al., 1996). Specimens were ground and polished on a Struers LaboPol-5 grinder/polisher equipped with a LaboForce-3 power head. Grinding can be classified as 2 steps: plane grinding (PG) and fine grinding (FG). In the PG step, the diamond grinding disc was applied to remove the damaged surface resulting from the sectioning operation and to obtain a surface flat. A Struers MD-Allegro disc was used in the FG step to eliminate the deformation introduced during the PG step. The polishing comprised two steps: diamond polishing 1 using a Struers MD-Pan disc (DP1) and the diamond polishing 2 with a MD-Mol disc (DP2). The grinding and polishing procedures were adapted from the Metalog Guide (Struers) (Bjerregaad et al., 1996) and shown in detail in Table 3.6.

3.1.3.6 Optical Microscopy

Cross sections of the conventional WC-12 wt% Co coatings sprayed with HVOLF and HVOGF were investigated by optical microscopy (Nikon FX-35 with an attached Microflex UFX-II camera). The samples were prepared as outlined in section 3.1.3.5. In addition, the coatings were etched for 3 s with Murakami's reagent consisting of

10 g potassium ferricyanide ($K_3Fe_3(CN)_6$), 10 g potassium hydroxide (KOH) and 100 ml water (Vander Voort, 1999). Carbide grains are outlined and slightly darkened by Murakami's reagent. It also attacks, rapidly, complex carbides such as W_2C, Co_6W_6C and Co_3W_3C (Vander Voort, 1999; Haller, 1998).

3.1.3.7 Transmission Electron Microscopy (TEM)

Microstructural and crystallographic investigations of coatings were performed on a JEOL 2000-FX-II TEM at 200 kV with a LaB_6 thermal electron source. Bright field (BF) and dark field (DF) imaging, selected area electron diffraction (SAD) techniques and microanalysis (EDS) were employed.

TEM samples were prepared from thin discs, 3 mm in diameter, taken parallel to the substrate-coating interface, which were cut by a wire spark machine. The discs were ground on the coating side first and then on the other side to remove the substrate. There were then dimpled and polished down to a thickness of 20 μm using 6 μm and 1 μm diamond slurries. Each disc was then resin bonded (Alradite) on a copper ring to support it when placed on the sample holder of an ion beam thinner. The final thinning process to perforation was carried out by an ion beam thinner (Fischione model 1010) with 5.8 kV Ar ion beam using an incidence angle of 15°. The resulting thin discs were cleaned with acetone and demagnetised before examination in the TEM.

3.1.3.8 Microhardness Measurement

Microhardness testing was performed using a Leco M-400 microhardness tester on polished cross sections of coatings employing a 300 gf load and a dwell time of 15 sec. Ten measurements were taken along the mid-plane of the coating transverse section on each specimen. The average hardness is quoted along with the standard deviation.

3.1.3.9 Profilometry and Roughness Measurement

The roughness and the profile of the as sprayed coatings were measured by a Surfcom profilometer (Advanced Metrology System Ltd., Leicester, UK). A diamond stylus was traversed across the coating with a tracing speed of 0.3 mm s^{-1}, cut off of 0.8 mm and transverse length of 4 mm. Each sample was measured at 5 random locations with the average and standard deviation of the Ra values being quoted.

3.2 Sliding Wear Testing (Ball-on-Disc)

3.2.1 Material and Specimen Preparation

3.2.1.1 Sintered WC-11 wt% Co

Discs of sintered WC-11 wt% Co (ϕ 36.8 mm x 5.5 mm in thickness) containing WC grains approximately 2 μm in size were obtained from Marshalls Hard Metals Ltd.,

UK. This was used as a reference material for the sliding wear experiments. The hardnesses of the sintered disc were measured as previously stated.

3.2.1.2 Ceramic Ball (Al_2O_3)

A sintered ceramic ball (Al_2O_3), 9.6 mm diameter, was supplied by Dejay Distribution Ltd., UK. Aluminium oxide (99.5% Al_2O_3) was chosen as the counterface ball material since it is reported (Jacobs et al., 1999) that this results in a high fraction contact with such coatings, thus promoting accelerated wear. Microhardness tests were also performed on the Al_2O_3 balls.

3.2.1.3 Disc Preparation

The HVOF-sprayed steel discs, 38 mm diameter and 6 mm thickness, were employed for the sliding wear tests. Sintered WC-Co and coated discs were prepared by grinding the top surface down to 1 μm by the lapping procedure, as described in section 3.1.3.5.

3.2.2 Sliding Wear Testing

Sliding wear tests on the coatings and sintered WC-Co reference materials were performed using a conventional ball-on-disc apparatus, shown schematically in Fig. 3.3. The ball-on-disc tests were performed under different loads with a sliding distance of 5000 m and a sliding speed of 0.5 m s^{-1}. The tests were carried out at room temperature without lubrication. A new sintered ceramic ball (Al_2O_3) was employed

as the counterface for each test. Both ball and disc samples were cleaned with ethanol and dry compressed air before and after testing.

Wear was monitored by a linearly variable differential transformer (LVDT) connected to a data logger. The LVDT measured the wear displacement by recording the vertical movement of the load arm relative to the initial starting level of the disc. Calibration of the LVDT was performed using a movement drum micrometer. A vertical displacement of 0.86 mm resulted in a 1 V change in output. The signal of the LVDT was monitored by the data logger at 2 Hz during the test.

In preliminary experiments, mild steel discs were slid against Al_2O_3 balls. It was found that both materials were worn, as a result the LVDT displacement could not report the precise wear of the disc. This problem is explained in Fig. 3.4. Fig. 3.4a shows the initial set up of a wear test. If only the ball wears, the distance 'x' will be measured directly by the LVDT (Fig 3.4b). If both the ball and disc wear by an amount 'z' and 'y' respectively, the LVDT will measure 'y+z' as a function of time but it is not possible to deconvolute this (Fig 3.4c). Therefore, the results of wear displacement measured by the LVDT were not reported in this work.

3.2.3 Calculation of Volume Loss of Discs and Balls

The wear track of the disc was measured using a profilometer to obtain the overall volume loss of the disc. This was obtained by measuring the average cross-sectional area of the track along 4 traces of the wear track. The volume loss of the disc was obtained by calculating:

$$V = 2\pi \times r_{wd} \times A \qquad (1)$$

r_{wd} = the average radius of wear scar of a disc measured from the middle of wear scar

A = the average cross-sectional area for 4 traces of the wear track with a profilometer.

The wear of the ball resulted in a near circular flat being formed, which it was assumed, represented the removal of a spherical cap of material. The diameter of the worn surface of the ball was scanned with a scanner and estimated from an image using an image analysis program. The volume loss of the ball was calculated by the following equations (Shipway, 1999). A diagram of a ball worn corresponding to the equations is shown in Fig. 3.5. The average wear rate of the ball was calculated by dividing the total volume loss by the total distance slid.

$$d = r - \sqrt{(r^2 - a^2)} \qquad (2)$$

$$V = \pi d^2 (r - \frac{d}{3}) \qquad (3)$$

where d = the depth of wear scar

r = the radius of the ball

a = the radius of the scar

V = the volume loss of the ball

3.2.4 Investigation of Worn Surface and Debris

A SEM (JEOL-6400) was employed to investigate the plan-view and the cross-sections of the worn surfaces of discs, the worn surfaces of balls and loose wear debris. The SEM was operated at 20 kV for plan view and cross section of worn surfaces of the discs and at 15 kV for the worn surfaces of the balls and debris. Clear Perspex sheets were placed on the worn surface with glue (Araldite) to protect the worn surfaces. Cross sections through the wear track on the worn surfaces of discs were made parallel to the sliding direction at that point. These samples were prepared by cutting with a precision diamond blade, mounting in cold-mounting epoxy resin, grinding and polishing by the lapping procedure. All samples were sputter-coated with gold for SEM imaging. Energy dispersive spectroscopy was also employed for quantitative analysis in the wear track.

Table 3.1 The details of the commercially produced powders.

Powder	Powder type	Powder supplier	Nominal size
Conventional powder			
1. WC-12wt%Co (M)	Sintered and crushed	Metallisation Ltd., UK	-45+15 μm
2. WC-17wt%Co (P)	Sintered and crushed	Praxair Surface Technologies Inc. of Indianapolis, USA	-45+11 μm
3. WC-17wt%Co (M)	Agglomerated and sintered	Metallisation Inc., UK	-45+15 μm
Nanoscale powder			
1. WC-12wt%Co(N)	Spray dried and converted	Nanodyne Inc. of New Brunswick, USA	-106+38 μm

NB : M = Metallisation Powder , P = Praxair Powder, N = Nanocarb Powder

Table 3.2 Composition of starting powders.

Powder	Composition (wt%)				
	W	Co	Total C	Fe	Ni
Conventional powder					
1. WC-12wt%Co (M)	82.20	11.41	5.13	0.60	-
2. WC-17wt%Co (P)	77.32	17.10	4.98	0.2	-
3. WC-17wt%Co (M)	77.98	16.9	4.92	≤ 0.1	≤ 0.1
Nanoscale powder					
1. WC-12wt%Co (N)	81.68	12.12	6.20	-	-

Table 3.3 Spraying parameters of WC-17wt%Co (M) and WC-12wt%Co (M) sprayed with the liquid-fuel gun (HVOLF).

Powder	WC-17wt%Co (M)	WC-12wt%Co (M)
Spraying parameters	**Value**	
Oxygen flow rate (l min^{-1})	833	824
Fuel (Kerosene) flow rate (l min^{-1})	0.5	0.5
Nozzle length (mm)	200	200
Spray distance (mm)	356	356
Powder ports used	2	2
Carrier gas (N_2) flow rate (l min^{-1})	6	6
Powder feed rate (g min^{-1})	69	77
Number of passes	30	30
Substrate velocity (m s^{-1})	1	1
Gun traverse speed (mm s^{-1})	5	5

Table 3.4 Spraying parameters of WC-17wt%Co (P) and WC-12wt%Co (M) sprayed with HVOGF.

Powder	WC-17wt%Co (P)	WC-12wt%Co (M)
Spraying parameters	**Value**	
Oxygen flow rate (l min^{-1})	241	241
Fuel gas (H_2) flow rate (l min^{-1})	642	642
Total flow (l min^{-1})	883	883
O_2/Fuel (% Stoichiometric)	75	75
Carrier gas (N_2) flow rate (l min^{-1})	17	17
Combustion chamber (mm)	22	22
Nozzle length (mm)	120	120
Spray distance (mm)	300	300
Powder feed rate (g min^{-1})	41	42
Number of passes	30	30
Substrate velocity (m s^{-1})	1	1
Gun traverse speed (mm s^{-1})	5	5

Table 3.5 Spraying parameters of WC-12wt%Co (N) sprayed with HVOGF.

Spraying parameters	**Value**			
Run No.	1	2	3	4
Oxygen flow rate (l min^{-1})	212	212	193	193
Fuel gas (H_2) flow rate (l min^{-1})	623	623	642	642
Total flow (l min^{-1})	835	835	835	835
O_2/Fuel (% Stoichiometric)	68	68	60	60
Carrier gas (N_2) flow rate (l min^{-1})	21	21	21	21
Combustion chamber (mm)	22	22	22	12
Nozzle length (mm)	120	120	120	120
Spray distance (mm)	150	200	200	200
Powder feed rate (g min^{-1})	9	31	27	25
Number of passes	30	40	40	40
Substrate velocity (m s^{-1})	1	1	1	1
Gun traverse speed (mm s^{-1})	5	5	5	5

Table 3.6 The grinding and polishing procedures: lapping procedure (adapted from Bjerregaard et al., 1996) with reference to Struers materials.

Step	**PG**	**FG**	**DP1**	**DP2**	**DP3**
Type of Disc	Diamond Grinding Disc	MD-Allegro	MD-Pan	MD-Pan	MD-Mol
Abrasive	-	Diamond	Diamond	Diamond	Diamond
Grit	#220	-	-	-	-
Grain Size	-	9 μm	6μm	3 μm	1μm
Lubricant	Water	DP-Blue	DP-Blue	DP-Blue	DP-Blue
RPM	300	150	150	150	150
Force (unit)	2	4	3	3	2
Time	30 s - 1 min	5 min	5 min	5 min	3 min

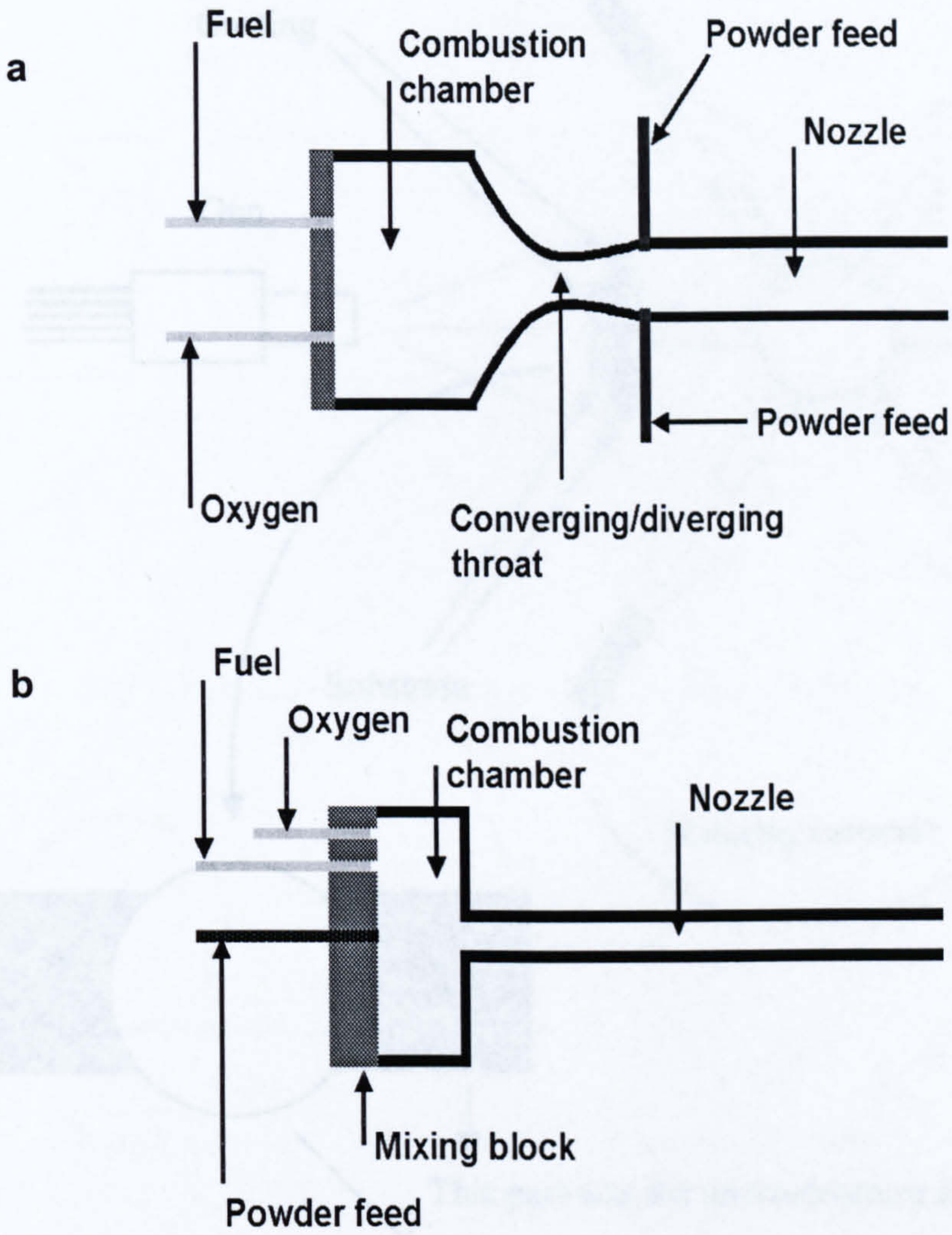

Fig. 3.1 Schematic diagrams of the design of
(a) HVOLF (b) HVOGF

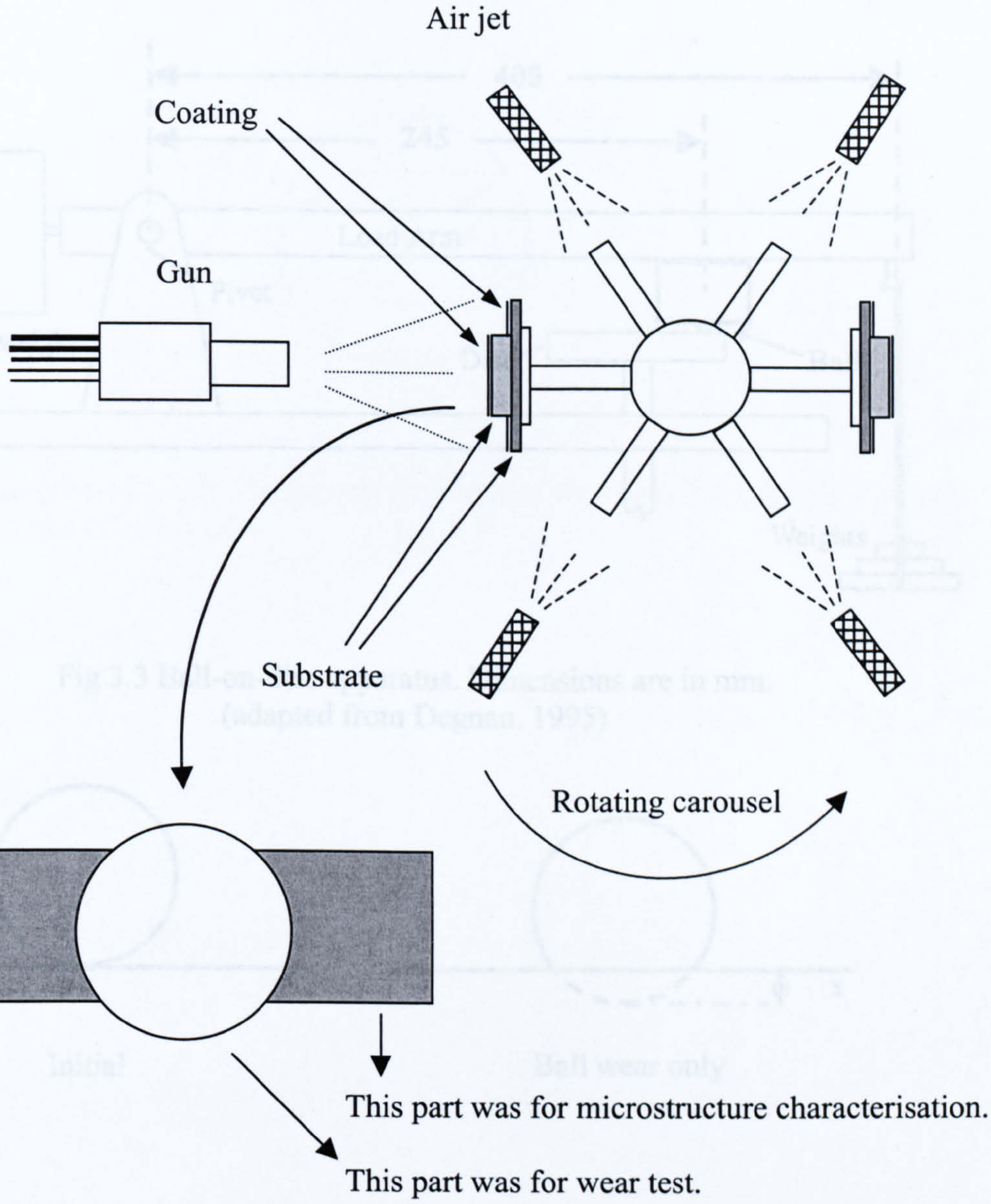

Fig. 3.2 Schematic diagram (plan view) of spray set-up.

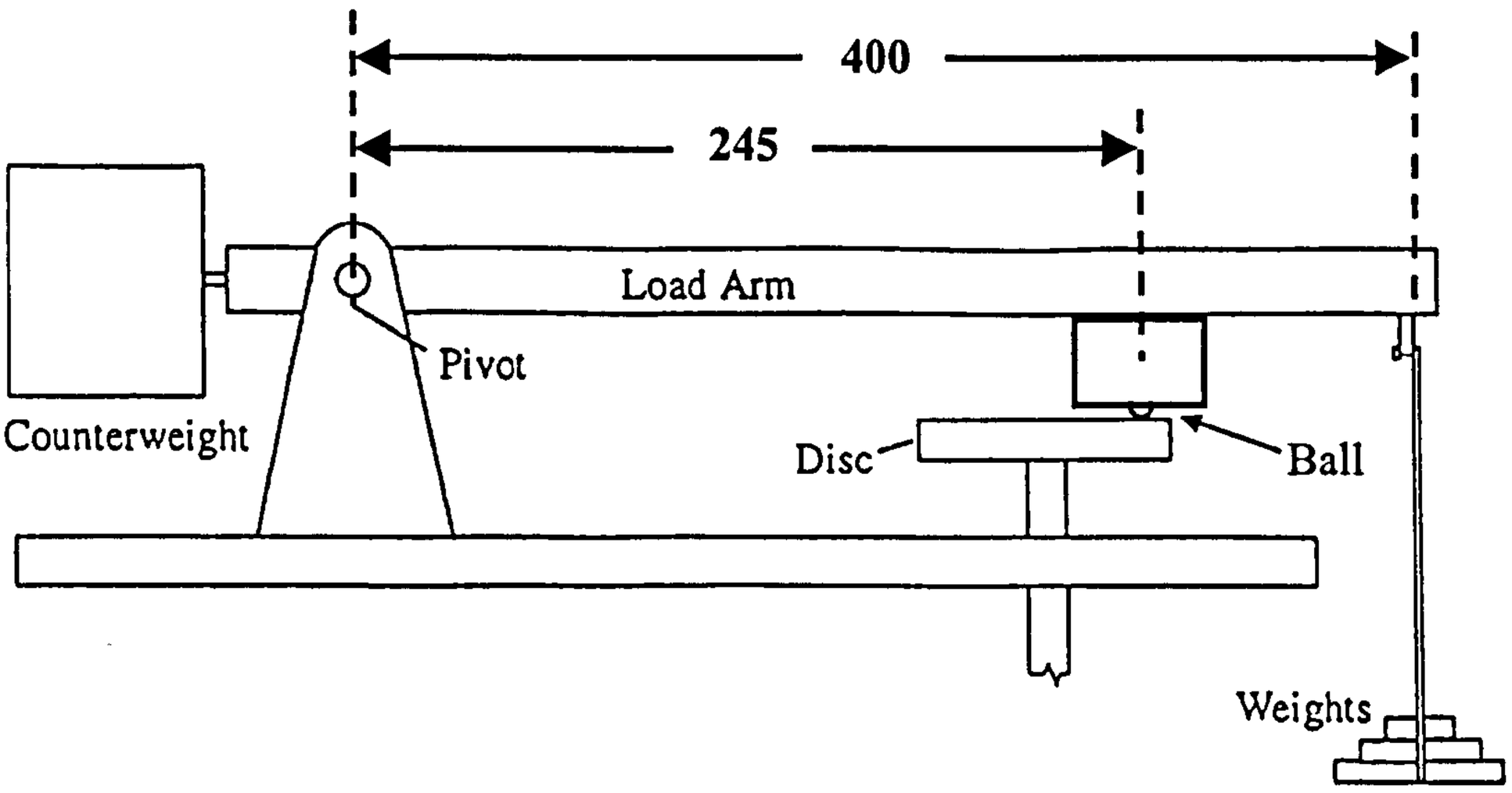

Fig 3.3 Ball-on-disc apparatus. Dimensions are in mm.
(adapted from Degnan, 1995)

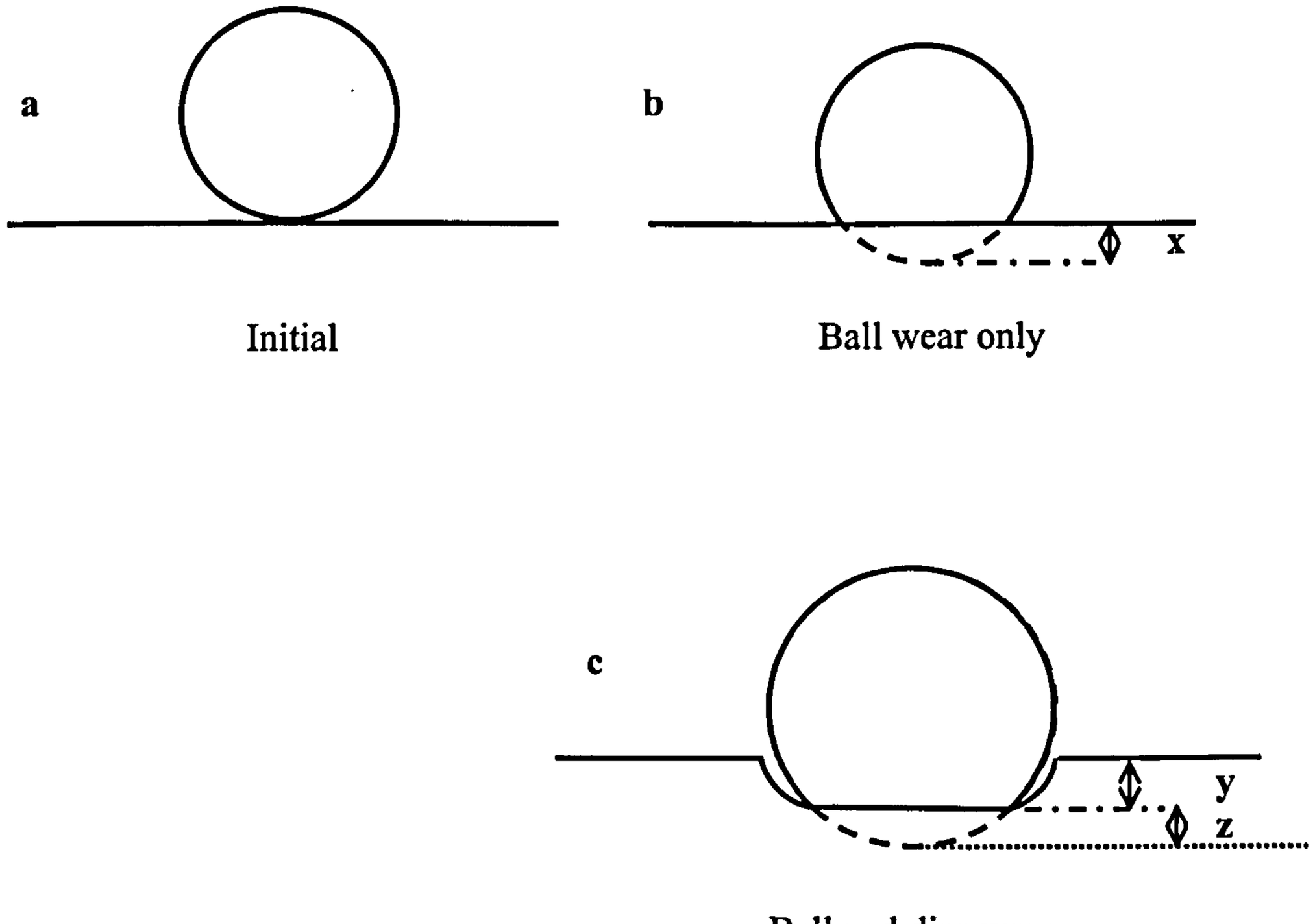

Fig. 3.4 Schematic of (a) an initial set up, (b) a ball worn and (c) a ball and a disc worn.

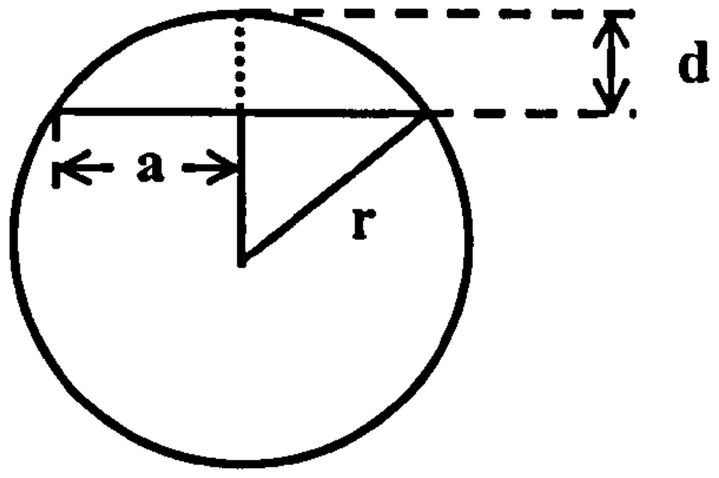

Fig. 3.5 A diagram of a ball worn shows the depth of wear scar (d), the radius of a ball (r) and the radius of a scar (a).

Chapter 4

Results : Characterisation of HVOF Sprayed WC-Co Coatings

The characterisation of conventional and nanaoscale powder and coatings, sprayed with high velocity oxy-liquid fuel (HVOLF) and high velocity oxy-gas fuel (HVOGF), is described in this chapter.

4.1 Characterisation of Powder Feedstock

4.1.1 Morphology and Microstructure of the Powder

The external morphologies and cross sections of the conventional WC-12 wt% Co powder, the nanoscale WC-12 wt% Co powder and two different types of the conventional WC-17 wt% Co powder were examined by SEM (Fig. 4.1). The conventional WC-12 wt% Co powder, produced by sintering and crushing, has a blocky, angular shape and is fairly dense, as shown in Figs. 4.1a and 4.1b. The powder was received with a nominal size distribution (-45+15) μm. The nanoscale WC-12 wt% Co powder, produced by a spray conversion process (McCandlish et al., 1990), exhibits a spherical morphology (Fig. 4.1c) with a nominal size distribution

(-106+38) μm. The polished cross section shows a very porous microstructure with a shell about 10 μm in thickness (Fig. 4.1d). The conventional WC-17 wt% Co powder, supplied by Metallisation Ltd., was manufactured by the agglomerating and sintering method with a nominal size distribution (-45+15) μm. The powder, therefore, had a spheroidal morphology with high levels of porosity (Figs. 4.1e and 4.1f). The conventional WC-17 wt% Co, supplied by Praxair Surface Technologies Inc., has an angular morphology and is fairly dense (Figs. 4.1g and 4.1h). This powder was produced by sintering and crushing with a nominal size distribution (-45+11) μm. The powders, received from Metallisation Ltd. and Praxair Surface Technologies Inc., were designated as M and P, respectively.

High magnification cross sections of the powders are presented in Fig. 4.2. A typical microstructure of WC-Co powder consists of angular particles of WC embedded in metallic Co. Also cracks and pores can be found due to the manufacturing process. The conventional WC-12 wt% Co powder has a WC grain size in the range of 1-7 μm, as shown in Fig. 4.2a. Fig. 4.2b shows the carbide grain size of the nanoscale WC-12 wt% Co powder in the range of 100 - 600 nm. Figs. 4.2c and 4.2d show that the WC grain size of the two different types of the conventional WC-17 wt% Co has a similar range (see section 4.1.4). Line analysis was used to measure the carbide grain size of the conventional powders from images such as these. The results are presented in the section 4.1.4.

4.1.2 Phases within Powders

An XRD spectrum of the conventional WC-12 wt% Co powder is shown in Fig. 4.3a in which the peaks resulting from the primary phases WC (hexagonal) and Co (FCC) are indexed. A small amount of Co_3W_3C phase is also found. In the XRD diffraction spectra of the nanoscale WC-12 wt% Co and both types of the conventional WC-17 wt% Co powders, only WC and Co peaks are observed, as shown in Figs. 4.3b, 4.3c and 4.3d, respectively.

4.1.3 Powder Size Distribution

The results of powder size distribution analysis are presented in Fig. 4.4. The conventional WC-12 wt% Co powder shows the median size about 30 μm, whilst the nanoscale WC-12 wt% Co shows a much larger median size (~ 47 μm), as exhibited in Figs. 4.4a and 4.4b. The nanoscale WC-12 wt% Co powder has particle size distribution ranging from 2 μm - 100 μm at 5 % and 95 % of cumulative, respectively. It indicates that the nanoscale WC-12 wt% Co powder has a much larger spread of sizes than the conventional WC-12 wt% Co powder, which has a particle size distribution ranging from 10 μm - 60 μm.

A comparison of the median size of the conventional WC-17 wt% Co (M) powder (~ 23 μm) and the conventional WC-17 wt% Co (P) powder (~ 42 μm) shows a significant difference, as shown in Figs. 4.4c and 4.4d. Also, the particle size distribution between 5 % - 95 % of cumulative of the conventional WC-17 wt% Co

(P) powder (11 μm - 80 μm) revealed a higher proportion of large particles than the conventional WC-17 wt% Co (M) powder (7 μm - 53μm).

4.1.4 Carbide Volume Fraction and Grain Size Analysis

Table 4.1 shows the results of the phase volume fraction and carbide grain size of the conventional powders. The weight percentages of the phases were calculated from the measured volume fractions and the values obtained were compared with the quoted values. For the WC-12 wt% Co powder, the quoted and measured values are close. However, for the WC-17 wt% Co powder, the measured carbide volume fractions are significantly higher than those quoted. This may result from the variability in apparent WC volume fraction in different cross sections and from the difficulty in accurately determining the edge position of carbide particles when the proportion of soft Co-binder is increased. The average carbide grain sizes obtained from the measurements are also shown in Table 4.1.

4.2 Characterisation of the Conventional WC-12 wt% Co Coating Sprayed by the HVOLF Process

The conventional WC-12 wt%Co powder was sprayed by the HVOLF gun, with the spray parameters indicated in Table 3.3. The principal microstructural features are described in the following sections.

4.2.1 X-Ray Diffraction

The XRD pattern of the coating clearly shows the primary peaks indexed to WC (hexagonal) and W_2C (hexagonal) along with a broad diffuse peak between $2\theta = 37°$-$46°$ (Fig. 4.5b). This broad diffuse peak indicates an amorphous or nanocrystalline material.

4.2.2 Scanning Electron Microscopy

The different phases in a cross section of the coating can be seen in a BSE-SEM micrograph (Fig. 4.6a). The coating shows little porosity with a homogeneous distribution of carbide particles. The microstructure at high magnification shows blocky carbide particles some with rounded edges varying in size from 1 μm to 4 μm within a Co-based matrix exhibiting different shades of grey contrast (Fig. 4.6b). BSE-SEM images exhibit contrast based on the mean atomic number. A material with a high average atomic number, such as W, WC and W_2C, shows very bright contrast, whereas the Co-binder phase shows different grey shades resulting from the different amount of W and C dissolved in it. From the comparison between the microstructure of the powder and the coating, it can be seen that the WC particles still have a basically angular shape in the darker binder phase. On the other hand, the WC particles in the brighter binder phase have more rounded edges and some have a white layer either partially or completely enclosing them. The white layer is probably the W_2C observed in the XRD analysis. Also, pores scattered randomly throughout the coating can be found.

4.2.3 Etched Structure

The microstructure of the coating etched by Murakami's reagent was investigated by optical microscopy. This reagent is normally employed for revealing the microstructure of powder metallurgy WC-Co alloys; the carbide grains are outlined and darkened slightly but the Co-binder is unaffected (Vander Voort, 1999).

Fig. 4.7 shows the microstructure at low magnification. It can be seen that the dark areas in the optical microscope are equivalent to the bright areas in the BSE-SEM micrographs (Fig. 4.6b). From the results above, the dark etched areas are probably the Co based binder with high levels of W and C in solution. This results from dissolution of WC into the Co-binder during spraying; it is this material which results in a broad diffuse peak found in the XRD analysis.

The etched coating was also examined by SE-SEM. Fig. 4.8a shows the edges of lamellar splats attacked by the etchant. At high magnification (Fig. 4.8b), it can be seen that the etchant attacks the edges of the splats, primarily the regions where WC has undergone extensive dissolution into the binder phase. The core WC splats still have an angular shape of carbide particles within an unmelted Co-binder

4.2.4 Thickness, Deposition Efficiency, Hardness, Roughness and Volume Fraction Analysis

The thickness of the coating, deposition efficiency, microhardness, roughness and phase volume fraction are shown in Table 4.2. The coating was obtained from

spraying 30 passes of the gun. An average deposition efficiency (%) was calculated by:

$$\text{Deposition efficiency (\%)} = \frac{\text{Total powder used}}{100} \times \left(\frac{\text{Area of a carousel}}{\text{Area of a disc}} \right)$$

Microhardness measurements were performed on a ground and polished cross section of coating. Phase volume fraction was measured by random point counting on an area of about 9276 μm^2 at a magnification of x3000.

4.2.5 Transmission Electron Microscopy

To investigate in detail the microstructure of the coating, a TEM study was carried out. Most carbide particles observed were WC particles which suggests a high retained fraction in agreement with the XRD pattern.

- **Carbide Structures (WC and W_2C)**

Fig. 4.9 shows TEM images of carbide particles, resulting selected area diffraction (SAD) patterns and schematic diagrams of SAD patterns indexed with the aid of CaRIne computer software. Fig. 4.9a shows a bright field image of two carbide particles in the Co-based matrix. A high magnification image of a particle 'A' (Fig. 4.9b) clearly shows the structural defects within the particle, namely dislocations and stacking faults. Fig. 4.9c shows a SAD pattern of a particle 'A' indexed to WC (Fig 4.9d). A dark field image using the objective aperture in spot A_1 (in Fig. 4.9c) is shown in Fig. 4.9e. The SAD pattern of particle 'B' is also indexed to WC (Figs. 4.9f and 4.9g). A dark field image of a spot 'B' is taken from a spot B_1, (Fig. 4.9h).

Generally, dislocations and stacking faults are found with high density in each WC particle.

Fig. 4.10a indicates a bright field image of a cluster of small particles. The SAD pattern from the particles in Fig. 4.10a is in the form of a ring diffraction pattern (Fig. 4.10b). When indexed (Fig. 4.10d), this showed the spotty rings to result from W_2C with more distinct spots from WC grains. A diffuse ring indicated the presence of an amorphous / nanocrystalline binder. A dark field image taken from a spot 'A' (indexed to WC) shows a WC particle lit up (Fig. 4.10c). The ring diffraction pattern came from W_2C, as shown in Fig. 4.10d. Moreover, a particle made up of WC and W_2C has been formed, as shown in Fig. 4.11a. A bright field image exhibits a rounded particle surrounded with a thick layer. The SAD pattern of that particle is indexed as WC and W_2C (Fig. 4.11b). A dark field image formed from a diffraction spot indexed to W_2C (spot circled in Fig. 4.11b) is shown in Fig. 4.11c, showing the outer layer is W_2C. Therefore, it can be concluded that the core WC is surrounded with W_2C layer. Also, WC and W_2C have an orientation relationship with the same zone axis, namely $[\bar{1}00]$.

- **Co-Based Matrix**

Fig. 4.12a shows a bright field image at low magnification of carbide particles embedded in a Co-based matrix. A bright field image taken from the area 'A' is shown in Fig. 4.12b. The SAD pattern of this area (Fig.4.12c) shows diffuse diffraction rings, indicating the material is amorphous / nanocrystalline. A dark field image using the objective aperture over the strongest line (as indicated in Fig. 4.12c) is revealed in Fig. 4.12d. It can be seen that nanocrystalline particles are lit up. Fig. 4.13a shows a

bright field image of carbide particles embedded in a Co-based matrix at low magnification. The SAD patterns of carbide particles 'A' and 'B' are shown in Figs. 4.13b and 4.13c, respectively. The patterns were both indexed to WC (Figs. 4.13d and 4.13e). An EDS analysis was performed on both the WC particles and the Co-based matrix with an electron beam diameter 50 nm. The spectra, taken from the three positions in Fig 4.13a, are shown in Fig. 4.14. The spectrum taken from the Co-based matrix exhibits substantial W peaks. This confirms that W is dissolved in the Co-based matrix.

4.3 Characterisation of the Conventional WC-12 wt% Co Coating Sprayed by the HVOGF Process

The conventional WC-12 wt% Co powder was sprayed by the HVOGF with the spray parameters given in Table 3.4. The coating is characterised by the following sections.

4.3.1 X-Ray Diffraction

The XRD spectrum of the WC-12 wt% Co coating sprayed by the HVOGF gun is shown in Fig. 4.5c and clearly shows the presence of WC (hexagonal) peaks and prominent peaks of W_2C (hexagonal). A small amount of W (BCC) is also observed. Furthermore, two broad diffuse peaks between $2\theta = 37° - 45°$ and $2\theta = 68° - 80°$ can be seen. The complete XRD trace is shown in Appendix 2.

Comparison of the XRD traces of the HVOLF and HVOGF sprayed WC-12 wt% Co coatings, shown in Figs. 4.5b and 4.5c, show clearly that there is significantly higher

amounts of W_2C in the HVOGF sprayed coating. Also metallic tungsten (W) is present only in the HVOGF sprayed coating. Moreover, the XRD traces of both coatings show little difference in the intensities of the diffuse diffraction areas correlating with the degree of decomposition. The XRD spectrum of the HVOGF sprayed WC-12 wt% Co coating exhibits higher intensity of the diffuse diffraction area than that of the HVOLF sprayed WC-12 wt% Co coating. This means that the HVOGF sprayed WC-12 wt% Co coating undergoes more decomposition during spraying.

4.3.2 Scanning Electron Microscopy

The backscattered image of a coating cross section is shown in Fig. 4.15a. The coating exhibits a fine and dense structure. Fig. 4.15b, at higher magnification, shows a microstructure with a binder phase having a wide range of shades of grey. Some of the binder phase has high brightness indicating substantial dissolution of W. Carbide particle sizes vary from 0.5 μm to 8 μm. The blocky carbide particles are found in the dark binder phase, whereas, the round edge carbide particles are observed in the bright binder phase. Clearly, some carbide particles which are in the brighter binder phase are surrounded by partial or continuous white layers at their edges. Pores with different sizes and shapes are randomly distributed throughout the coating.

4.3.3 Etched Structure

Fig. 4.16 shows the cross sectional microstructure of coating etched with Murakami's reagent. It can be seen that there is considerably more dark etched region than in Fig. 4.7.

Under high magnification, the etched coating was investigated by SE-SEM. The unetched area shows unmelted material consisting of carbide particles in Co based matrix (Fig. 4.17a). A large area of this coating has been attacked by the etchant. This results from a higher degree of melting of the powders during spraying. Under high magnification (Fig. 4.17b), it can be seen that the etchant attacks the molten area of the binder phase.

4.3.4 Thickness, Deposition Efficiency, Hardness, Roughness and Volume Fraction Analysis

The thickness, deposition efficiency, average hardness and roughness of the as-sprayed coating and phase volume fraction measured on an area of about 7570 μm^2 at a magnification of x2500, x3000 and x3500 are shown in Table 4.2.

4.3.5 Transmission Electron Microscopy

A detailed investigation of the coating characteristics was carried out by TEM.

- **Carbide structures (WC and W_2C)**

Fig. 4.18a shows a bright field TEM image of a carbide particle with an angular shape and sharp edges. The selected area diffraction (SAD) pattern (Fig. 4.18b) confirmed this to be a WC particle with a [001] zone axis as indexed in Fig. 4.18c. A dark field image taken from the diffraction spot marked by a circle in Fig. 4.18b is shown in Fig. 4.18d.

A close observation of another carbide particle (Fig. 4.19a) indicates the presence of small particles at the edge of a carbide particle, as indicated by arrows. The SAD pattern of the core particle is shown in Fig. 4.19b and is indexed to WC in Fig. 4.19c. Again, Fig. 4.20a shows a bright field image of a carbide particle with small particles precipitates on their edges. The precipitates grow preferentially on specific carbide crystallographic planes. The SAD pattern of that carbide particle is shown in Fig. 4.20b and indexed to WC (Fig. 4.20c). Using the diffraction spot marked by a circle in Fig. 4.20b, the dark field image, as shown in Fig. 4.20d, is formed. Fig. 4.20e shows the precipitates at high magnification. The SAD pattern taken from the precipitates in a position 'A' (Fig. 4.20a) is presented in Fig. 4.20f. The pattern consists of two overlapping diffraction patterns, analyzed to be WC with [$\bar{3}$ $\bar{2}$ 2] zone axis and W_2C with [$\bar{3}$ $\bar{2}$ 1] zone axis as indicated in Figs. 4.20g and 4.20h, respectively. Another core carbide particle (Fig. 4.21a) was shown by indexing of its SAD pattern (Fig. 4.21b) to be WC (Fig. 4.21c) with a [2 $\bar{1}$ 1] zone axis. A diffraction spot in a circle was taken to produce a dark field image (Fig. 4.21d). The structures surrounding the core WC particle show a nodular form. Fig. 4.21e shows a bright field image at the rim of a WC particle and Fig. 4.21f shows the diffraction pattern from the marked nodule indexed to be W_2C with [$\bar{1}$ $\bar{1}$ 1] zone axis

(Fig. 4.21g). A dark field image taken from the diffraction spot marked with a circle is shown in Fig. 4.21h indicating that these nodules are indeed W_2C. The interface between W_2C and WC is quite sharp and smoothly curved in some areas. The interface between W_2C and the binder phase also presents a smooth curvature. Furthermore, the core WC particles often display defects and dislocations, while these are never observed in W_2C. A W_2C particle not attached to a WC particle (the W_2C may have precipitated independently or the section of the sample may not include the WC core) is shown in Fig. 4.22a with its SAD pattern and indexing shown in Figs. 4.22b and 4.22c, respectively. The diffraction spot in a circle is used to form a dark field image (Fig. 4.22d). A cluster of W_2C particles are also found, as shown in Fig. 4.23a and confirmed by the SAD pattern in Fig. 4.23b.

4.4 Characterisation of the Nanoscale WC-12 wt% Co Coating Sprayed by the HVOGF Process

The nanoscale powder was sprayed by the HVOGF gun. Four runs were performed with different spray parameters as indicated in Table 3.5. The coating characterisation is described in the following sections.

4.4.1 X-Ray Diffraction

Fig. 4.24 shows the XRD patterns of HVOGF sprayed nanoscale WC-12 wt%Co coatings. The XRD patterns of all runs exhibit WC and two large broad peaks between $2\theta = 37^\circ$ - 46° and $2\theta = 68^\circ$ - 80°. Peaks indexed to W_2C and metallic tungsten (W) are clearly obvious. Moreover, a peak which is possibly from a complex

carbide (Co_3W_3C) can be found at $2\theta = 42.6^{\circ}$ in the XRD spectrum of run number 3 (Fig. 4.24d). The XRD spectra clearly show that the nanoscale powder sprayed with HVOGF results in a higher degree of decomposition than the conventional materials, i.e., a higher amount of WC decomposes to W_2C, W and Co_3W_3C.

4.4.2 Scanning Electron Microscopy

The cross sectional BSE-SEM images of HVOGF nanoscale WC-12 wt% Co coatings from the spray runs are shown in Fig. 4.25. As shown in Table 3.5, for 'Run 1' 30 passes were used to form the coating, a very low powder feed rate (9 g min^{-1}) was also employed. 'Run 2', 'Run 3' and 'Run 4' were sprayed with 40 passes with high powder feed rate (~ 30 g min^{-1}), the thickness typically was 100 μm thick. As a result of a smaller number of passes and lower powder feed rate, the coating from 'Run 1' is very thin with large degree of porosity. Cracks are also observed along splat boundaries. Porosity increases in the order 'Run2': 'Run 4': 'Run 3': 'Run 1'. Therefore, the spray parameters for 'Run 2' were selected for spraying the nanoscale WC-12 wt% Co powder with (-90+53) μm size to produce wear test samples.

At low magnification (Fig. 4.25b), the microstructure of the coating generally presents different grey shades, i.e., ranging from bright to dark grey. A variety of pores sizes can be found and cracks are also observed along the interface of splats. A cross sectional microstructure at higher magnification (Fig. 4.26) reveals different binder grey shades. A large number of rounded bright particles are found in the bright binder areas while blocky carbide particles are observed in the dark binder areas. The details

of microstructure are further investigated with TEM due to the very small size of carbide grains.

4.4.3 Thickness, Deposition Efficiency, Hardness and Roughness

The thickness, deposition efficiency, hardness and roughness of the as-sprayed coating are shown in Table 4.3.

4.4.4 Transmission Electron Microscopy

When the HVOGF nanoscale WC-12 wt% Co coating was examined in the TEM. Rounded carbide particles and angular-shaped carbide particles with precipitation on their edges were often observed. TEM images of them are described below.

- **Carbide Structures (WC, W_2C and W)**

Fig. 4.27a indicates a bright field image of a carbide particle with precipitation on its edges. The SAD pattern (Fig. 4.27b) is indexed as a WC particle (Fig. 4.27c). A dark field image of that particle is produced from the diffraction spot as marked with a circle, (Fig. 4.27d). Again, a carbide particle with an angular shape is shown in Fig. 4.28a. The SAD pattern (Fig. 4.28b) is indexed to WC (Fig. 4.28c). The diffraction spot in the circle is taken to produce a dark field image (Fig. 4.28d). Two distinct features 'A' and 'B' are seen in the WC particle. EDS microanalysis was carried out on those features, with the resulting spectra shown in Figs. 4.28e and 4.28f. It shows that 'A' has a very high Co content, whereas 'B' shows very low counts and may be a void.

A large number of rounded carbide particles are found in the coating as seen, for example, in a bright field image in Fig. 4.29a. The selected area (SA) aperture covered on the area around a particle 'A' reveals the combined diffraction patterns (Fig. 4.29b) indexed to W_2C (Fig. 4.29c). A dark field image produced from the circled diffraction spot in Fig. 4.29b shows two particles lit up (Fig. 4.29d). This is because the size of the SA aperture projected on the image covers a large area with diameter about 300 nm leading to combined diffraction patterns and a weak diffuse ring from the amorphous binder. Fig. 4.30a shows a cluster of particles in a Co rich binder phase. The SAD pattern with the aperture over a large area produced a diffuse ring and small spots tending to form continuous ring patterns (Fig. 4.30b). These are indexed to W in an amorphous binder. A dark field image produced from the circled diffraction spot is shown in Fig. 4.30c.

4.5 Characterisation of the Conventional WC-17 wt% Co Coating Sprayed by the HVOLF Process

The conventional WC-17 wt% Co powder manufactured by the agglomerating and sintering process was sprayed with HVOLF using the spray parameters given in the Table 3.3. The results of the microstructual investigation are presented in the following sections.

4.5.1 X-Ray Diffraction

Fig. 4.31 shows the X-ray diffraction patterns of the conventional WC-17 wt% Co powder and coating. WC peaks are predominant with small W_2C peaks present in the coating. Also a broad diffuse peak between $2\theta = 38^\circ - 46^\circ$ can be seen.

4.5.2 Scanning Electron Microscopy

At low magnification, the coating exhibits a low porosity structure with fine carbide particles, as shown in Fig. 4.32a. A high magnification image of Fig. 4.32b shows carbide particles ranging in size from 1 - 4 μm, and pores, with a range of sizes, randomly distributed in the coating. The matrix exhibits different grey shades. A small number of carbide particles with white layers on their edges are found in the bright binder phase. On the other hand, blocky carbide grains with somewhat rounded edges are observed in the dark binder phase.

4.5.3 Thickness, Deposition Efficiency, Hardness, Roughness and Volume Fraction Analysis

The thickness, deposition efficiency, average hardness and roughness (Ra) of the as-sprayed coating are shown in Table 4.2 along with the phase volume fraction of WC and Co analyzed from an area of 7228 μm^2 at a magnification of x3000 and x3500.

4.5.4 Transmission Electron Microscopy

- **Carbide structure (WC)**

An example of a bright field image of two carbide particles (Fig. 4.33a) shows carbide 'A' with an irregular shape and carbide 'B' with line defects inside. The SAD patterns of both particles index to WC (Figs. 4.33b and 4.33c) with [$\bar{1}$ $\bar{1}$ 0] and [1 $\bar{1}$ 0] zone axes (Figs. 4.33d and 4.33e). A dark field image of particle 'A' and 'B' are formed from diffraction spots marked on their respective diffraction patterns and presented in Figs. 4.33f and 4.33g. In Figs. 4.33b and 4.33c, weak rings are visible because the SA is partly over the matrix. Hence in the dark field images, the matrix is also diffracting to the image.

- **Matrix Phase**

Fig. 4.34 presents a bright field image with three carbide particles indexed to WC and diffuse diffraction rings confirming the Co-binder is amorphous. EDS microanalysis performed on a WC particle 'A' and the binder at a position '1' are shown in Fig. 4.35. The EDS spectrum of the binder phase shows that significant W is present in the binder indicating that WC has dissolved into it.

4.6 Characterisation of the Conventional WC-17 wt% Co Coating Sprayed by the HVOGF Process

The conventional WC-17 wt% Co powder produced by sintering and crushing was sprayed with HVOGF under the spray parameters given in Table 3.4. The coating was characterised as follows:

4.6.1 X-Ray Diffraction

Figs. 4.36a and 4.36b show the XRD patterns of powder and coating, respectively. It can be seen that a number of microstructural changes have taken place during the spraying process. The coating still exhibits substantial WC peaks and the presence of W_2C peaks. A broad peak is also found between $2\theta = 38^\circ - 46^\circ$. This results from the formation of an amorphous binder phase.

4.6.2 Scanning Electron Microscopy

The microstructure of the coating observed in the SEM in SEI mode at low magnification shows a lamellar structure with a rather high level of porosity spread throughout the coating (Fig. 4.37a). At high magnification, the cross section of coating imaged in BEI mode shows the matrix with different grey shades. EDS analysis was carried out to measure the amount of W, C and Co in the regions with different grey shades, as shown in Table 4.4. It can be seen that different shades of grey in the matrix result from the variable levels of W and C dissolved in the binder. Significant amounts of W are found in the bright binder phase, whereas, these are

much reduced in the dark binder. The carbide sizes are about 1 - 4 μm. Also, rounded carbide particles with white layer on their edges are observed in the bright binder phase. Blocky carbide particles are found in the dark grey binder (Fig. 4.37b).

4.6.3 Thickness, Deposition Efficiency, Hardness, Roughness and Volume Fraction Analysis

The thickness, deposition efficiency, hardness, roughness (Ra) and volume fractions of the various phases are all shown in Table 4.2.

4.6.4 Transmission Electron Microscopy

A detailed observation of the coating was characterised by a former Ph.D. student, Stewart (1998). A summary of the main points is reported. Stewart (1998) found that blocky carbide particles confirmed to be a WC showed high densities of dislocation and stacking faults. The core WC particles surrounded with both discrete and completely W_2C without dislocations or stacking faults were also observed. The carbide particles were embedded in an amorphous binder matrix. The carbide particles of W_2C and W were not observed.

Table 4.1 Volume fraction and carbide grain size analysis of powder feedstock calculated by quantitative image analysis.

Conventional Powder	Measured volume fraction		Calculated Weight percent		Mean carbide size
	%WC	%Co	%WC	%Co	(μm)
1. WC-12 wt% Co	81	19	88	12	~ 1.5
2. WC-17 wt% Co (M)	82	18	88	12	~ 0.7
3. WC-17 wt% Co (P)	85	15	91	9	~ 1

Table 4.2 The thickness, deposition efficiency, hardness, roughness and volume fraction analysis of conventional WC-Co coatings.

Coating	Thickness/passes (μm)/	Deposition Efficiency (%)	Hardness (kgf mm^{-2})	Roughness (Ra)	Volume fraction	
					%WC	%Binder phase
HVOLF WC-12 wt% Co	200 / 30	30	1237 ± 93	3.5 ± 0.3	76	24
HVOGF WC-12 wt% Co	200 / 30	52	1288 ± 86	4.6 ± 0.3	67	33
HVOLF WC-17wt%Co(M)	260 / 30	35	1333 ± 54	2.5 ± 0.3	82	18
HVOGF WC-17wt%Co (P)	200 / 30	48	1283 ± 74	4.5 ± 0.3	55	45

Note ± : standard deviation

Table 4.3 The thickness, deposition efficiency, hardness and roughness of the HVOGF sprayed nanoscale WC-12 wt% Co coatings (details of different runs are given in Chapter 3).

Run Number	Thickness/passes (μm)/	Deposition Efficiency (%)	Hardness (kg mm^{-2})	Roughness (Ra : μm)
1	~ 30-50 / 30	35	Not measurable	4.3 ± 0.4
2	~ 110 / 40	36	1206 ± 64	4.7 ± 0.4
3	~ 130 / 40	37	1170 ± 88	6.2 ± 0.4
4	~ 130 / 40	50	1178 ± 111	5.0 ± 0.3

Note ± : standard deviation

Table 4.4 EDS spot analysis for the dark and bright grey binder of the HVOGF sprayed conventional WC-17 wt% Co (P) coating.

	Bright area		Dark area	
Element	At%	Wt%	At%	Wt%
W	40 ± 10	79 ± 8	17 ± 4	54 ± 4
Co	25 ± 10	16 ± 7	40 ± 4	37 ± 2
C	36 ± 13	5 ± 3	42 ± 8	8 ± 3

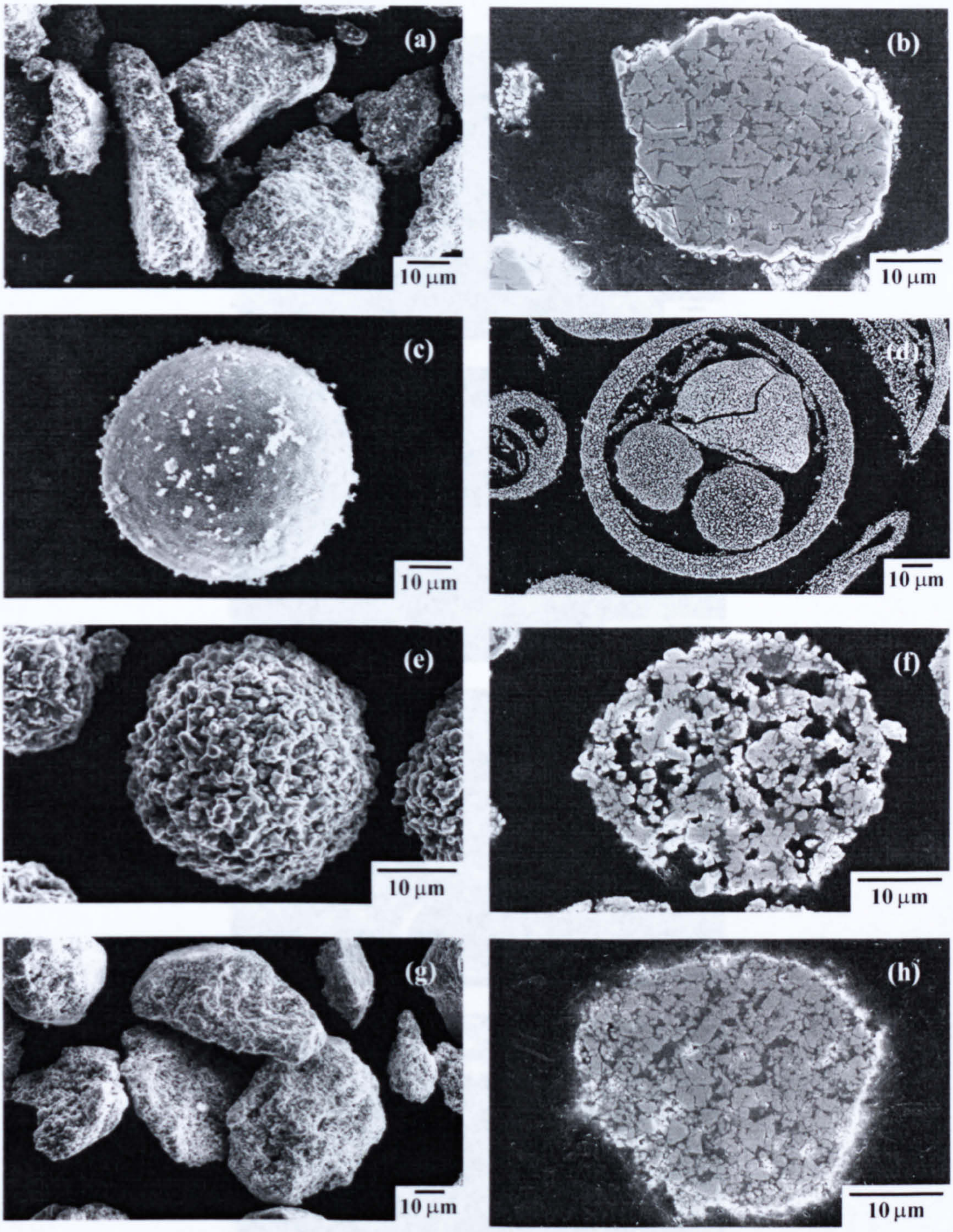

Fig. 4.1 SEM images showing the morphologies and cross sectional microstructure of WC-Co powders.

(a) Blocky and angular morphologies of the conventional WC-12 wt% Co powder.
(b) Cross section at low magnification of (a) exhibiting a fairly dense structure.
(c) Spherical morphology of the nanoscale WC-12 wt% Co powder.
(d) Cross section at low magnification of (c) showing a hollow structure with 10 μm thick shell.
(e) Spherical morphology of the conventional WC-17 wt% Co (M) powder.
(f) Cross section at low magnification of (e) showing a very porous structure.
(g) Angular morphology of the conventional WC-17 wt% Co (P) powder.
(h) Cross section at low magnification of (g) revealing a fairly dense particle.

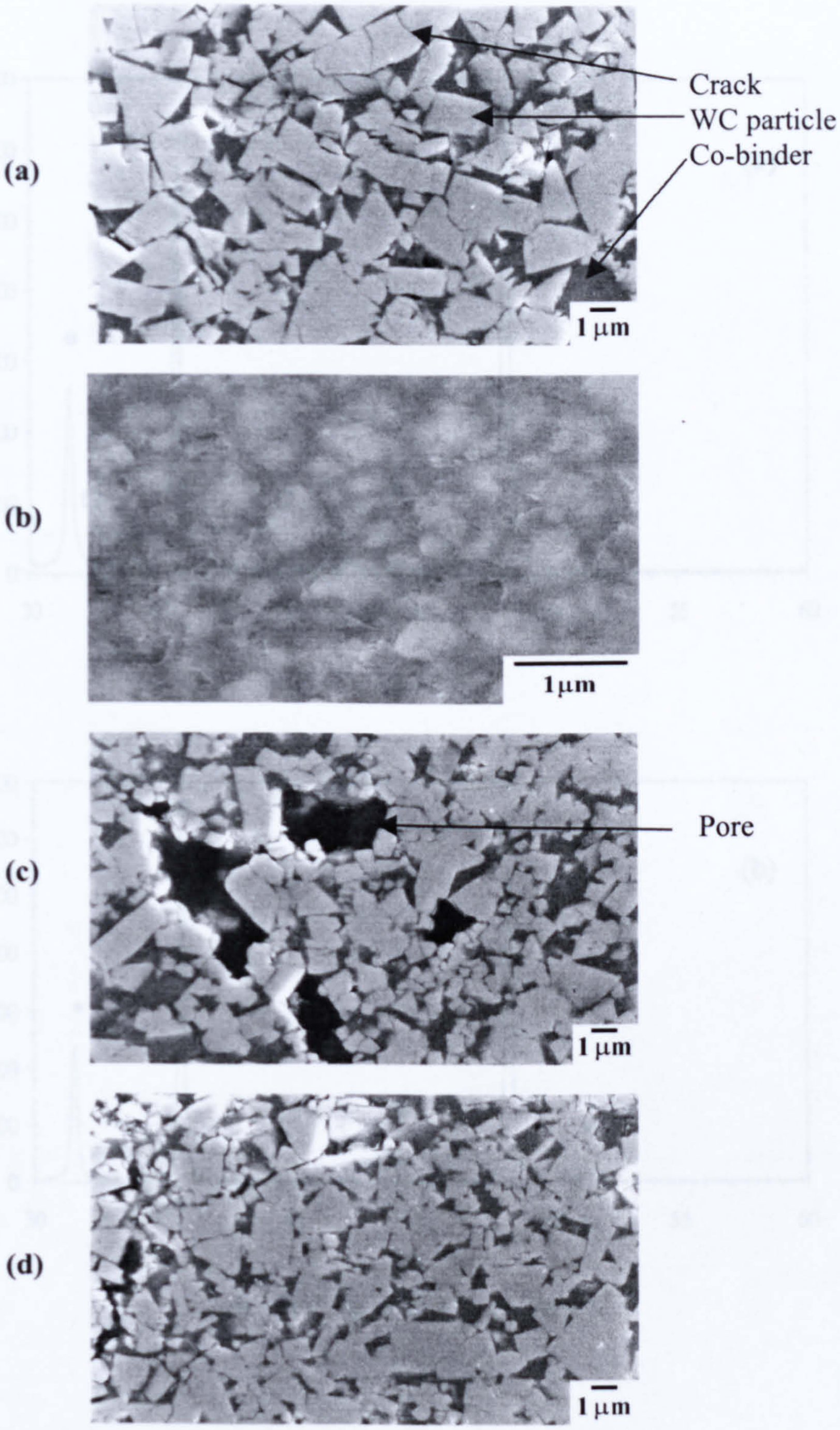

Fig. 4.2 Microstructure at high magnification of the WC-Co powders showing angular particles of WC embedded in the metallic Co. Cracks and pores are also observed.

(a) The conventional WC-12 wt% Co powder
(b) The nanoscale WC-12 wt% Co powder
(c) The conventional WC-17 wt% Co (M) powder
(d) The conventional WC-17 wt% Co (P) powder

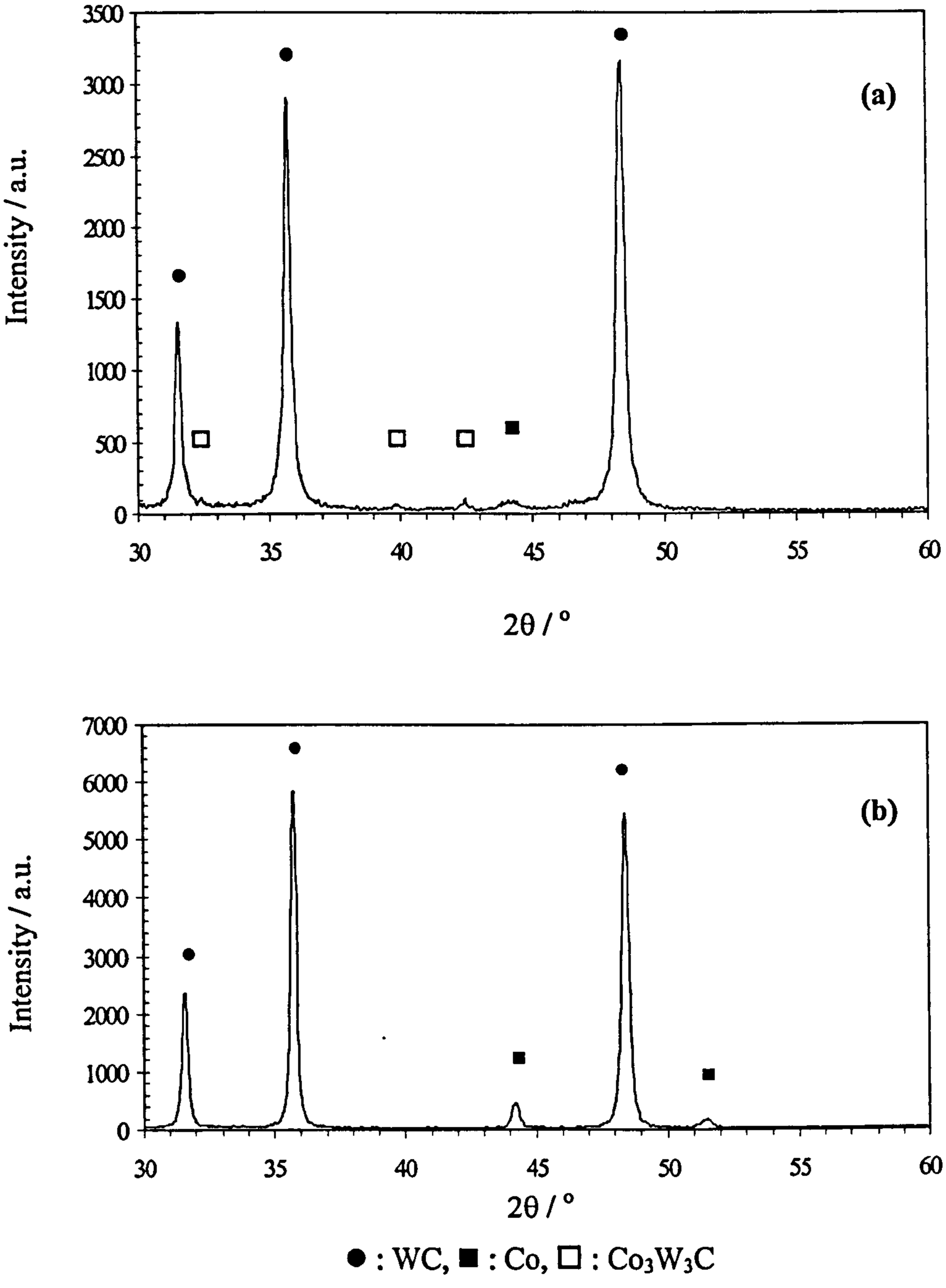

Fig. 4.3 showing the XRD patterns of (a) the conventional WC-12 wt% Co powder showing WC, Co and a small amount of Co_3W_3C peaks, (b) the nanoscale WC-12 wt% Co powder revealing WC and Co peaks.

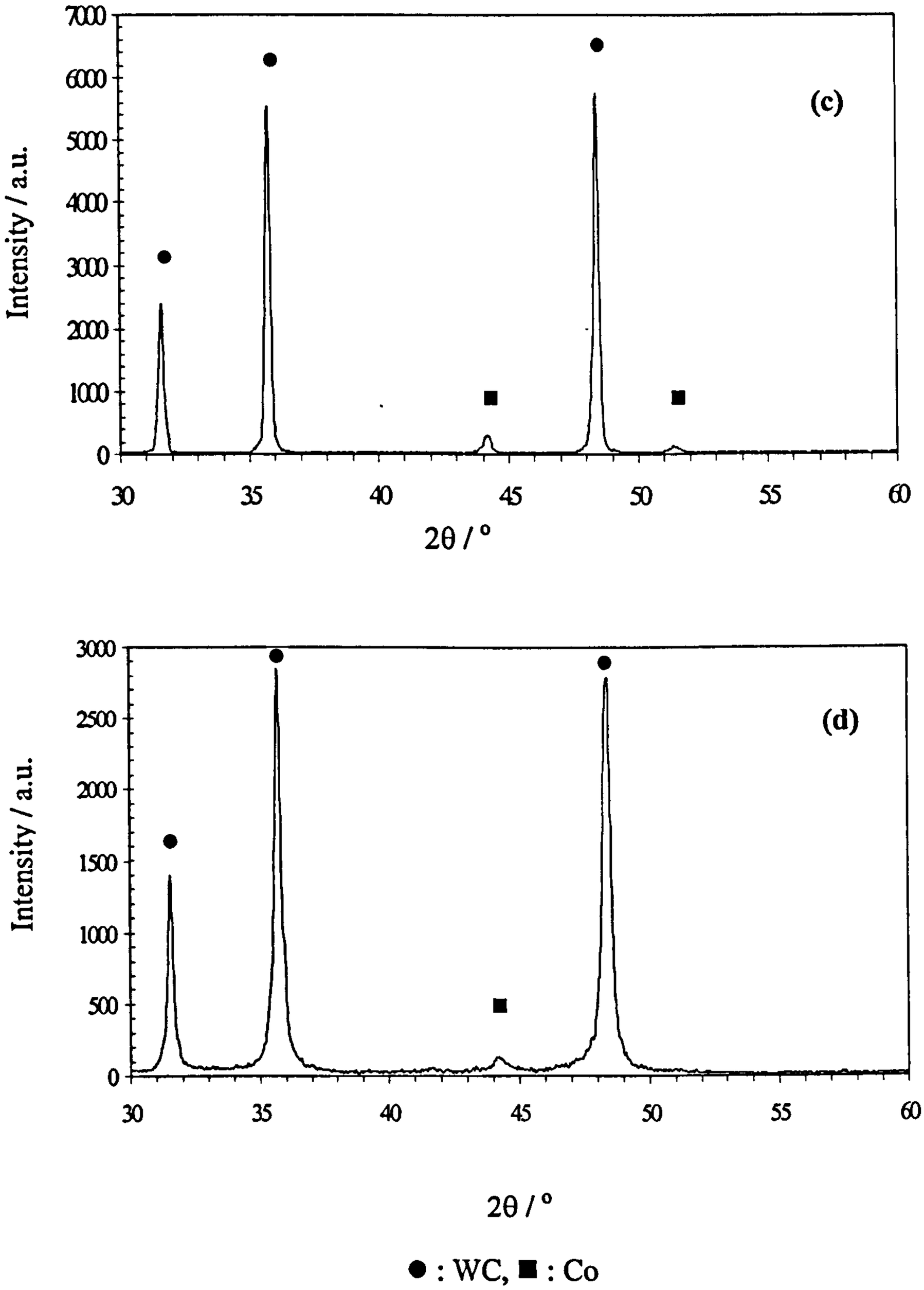

Fig. 4.3 (cont.) showing the XRD patterns of c) the conventional WC-17 wt% Co (M) powder showing WC and Co peaks, d) the conventional WC-17 wt% Co (P) powder indicating WC and Co peaks.

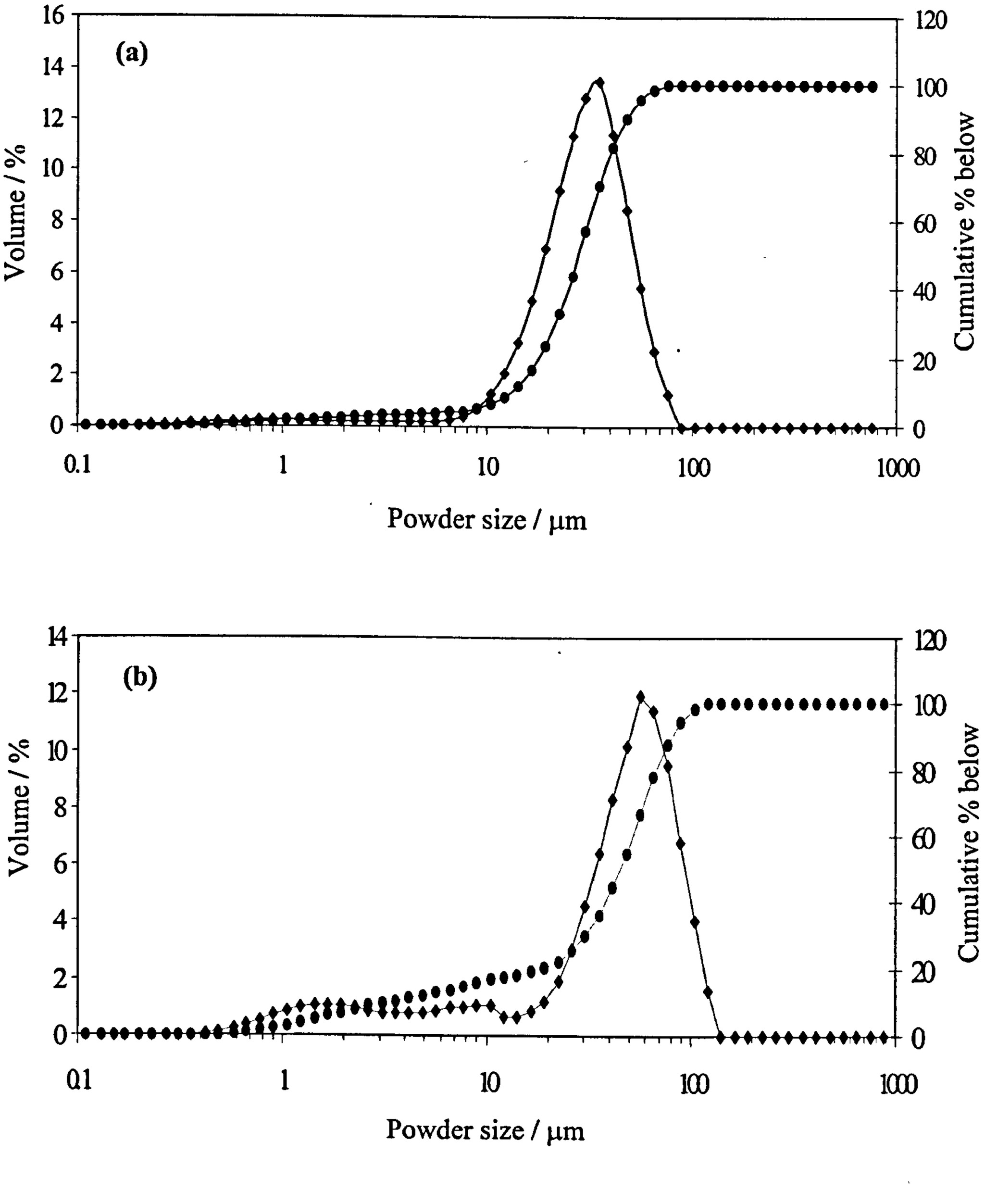

Fig.4.4 showing powder distribution of (a) the conventional WC-12 wt% Co powder, (b) the nanoscale WC-12 wt% Co powder.

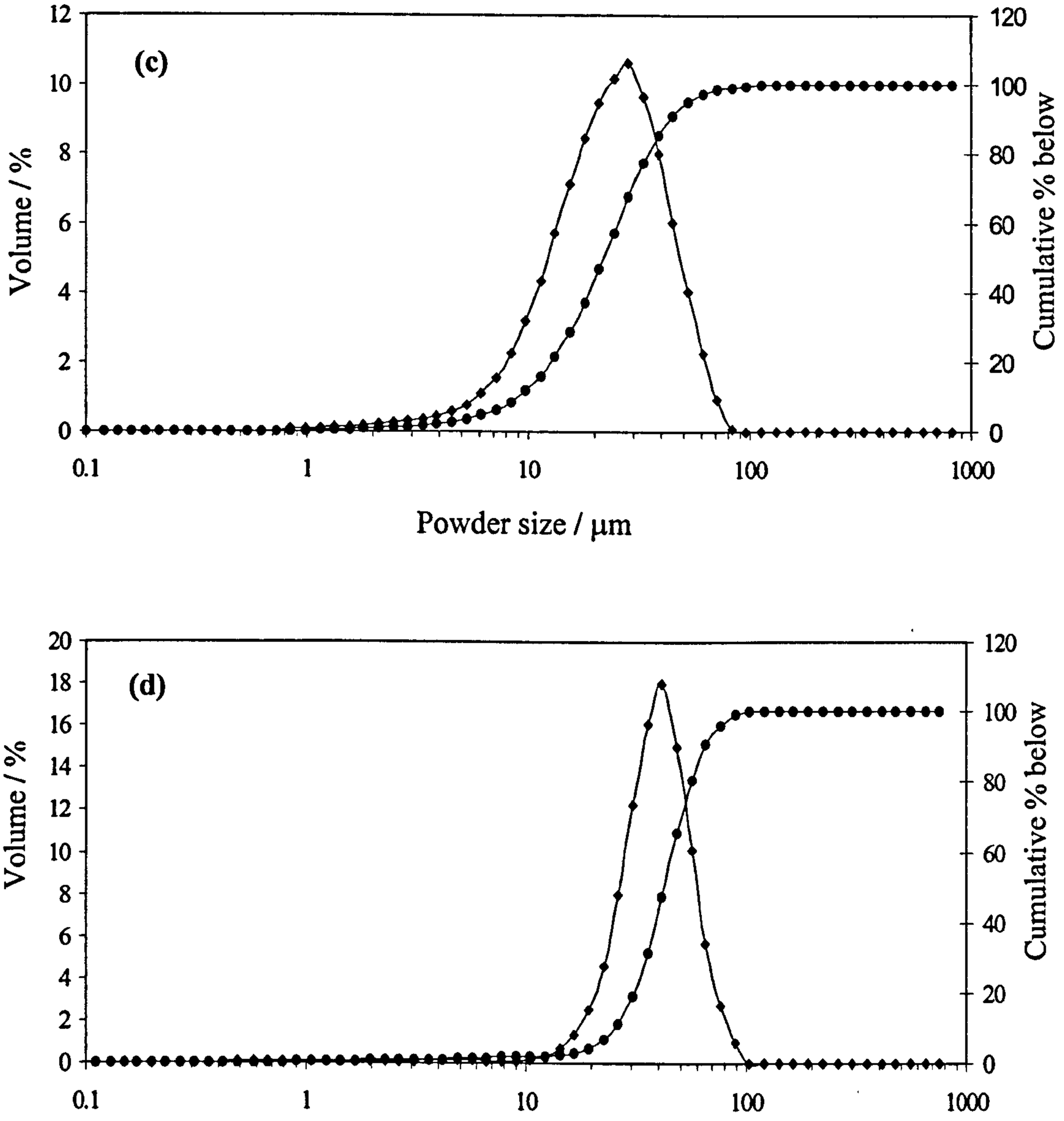

Fig.4.4 (cont.) showing powder distribution of (c) the conventional WC-17 wt% Co (M) powder, (d) the conventional WC-17 wt% Co (P) powder.

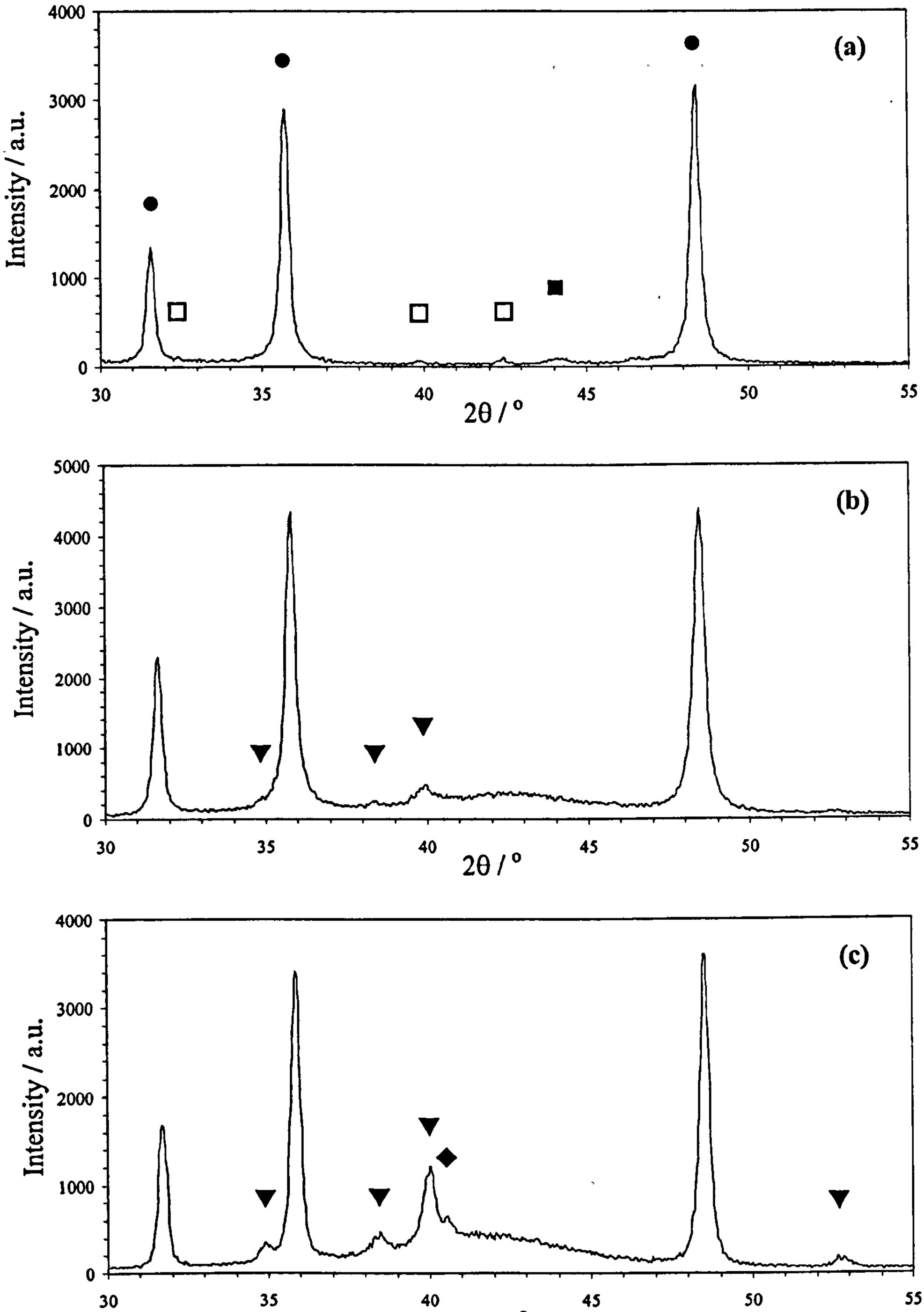

Fig 4.5 The XRD spectra of (a) the conventional WC-12 wt% Co powder; (b) the HVOLF sprayed WC-12 wt% Co coating. In the coating, in addition to WC, a small amount W_2C is observed with a broad diffuse peak between $2\theta = 37°$-$46°$ and (c) the HVOGF sprayed conventional WC-12 wt% Co coating showing WC peaks, prominent W_2C peaks and a small W peak.

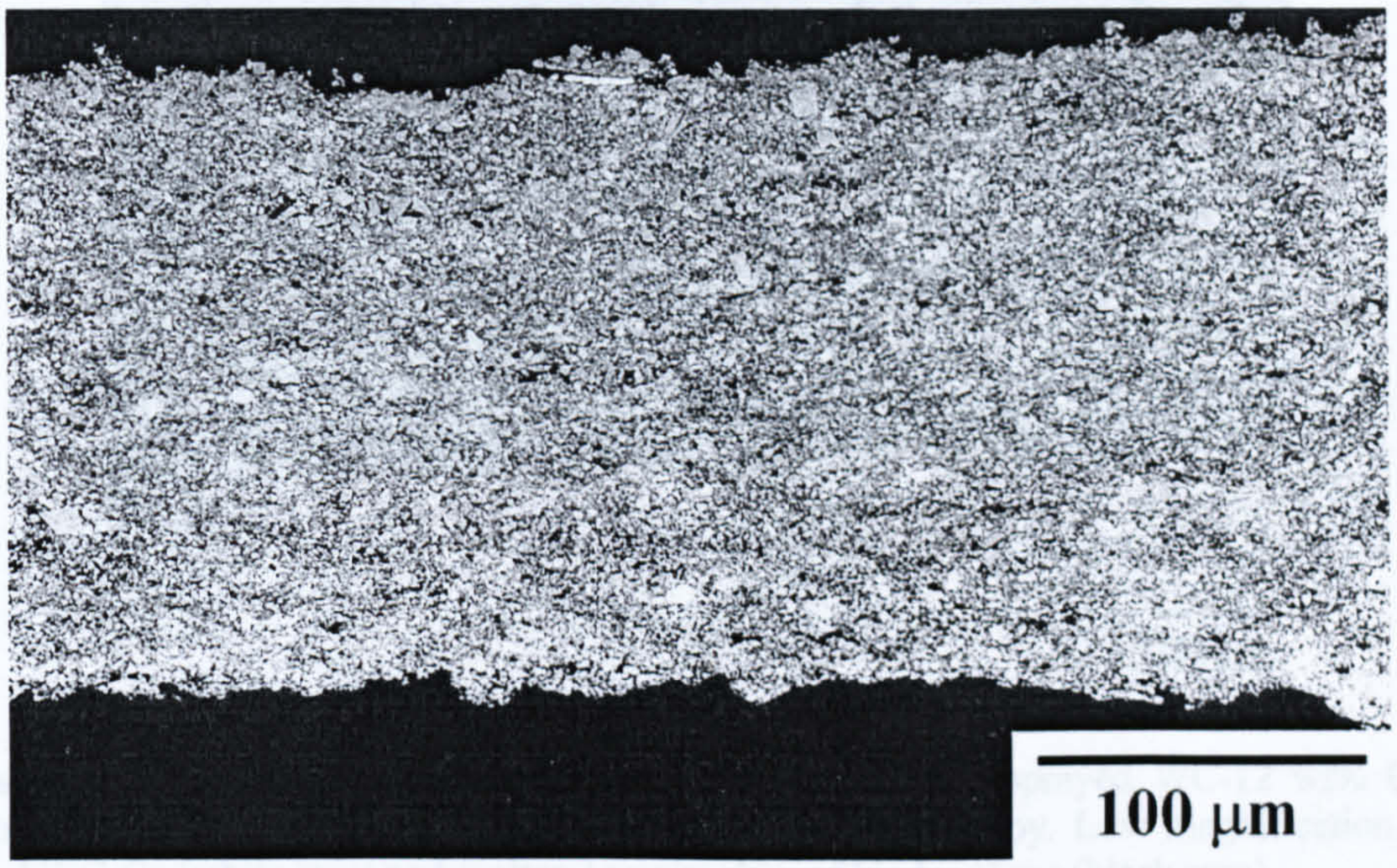

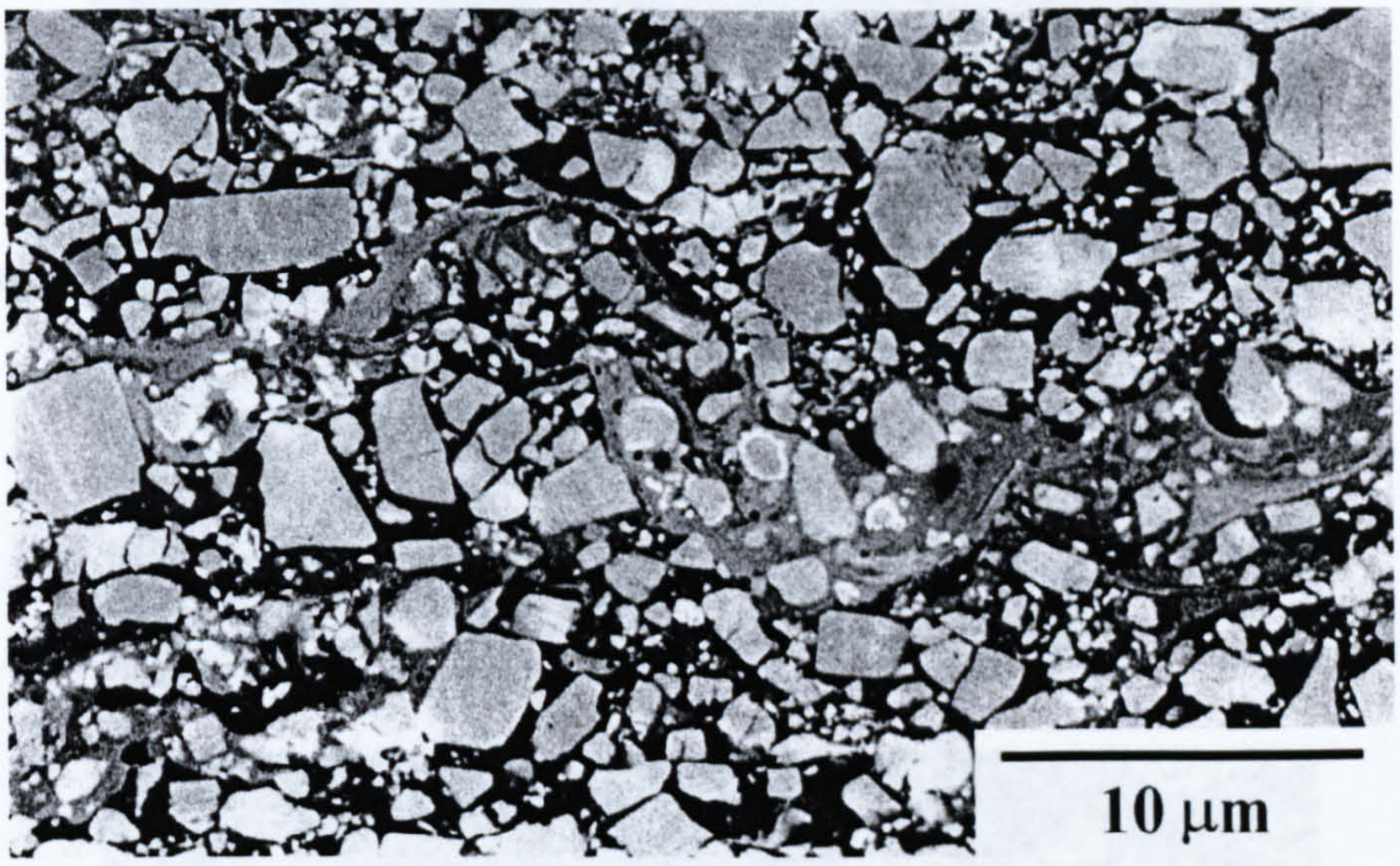

Fig. 4.6 A cross sectional microstructure of HVOLF sprayed the conventional WC-12 wt% Co showing (a) a small amount of porosity with homogeneous distribution of carbide particles at low magnification and (b) blocky carbides with somewhat rounded edges, different grey shades of binder phase and white layer at the edges of some carbide particles in the brighter binder matrix.

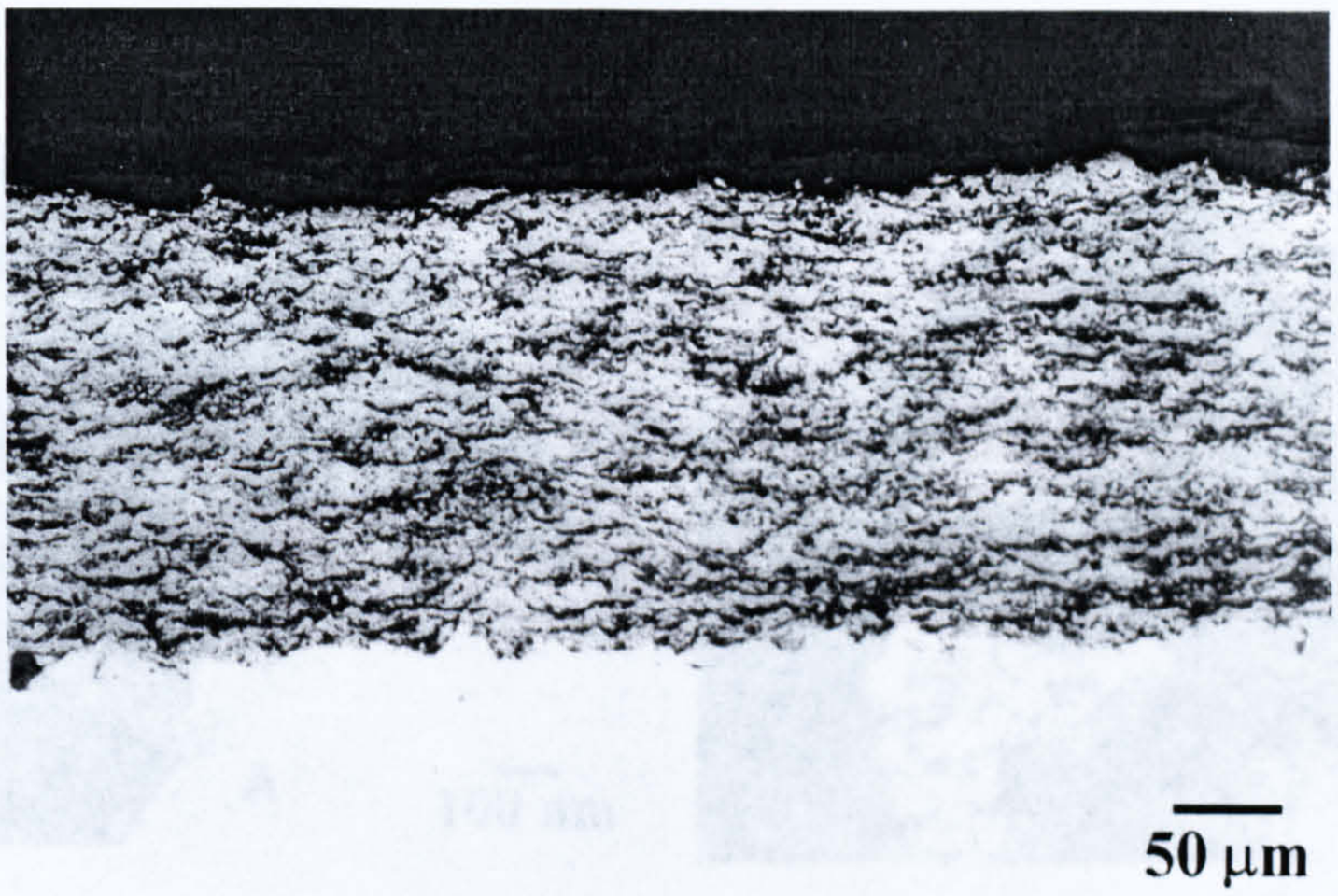

Fig. 4.7 showing the cross sectional microstructure of the HVOLF sprayed WC-12 wt% Co coating etched with Murakami's reagent and observed by an optical microscopy. Low magnification indicating the unmelted WC-Co (white area) and molten / semimolten of binder phase (black area).

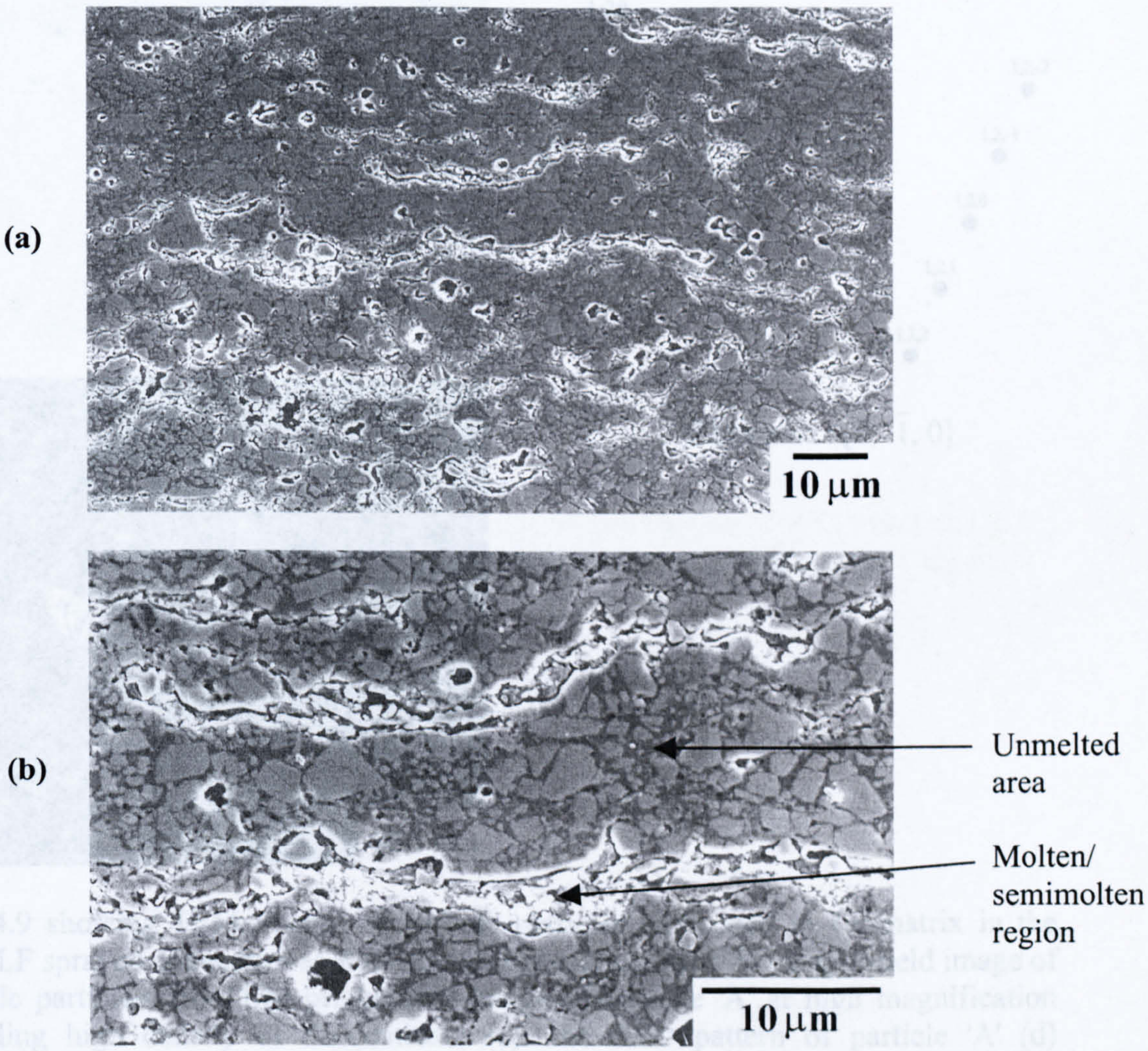

Fig. 4.8 showing the cross sectional microstructure of the HVOLF sprayed WC-12 wt% Co observed by SEM (SE mode). The microstructure was etched with Murakami's reagent. (a) Low magnification showing lamellar splat structure. (b) High magnification showing the edges of the splats attacked with etchant.

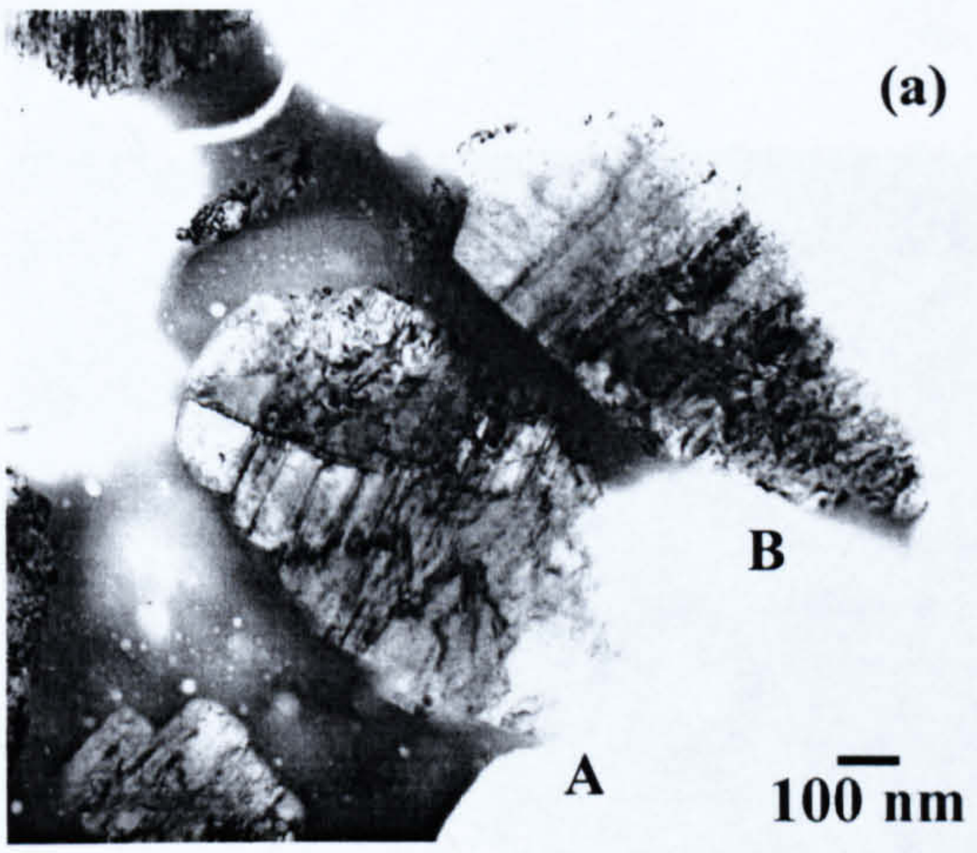

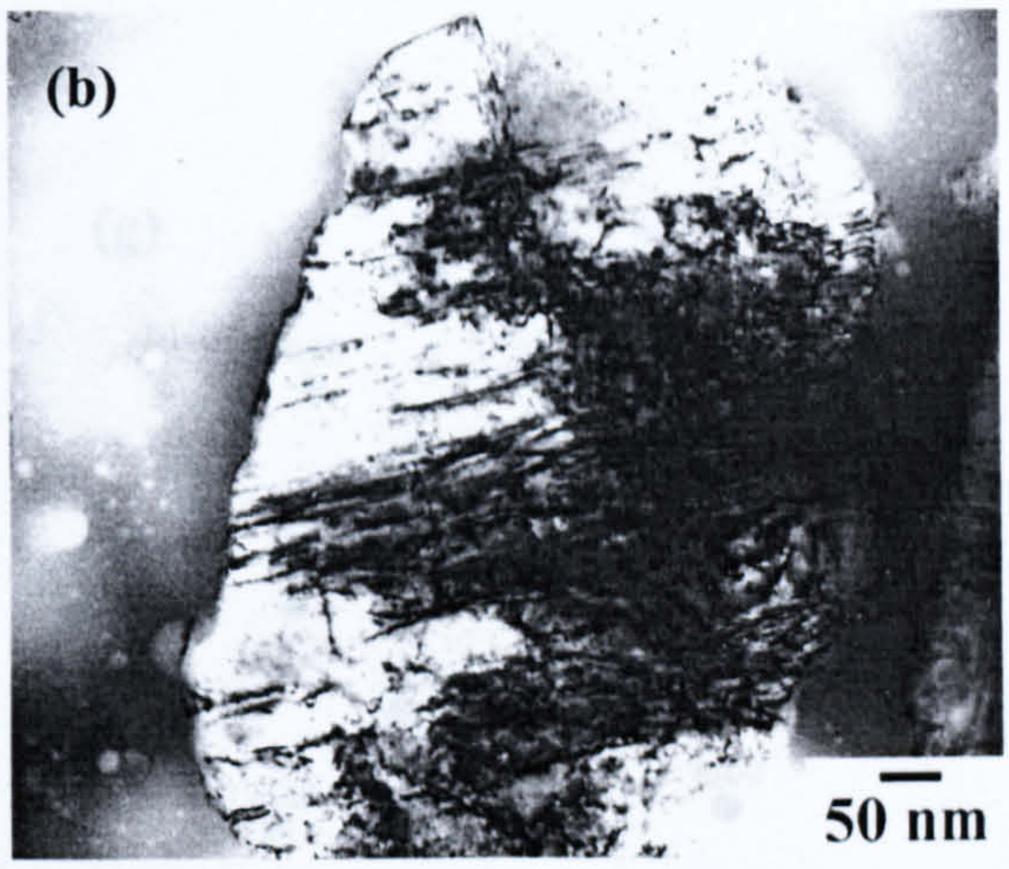

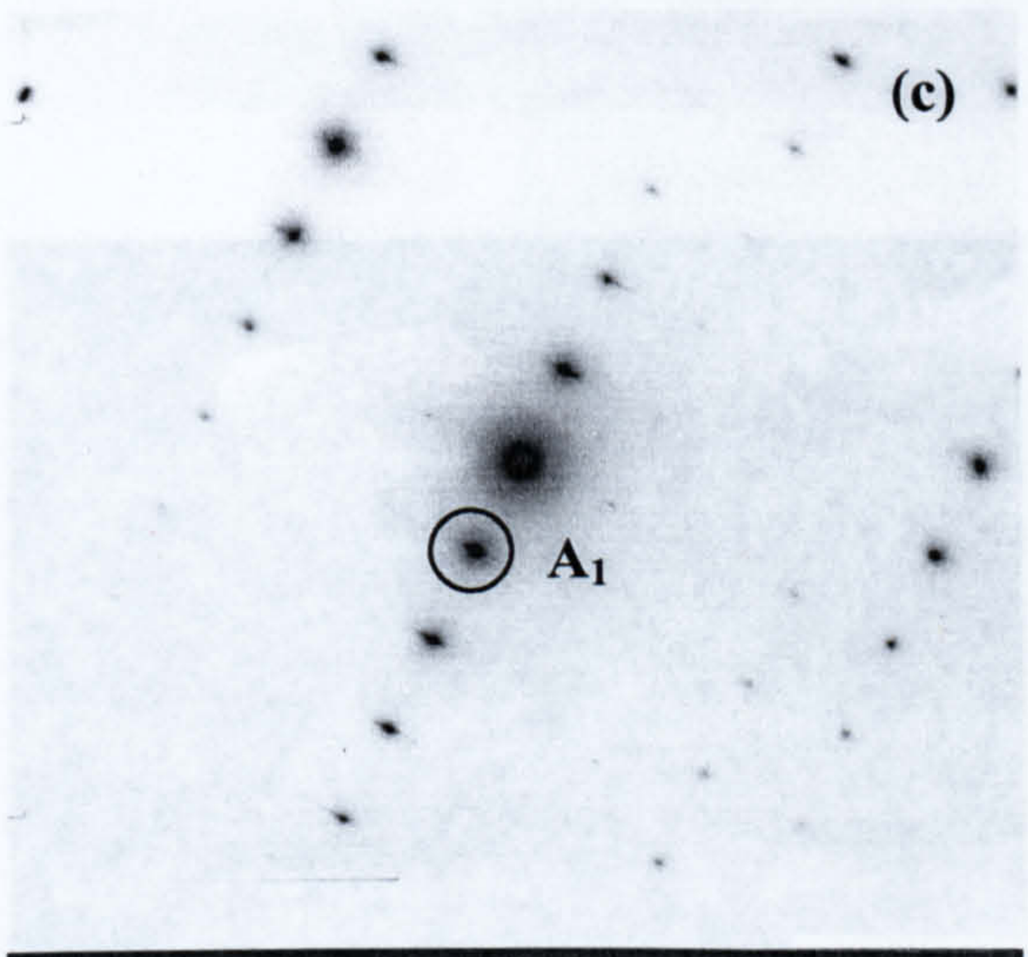

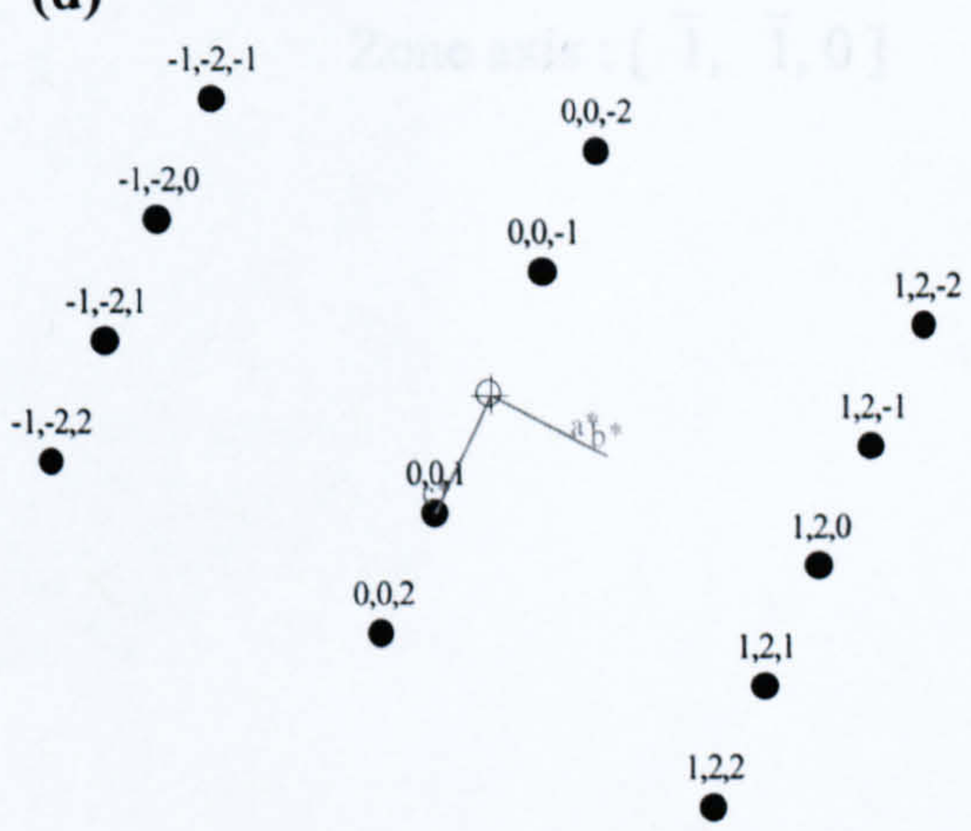

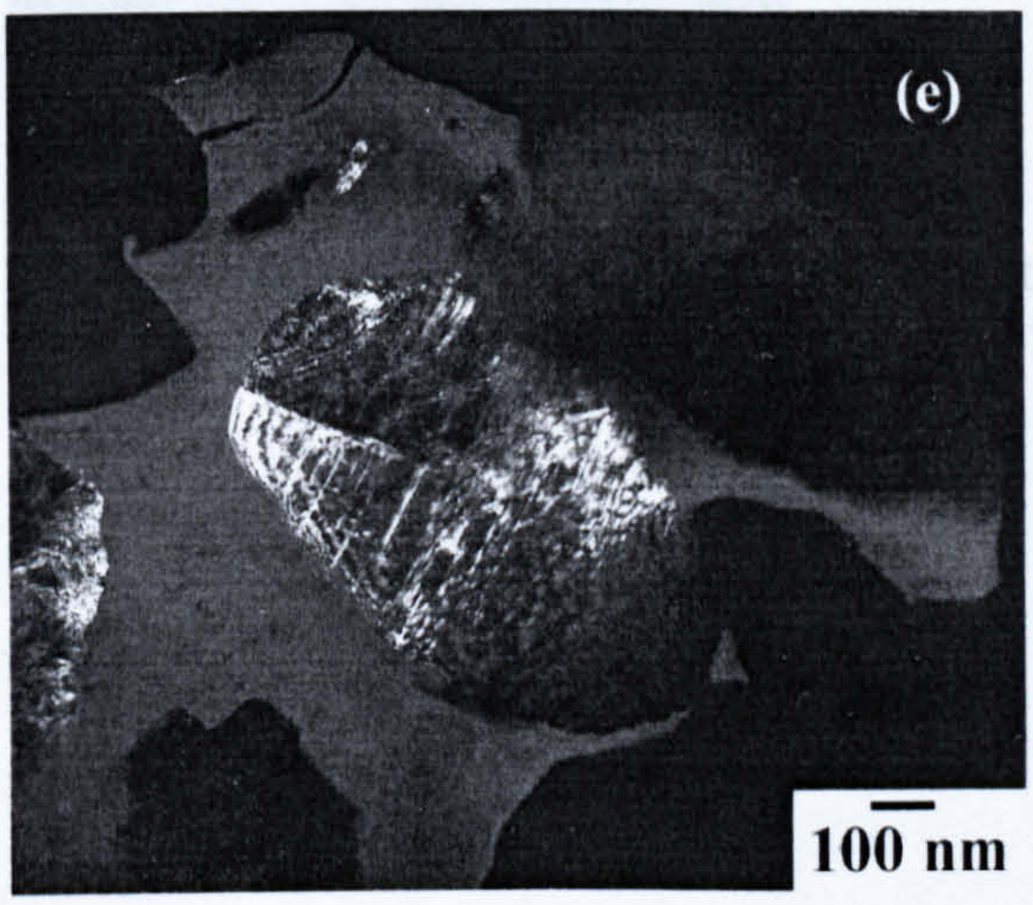

Fig. 4.9 showing TEM images of carbide particles embedded in Co-matrix in the HVOLF sprayed conventional WC-12 wt% Co coating. (a) TEM bright-field image of carbide particles; (b) TEM bright field image of particle 'A' at high magnification revealing high density of dislocations; (c) The SAD pattern of particle 'A' (d) Schematic of (c) confirming WC with [2, $\bar{1}$, 0] zone axis; (e) TEM dark field image of particle 'A' produced from diffraction spot 'A_1'.

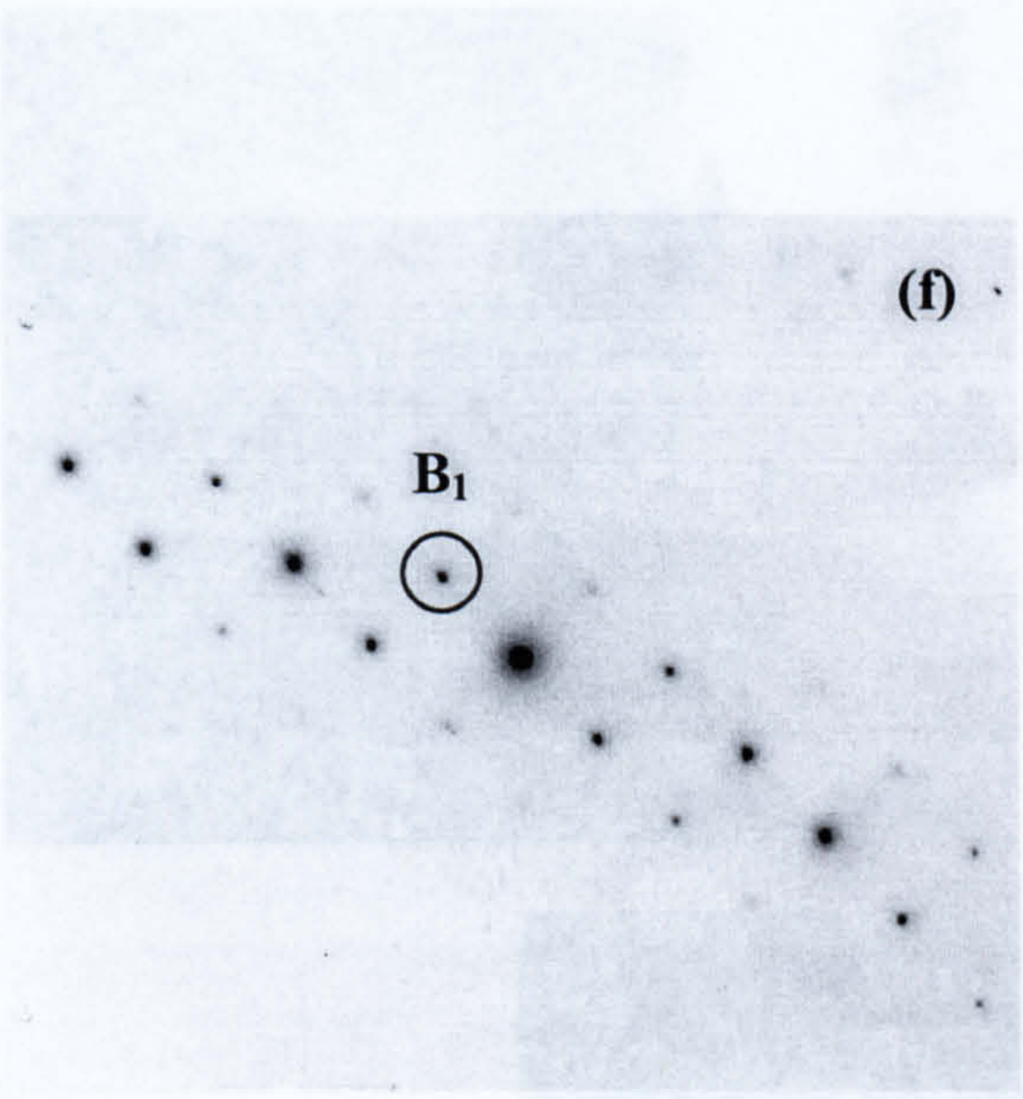

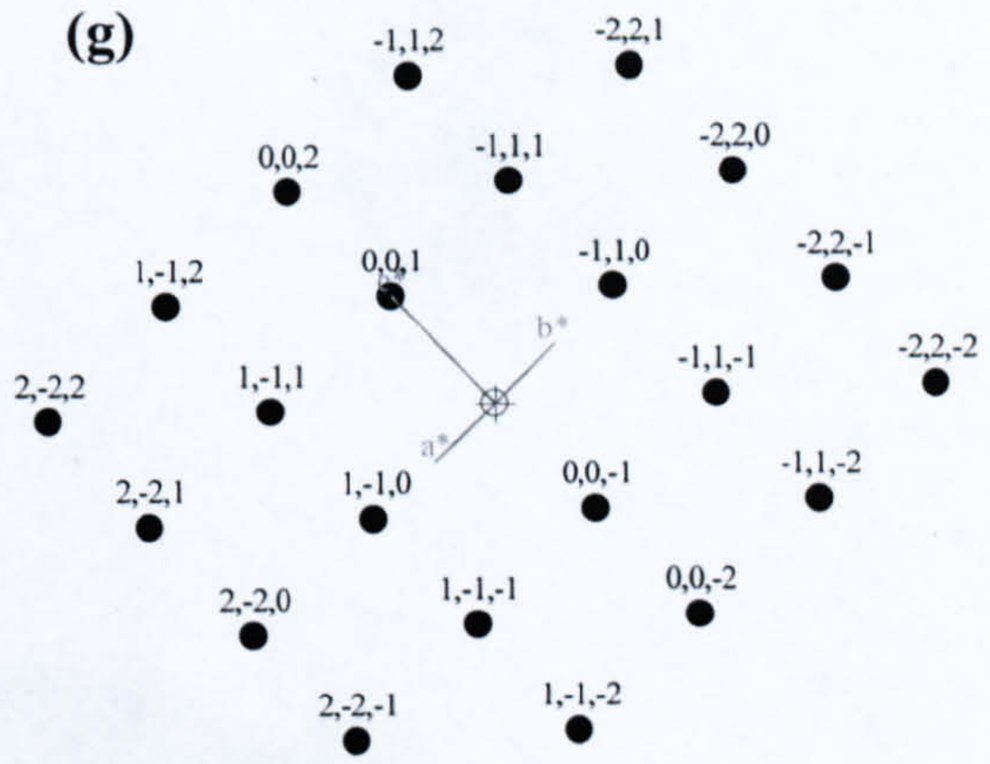

Zone axis : [$\bar{1}$, $\bar{1}$, 0]

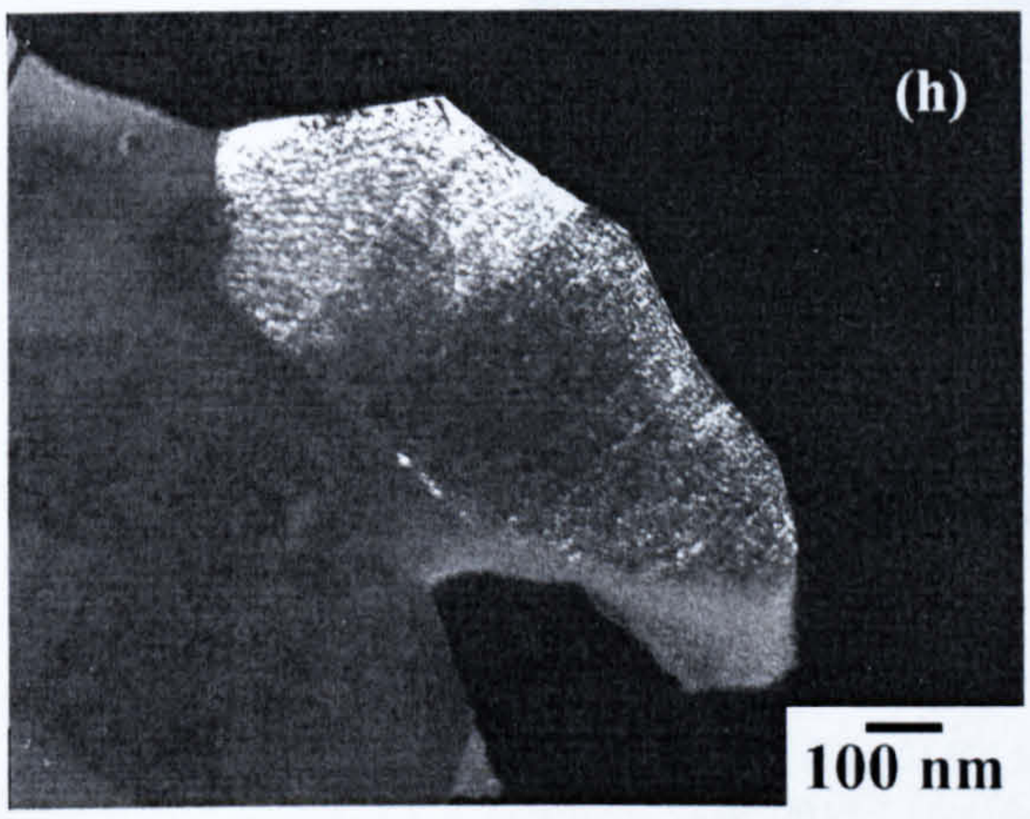

Fig. 4.9 (cont.) (f) The SAD pattern of particle 'B' (g) relating to WC with [$\bar{1}$, $\bar{1}$, 0] zone axis (h) a dark field image of particle 'B' taken from a diffraction spot 'B_1' in (f).

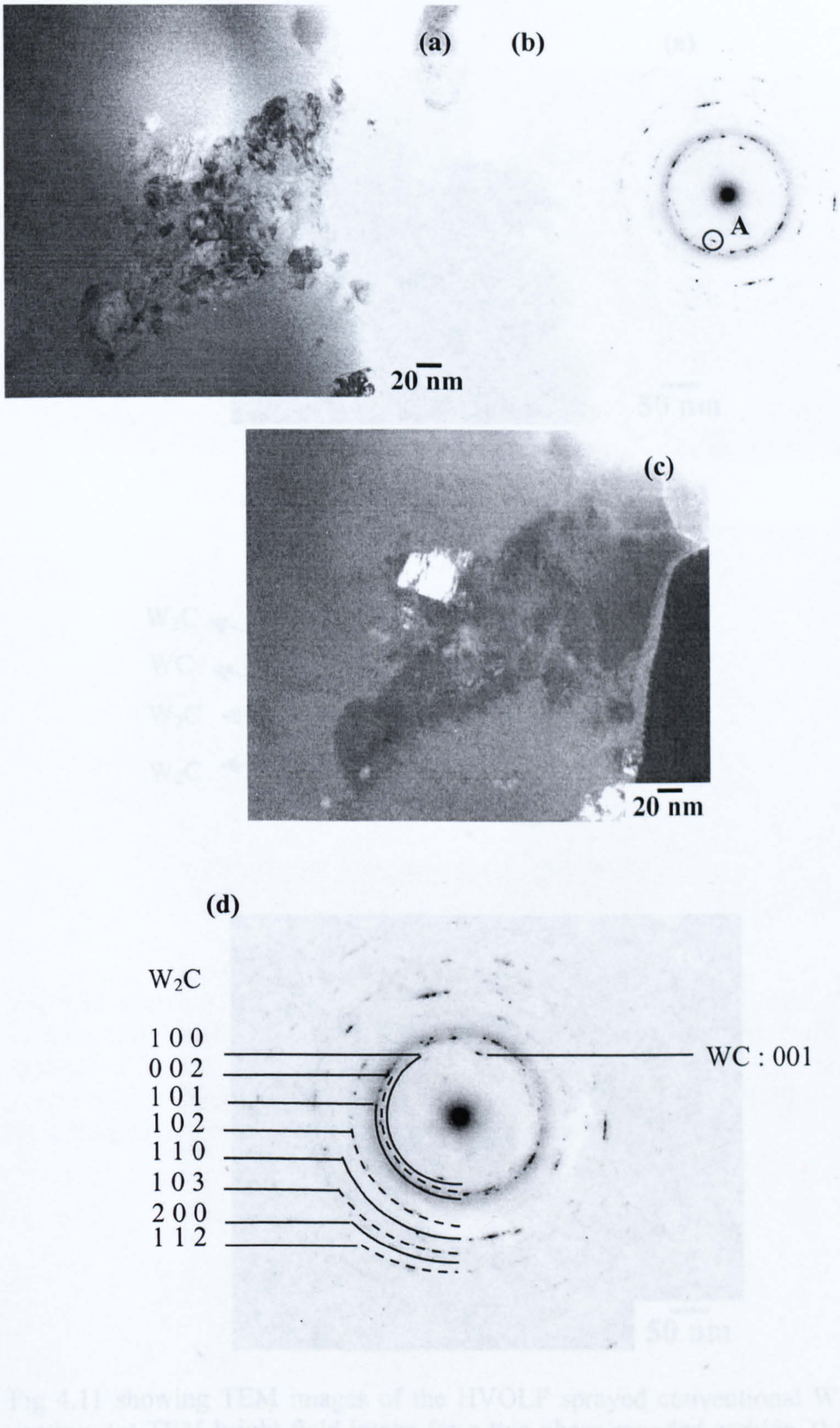

Fig. 4.10 showing TEM images of the HVOLF sprayed conventional WC-12 wt% Co coating. (a) TEM bright field image of a cluster of carbide particles in Co-matrix, (b) The SAD pattern taken from (a), (c) TEM dark field image produced from a diffraction spot 'A' in (b), (d) Corresponding to (b) showing ring diffraction patterns of W_2C and a diffraction spot of WC.

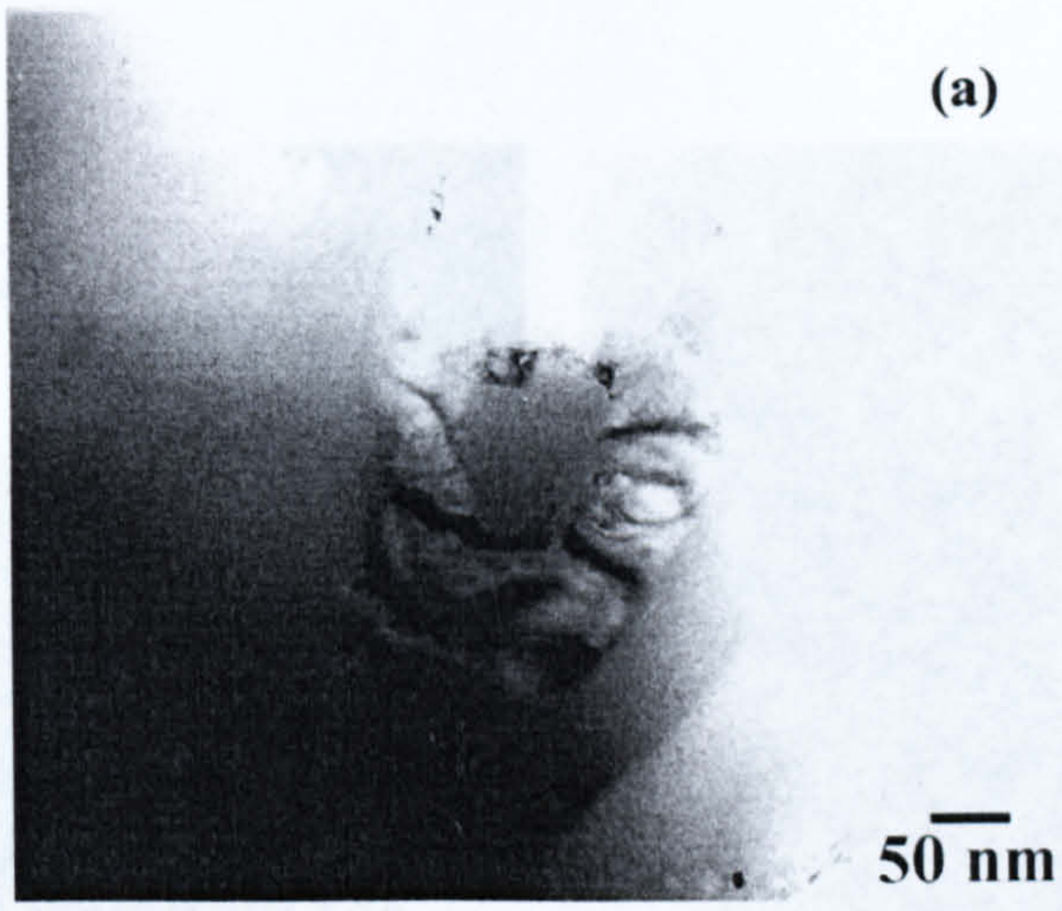

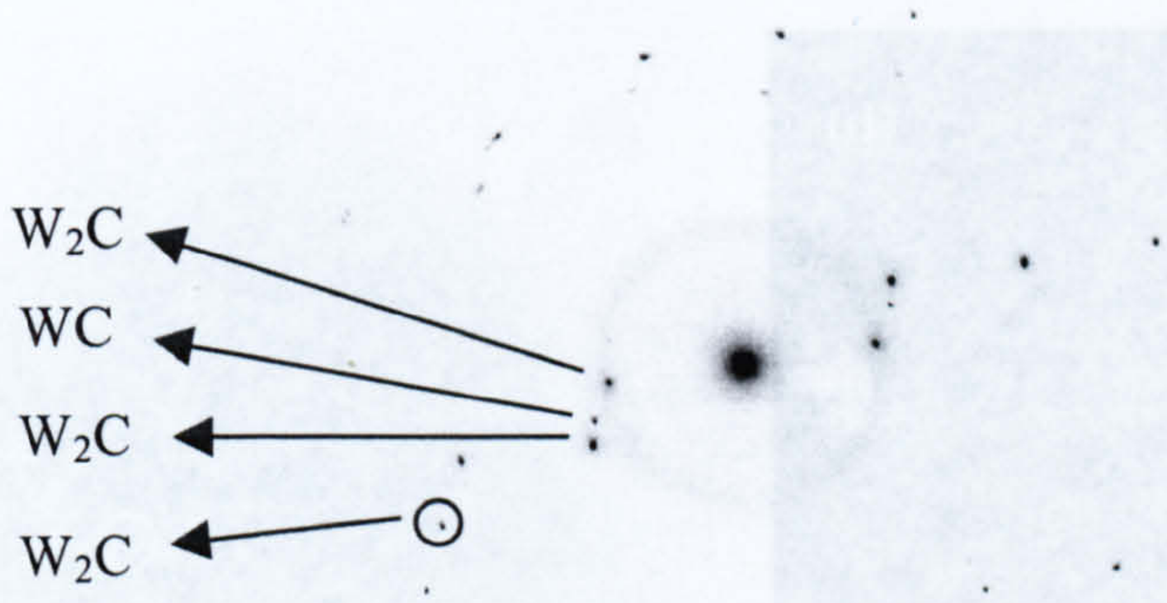

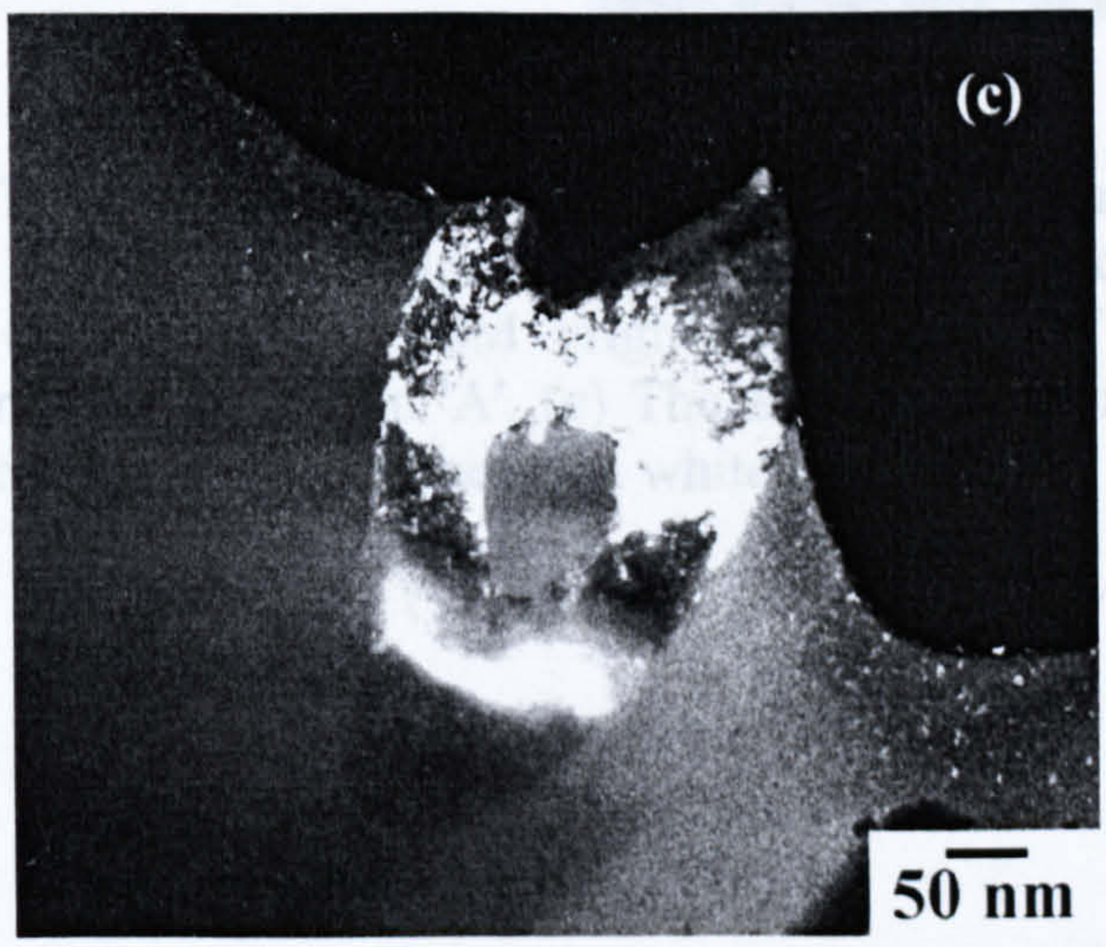

Fig 4.11 showing TEM images of the HVOLF sprayed conventional WC-12 %Co coating. (a) TEM bright field image for a two phase rounded carbide, (b) The SAD pattern showing the WC core and the W_2C surrounded with the core WC, (c) TEM dark field image taken from a diffraction spot in a black circle indexed to W_2C.

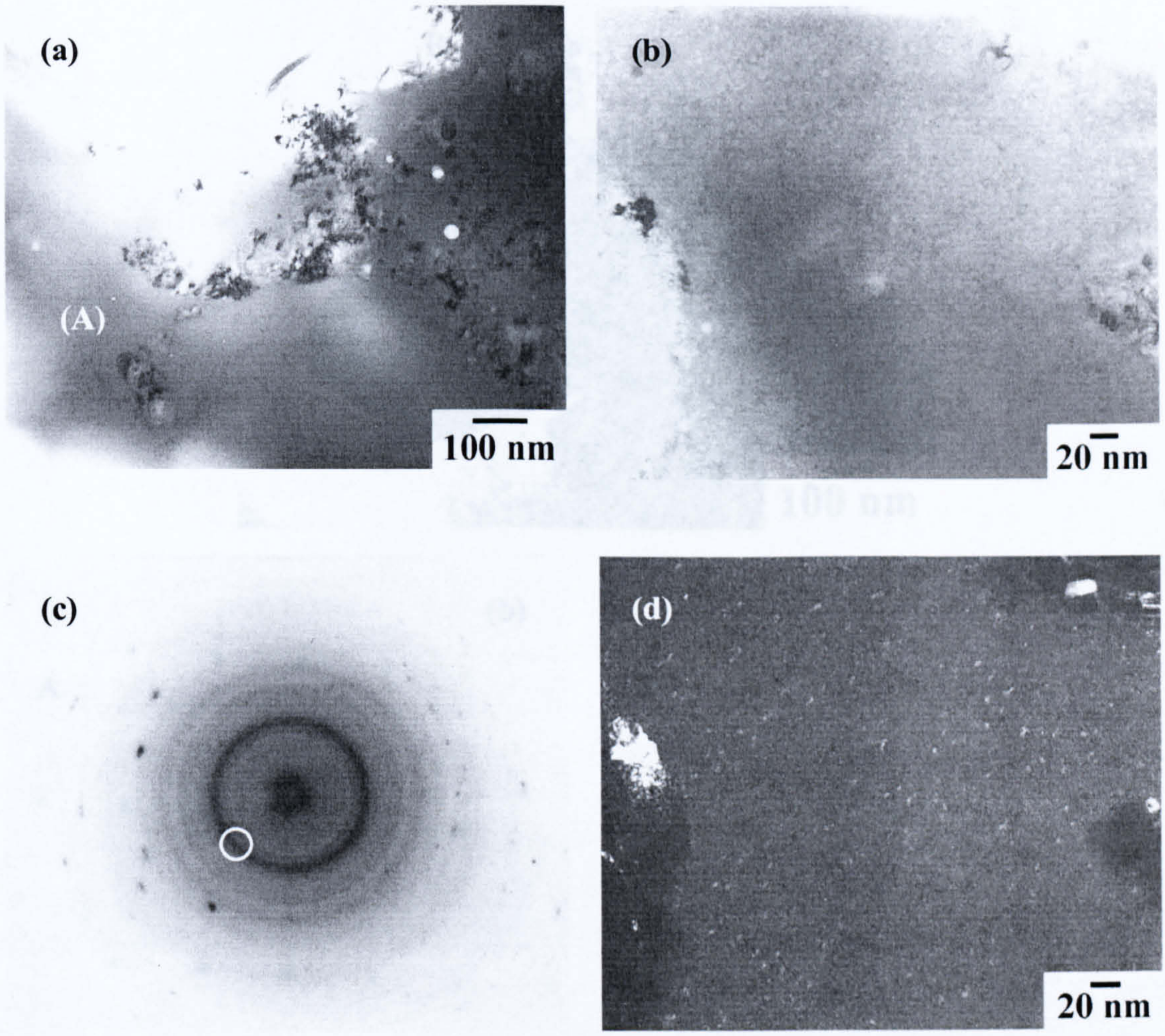

Fig 4.12 showing TEM images of the HVOLF sprayed conventional WC-12 %Co coating. (a) TEM bright field image at low magnification of carbide particles embedded in the Co-matrix, (b) TEM bright field image of Co-matrix at high magnification taken from a position 'A', (c) The SAD pattern of (b), (d) TEM dark field image produced from diffracted beam in white circle in (c).

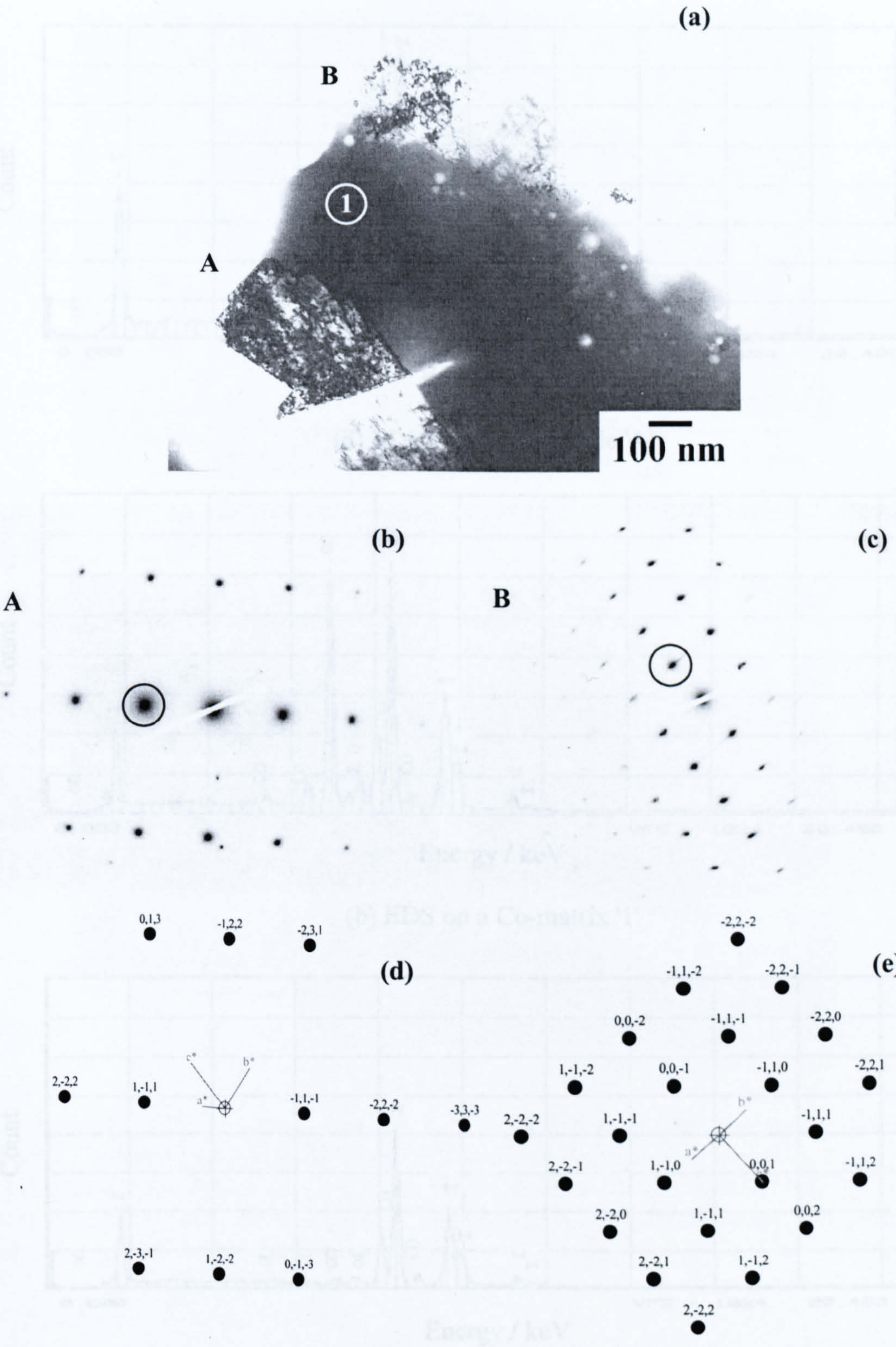

Fig. 4.13 showing TEM images of the HVOLF sprayed conventional WC-12 %Co coating. (a) TEM bright field image showing carbide particles in Co-matrix, (b) and (c) Showing the SAD patterns of particles 'A' and 'B', respectively, (d) and (e) Corresponding to (b) and (c) indexed to WC with [$\bar{4}$, $\bar{3}$, 1] and [$\bar{1}$, $\bar{1}$, 0] zone axes, respectively.

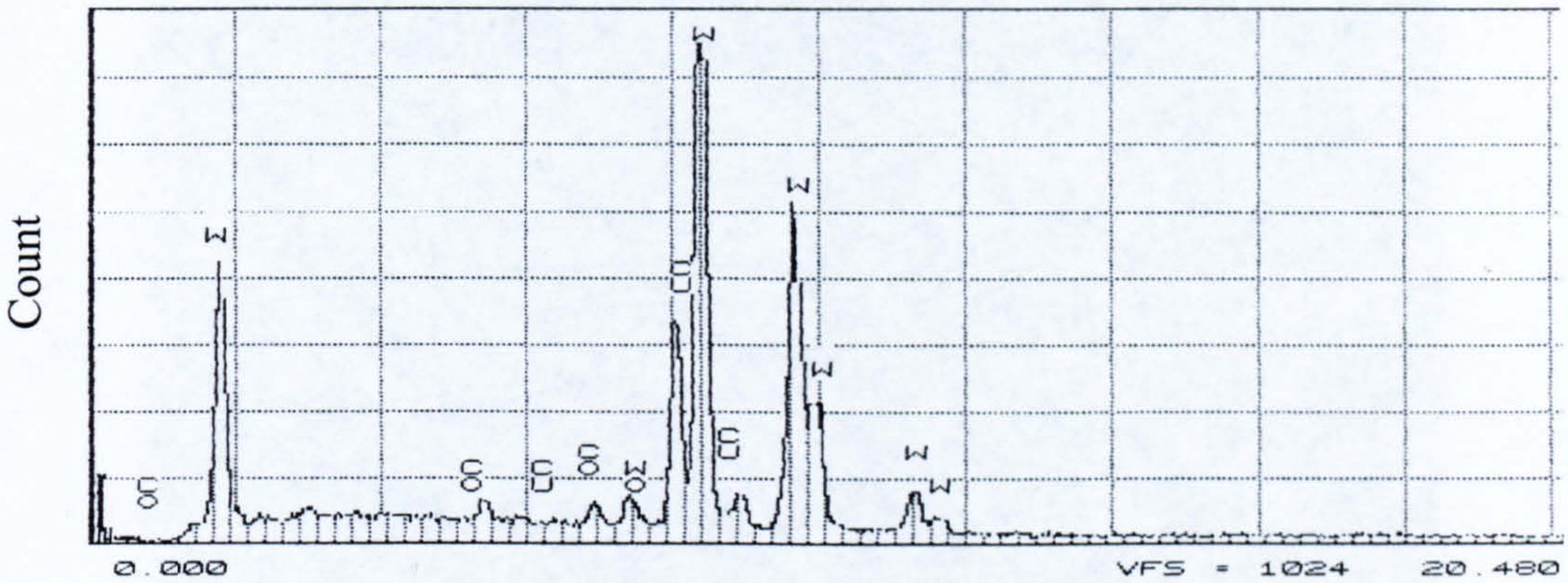

(a) EDS on a WC particle 'A'

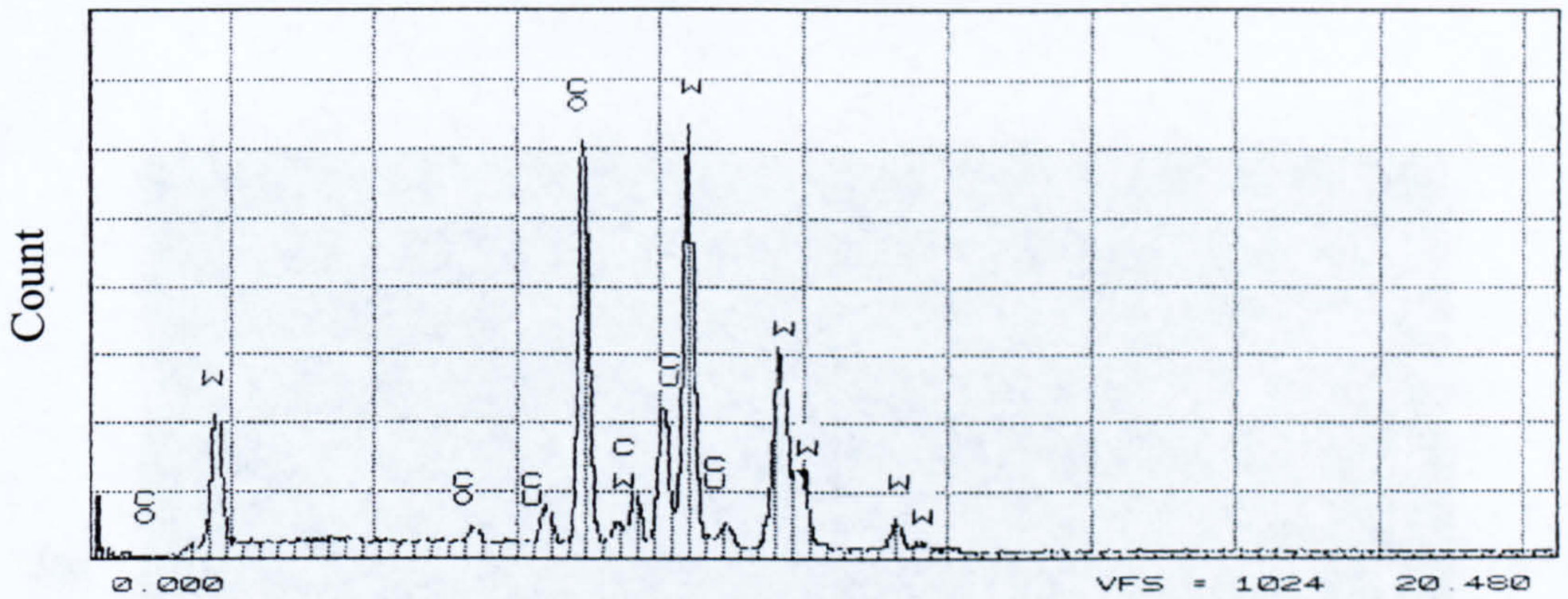

(b) EDS on a Co-matrix '1'

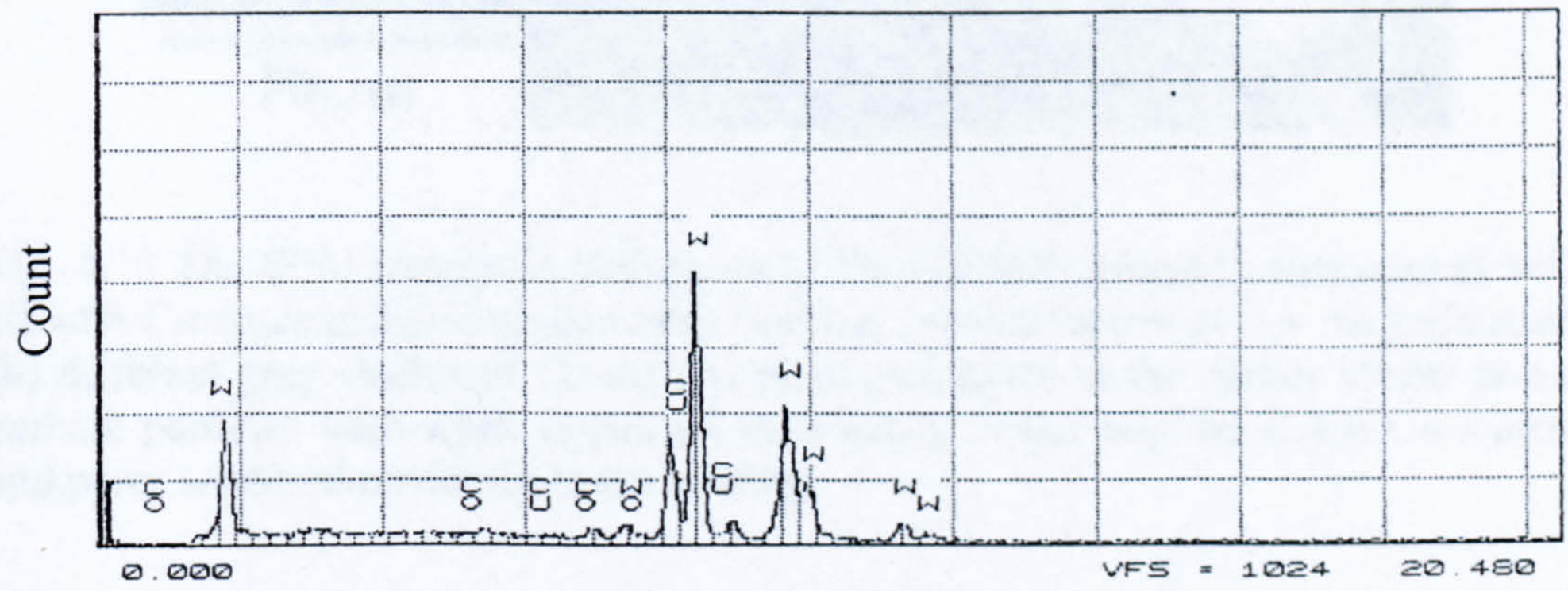

(c) EDS on a WC particle 'B'

Fig. 4.14 The EDSA spectra taken from a TEM bright field image in Fig 4.13 (a) showing the spectrum of WC particle 'A', (b) showing the spectrum of the Co-matrix at position '1', (c) showing the spectrum of WC particle 'B'.

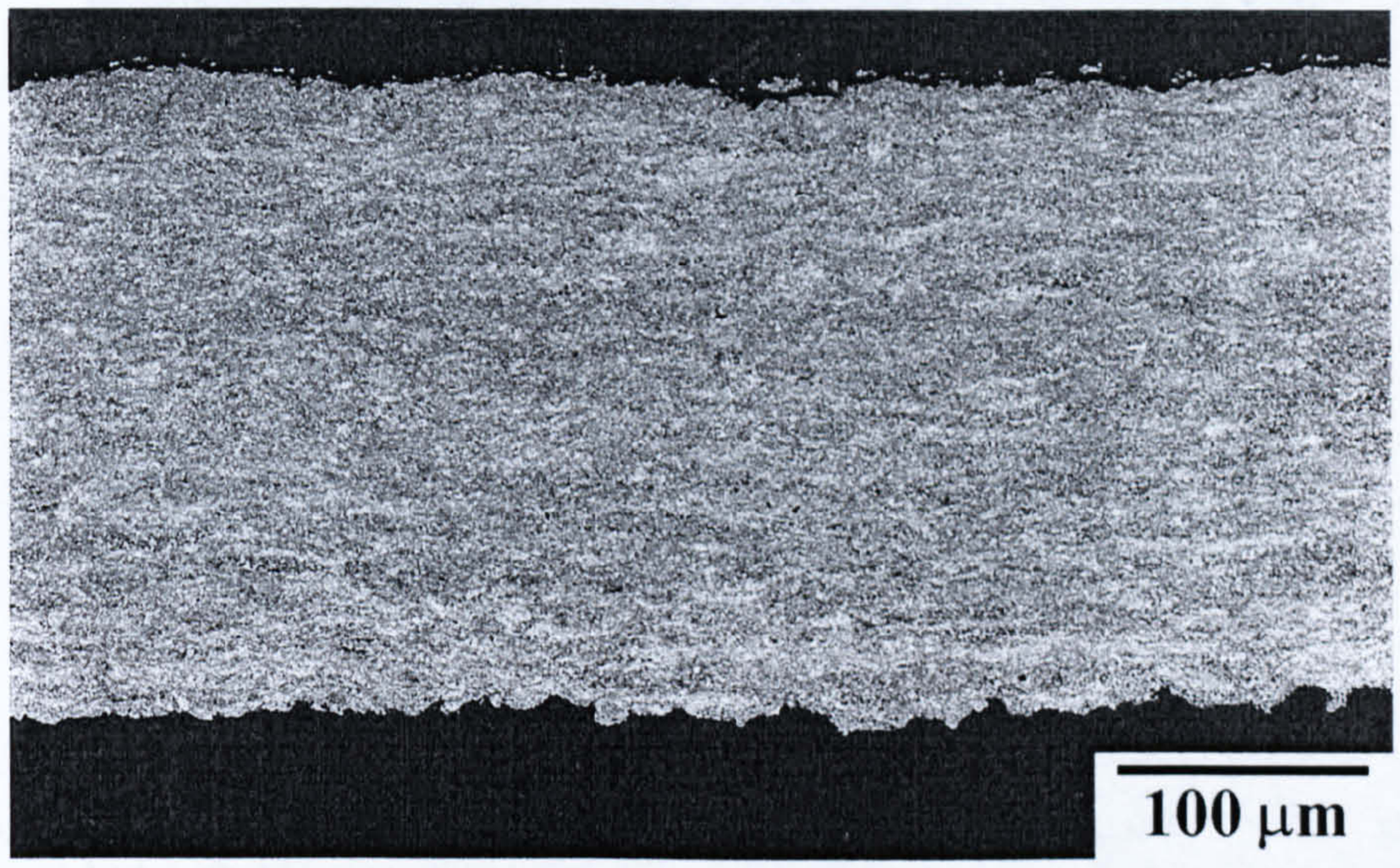

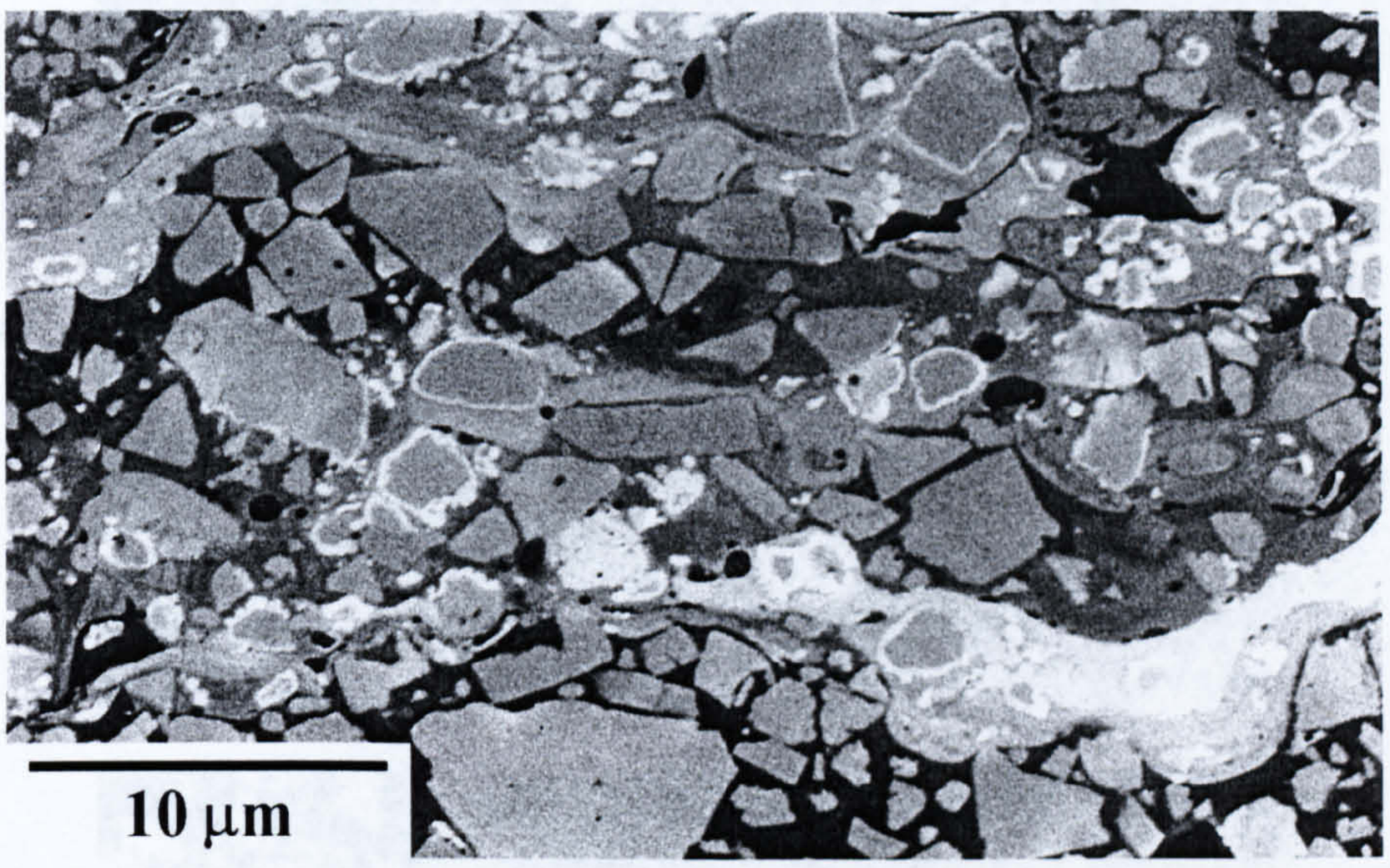

Fig. 4.15 The SEM images in BSI mode of the HVOGF sprayed conventional WC-12 wt% Co coating showing (a) a very fine and dense structure at low magnification, (b) different grey shades of Co-matrix, blocky carbides in the darker binder phase, carbide particles with white layers on their edges in the brighter shade Co-matrix, and pores scattered randomly in the coating.

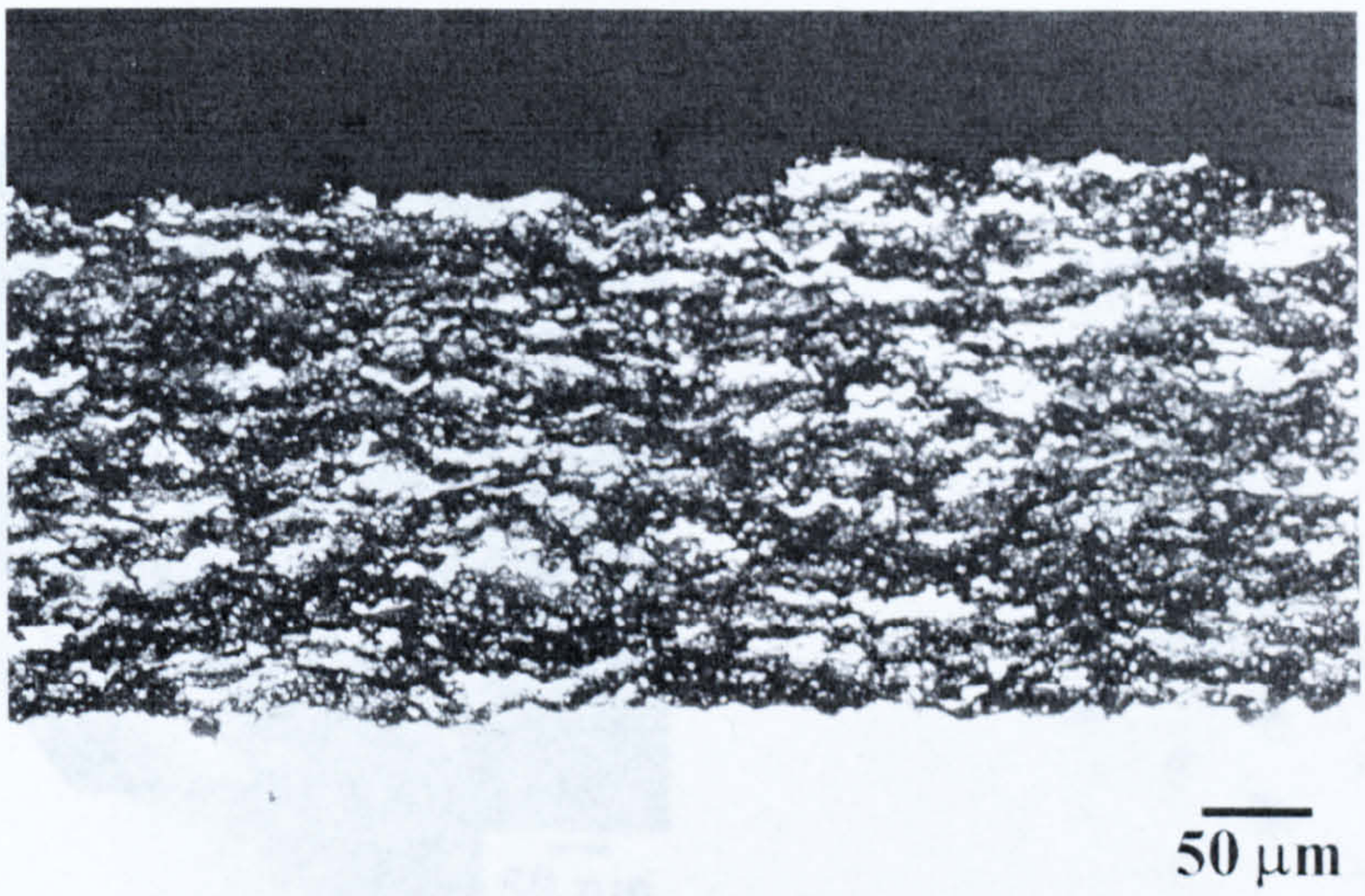

Fig. 4.16 Optical micrographs of the cross section of the HVOGF sprayed WC-12 wt% Co coating etched with Murakami's reagent. Low magnification shows the higher amount of the dark area (molten or semi-molten areas) than the white area (unmelted areas).

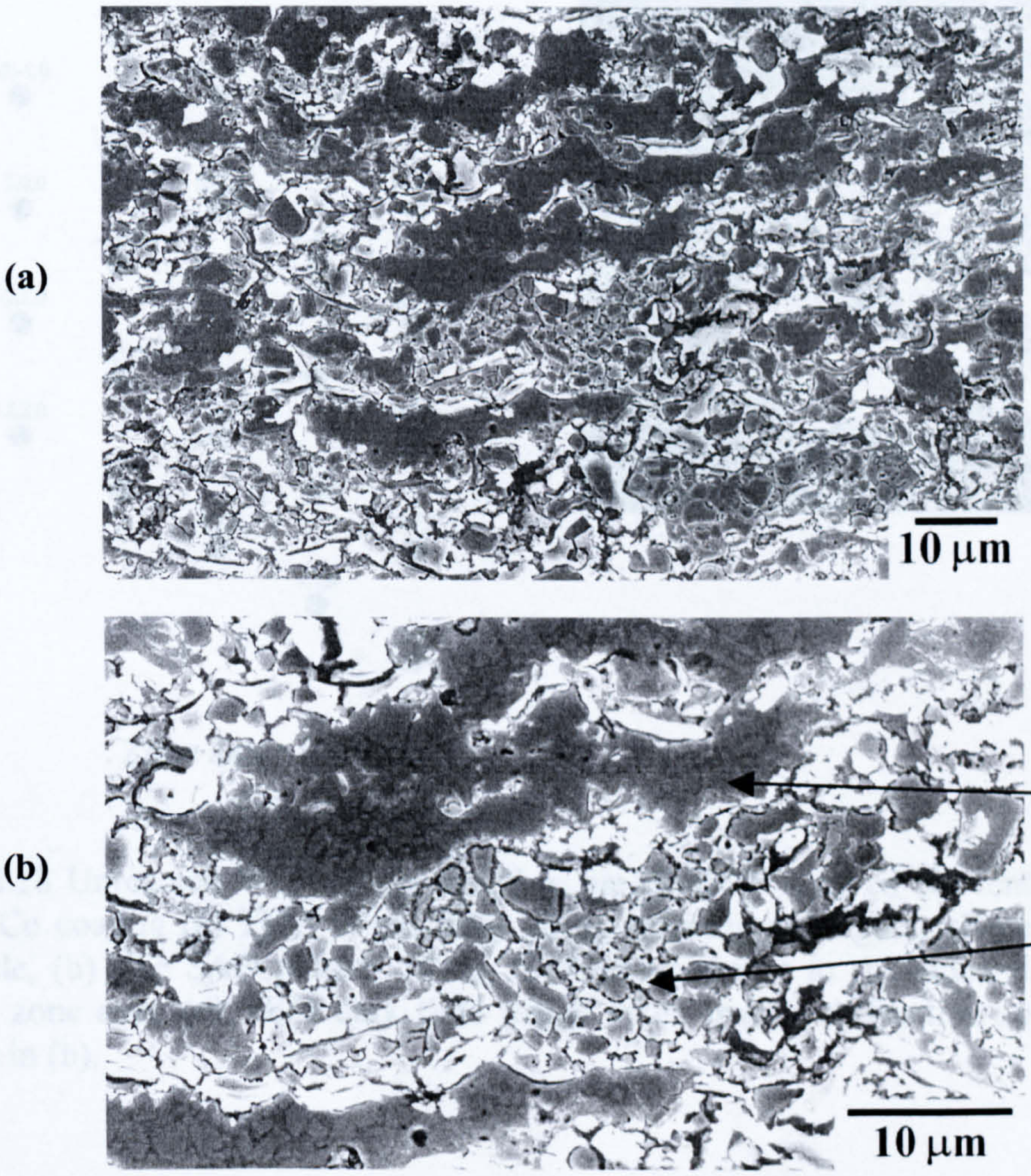

Fig. 4.17 Cross sectional SEM images in SEI mode of the HVOGF sprayed conventional WC-12 wt% Co coating (a) Microstructure at low magnification showing the splat structures with a higher amount of molten and semimolten regions. (b) A high magnification image showing unmelted regions of WC-Co particle and semimolten particle indicating melting of the Co matrix.

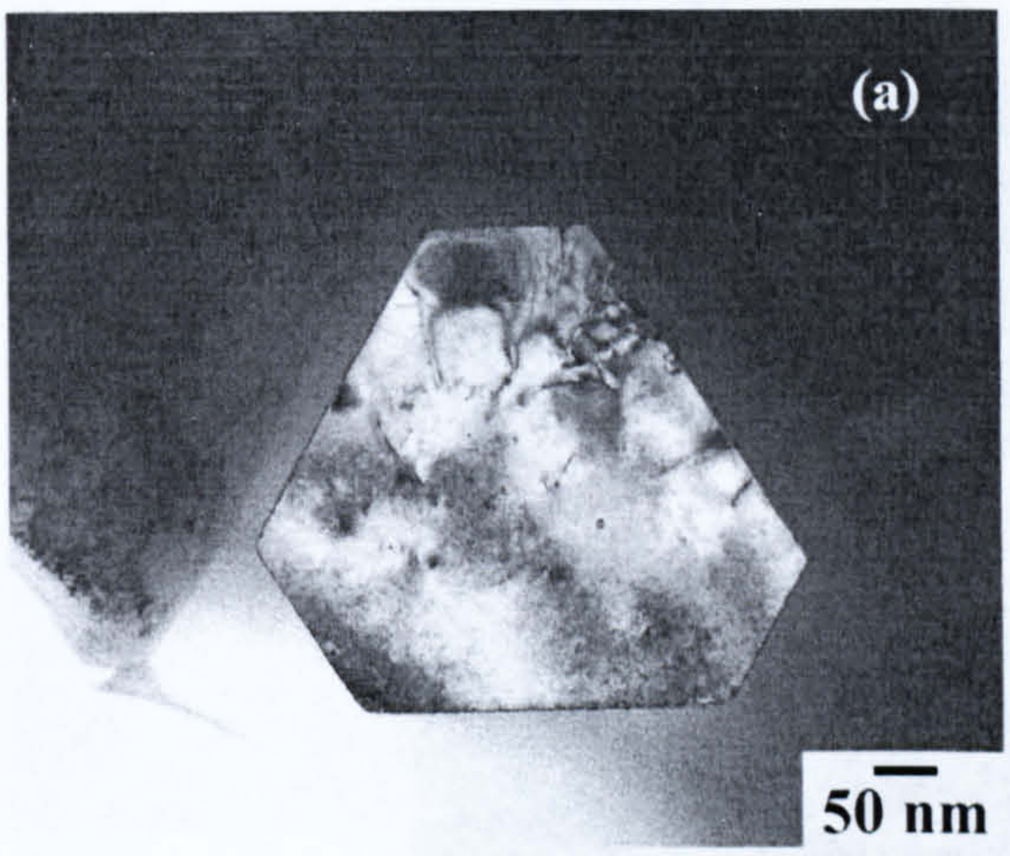

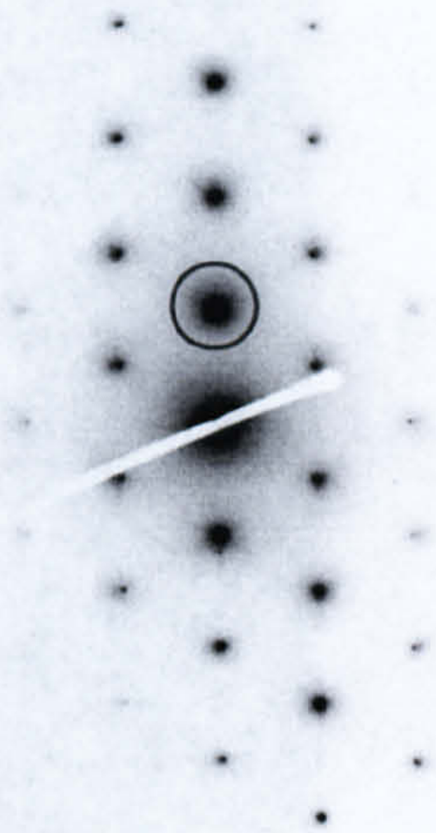

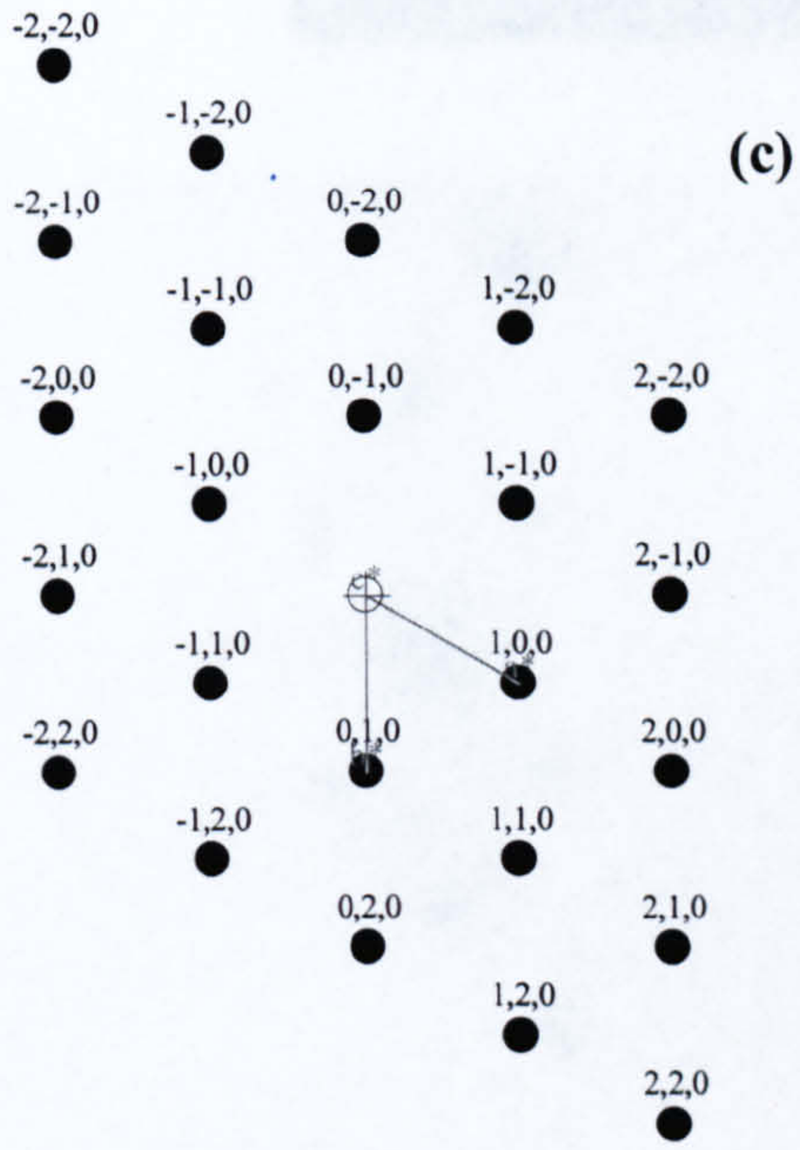

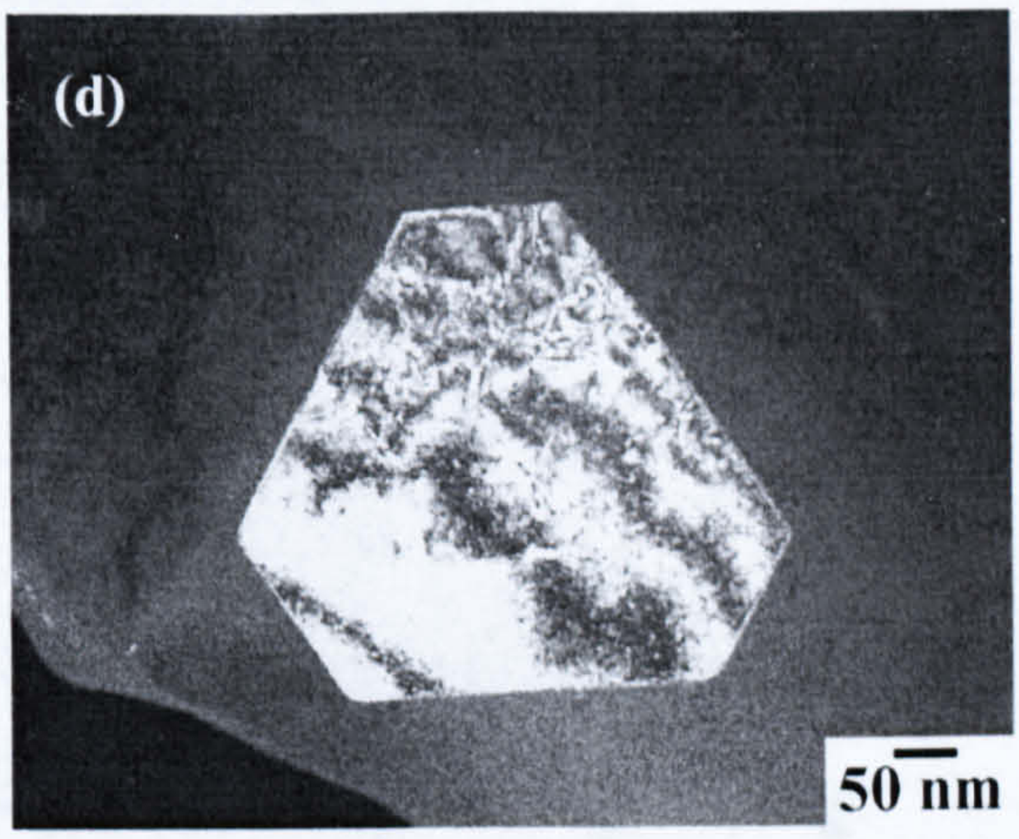

Fig. 4.18 Unreacted WC particle found in the HVOGF sprayed conventional WC-12 wt% Co coating (a) TEM bright field image showing an angular shape of a carbide particle, (b) The SAD pattern of (a), (c) Corresponding to (b) indexed to WC with [001] zone axis, (d) TEM dark field image taken from a diffraction spot in a black circle in (b).

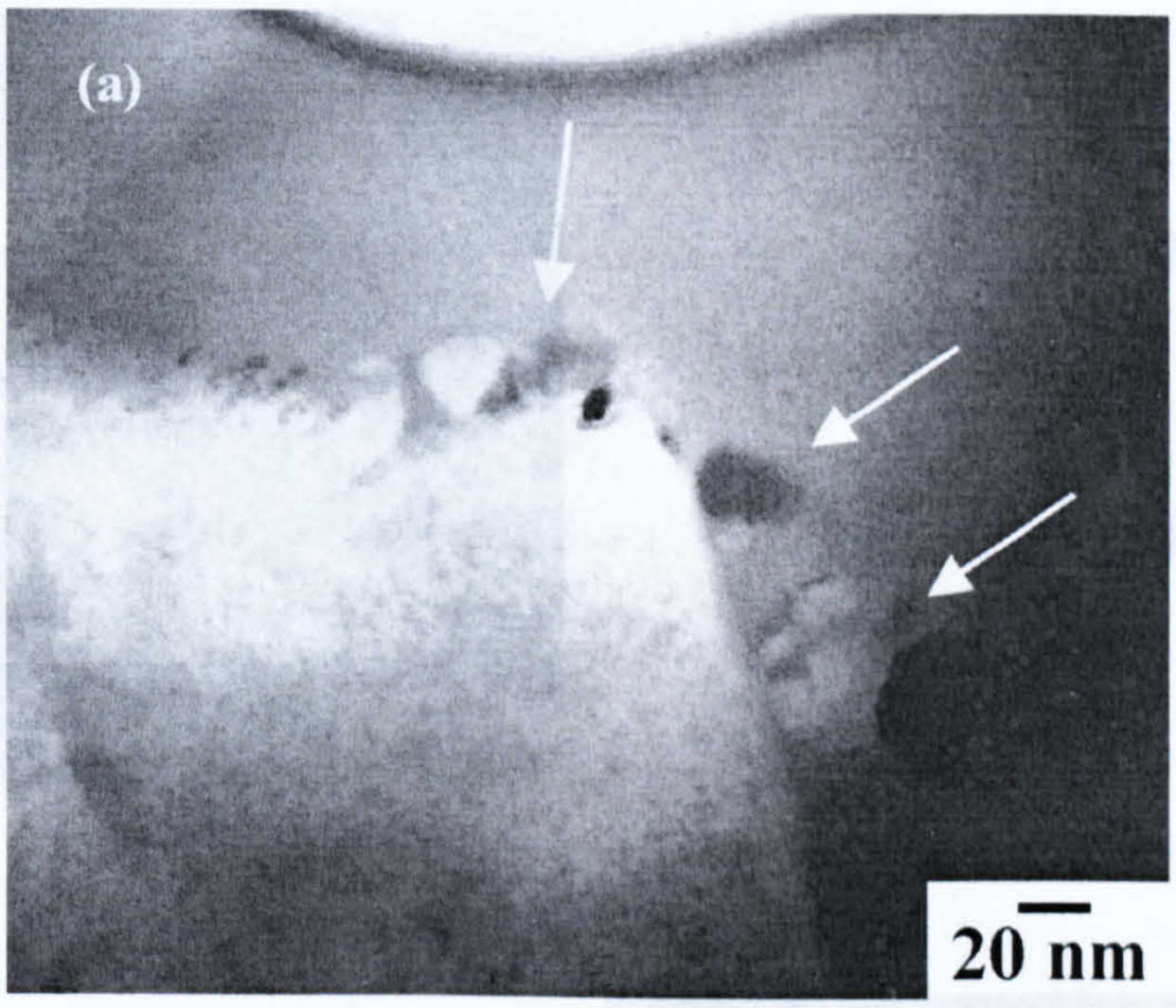

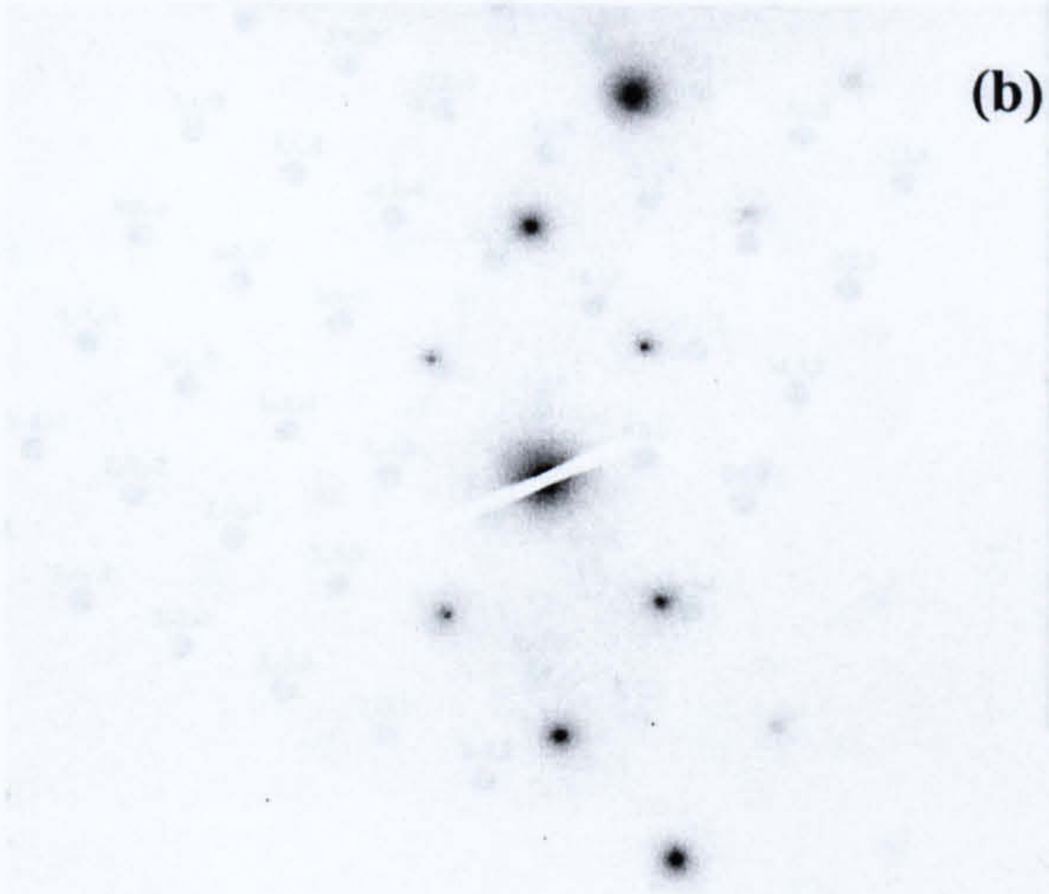

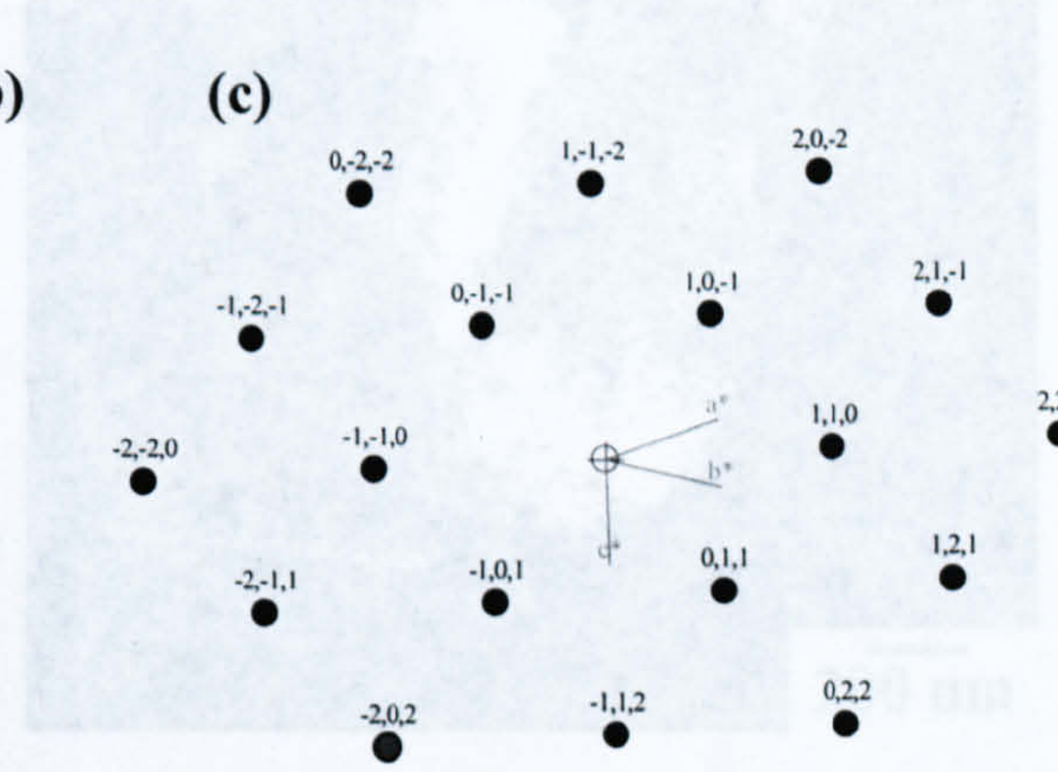

Zone axis : [1 $\bar{1}$ 1]

Fig. 4.19 Reacted carbide particle in the HVOGF sprayed conventional WC-12 wt% Co coating (a) TEM bright field image of a carbide particle showing precipitation formation at its edges (as indicated by the arrows), (b) The SAD pattern of a core particle, (c) Relating to (b) confirmed to WC with [1 $\bar{1}$ 1] zone axis.

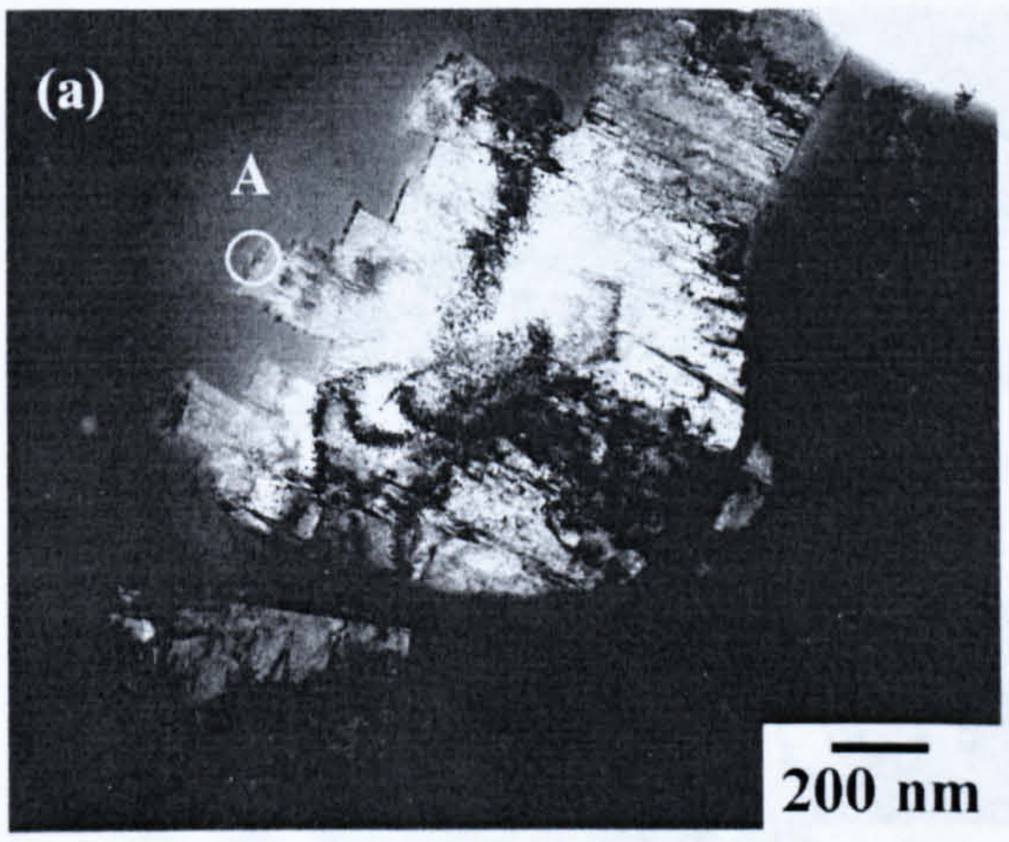

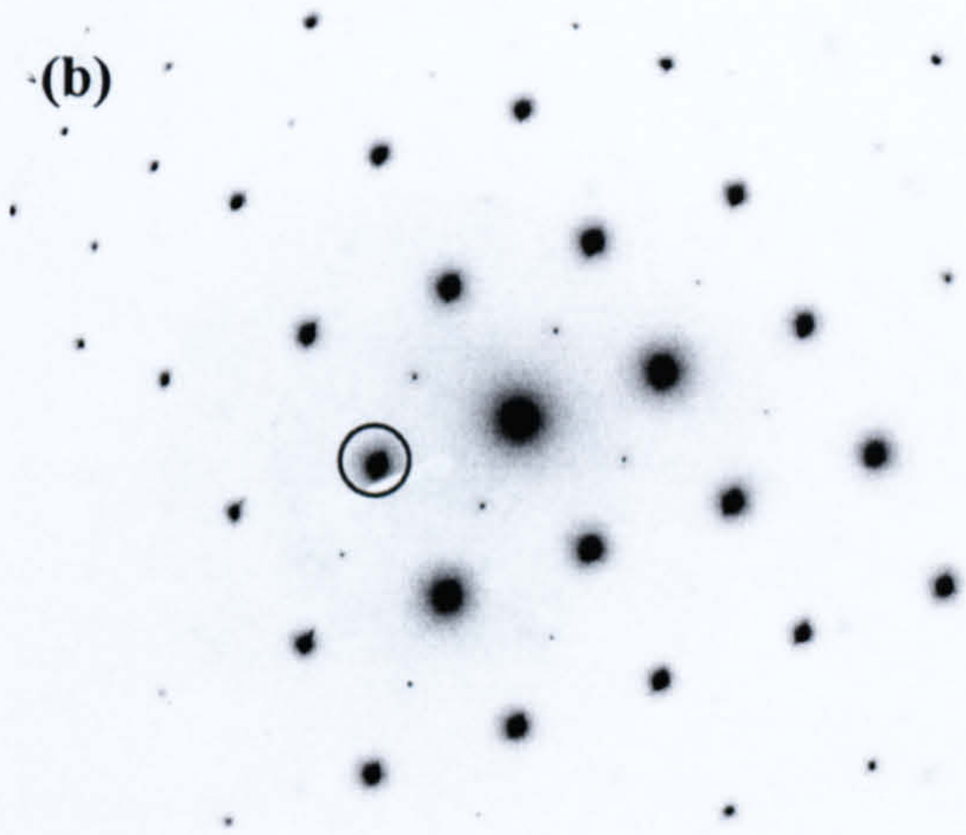

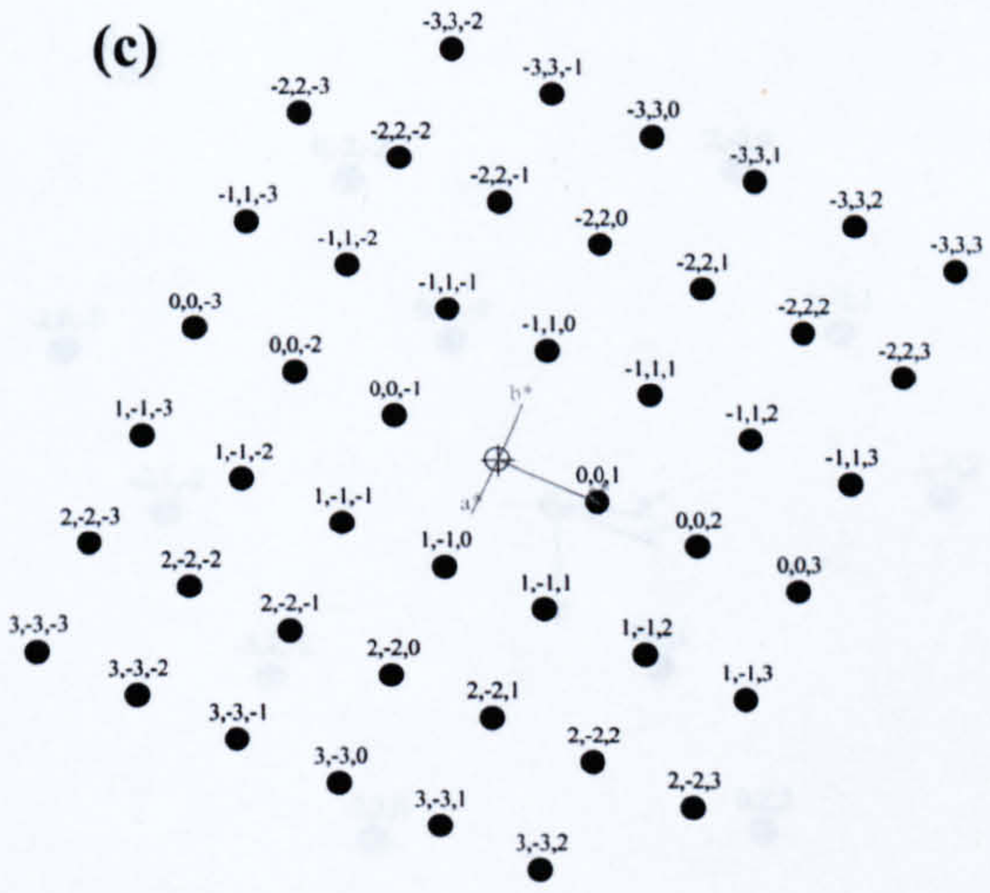

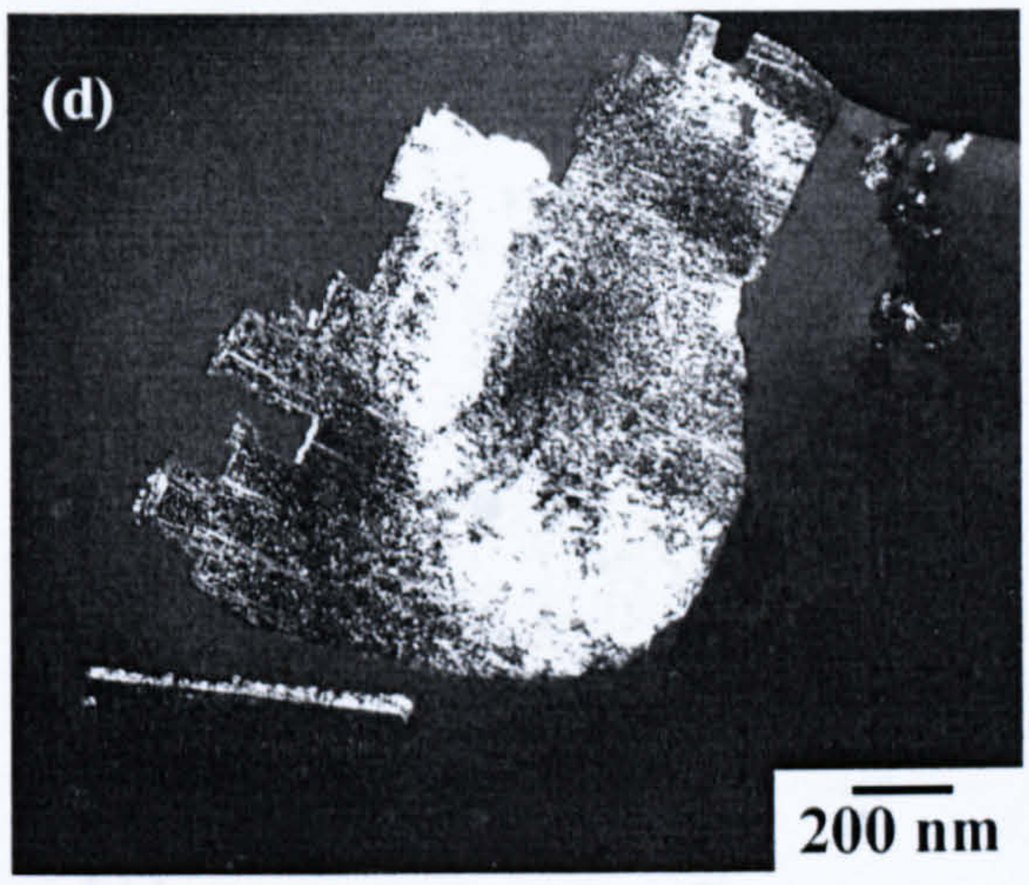

Zone axis : [$\bar{1}$ $\bar{1}$ 0]

Fig. 4.20 Reacted a carbide particle in the HVOGF sprayed conventional WC-12 wt% Co coating (a) TEM bright field image revealing a carbide particle with a step-edge and precipitate formation at its edges, (b) The SAD pattern of a core carbide particle, (c) Relating to (b) indexed to WC with [$\bar{1}$ $\bar{1}$ 0] zone axis, (d) TEM dark field image taken from a diffraction spot in a black circle in (b).

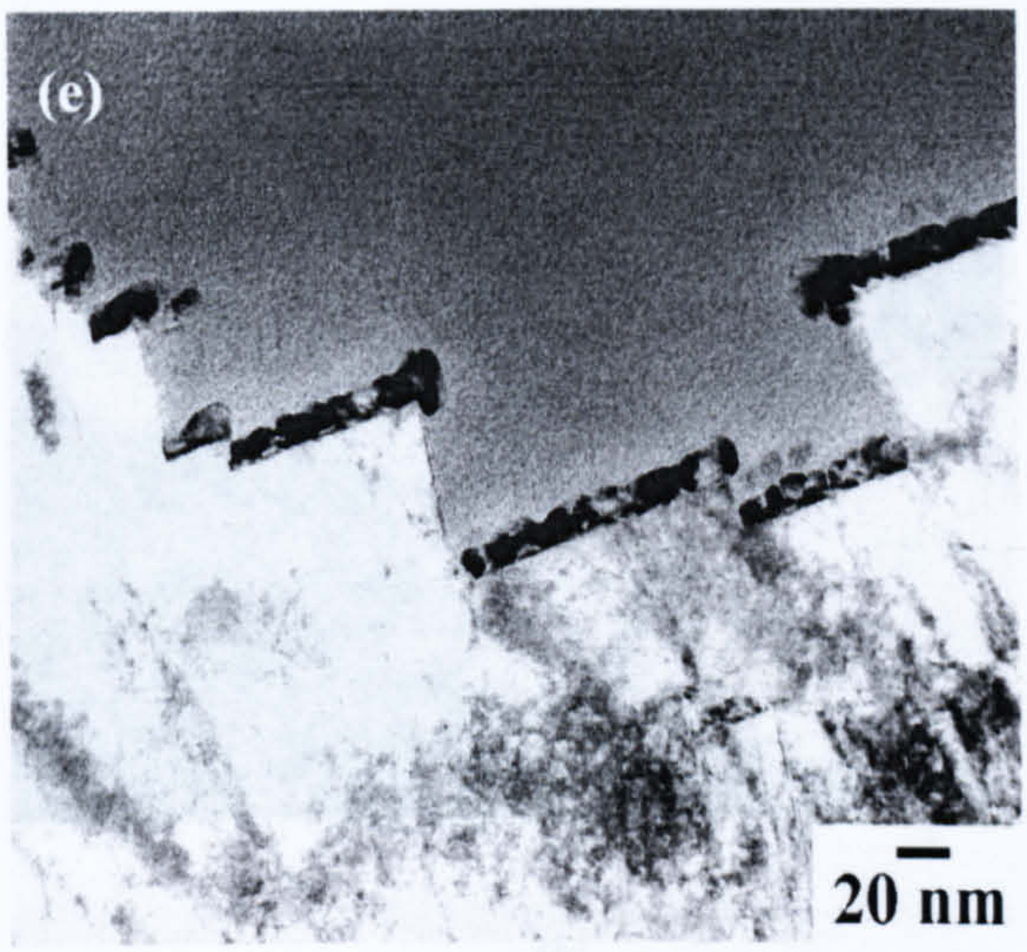

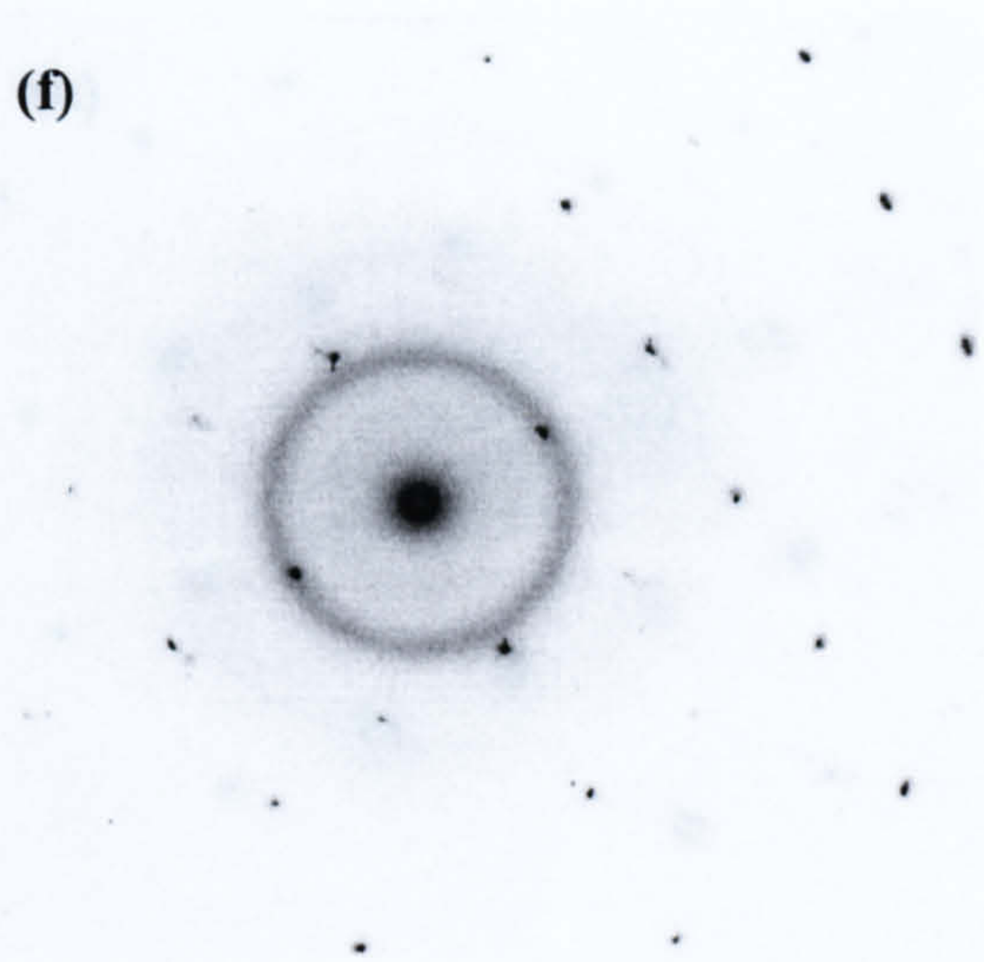

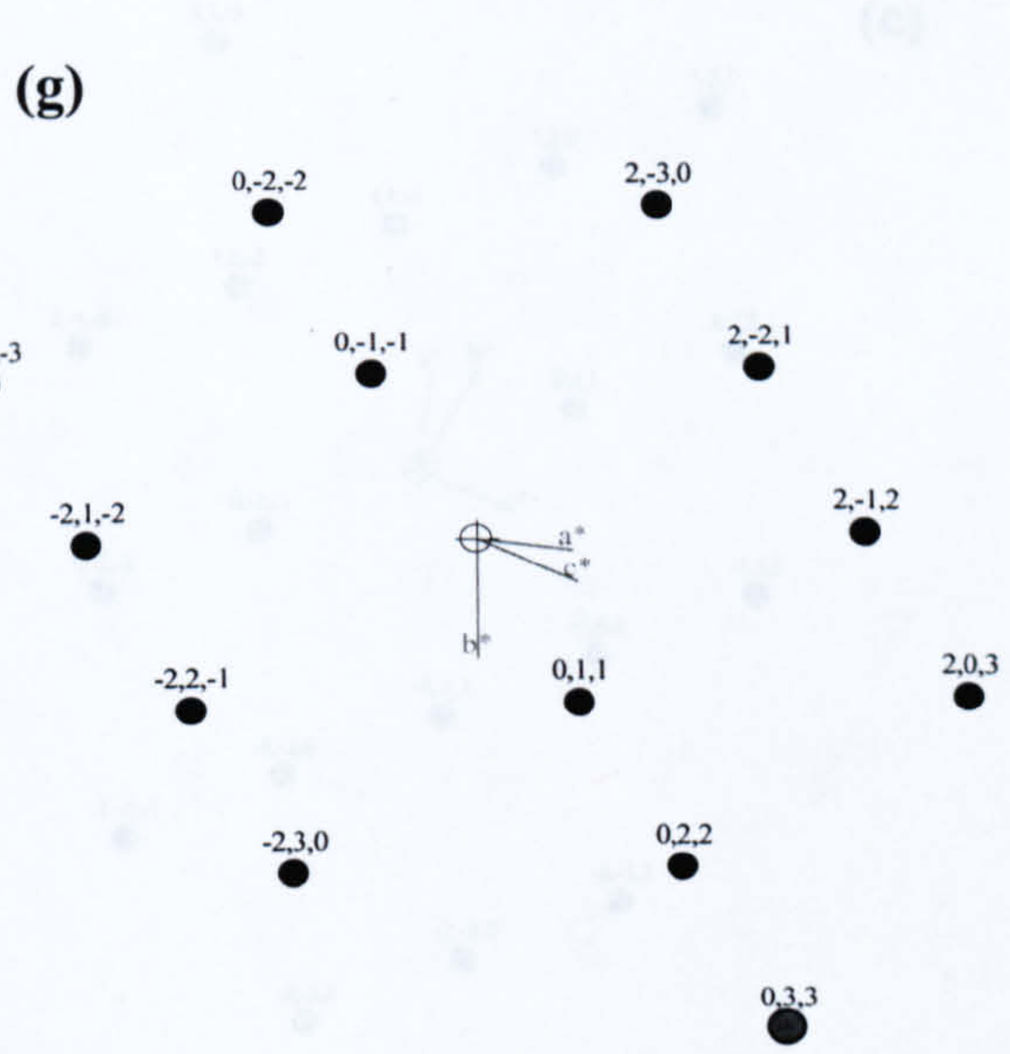

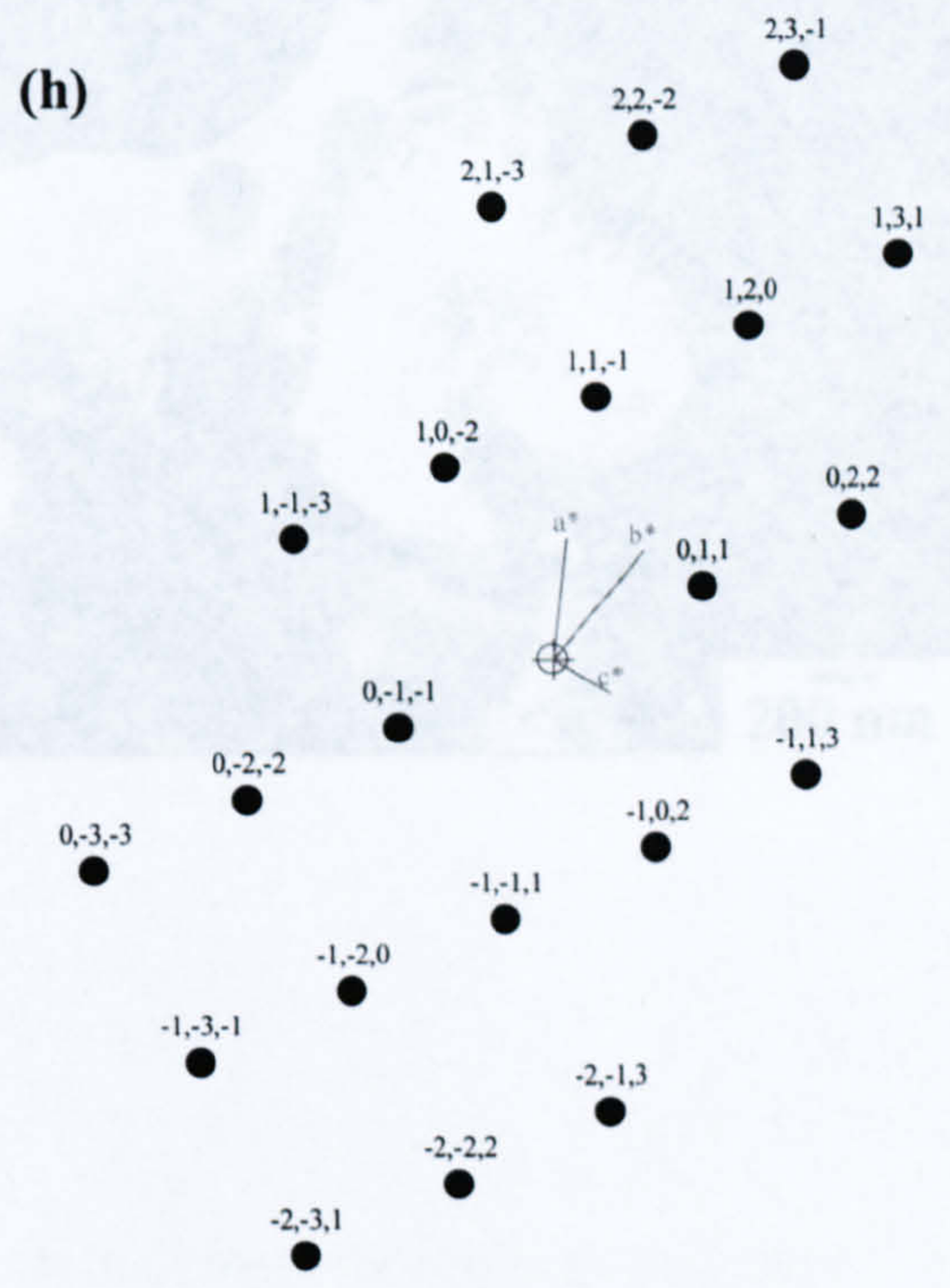

Fig. 4.20 (cont.) (e) At high magnification at the edge of a WC particle showing precipitate formation, (f) The SAD pattern at the precipitate from a position 'A' in (a), (g) and (h) Corresponding to (f) confirmed to WC with [$\bar{3}$ $\bar{2}$ 2] zone axis and W_2C with [$\bar{3}$ $\bar{2}$ 1] zone axis.

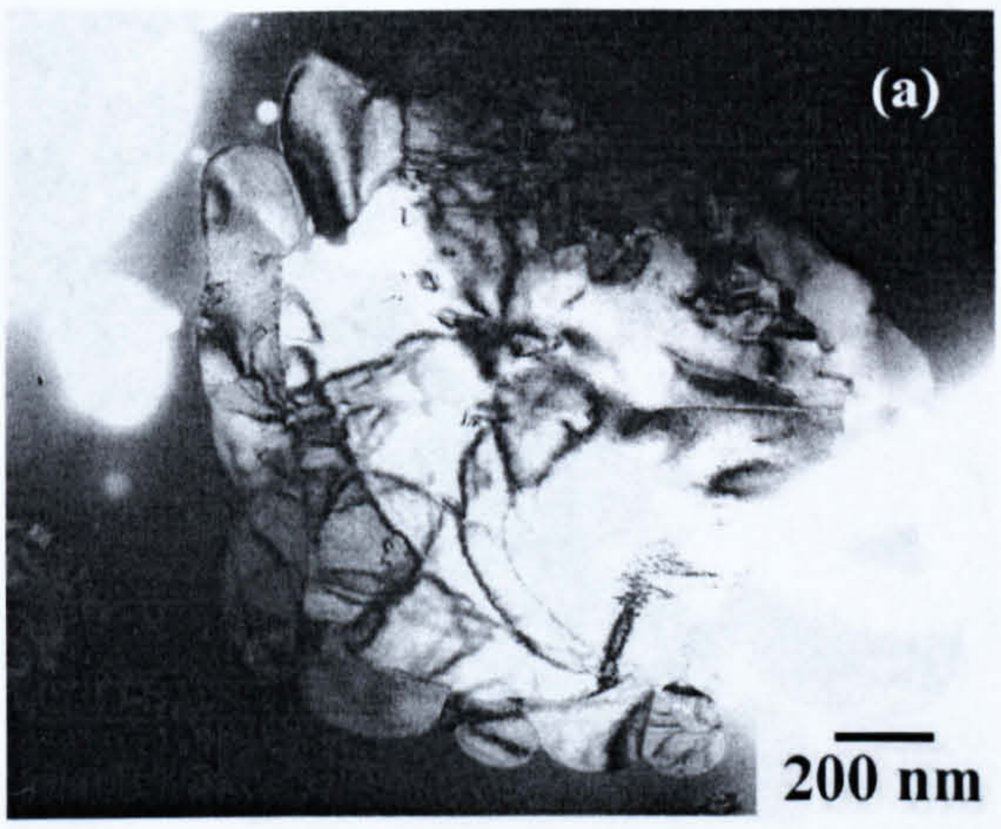

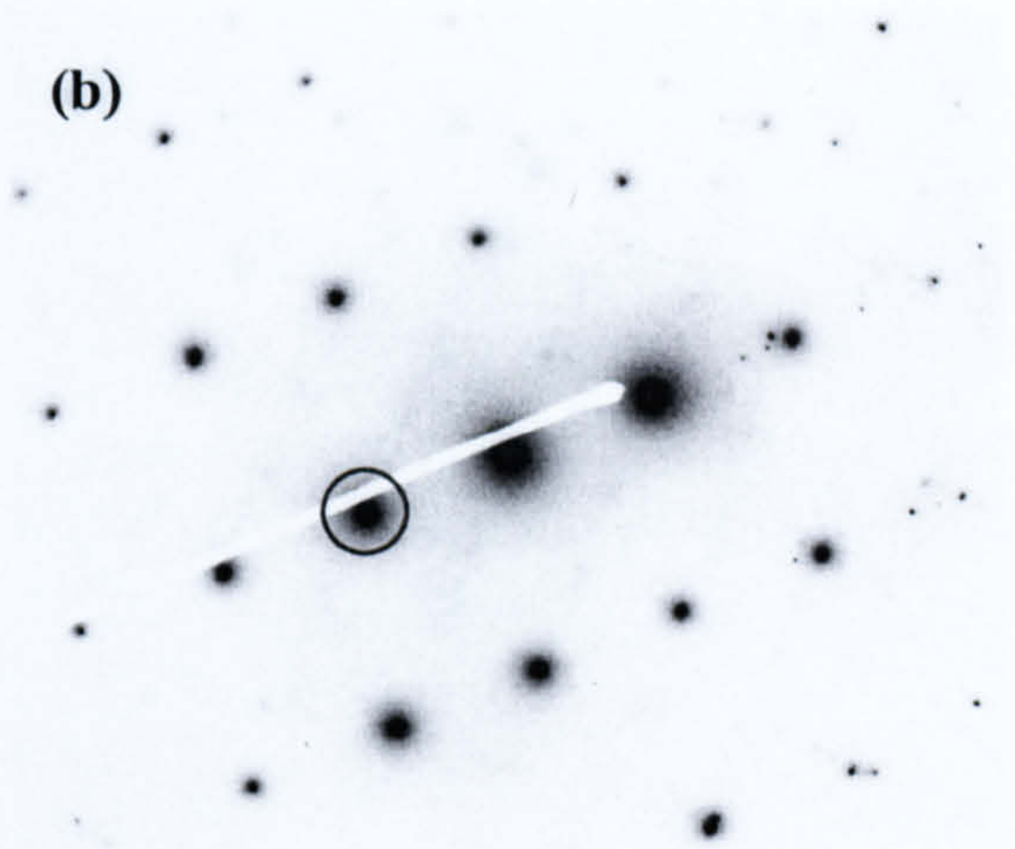

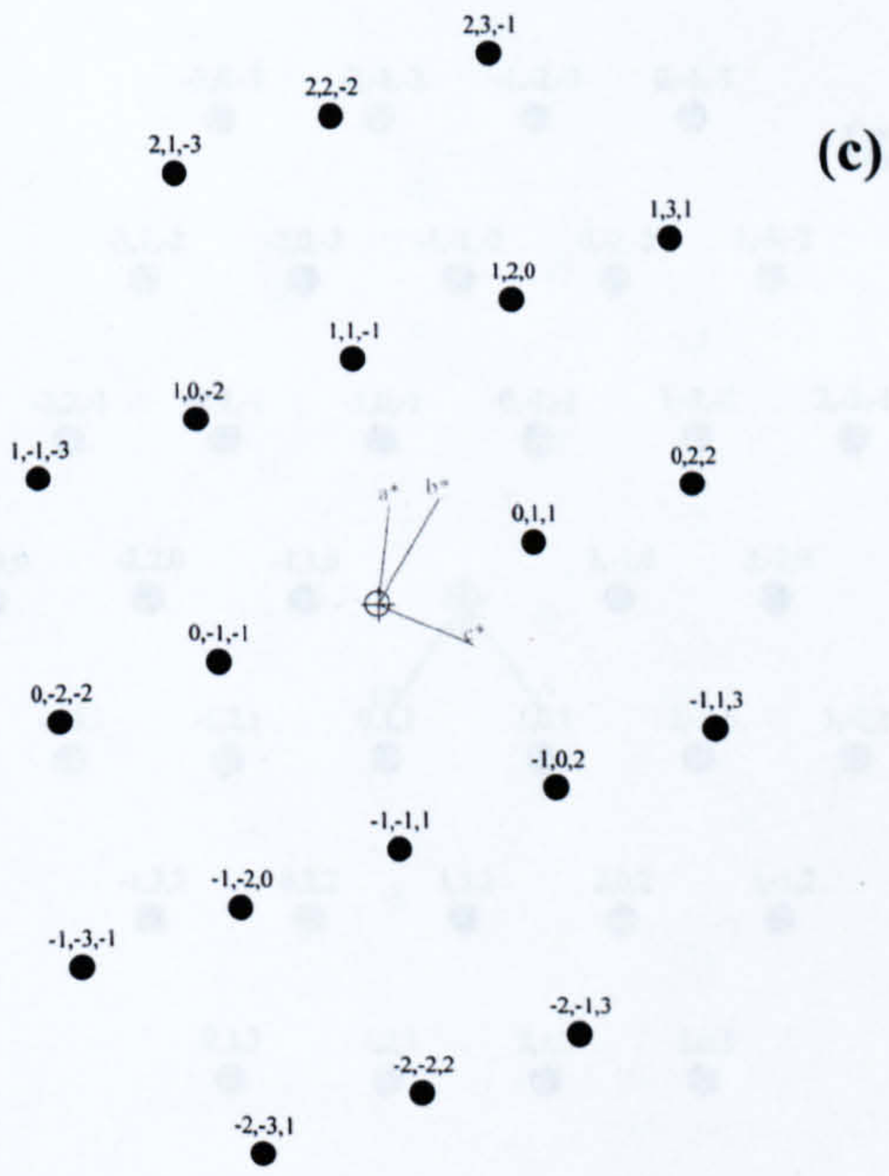

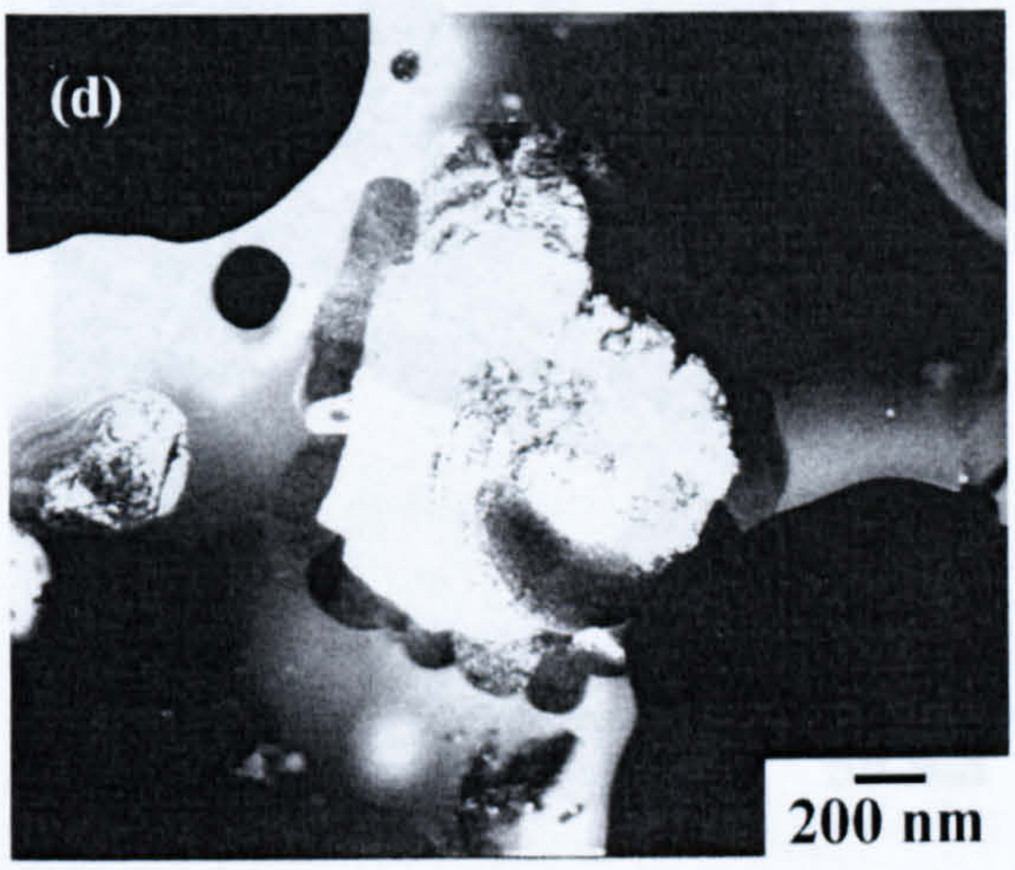

Fig. 4.21 Reacted carbide particle in the HVOGF sprayed conventional WC-12 wt% Co (a) TEM bright field image showing a carbide particle surrounded with a discrete layer, (b) The SAD pattern of a core carbide particle, (c) Relating to (b) confirmed to WC with [2 1 1] zone axis, (d) TEM dark field image of a core WC particle taken from a diffraction spot in a dark circle from (b).

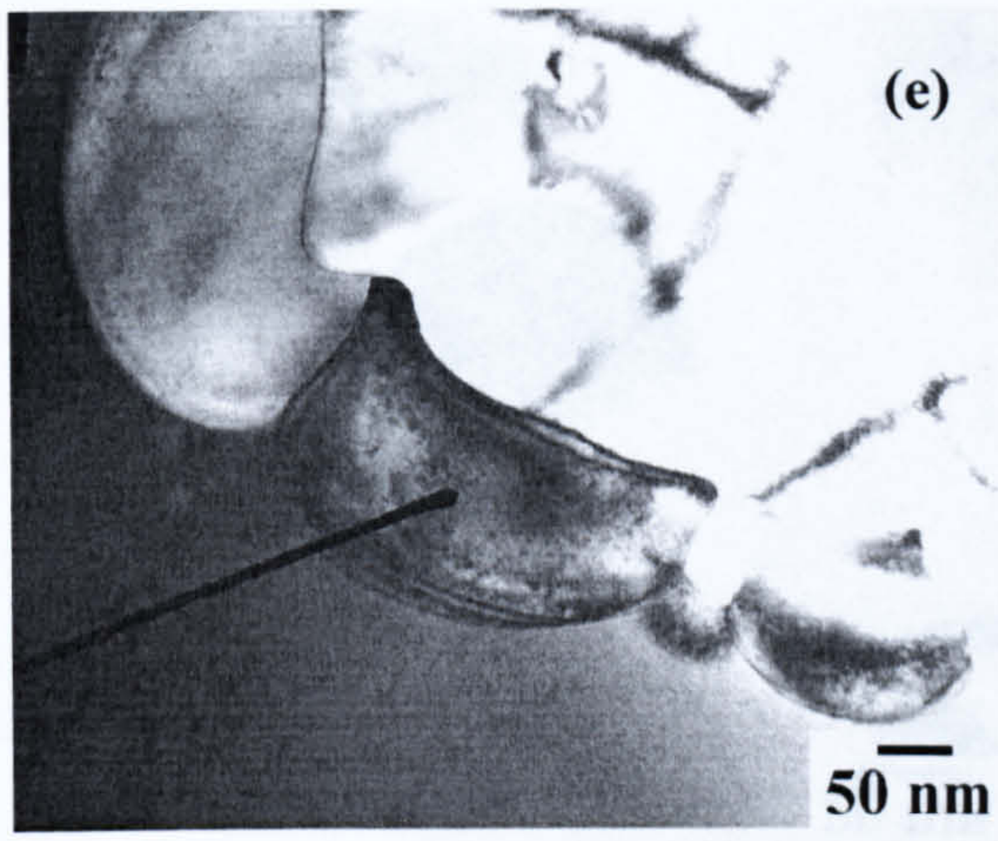

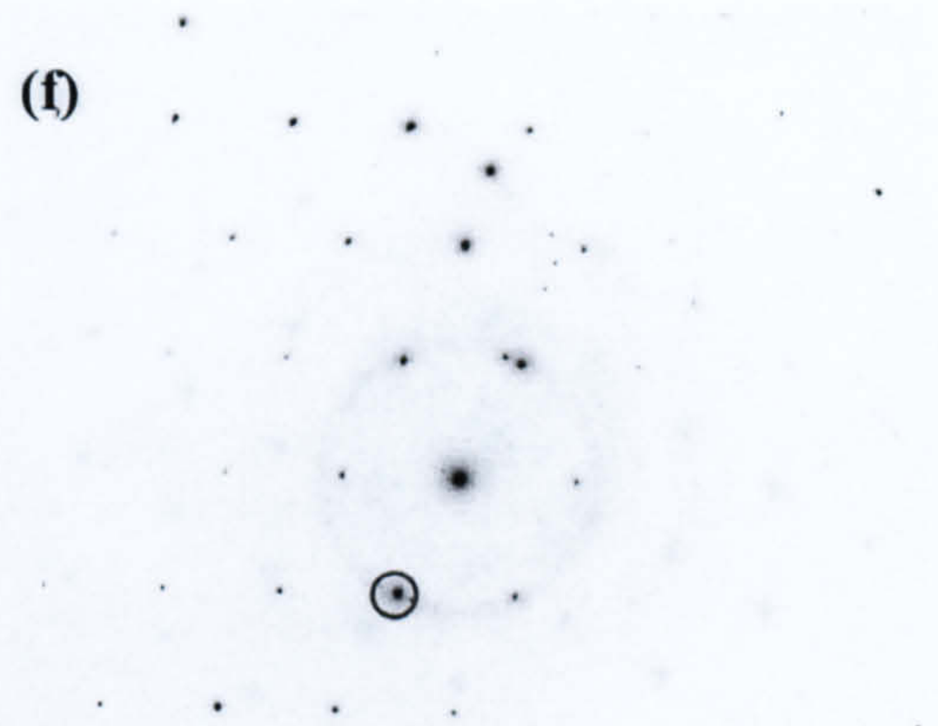

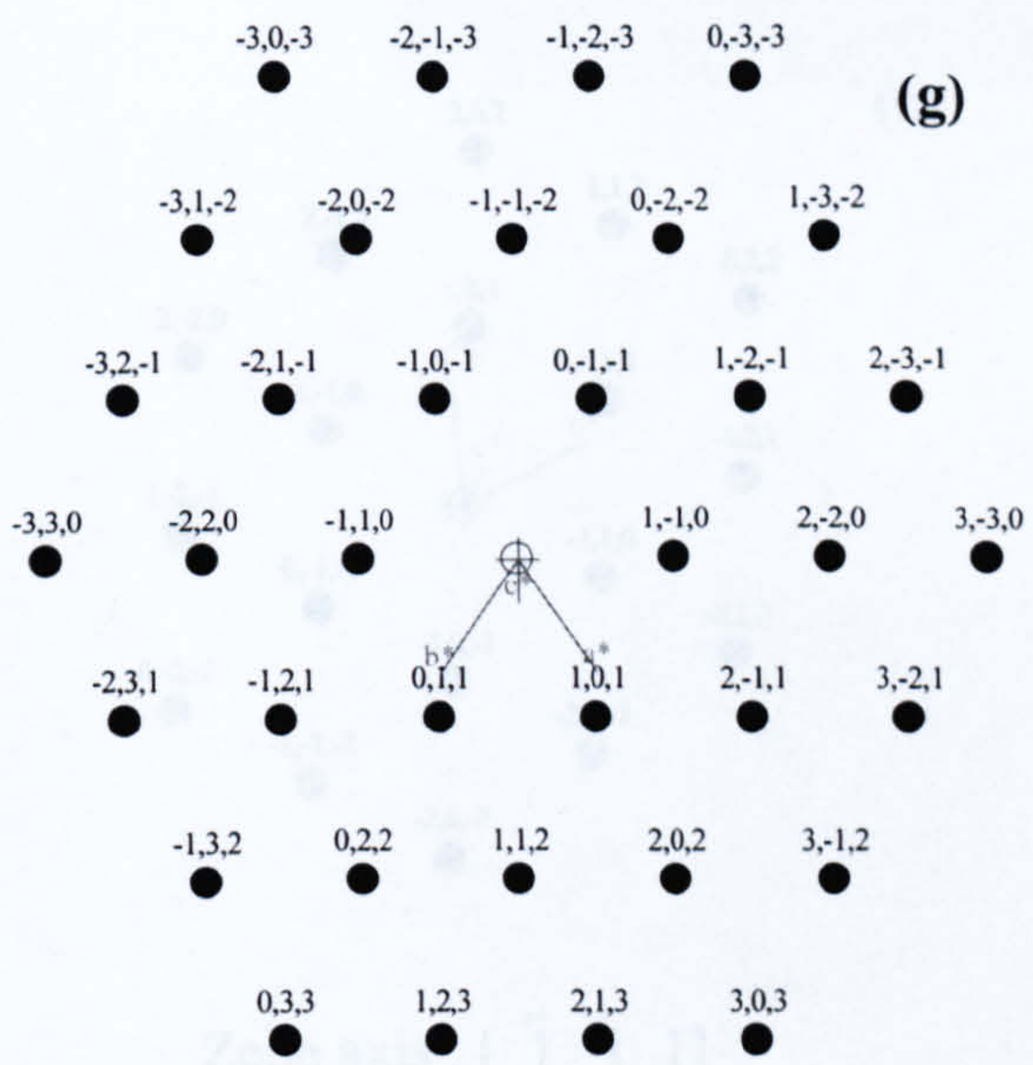

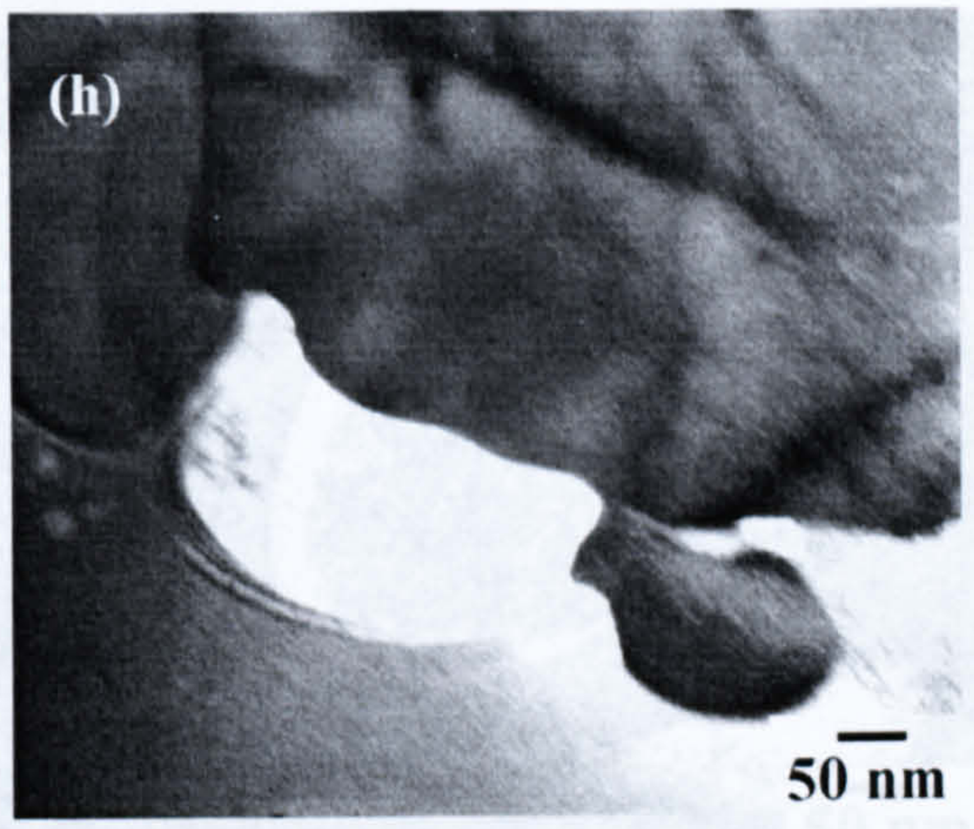

Zone axis : [$\bar{1}$ $\bar{1}$ 1]

Fig. 4.21 (cont.) (e) TEM bright field image at high magnification on their edges, (f) The SAD pattern produced from a discrete layer at the pointer, (g) Corresponding to (f) indexed to W_2C with [$\bar{1}$ $\bar{1}$ 1] zone axis, (h) TEM dark field image taken from a diffraction spot in a dark circle in (f).

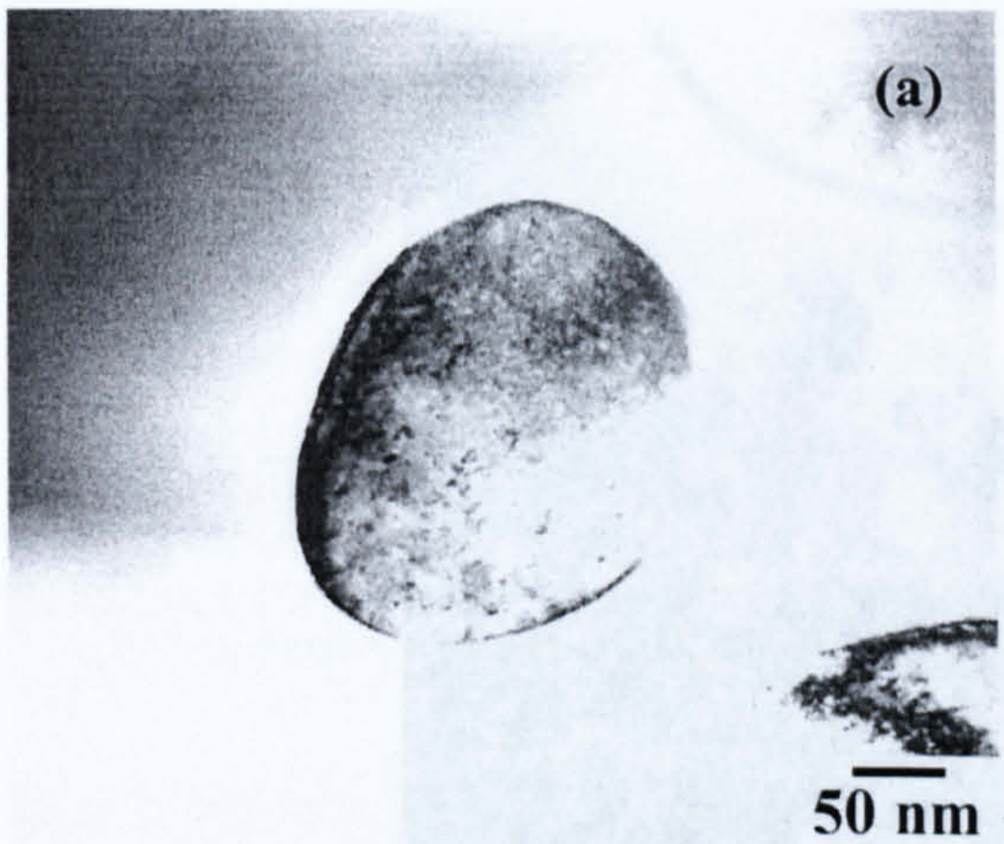

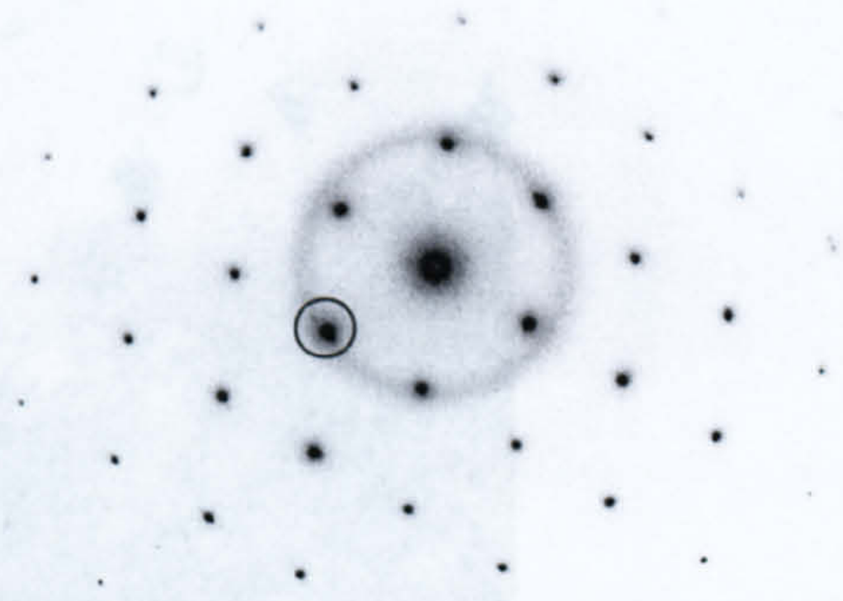

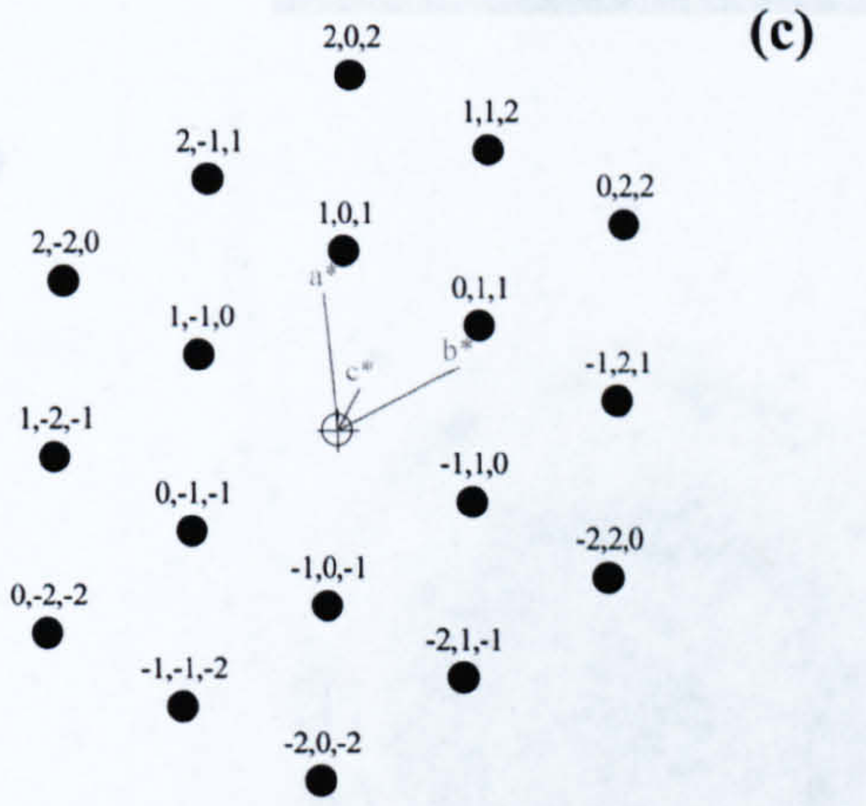

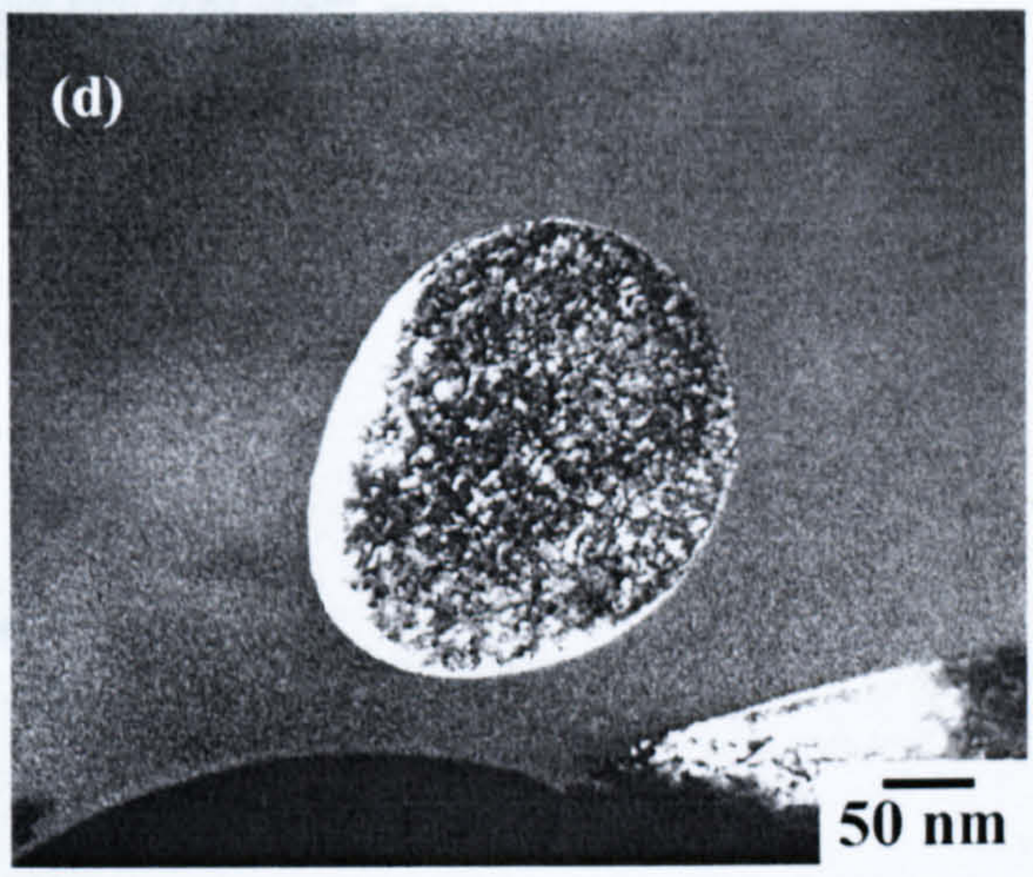

Zone axis : [$\bar{1}$ $\bar{1}$ 1]

Fig. 4.22 A rounded carbide particle in the HVOGF sprayed conventional WC-12 wt% Co coating. (a) TEM bright field image, (b) The SAD patterns of (a) with a diffuse ring pattern, (c) Relating to (b) indexed to W_2C with [$\bar{1}$ $\bar{1}$ 1] zone axis, (d) TEM dark field image of a W_2C particle produced from a diffraction spot in a dark circle in (b).

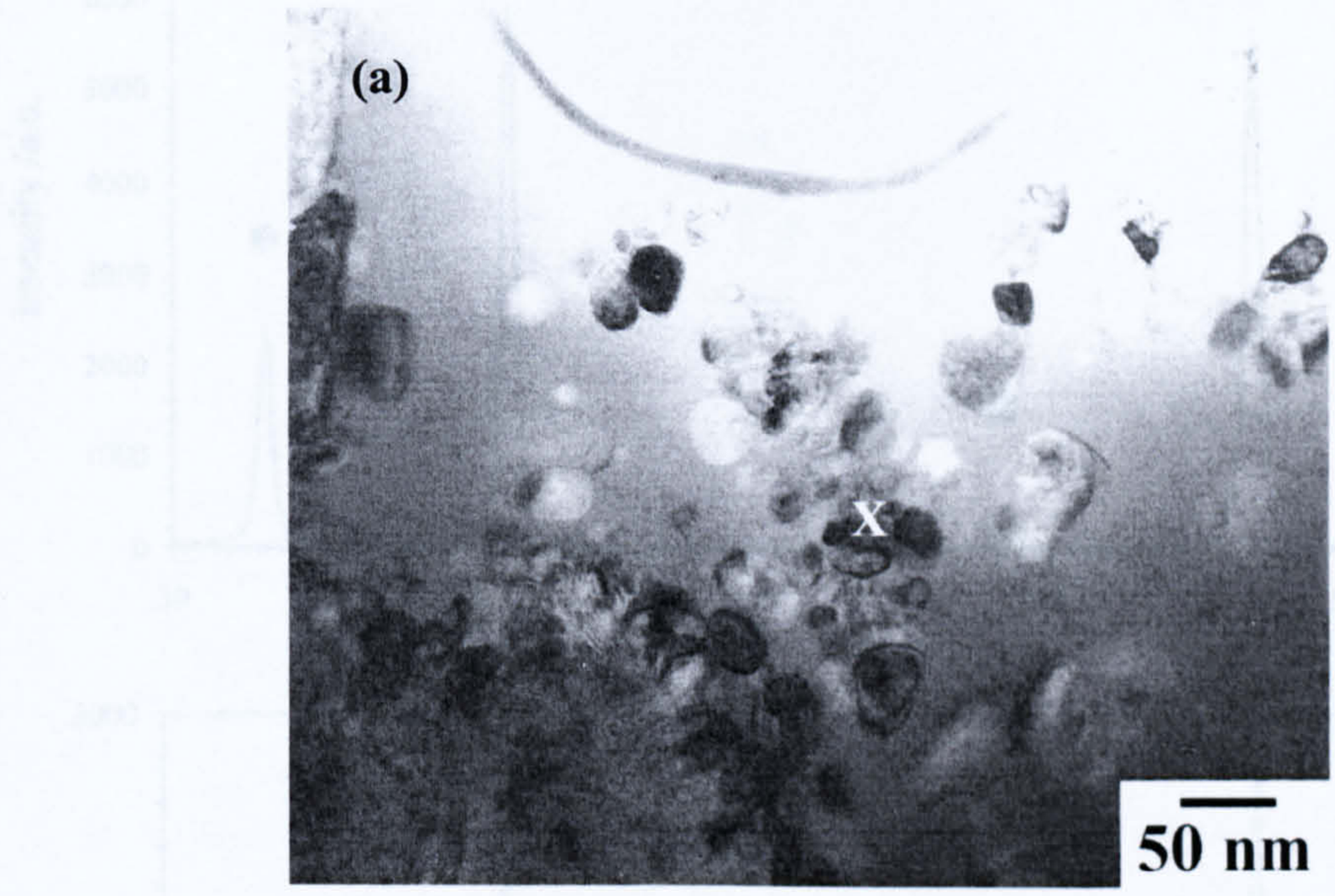

Fig. 4.23 (a) A TEM bright field image revealing a cluster of carbide particles in Co based matrix, (b) The SAD pattern taken from the area around 'X' in (a) shows ring diffraction patterns confirmed to W_2C.

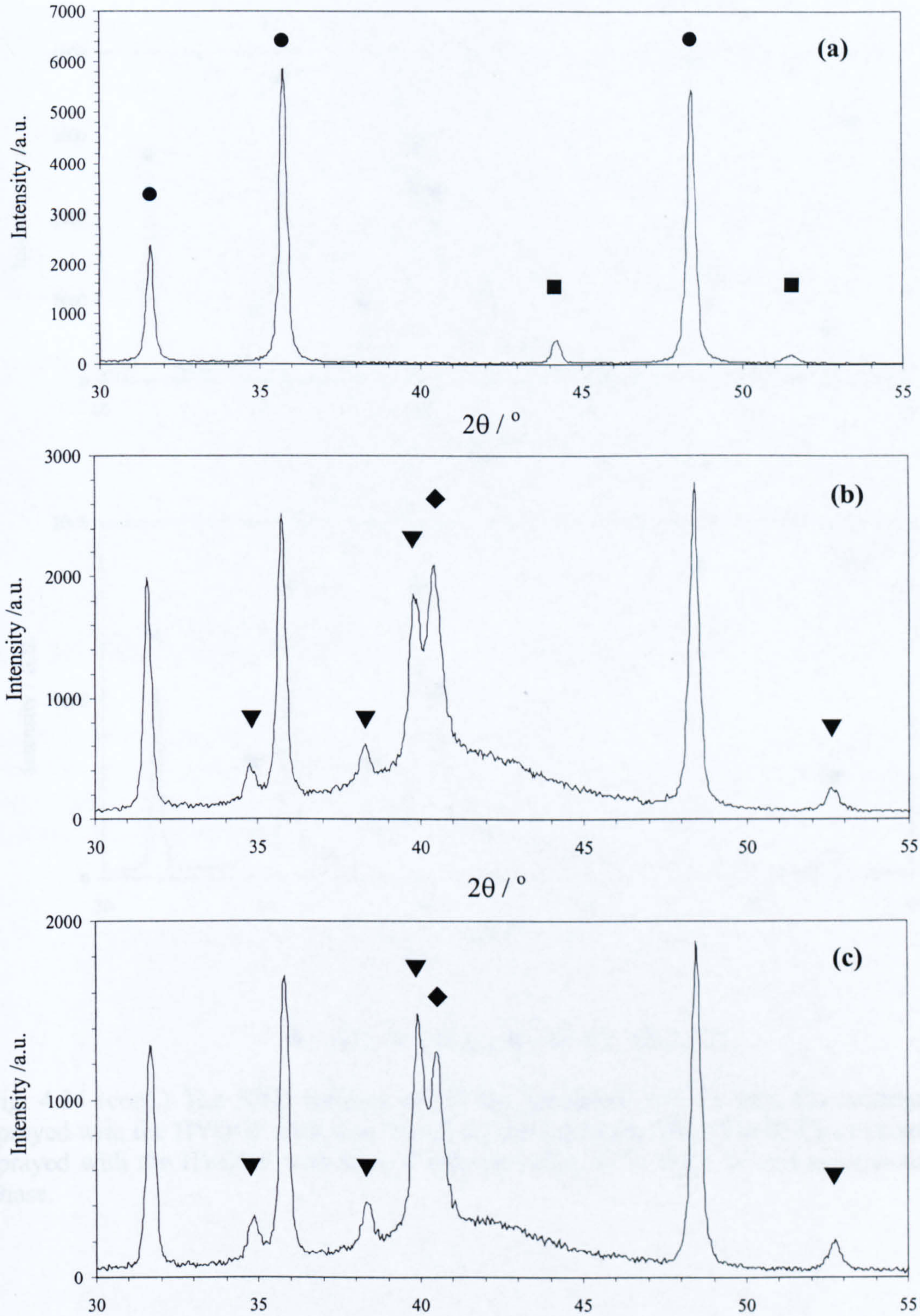

Fig. 4.24 The XRD patterns of (a) the nanoscale WC-12 wt% Co powder showing WC and Co peaks, (b) the nanoscale WC-12 wt% Co coatings sprayed with the HVOGF with Run '1' and (c) the nanoscale WC-12 wt% Co coatings sprayed with the HVOGF with Run '2' revealing WC, W_2C, W and amorphous phase.

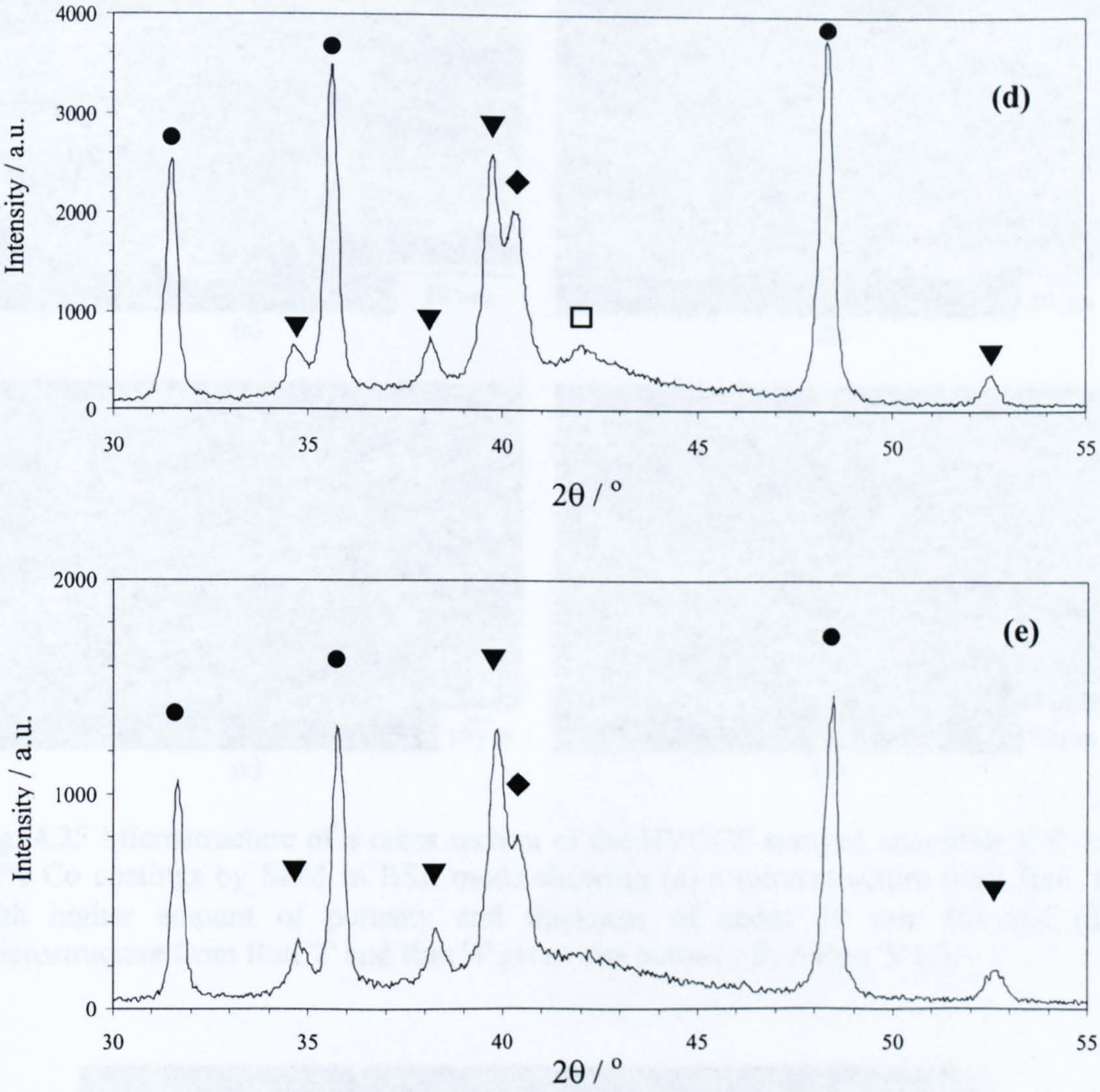

Fig. 4.24 (cont.) The XRD patterns of (d) the nanoscale WC-12 wt% Co coatings sprayed with the HVOGF with Run '3' and (e) the nanoscale WC-12 wt% Co coatings sprayed with the HVOGF with Run '4' also revealing WC, W_2C, W and amorphous phase.

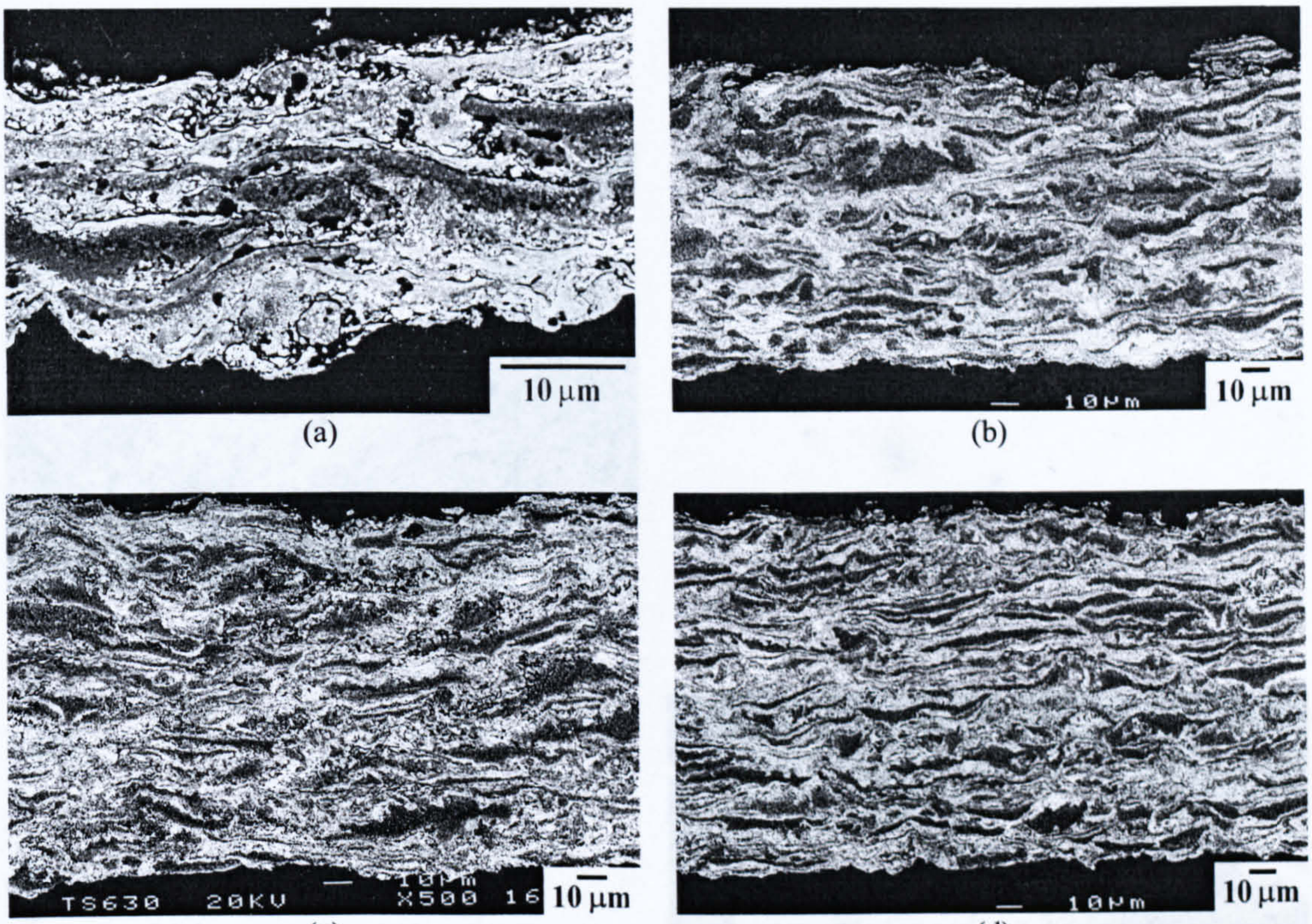

Fig. 4.25 Microstructure of a cross section of the HVOGF sprayed nanoscale WC-12 wt% Co coatings by SEM in BSE mode showing (a) a microstructure from Run '1' with higher amount of porosity and thickness of about 30 μm. (b) and (d) Microstructure from Run '2' and Run '4' gives less porosity than Run '3' (c).

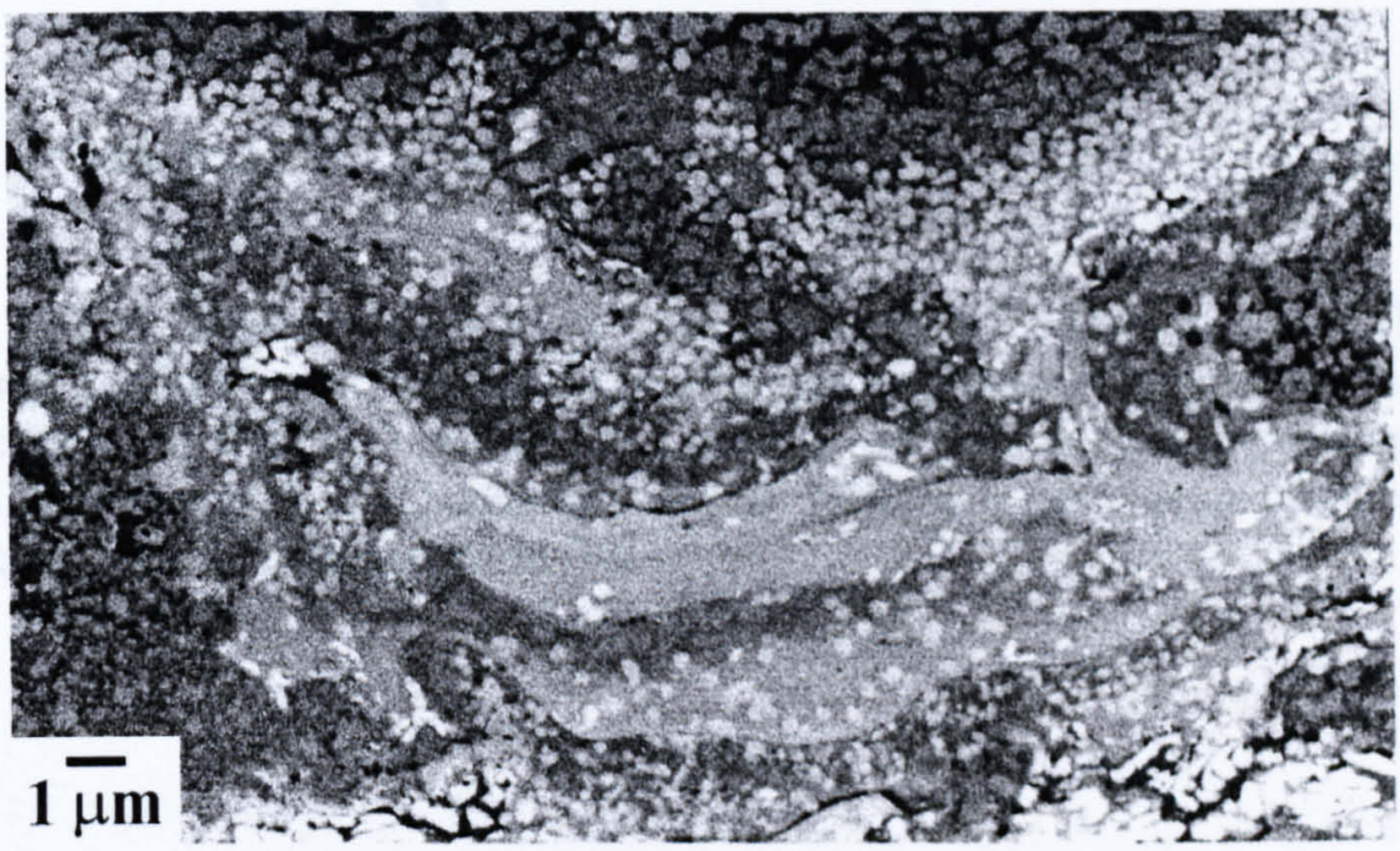

Fig. 4.26 Cross section of the HVOGF sprayed nanoscale WC-12 wt% Co coating (Run '2') at high magnification reveals different binder grey shades; the majority of rounded particles with high brightness are observed in the brighter binder matrix.

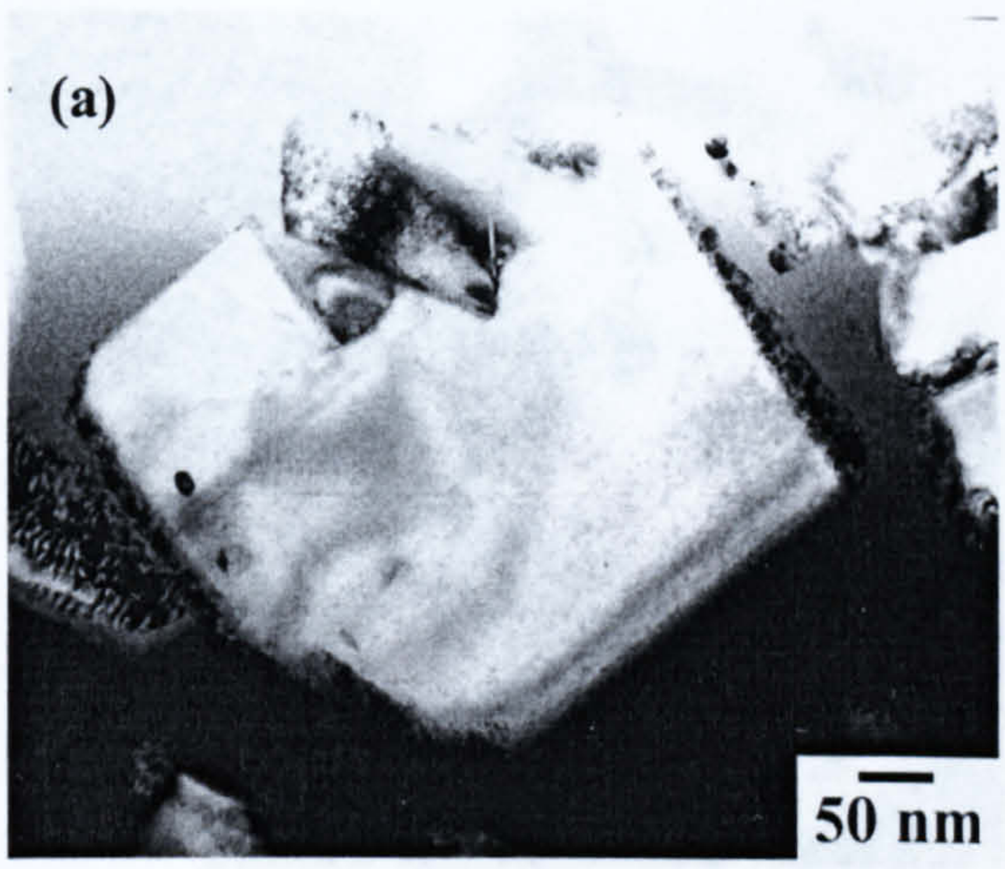

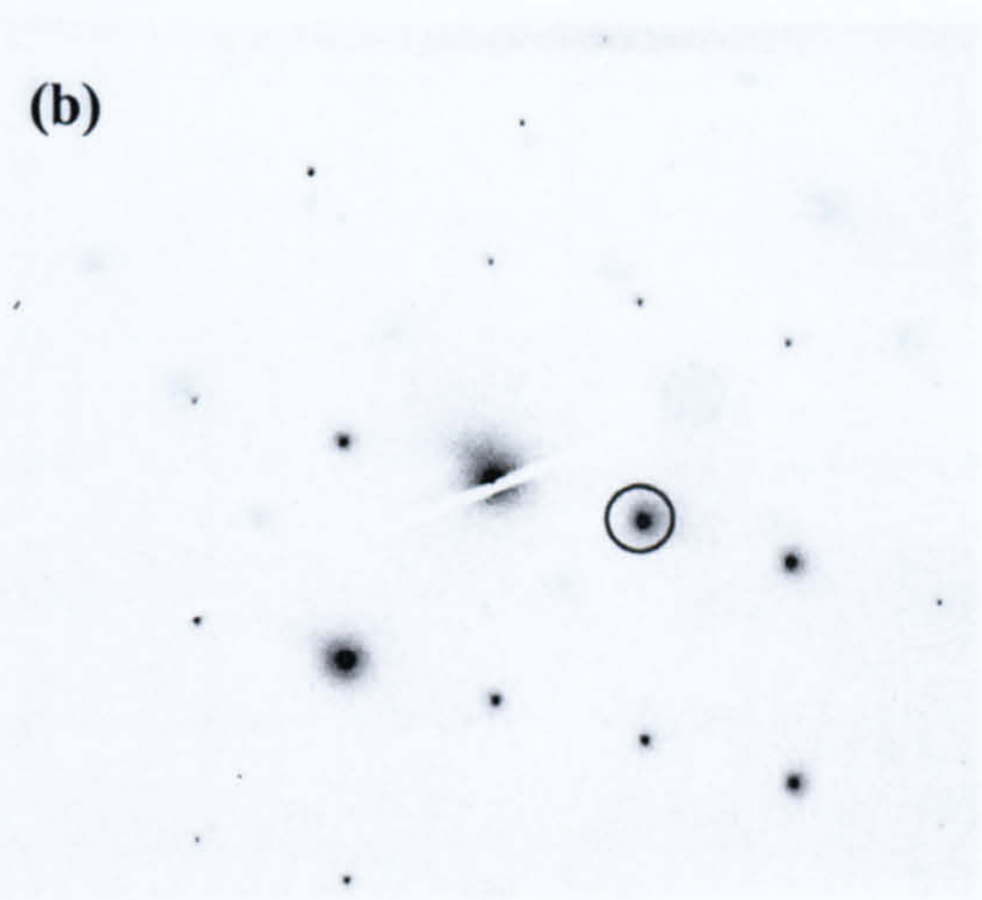

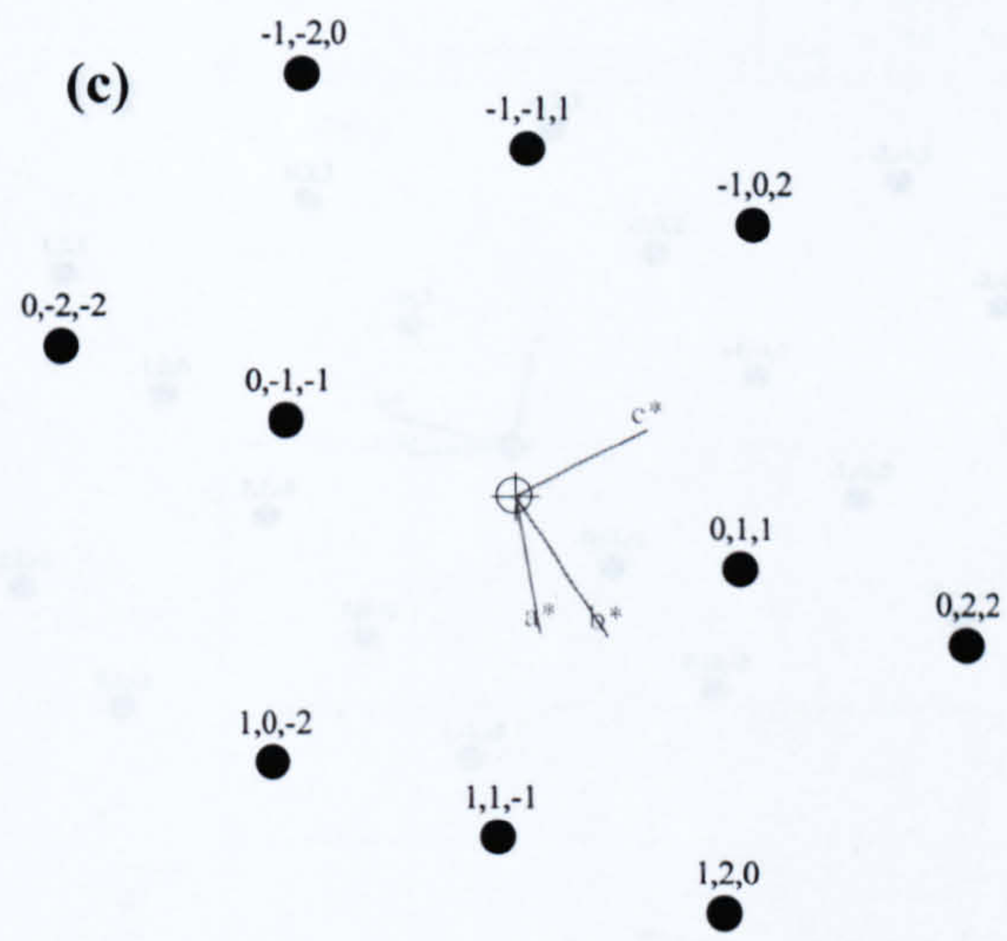

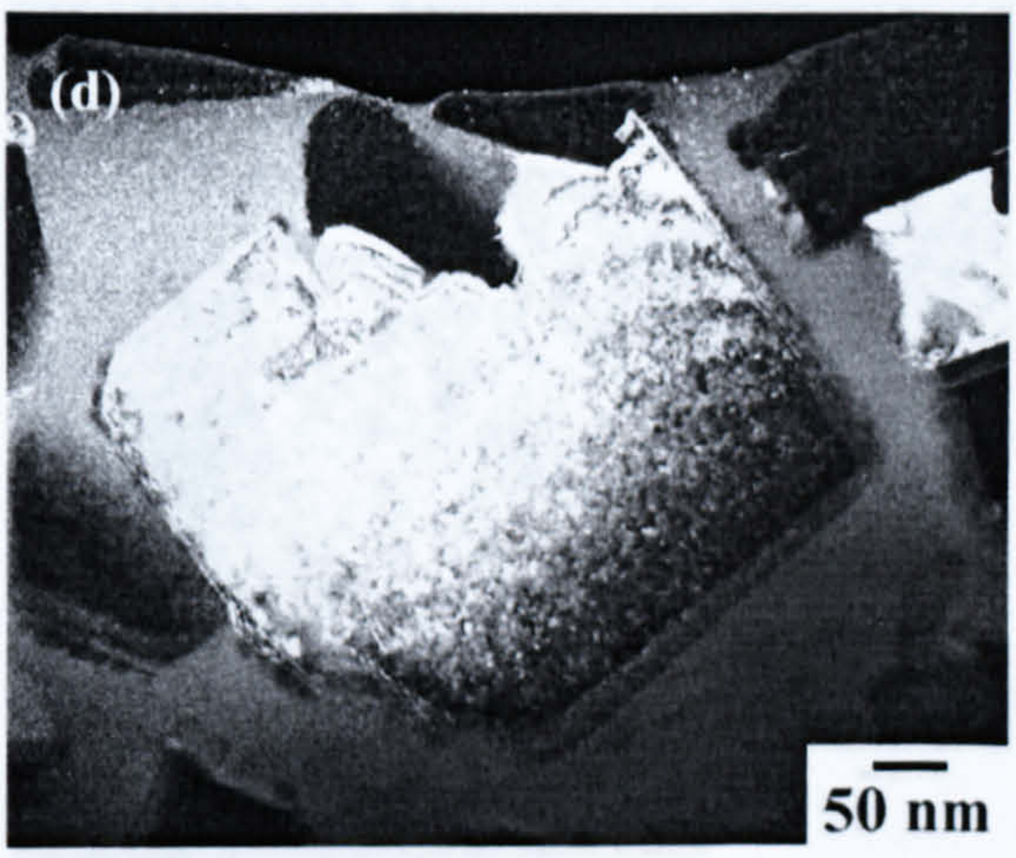

Zone axis : [2 $\bar{1}$ 1]

Fig. 4.27 TEM images of the HVOGF nanoscale WC-12 wt% Co coating (Run '2') indicating (a) TEM bright field image of a carbide particle with precipitate formation on its edges, (b) the SAD pattern of a carbide particle, (c) corresponding to (b) indexed to WC with [2 $\bar{1}$ 1] zone axis and (d) TEM dark field image produced from a diffraction spot in a dark circle in (b).

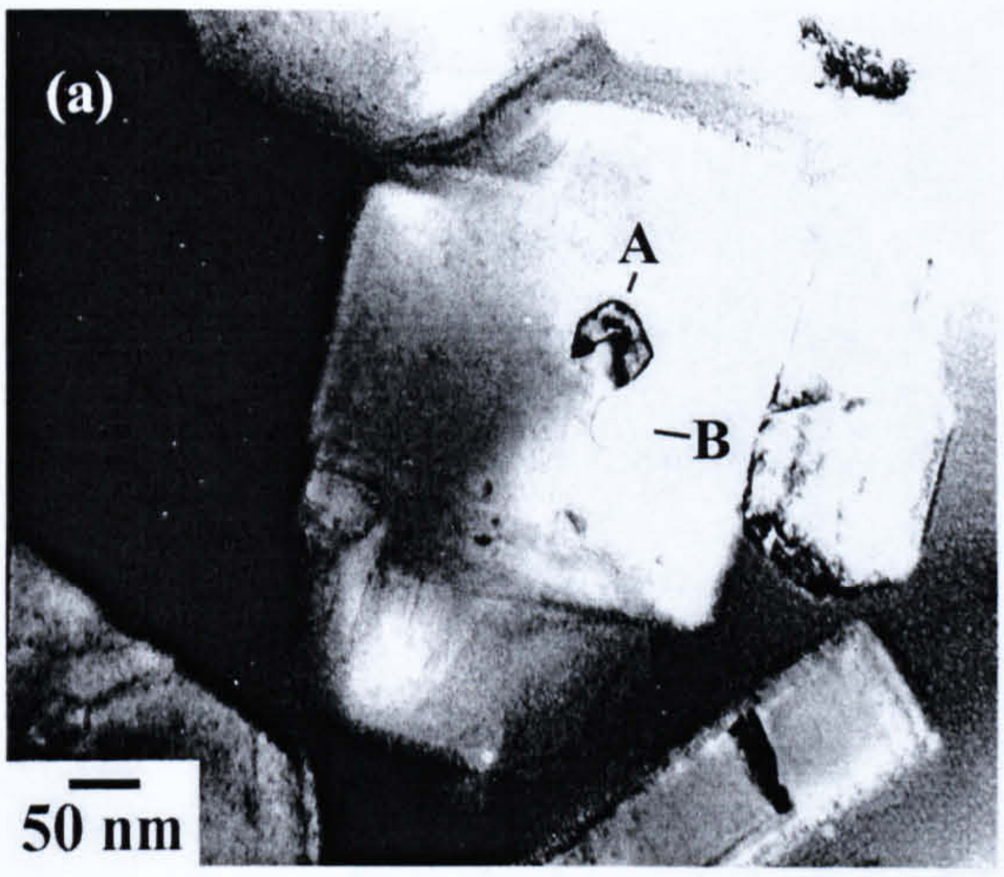

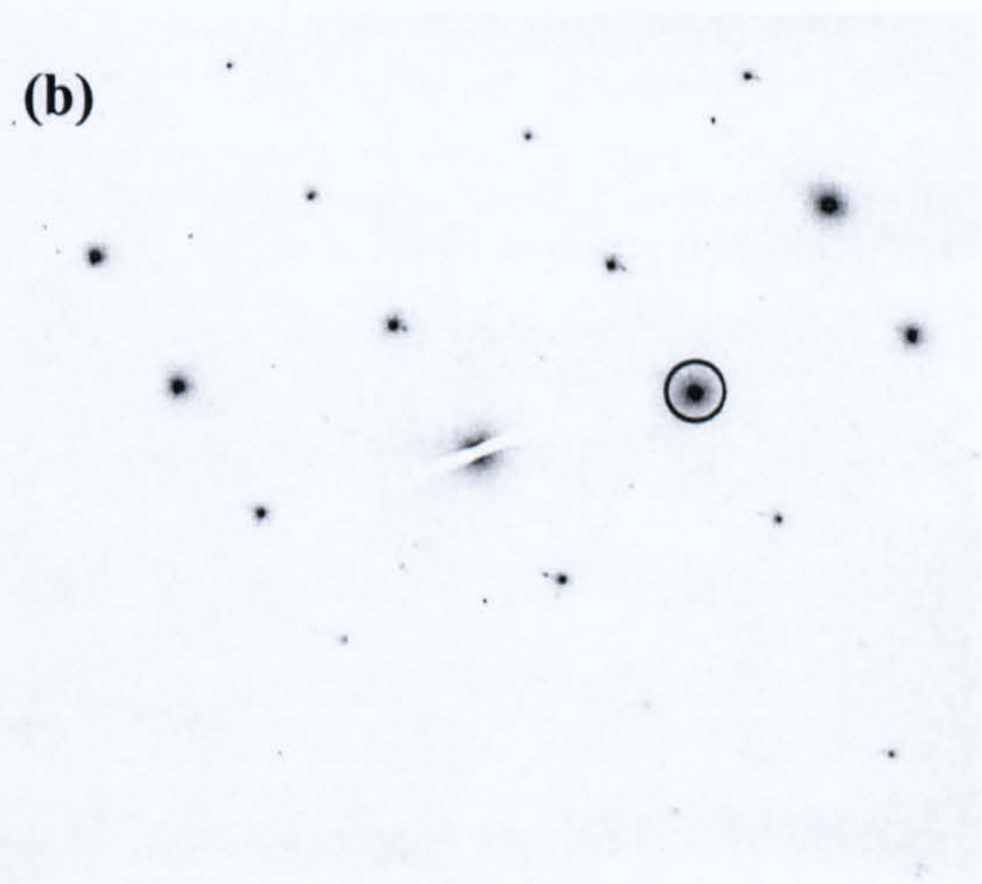

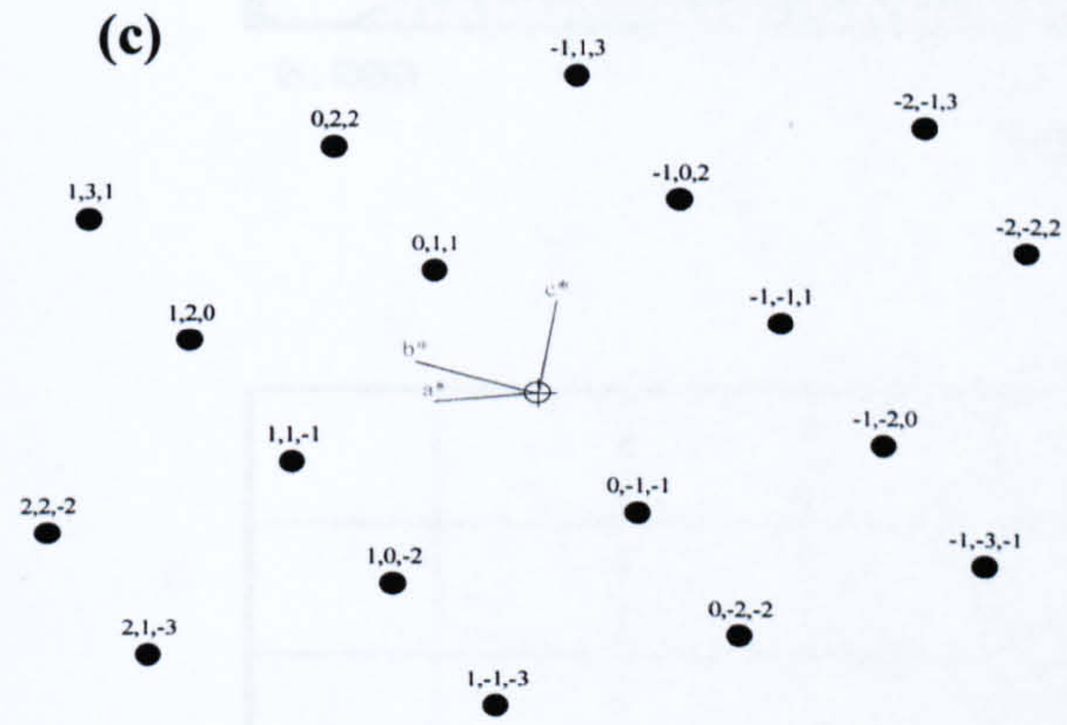

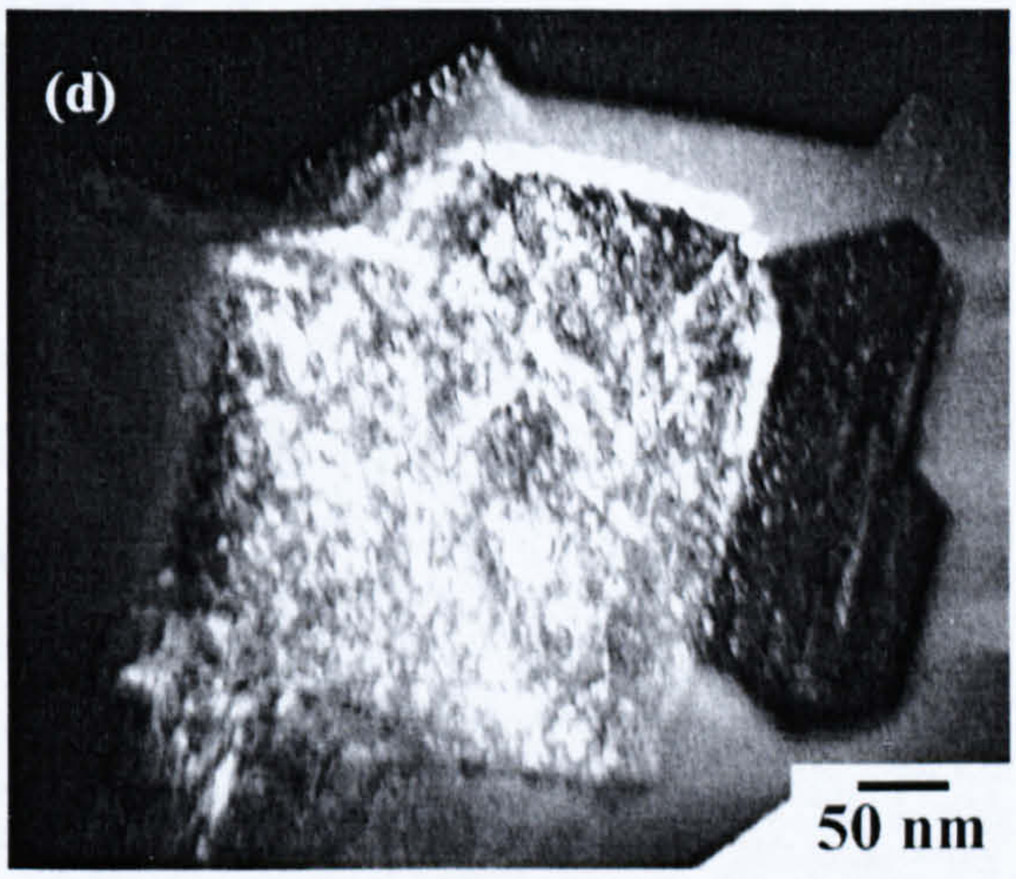

Zone axis : [2 $\bar{1}$ 1]

Fig. 4.28 TEM images of the HVOGF nanoscale WC-12 wt% Co coating (Run '3'). (a) TEM bright field image showing a carbide particle with precipitate formation on its edges and a small feature at position 'A' and 'B', (b) the SAD pattern of a carbide particle, (c) corresponding to (b) indexed to WC with [2 $\bar{1}$ 1] zone axis and (d) TEM dark field image taken from a diffraction spot in a dark circle in (b).

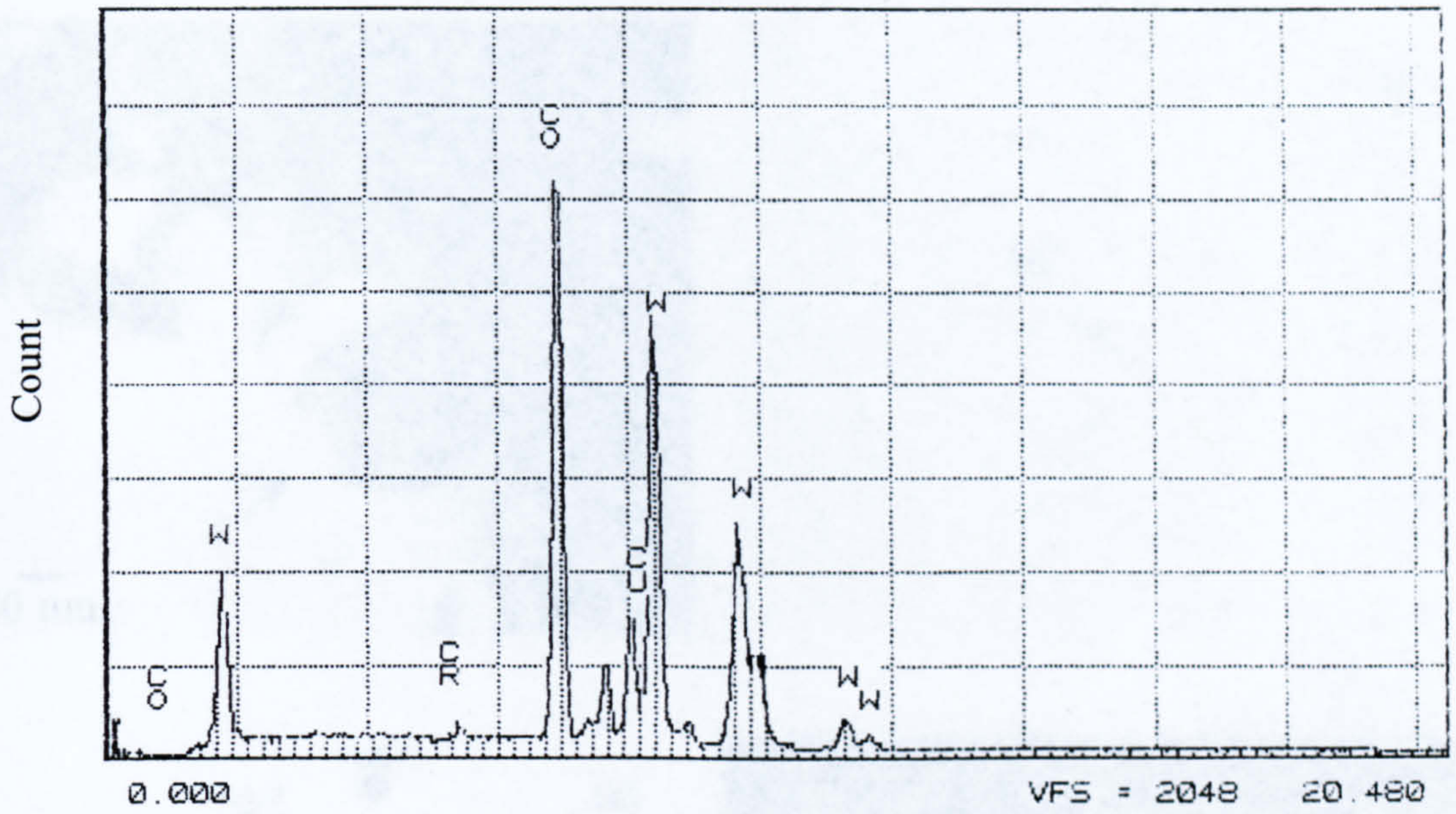

(e)

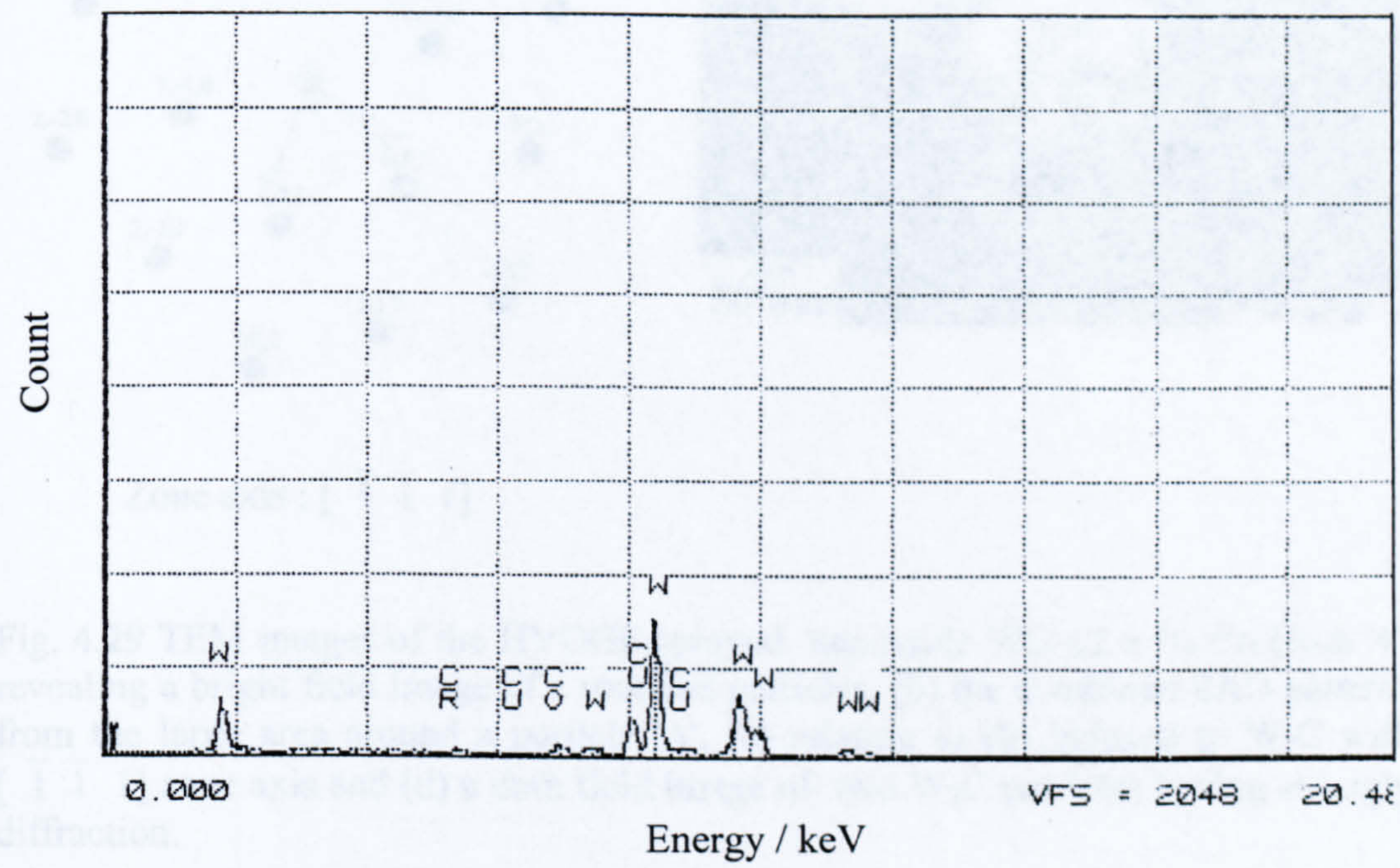

(f)

Fig. 4.28 (cont.) (e) An EDSA spectrum taken from a position 'A' in (a) showing the appearance of Co in a carbide particle, (f) An EDSA spectrum taken from a position 'B' reveals very low count levels for all elements including W and Co.

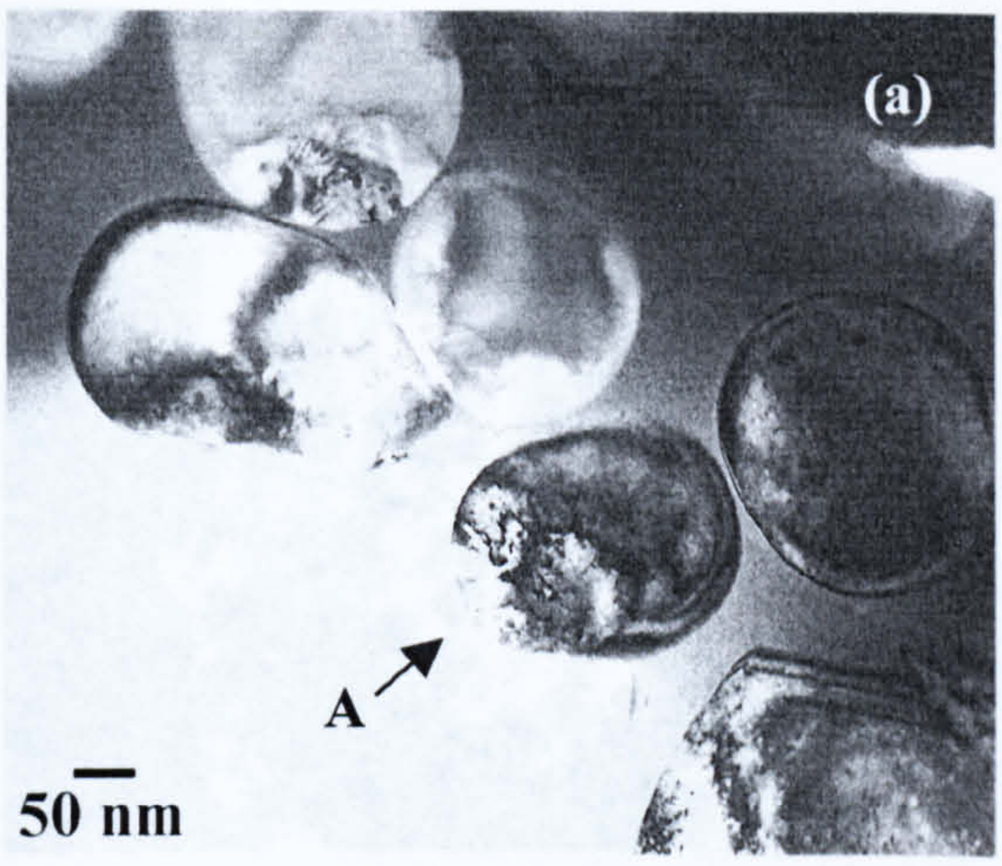

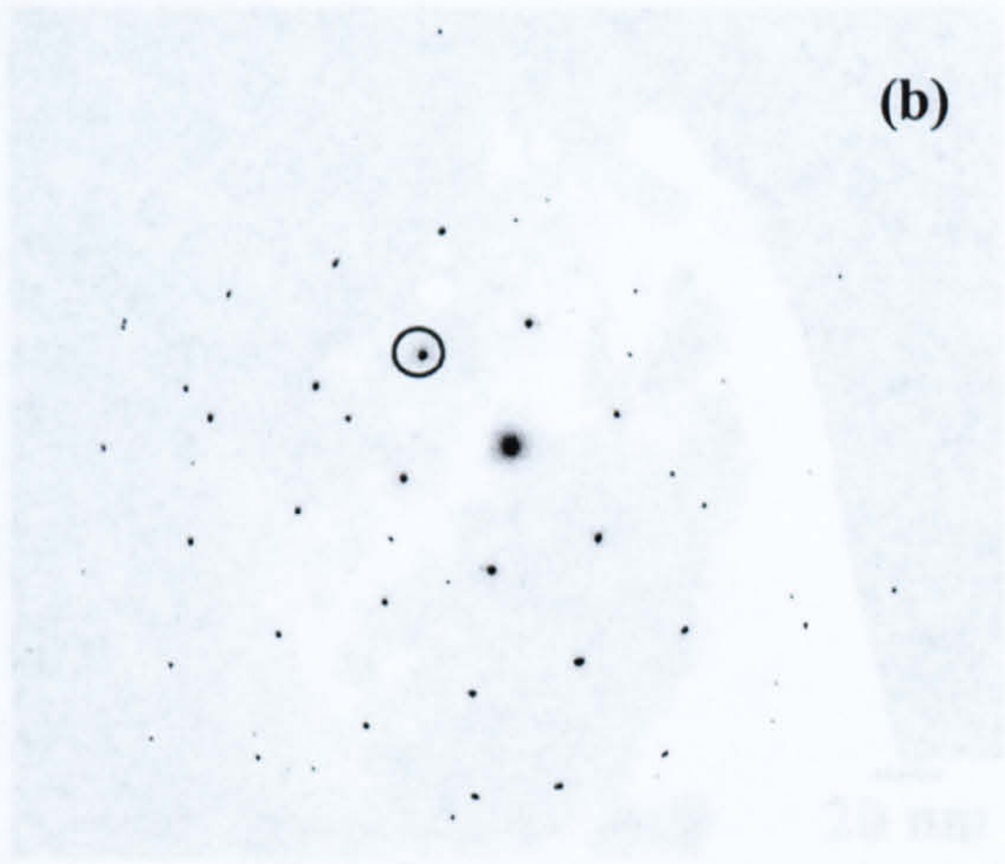

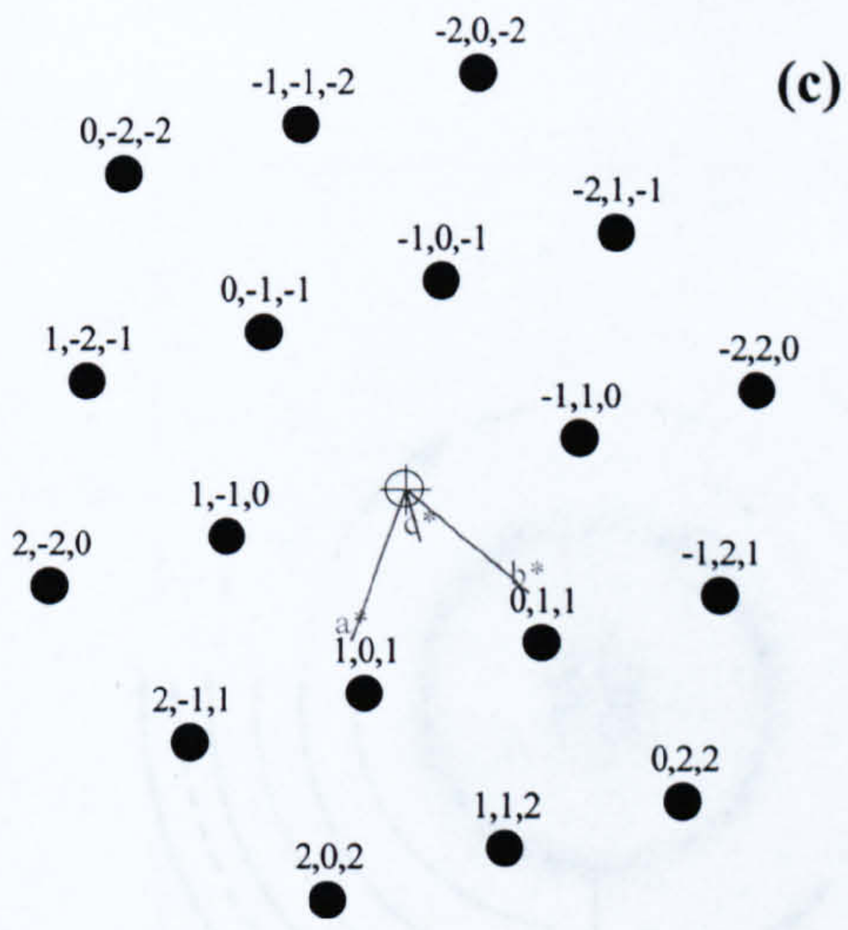

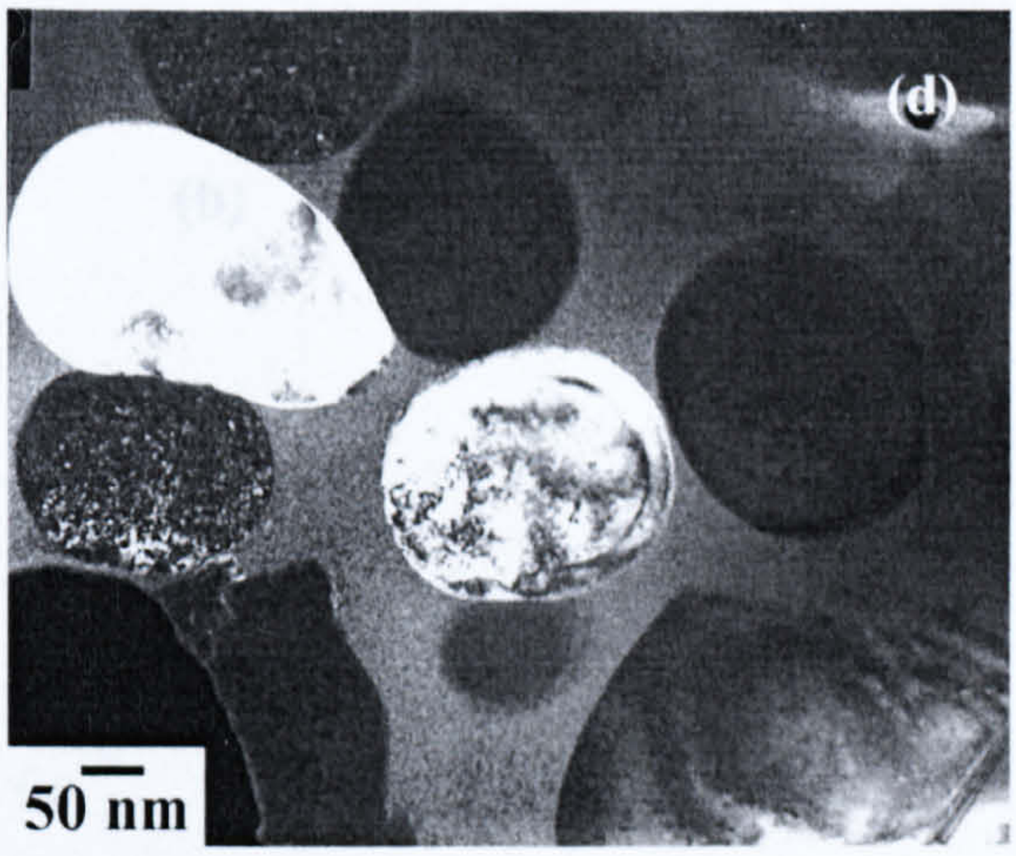

Zone axis : [$\bar{1}$ $\bar{1}$ 1]

Fig. 4.29 TEM images of the HVOGF sprayed nanoscale WC-12 wt% Co (Run '4') revealing a bright field image of a rounded particles, (b) the combined SAD patterns from the large area around a particle 'A', (c) relating to (b) indexed to W_2C with [$\bar{1}$ $\bar{1}$ 1] zone axis and (d) a dark field image of two W_2C particles having strongly diffraction.

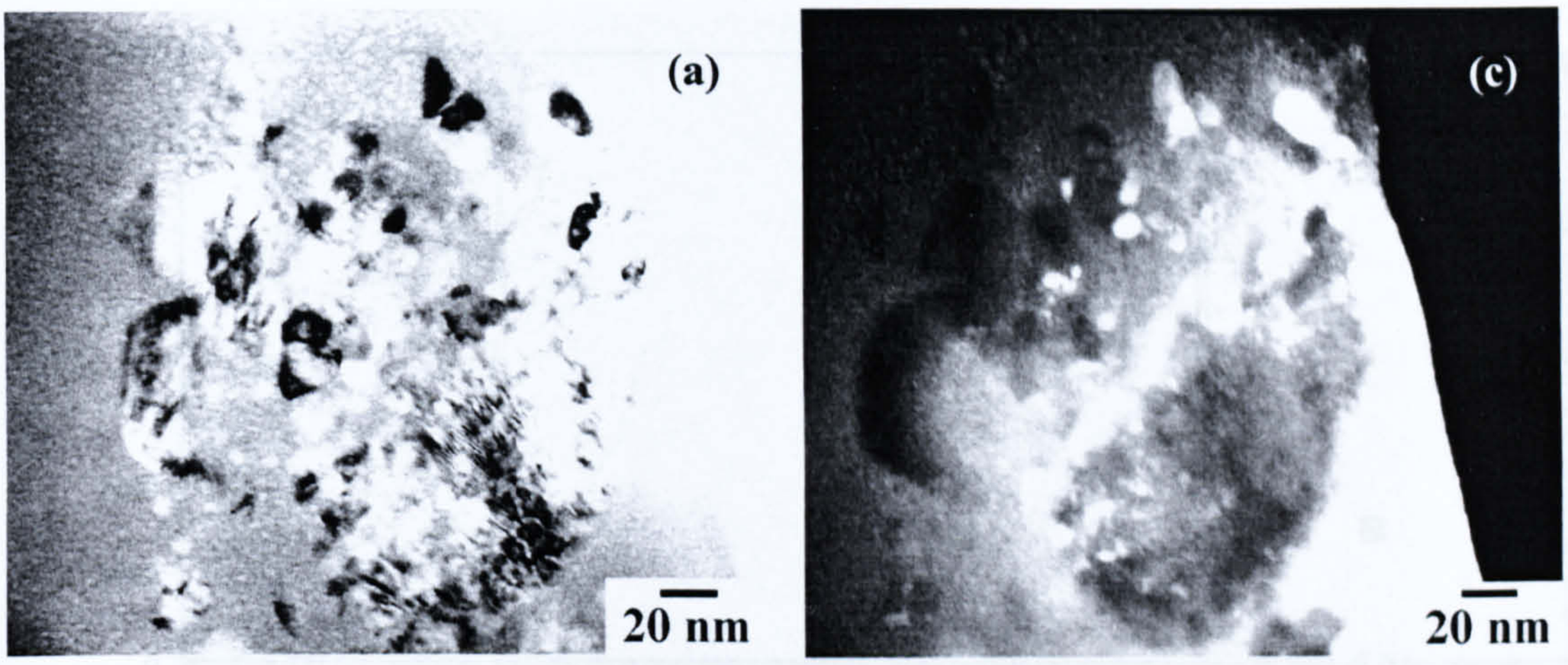

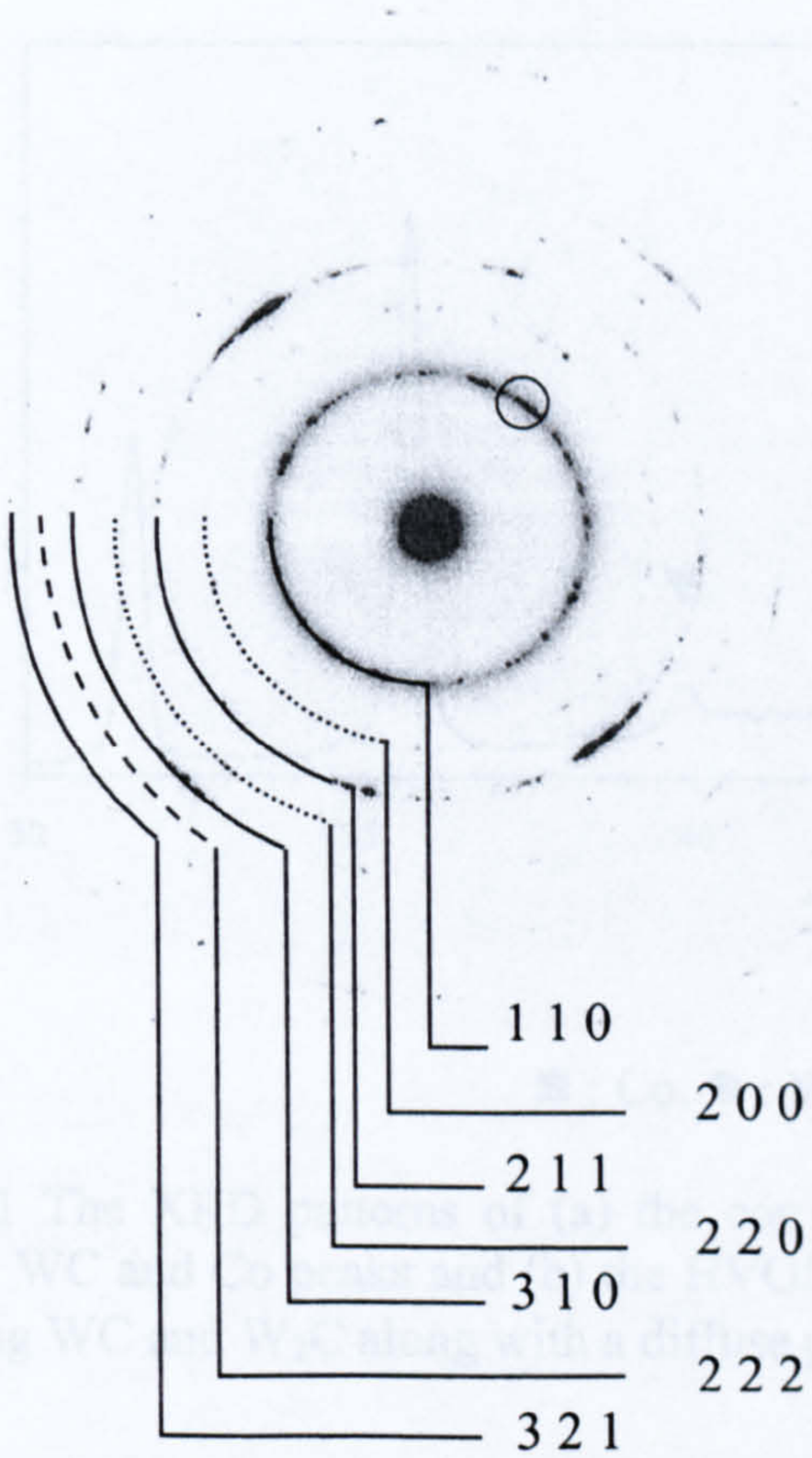

Fig. 4.30 TEM images of the HVOGF sprayed nanoscale WC-12 wt% Co coating (Run '2') exhibits (a) a bright field image of a cluster of carbide particles, (b) the SAD pattern with diffraction ring patterns indexed to W and (c) a dark field image taken from a ring in a dark circle.

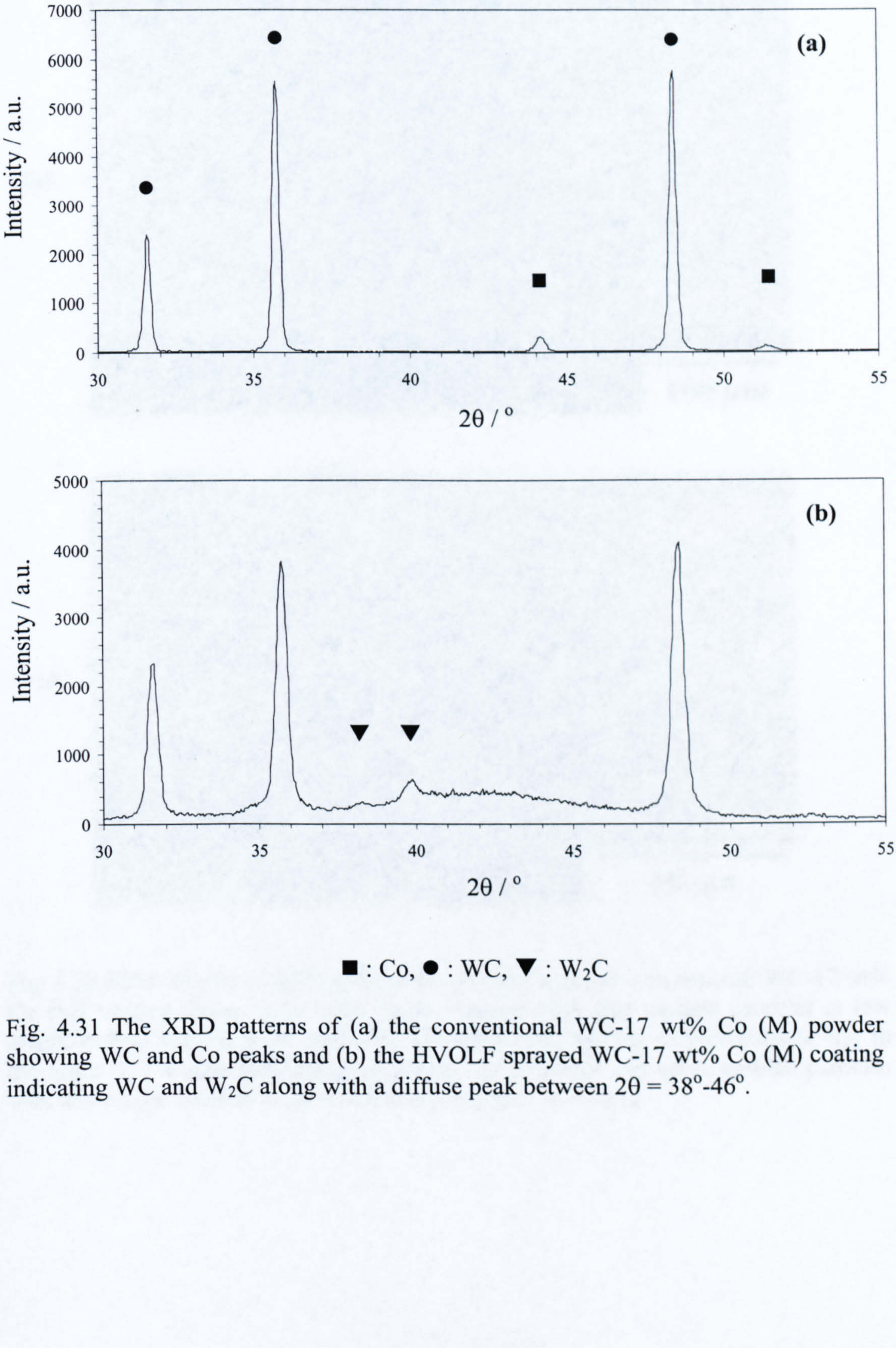

Fig. 4.31 The XRD patterns of (a) the conventional WC-17 wt% Co (M) powder showing WC and Co peaks and (b) the HVOLF sprayed WC-17 wt% Co (M) coating indicating WC and W_2C along with a diffuse peak between $2\theta = 38^{o}$-46^{o}.

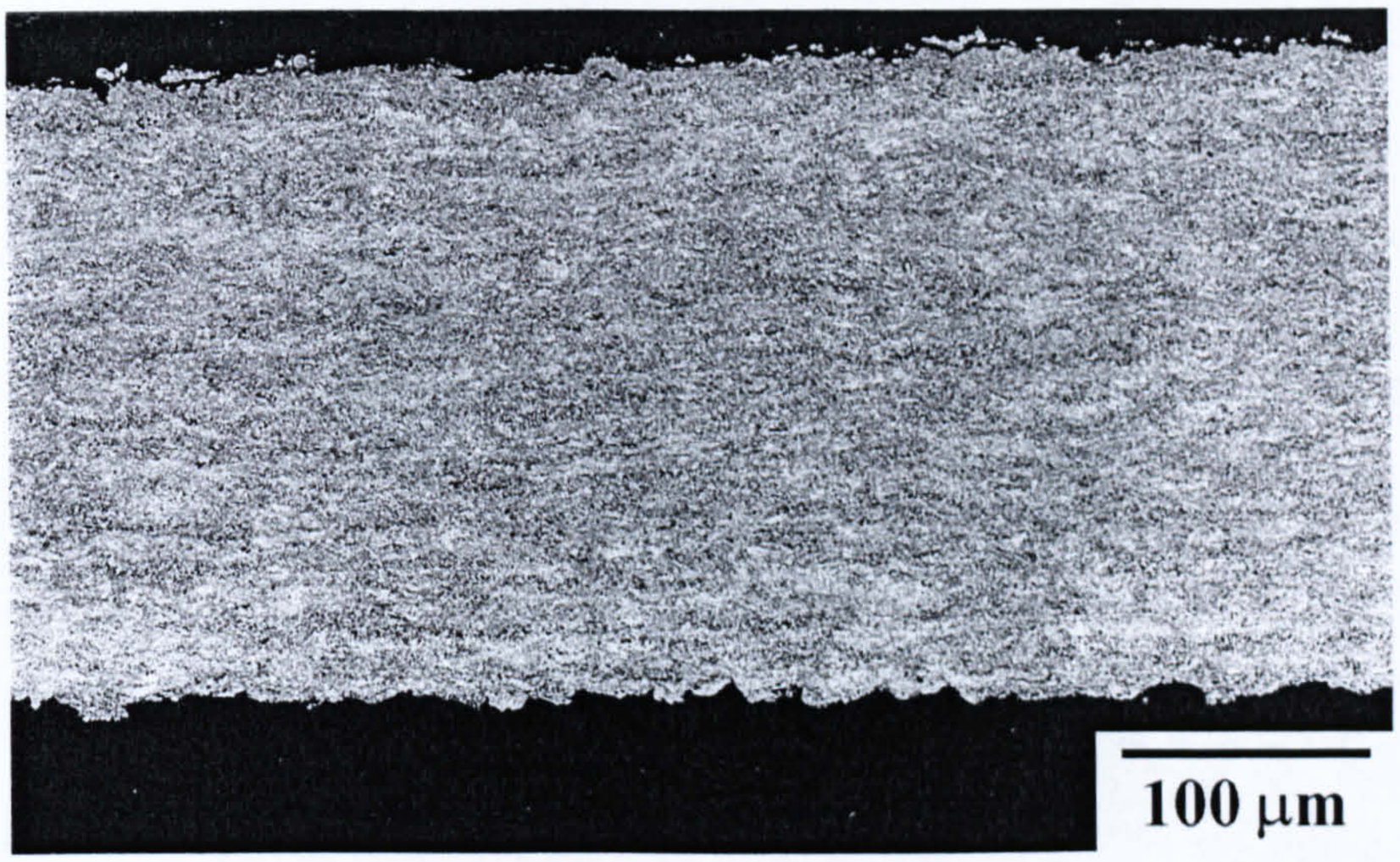

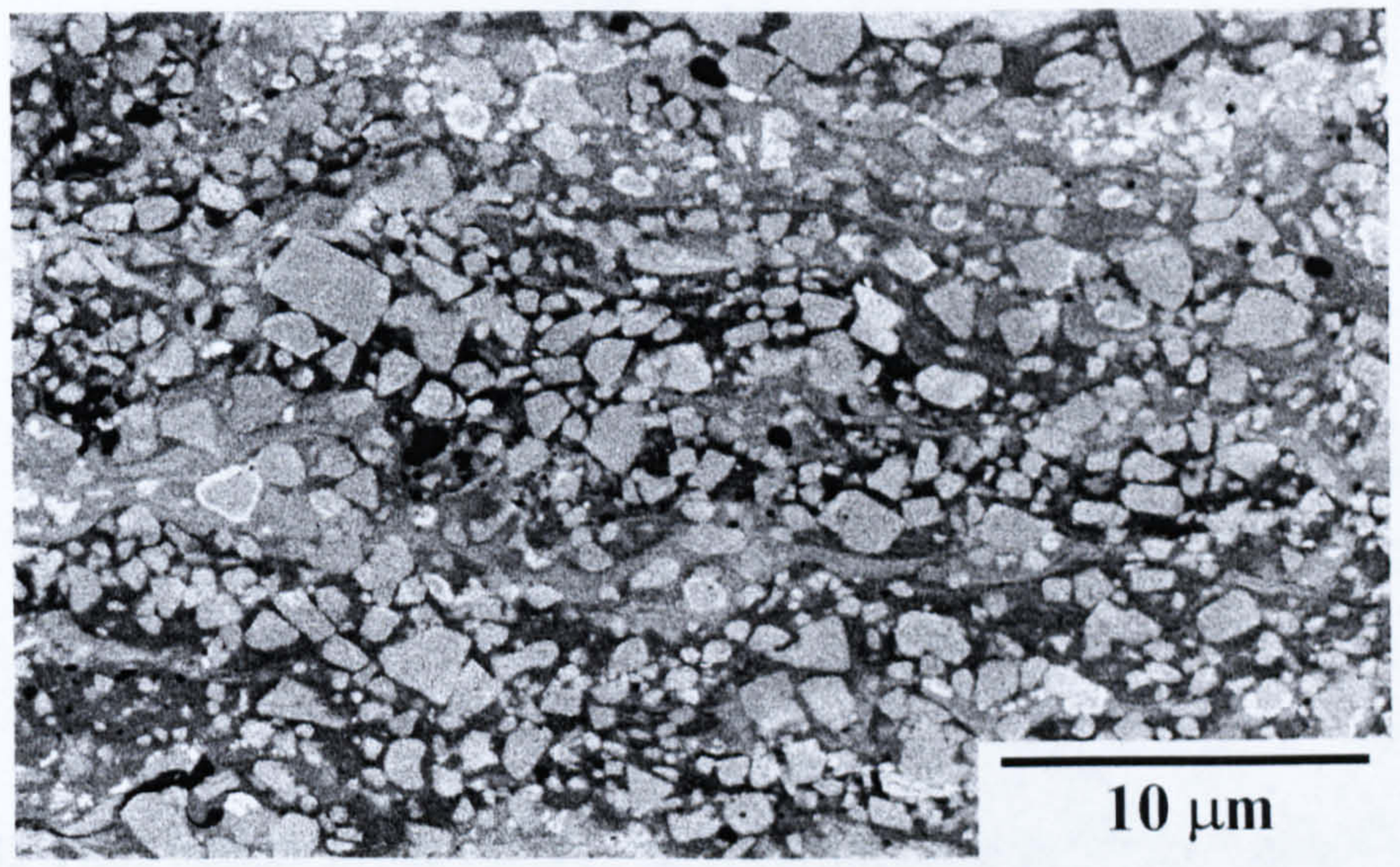

Fig. 4.32 SEM images in BSI mode of the HVOLF sprayed conventional WC-17 wt% Co (M) coating shows (a) a very dense structure with fine carbide particles at low magnification and (b) pores scattered throughout the coating, carbide particle size in the order of 1-4 μm, different grey shades of Co-matrix and some carbide particles with white layer on their edge found in the brighter Co-matrix.

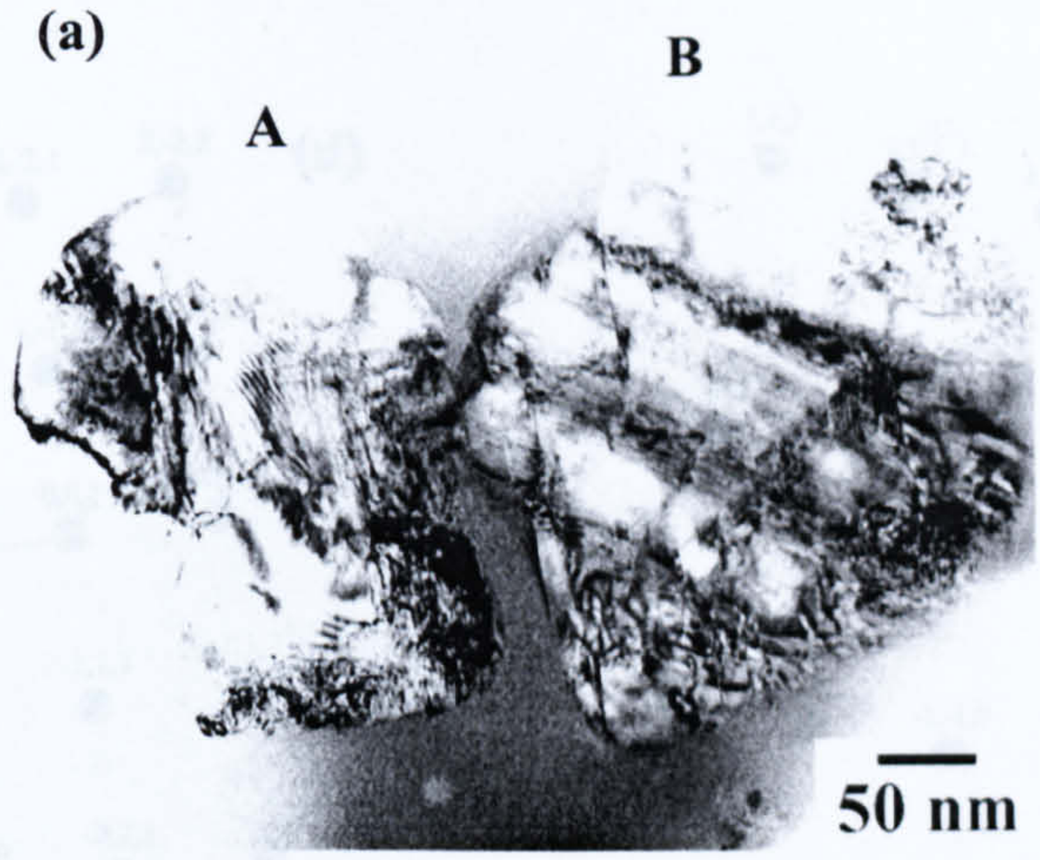

Fig. 4.33 TEM images of the HVOLF sprayed conventional WC-17 wt% Co coating (M) exhibiting (a) a bright field image of carbide particles 'A' and 'B' with their SAD patterns in (b) and (c), respectively. Weak diffuse rings are also visible in their SAD patterns.

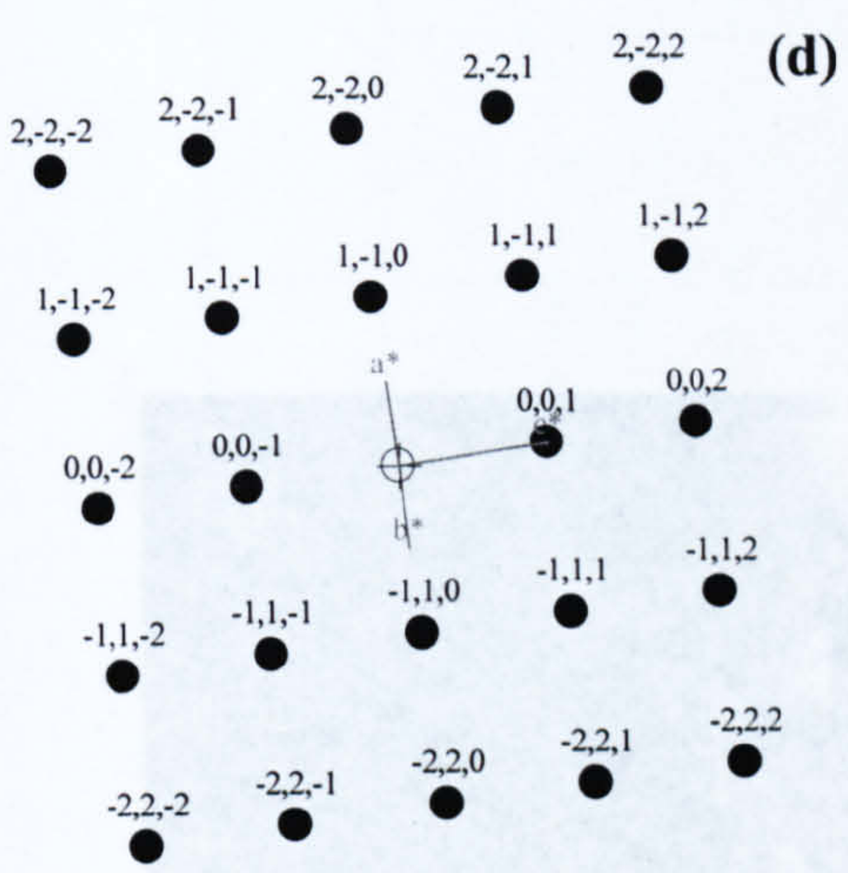

Zone axis : [$\bar{1}$ $\bar{1}$ 0]

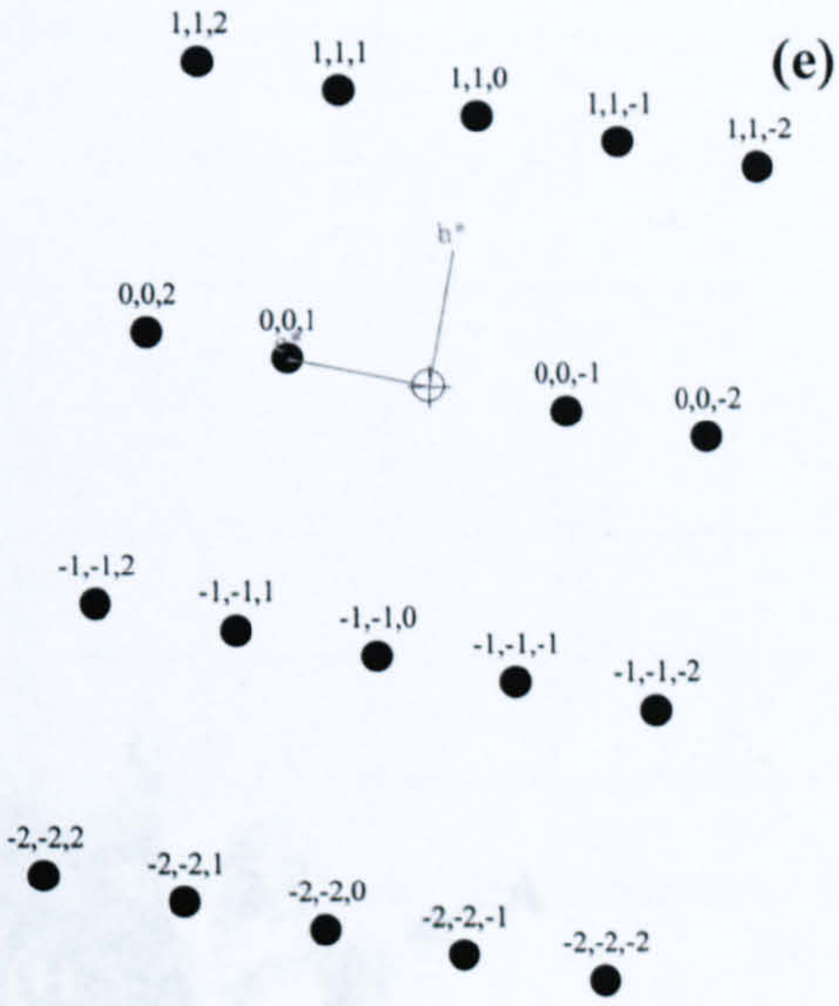

Zone axis : [1 $\bar{1}$ 0]

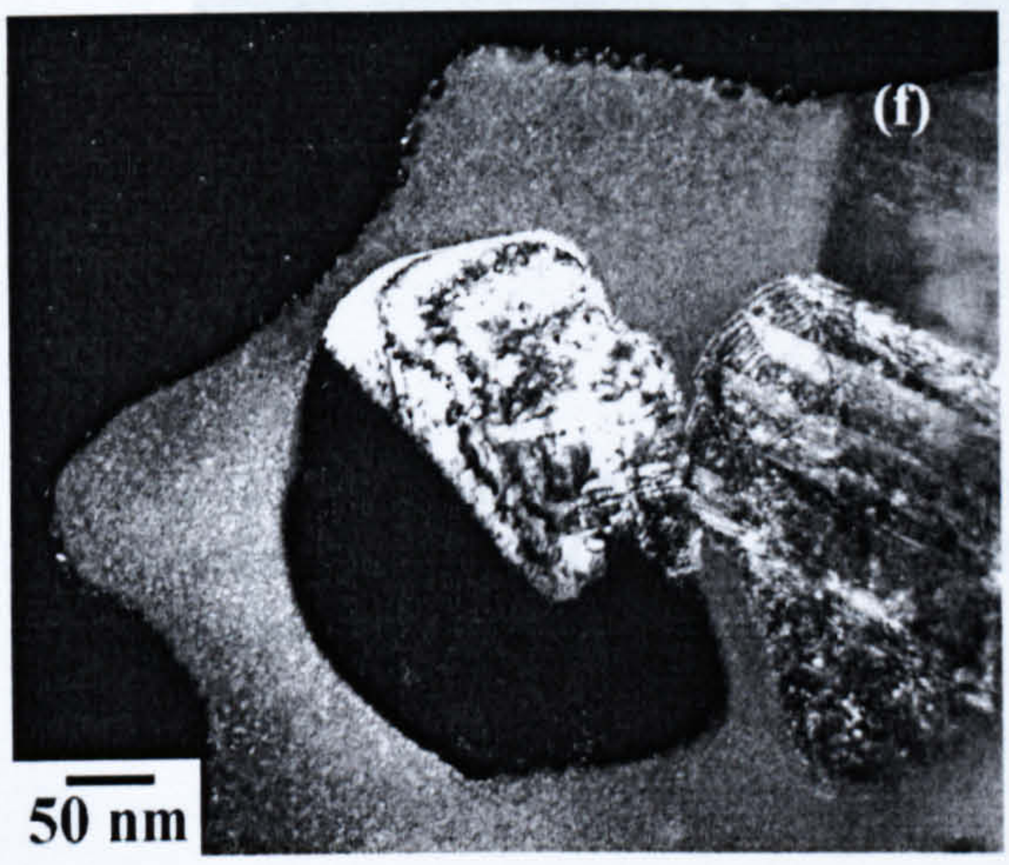

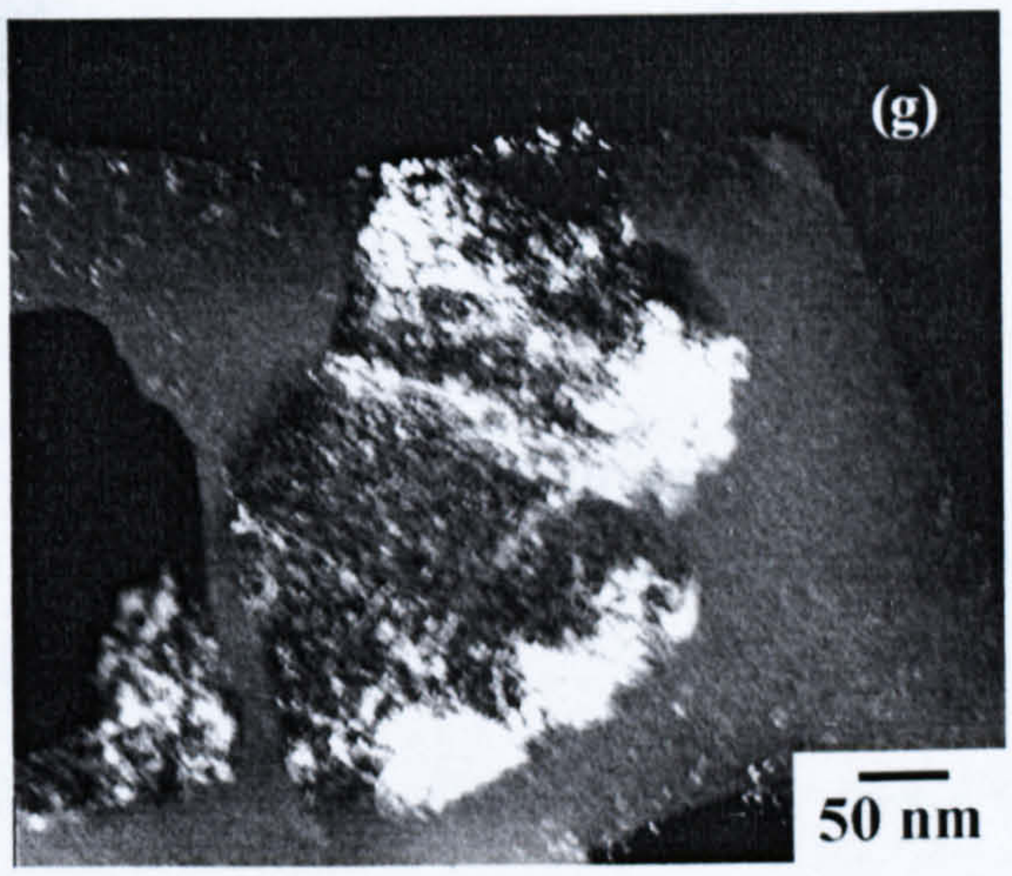

Fig. 4.33 (cont.) (d) and (e) related to (b) and (c) respectively are both indexed to WC both with [$\bar{1}$ $\bar{1}$ 0] and [1 $\bar{1}$ 0] zone axes, respectively. (f) and (g) show dark field images of 'A' and 'B', respectively.

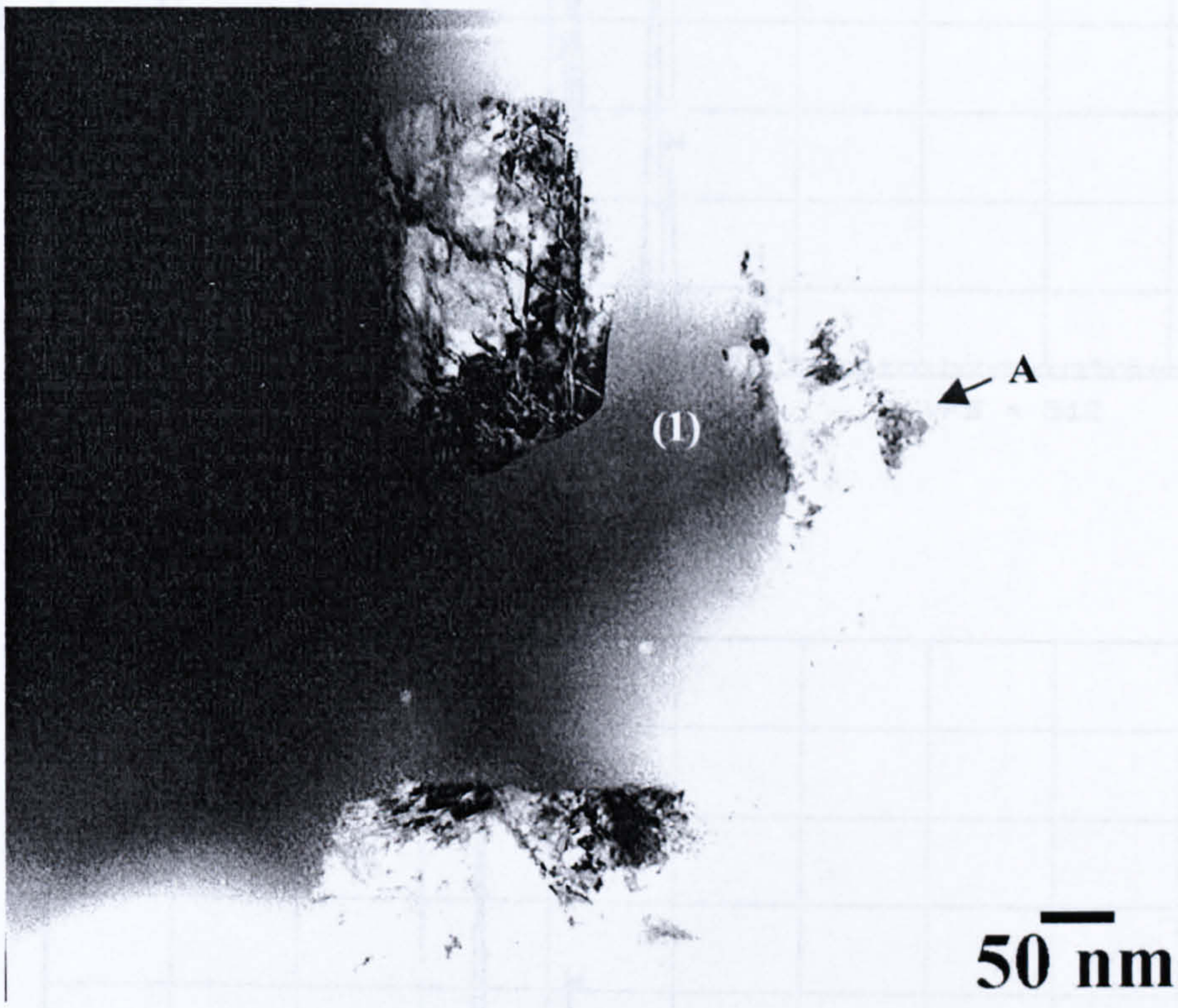

Fig 4.34 (a) showing a TEM bright field image of the HVOLF sprayed conventional WC-17 wt% Co (M) coating with three carbide particles indexed to WC in the Co-matrix.

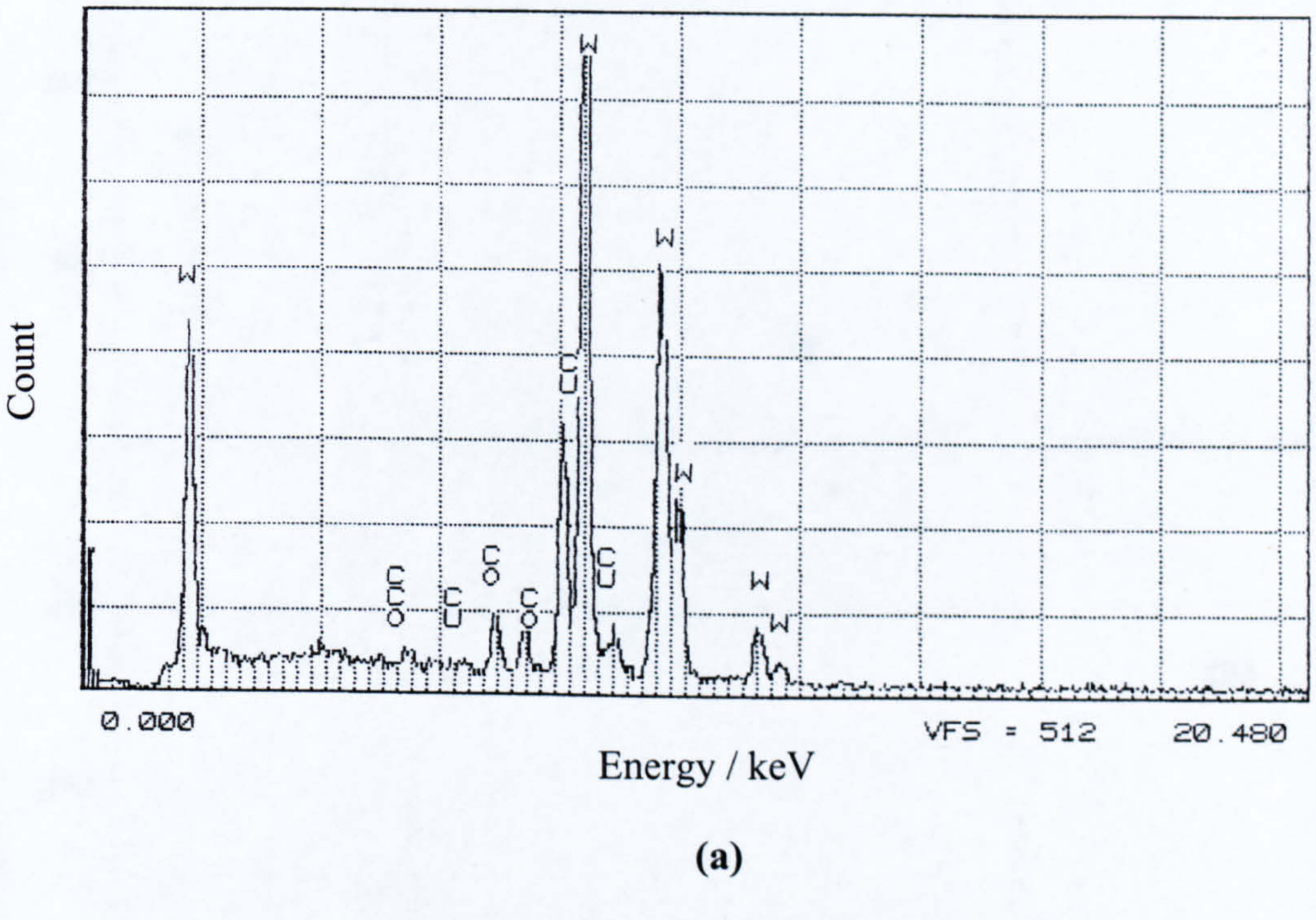

(a)

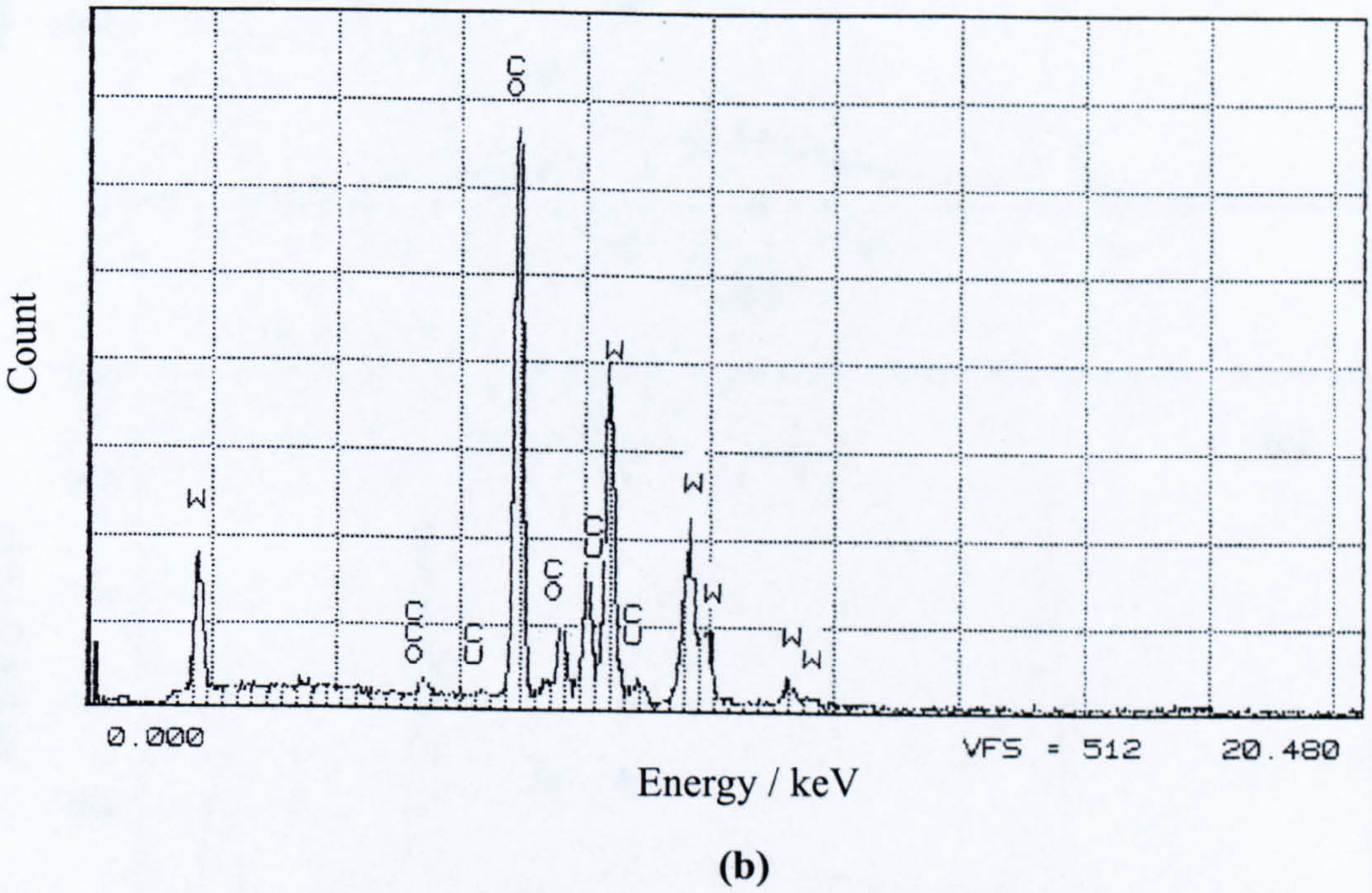

(b)

Fig. 4.35 presents EDSA spectra taken from the image shown in Fig. 4.35 (a) from a particle 'A' and (b) from the Co based matrix in position '1' showing the appearance of an amount of W in Co based matrix.

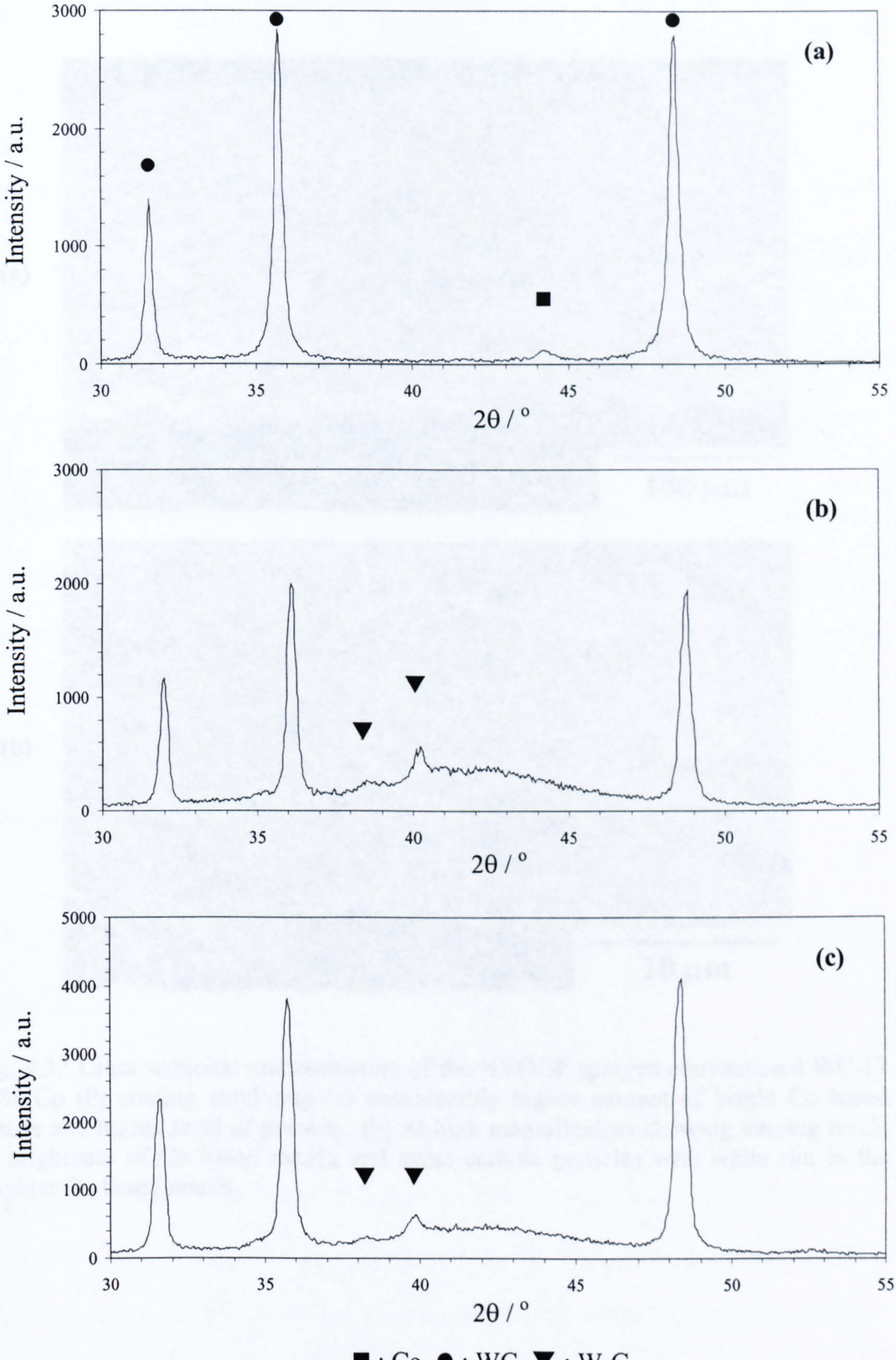

Fig. 4.36 XRD patterns of (a) the conventional WC-17 wt% Co (P) powder showing WC and Co peaks, (b) the coating sprayed with the HVOGF indicating WC and W_2C along with a diffuse peak between $2\theta = 38^{\circ}$-46° and (c) the (M) coating sprayed with the HVOLF indicating WC and W_2C along with a diffuse peak.

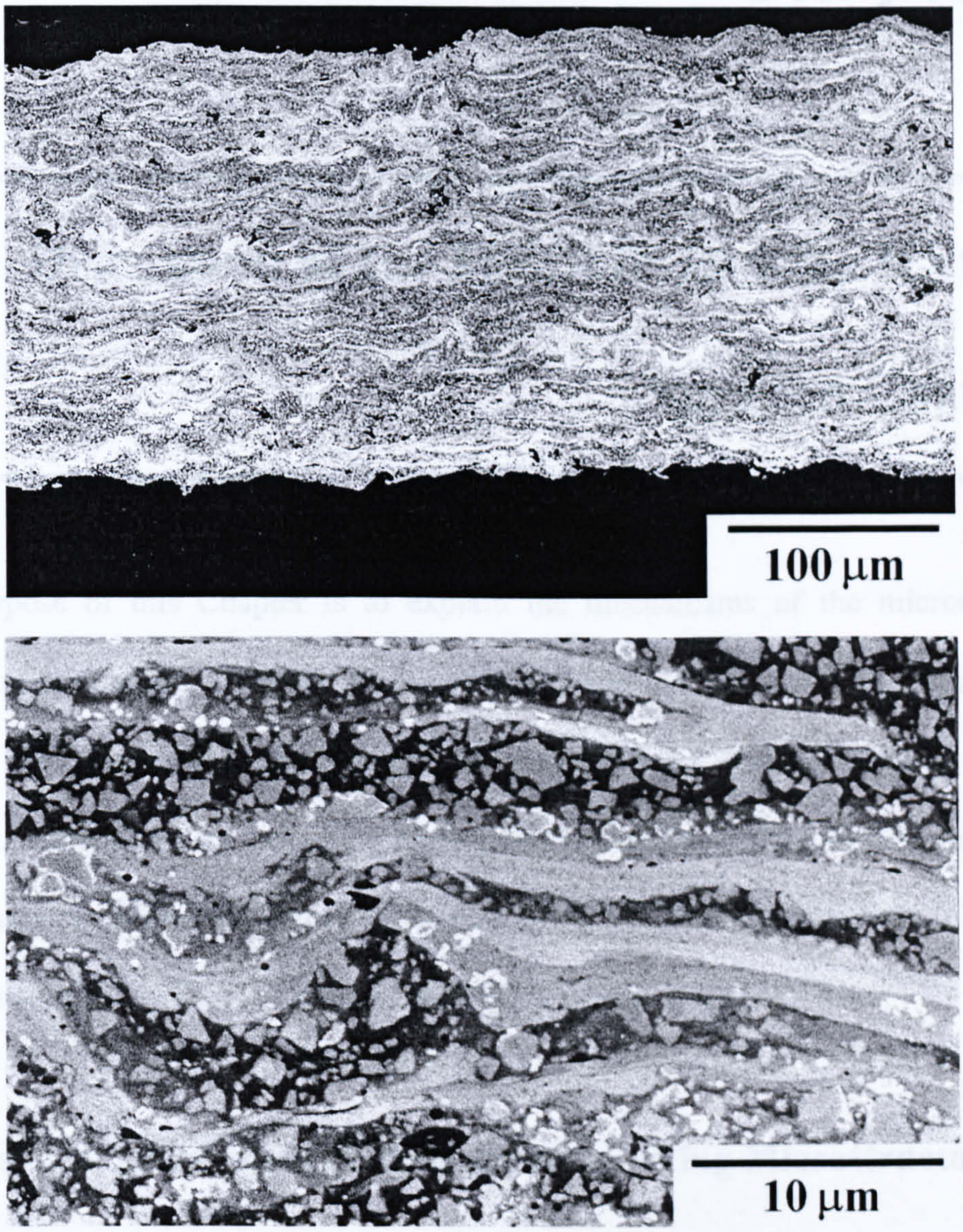

Fig. 4.37 Cross sectional microstructure of the HVOGF sprayed conventional WC-17 wt% Co (P) coating exhibiting (a) considerably higher amount of bright Co based matrix and higher level of porosity. (b) At high magnification showing varying levels of brightness of Co based matrix and some carbide particles with white rim in the brighter Co based matrix.

Chapter 5

Discussion of the HVOGF and the HVOLF Sprayed Coatings

The purpose of this Chapter is to explain the mechanisms of the microstructure formation in coatings deposited by the HVOGF and the HVOLF spray guns and to discuss the parameters (such as the characteristics of starting powder, particle velocity, temperature etc.) affecting the microstructure. The main part is to propose an outline model of the microstructure formation for the different behaviour of WC-Co particles sprayed by the HVOGF and the HVOLF spray guns.

5.1 Physical and Chemical Phenomena Affecting Microstructure Formation

The purpose of this section is to discuss, in a semi-quantitative manner, the physical and chemical phenomena which influence the microstructure formation in the coating. In general terms, coating formation involves injecting WC-Co cermet powders into a high temperature, high velocity gas jet. The particles then strike a solid substrate and successive deposits adhere together to form a thick coating. The main phenomena occurring can be described under the following headings:

- Particle heating and particle melting
- Particle acceleration
- Chemical reactions between the particles and the surrounding gas
- Particle impact, spreading and solidification at high cooling rate

5.1.1 Particle Heating and Particle Melting

Particle heating occurs as a result of heat transfer from the high temperature gas to the particle. Some fundamental differences exist between the HVOGF (Top Gun) and HVOLF (Met-Jet II) systems. Gun geometries are shown schematically in Fig. 3.1. It can be seen that powder is injected in different positions for the different processes. In the HVOGF process, powder is injected via the back of the gun, and as a result the powder passes through the hottest zone in the combustion chamber. Thus, the WC-Co powder sprayed by the HVOGF process is expected to have a higher level of melting than the WC-Co powder sprayed by the HVOLF process. In the HVOLF process, powder is fed into the gas downstream of the throat of the gun. Thus the powder does not pass through the hottest zone in the combustion chamber.

According to Gu (2000), centreline gas temperature and velocity in the HVOGF process using propylene as fuel gas are about 2700 K and 1500 m s^{-1}, respectively. Gas temperature and gas velocity were calculated using fuel and oxygen flows similar to that employed in this work. These give particle acceleration and heating values as shown in Fig. 5.1. The data can be used to estimate roughly the temperature and velocity of WC-12 wt% Co powder sprayed by the HVOGF process using hydrogen as fuel gas instead of propylene. Assuming no temperature gradients within particles

and neglecting latent heat of melting, it is predicted that particles which has sizes ranging from 20 - 40 μm reach temperatures between 1500 - 2000 K (1200 - 1700 °C) (Fig. 5.1a) and particle velocities between 300 - 400 m s^{-1} (Fig. 5.1b). Clearly, small particles reach a much higher maximum temperature than larger particles. The melting temperature of Co is 1768 K (1495 °C) and so particles in the size range up to 30 μm are expected to undergo partial melting.

The HVOLF gun has not been modelled in such detail. However, Gu (2001) conducted computational modelling of Inconel 625 powder sprayed by the HVOLF process using kerosene as fuel gas (Fig. 5.2). It was shown that the centreline gas temperature and velocity were 2300 K and 1700 m s^{-1}, respectively, i.e. a significantly lower temperature and higher velocity than in the HVOGF process. The data obtained from this computational modelling can be applied to give an approximate powder temperature and velocity of WC-12 wt% Co powder sprayed by the HVOLF process. Hence, in the HVOLF system particle velocities are expected to be higher (residence times shorter) and particle temperatures will be expected to be lower than in the HVOGF system. In the WC-Co system it has largely been assumed that temperature gradients in the particle can be neglected. However, evidence is growing (e.g. Figs. 4.8b and 4.17b) that this is not a good assumption. Instead, the particles which begin to melt can be considered as having a structure as shown in Fig. 5.3. It is possible that in the HVOGF system the unmelted core in these particles which form the coating will be small and melted zone large. In the HVOLF system, it is likely that melted zone is small and solid core large. Fig. 5.4 illustrates schematically how powders of different sizes within the typical size distribution might be expected to behave.

5.1.2 Dissolution of WC in Molten Cobalt

Heating the WC-Co powder above the melting point of pure Co at 1768 K (1495 °C) the Co-binder begins to melt. The particle temperature is not homogeneous throughout, i.e., the particle core has a lower temperature than the particle shell. WC particles begin to dissolve in the liquid Co-binder at the temperature around 1600 K (~ 1326 °C), as shown in the vertical of section of Fig. 5.5 (Fernández-Guillermet, 1989). Thus, WC dissolution causes a considerable increase of W and C in solution in Co near a WC particle/liquid Co interface. Fig. 5.6 shows the projection of the liquidus surface of Co-W-C system (Fernández-Guillermet, 1989). It is apparent that WC particles begin dissolving in the liquid Co at a temperature of between 1548 and 1599 K. At a temperature of 1773 K, approximately 30 wt% W and 3 wt% C can dissolve in the liquid Co. It is evident that at higher temperature, further dissolution of WC occurs. Moreover, the dissolution of WC particles must result in a decrease of the volume fraction of WC in the coating (Stewart et al., 2000).

As mentioned previously regarding WC dissolution, the dissolution rate of WC was studied at a temperature of 1450 °C with turbulent stirring in the liquid Co (Lavergne and Allibert, 1999). The dissolution rate of WC calculated with the aid of the Berthoud equation (Lavergne and Allibert, 1999) was reported to give rate constants of 5.0×10^{-5} and 4.9×10^{-5} m s^{-1}, respectively for W and C.

From the calculation using Berthoud equation (see details in Appendix 3), it was found that in 2 milliseconds an average size of a WC grain of 1 μm diameter gives solute content (W) in the liquid Co 0.8 times the equilibrium value. Furthermore the

calculation also shows that in 2 milliseconds small WC grain sizes give a higher proportion of solute content than large WC grain sizes. Thus, it can be stated that WC grains with a nanoscale-size are dissolved more rapidly than WC grains with a microscale-size. Also, the longer the exposure time in the hot flame temperature, the greater the level of dissolution that results.

In addition, it is possible to estimate the binder thickness as a function of the WC size (see Appendix 3). For example, a WC grain with a 1 μm diameter has a diameter of the Co-binder surrounding the WC grain of 1.1 μm. Moreover, the estimated total volume of W lost from the WC by dissolution is 43.6×10^{-21} m^3. Due to WC dissolution during spraying, this reduces the WC grain size from 1 to 0.97 μm diameter assuming that no W or C is lost from the equilibrium system. The next section reveals that this is an incorrect assumption and so underestimates the degree of WC dissolution.

5.1.3 Oxidation in the Gas Stream

During flight, between the exit of the gun nozzle and impact with the substrate (a distance of 200 - 300 mm) the particles are exposed to high levels of oxygen. From the air itself and also due to excess O_2 in the combustion gas. Korpiola et al. (1995) claim that the partial pressure of oxygen increases to ~ 0.06 atm at the distance of 150 mm from the gun exit. Therefore, it is clear that oxidation reactions can occur during powder particles exposed in the hot flame temperature.

For oxidation occurring at the gas/powder particle interface, the oxygen can react directly with carbide particles which are at the free surface of heated powders (solid state reaction). The result is that W_2C and W are formed directly from WC particles. The occurrence of the direct oxidation of WC particles has been proposed by a number of researchers (Nerz et al., 1991; Fincke et al., 1994; Harvey et al., 1995; Khan et al., 1997; Vinaya et al., 1985).

In contrast, it is clearly apparent that BSE-SEM images of WC-Co coatings show different grey shades of the Co-binder matrix and very bright shells surrounding the carbide particles (e.g. Figs. 4.15 and 4.37). It is evident from Stewart et al. (2000) that the different grey shades of the Co binder matrix result from the different W compositions. Thus, another model of oxidation is that it occurred in the liquid Co-binder during spraying.

In the previous section 5.1.2, dissolution of WC in molten Co was discussed. The WC particle/liquid Co interface contains high concentrations of W and C. Oxygen can diffuse easily into the rim of molten particles (the liquid Co) and react with C to form CO gas (liquid state reaction). Fig. 5.7 shows the Ellingham diagram for oxidation of liquid Co phase (Stewart, 1998). The favourable reaction of oxygen forming CO gas is $2C + O_2 \rightarrow 2CO_{(g)}$ at the temperature exceeding 1768 K (Stewart, 1998). Hence, oxidation causes C depletion of the liquid Co. However, the depletion of C at the rim of molten particle leads to further dissolution of WC particles in the liquid Co-binder in an attempt to maintain equilibrium between Co(W,C) and WC.

Thus, oxidation of solid WC and the liquid state reaction with O_2 both causes C depletion. The net result of decarburisation is a difference in the amount of C between the inner and the outer regions of particles and a reduced carbon content of the coating compared with the original powder (typically 3.5 wt% C compared with ~5 wt% C initially in the powder (Stewart, 1998)).

5.1.4 Particle Impact and Solidification

As mentioned above, WC dissolves in the liquid Co, and C in the liquid Co reacts with oxygen causing C depletion. Thus, it is likely that there is considerable W enrichment and C depletion near the WC/liquid Co interface. Prior to powder particles impacting on the substrate, the powder temperature is decreasing relatively slowly. When powder particles impact on the substrate, they are cooled down rapidly, as a result of heat transfer to the substrate. W_2C, W and an amorphous binder phase all are formed during solidification. Although, the cooling rate of splats is estimated to be 10^6 - 10^7 K s^{-1} (Sampath and Herman, 1996), powder particles will also experience some reheating as successive layers of splats are built up. This may result in nanocrystalline formation from an originally amorphous binder phase.

Due to the rapid solidification of splats, the ternary equilibrium phase diagram cannot be used to accurately analyze phase transformations. Fig. 5.6, however, it can assistance understanding the presence of a W_2C shell, which forms during solidification, surrounding a WC core. When the powder temperature drops to ~ 2200 K, the melt composition at equilibrium resulting from WC dissolution is shown by the solid circle. The result of oxidation causes C decrease in the liquid Co phase. Thus,

the melt composition could be as shown by the open circle, which is much closer to the M_2C phase field. As the powder particle is rapidly solidified, a retained WC core still exists whereas the areas around a WC core form W_2C using the WC as a nucleation site. Moreover, it is unlikely that M_6C and $M_{12}C$ are formed because of their complex crystal structure, whist it is possible to form an amorphous structure from the Co-rich matrix phase.

5.2 Comparison with Experimental Observations

Fig. 5.8 shows a schematic model of the development of solidified structures in the HVOGF and HVOLF deposits. As a WC-Co powder particle is exposed to the hot flame temperature, the particle temperature increases (Figs. 5.8a and 5.8d). The Co-binder begin to melt, WC particles dissolve in the liquid Co leading to high concentrations of W and C at the WC particle/liquid Co interface. Oxygen reacts with C in the liquid Co at the rim of a molten particle causing C depletion of the liquid Co. The C depletion promotes further WC dissolution into the liquid Co, and as a result, the regions near the WC/liquid Co interface contain W enrichment and C depletion. The result of the WC dissolution and decarburisation is manifested by different grey shades of the Co-binder matrix observed by BS-SEM imaging (e.g. Fig. 4.37b). EDS analysis (Table 4.4) in the HVOGF sprayed WC-17 wt% Co (P) coating (Fig. 4.37b) indicates that the bright binder matrix (or the areas near the WC/liquid Co interface) contains increased W and lower C concentrations, whilst the dark binder matrix at the WC core contains less W and higher C concentrations, because of less dissolution and less oxidation. Thus, it can be stated that the regions of bright binder matrix, where a greater degree of dissolution and oxidation occurs, contains small WC grain sizes and

reduced volume fraction of WC grains. Whereas the regions of dark binder matrix, where less dissolution and oxidation occurs, contains large WC grain sizes and a high volume fraction of WC grains (Stewart, 1998).

Regarding the degree of melting, Figs. 4.8 and 4.17 show significant differences between the conventional WC-12 wt% Co coatings sprayed by the HVOLF and HVOGF systems. The HVOGF sprayed coating (Fig. 5.9b) shows more blue area than the HVOLF sprayed coating (Fig. 5.9a). The blue areas are etched regions attacked by Murakami's reagent. This reagent generally does not attack pure Co-binder and only slightly attacks WC. However, Murakami's reagent will attack W_2C, eta phase (i.e. Co_3W_3C and Co_6W_6C) (Tomita et al., 1993) and nanocrystalline/amorphous phase (Korpiola and Vuoristo, 1996). Thus, the blue areas (or reacted areas) can be identified as W_2C, eta phase (Co_3W_3C and Co_6W_6C) and nanocrystalline/amorphous phase. Therefore, the etched microstructure support the model in Figs. 5.8b and 5.8e that WC-Co powders sprayed by the HVOGF process undergo a higher degree of melting and then as a result greater degree of WC dissolution, because of higher gas temperatures and longer residence times, than those sprayed by the HVOLF process.

When the powder particles impact on the substrate, they solidify rapidly leading to new phase formations (such as W_2C, W and amorphous binder phase), as shown in Figs. 5.8c and 5.8f. TEM observations in the conventional WC-12 wt% Co powder sprayed with the HVOGF and HVOLF processes show rounded edges for two retained WC particles, which have been partially dissolved (Fig. 4.9). It is also found that a WC particle still has an angular shape because it did not reach a high enough temperature to begin to dissolve (Fig. 4.18). In the bright binder matrix, the liquid

composition will be varied through the areas. This results in W_2C and sometimes W formations. Fig. 4.19 exhibits the precipitation formation (identified by arrows) observed on the surface of a WC particle. It is clearly shown that the W_2C precipitates (Fig. 4.20e) and grows (Fig. 4.21a) on the edges of WC particles. Surface observations at high magnification (Fig. 4.21e) reveal discrete W_2C nodes with a smooth curvature of the W_2C/Co-binder matrix interface. Also, a WC particle surrounded with a continuous W_2C shell is shown in Fig. 4.11. From these results, it is believed that WC grains behave as likely nucleation sites for W_2C precipitation and growth. It is also confirmed that W_2C containing neither dislocations nor stacking faults, therefore, is formed after impacting. Furthermore, in the other areas a cluster of W_2C particles were present (Fig. 4.23), and an isolated W_2C particle with rounded shape (Fig. 4.22) can be observed. In the region containing a high concentration of W, it can be found a cluster of W, for example in the HVOGF sprayed nanoscale WC-12 wt% Co (Fig. 4.30).

Due to the dissolution of WC particles, the Co-binder matrix contains the amount of W and C to form the Co(W,C) phase. When the Co-binder by analysed TEM, the SAD pattern of the Co-binder shows diffuse rings indicating an amorphous phase (Fig. 4.12c). A TEM dark field image produced from the diffracted beam in Fig. 4.12c reveals nanocrystalline particles ranging from 5 - 10 nm in size (Fig. 4.12d). Therefore, it can be stated that the Co-binder matrix contains amorphous /nanocrystalline phases.

The results from TEM analyses of coatings sprayed with the HVOGF and HVOLF processes were used to propose a model of microstructure development. This is shown schematically in Fig 5.8. In outline, the model consists of the following:

1) As the WC-Co powders are exposed to the hot flame temperature, Co starts melting (at temperature exceeding 1768 K (1495 °C)). The degree of melting mainly depends on the dwell time and the flame temperature causing different behaviour for the WC-Co powder sprayed by different guns. The WC-Co powder sprayed by the HVOGF process experiences higher temperatures and longer dwell times in the hot regions of the flame than for the HVOLF process. Thus, the powder particles sprayed by the HVOGF process have larger areas of molten Co than those sprayed by the HVOLF process.

2) As soon as the Co melts, WC begins to dissolve to the liquid Co-binder matrix, leading to a decrease of carbide particle sizes. WC dissolution generates high densities of W and C in the liquid Co.

3) Oxygen diffuses rapidly into the liquid Co and reacts with C to form CO(g). The favourable reaction will be $2C + O_2 \rightarrow 2CO(g)$. Hence, C content near the rim of the powder particles is decreased by oxidation. This promotes further WC dissolution.

4) New phases are formed at the high cooling rate (10^6 - 10^7 K s^{-1}) of splats, resulting also in amorphous/nanocrystalline formation of the Co-rich phase. C deficiency, due to oxidation, results in W_2C and W formation depending on the degree of

decarburisation. It can be shown that W_2C is precipitated and grows on the surface of WC particles which act as nucleation sites. Also, an isolated W_2C particle, a cluster of W_2C and clusters of W nanocrystallines are formed in an amorphous /nanocrystalline binder phase. Analysis of the binder phase confirms that nanocrystalline Co(W,C) is formed in an amorphous binder phase. Moreover, the WC particles are still retained in the coating.

5.3 Effect of Spray Process on Microstructure Formation

WC-12 wt% Co and WC-17 wt% Co conventional powders were sprayed by both processes. In the case of WC-12 wt% Co the powders used in the HVOGF and HVOLF processes were identical. However, there were some differences in powder, namely WC-12 wt% Co starting powder contains Co_3W_3C in addition to WC and Co. Nevertheless, it is believed that the major differences in coatings from WC-17 wt% Co powders were due to different process conditions generated in the HVOGF and HVOLF processes. In this section, the major microstructural differences between the HVOGF and HVOLF coatings will be assessed for each composition, they will be related to previous work and the microstructure formation analysed in terms of the concepts set out in section 5.1.

5.3.1 WC-12 wt% Co

The conventional sintered and crushed WC-12 wt% Co powder was sprayed by the HVOGF and HVOLF process. As mentioned previously, regarding the differences of

both processes (section 5.1.1), it can stated that the HVOLF process produces higher gas velocities and lower gas temperatures than the HVOGF process.

The XRD spectra of the HVOLF and the HVOGF sprayed WC-12 wt% Co coatings are shown in Figs. 4.5b and 4.5c, respectively. As expected, there is a far greater degree of decomposition during the spraying of the WC-12 wt% Co powder with the HVOGF process, compared to spraying with the HVOLF process. Similar conclusions have been reached by a number of workers in this area (e.g. Schwetzke and Kreye, 1999). Decomposition is indicated in the XRD spectra of Fig. 4.5c by the presence of an amorphous broad diffuse peak and the formation of W_2C and W, all of which are more evident in the HVOGF sprayed WC-12 wt% Co coating.

Optical images of both coatings etched by Murakami's reagent are shown in Fig. 5.9. It can be observed that the HVOGF coating contains a higher proportion of molten/semimolten areas than the HVOLF coating. The molten/semimolten areas contains very small and rounded edged carbide particles, whilst unmelted areas contain carbide particles with angular shapes.

BSE-SEM images of Figs. 4.6b and 4.15b show significant variations of grey shades of the Co-binder matrix resulting from WC dissolution. As a result of greater degree of dissolution, the HVOGF sprayed coating contains a lower volume fraction of carbide phase (67%) than the HVOLF sprayed coating (76%), as shown in Table 4.2. Also, a greater degree of dissolution is indicated by greater amounts of reacted carbide particles surrounding WC particles with discrete or continuous white layers. These results prove that the powder particles sprayed with the HVOGF process

undergoes a larger degree of dissolution of carbide particles. Many researchers (for example Verdon et al., 1998; Stewart et al., 1998; Guilemany et al., 1999 a, b) are in agreement that the WC particles dissolve into the liquid Co and thus support the proposed model.

The extent of melting and dissolution will depend, to some extent on the time that particle remains in the hot flame temperature. Spraying with the HVOLF process promotes reduced levels of particle melting and dissolution of carbides, often termed decomposition. Control of decomposition is important as it is thought to be a problem in the formation of a wear resistant coating, as it results in a binder phase which is brittle and thus a coating is less resistant to wear.

The reasons for greater decomposition of the powder during spraying with the HVOGF process are that (i) the powder is injected directly into the combustion chamber in the HVOGF process (Fig. 3.1b) whereas in the HVOLF system the particles are injected into nozzle downstream of combustion (Fig. 3.1a); (ii) due to the converging-diverging throat in the HVOLF process, the gas velocity (and thus the particle velocity) is much higher leading to reduced dwell times of the particles in the hot gas. However, due to higher particle velocities (500 - 700 m s^{-1}; Gu, 2001), mechanical damage on impact results in a greater proportion of carbide grains which exhibit fracture (Fig. 4.6b).

Prior to impacting, a powder particle consists of a solid core containing solid carbide particles which have not dissolved and liquid Co (containing W and C, as well as Co) at the rim of a powder. After impacting, phases will precipitate from the

supersaturated binder phase, forming W_2C shells around existing WC particles (Fig. 4.21), isolated and clustered W_2C particles (Figs. 4.22 and 4.23) and clusters of W nanocrystallines (Fig. 4.30), as discussed in section 5.1.4. The final microstructure of both coatings (Figs. 4.6b and 4.15b) shows significant differences resulting from the degree of dissolution of powder sprayed by each process (as mentioned in a previous section). Due to the high powder velocities sprayed by the HVOLF process, it is apparent that there are more dislocations or stacking faults in the retained WC particles (Fig. 4.9), compared with the retained WC particles in the HVOGF sprayed coatings (Fig. 4.21a).

The powder particles sprayed by the HVOLF process have reduced levels of particle melting and dissolution of carbides. This has an influence on the hardness of the coatings. In contrast, Schwetzke and Kreye (1999) reported that the hardness value of the agglomerated and sintered WC-17 wt% Co coating sprayed by the JP-5000 (same as the HVOLF process) had significant higher hardness value (1490 $HV_{0.3}$) than that coating sprayed by the Top-Gun (1080 $HV_{0.3}$). The hardness of the HVOLF sprayed WC-12 wt% Co coating is rather lower than the HVOGF sprayed WC-12 wt% Co coating (Table 4.2) in this work due to less brittle phases (W_2C). However, the velocity is not the main factor on the degree of decomposition only. Other factors also affect the decomposition such as spray distance and fuel : oxygen ratio (Knight et al., 1994).

Moreover, high velocity of particles also has an affect to the surface roughness of as-sprayed coating, i.e., the HVOLF sprayed WC-12 wt% Co coating has lower surface roughness than the HVOGF sprayed WC-12 wt% Co coating.

5.3.2 WC-17 wt% Co

Conventional WC-17 wt% Co powders are produced by two different manufacturing processes, namely agglomerated and sintered (M), and sintered and crushed (P). Internal morphology of the WC-17 wt% Co (M) shows a very porous structure, whilst the WC-17 wt% Co (P) reveals small amounts of porosity (Fig. 4.2).

These were sprayed by the HVOLF and HVOGF processes. The XRD traces of both coatings (Fig. 4.36) show no significant difference in the presence of an amorphous broad diffuse peak and the formation of W_2C. In the BSE-SEM images, it is clearly shown that the HVOLF sprayed WC-17 wt% Co (M) coating (Fig. 4.32a) has a higher level of density than the HVOGF sprayed WC-17 wt% Co (P) coating (Fig. 4.37a). Observations of the cross sectional images at high magnification, in Figs. 4.32b and 4.37b, show significantly different microstructures resulting from the different morphology of the starting powder.

As mentioned previously, the WC-17 wt% Co (P) powder has an angular shape with low porosity in the structure. When the powder particles are exposed to the high flame temperature, the Co-binder at the rim of the particles will begin to melt. The mechanisms of WC dissolution, oxidation and microstructure formations of WC-17 wt% Co (P) coating are similar to the conventional WC-12 wt% Co powder sprayed by the HVOGF process. Due to high levels porosity of the WC-17 wt% Co (M) powder sprayed by the HVOLF process, this possibly allows melting of the Co-binder within the particle as well as at the rim because of a greater degree of efficient heat transfer (Khan et al., 1997). Thus, the microstructure of the HVOLF sprayed WC-17

wt% Co (M) coating (Fig. 4.32b), does not clearly show core particles and dissolution areas (bright shell) around a core particle.

The agglomerated and sintered WC-17 wt% Co (M) powder, sprayed by the HVOGF process, will achieve higher particle temperature and lower particle velocity compared to spraying by the HVOLF process (as mentioned previously in section 5.1.1). Large proportions of powder are melted, both at the rim of the powder and also inside the powder, which lead to high proportions of WC dissolution. Decarburisation is favourable because the powder particles have a porous structure which allows oxygen within the particle during flighting (Khan and Clyne, 1996). Thus, due to high particle temperature, long dwell time and probably greater degree of decarburisation, it will promote WC dissolution into the liquid Co, leading to the presence of larger proportions of an amorphous phase and new phase formations (e.g. W_2C and W).

Observations of TEM images of the HVOLF sprayed WC-17 wt% Co (M) coating show agglomerated WC particles (Figs. 4.33f and 4.33g) resulting from the manufacturing process of this powder. It can be seen that dislocations or stacking faults in the WC particles in the HVOLF sprayed WC-17 wt% Co (M) (Fig. 4.33a) are in higher proportions than those in the HVOGF sprayed WC-17 wt% Co (P) coating (as shown elsewhere, Stewart, 1998). This results from high powder velocity using the HVOLF process.

From the comparisons of the volume fraction of carbide particles, roughness and hardness, it is evident that the volume fraction of carbide phase in the HVOGF sprayed WC-17 wt% Co (P) coating dramatically decreases, leading to a higher

degree of decomposition (Tables 4.1 and 4.2). The XRD spectrum of the HVOGF sprayed WC-17 wt% Co (P) coating shows the presence of an amorphous phase and a small amount of W_2C. The carbide particles are scattered nonuniformly throughout the coating (Fig. 4.37b), i.e., there are less carbide particles embedded in the bright binder matrix. The as-sprayed coating roughness of the HVOLF sprayed WC-17 wt% Co (M) coating is less than the HVOGF sprayed WC-17 wt% Co (P) coating (Table 4.2) which is a function of the higher impact velocities of particles sprayed with the HVOLF process. The hardness value of the HVOLF sprayed WC-17 wt% Co (M) coating is higher than the HVOGF sprayed WC-17 wt% Co (P) coating as a result of lower porosity within the coating.

5.4 Effect of Powder Composition on Microstructure Formation

WC-12 wt% Co and WC-17 wt% Co powders, produced by the sintered and crushed method, have a different mean carbide size (as reported in Table 4.1), namely, ~1.5 μm and ~1 μm, respectively, as shown in Figs 4.2a and 4.2d.

Both powders were sprayed with the HVOGF process using the same spraying parameters in Table 3.4. The XRD patterns of the HVOGF sprayed WC-12 wt% Co coating (Fig.4.5c) shows peaks indexed to W_2C and W present together with retained WC peaks and a broad diffuse peak. The XRD peak of the HVOGF sprayed WC-17 wt% Co (P) coating exhibits retained WC peaks, W_2C peaks and a broad diffuse peak. The results indicate the HVOGF sprayed WC-12 wt% Co coating shows a higher degree of decomposition of primary WC particles than the HVOGF sprayed WC-17 wt% Co (P) coating. Moreover, the WC particles preferentially decompose to W_2C or

metallic W in the WC-12 wt% Co powder feedstock when it contains a small amount of Co_3W_3C, as shown in Fig. 4.3a (Li et al., 1996).

5.5 Effect of WC Grain Size on Microstructure Formation

Nanoscale WC-12 wt% Co and conventional WC-12 wt% Co powders which have the carbide size ranging from 100 - 600 nm and a mean carbide size of 1.5 μm (Table 4.1), respectively, were used to spray by the HVOGF process to obtain coatings. Nanoscale WC-12 wt% Co powder shows a spherical morphology (Fig. 4.1c). The cross sectional image reveals a very porous structure with a shell about 10 μm in thickness (Fig. 4.1d). Both powders were sprayed using hydrogen as the fuel gas, other spray parameters are presented in Table 3.5. In general, the XRD patterns of the nanoscale WC-12 wt% Co coatings show peaks indexed to WC, W_2C, W and two large broad peaks between $2\theta = 37° - 46°$ and $2\theta = 68° - 80°$. In particular, the coating in 'Run 3' exhibits a peak of complex carbide (Co_3W_3C) at $2\theta = 42.6°$. The XRD spectrum of the conventional WC-12 wt% Co coating shows peaks corresponding to WC, W_2C and W and two broad diffuse peaks as the same angles as the nanoscale coating. From a comparison between the XRD spectra of the HVOGF sprayed nanoscale (Fig. 4.24) and conventional WC-12 wt% Co coatings (Fig. 4.5c), it can be suggested that the nanoscale coating undergoes more decomposition than the conventional coating. From the calculation, Appendix 3, it can be explained that smaller WC grains and longer exposure times leads to greater amounts of solute content (W) in the liquid Co, resulting in a higher degree of dissolution. In the nanoscale coating, the overall intensity of WC is reduced whereas the overall intensity of W_2C and W are increased. The increase in the degree of decomposition is a result

of the morphology of powder, i.e., porous structure. When the nanoscale powder is heated, it can rapidly react with the gaseous environment (O_2) resulting from its high surface area (Kear et al., 2000).

The hardness values of all the spray runs of the HVOGF sprayed nanoscale WC-12 wt% Co coatings are lower than the HVOGF sprayed conventional WC-12 wt% Co coating, as shown in Tables 4.2 and 4.3. Despite the significance of the WC degradation, micropores in the coating probably result in a decrease in hardness values (Strutt, 1998). One possible cause of the porosity in these coatings is that they are deposited from powder with a wide size distribution that is not well suited to HVOF spraying. Ideally, the size distribution showed be in the range 15 – 45 μm. The wide size range will result in some particles which are greatly overheat, whilst others will be poorly melted. This is a possible reason for increased porosity and reduced hardness.

SEM observations of the cross section of the HVOGF sprayed nanoscale WC-12 wt% Co coating from 'Run 2' (Fig. 4.26) show different grey shades of Co-binder matrix. A significant number of rounded particles with high brightness are found in the bright binder matrix, whereas blocky carbide particles are observed in the dark binder matrix. At high magnification, the microstructure of the HVOGF sprayed WC-12 wt% Co coating shows blocky carbide particles, some with rounded morphology, within the Co-binder matrix which also exhibits different shades of grey contrast (Fig. 4.15b). A BSE-SEM image shows that the WC particles still have an angular shape in the darker binder phase. Conversely, the WC particles in the brighter binder phase have more rounded edges and some have a white layer (W_2C) either partially or

completely enclosing them. Also, pores scattered randomly throughout the coating can be found.

TEM observations of the nanoscale coating (Run '2') clearly shows significant numbers of carbide particles with precipitates on their edges, for example, Fig. 4.27 reveals a core carbide particle indexed to WC with precipitate formation. Co in carbide particles can also be found, however this is present in the original spray powder which results from the powder manufacturing process (Fig. 4.28). This observed Co precipitates in a WC particle corresponds with the work of Mohan and Strutt (1996 a, b). A large amount of rounded carbide particles confirmed to W_2C are observed. Also a cluster of carbide particles is found (Fig. 4.30). The SAD pattern shows diffraction rings indexed to W element (Fig. 4.30b). The comparison between the HVOGF sprayed nanoscale and conventional WC-12 wt% Co coatings, it is found that the nanoscale coating shows larger amount of core WC particles with precipitate formation on their edges and spherical W_2C particles than the conventional coating. Also, a cluster of W nanocrystallites is only found in the nanoscale coating.

5.6 Influence of Spray Parameters on Nanoscale Coating Structure

Nanoscale WC-12 wt% Co powder was sprayed with the HVOGF process using the conditions shown in Table 3.5. The coating from 'Run 1' was very thin resulting from the lower powder feed rate (Fig. 4.25a). Also, a large amount of porosity in the coating is clearly observed. An increase of the powder feed rate is believed to decrease the porosity of the coating (Voyer and Maple, 2000). A higher powder feed

rate might also decrease an overheating of the powder particles. Thus, a decrease in the overheating of the powder particles may decrease the porosity.

Comparing the coatings from 'Run 2' (68 %stoichiometric) and from 'Run 3' (60 %stoichiometric) in Table 3.5, it is found that an increase of the oxygen percent stoichiometric decreases the porosity by a small amount. As a result of an increase of the oxygen percent stoichiometric (Fig. 5.10), the temperature of the combustion flame is increased resulting in powders reaching higher temperatures. As the temperature of particles increases, the level of porosity decreases because the powder particles reach a better molten state. From this finding, it is found that the level of porosity in the coating from 'Run 3' (Fig. 4.25d) is a little higher than that in the coating from 'Run 2' (Fig. 4.25c). However, there is no distinct difference in the decomposition between both coatings, because the flame temperatures are still relatively close, i.e., the flame temperatures using the spray parameters of 'Run 2' and 'Run 3' are about 2800 °C and 2740 °C, respectively.

The influence of the size of the combustion chamber is illustrated by the XRD spectra of the coatings from 'Run 3' (Fig. 4.24d) and from 'Run 4' (Fig. 4.24e). It is shown that the intensity of W peak seems to be decreased in 'Run 4'. A complex carbide peak (Co_3W_3C) is also nearly absent in 'Run 4'. The size of combustion chamber has an effect on the flame temperature, namely, longer combustion chambers produce higher temperature because of increased residence time of powder, and are generally used to spray higher melting point materials (Gu, 2000). Different sizes of combustion chamber: 22-mm and 12-mm were used to spray the coatings from 'Run 3' and 'Run 4', respectively (Table 3.5). Since particles have shorter residence times in the region

where they travel slowly, they will heat less and decompose less in 'Run 4' compared to 'Run 3'.

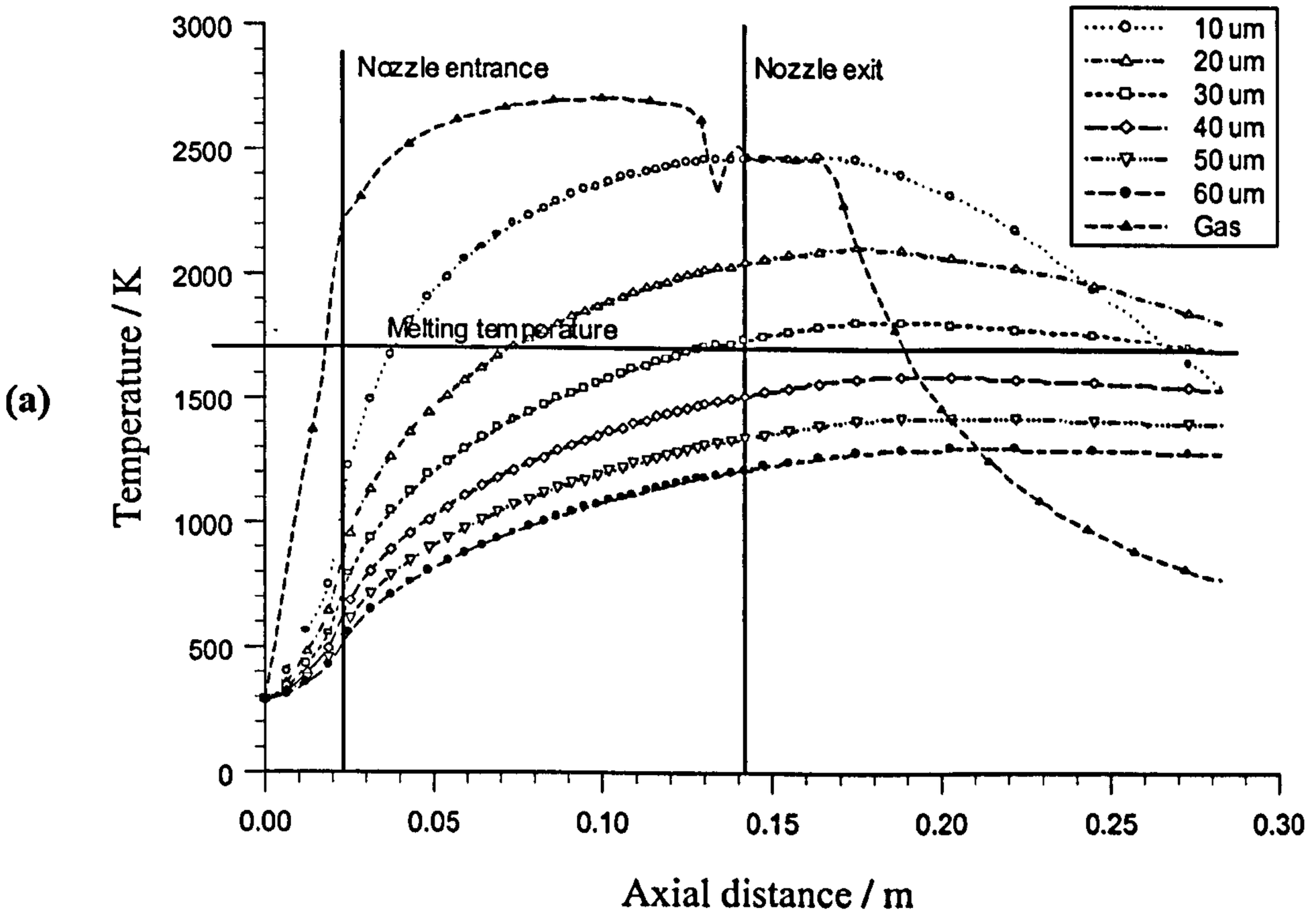

Fig. 5.1 Conventional WC-17 wt% Co (P) powder in the HVOGF spray gun showing (a) particle temperatures and (b) particle velocity with different sizes from 22-mm chamber (reprinted from Gu, 2000).

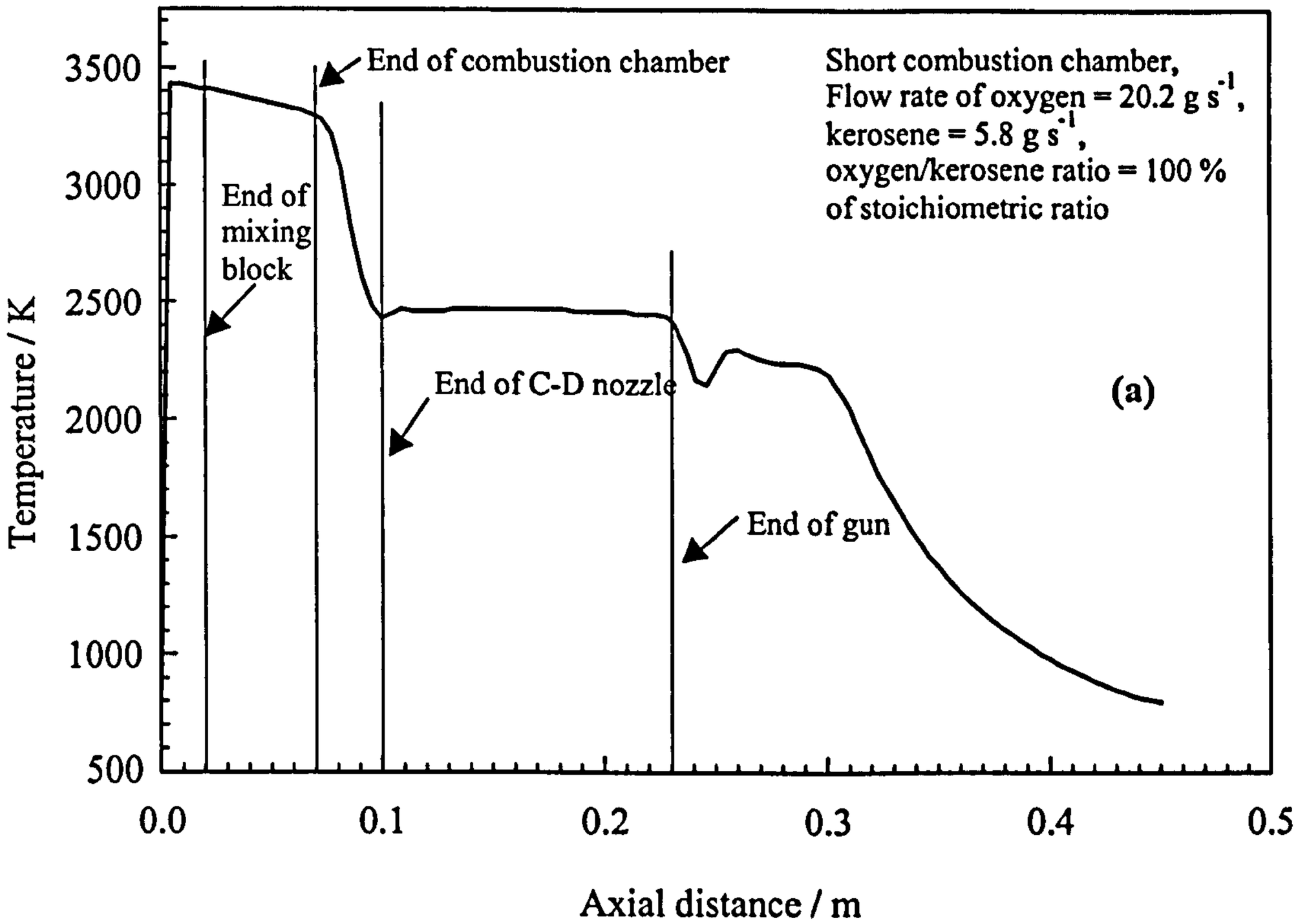

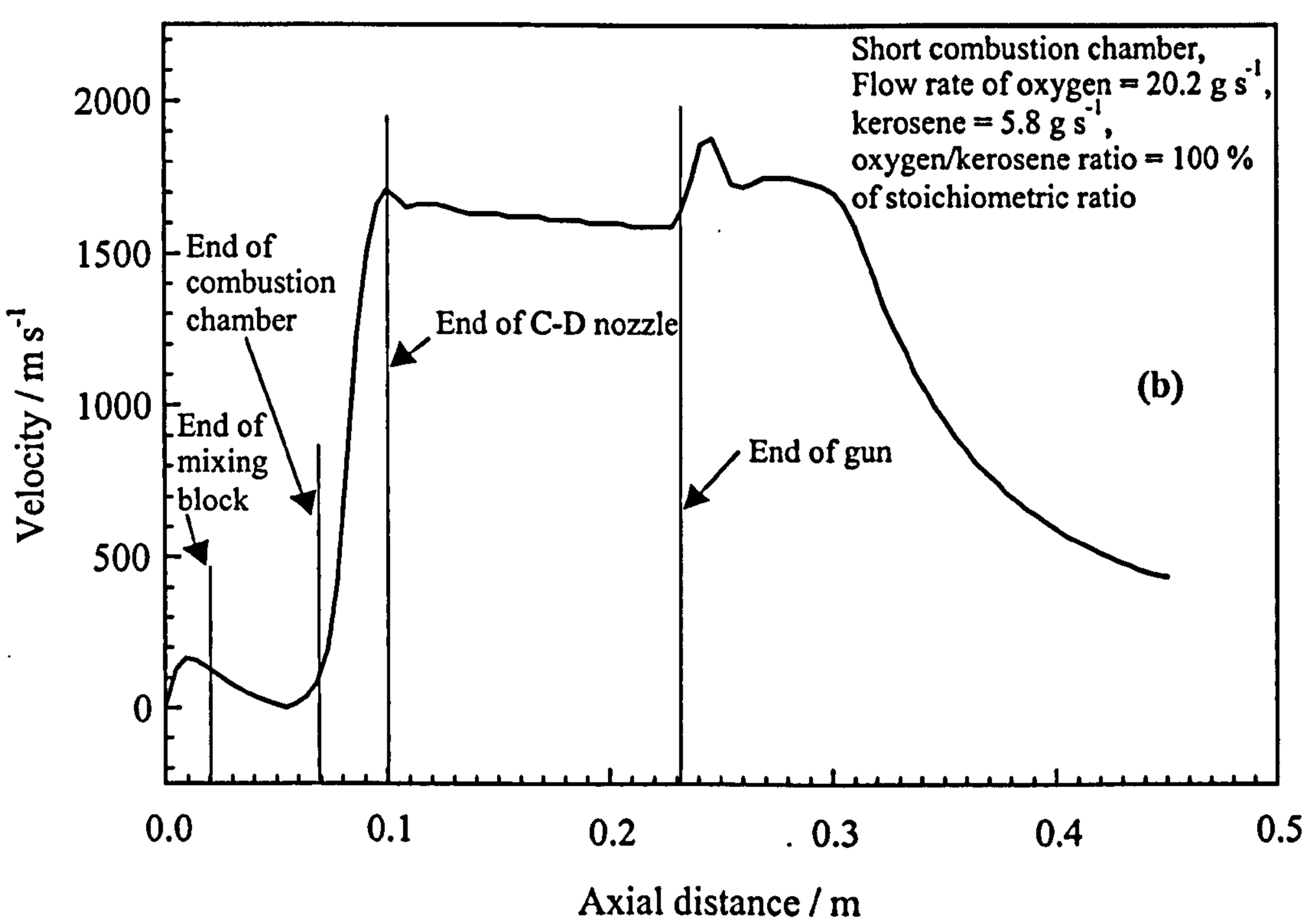

Fig. 5.2 Centreline of (a) gas temperature and (b) gas velocity using the HVOLF process (reprinted from Gu, 2001).

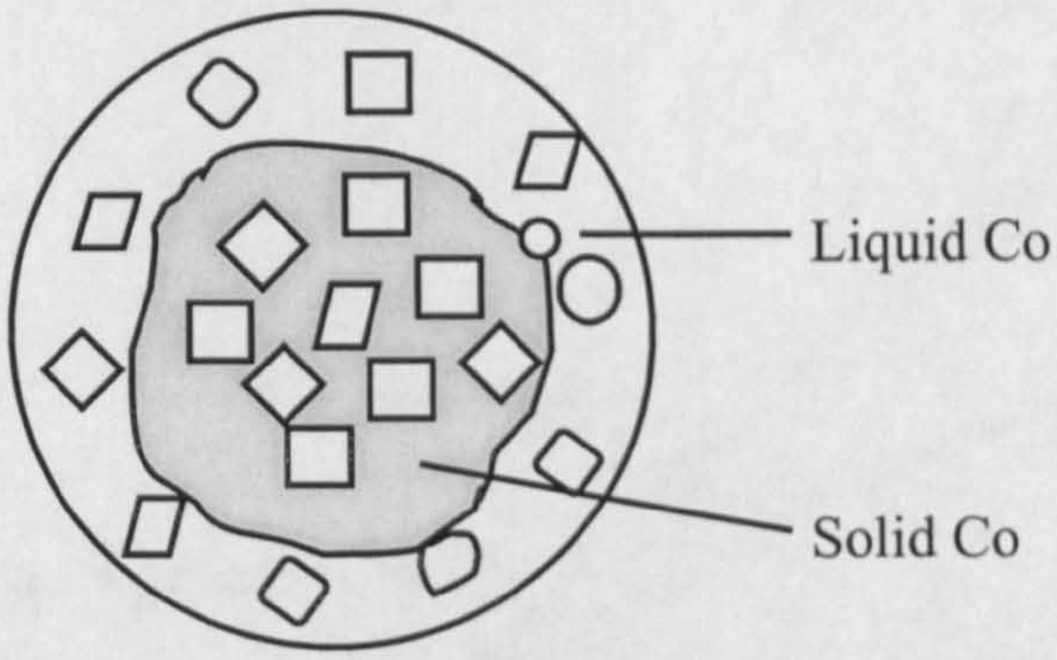

Fig. 5.3 A schematic image of WC-Co powder exposed in the hot flame temperature.

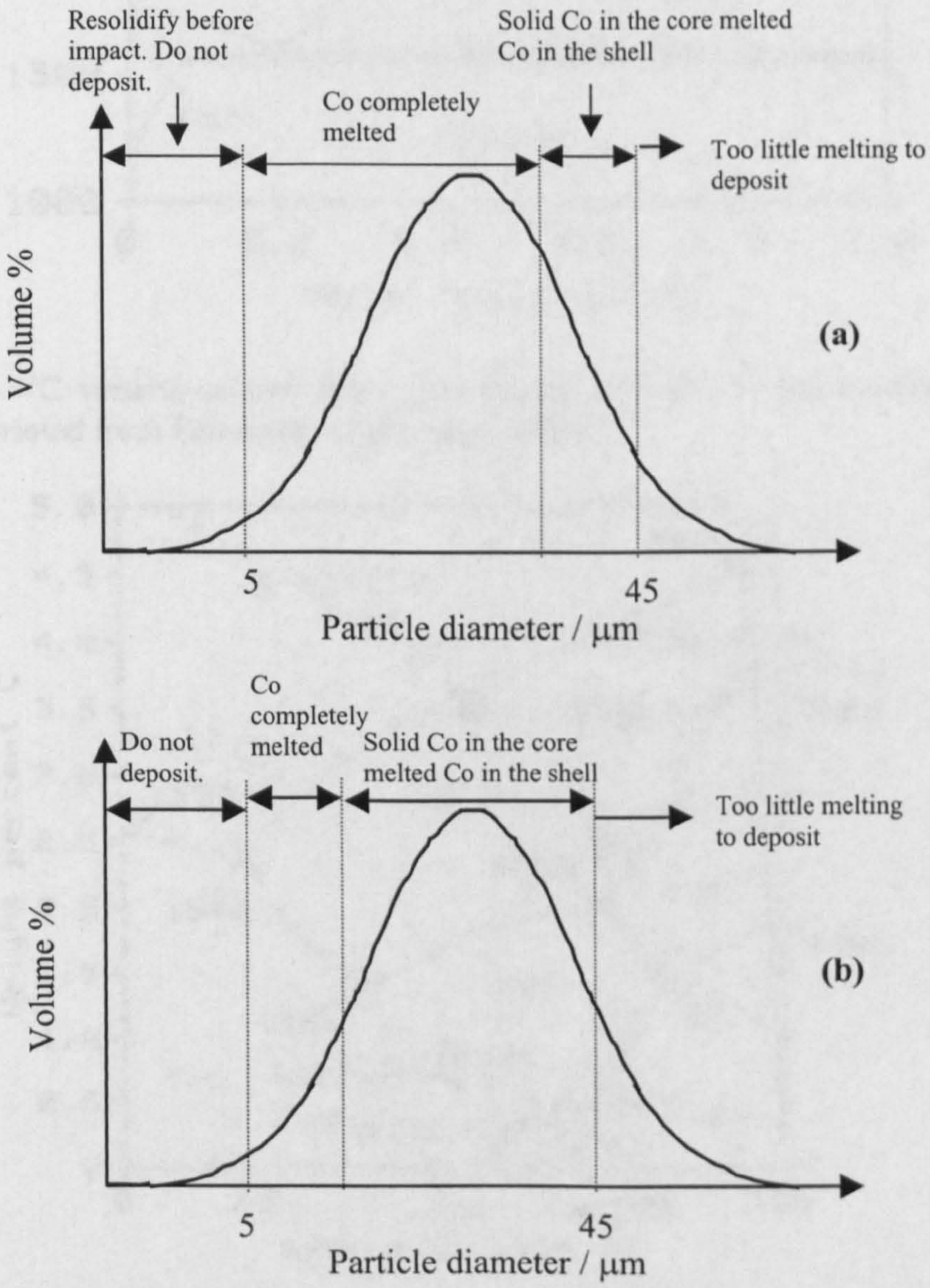

Fig. 5.4 Schematic of powder behaviour in
(a) the HVOGF system and (b) the HVOLF system.

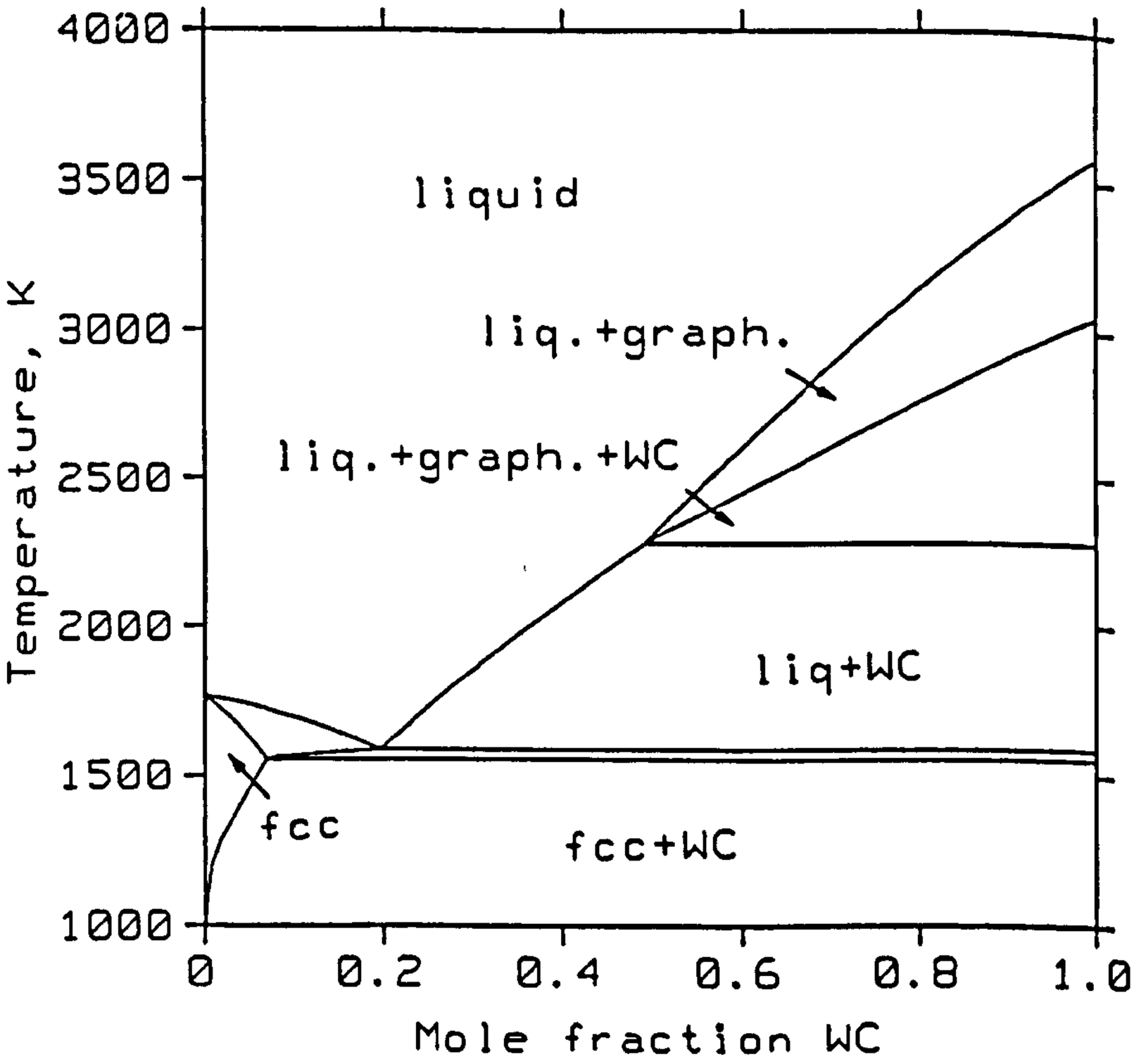

Fig. 5.5 Co-WC vertical section from pure Co to pure WC of the Co-W-C phase diagram (reprinted from Fernández-Guiliermet, 1989).

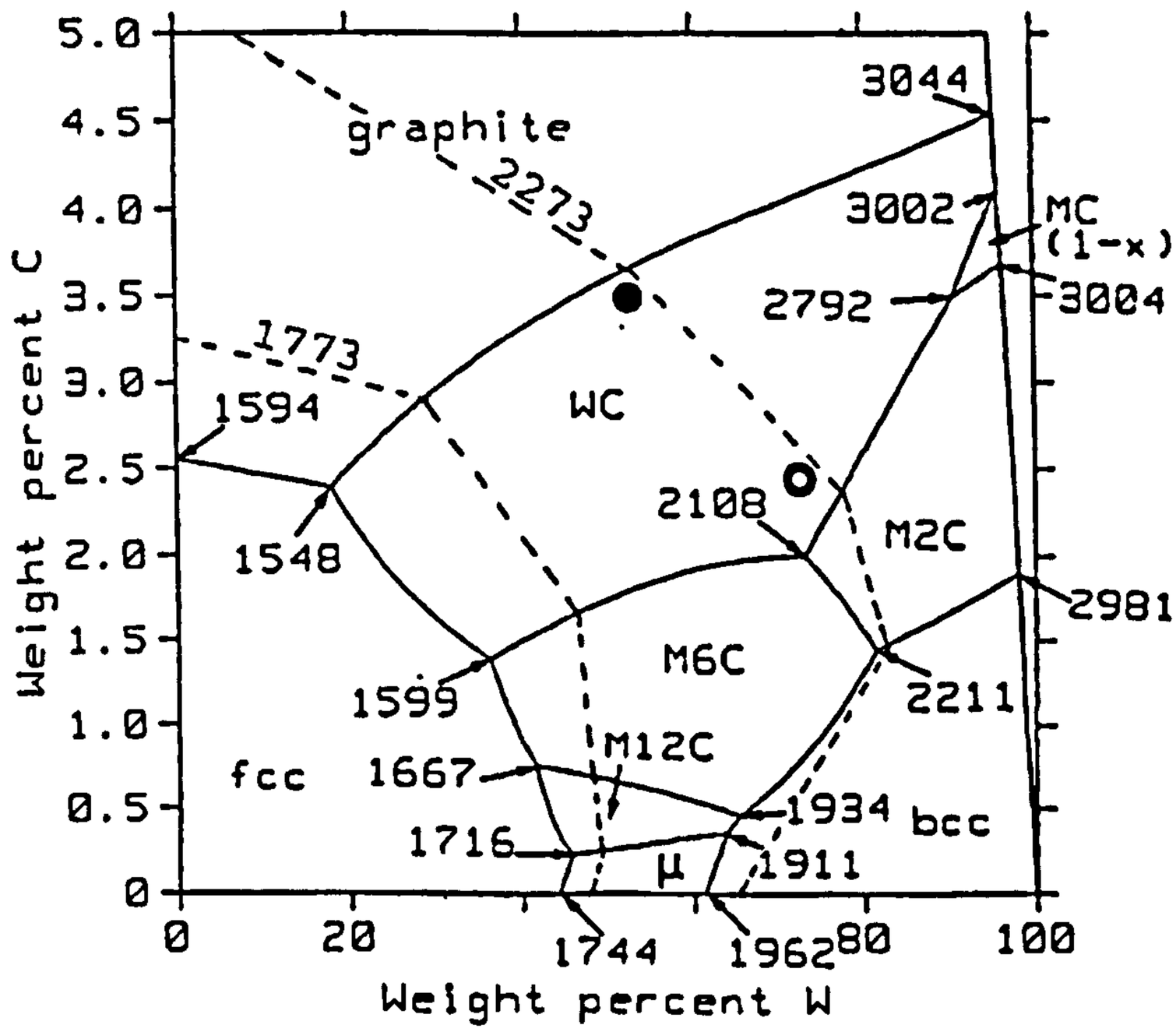

Fig. 5.6 The projection of the liquidus surface of the Co-W-C system. Temperature values are given in kelvin. Solid line shows the calculation of liquid phase composition in equilibrium. Dash line estimates isotherms at 1773 K and 2273 K (reprinted from Fernández-Guiliermet, 1989).

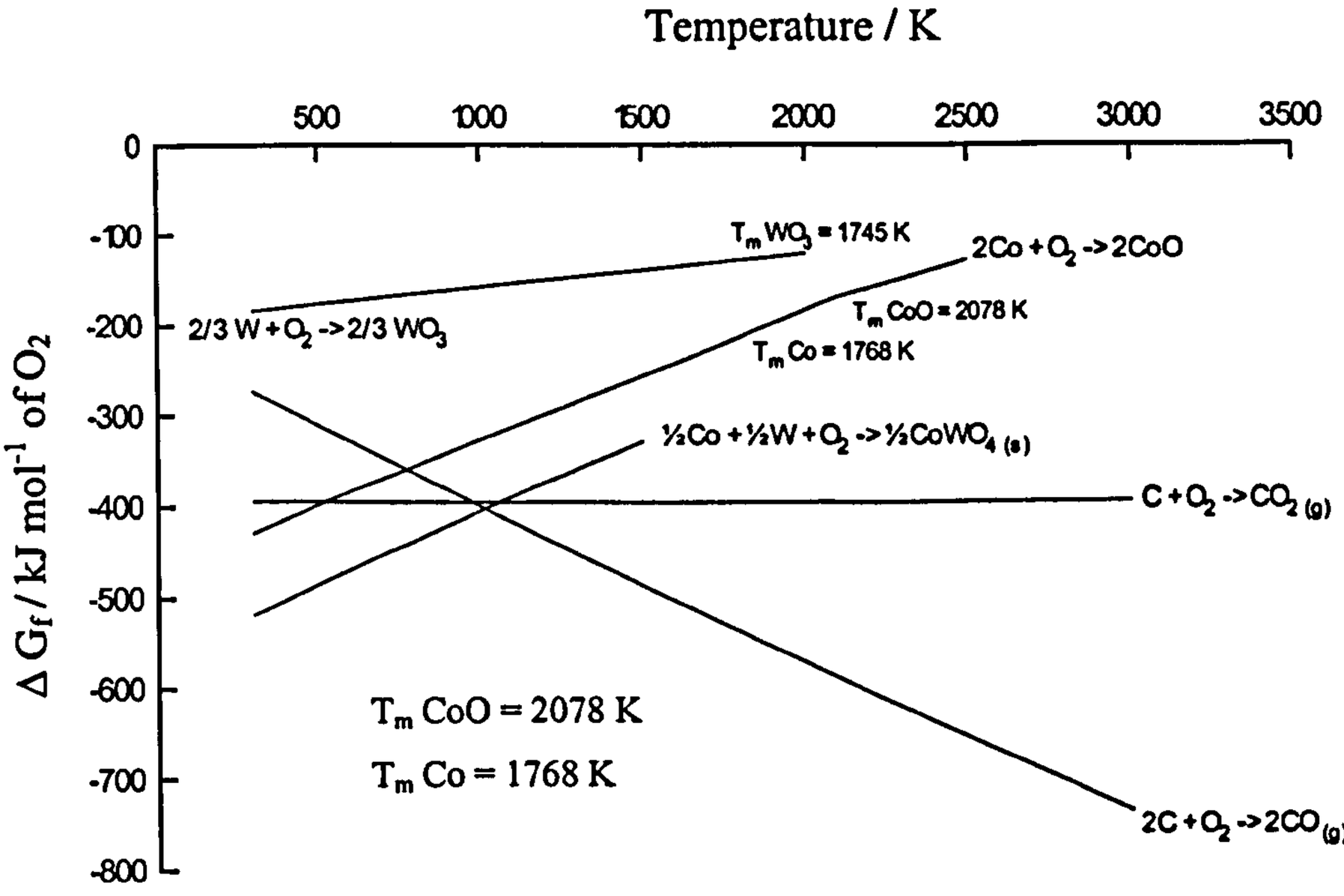

Fig. 5.7 The Ellingham diagram showing oxidation occurring in the liquid Co phase (reprinted from Stewart, 1998).

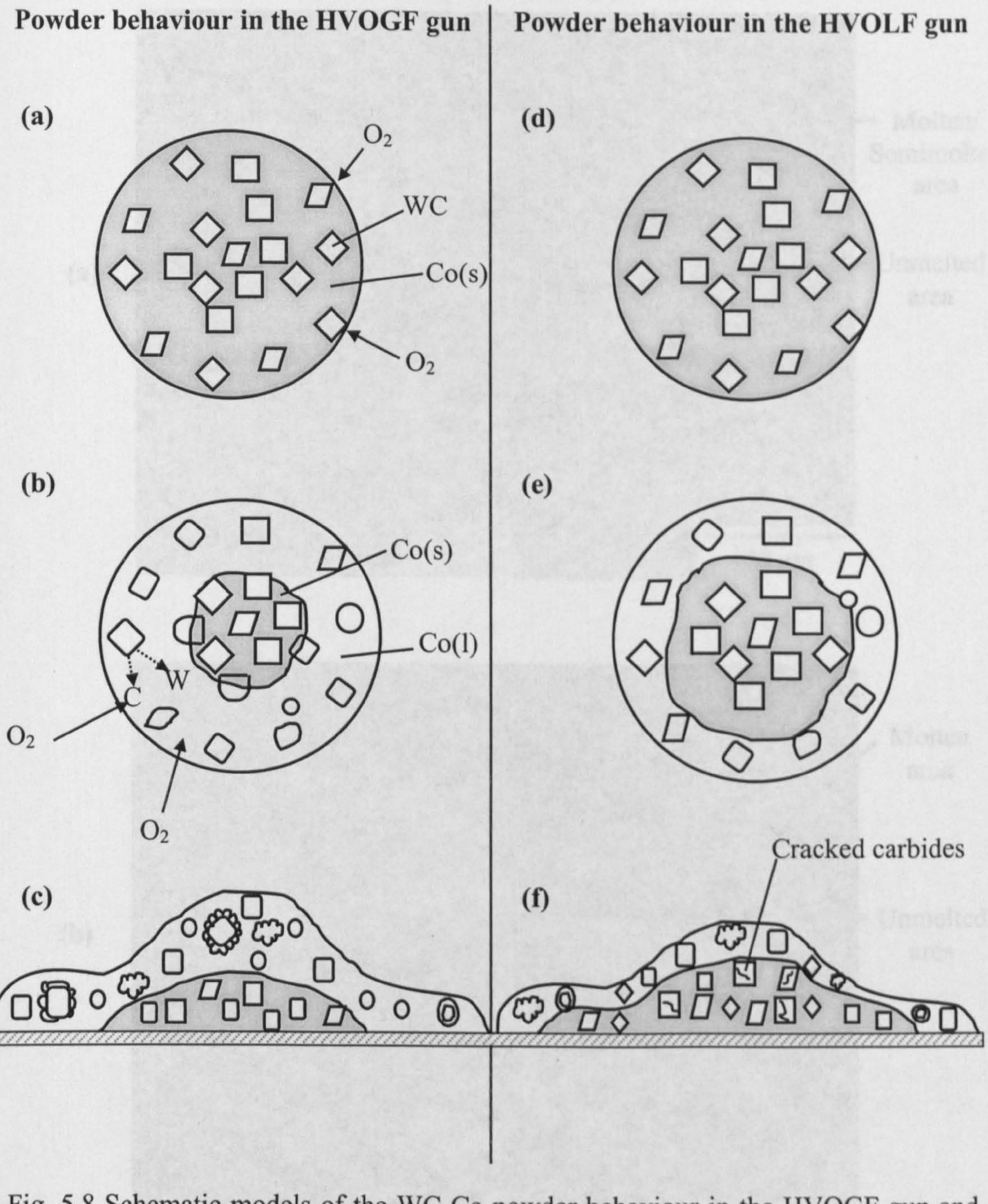

Fig. 5.8 Schematic models of the WC-Co powder behaviour in the HVOGF gun and in the HVOLF gun showing:
(a) and (d) heated powder in the hot flame temperature and solid state reaction of decarburisation on the WC particles at free surface of powder,
(b) and (e) WC carbide particles dissolving into the liquid Co binder and oxygen diffusing into liquid Co binder to react with C (decarburisation),
(c) and (f) powder impacting onto the substrate and forming W_2C, W and Co(W,C) nanocrystalline or amorphous binder phase.

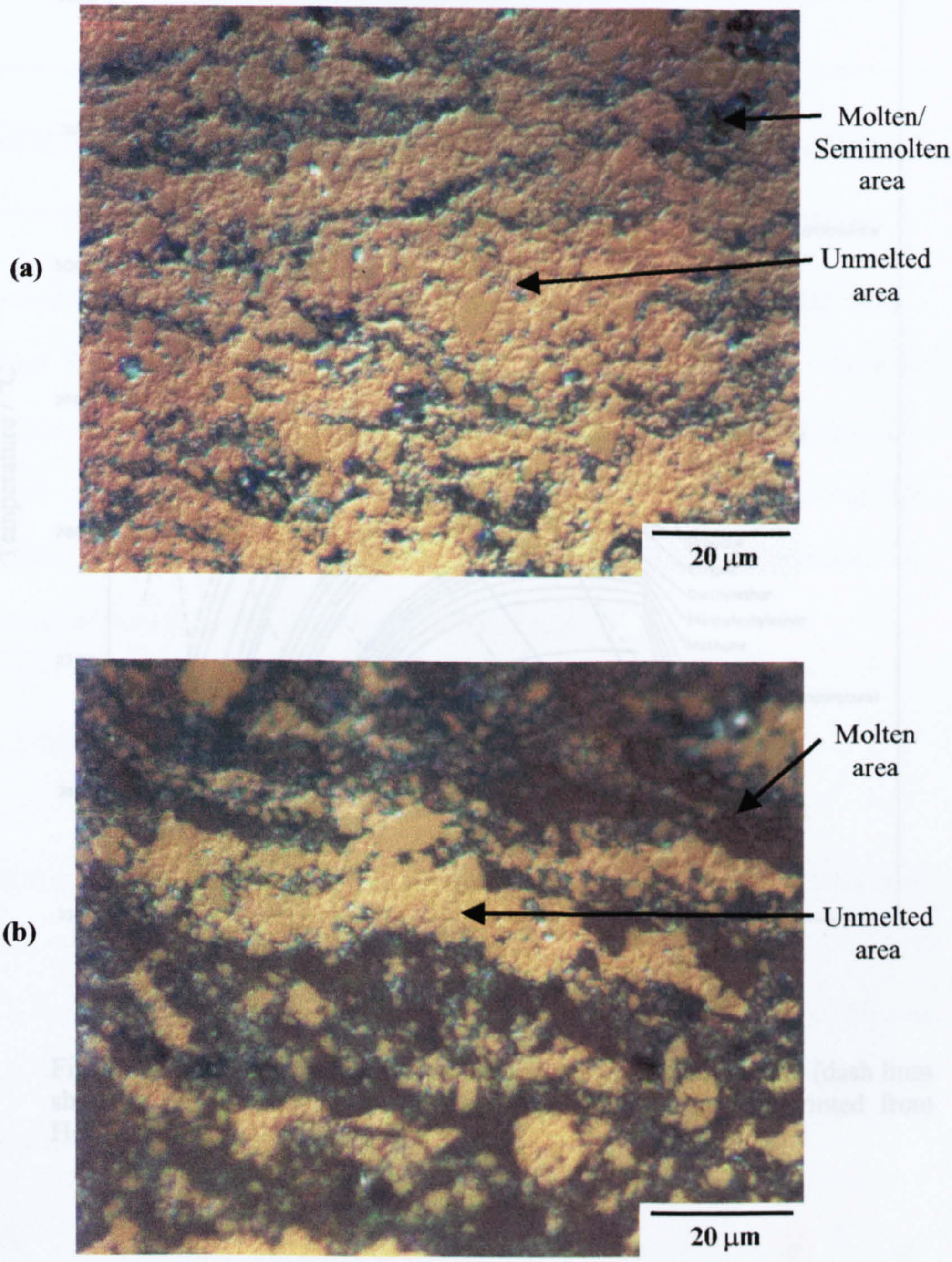

Fig. 5.9 Optical images of (a) the HVOLF and (b) the HVOGF sprayed WC-12 wt% Co coatings etched with Murakami's reagent showing unmelted areas (yellow areas) and molten/semimolten areas (blue areas).

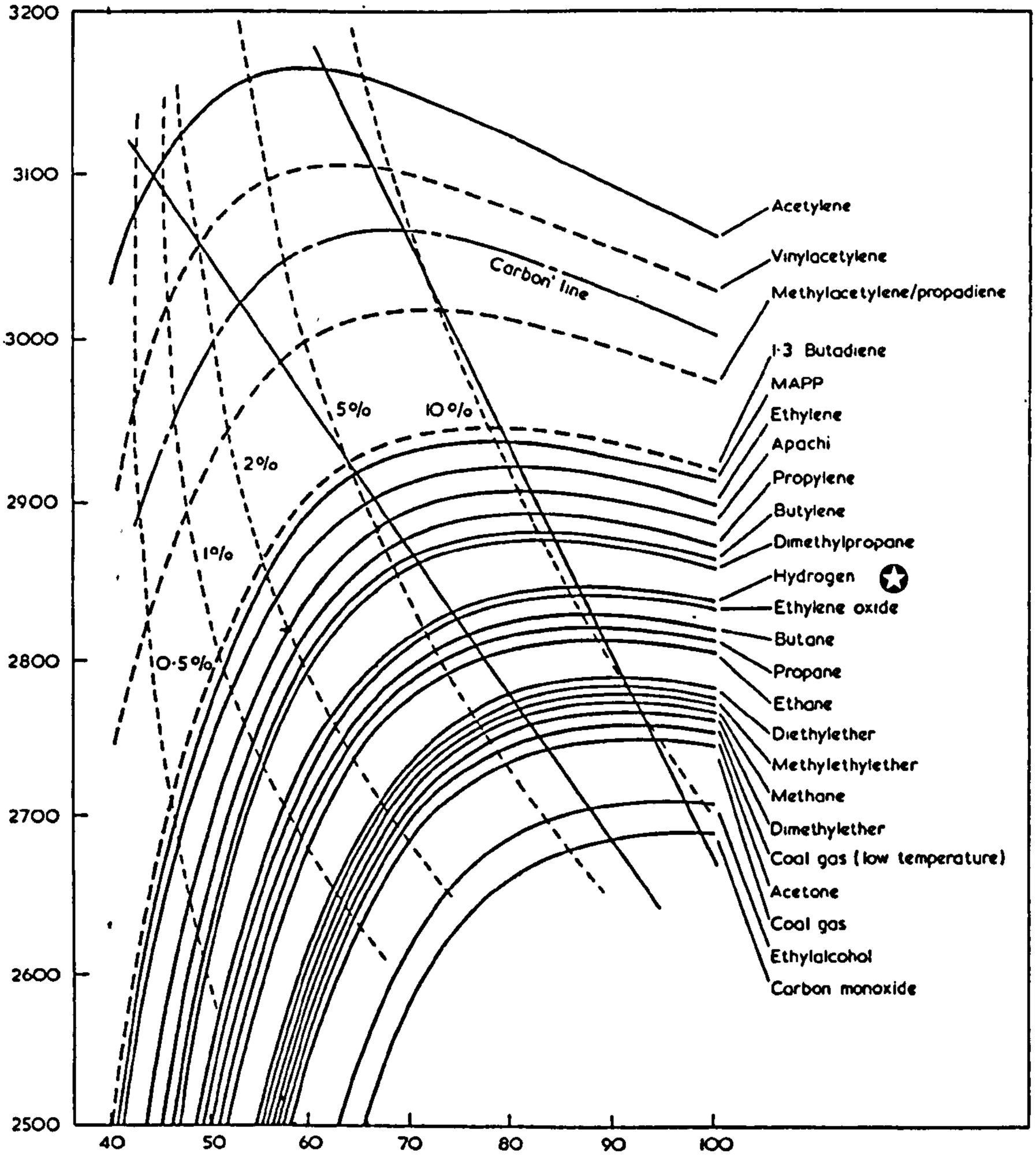

Fig. 5.10 Flame temperature versus oxygen percent stoichiometric (dash lines showing excess oxygen on the flame temperature chart) (reprinted from Hewitt, 1972).

Chapter 6

Sliding Wear Test Results and Wear Behaviour

This chapter describes the ball-on-disc (BOD) sliding wear test results of the sprayed coatings. Sintered WC-Co (WC-11 wt% Co) was also used as a reference material for the BOD sliding wear test. Both sintered WC-Co and coated discs were slid against an alumina ceramic ball. The results are reported in terms of the average wear rate, calculated by dividing the total volume loss by the total sliding distance. The structures of worn surfaces and debris are presented.

6.1 Sintered Ceramic Ball

A sintered ceramic ball of 9.525 mm diameter was used for the BOD sliding wear tests against sintered WC-Co and coated discs. The ball composition was 99.5 wt% Al_2O_3 having a hardness value of 1726 ± 83 kgf mm^{-2} (HV_{300g}). The morphology of the surface of the as-received ball is shown in Fig. 6.1. It indicates that there are a large number of pores on the surface, which have a range of sizes.

6.2 Wear Behaviour of Sintered WC-Co and Coated Discs

The results of hardness, roughness and the BOD wear tests are summarised in Table 6.1. The hardness (HV_{300}) of the sintered cemented carbide was 1500 ± 28 kgf mm^{-2},

whereas the hardnesses of WC-Co coatings were in the range of 1200-1300 kgf mm^{-2}. It is notable that the HVOLF WC-17 wt% Co (M) coating had the highest hardness, despite it having a high fraction of binder phase. The roughness of the polished surfaces were measured by a profilometer. The average roughness Ra (μm) of the polished surface before testing was 0.03 - 0.05 μm for the sintered WC-Co and the conventional coatings, and a little higher at 0.04 - 0.17 μm for the nanoscale coating where some pullout during preparation occurred. The standard error in the mean for four volume loss measurements is quoted as the error in the disc wear rate.

The worn surfaces of sintered WC-Co discs and coated discs were measured by a profilometer to obtain the area of the material loss and subsequently to calculate the volume loss as set out in Chapter 3. The amount of material loss in sliding wear is proportional to the load and distance slid. Fig. 6.2 shows the wear rate (averaged over 5000 m) of the sintered WC-Co and coated discs plotted on a log scale versus the applied load. As can be seen from the graph, at the lowest load of 1.9 kg, the sintered WC-Co had the lowest wear rate whereas the HVOLF sprayed conventional WC-17 wt% Co (M) coating had the highest wear rate. However, the HVOGF sprayed conventional WC-12 wt% Co coating shows a wear resistance greater than any of the other HVOF sprayed coatings. At a load between 4 and 7 kg, there is a transition in sliding wear rate between mild wear at low loads and severe at high loads. Under a load of 10 kg, the sintered WC-Co displays the highest wear rate while the HVOLF sprayed conventional WC-12 wt% Co coating shows the lowest wear rate. The wear rates at a low load of 1.94 kg and 3.57 kg of sintered WC-Co and coated discs are more clearly shown in the bar charts of Figs. 6.2b and 6.2c.

6.2.1 Wear Behaviour of the Sintered WC-Co

6.2.1.1 The Effect of Sliding Distance

The wear volume and average wear rate of the sintered WC-Co at 5.2 kg load as a function of sliding distance is summarised in Table 6.2. As can be seen from the graph (Fig. 6.3), the wear volume loss is high up to around 1000 m of sliding; following this, there is a significant reduction in wear volume loss and a steady state wear volume loss is reached.

6.2.1.2 Microstructural Observation of Worn Surfaces of Sintered WC-Co

The sintered WC-Co basically consists of brittle WC grains, approximately 2 μm in size, in a metallic Co-binder (Fig. 6.4a). The carbide grains show a very flat surface. After BOD testing, the microstructure of the worn surface of the sintered WC-Co discs tested at 1.9 kg, 3.57 kg and 10.1 kg is illustrated. Figs. 6.4b - 6.4d show plan view images of the wear track tested under a 1.9 kg load. At low magnification, the sintered WC-Co disc shows a smooth surface with the wear track about 0.3 mm in width (Fig. 6.4b). In the middle of the wear track, the occurrence of cobalt-extrusion and clusters of carbide grain pull out (resulting from lack support of Co-binder) can be observed (Fig. 6.4c). Fine wavy features on the carbide grains themselves were found on the rim of the wear track (Fig. 6.4d).

The profile of a track resulting from wear under a load of 3.57 kg is shown in Fig. 6.5a. The depth of the wear scar is approximately 0.2 μm, apart from a deep narrow

groove nearly 1 μm deep. Figs. 6.6a and 6.6b shows the corresponding worn surface. At low magnification, the sintered WC-Co disc shows very little damage on the surface with the wear track being about 1 mm in width (Fig. 6.6a). The wear track exhibits a smooth surface. Again, high magnification images indicate that Co-binder extrusion had occurred along with subsequent loss of carbide grains (Fig. 6.6b). Also, a few cracks on the carbide grains can be observed, as indicated by the arrows on the Fig. 6.6b.

Fig. 6.5b reveals the wear track of the sintered WC-Co tested under a load of 10.1 kg. This track is about 90 μm in depth. The sintered disc shows the most severely worn surface with a wear track about 3.7 mm wide (Fig. 6.7a). In the middle of the wear track, a transferred layer consisting of small particles of debris stuck in the wear track can be observed (Fig. 6.7b). Investigation of the transferred layer with BSE-SEM shows the presence of finely comminuted carbide particles and cracking within the transferred layer (Figs. 6.7c and 6.7d). Near the rim of the wear track, the unworn surface on the left-hand side can be observed next to the transferred layer on the right (Fig. 6.7e). Severe wear can be seen to occur very close to the unworn region. Generally, the wear debris is made up of very fine agglomerated particles, as shown in Fig. 6.7f; also plate-like debris is observed, resulting from removal and loss of the transferred layer, Fig. 6.7g.

6.2.2 Microstructural Observation of the Worn Surface of HVOLF Sprayed Conventional WC-12 wt% Co Coating

The plan view of the surface of the HVOLF sprayed WC-12 wt% Co coating worn under a load of 1.9 kg is illustrated in Fig. 6.8. The microstructure of the unworn surface exhibits a smooth surface with a number of pores and cracks in the carbide grains (Fig. 6.8a). The worn surface of the coating shows a generally smooth surface with a small number of pits (Fig. 6.8b). The wear track was around 1.5 mm in width. Fig. 6.8c shows a high magnification image from the middle of the wear track. It was found that a large number of pits had been formed. A significant amount of cracking was observed in the carbide grains themselves. This results in considerable fragmentation of carbide grains.

The surface of the coated disc worn under a load of 3.57 kg reveals more severe wear, as shown in Fig. 6.9a. The wear track is twice the width of that worn under a load of 1.9 kg. The track shows a large number of pits and delamination. Surface observations at high magnification reveal the lack of binder phase in some regions of the surface (Fig. 6.9b). This binder had been rapidly removed resulting in carbides which lacked support and thus prone to removal. In this case, cracking of the actual carbide grains is also observed. Little evidence for significant sub-surface cracking can be observed in the cross-section through this wear track, Fig. 6.9c, although there is some evidence for carbide pullout leading to pit formation.

The track following wear under a load of 10.1 kg has a width of about 3.5 mm, this shows the most severe wear and a large amount of delamination (Fig. 6.10a). The

observation of wear scar at high magnification indicated that it is covered with a transferred layer, showing severe plastic deformation (Fig 6.10b). This transferred layer in 'A' was examined by EDS spot analysis which indicated the presence of mainly Al and W as well as some traces of Co (oxygen and carbon were not analyzed). A high magnification image of the transferred layer shows a large amount of fine debris stuck in the wear scar, Fig 6.10c. Again, Figs. 6.10d and 6.10e show the microstructure of the transferred layer at high magnification. The observation by BSE-SEM shows that there are substantial amounts of very fine tungsten carbide particles (the bright phase) embedded in the transferred layer. This results from fragmentation of carbide particles during testing. The morphology of the wear debris is shown in Fig. 6.10f. The wear debris consists of agglomerated fine particles and plate-like debris, resulting from delamination of the transferred layer.

6.2.3 Microstructural Observation of the Worn Surface of HVOGF Sprayed Conventional WC-12 wt% Co Coating

The unworn surface of the HVOGF sprayed WC-12 wt% Co coating exhibits a flat surface with a small number of micropores, as shown in Fig. 6.11a. The coated disc worn under a load of 1.9 kg reveals a wear track about 1.3 mm in width. SEM observation at low magnification shows a rather smooth surface with a large number of pits (Fig. 6.11b). A high magnification image taken from the middle of the wear track (Fig 6.11c) shows a flat surface with carbide grains standing proud of the binder phase, and a few holes resulting from the removal of carbide grains. Also, less cracking of the carbide grains can be seen than in the corresponding HVOLF sprayed sample (Fig. 6.8c).

For the coating tested under a load of 3.57 kg, the wear track exhibits a smooth surface with a number of pits and a small amount delamination (Fig. 6.12a). A high magnification image towards the rim of the wear track (Fig. 6.12b) shows the smooth surface of carbide grains; individual carbide grains are standing proud of the matrix indicating preferential wear of the matrix phase. Pores are also observed which result from pullout of the carbide grains. A SEM cross-sectional image of the wear scar (Fig. 6.12c) shows good adhesion of carbide grains at the wearing surface (there is little pullout despite the small size of some of the carbide grains). However, sub-surface cracking is seen which will result in the formation of large pits. There appears to be less removal of matrix than in the corresponding HVOLF coating.

For the coated disc, tested under a load of 10.1 kg, severe wear is observed (Fig. 6.13a). The surface morphology reveals similar features throughout the wear track. A high magnification image from the middle of the wear track (Fig. 6.13b) shows a plastically deformed transferred layer with evidence of some cracking of the transferred layer and fine debris stuck in the wear track. Samples of the debris observed are shown in Fig. 6.13c. The debris is comprised of very fine particles, generally less than 5 μm in size, agglomerated together to form bulk debris particles.

6.2.4 Microstructural Observation of the Worn Surface of HVOGF Sprayed Nanoscale WC-12 wt% Co Coating

The unworn surface of the HVOGF sprayed nanoscale WC-12 wt% Co coating reveals a large number of micropores scattered throughout the surface, as shown in Fig. 6.14a. The worn surface of the coating tested under a load of 1.9 kg reveals a

wear track of approximately 1.6 mm in width, Fig. 6.14b. A large number of pits and a small amount of delamination can be observed in the wear scar. Microstructural observations at high magnification (Fig. 6.14c) illustrate considerable material loss from the wear track. Carbide grains again seem to stand proud of the matrix. Also, large cracks can be seen in the wear track, as indicated by an arrow 'A', and areas where both carbide and matrix have been lost together resulting in pit formation, as indicated by arrows 'B'. Some of the pits have been filled with wear debris, as indicated by an arrow 'C'.

The wear track on the coating tested under a load of 3.57 kg exhibits significant pitting and delamination (Fig. 6.15a). A plan view at high magnification shows large amounts of material loss from the wear track and severe cracking, Fig. 6.15b. The cross-sectional image through the wear track (Fig. 6.15c) reveals deep sub-surface cracking, with cracks running approximately parallel to the wear surface. The cracks are observed to run predominantly in the areas of the microstructure where W and W_2C particles have formed.

For the coating tested under a load of 10.1 kg, the wear track is about 3.5 mm in width and shows a significantly higher degree of delamination and transferred layer formation (Fig. 6.16a). Surface observations at high magnification in the middle of the wear track exhibit severe cracks on the surface, Fig. 6.16b. Such cracking results in the high rate of material loss. Also the transferred layer and debris are seen. Fig. 6.16c reveals an area of material loss covered by the transferred layer.

6.2.5 Microstructural Observation of the Worn Surface of HVOLF Sprayed Conventional WC-17 wt% Co (M) Coating

Fig. 6.17a shows a polished surface of the HVOLF sprayed WC-17 wt% Co coating which contains a few micropores. The worn surface of the coating tested under a load of 1.9 kg exhibits a smooth surface with a small amount delamination and porosity. At low magnification, the worn surface shows a wear track about 1.3 mm in width, Fig. 6.17b. The microstructure at high magnification at the rim of the wear track indicates material loss in some regions and fragmented carbide grains (Fig. 6.17c). Images from the middle of the wear track show the smooth surface of carbide grains where they are standing proud of the matrix phase (Fig. 6.17d). The worn surface also shows a small track around an original feedstock powder particle, which probably resulted from an insufficient degree of melting, and thus resulted in poor bonding between this particle and the rest of the coating.

The plan view images of the coating disc worn under a load of 3.57 kg are shown in Fig. 6.18. The coated disc reveals severe wear with delamination, Fig. 6.18a. Surface observations at high magnification on the rim of the wear track (Fig. 6.18b) show some pores resulting from the removal of carbide grains, which lacked sufficient support. In the middle of the wear track (Fig. 6.18c), the severe worn surface and transferred layer with embedded fragmented carbide grains can be observed. Examination of the cross-sectional image of the wear track by BSE-SEM (Fig. 6.18d) shows little evidence of sub-surface cracking in the binder phase or for carbide pullout and pitting. Cracks in the carbide grains can also be observed.

The plan view image of the surface, worn under a load of 10.1 kg exhibits severe damage on the surface (Fig. 6.19a). At high magnification (Fig. 6.19b) significant plastic deformation and cracking can be observed with a large amount of the surface covered by the transferred layer. Observations of the transferred layer indicate that it contains a large number of small fragmented carbide grains (Figs. 6.19c and 6.19d).

6.2.6 Microstructural Observation of the Worn Surface of HVOGF Sprayed Conventional WC-17 wt% Co (P) Coating

The polished surface of a coated disc (HVOGF sprayed WC-17 wt% Co coating) shows a smooth surface with a few pores (Fig. 6.20a). The regions where carbide dissolution has been significant can be clearly seen (fewer carbide particles and less contrast between the matrix and carbides). Following wear under a load of 1.9 kg (Fig. 6.20b), a fairly smooth surface with a high number of pits can be seen. The wear track is about 1 mm in width. Fig. 6.20c shows the worn surface in the middle of the wear track at high magnification. It can be seen that the carbide grains protrude from the binder phase. Compacted debris and pores resulting from material loss can also be observed.

The profile of the wear track resulting from wear under a load of 3.57 kg is shown in Fig. 6.21a. The depth of the wear track is about 2 μm. The worn surface of the coating under a load of 3.57 kg shows severe wear with significant delamination and transferred layer formation (Fig. 6.22a). Pits can also be observed. The wear track is three times wider than that produced by wear under a 1.9 kg load. Observation of the transferred layer clearly shows plastically deformed material and fractured carbide

grains (Fig. 6.22b). Fig. 6.22c shows cracking of the carbide grains which will lead to their fragmentation. The fragmented carbide grains are removed and leave pores. A cross-sectional image of the worn surface indicates severe sub-surface cracking parallel to the sliding direction, resulting in the removal of large sections of the coating. The cracks predominantly run in the reacted regions of the coating, Fig 6.22d.

The profile of the coating tested under a load of 10.1 kg shows a wear track about 5 μm in depth (Fig. 6.21b). Surface observations of the wear scar reveal a severely worn surface (Fig. 6.23a). A significant amount of delamination and transferred layer formation can be observed throughout the wear track. Fig. 6.23b shows the microstructure of the worn surface at the rim of the wear track. It can be seen that carbide grains in the wear track are broken down during the test. The worn surface in the middle of the track indicates transferred layer formation, cracks on the worn surface, debris stuck in the wear track and material loss in some regions, Fig. 6.23c.

6.3 Comparison of the Wear Behaviour of Sintered WC-Co and Sprayed Coatings

The wear behaviour of the sintered WC-Co and various coatings differ as a result of their different microstructures.

Wear of the sintered WC-Co results from extrusion of the Co-binder phase, i.e., the Co-binder is smeared on the surface, as shown in Fig. 6.4c. Moreover, it can be found that the WC grains have slipped relative to each other within the structure (Fig. 6.6b).

Also, cracks can be found in the carbide grains. Fractured carbide grains are then susceptible to removal during further wear exposure. Worn surfaces generated at high load show, at high magnification, a large amount of transferred layer deformed on the surface, as seen in Figs. 6.7c and 6.7d. This transferred layer results from accumulation of small fragments of WC grains, binder phase and debris from the Al_2O_3 ball. The carbide grains and alumina may generate abrasive wear as well as sliding wear.

The conventional sintered and crushed WC-12 wt% Co powder was sprayed with both the HVOGF and HVOLF guns. As described in sections 4.2 and 4.3, the particles sprayed with the HVOLF gun arrived with a solid core and semimolten shell. Therefore, the worn surface of the HVOLF sprayed WC-12 wt% Co coating in Fig. 6.9b shows some molten regions which exhibit less wear and carbide-matrix decohesion in the unmelted region. The wear mechanism of the HVOLF sprayed WC-12 wt% Co coating results from the removal of the binder phase due to poor bonding between carbide grains and binder phase, as seen in Fig. 6.9b. Cracks are frequently found in carbide grains causing carbide loss, Fig. 6.8c, and resulting in pit formation, Fig. 6.9c. Also, a cross-sectional image of a worn surface indicates a number of cracks in the carbide grains indicated by the arrow at the wearing surface. Surface observations on the worn surface at high loads (Fig. 6.10) reveal the appearance of a large amount of delamination and transferred layer. The BSE-SEM image (Fig. 6.10e) shows small fragments of carbide grains in the transferred layer.

Due to a high degree of melting and consequent good bonding between the carbide grains and Co - rich binder, the primary wear of the HVOGF sprayed WC-12 wt% Co

coating occurs by sub-surface cracking, as shown in Fig. 6.12c. This can generate significant material loss. However, material loss can still result from pits arising from the removal of carbide grains owing to lack of support of the matrix phase (Fig. 6.12b). The surface worn at high loads indicates no significantly different morphology from the surface of the HVOLF sprayed WC-12 wt% Co coating worn at high loads.

The nanoscale WC-12 wt% Co coating exhibits a highly melted and decarburised layer associated with the formation of W_2C and W, as shown in Fig.4.26. Wear of this coating proceeds by cracking in the regions rich in W_2C and W, Fig. 6.15c. This leads to surface spallation and rapid wear. Correspondingly, the plan view images (Figs. 6.14c and 6.15b) of worn surface show a considerable amount of material loss and severe cracking on the surface. The surface worn at high loads shows severe damage with cracks and pores filled up with transferred layer material (Figs. 6.16b and 6.16c).

WC-17 wt% Co (M) powder produced by agglomerating and sintering was sprayed with the HVOLF gun. This powder had a porous structure (Fig. 4.1e), which has an effect on the degree of melting and consolidation on impact. The wear of the coating sprayed by the HVOLF system from this powder initially proceeds by the removal of the binder phase leading to individual carbide grains protruding from the surface, Fig. 6.17d. Holes resulting from the removal of carbide grains because of lack support of the binder phase can be found, Fig. 6.18b. Also, cracks can be observed in the carbide grains, Fig. 6.17d. Observations of a cross-section of a worn surface show little sub-surface cracking and little evidence of carbide grain pullout to form pores. Surfaces worn at high loads show severe damage with a large degree of transferred layer

formation and delamination. Small fragmented carbide grains are found in the transferred layer.

WC-17 wt% Co (P) powder produced by sintering and crushing was sprayed with the HVOGF gun. Wear of this coating results from the removal of the binder phase resulting in individual carbide grains protruding from the surface, Fig. 6.20c. Cracks can be found in the carbide grains (Fig. 6.22c). This leads to fragmentation of the carbide grains and their removal. Moreover, regions of material loss resulting in pore formation can be observed. Observations on a cross-section through a worn surface show severe sub-surface cracking either parallel or perpendicular to the surface, Fig. 6.22d. This will result in material loss in large sections.

6.4 Wear Behaviour of the Al_2O_3 Ball Slid Against Sintered WC-Co and Sprayed Coatings

The results for the wear rate of Al_2O_3 balls sliding against sintered WC-Co and coated discs are shown in Table 6.3 and the wear rate is plotted on a log scale in Fig. 6.24. It can be seen that the wear rate of a ball slid against the sintered WC-Co disc was, at all loads, considerably lower than that of the balls slid against any of the coatings. Again, a transition between low-rate wear and high-rate wear occurred between about 3 and 7 kg. The wear rate of Al_2O_3 balls at low loads of 1.94 kg and 3.57 kg are clearly visible in Figs. 6.24b and 6.24c.

To clearly understand the wear behaviour at the low loads, the balls worn under a 3.57 kg load slid against the sintered WC-Co, the HVOGF sprayed WC-12 wt% Co

coating and the HVOGF sprayed WC-17 wt% Co (P) coating were observed with the SEM.

6.4.1 Microstructural Observation of the Worn Surface of Al_2O_3 Slid Against Sintered WC-Co

The wear scar on a ball worn at a load of 3.57 kg was about 1.4 mm diameter, Fig. 6.25a. The worn surface at high magnification in the centre of the worn ball probably shows the grain structure of the Al_2O_3, Fig. 6.25b. Some regions were analyzed by EDS. A region in a position '1' shows a strong peak of W and a small peak of Al, Fig. 6.26a. This is probably wear debris embedded into a pore that has formed. The results of an EDS analysis at positions '2' and '3' indicate a significant peak of Al (Figs. 6.26b and 6.26c).

6.4.2 Microstructural Observation of the Worn Surface of Al_2O_3 Slid Against HVOGF Sprayed WC-12 wt% Co Coating

The scar on Al_2O_3 ball worn under a load of 3.57 kg is approximately 3 mm diameter with pores and ploughing at its centre (Fig. 6.27a). Observations of this surface reveal a more severely worn surface with a smeared transfer layer (Fig. 6.27b). The worn surface at the bottom of the ball (Fig. 6.27c) was analyzed at positions '1', '2' and '3'. The EDS peaks of those areas are shown in Figs. 6.28a - 6.28c. Position '1' in the lighter area (Fig. 6.28a) is made up of comminuted debris exhibiting Al and W peaks whereas the position '2' in the darker area (Fig. 6.28b) shows a strong peak of Al with

small traces of W. Debris trapped in a hole at the position '3' reveals peaks consisting of Al and W (Fig. 6.28c).

6.4.3 Microstructural Observation of the Worn Surface of Al_2O_3 Slid Against HVOGF Sprayed WC-17 wt% Co (P) Coating

A ball slid against the coated disc under a load of 3.57 kg exhibits significant severe wear with a scar 3.8 mm diameter, Fig. 6.29a. Observations on the worn surface show smearing of the transferred layer (Fig. 6.29b). The SE-SEM image at high magnification indicates that the transferred layer at position '1' is composed of fractured carbide grains and Co-binder matrix (Fig. 6.29c). Also, a large amount of fine debris is found in the worn surface (Fig. 6.29d).

6.5 Comparison of the Wear Behaviour of Al_2O_3 Ball Slid Against the Sintered WC-Co and Sprayed Coatings

The wear rate of balls slid against the sintered WC-Co and coated discs are plotted in Fig 6.24. It is clear that the wear rate of a ball slid against the sintered WC-Co is the lowest. Comparison between balls slid against coated discs at low load indicate that against HVOGF sprayed WC-12 wt% Co coating the lowest wear rate occurs, whilst a ball slid against HVOGF sprayed nanoscale WC-12 wt% Co coating has the highest wear rate. At loads between 3-9 kg, the wear rates of balls slid against coated discs change in order because they are in the transition period. At high loads, a ball slid against HVOGF sprayed WC-17 wt% Co (P) coating exhibits the lowest wear rate,

whereas a ball slid against HVOGF sprayed WC-12 wt% Co coating shows the highest wear rate. Furthermore, in all cases the ball scar was circular.

Figs. 6.25, 6.27 and 6.29 show the surface morphologies of balls worn against sintered WC-Co, HVOGF sprayed WC-12 wt% Co coating and HVOGF sprayed WC-17 wt% Co (P) coating. It can be seen that a ball slid against HVOGF sprayed WC-17 wt% Co (P) coating shows the most severe worn surface followed by HVOGF sprayed WC-12 wt% Co coating and then sintered WC-Co. The surface worn under a low load against sintered WC-Co exhibits a smooth surface with a few pores (Fig. 6.25a). Worn surface observations on balls slid against HVOGF sprayed WC-12 wt% Co coating and HVOGF sprayed WC-17 wt% Co (P) coating have similar wear mechanism, as shown in Figs. 6.27 and 6.29. Worn surfaces reveal smearing of transferred layer with fractured carbide grains embedded and fine debris trapped in it.

From the graphs of the wear rates of balls (Fig. 6.24) and discs (Fig. 6.2) shows that the wear rate of balls increases as the wear rate of discs increases. The graph of the wear rate of balls and discs are replotted and illustrated in Fig. 6.30. Wear debris from either the disc or ball will cause wear of the other material in the couple by abrasive wear.

Table 6.1 Results of hardness and roughness of polished surfaces of wear specimens and wear rate of sintered carbide and coated discs.

Specimen	Hardness HV_{300}	Roughness (μm)	BOD conditions		Disc wear / (10^{-10}) m^3	Disc wear rate / (10^{-15}) $m^3 m^{-1}$	Error in disc wear rate (%)
			Load (kg)	Distance (m)			
Sintered carbide	1500±28	0.04-0.05	1.94	5000	0.042	0.83	6.05
			2.75	5000	0.043	0.86	18.26
			3.57	5000	0.130	2.60	20.72
			5.20	5000	1.080	21.60	14.18
			6.83	2715.5	48.810	1797.46	2.99
			8.46	1138	117.680	10340.95	2.90
			10.09	1148	139.280	12132.40	1.85
			18.24	501	128.344	25617.56	1.83
HVOLF Conv. WC-12 wt% Co	1237±93	0.03-0.05	1.94	5000	1.013	20.26	61.15
			3.57	5000	2.563	51.25	10.08
			6.83	395	7.392	1871.39	13.11
			10.09	281	7.937	2819.43	21.30
HVOGF Conv. WC-12 wt% Co	1288±86	0.03-0.05	1.94	5000	0.108	2.17	8.86
			3.57	5000	0.508	10.17	9.05
			6.83	386.5	5.590	1446.31	12.51
			10.09	152.5	6.815	4468.98	14.24
HVOGF Nano. WC-12 wt% Co	1206±64	0.04-0.17	1.94	5000	1.823	36.46	34.90
			3.57	5000	1.815	36.29	13.74
			6.83	370	6.022	1627.57	5.18
			10.09	184.5	10.887	5900.81	16.24
HVOLF Conv. WC-17 wt% Co (M)	1333±54	0.03-0.04	1.94	5000	2.096	41.92	69.08
			3.57	5000	4.770	95.40	25.65
			6.83	301	10.910	3624.58	29.47
			10.09	202	14.753	7303.47	19.37
HVOGF Conv. WC-17 wt% Co (P)	1283±74	0.03	1.94	5000	0.150	2.99	6.02
			3.57	5000	5.294	105.88	25.02
			6.83	885	8.148	920.68	7.71
			10.09	422	12.300	2914.69	22.33

Table 6.2 Wear volume and average wear rate of sintered carbide at 5.2 kg load with different sliding distances.

Specimen	BOD conditions		Disc wear / (10^{-10}) m^3	Disc wear rate / (10^{-15}) $m^3 m^{-1}$	Error in disc wear rate (%)
	Load (kg)	Distance (m)			
Sintered carbide	5.20	250	0.199	39.80	19.55
		500	0.472	47.20	15.13
		3000	0.737	24.57	16.42
		5000	1.080	21.60	14.18

Table 6.3 Wear rate of Al_2O_3 ball slid against sintered carbide and coated discs.

Specimen	BOD conditions		Ball wear / (10^{-9}) m^3	Ball wear rate / (10^{-15}) $m^3 m^{-1}$
	Load (kg)	Distance (m)		
Sintered carbide	1.94	5000	0.0008859	0.18
	2.75	5000	0.0073	1.46
	3.57	5000	0.0397	7.94
	5.20	5000	0.1938	38.76
	6.83	2715.5	3.0699	1130.51
	8.46	1138	4.7957	4214.15
	10.09	1148	3.5585	3099.74
	18.24	501	3.6077	7201.00
HVOLF Conv. WC-12 wt% Co	1.94	5000	0.279	55.80
	3.57	5000	1.912	382.40
	6.83	395	4.1363	10471.65
	10.09	281	4.1135	14612.79
HVOGF Conv. WC-12 wt% Co	1.94	5000	0.0045	0.90
	3.57	5000	0.2942	58.84
	6.83	386.5	5.1592	13348.51
	10.09	152.5	4.9749	32622.30
HVOGF Nano. WC-12 wt% Co	1.94	5000	0.5082	101.64
	3.57	5000	0.4230	84.60
	6.83	370	3.5030	9467.57
	10.09	184.5	5.1968	28166.94
HVOLF Conv. WC-17 wt% Co (M)	1.94	5000	0.1694	33.88
	3.57	5000	2.5751	515.02
	6.83	301	5.7043	18951.16
	10.09	202	6.2504	30942.57
HVOGF Conv. WC-17 wt% Co (P)	1.94	5000	0.0327	6.54
	3.57	5000	3.0359	607.18
	6.83	885	3.2613	3685.08
	10.09	422	4.2000	9952.61

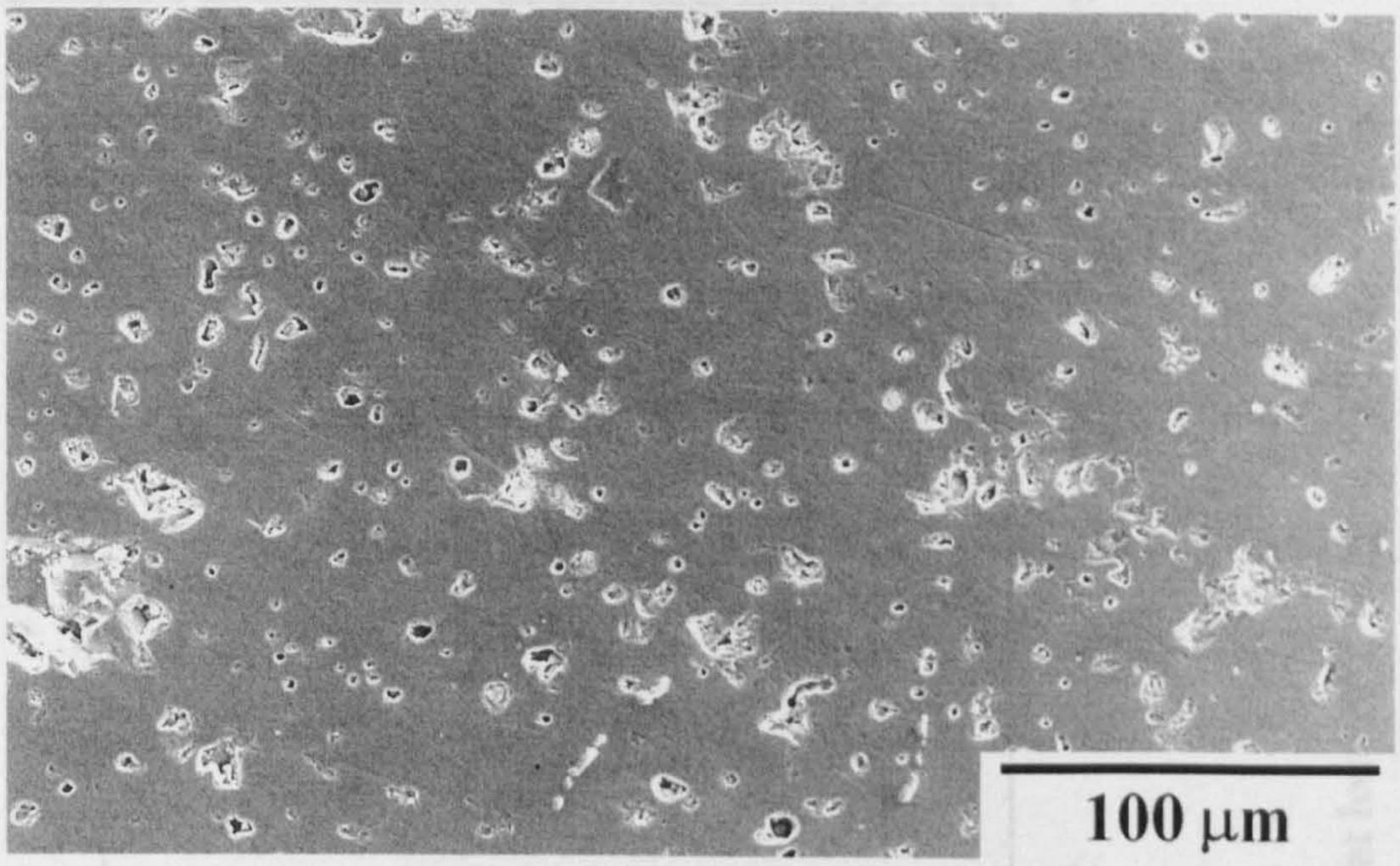

Fig 6.1 Microstructure of as-received a sintered ceramic ball (Al_2O_3) with pores of a range of sizes.

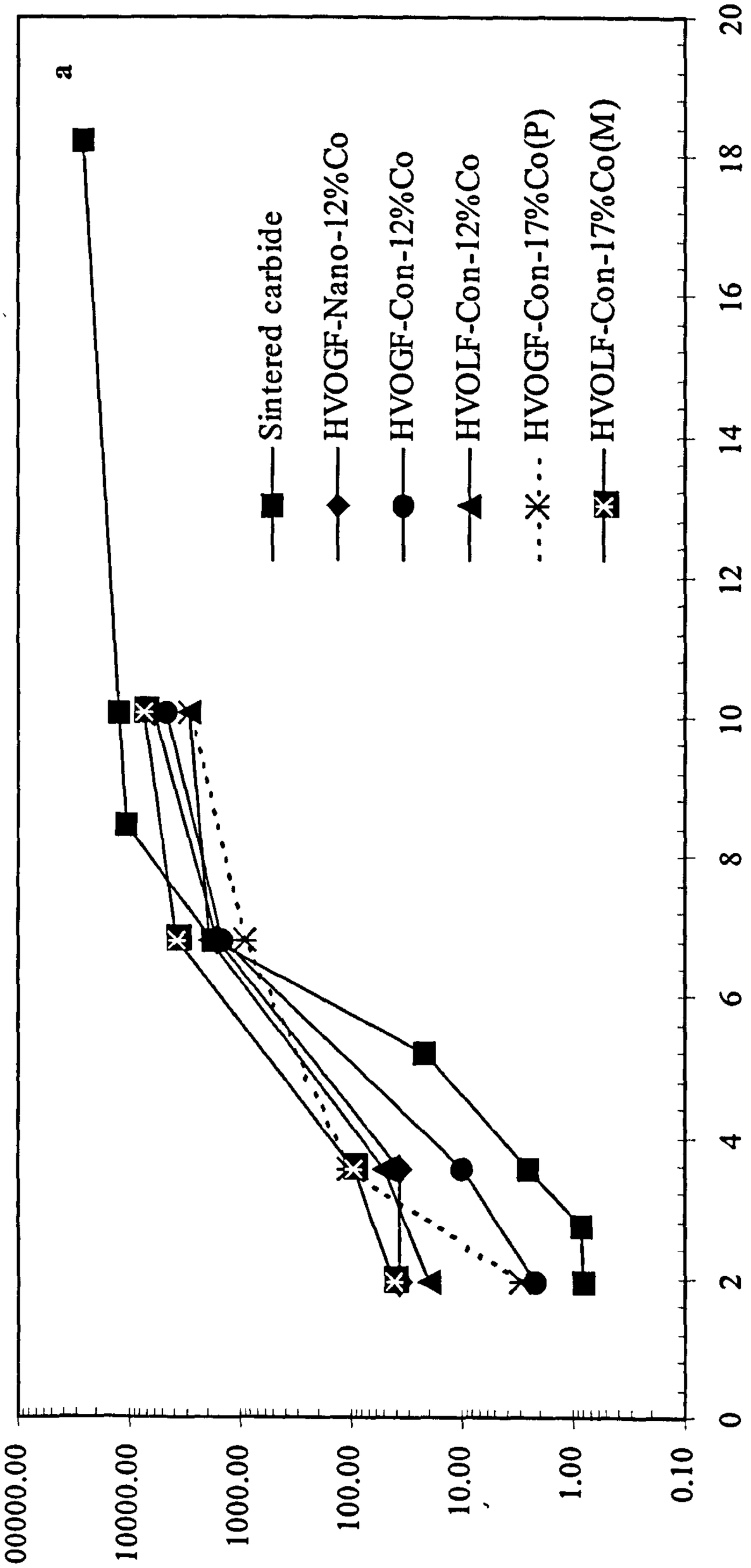

Fig. 6.2 Wear rate of sintered carbide and coated discs (a) at load of 1.94 kg to 10.09kg.

Note : ΔV_D = the volume loss of WC-Co disc per unit sliding distance

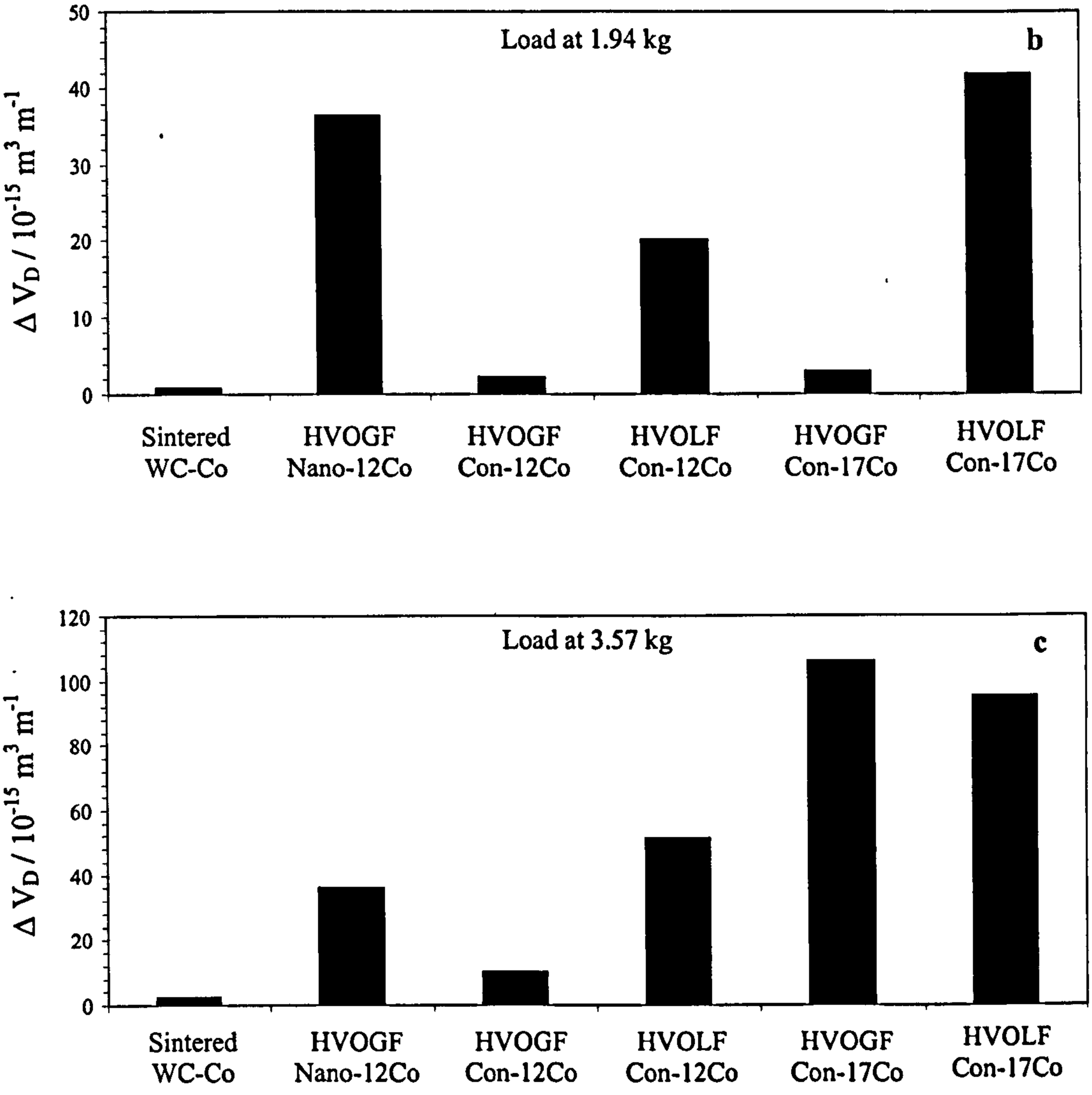

Fig.6.2 (cont.) Wear rate of sintered carbide and coated discs (b) at load of 1.94 kg and (c) at load of 3.57 kg.

Note : ΔV_D = the volume loss of WC-Co disc per unit sliding distance

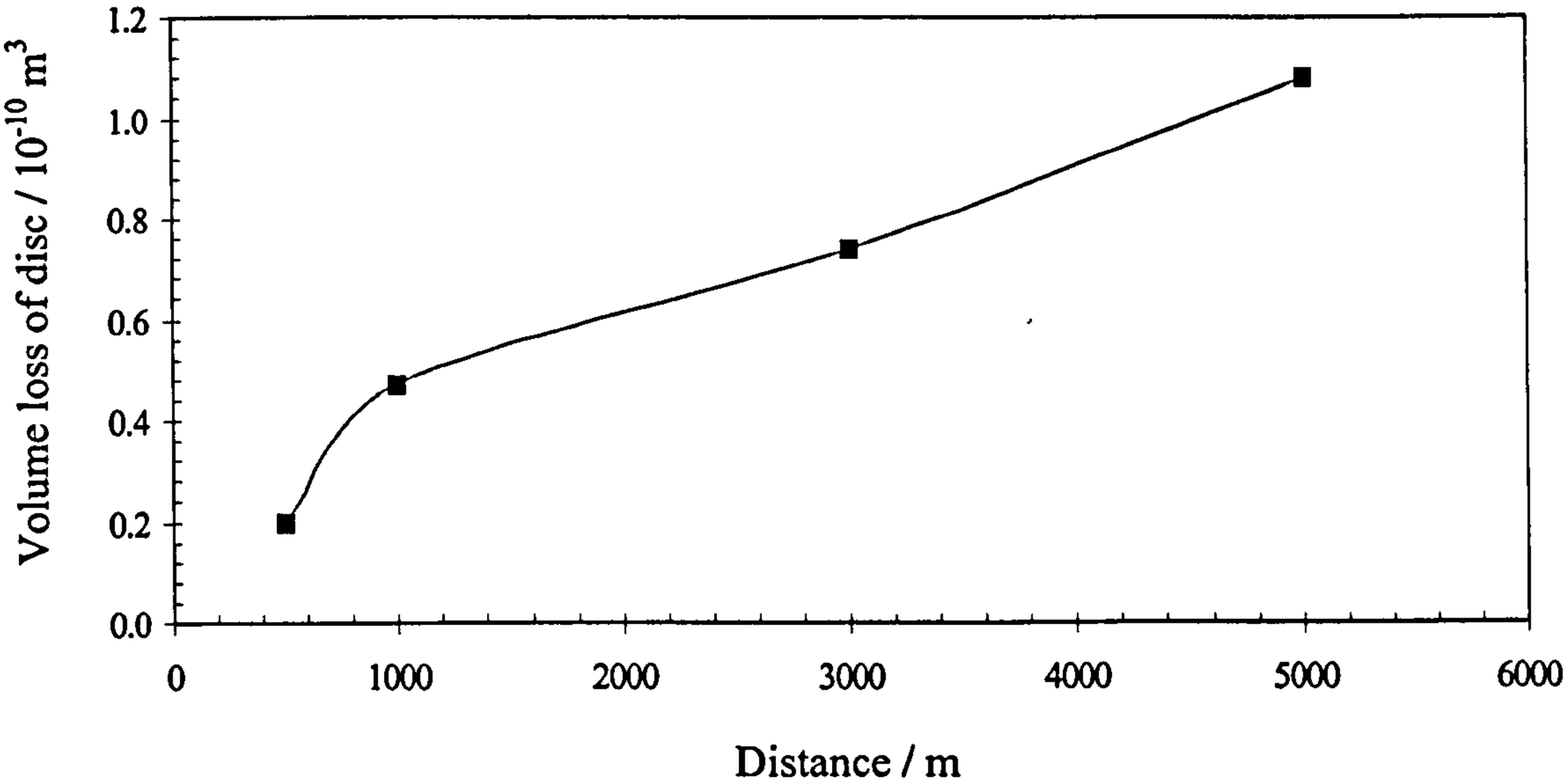

Fig. 6.3 Wear volume loss of the sintered carbide tested under a load of 5.2 kg with different sliding distances.

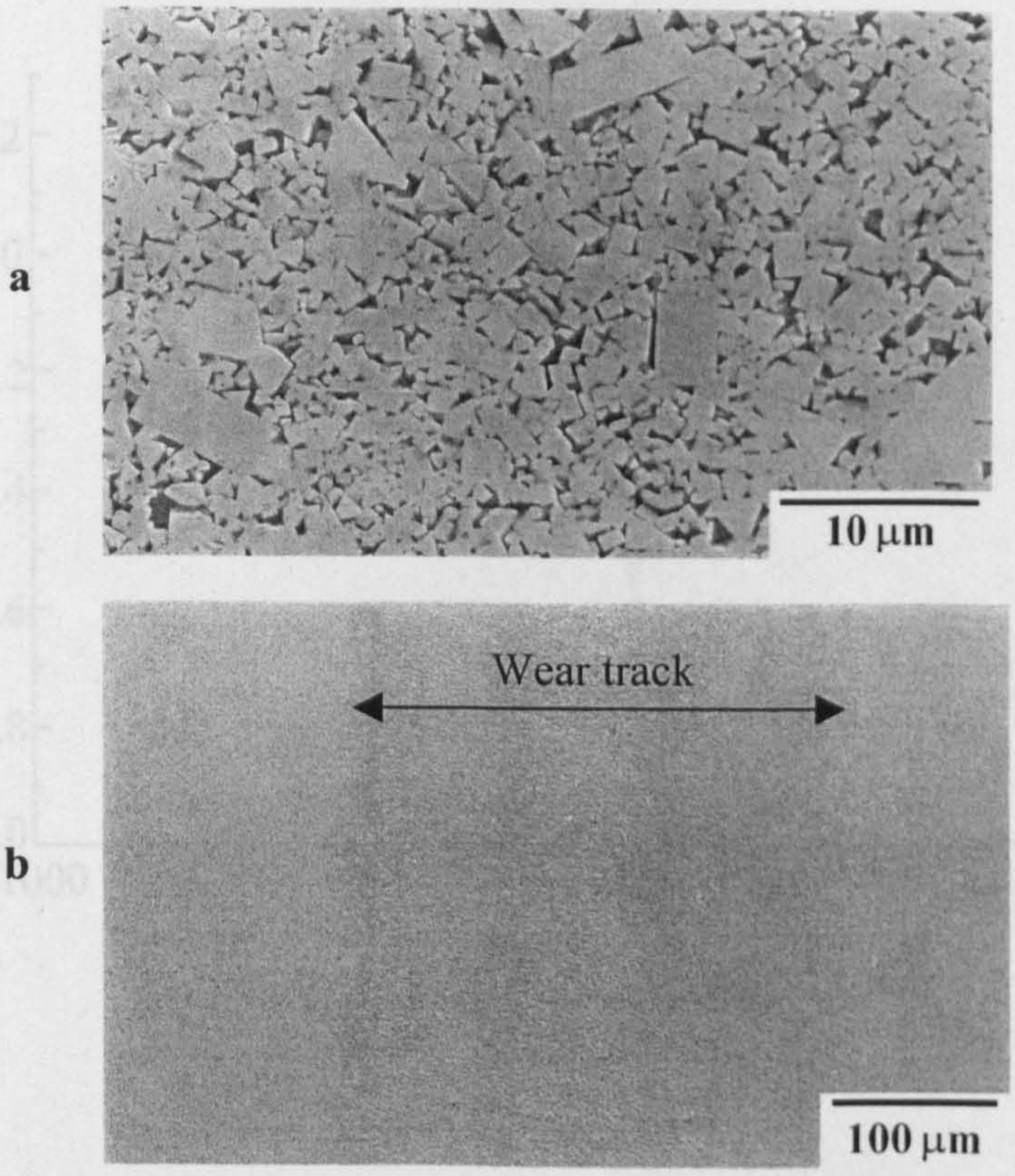

Fig. 6.4 SEM images of sintered carbide showing (a) an unworn surface with carbide grains about 2 μm, (b) a surface worn under a 1.94 kg load showing smooth surface with little damage, (c) worn surface from the middle of the wear track showing pure Co extrusion, carbide grains pullout and (d) worn surface at the rim on the right of the wear track showing fine wavy features on carbide grains (sliding direction from top to bottom).

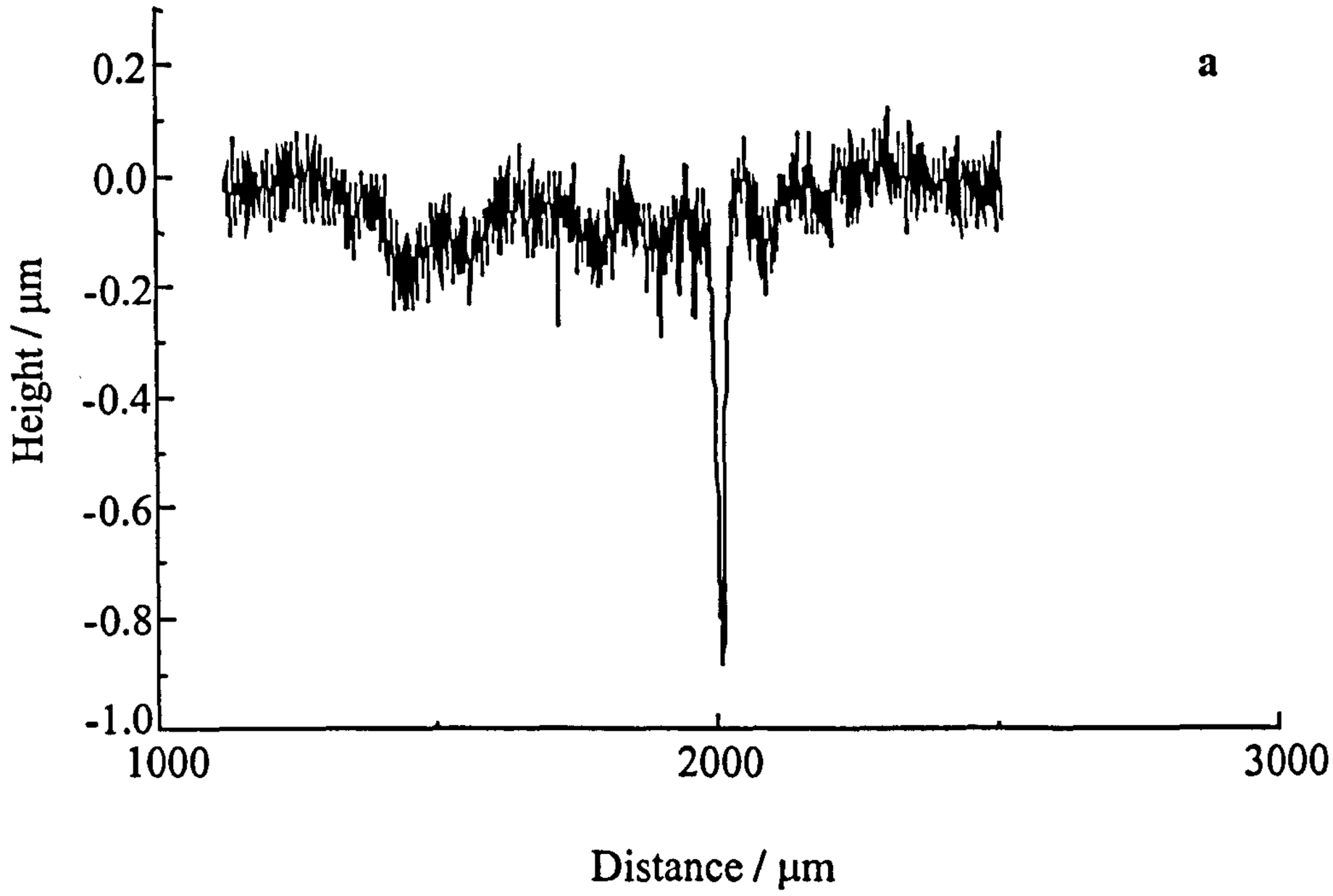

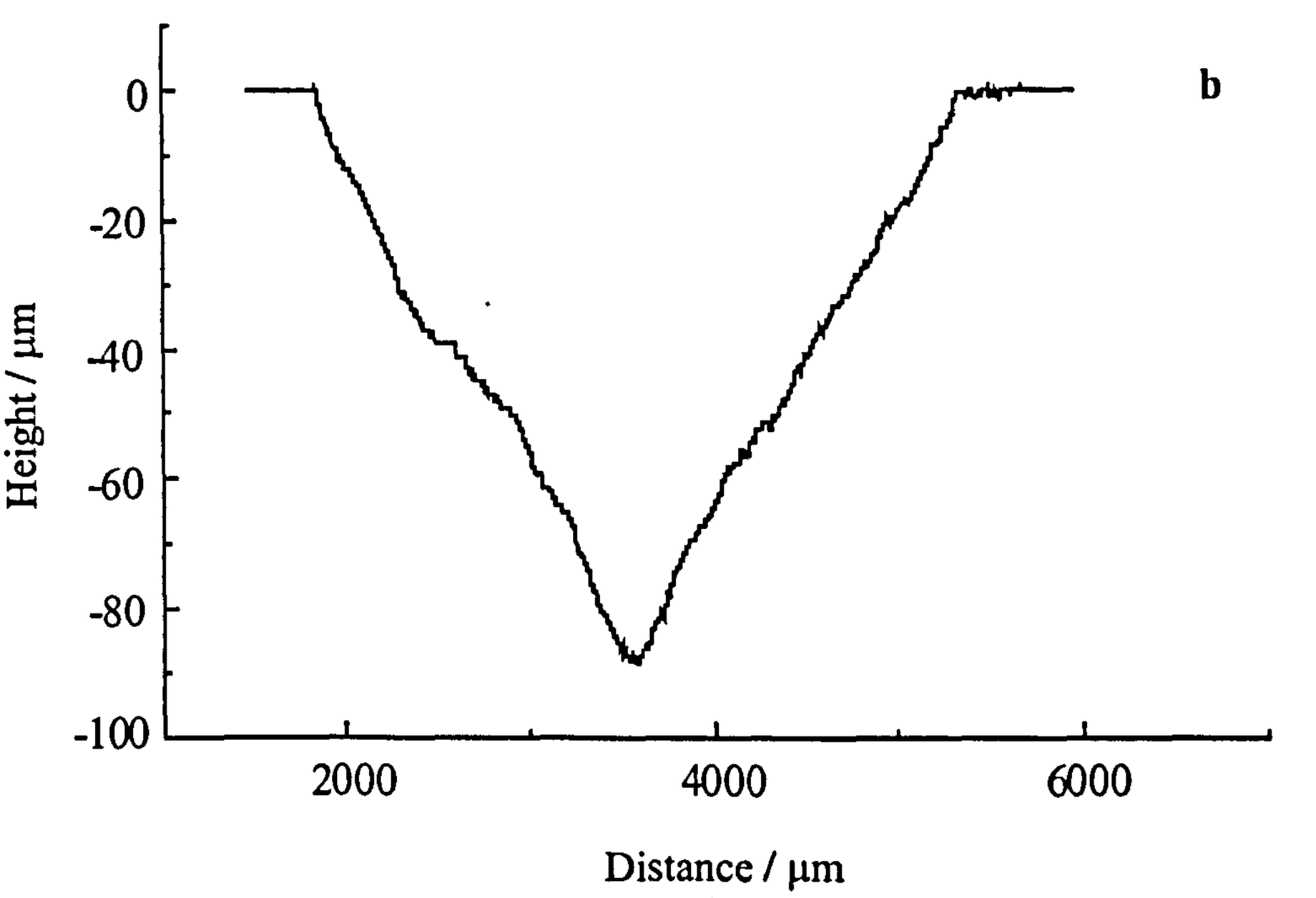

Fig. 6.5 Wear track profile of sintered carbide slid under different loads (a) 3.57 kg and (b) 10.1 kg.

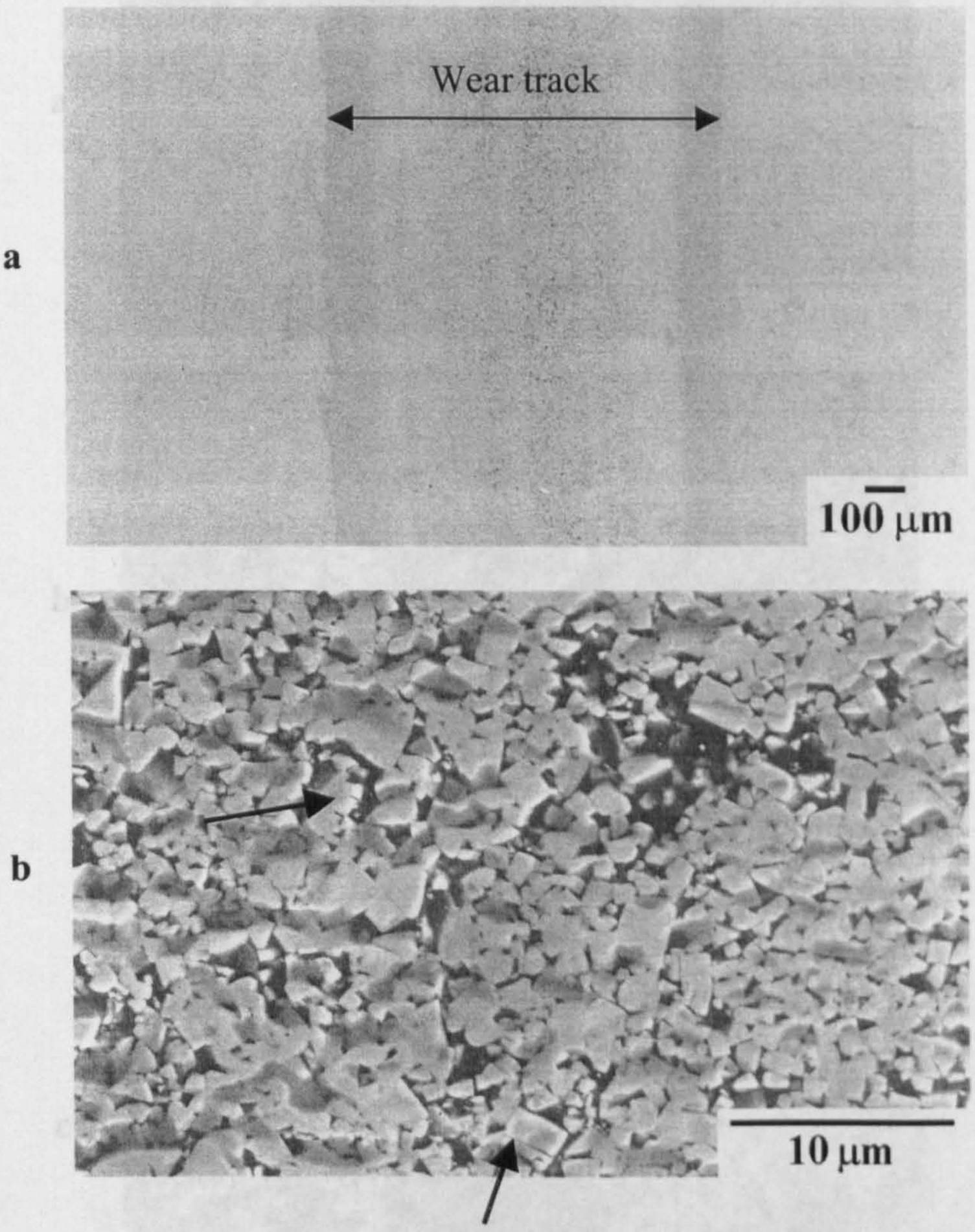

Fig. 6.6 SEM images of surface of sintered carbide worn under a load of 3.57 kg indicating (a) the wear track with smooth surface and (b) worn surface from the middle of the wear track showing the removal of binder phase and carbide grains and cracks (as indicated by arrows) on carbide grains (sliding direction from top to bottom).

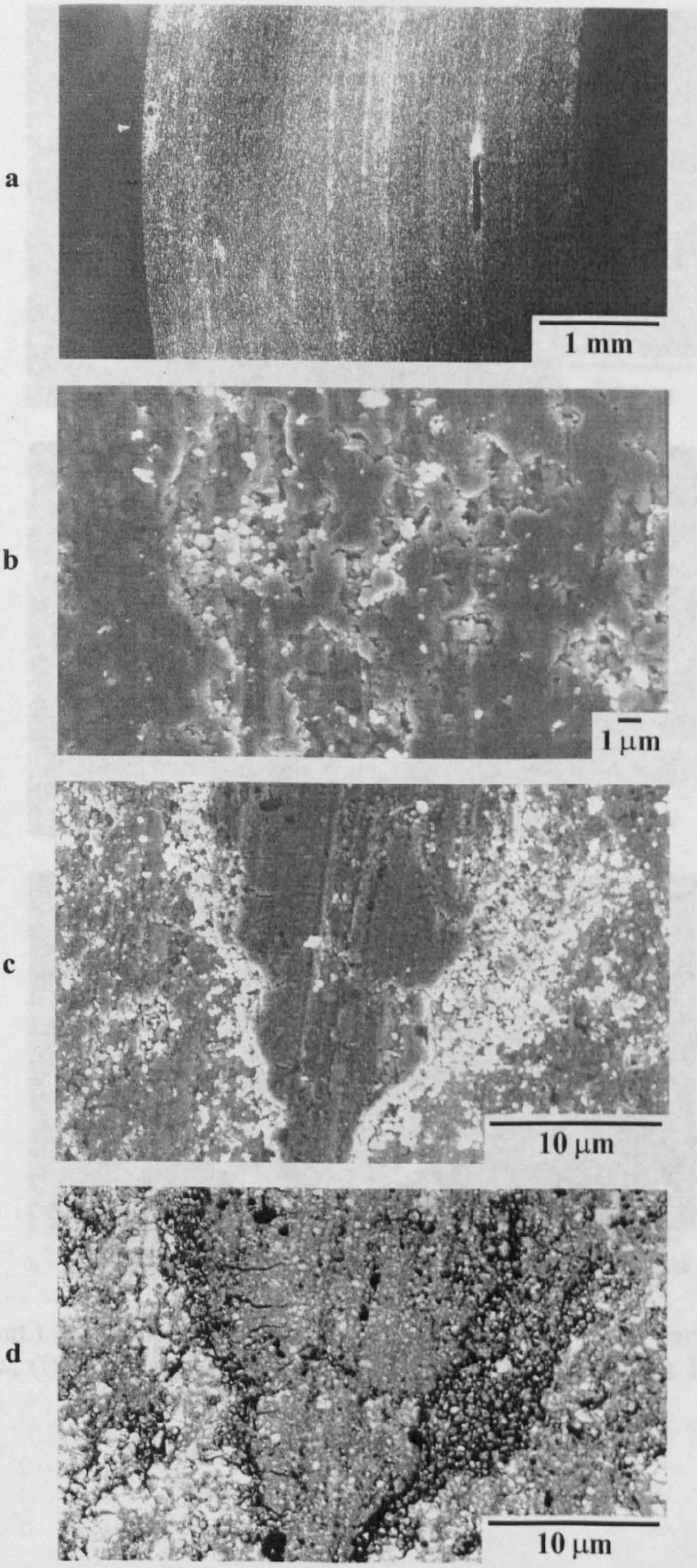

Fig. 6.7 SEM images of the surface sintered carbide worn under a load of 10.1 kg indicating (a) the wear track, (b) worn surface from the middle of the wear track, (c) and (d) transferred layer with SE-SEM imaging and BSE-SEM imaging, respectively, showing fragmented carbide grains in it (sliding direction from top to bottom).

e

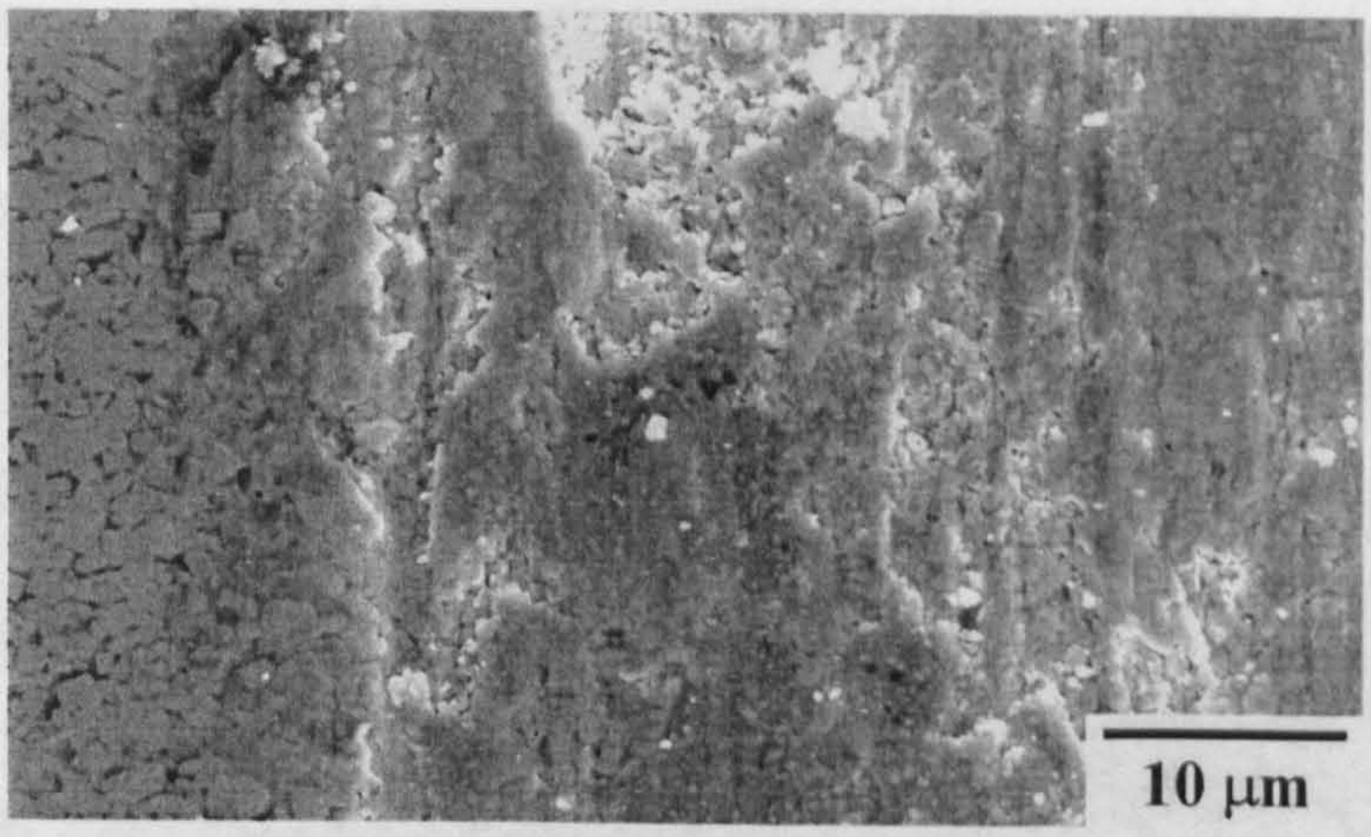

f

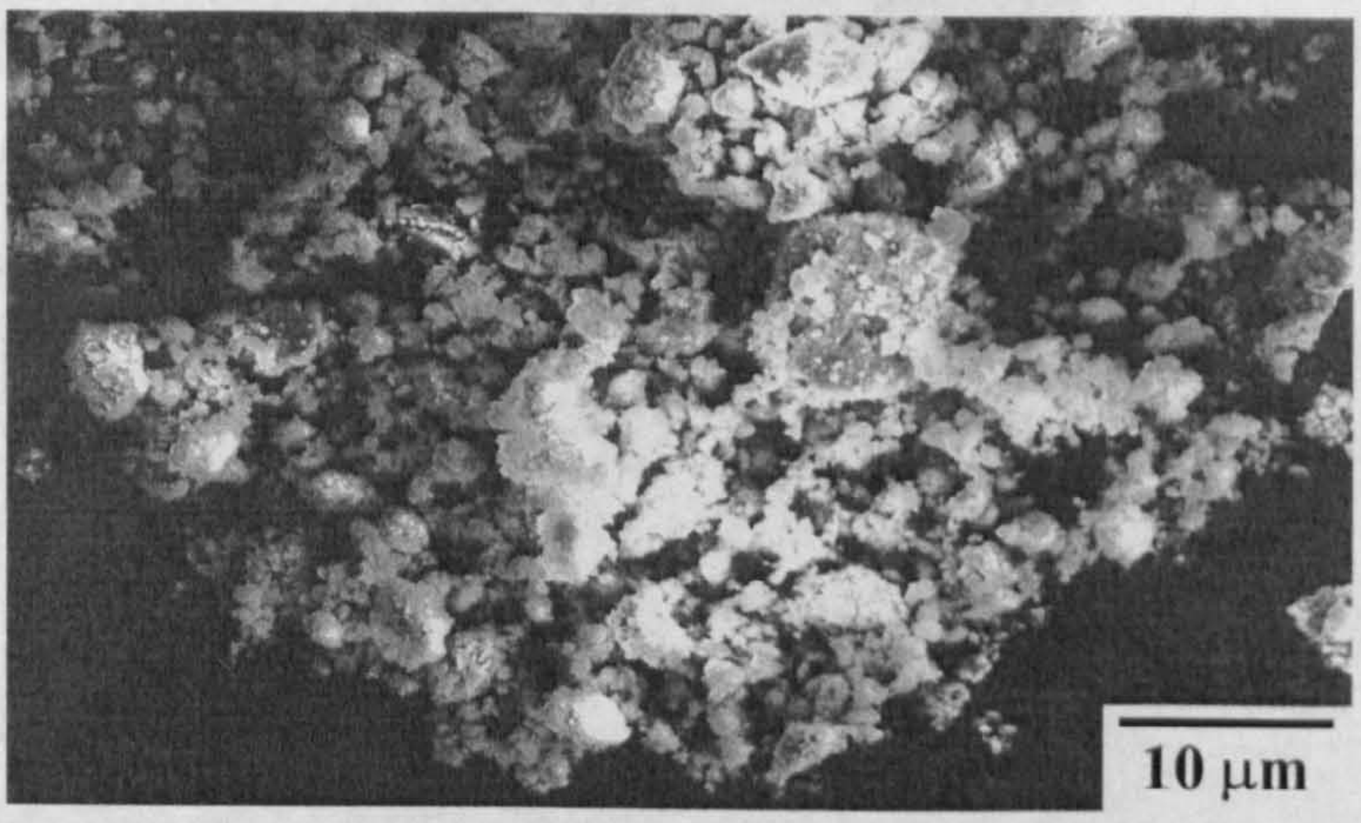

g

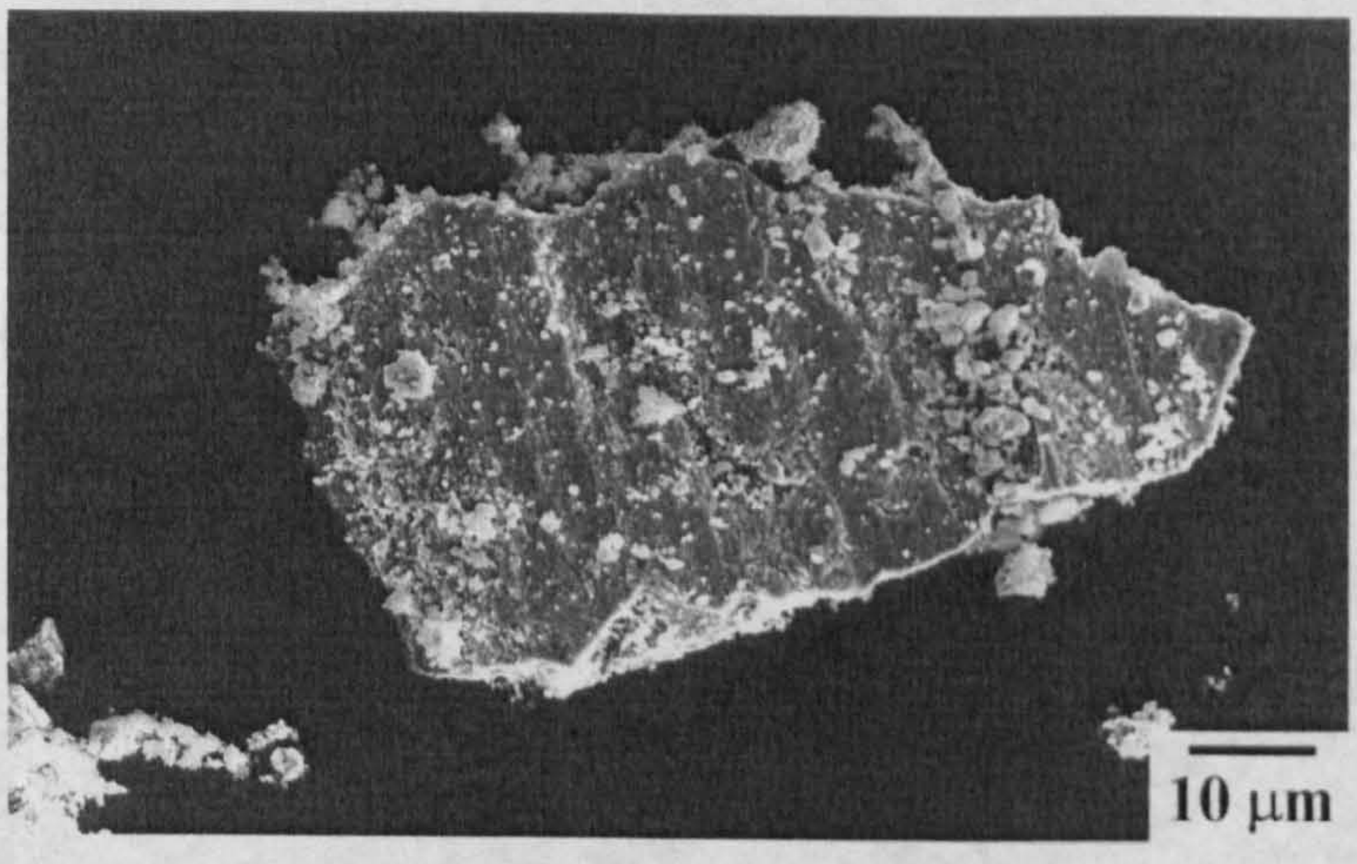

Fig. 6.7 (cont.) (e) worn surface at rim on the left of the wear track revealing the material loss, (f) agglomerated fine debris and (g) plate-like debris from transferred layer.

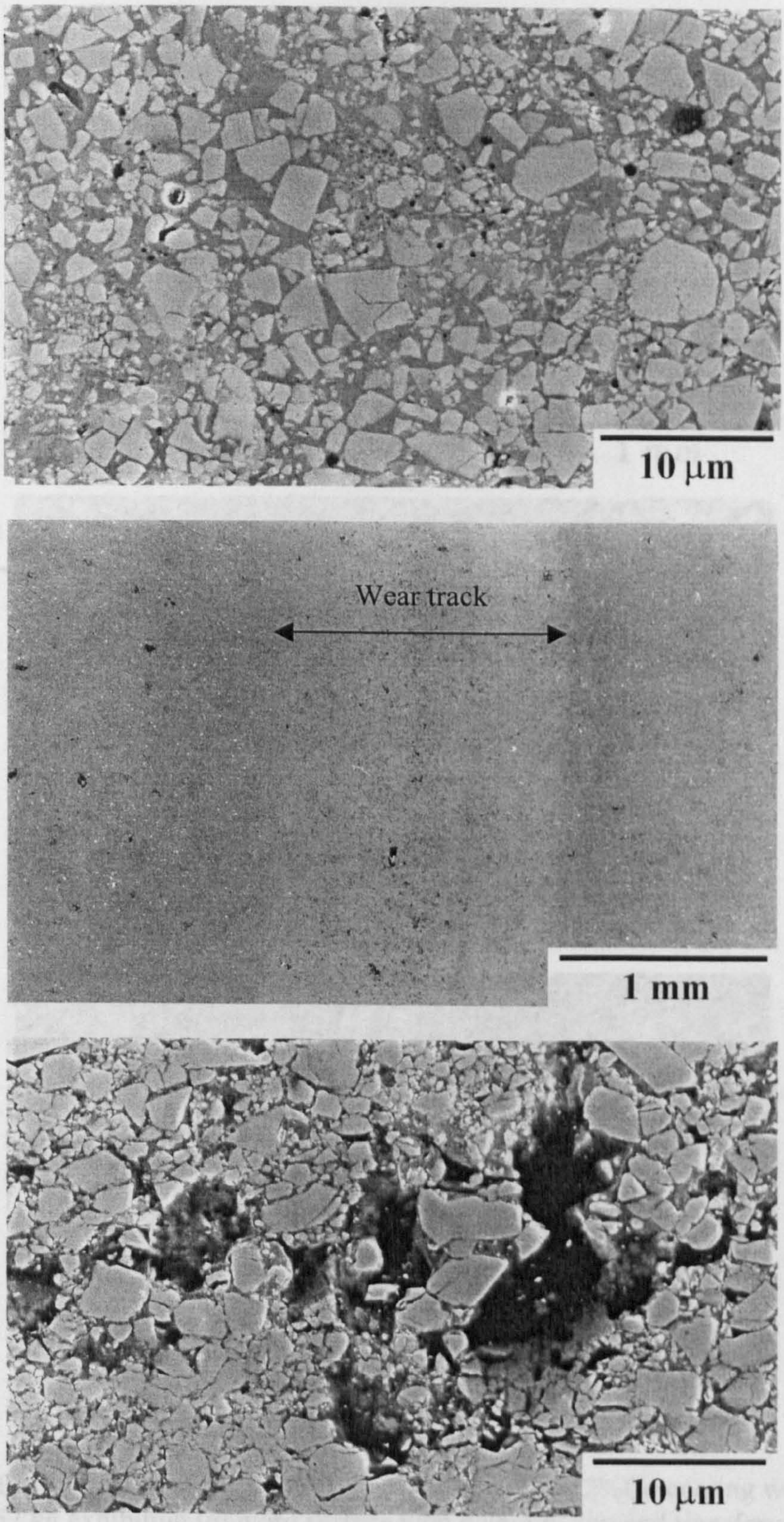

Fig. 6.8 SEM images of HVOLF sprayed WC-12 wt% Co coating showing (a) unworn surface with pores and cracks in carbide grains, (b) surface worn under a load of 1.94 kg showing smooth surface with few pits and (c) worn surface from the middle of the wear track revealing an area of material loss and cracks in the carbide grains (sliding direction from top to bottom).

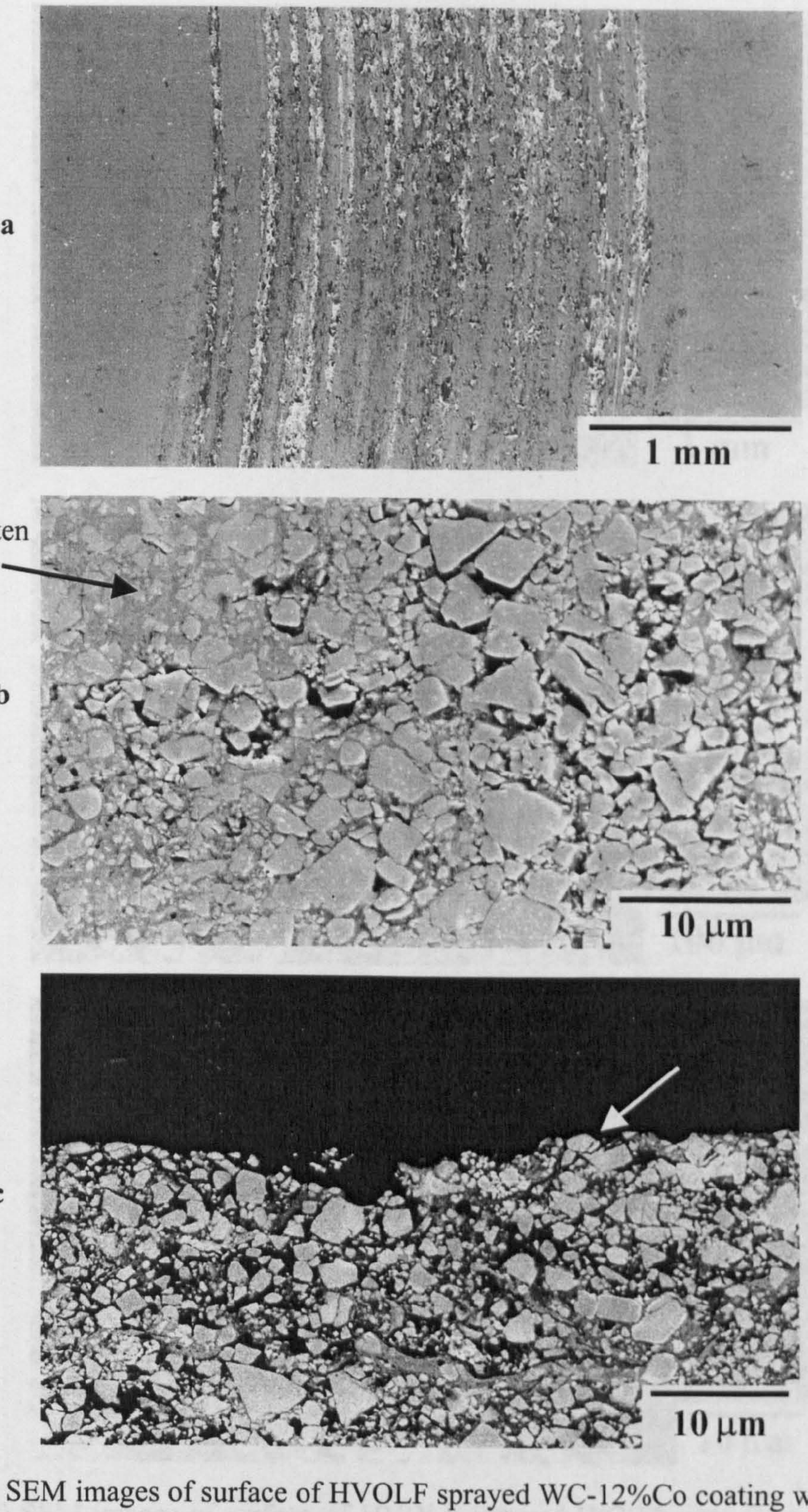

Fig. 6.9 SEM images of surface of HVOLF sprayed WC-12%Co coating worn under a load of 3.57 kg exhibiting (a) worn surface with delamination and transferred layer, (b) worn surface toward the rim of the wear track showing the removal of binder phase and cracks in carbide grains and (c) cross-sectional image revealing no significant sub-surface cracking (a and b: sliding direction from top to bottom, c: sliding direction parallel to the coating).

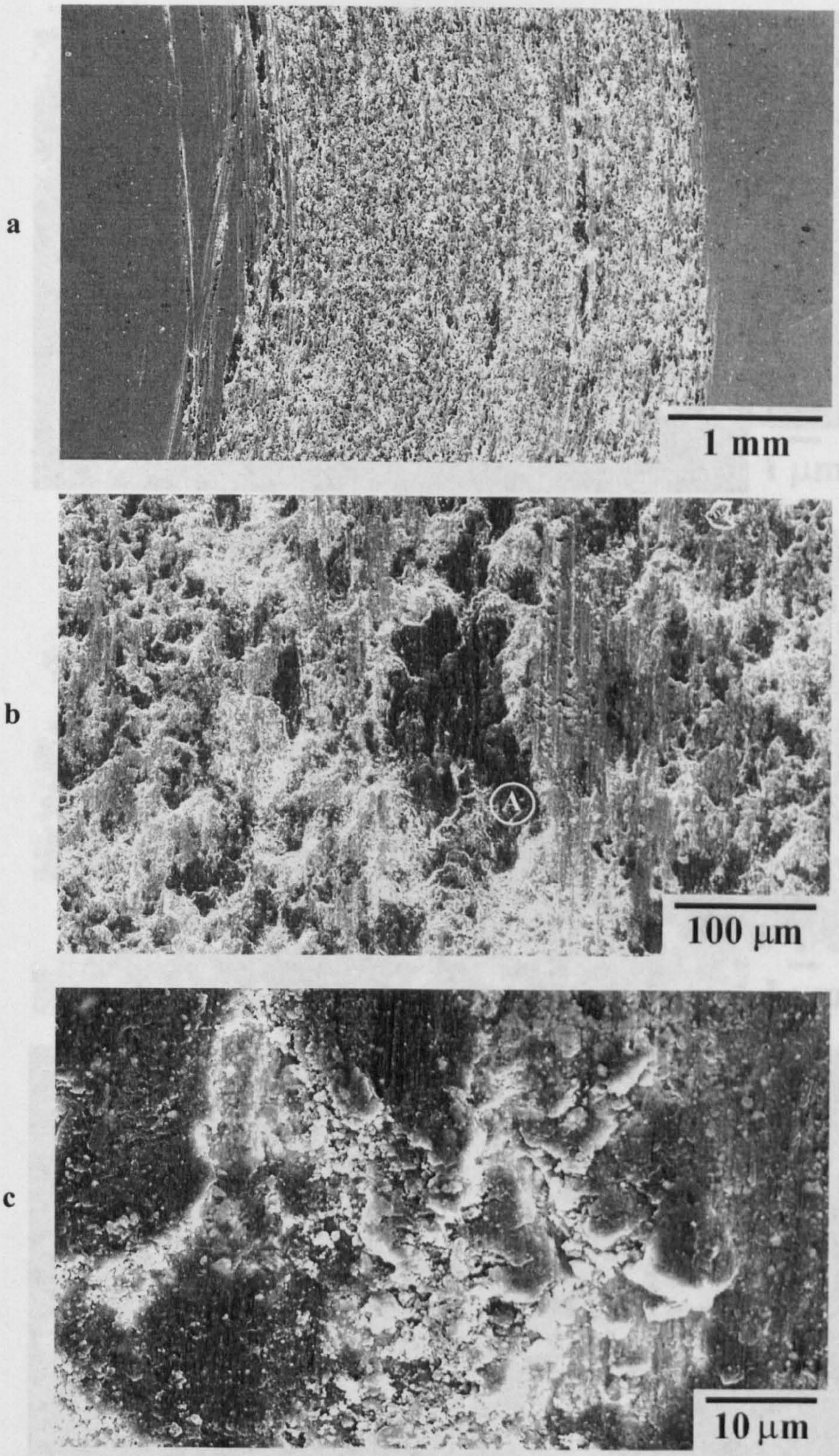

Fig 6.10 SEM images of surface of HVOLF sprayed WC-12 wt% Co coating worn under a load of 10.1 kg indicating (a) severely worn surface with delamination and transferred layer, (b) high magnification of worn surface in the wear track showing transferred layer and delamination, (c) high magnification on transferred layer showing cracking and fine debris trapped in the wear track (sliding direction from top to bottom).

d

e

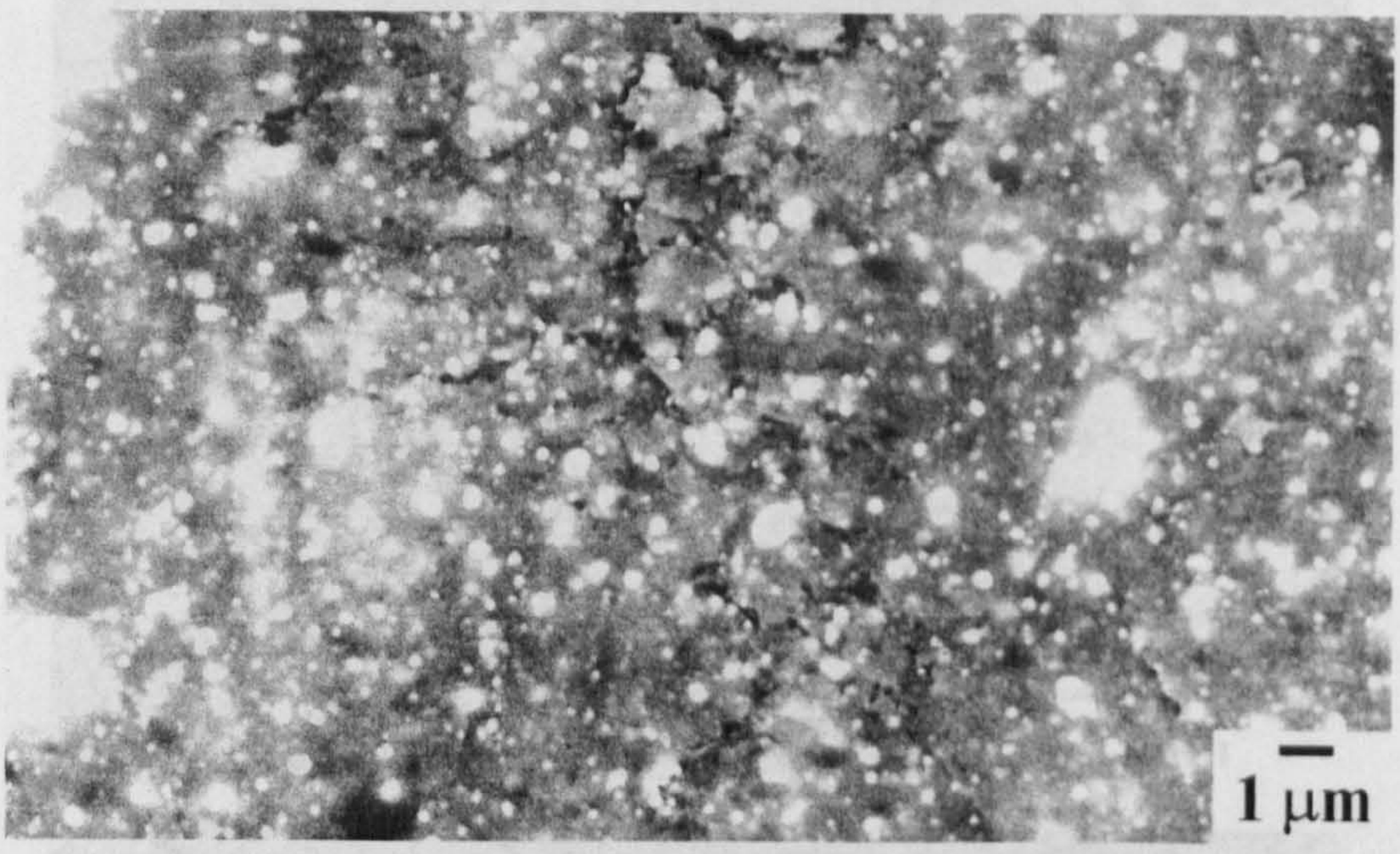

f

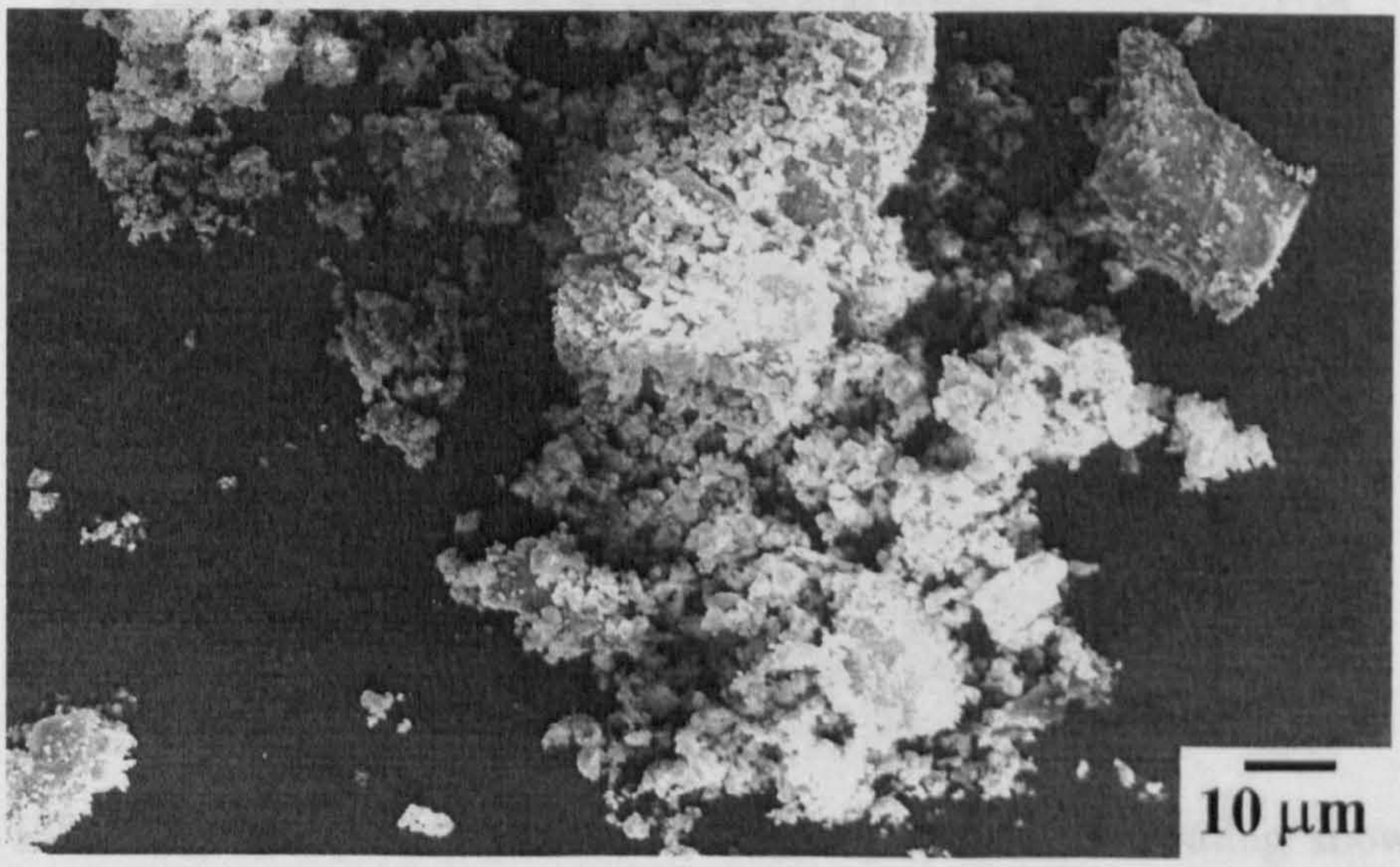

Fig. 6.10 (cont.) (d) and (e) high magnification SE-SEM image and BSE-SEM image, respectively, of transferred layer showing small fragmented carbide grains and (f) wear debris containing agglomerated fine particles and plate-like debris.

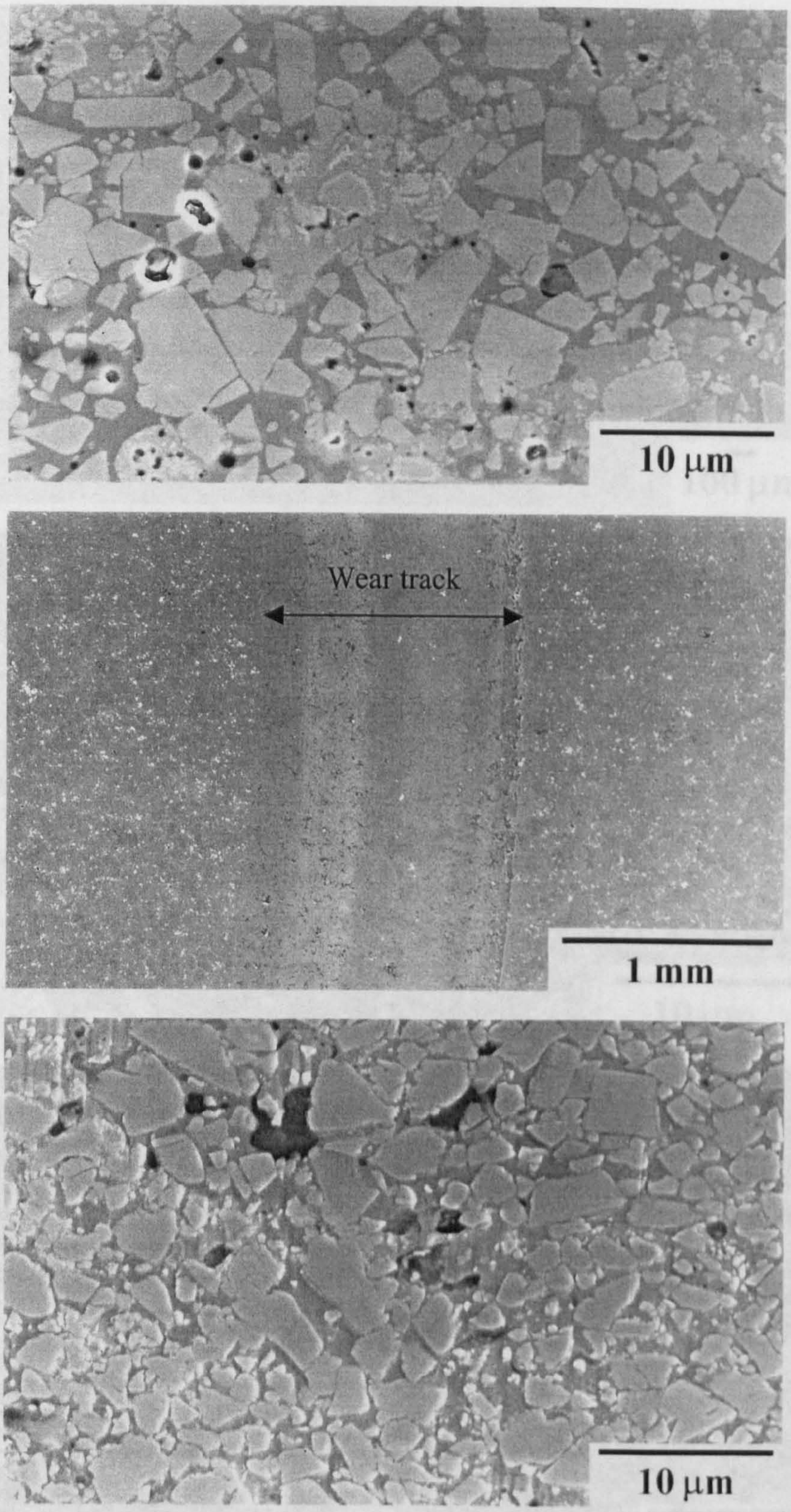

Fig. 6.11 SEM images of HVOGF sprayed WC-12 wt% Co coating showing (a) unworn surface with micropores, (b) surface worn under a load of 1.94 kg showing smooth surface with pits and (c) worn surface from the middle of the wear track showing preferential wear of matrix phase, carbide grains standing proud of the matrix, holes resulting from the removal of carbide grains (sliding direction from top to bottom).

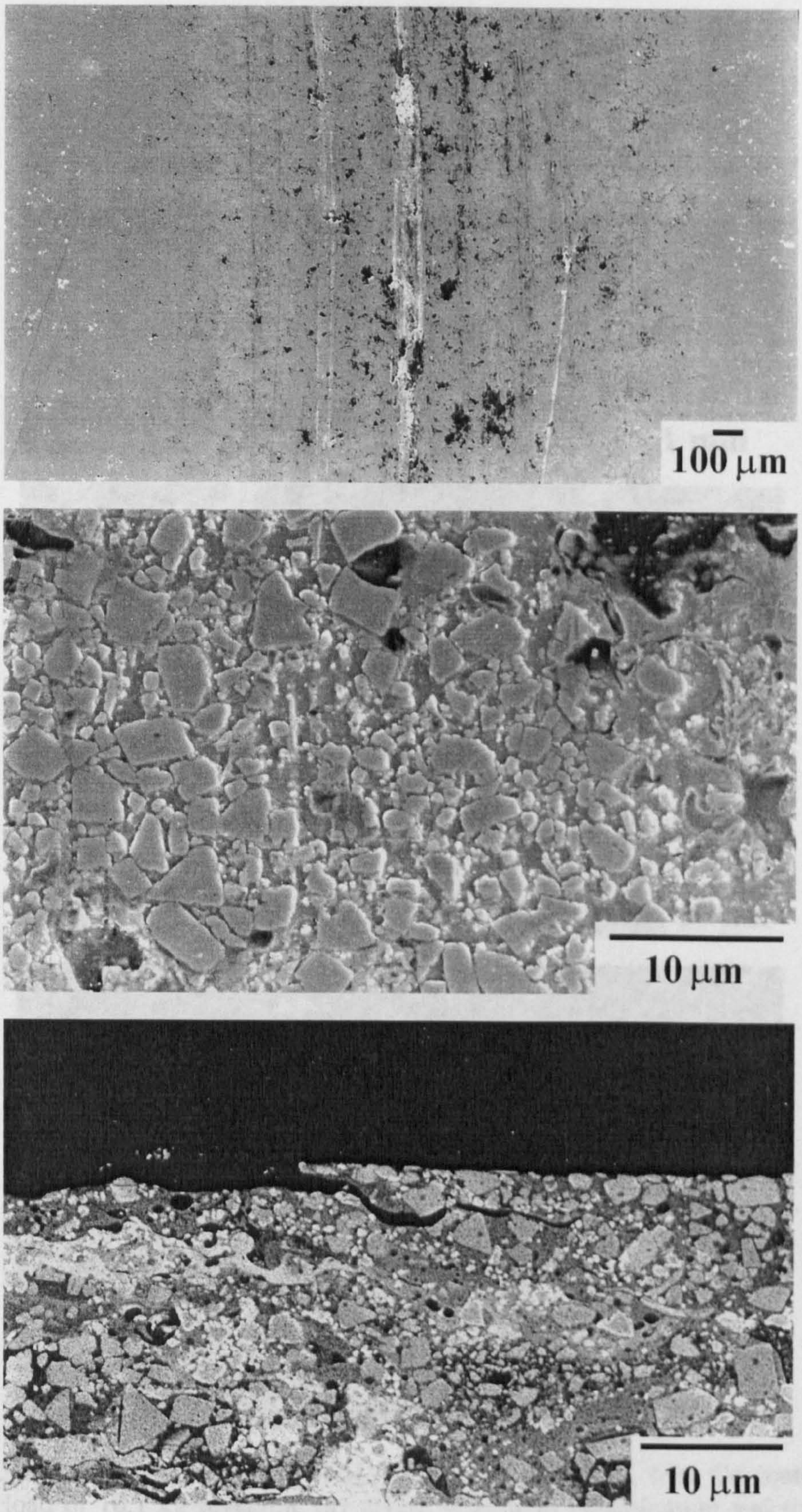

Fig. 6.12 Surface of HVOGF sprayed WC-12 wt% Co coating worn under a load of 3.57 kg exhibiting (a) wear track with pitting and delamination, (b) worn surface at high magnification showing wear of the binder phase, carbide grains protruding from the surface and carbide grains pullout, (c) a cross-sectional image showing sub-surface cracking and good adhesion of carbide grains at the wearing surface (a and b: sliding direction from top to bottom, c: sliding direction parallel to the coating).

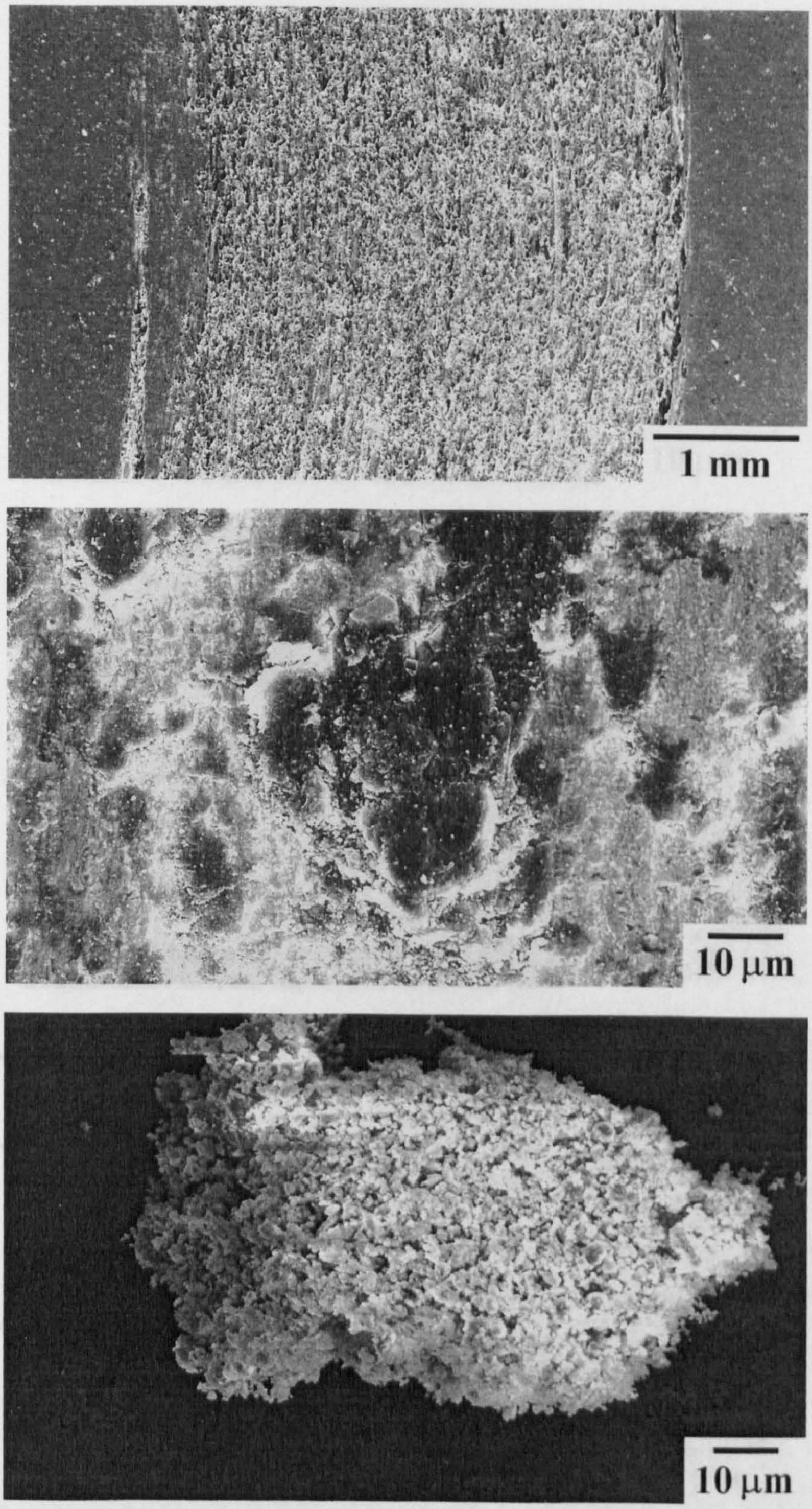

Fig. 6.13 SEM images of surface of HVOGF sprayed WC-12 wt% Co coating worn under a load of 10.1 kg revealing (a) severe wear with delamination and transferred layer, (b) high magnification image on the transferred layer and (c) agglomerated fine debris (sliding direction from top to bottom).

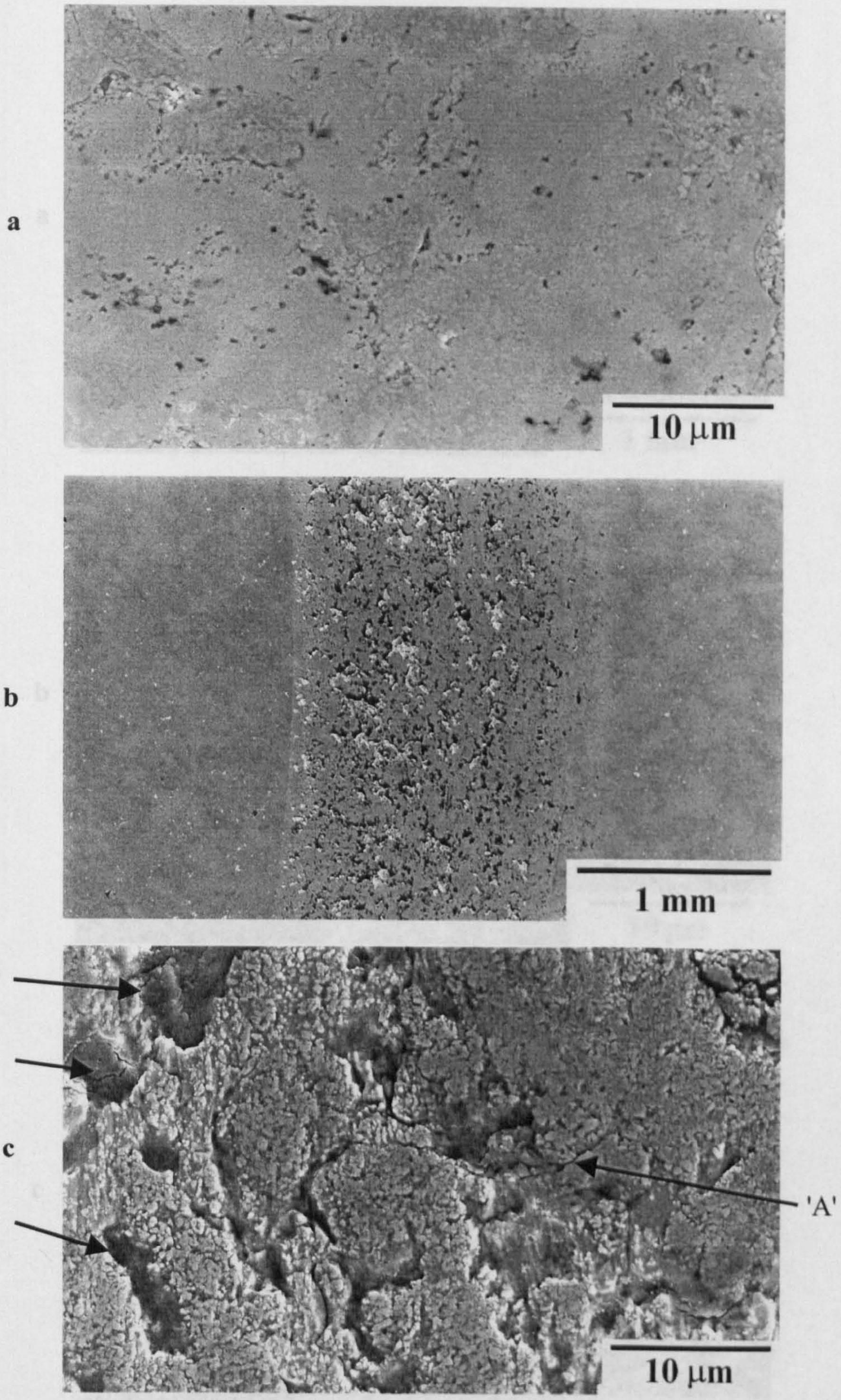

Fig. 6.14 SEM images of HVOGF sprayed nanoscale WC-12 wt% Co coating showing (a) unworn surface with micropores, (b) surface worn under a load of 1.94 kg showing smooth surface with severe pitting and delamination and (c) worn surface in the wear track indicating a large amount of material loss (as indicated by arrows 'B'), severe cracking (as indicated by arrows 'A'), and seemingly carbide grains standing out of the matrix phase (sliding direction from top to bottom). An arrow from 'C' shows that some of the pits have been filled with wear debris.

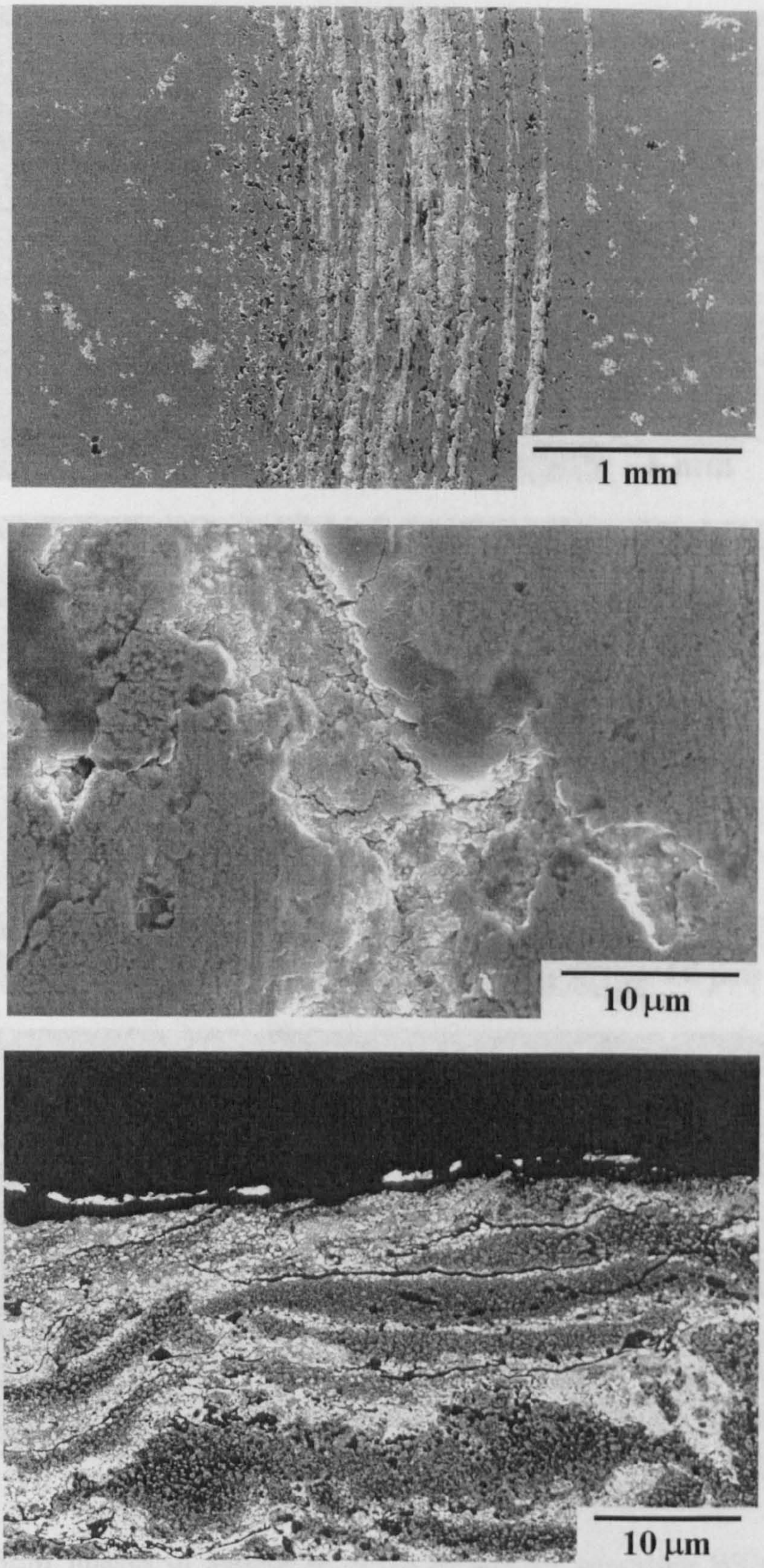

Fig. 6.15 SEM images of surface of HVOGF sprayed nanoscale WC-12 wt% Co coating worn under a load of 3.57 kg exhibiting (a) significant pitting and delamination, (b) large amounts of material loss and severe cracking and (c) a cross-section of worn surface showing sub-surface cracking with cracks running in the area of W and W_2C formation (a and b: sliding direction from top to bottom, c: sliding direction parallel to the coating).

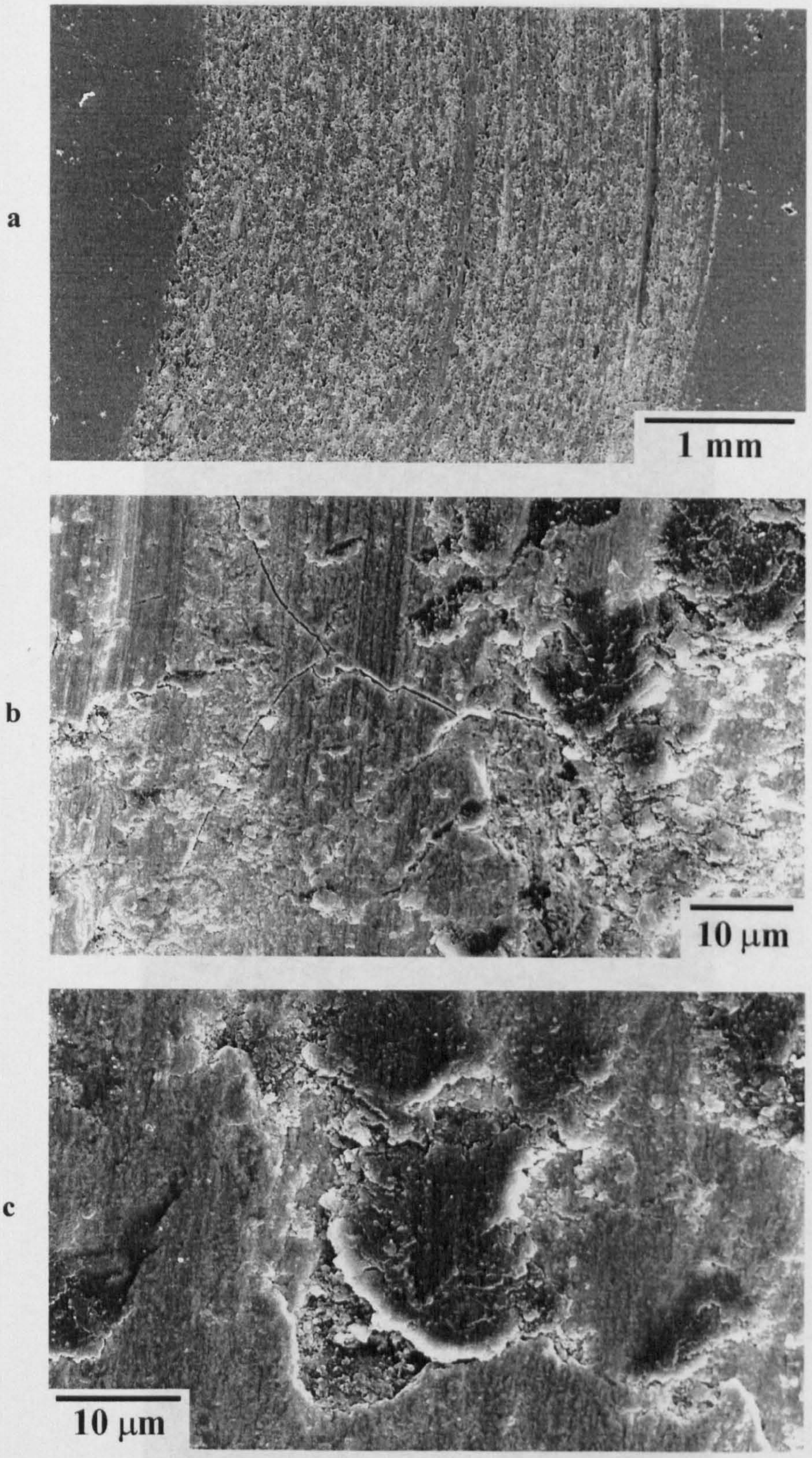

Fig. 6.16 SEM images of surface of HVOGF sprayed nanoscale WC-12 wt% Co coating worn under a load of 10.1 kg illustrating (a) severe worn surface with pitting and delamination, (b) severe crack in the worn surface and (c) a large area of material loss and filled up with transferred layer (sliding direction from top to bottom).

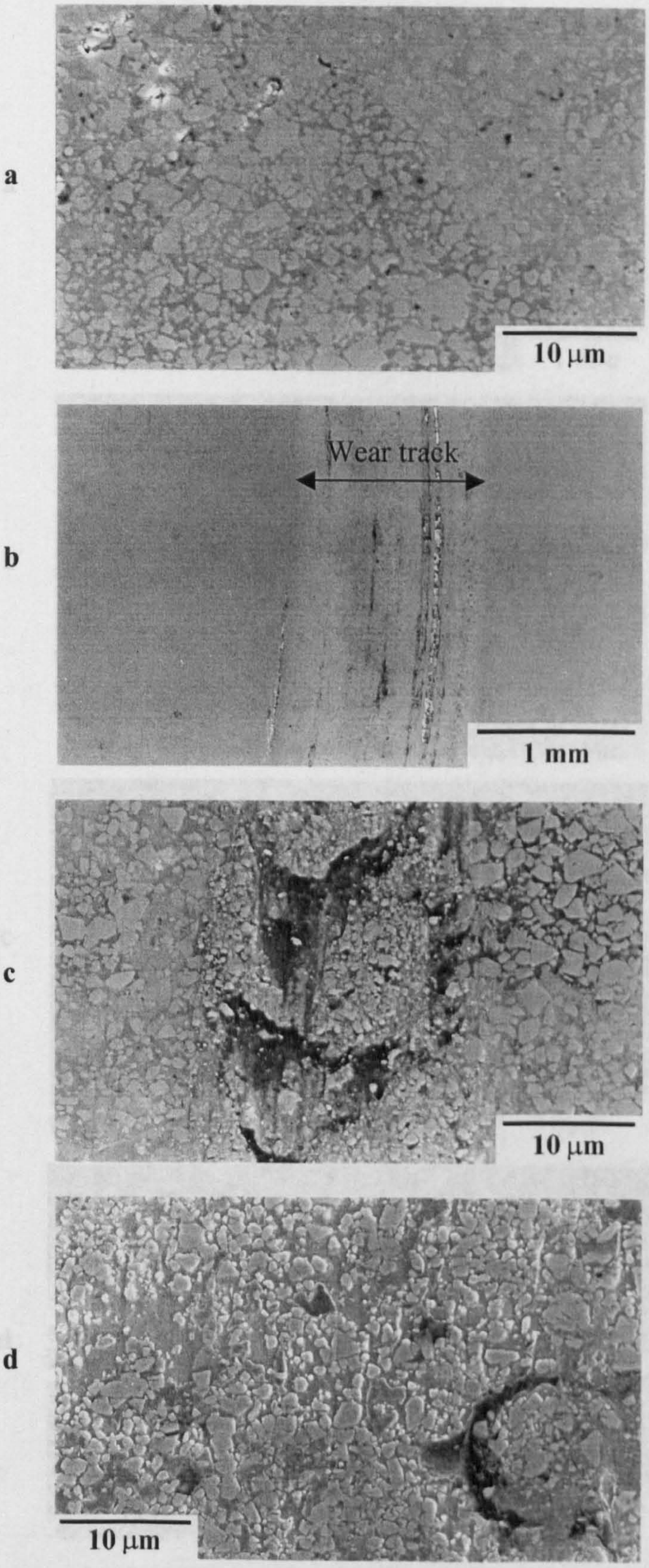

Fig. 6.17 SEM images of HVOLF sprayed WC-17 wt% Co (M) coating show (a) unworn surface with a few pores, (b) surface worn under a load of 1.9 kg revealing smooth surface with little delamination and transferred layer, (c) worn surface at rim of the wear track showing material loss and fragmented carbide grains and (d) worn surface from the middle of the wear track showing the removal of carbide phase and carbide grain standing proud of the matrix phase (sliding direction from top to bottom).

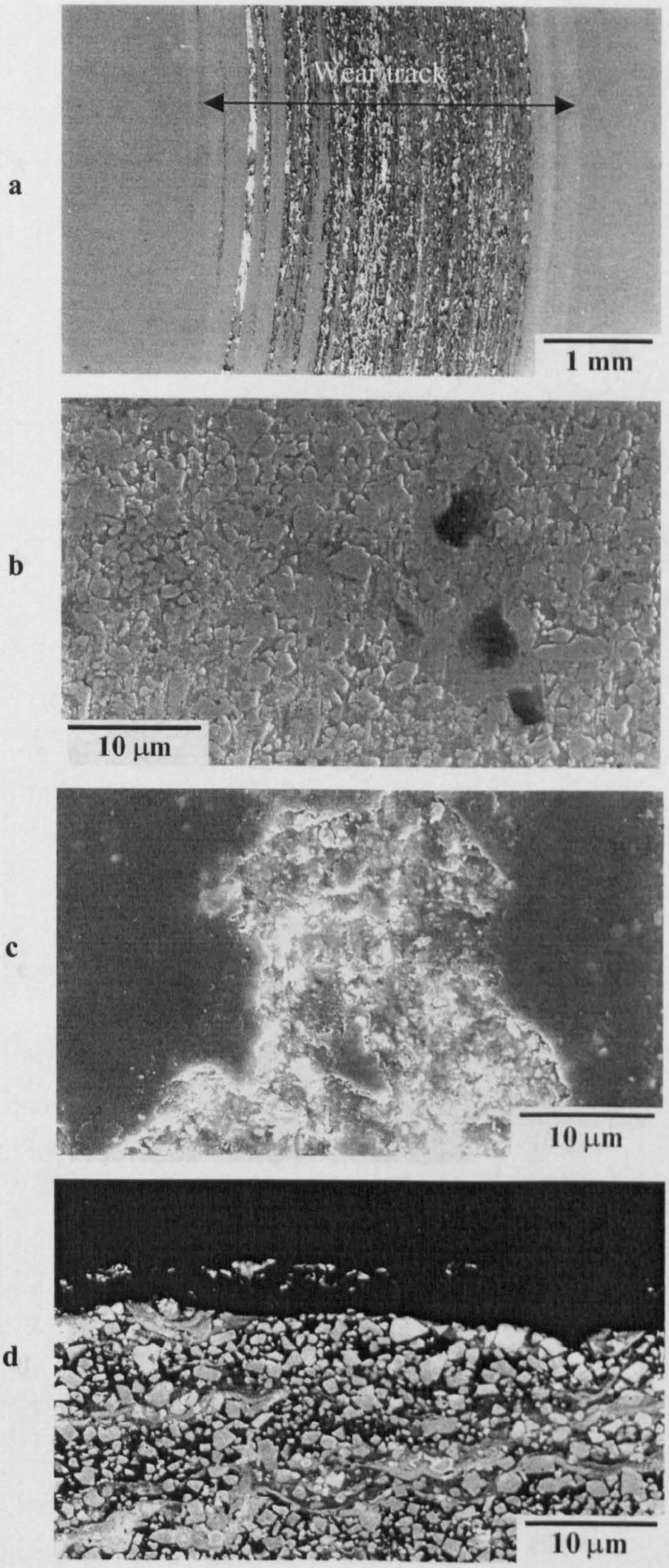

Fig. 6.18 SEM images of surface of HVOLF sprayed WC-17 wt% Co (M) coating worn under a load of 3.57 kg indicating (a) severe wear with delamination, (b) worn surface at rim of the wear track showing some pores resulting from carbide grain pullout and carbide grains standing proud of the surface, (c) transferred layer in the middle of the wear track and (d) a cross-section of worn surface indicating little evidence of subsurface cracking in the binder phase and carbide grains pullout (a, b and c: sliding direction from top to bottom, d: sliding direction parallel to the coating).

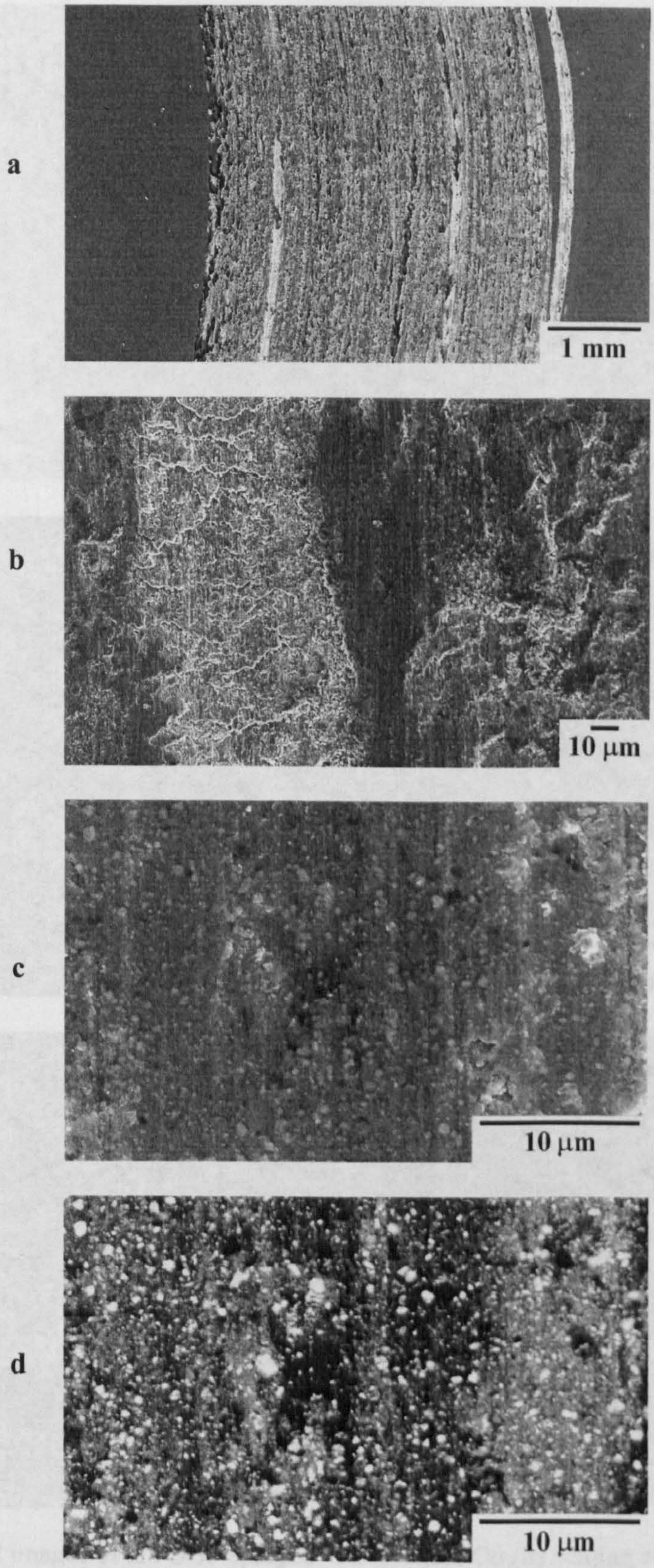

Fig. 6.19 SEM images of surface of HVOLF sprayed WC-17 wt% Co (M) coating worn under a load of 10.1 kg showing (a) severe worn surface with delamination, (b) plastic deformation of worn surface and transferred layer, (c) and (d) SE-SEM and BSE-SEM images on the transferred layer, respectively, showing fine fractured carbide grains in it (sliding direction from top to bottom).

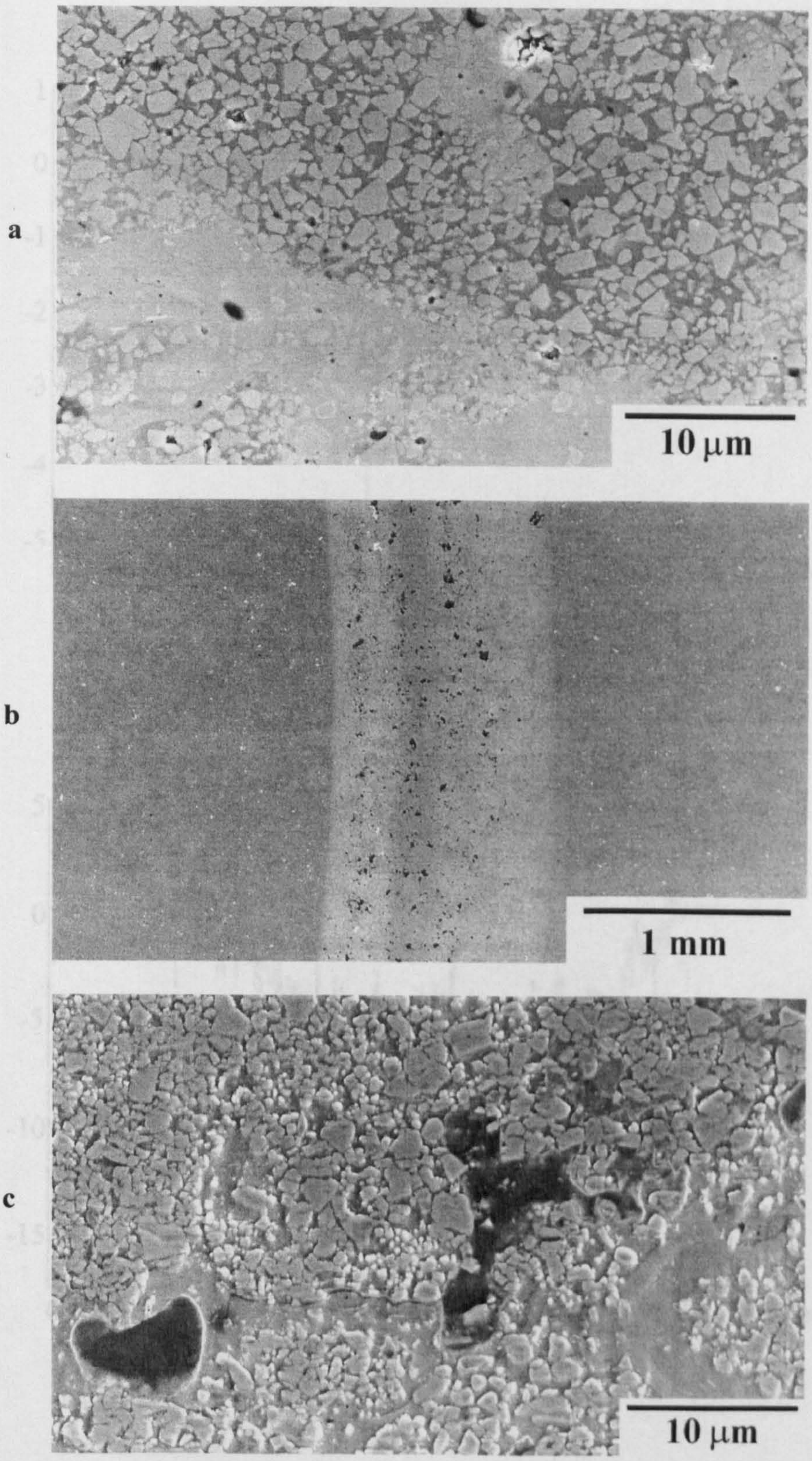

Fig. 6.20 SEM images of HVOGF sprayed WC-17 wt% Co (P) coating revealing (a) unworn surface with a few pores, (b) surface worn under a load of 1.94 kg showing a fairly smooth surface with a number of large pits and (c) worn surface at high magnification in the middle of the wear track showing carbide grains protruded resulting from rapid wear of the binder phase, pores resulting from material loss and cracks in the carbide grains and at the interface of powder particle (sliding direction from top to bottom).

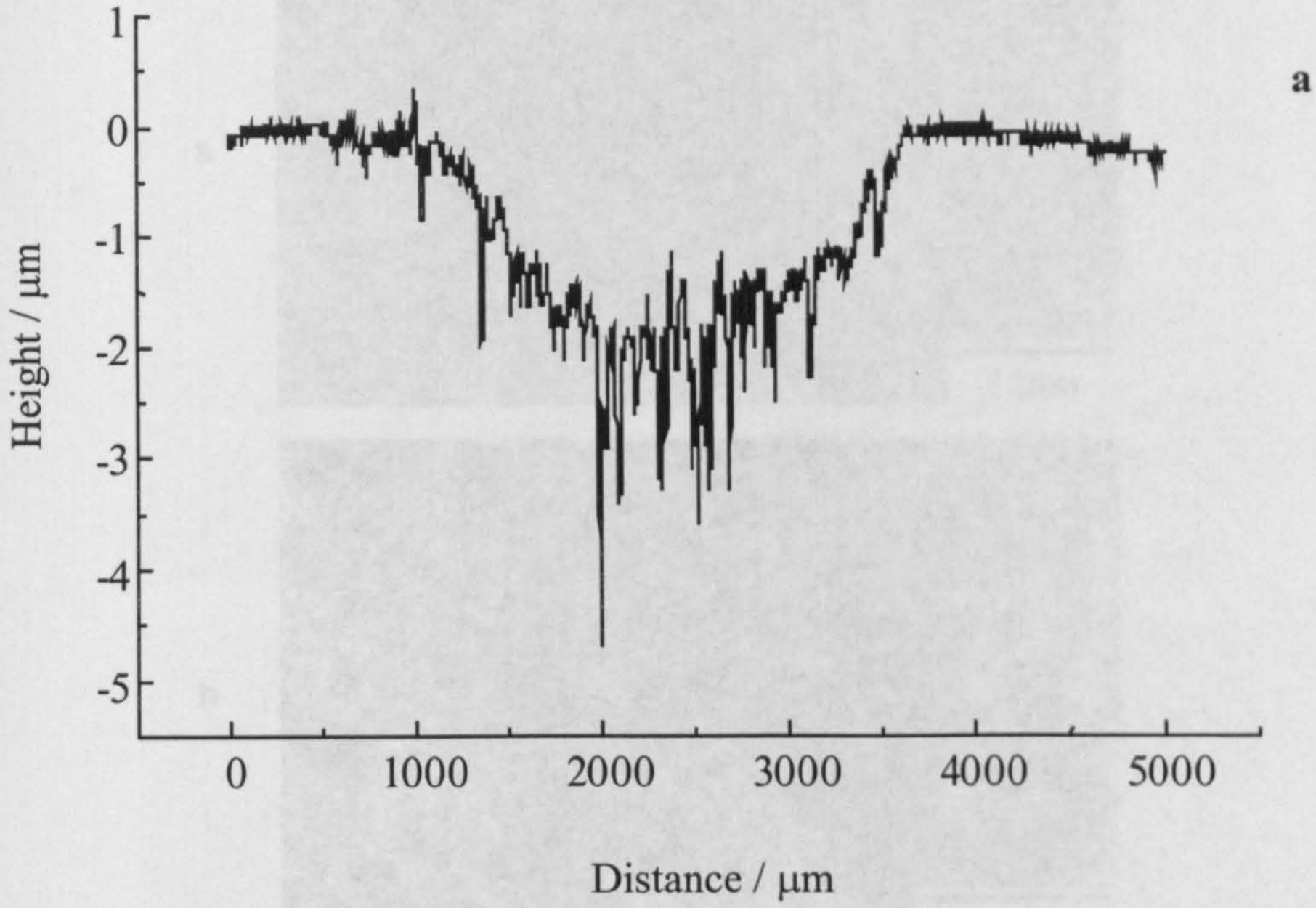

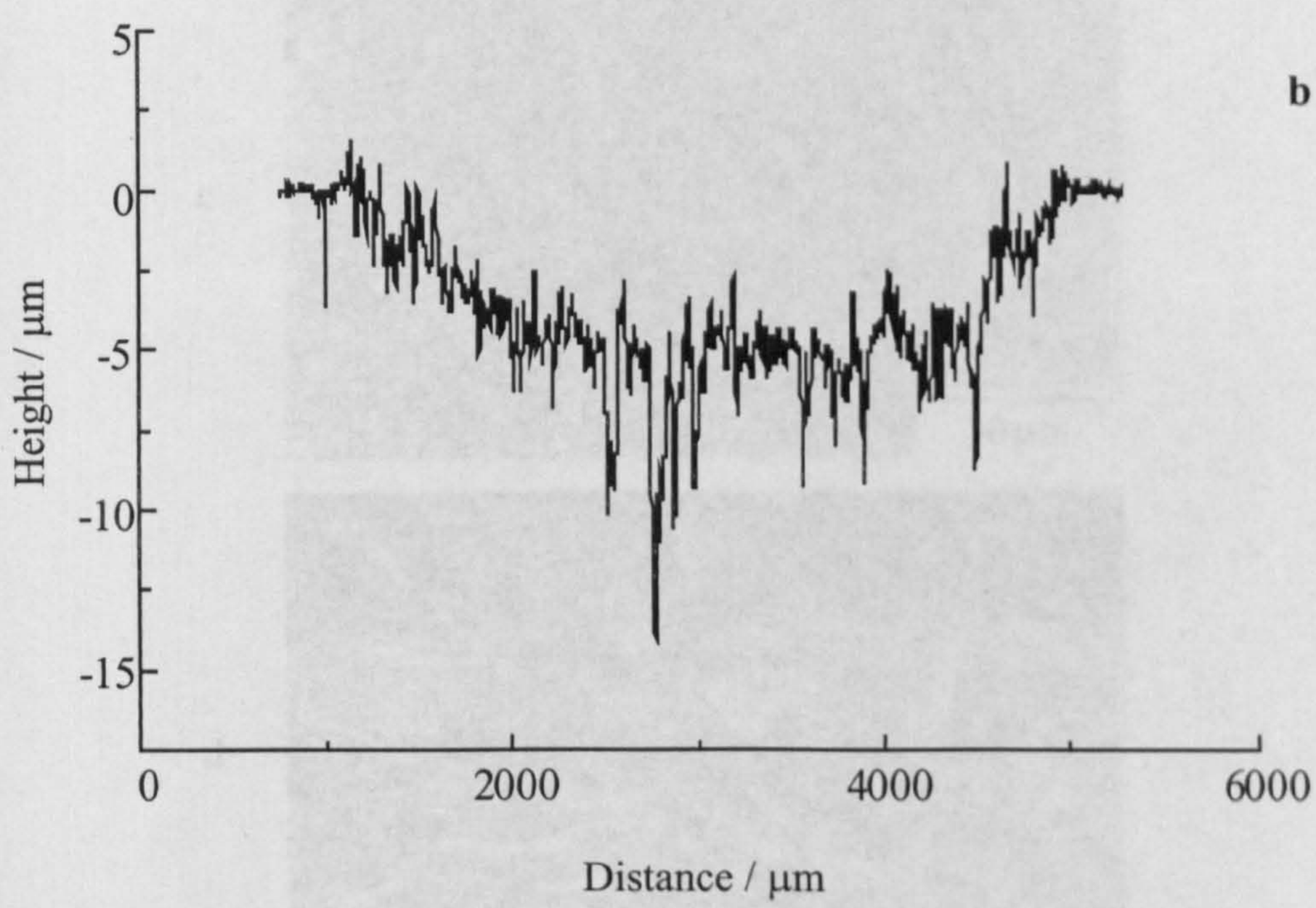

Fig. 6.21 Wear track profile of HVOGF sprayed WC-17 wt% Co (P) coating slid under different loads (a) 3.57 kg and (b) 10.1 kg.

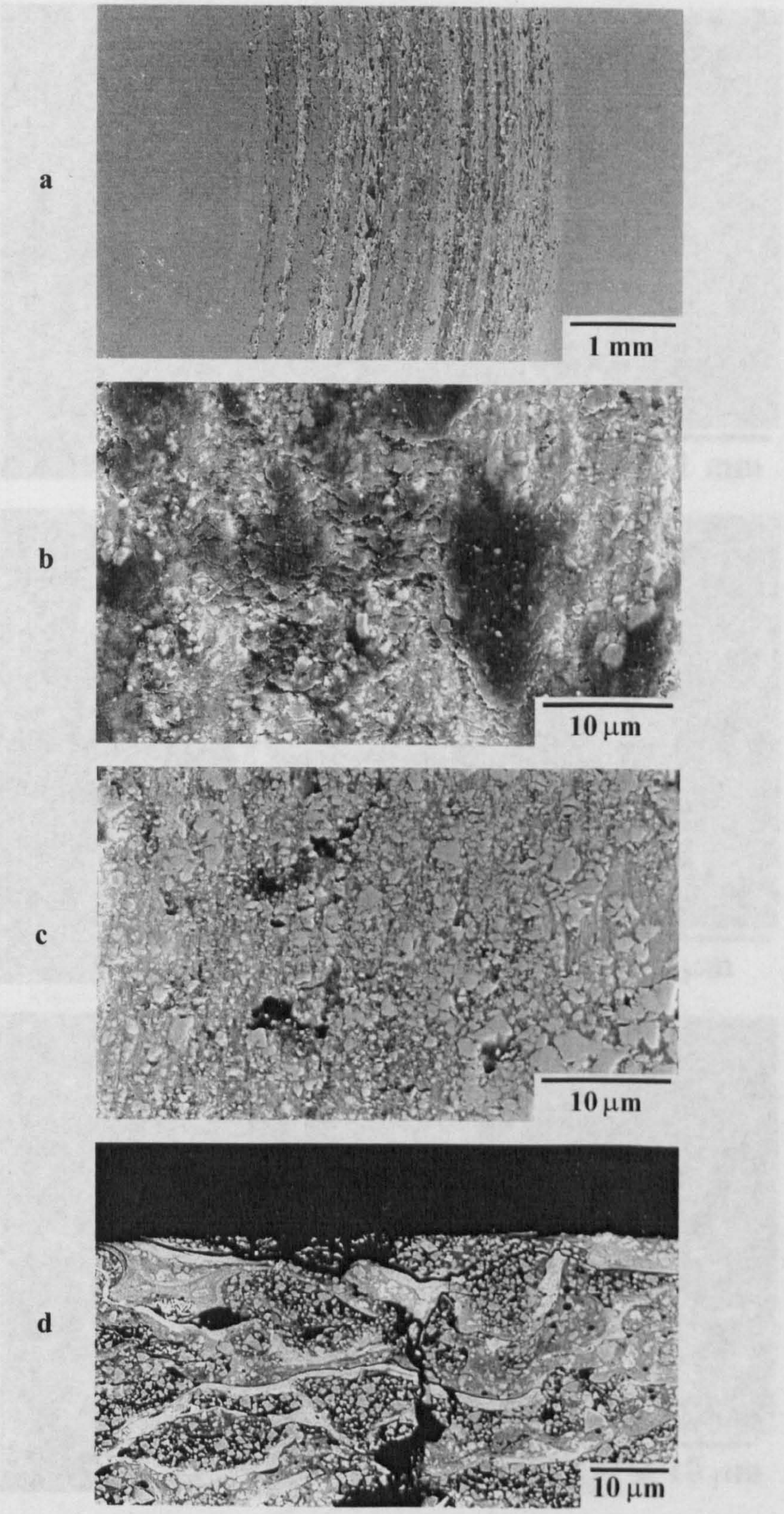

Fig. 6.22 SEM images of surface of HVOGF sprayed WC-17 wt% Co (P) coating worn under a load of 3.57 kg showing (a) severe wear with delamination and transferred layer, (b) plastic deformation of transferred layer and fractured carbide grains, (c) worn surface in the middle of the wear track revealing cracks in carbide grain and (d) a cross-section of worn surface showing sub-surface cracking and a large area of porosity (a - c: sliding direction from top to bottom and d: sliding direction parallel to the coating).

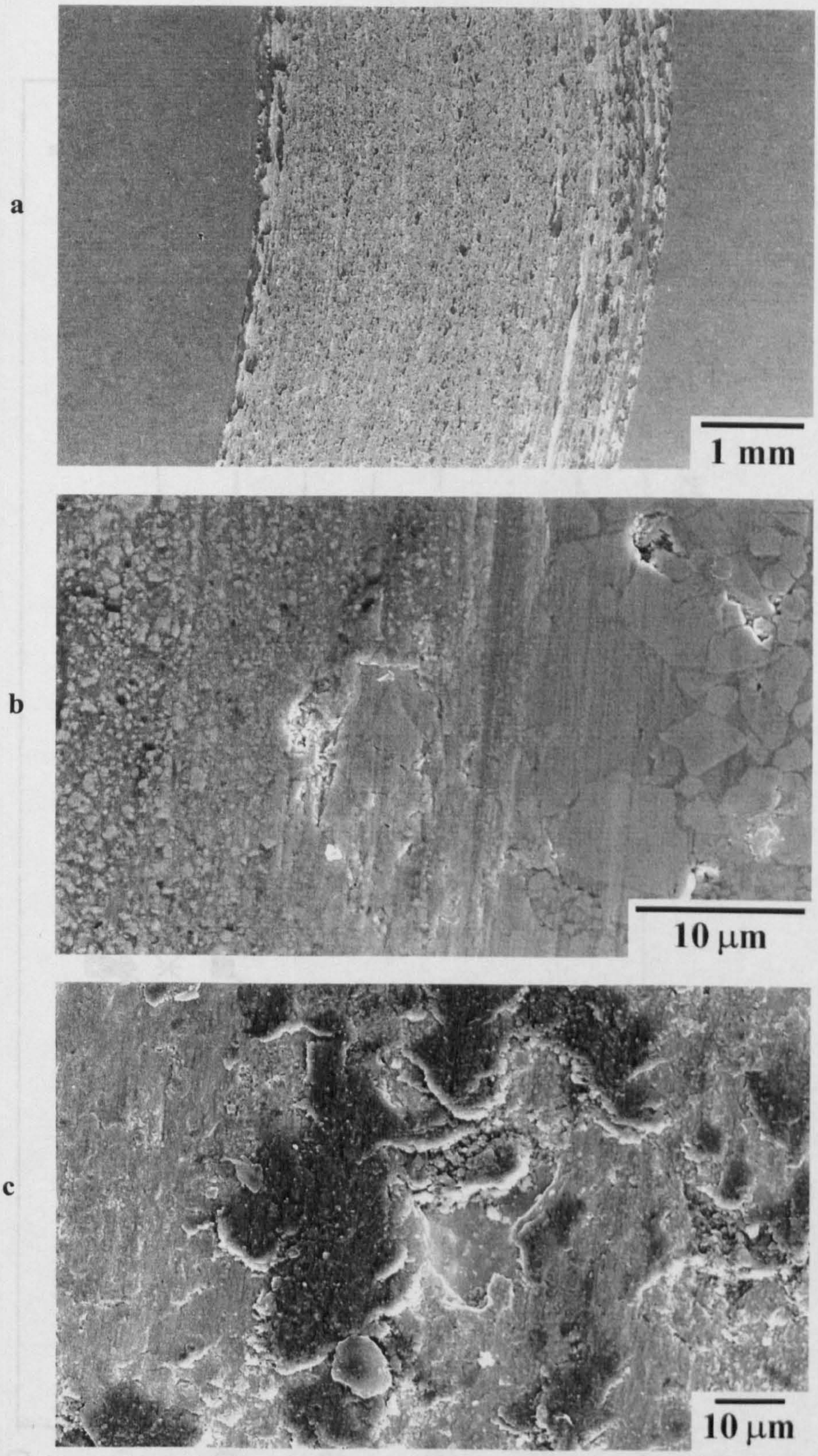

Fig. 6.23 SEM images of surface of HVOGF sprayed WC-17 wt% Co (P) coating worn under a load of 10.1 kg exhibiting (a) severely worn surface with a large amount of delamination, (b) worn surface at rim of the wear track showing fractured carbide grains and (c) worn surface in the middle of the wear track revealing transferred layer, cracks in the worn surface, debris trapped in the wear track and material loss in some regions (sliding direction from top to bottom).

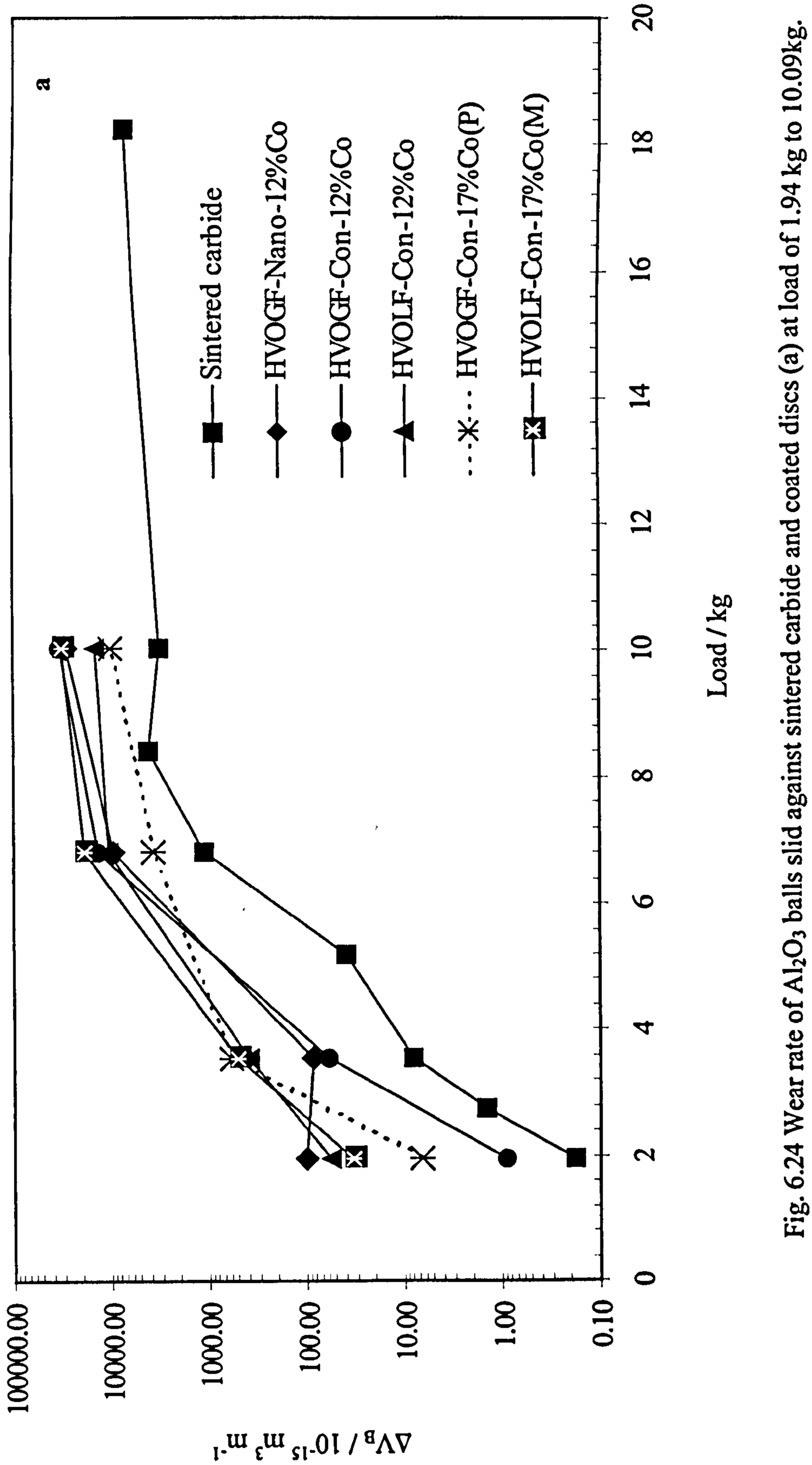

Fig. 6.24 Wear rate of Al_2O_3 balls slid against sintered carbide and coated discs (a) at load of 1.94 kg to 10.09kg.

Note : ΔV_B = the volume loss of ball per unit sliding distance

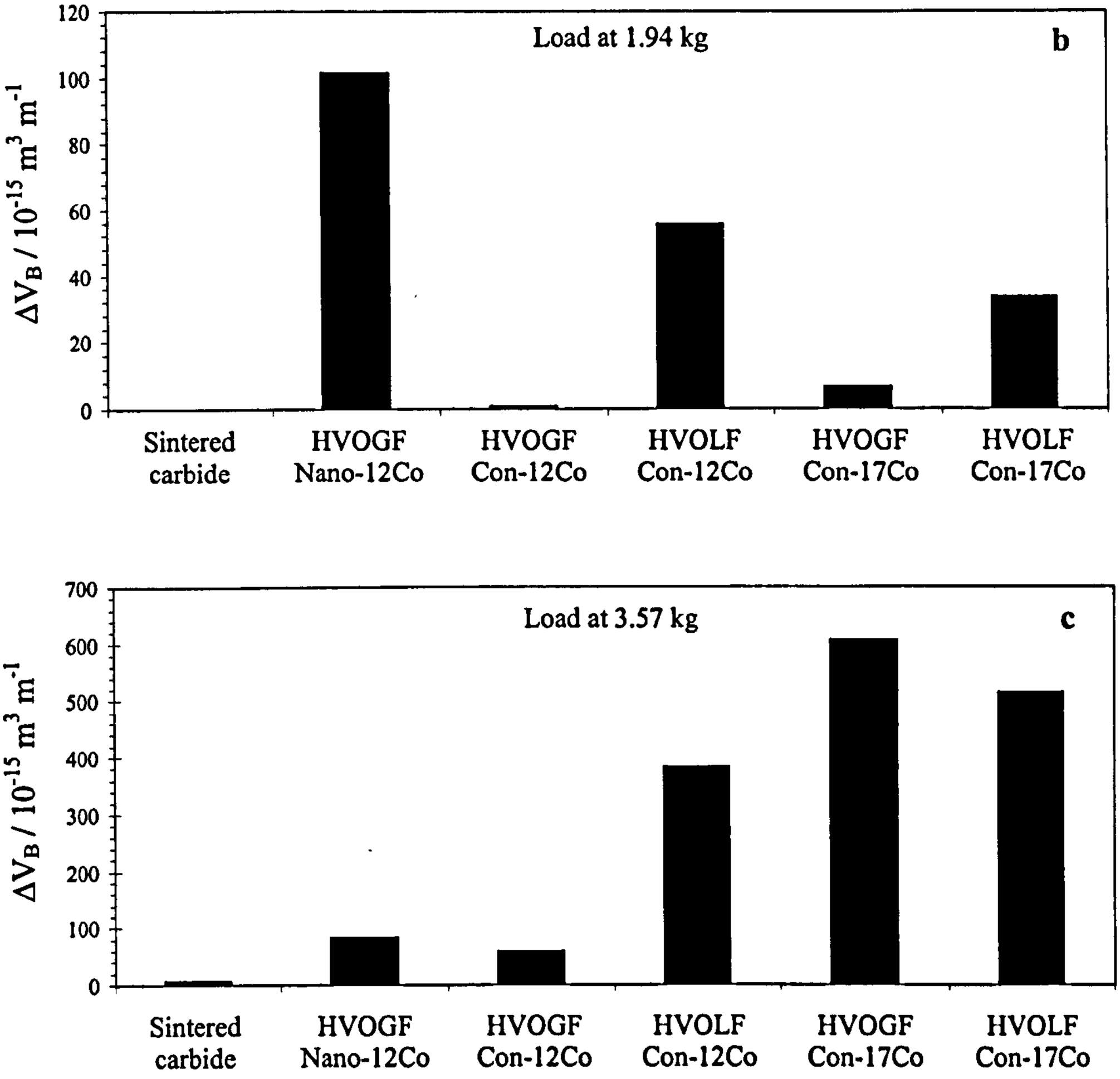

Fig. 6.24 (cont.) Wear rate of Al_2O_3 balls slid against sintered carbide and coated discs (b) at load of 1.94 kg and (c) at load of 3.57 kg.

Note : ΔV_B = the volume loss of ball per unit sliding distance

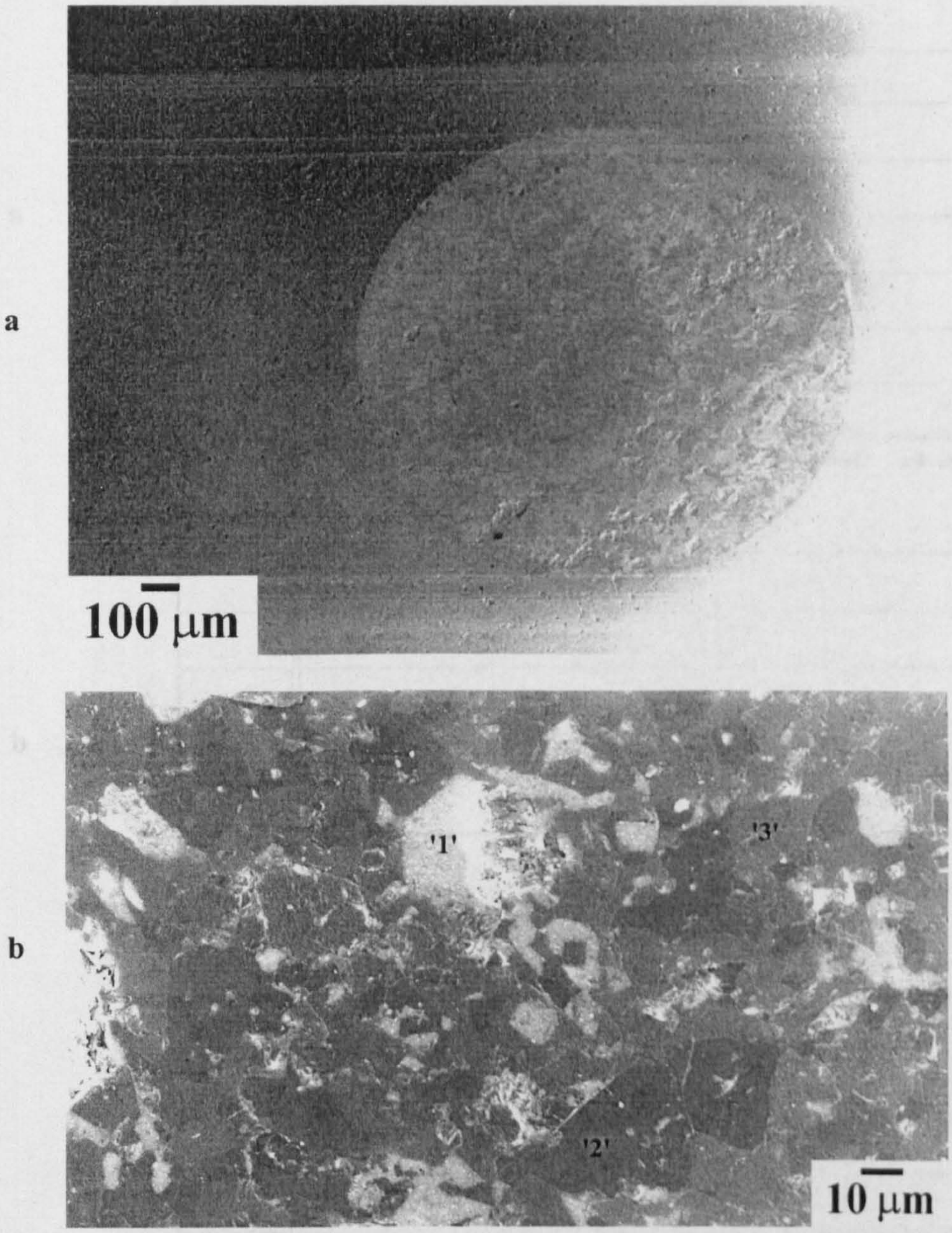

Fig. 6.25 Worn surface of Al_2O_3 ball slid against sintered carbide disc at load 3.57 kg showing (a) the wear scar with material loss leading to pore formation and (b) high magnification image in the centre of the wear scare indicating the grain structure of Al_2O_3 and holes filled up with mixed wear debris.

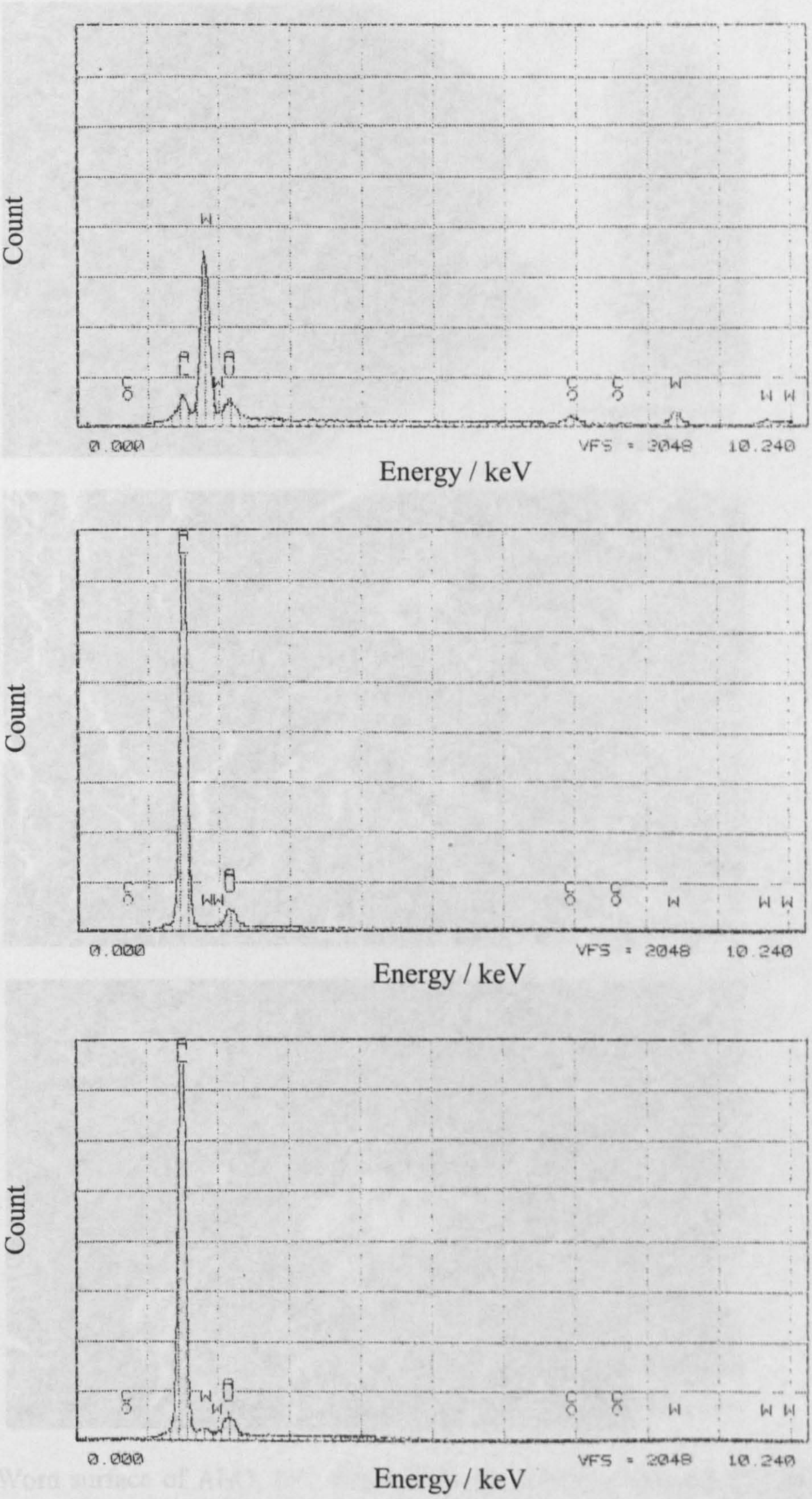

Fig. 6.26 EDS analysis of the worn surface of Al_2O_3 ball slid against sintered carbide disc under a load of 3.57 kg at (a) position '1', (b) position '2', and (c) position '3' as indicated in Fig. 6.25b.

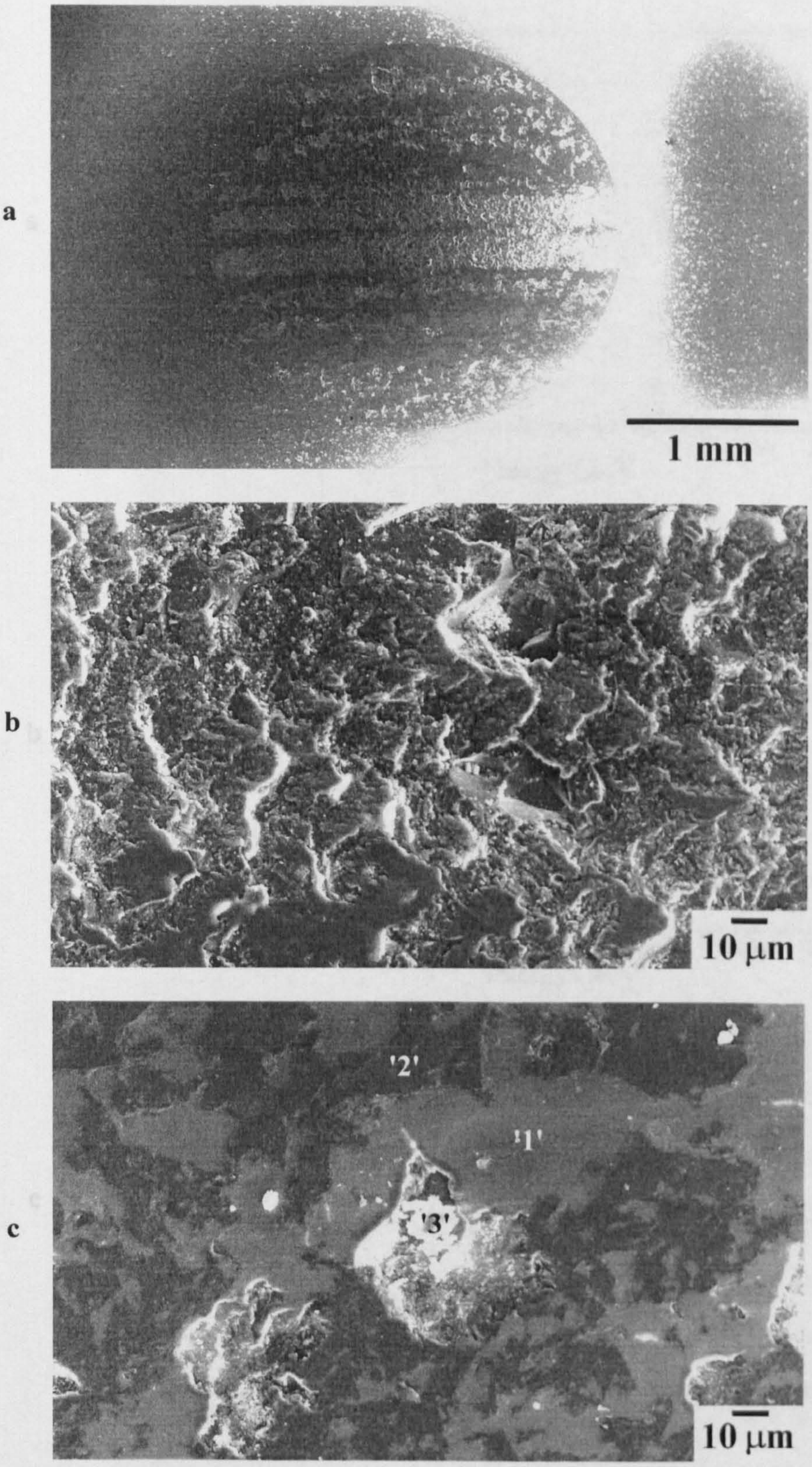

Fig. 6.27 Worn surface of Al_2O_3 ball slid against the HVOGF sprayed WC-12 wt% Co coating under a load of 3.57 kg showing (a) wear scar with pores and smearing at the centre, (b) high magnification image at the centre of wear scar revealing plastic deformation smearing in some regions and (c) high magnification image at the bottom of the wear scar indicating holes, mixed wear debris trapped in the wear scar.

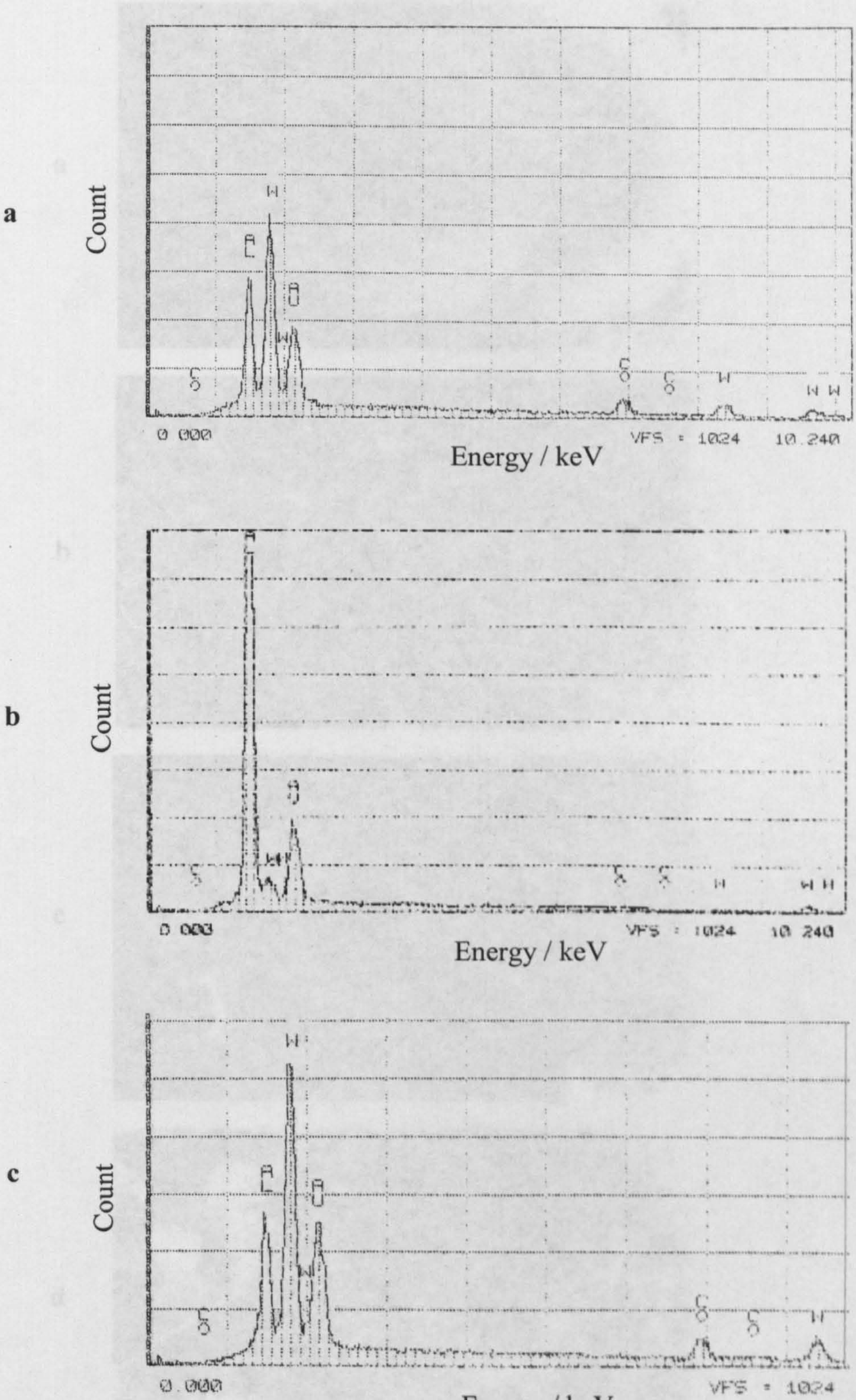

Fig. 6.28 EDS analysis of the worn surface of Al_2O_3 ball slid against the HVOGF sprayed WC-12 wt% Co coating under a load of 3.57 kg in Fig. 6.27c at (a) position '1', (b) position '2' and (c) position '3'as marked in Fig. 6.28c.

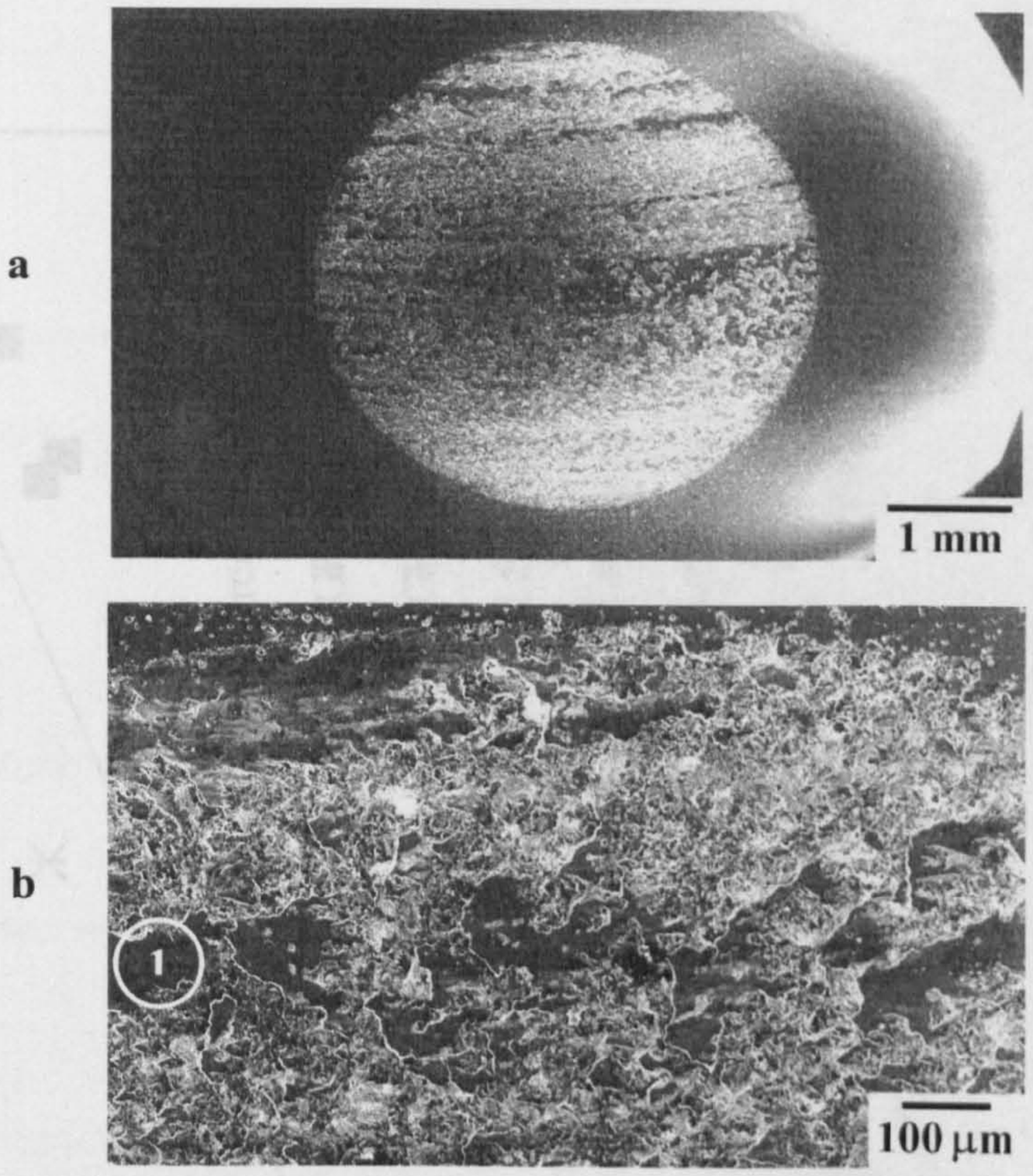

Fig. 6.29 Worn surface of Al_2O_3 ball slid against the HVOGF sprayed WC-17 wt% Co (P) coating under a load of 3.57 kg illustrating (a) severely worn surface with delamination, (b) worn surface at the top of wear scar, (c) high magnification SE-SEM image from position '1' in (b) showing debris build up with fractured carbide grains and (d) high magnification at the centre of the worn surface showing smearing on the worn surface and debris trapped inside.

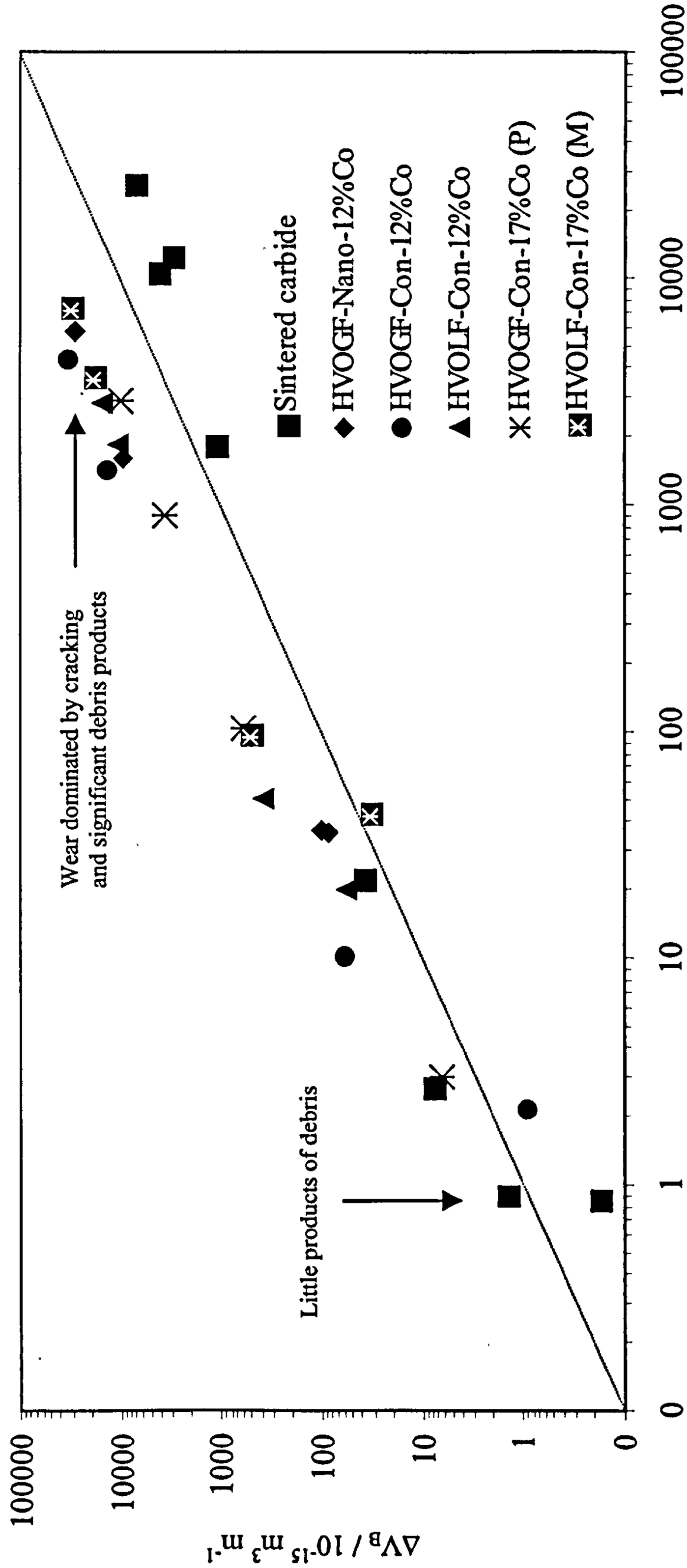

Fig. 6.30 The wear rates of balls and discs. A dot line represents a line of slope unity.

Note : ΔV_B = the volume loss of ball per unit sliding distance

ΔV_D = the volume loss of disc per unit sliding distance

Chapter 7

Discussion of Sliding Wear Behaviour of Sintered WC-Co and WC-Co Coatings

In this chapter will be found the discussion of the sliding wear behaviour of the sintered WC-11 wt% Co and the WC-Co coatings in terms of their microstructure. The wear behaviour of the WC-Co coatings is discussed and compared in terms of the different types of feedstock powder production, WC grain size, Co content and the HVOF spray system used to deposit the coatings.

7.1 Wear Behaviour of Sintered WC-Co

As seen in Fig. 6.2, in the lower load range, the sintered WC-Co has a lower wear rate than any of the WC-Co coatings. This may be related to its high hardness (1500 kgf mm^{-2}) and ideal cermet microstructure. The sintered WC-Co is worn at a load of 5.2 kg with different sliding distances of 500 m to 1000 m (Fig. 6.3). After a distance of 1000 m, the volume losses increase linearly with sliding distance indicating Archard type wear behaviour following an initial running in period.

The wear behaviour of the sintered WC-Co can be observed from surfaces worn at a low load in Figs. 6.4 and 6.6. Wear of the sintered WC-Co results from extrusion of

Co from between the WC grains, as shown in Fig. 6.4c. The WC grains can subsequently be removed leaving areas devoid of carbides (Fig. 6.6b). Additionally, a few cracks in the WC grains can be observed. Following cracking, it is highly likely that WC grains will be fragmented and removed, again, resulting in areas devoid of carbide particles. Sheikh-Ahmad and Bailey (1999) have also reported similar fragmentation of WC grains and their subsequent removal. This wear mechanism is able to operate since the binder phase is ductile in such a sintered system. Such a wear mechanism for the sintered WC-Co materials has been previously proposed by Larsen-Basse (1985).

A severely worn surface of the sintered WC-Co, following testing under a high load (Fig. 6.7), shows evidence of a transferred layer containing comminuted WC grains (Figs. 6.7c and 6.7d). The wear debris reveals very fine agglomerated particles (Fig. 6.7f) and some plate-like debris resulting from delamination of the transferred layer (Fig. 6.7g). The presence of the transferred layer and the formation of plate-like debris are consistent with the model of wear debris formation proposed by Sasada et al. (1979), as previously discussed in section 2.7.5.1.

7.2 Wear Behaviour of WC-Co Coatings

7.2.1 The Role of Coating Spray Process

Conventional sintered and crushed WC-12 wt% Co powder was sprayed by the HVOGF and the HVOLF spray systems. The XRD spectra of both coatings in Fig. 4.5 show that the HVOGF coating had a higher proportion of W_2C than the HVOLF

coating. This indicates that the HVOGF process results in a higher degree of reaction during spraying. BSE-SEM images of both coatings also reveal a larger amount of decomposition in the HVOGF sprayed coating (Fig. 4.15) when compared with the HVOLF coating (Fig. 4.6). Decomposition during spraying results in a large number of particles surrounded by a white layer (confirmed to W_2C) and different grey shades in the Co-based binder matrix due to substantial dissolution of tungsten carbide (Fig. 4.15).

Wear behaviour of the HVOGF sprayed coating at a low load of 1.94 kg and 3.57 kg shows evidence of preferential wear of the Co-binder matrix, as shown in Figs. 6.11c and 6.12b, which causes slight relief between the WC grains and the matrix. The appearance of pores in the worn surface is a result of the pullout of carbide particles. Additionally, a cross section of the HVOGF sprayed coating (Fig. 6.12c) provides evidence of good adhesion of the carbide grains at the wearing surface with some sub-surface cracking. Wear behaviour at a high load of 10.1 kg (Fig. 6.13) shows severe wear with delamination and transferred layer. The agglomerated fine debris is shown in Fig. 6.13c.

The HVOLF sprayed coating exhibits a lower level of decomposition during spraying, indicated by the XRD spectrum (Fig. 4.5) and the cross sectional BSE-SEM image (Fig. 4.6). A number of researchers have reported that the formation of W_2C is detrimental for wear resistance (Ahn and Lee, 1998; Jacobs et al., 1998; Voyer and Marple, 1999). However, in this work, it has been shown that the HVOLF sprayed coating (with a low degree of decomposition) exhibited a wear rate ten times greater than the HVOGF sprayed coating at the lowest load employed, as shown in Fig. 6.2.

Examination of Fig. 6.9b indicates that the matrix phase is being preferentially removed to a significant depth which may result from its high ductility associated with its low levels of W and C in solution. Another point which may influence the wear behaviour of the HVOLF sprayed coating is the degree of powder melting during spraying. In Fig. 4.8 the structure can be seen to be made up of unmelted areas with molten or semimolten regions. The same regions can be seen in the wear scar in Fig. 6.9b. The semimolten areas reveal less wear whilst the unmelted regions exhibit substantial carbide-matrix decohesion. WC grains in the decohered regions also exhibit cracking (Fig. 6.9b) which is rarely observed in the HVOGF sprayed coating (Fig. 6.11). The cross sectional microstructure shows a high level of primary carbide and little evidence for decomposition during spraying (Fig. 6.9c). However, large volumes of material are still being removed from the surface.

Generally, wear of these coatings may proceed by loss of carbides (by pullout or fragmentation) or by subsurface cracking. Subsurface cracking is dominant in the coatings which show a high degree of reaction (the HVOGF sprayed coatings) due to embrittlement of the binder phase by substantial dissolution of W and C into it during spraying. Such subsurface cracking has been seen in similar coatings in abrasive wear situations (Stewart et al., 1999). As a result, there has been a move to reduce the degree reaction during spraying through the use of HVOLF guns. In this latter situation, a conventional dense WC-12 wt% Co powder particle (Fig. 4.2a) just prior to impact consists of a molten/semimolten shell around a solid core (Fig. 5.7). WC-12 wt% Co powder sprayed by the HVOLF process has higher powder velocity (~600 m s^{-1}) than the powder sprayed by the HVOGF process (~400 m s^{-1}) (Sai, 2000; 2001). On impact, the solid core is deformed to some extent, which results in fracture

of some carbides and carbide-matrix decohesion. It can be clearly seen that carbide grains break up into small grains in the HVOLF coating resulting from higher impact forces (Fig. 4.6b) when compared with the HVOGF coating (Fig. 4.15b). Whilst bond disruption and carbide cracking is not very obvious in the as-sprayed state, its existence is made clear following wear, when carbide decohesion and fracture is only observed in the unmelted regions (Fig. 6.9b). In contrast, the HVOGF sprayed particles impact with the substrate at lower velocities, and, due to enhanced heating of these particles during spraying, may not have an unmelted core at all. As illustrated in Fig. 5.8, these particles will not suffer the mechanical disruption associated with the spraying with the HVOLF system.

7.2.2 The Roles of WC Grain Size and Powder Production

Nanoscale WC-12 wt % Co powder containing carbide size in the range of 100 - 600 nm was produced by a spray conversion process resulting in a porous spherical morphology. The nanoscale WC-12 wt% Co powder was sprayed by the HVOGF process. A comparison between the HVOGF sprayed nanoscale WC-12 wt% Co and conventional WC-12 wt% Co coatings is discussed.

The XRD spectrum of the HVOGF sprayed nanoscale coating (Fig. 4.24b) reveals a higher proportion of W_2C and W compared to the HVOGF sprayed conventional coating. It can be stated that a larger degree of WC decomposition occurred in the HVOGF sprayed nanoscale coating. This is because a decrease in carbide grain size increases surface area of carbide over which dissolution into the liquid matrix can occur, leading to high degree of decomposition (Sudaprasert et al., 2002). Other

workers have shown that larger amounts of W_2C results in higher hardness values (Usmani et al., 1997; Jacobs et al., 1999). Nevertheless, the hardness of the HVOGF sprayed nanoscale coating (1206 ± 64 kgf mm^{-2}) is comparable to that of the HVOGF sprayed conventional coating (1288 ± 86 kgf mm^{-2}). The reason for this is that the existence of nanoscale/microscale porosity plays an important role in the hardness of the nanoscale coating (Strutt, 1998; Kear et al., 2000). The reasons for the high porosity levels in the nanoscale coating (as shown in Fig. 6.14a) are not entirely clear.

When examining the wear behaviour of the nanoscale WC-12 wt% Co coatings sprayed by HVOGF, it can be seen that it is indeed the highly decarburised layers (associated with the formation of W_2C, W and the amorphous binder phase) which preferentially crack (Fig. 6.15c). These cracks lead to surface spallation and thus to rapid wear (Slavin and Nerz, 1990). As well as the work of Qaio et al. (2001), it has been shown that the degree of decarburisation in the coating sprayed with the nanoscale WC-Co powder is greater than that in the coating produced by the compact conventional WC-Co powder. Decarburisation results in the formation of brittle phases, in particular W_2C and the amorphous binder, which increase the hardness. However, the existence of brittle phases in the coating results in sliding wear by cracking and spallation. Severe cracking in the worn surface results in a large area of material loss filled up with transferred layers (Figs. 6.16b and 6.16c).

Different WC-Co powder production routes result in differences in powder morphology, WC grain size, WC grain size distribution, initial phases in the present starting powder and powder density. Khan et al. (1997) have also reported that in spraying of a conventional WC-17 wt% Co powder, the open agglomerated structure

was a significant effect on the formation of an amorphous phase. The open structure allowed more efficient heat transfer and thus the powder particle (Co-binder) begins melting from the surface as well as within the powder particle. Similar work by Li et al. (1996) argued that a compact powder (WC particles densely aggregated with Co) was the most difficult to decompose in the Jet-Kote gun. Thus, the appearance of decarburisation in the nanoscale coating may result from the powder morphology and surface area of per unit volume of the spray particles themselves rather than WC grain size (Kear et al., 2000; He et al., 2000).

In summary, wear behaviour of nanoscale and conventional WC-12 wt% Co coatings sprayed by the HVOGF process depends on powder morphology and WC grain size which relate to the degree of decomposition present. The nanoscale WC-12 wt% Co coating exhibits a high level of decomposition causing embrittlement and thus a high wear rate. There are two reasons leading to high level of decomposition of the nanoscale WC-12 wt% Co coating. The first is that the nanoscale powder exhibits a hollow morphology resulting in high surface area to volume ratio and thus rapid heating. The second is that the small carbide grain size results in an increase of surface area of WC grains allowing rapid WC dissolution. Thus, both reasons make nanoscale WC-12 wt% Co powder difficult to spray to form a wear resistant coating.

7.2.3 The Role of Co Content

The conventional WC-12 wt% Co and WC-17 wt% Co (P) powders, both produced by the sintering and crushing process and sprayed by the HVOGF gun are discussed in terms of Co content.

The hardness value of these coatings are not very different, despite the significant difference in initial volume fraction of carbide (Tables 4.1 and 4.2). Consideration of the WC-12 wt% Co powder (Fig. 4.2a) and the WC-17 wt% Co (P) powder (Fig. 4.2d), shows that the WC-12 wt% Co powder has a slightly larger WC grain size distribution than the WC-17 wt% Co powder. However, the BSE-SEM of the WC-12 wt% Co coating (Fig. 4.15b) exhibits a much larger grain size (see also wear scar, Fig. 6.11c) than the WC-17 wt% Co coating (Fig. 4.37b) (see also wear scar, Fig. 6.20c). It can thus be stated that the WC-17 wt% Co powder has undergone more dissolution during spraying. Also, the BSE-SEM image at low magnification shows that the WC-17 wt% Co coating is a generally more reacted structure (Fig. 4.37a). This may result from the higher Co volume fraction in the latter material promoting dissolution. The XRD spectra of both coatings (Figs. 4.5c and 4.36b) show the presence of a significant amorphous phase (indicated by a broad diffraction hump between 35° and 50° 2θ). Due to the dissolution of WC during spraying and the formation of new phases (W_2C, W and amorphous) on deposition, it is impossible to make definition comments from these spectra regarding the proportions of such phases. However, W is only present in the WC-12 wt% Co coating which also appears to have a larger proportion of W_2C phase.

The wear rates of the WC-17 wt% Co (P) coatings in the low load range are higher than those of the WC-12 wt% Co coatings. The WC-12 wt% Co coatings at a load of 1.94 kg shows a slightly worn surface revealing preferential wear of the Co-binder matrix causing slight carbide particle relief from the Co-binder matrix (Fig. 6.11). The worn surface of the WC-12 wt% Co coating shows a change in mechanism as load increases, namely, subsurface cracking is observed (Fig. 6.12c). The worn surface of

the WC-17 wt% Co (P) coating at a load of 1.94 kg again shows little damage (Fig. 6.20) in a similar way to the WC-12 wt% Co coating (Fig. 6.11) although more areas of carbide pullout are observed. It is noted that the carbide grain sizes in the WC-17 wt% Co (P) coating (Fig. 6.20c) are smaller than that in the WC-12 wt% Co coating (Fig. 6.11c). The worn surface of the WC-17 wt% Co (P) coating at a higher load (3.57 kg) shows severe wear with delamination, transferred layer, fractured carbide grains and subsurface cracking tending to spallation (in the cross-sectional BSE-SEM image) (Fig. 6.22).

Thus, it can be stated that wear of the HVOGF conventional WC-12 wt% Co and WC-17 wt% Co (P) coatings depend on the coating microstructures which in turn depend on the volume fraction binder matrix. Guilemany and De Paco (1998) have also studied the effect of percent of Co-binder matrix on the sliding wear behaviour of HVOF sprayed WC-Co coatings. They stated that wear resistance depended on the compositions of the metallic matrix in the starting powder, namely, WC-17 wt% Co coatings exhibited higher friction coefficients than WC-12 wt% Co coatings. Wear mechanisms also related to the content of Co-binder matrix.

7.3 Wear of Agglomerated and Sintered WC-17 wt% Co (M) Coating Sprayed by HVOLF

The WC-17 wt% Co (M) coating shows the lowest wear resistance of all the materials examined (Fig. 6.2). Wear of the WC-17 wt% Co (M) coating sprayed by the HVOLF process can be summarised by the following.

1. The agglomerated and sintered WC-17 wt% Co (M) powder, which has a small carbide grain size of 0.7 μm (Fig. 4.2c) and porous structure (Fig. 4.1d), was sprayed by the HVOLF process. Despite the low levels of heating, the effects of small carbide grain size and open structure lead to a high level of reaction (more W_2C and amorphous phase formation) compared to a dense powder particle with a larger grain size. As well as the study of Qiao et al. (2001), they have stated that decomposition will be favoured by small carbide grain sizes within the powder particles. However, whilst decomposition is reported to be deleterious to wear behaviour, low temperature spraying has been seen to result in coatings with poorer adhesion between the splats, again resulting in high rates of wear.

2. The WC-17 wt% Co (M) powder sprayed by the HVOLF process achieves high powder velocity tending to disrupt the carbide-matrix bond on impact. This, therefore, leads to increased rates of wear.

The poor wear performance of the WC-17 wt% Co (M) coating can be attributed to its small carbide grain size, the significant levels of reaction observed in the coating, and the disruption of carbide/matrix bonding which both lead to high rates of wear.

7.4 Wear of Al_2O_3 Ball

As seen in Fig. 6.24, across the complete load range employed, Al_2O_3 balls slid against sintered WC-Co have a lower wear rate than those slid against WC-Co coatings. The worn surfaces of Al_2O_3 balls slid against sintered WC-Co (Fig. 6.25a)

have a flatter wear scar than those slid against WC-Co coatings (Figs. 6.27a and 6.29a). In Fig. 6.25b, the worn surface of an Al_2O_3 ball slid against sintered WC-Co exhibits very fine debris and shows transferred material adhered to the Al_2O_3 ball. Fine debris (Fig. 6.29d) and transferred material (Fig. 6.29c) can be seen in the worn surface of the Al_2O_3 balls slid against WC-Co coatings. Moreover, the worn surface of Al_2O_3 balls slid against WC-Co coatings exhibited a smeared transfer layer (Figs. 6.27b and 6.29d) which was never seen on the surfaces of balls slid against sintered WC-Co. However, the worn surface the ball slid against the WC-17 wt% Co (P) coating (Fig. 6.29a) shows a larger quantity of smeared transfer layer than that of Al_2O_3 ball slid against WC-12 wt % Co coating (Fig. 6.27a). This may result from the difference of volume fraction of Co content.

Fig. 6.30 reveals a relation of the volume loss of discs and balls. It is apparent that wear rates (and thus mechanisms) of discs and balls change by orders of magnitude between low loads (left-hand side) and high loads (right-hand side). At the low loads, pore formation is a dominant wear mechanism with little production of debris. This results in low wear rates. At high loads, wear results from cracking leading to large amount of material loss and thus high wear rates. It is notable that there is a clear correlation between the wear rate of the ball and that of the disc over several orders of magnitude. When the disc wears, abrasive wear debris is produced which then abrades the ball. Such a process is self perpetuating.

7.5 Summary of Wear Mechanisms of Sintered WC-Co and WC-Co Coatings

The wear behaviour of sintered WC-Co and WC-Co coatings are different due to a significant difference of microstructure. Wear of sintered WC-Co proceeded by 1) Co-binder extrusion, 2) smearing of Co-binder, 3) cracks in the carbide particles leading to fragmented carbide and 4) the removal of carbide particles.

Wear of WC-Co depends mainly on coating microstructure which some argue depends more on the deposition method than on the starting powder used (Qiao et al, 2001). A number of workers have proposed mechanisms of wear for WC-Co coatings (Su and Lin, 1993; Ahn and Lee, 1998; Stoica and Ahmed, 2002; Jacobs et al., 1998). None of these models adequately describe the complex interactions between wear mechanism, deposition conditions and feedstock properties that have been observed in this work.

Rather than propose a new mechanism of wear, a number of broad interactions are highlighted below.

1. A heavily decomposed coating structure results from (i) porous powder (ii) high temperatures (iii) long residence times of particles in the flame (iv) small carbide size. Such coatings may exhibit good carbide retention and thus low wear rates. However, cracking of the brittle binder phase may also occur which leads to high wear rates. Which of these dominates depend on other factors such as detailed microstructure and loading conditions.

2. Decomposition can be reduced by altering one or more the factors outlined in 1. In this work, only the dense WC-12 wt% Co sprayed with the HVOLF exhibited little decomposition. Here, although no cracking of a brittle binder phase was observed, carbides were damaged by impact and their individual retention was poor. Future work must examine the complex interactions between powder morphology and spray condition in more detail.

Chapter 8

Conclusions

Four WC-Co powders, namely, conventional WC-12 wt% Co, two different powder types of conventional WC-17 wt% Co and a nanoscale WC-12 wt% Co powder, were deposited to form coatings using different spray systems: HVOGF and HVOLF guns. The resulting WC-Co coating microstructures were characterised and correlated with the spray system, WC grain size, spray parameters and Co content. Subsequently, the sliding wear rate of various WC-Co coatings was measured and related to the microstructural features of the WC-Co coatings. The following conclusions may be made:

8.1 Microstructure Formation

When a WC-Co powder particle is exposed to the hot flame temperature, the Co melts at temperature around 1768 K (~1495 °C). WC particles begin to dissolve in the liquid Co-binder, as shown in Fig. 5.5. When the powder particles exit the gun nozzle, they encounter high levels of oxygen travelling the 200 - 300 mm distance between the nozzle and the workpiece. Oxygen diffuses in the liquid Co-binder and reacts with the carbon in it, leading to carbon depletion at the rim of molten particle. This results in further dissolution of WC particles in the liquid Co-binder in an attempt to maintain equilibrium between Co(W,C) and WC. After impact with the substrate, the powder

particles are rapidly solidified (10^6 - 10^7 K s^{-1}) leading to the formation of W_2C, W and an amorphous phase. Powder particles will also experience some reheating as successive layers of splats are built up. This may result in nanocrystalline formation from an originally amorphous binder phase.

BSE-SEM images show different grey shades of the Co-binder matrix and very bright shells surrounding the carbide particles (e.g. Figs. 4.15 and 4.37). It is an evident that the different grey shades of the Co binder matrix result from the different W and C levels in the Co-binder. TEM observations demonstrate that W_2C precipitates and grows on the edges of WC particles. Clusters of W_2C and W are observed in the amorphouse/nanocrystalline Co(W,C) binder. Also, retained WC and isolated W_2C particles are also found.

8.2 Parameters Affecting the Microstructure and Properties of WC-Co Coatings

- **The Role of Different Gun Types**

WC-Co powders sprayed with different spray guns undergo different degrees of melting depending on powder feeder position, gun design and powder velocity. A higher degree of melting results in a higher degree of WC dissolution. Specifically in the Top-Gun, axial feeding of powder into the combustion chamber, relatively low particle velocities and high temperatures associated with the use of hydrogen fuel result in high particle temperatures and thus significant decomposition. However in the Met-Jet II, use of a kerosene fuel and radial feeding of powder into the nozzle

downstream of the combustion chamber results in higher particle velocities and lower temperatures and thus less decomposition.

- **Effect of Powder Composition**

Whilst there are a number of variations between the powders examined, it is generally observed that greater decomposition during spraying occurs as the cobalt binder content increases due to enhanced dissolution of WC. However, with lower binder content, more W_2C encapsulation of WC is observed, in certain cases.

- **The Role of WC Grain Size**

The smaller WC grain sizes lead to a higher degree of decomposition, which results from enhanced dissolution of WC grains.

- **The Role of Powder Morphology**

A porous WC-CO powder particle, which has a high ratio of particle surface to volume, can be melted more rapidly than a dense powder particle. Thus, a porous WC-Co powder exhibits more decomposition than a dense WC-Co powder, due to its high surface area which promotes high rates of heat transfer into the particle.

8.3 Sliding Wear Resistance and Wear Behaviour

The following conclusions can be made concerning the wear behaviour of sintered WC-Co and WC-Co coatings.

- The wear behaviour of the sintered WC-Co and the WC-Co coatings at the lowest loads tested (where wear rates are technologically interesting) indicate that the sintered WC-Co has the lowest wear rate.

- As known, both small WC grain sizes in the powder particle and particles with a porous structure lead to significant formation of an amorphous binder phase (more brittle phases), and thus enhanced wear. Therefore, Nanocarb WC-Co powder is not useful for an increase of sliding wear resistance under the spray conditions employed.

- WC-Co powder sprayed by the HVOGF process experiences high powder temperatures and long particle residence times in the hot gas jet. This results in a significant degree of decomposition leading to the formation of phases W_2C, W and amorphous. However, the HVOGF sprayed WC-12 wt% Co coating provides good bonding between splats. In contrast, WC-Co powder sprayed by the HVOLF process experiences lower powder temperatures and shorter particle residence times in the hot gas jet. The HVOLF sprayed WC-12 wt% Co coating displays less decomposition than its HVOGF sprayed counterpart. However, because of higher powder particle velocities on impact and a significant fraction of solid phase at this point, fragmentation and debonding of the carbide grains in the coating occurs, resulting in enhanced wear.

- Different gun types, spraying conditions and powder types must be optimized to yield as low a level of decomposition within the particles as possible whilst still maintaining enough heat input to engender strong bonding between splats and little disruption of the particle structure due to impact damage.

Chapter 9

Future Work

From the findings of this work, it is evident that the conventional WC-Co coatings sprayed by the HVOGF process, compared to those sprayed by the HVOLF process, show a higher degree of decomposition, leading to enhanced wear. However, the HVOGF sprayed WC-Co coatings exhibit higher wear resistance due to the reduction in fragmentation and debonding of the carbides. Thus, it would be desirable to reduce the degree of decomposition in WC-Co powder sprayed by the HVOGF process by optimisation of the spraying conditions (limiting decomposition and minimizing particle impact damage with good bonding).

Commercial WC-Co powders, produced by different manufacturing processes, display different powder morphologies and WC grain sizes. As known, small carbide grain sizes in the powder particles and porous structure of powder particles results in an increase of the degree of decomposition. Therefore, a second way to decrease the degree of decomposition is to optimise the WC-Co powder sprayed by the HVOGF process in terms of WC grain size and internal structure of the powder particles. A systematic study in this area would be desirable.

Another area of interest would be to spray nanoscale WC-Co powder by the HVOLF process in an attempt to achieve its promising properties in a thermally sprayed

coating. In the present study, the nanoscale WC-Co powder was only sprayed by the HVOGF process; spraying with the HVOLF process was unsuccessful due to the unsuitable particle size distribution causing deposition inside the nozzle. On the basis of a preliminary investigation, the problems of spraying the nanoscale WC-Co coating by the HVOLF may be overcome in two ways: by altering spraying parameters and by changing the size distribution characteristics of the nanoscale WC-Co powder.

Acknowledgements

I would like to express my gratitude to my supervisors, Prof. D.G. McCartney and Dr. P. Shipway for their advice and patience throughout the course of this PhD. I would like to thank the Royal Thai Government for financial support.

I would like to thank Dr. A. Horlock, Dr. D. Zhang for operating the spray equipment, Mr. K. Dinsdale, Dr. T. Burinprakhon and Dr. S. Wirojanupatum for training on the TEM. I also would like to thank Mrs. J. Armitage, Ms. N. Bock for training on the XRD, SEM and all staff in the Wolfson Building for technical assistance.

I would like to thank all my friends for making my life in England most enjoyable and memorable. Most importantly, I would like to express my deepest gratitude to my family and Lieutenant-Colonel Somphol Palathai for their support, love and encouragement.

Miss Tippaban Sudaprasert

November 2002

Appendix 1

A1.1 Powder Diffraction Standards

The powder diffraction standards are taken from the 1999 JCPDS-International Centre for Diffraction Data. The JCPDS files consisting of WC, Co, Co_3W_3C, W_2C and W are shown.

WC Tungsten Carbide		2θ (degree)	d (Å)	Intensity	h	k	l
System	Hexagonal	31.474	2.84	45	0	0	1
S.G.	P-6m2 (187)	35.626	2.518	100	1	0	0
a	2.9062	48.266	1.884	100	1	0	1
c	2.8378	63.979	1.454	20	1	1	0
Radiation	CuKa1λ	65.701	1.420	6	0	0	2
Standard no.	25-1047	73.064	1.294	25	1	1	1
		75.442	1.259	14	2	0	0
		77.101	1.236	30	1	0	2
		84.015	1.151	20	2	0	1
		98.734	1.015	14	1	1	2
		108.186	0.951	10	2	1	0
		109.026	0.946	1	0	0	3
		109.712	0.942	10	2	0	2
		117.292	0.902	20	2	1	1

Co Cobalt		2θ (degree)	d (Å)	Intensity	h	k	l
System	Cubic	51.830	2.0467	100	1	1	1
S.G.	Fm3m (225)	60.623	1.7723	40	2	0	0
a	3.5447	91.083	1.2532	25	2	2	0
Radiation	CoKa1λ	113.630	1.0688	30	3	1	1
Standard no.	15-0806	121.882	1.0233	12	2	2	2

α-W_2C Tungsten Carbide		**2θ (degree)**	**d (Å)**	**Intensity**	**h**	**k**	**l**
System	Hexagonal	34.524	2.5958	25	1	0	0
S.G.	P-3m1 (164)	38.029	2.3642	22	0	0	2
a	2.99704	39.569	2.2757	100	1	0	1
c	4.7279	52.300	1.7478	17	1	0	2
Radiation	CuKa1λ	61.861	1.4986	14	1	1	0
Standard no.	35-0776	69.769	1.3468	14	1	0	3
		72.839	1.2974	2	2	0	0
		74.979	1.2656	12	1	1	2
		75.984	1.2514	10	2	0	1
		81.328	1.1821	2	0	0	4
		85.228	1.1377	3	2	0	2
		91.472	1.0756	2	1	0	4
		100.510	1.0018	3	2	0	3
		103.472	0.9811	<1	2	1	0
		106.614	0.9606	5	2	1	1
		112.189	0.9281	3	1	1	4
		116.452	0.9061	1	2	1	2
		120.239	0.8884	2	1	0	5
		123.650	0.8738	1	2	0	4
		125.841	0.8651	1	3	0	0
		135.299	0.8329	3	2	1	3
		142.932	0.8124	2	3	0	2

W Tungsten		**2θ (degree)**	**d (Å)**	**Intensity**	**h**	**k**	**l**
System	Cubic	40.265	2.238	100	1	1	0
S.G.	Im3m (229)	58.276	1.582	15	2	0	0
a	3.1648	73.198	1.292	23	2	1	1
Radiation	CuKa1	87.024	1.1188	8	2	2	0
Standard no.	4-806	100.651	1.0008	11	3	1	0
		114.928	0.9137	4	2	2	2
		131.184	0.8459	18	3	2	1
		153.603	0.7912	2	4	0	0

Co_3W_3C Cobalt Tungsten Carbide		2θ (degree)	d (Å)	Intensity	h	k	l
System	Cubic	13.890	6.37	3	1	1	1
S.G.	Fd3m (227)	22.782	3.90	7	2	2	0
a	11.112	26.666	3.34	1	3	1	1
Radiation	CuKa1λ	28.035	3.18	1	2	2	2
Standard no.	27-1125	32.410	2.76	25	4	0	0
		35.450	2.53	40	3	3	1
		39.854	2.260	65	4	2	2
		42.399	2.130	100	5	1	1
		46.406	1.955	40	4	4	0
		49.380	1.844	3	4	4	2
		52.194	1.751	2	6	2	0
		54.403	1.685	1	5	3	3
		54.897	1.671	3	6	2	2
		59.510	1.552	13	5	5	1
		62.488	1.485	2	6	4	2
		64.473	1.444	12	7	3	1
		67.523	1.386	2	8	0	0
		69.284	1.355	19	7	3	3
		72.283	1.306	45	8	2	2
		73.924	1.281	11	7	5	1
		74.467	1.273	1	6	6	2
		78.453	1.218	4	9	1	1
		78.917	1.212	1	8	4	2
		81.332	1.182	2	6	6	4
		82.863	1.164	1	9	3	1
		87.290	1.116	13	7	5	5
		90.137	1.088	9	10	2	0
		91.644	1.074	8	9	5	1
		92.197	1.069	2	10	2	2
		98.861	1.014	2	10	4	2
		100.615	1.001	2	11	1	1
		104.997	0.9709	4	9	7	1
		105.601	0.967	2	8	8	2
		107.898	0.9527	8	10	6	0
		109.602	0.9426	1	9	7	3
		110.297	0.9386	1	10	6	2
		112.606	0.9258	10	12	0	0
		114.390	0.9164	5	11	5	1
		117.410	0.9014	13	12	2	2
		119.206	0.893	2	11	5	3
		122.394	0.879	2	12	4	0
		124.588	0.870	1	9	9	1
		127.995	0.857	4	10	8	2
		129.964	0.850	9	11	7	1
		130.547	0.848	4	10	6	6
		133.926	0.837	2	12	4	4
		135.912	0.831	16	13	3	1
		136.949	0.828	12	10	8	4
		140.263	0.819	10	12	6	2
		142.674	0.813	13	13	3	3
		147.501	0.8023	2	8	8	8

Appendix 2

A2 X-ray Diffraction Patterns of Starting Powders and Coatings

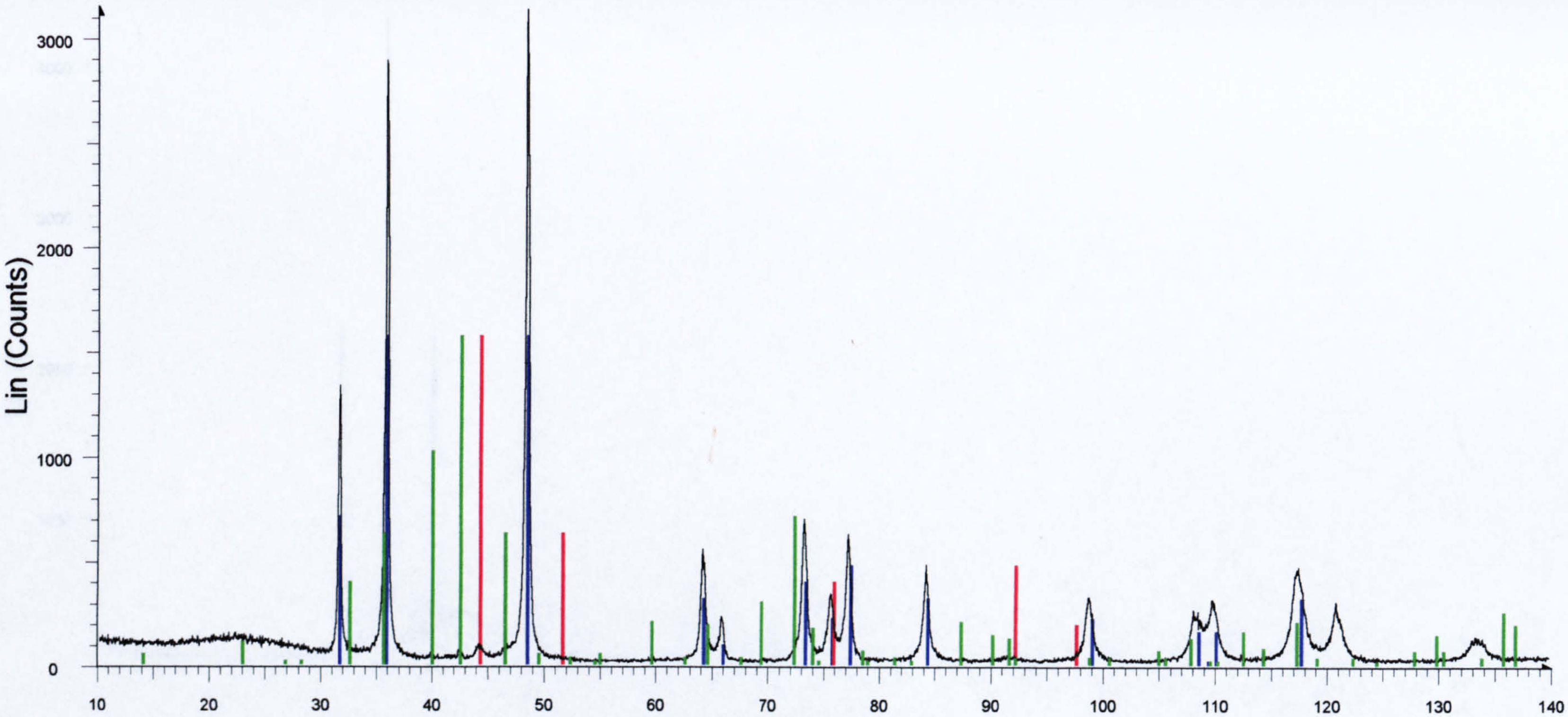

Conventional WC-12 wt% Co powder

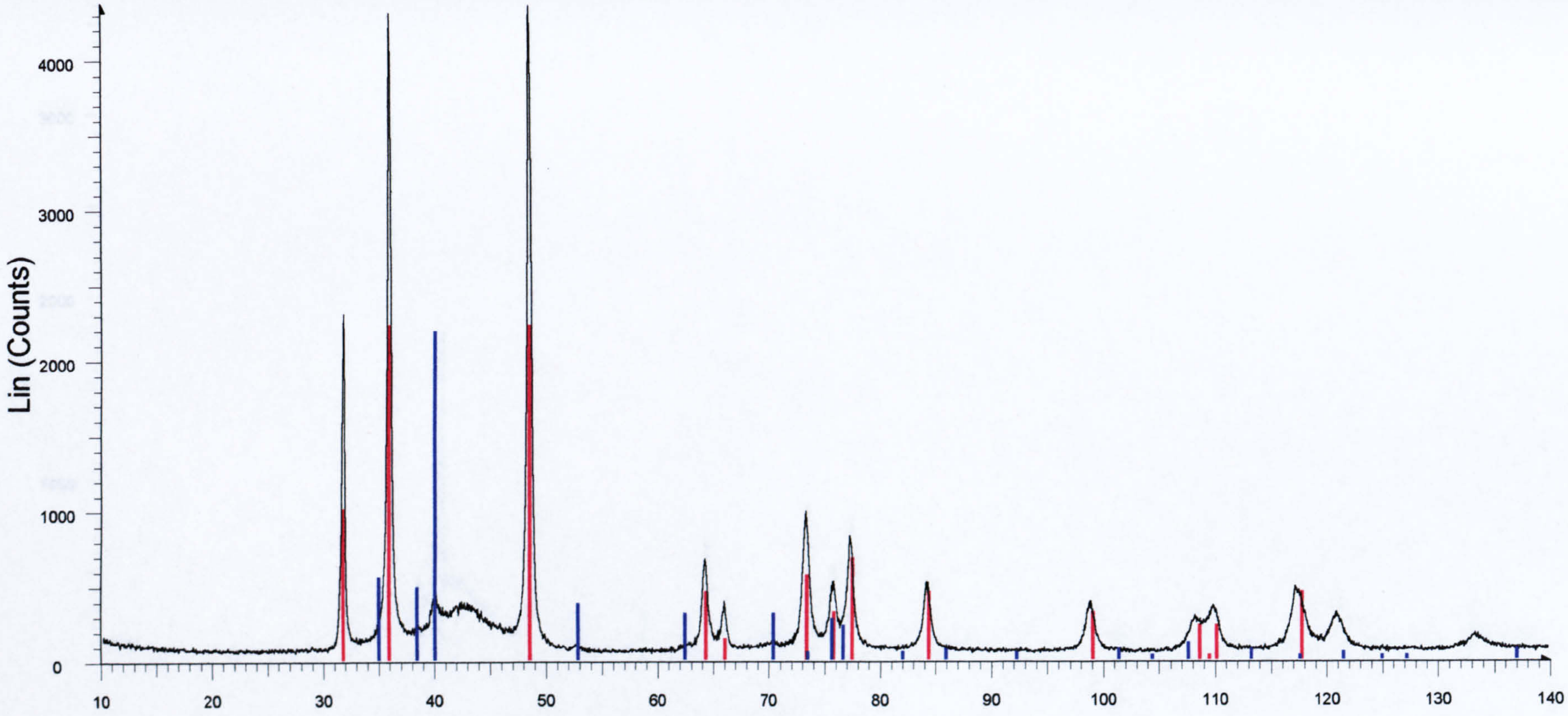

HVOLF sprayed conventional WC-12 wt% Co coating

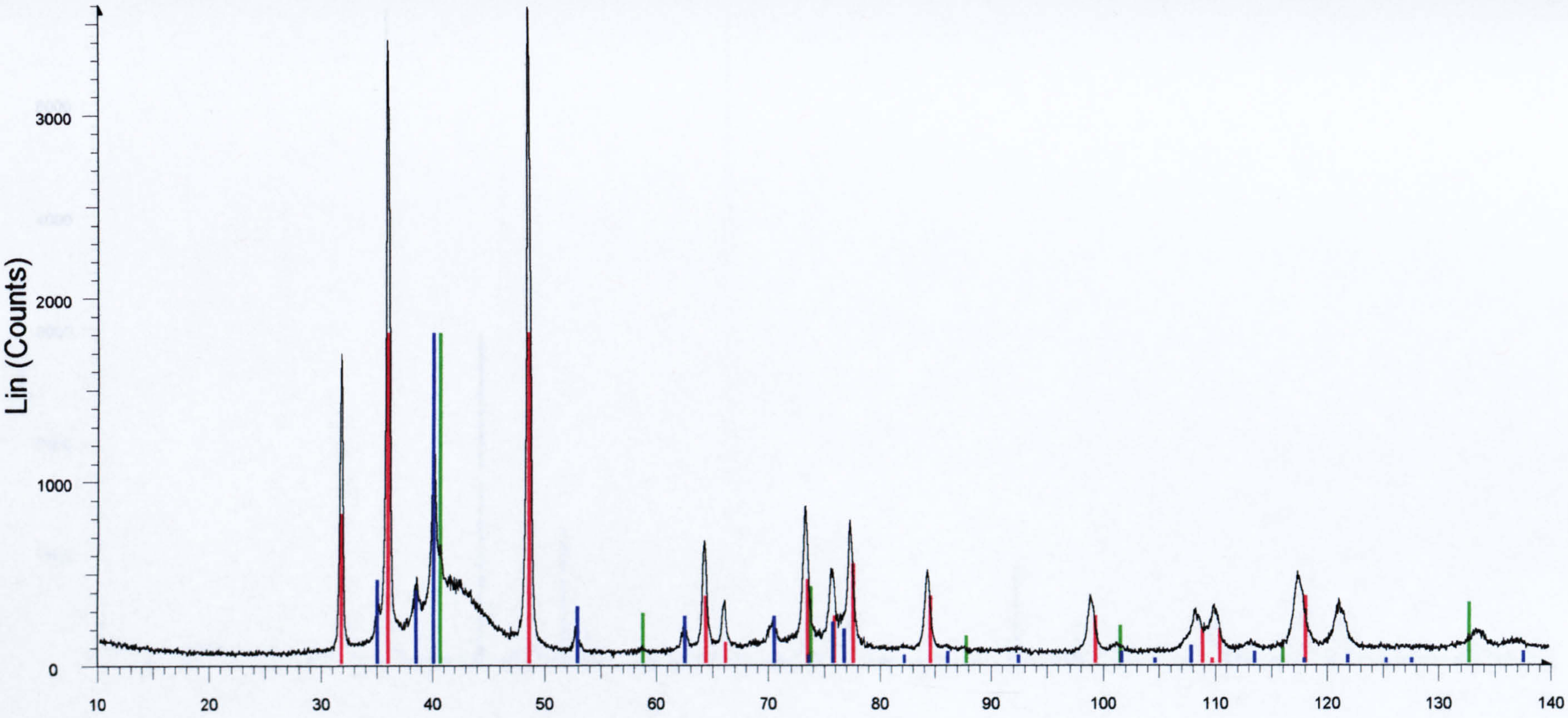

12CO420 - File: 12co420.raw - Type: 2Th/Th locked - Start: 10.000 ° - End: 140.000 ° - Step: 0.050 ° - Step time: 2. s - Temp.: 25 °C (Room) - Time Started: 0 s - 2-Theta: 10.000 ° - Theta: 5.
Operations: Import
25-1047 (*) - Unnamed mineral, syn [NR] - WC - Y: 50.00 % - d x by: 0.9955 - WL: 1.5406 - Hexagonal - a 2.9062 - b 2.90620 - c 2.8378 - alpha 90.000 - beta 90.000 - gamma 120.000 - Pri
35-0776 (*) - Tungsten Carbide - W2C - Y: 50.00 % - d x by: 0.9918 - WL: 1.5406 - Hexagonal - a 2.99704 - b 2.99704 - c 4.7279 - alpha 90.000 - beta 90.000 - gamma 120.000 - Primitive -
04-0806 (*) - Tungsten wolfram - W - Y: 50.00 % - d x by: 0.9936 - WL: 1.5406 - Cubic - a 3.1648 - b 3.16480 - c 3.16480 - alpha 90.000 - beta 90.000 - gamma 90.000 - Body-centred - Im3

HVOGF sprayed conventional WC-12 wt% Co coating

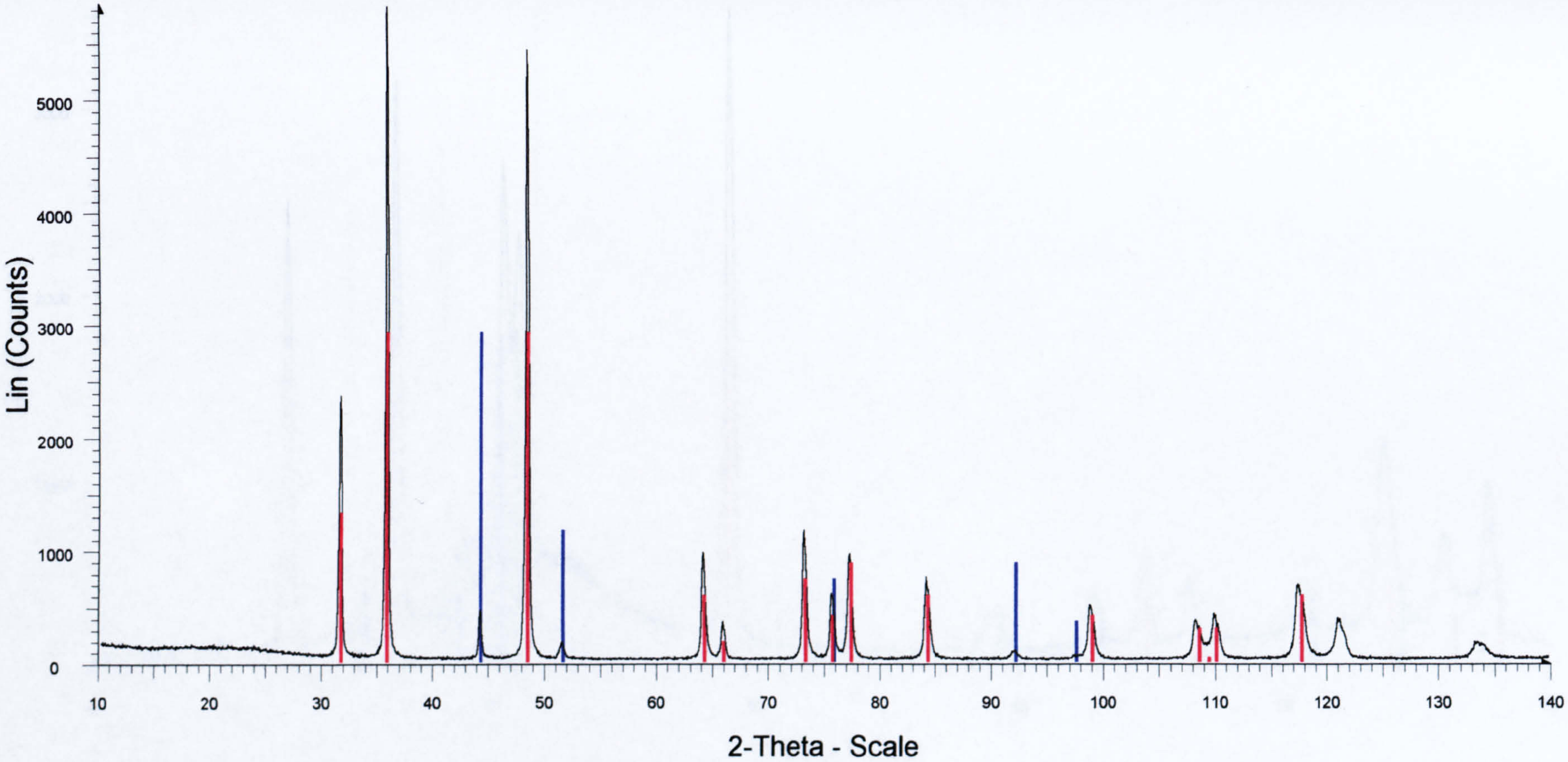

Nanoscale WC-12 wt% Co powder

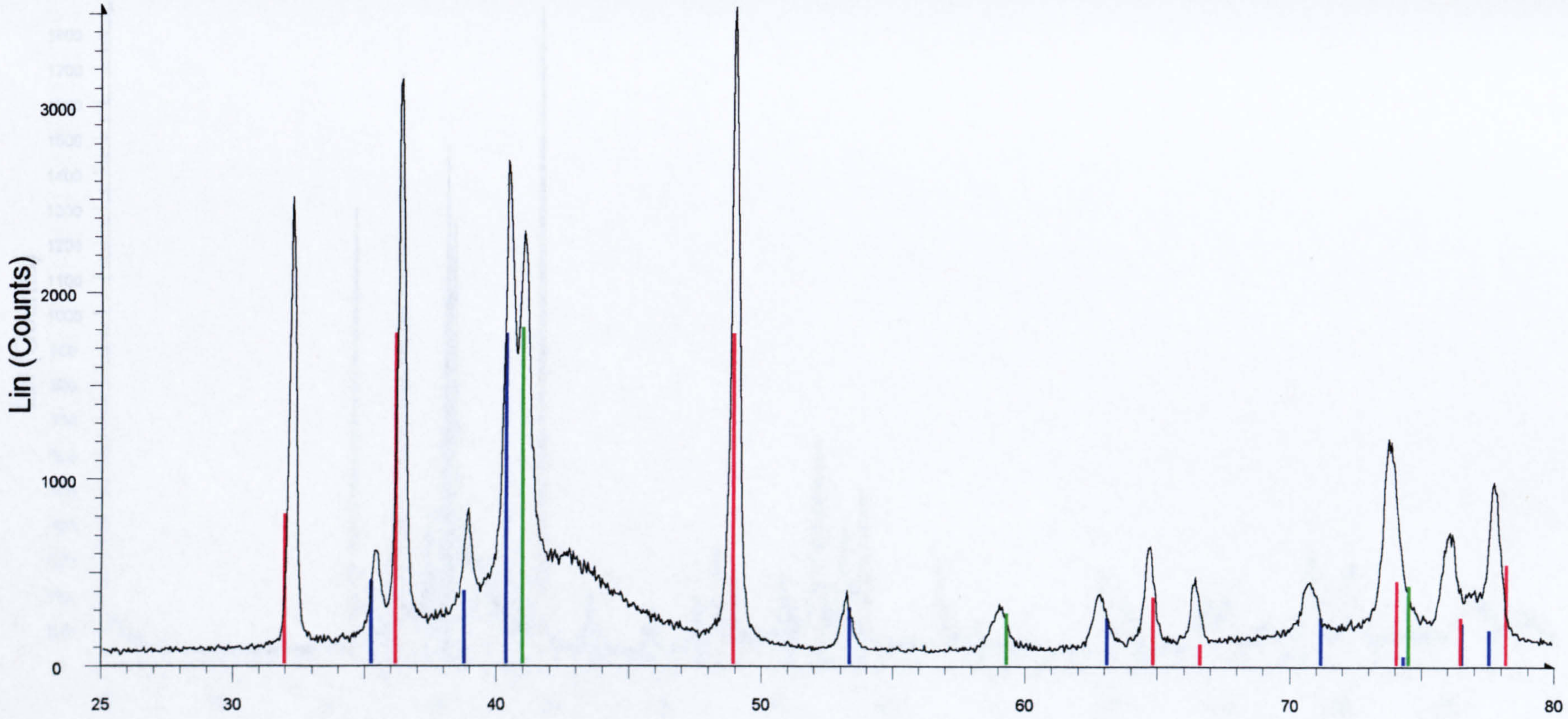

HVOGF sprayed nanoscale WC-12 wt% Co coating (Run 1)

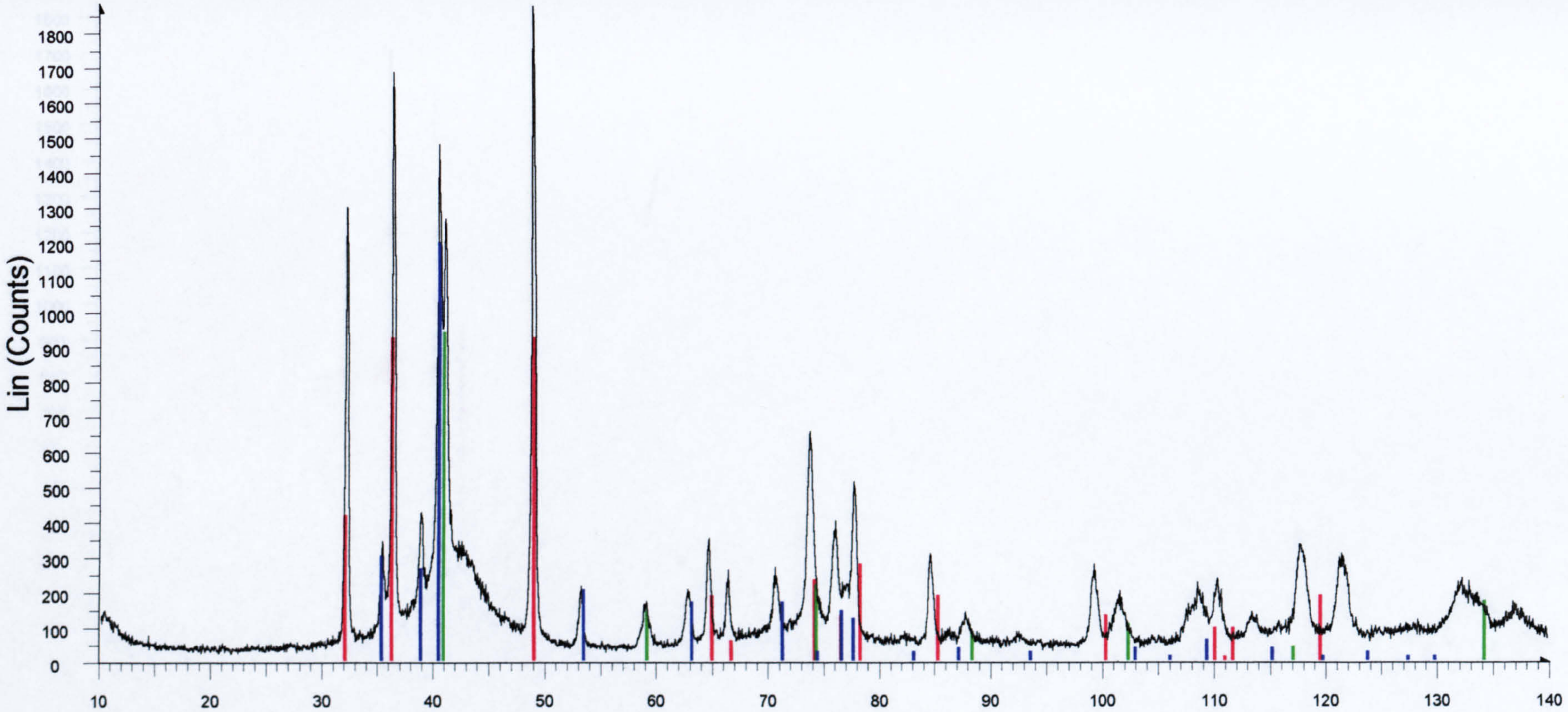

HVOGF sprayed nanoscale WC-12 wt% Co coating (Run 2)

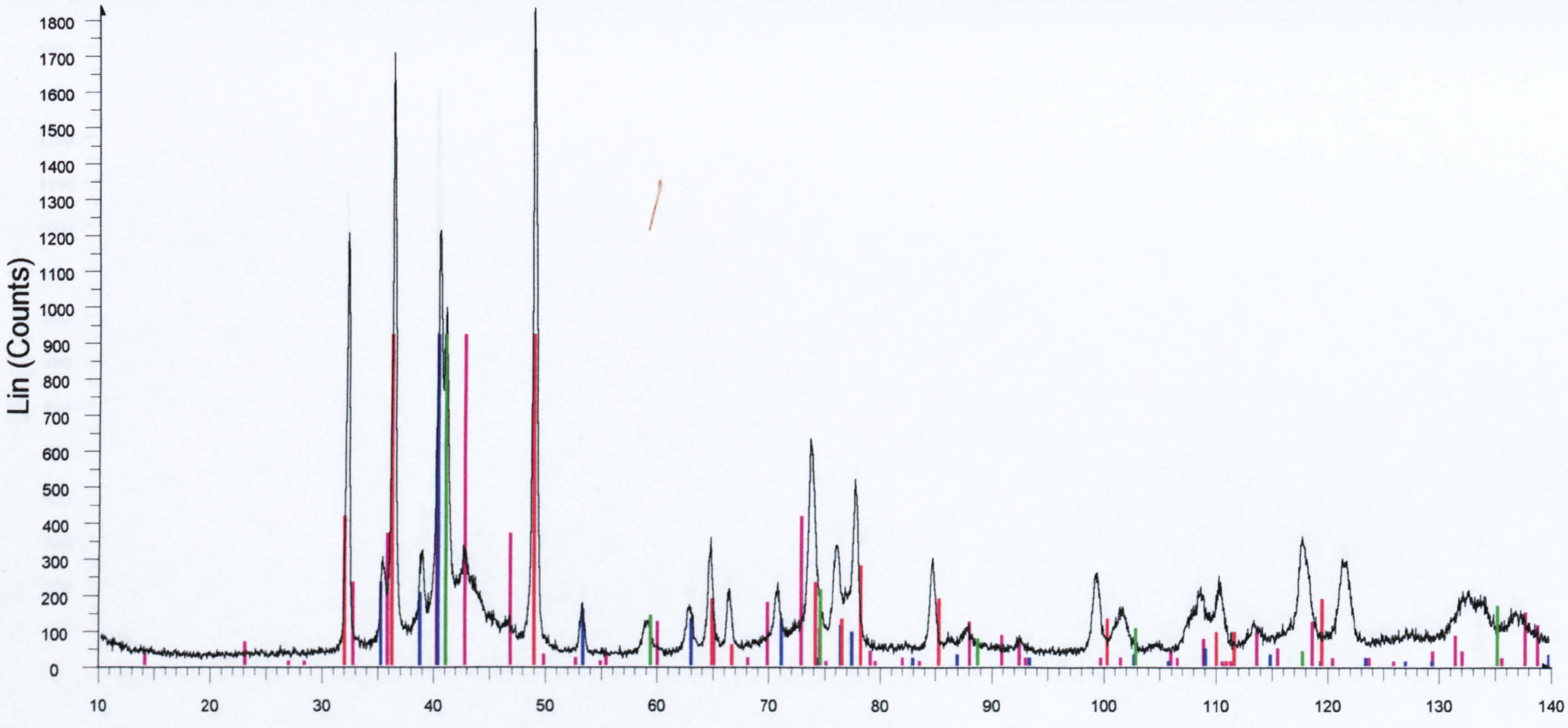

WC12CO31 - File: Wc12co31.raw - Type: 2Th/Th locked - Start: 10.000 ° - End: 140.000 ° - Step: 0.050 ° - Step time: 2. s - Temp.: 25 °C (Room) - Time Started: 0 s - 2-Theta: 10.000 ° - The
Operations: Import
04-0806 (*) - Tungsten wolfram - W - Y: 50.00 % - d x by: 0.9845 - WL: 1.5406 - Cubic - a 3.1648 - b 3.16480 - c 3.16480 - alpha 90.000 - beta 90.000 - gamma 90.000 - Body-centred - Im3
27-1125 (N) - Cobalt Tungsten Carbide - Co3W3C - Y: 50.00 % - d x by: 0.9936 - WL: 1.5406 - Cubic - a 11.112 - b 11.11200 - c 11.11200 - alpha 90.000 - beta 90.000 - gamma 90.000 - Fa
35-0776 (*) - Tungsten Carbide - W2C - Y: 50.00 % - d x by: 0.9845 - WL: 1.5406 - Hexagonal - a 2.99704 - b 2.99704 - c 4.7279 - alpha 90.000 - beta 90.000 - gamma 120.000 - Primitive -
25-1047 (*) - Unnamed mineral, syn [NR] - WC - Y: 50.00 % - d x by: 0.9882 - WL: 1.5406 - Hexagonal - a 2.9062 - b 2.90620 - c 2.8378 - alpha 90.000 - beta 90.000 - gamma 120.000 - Pri

HVOGF sprayed nanoscale WC-12 wt% Co coating (Run 3)

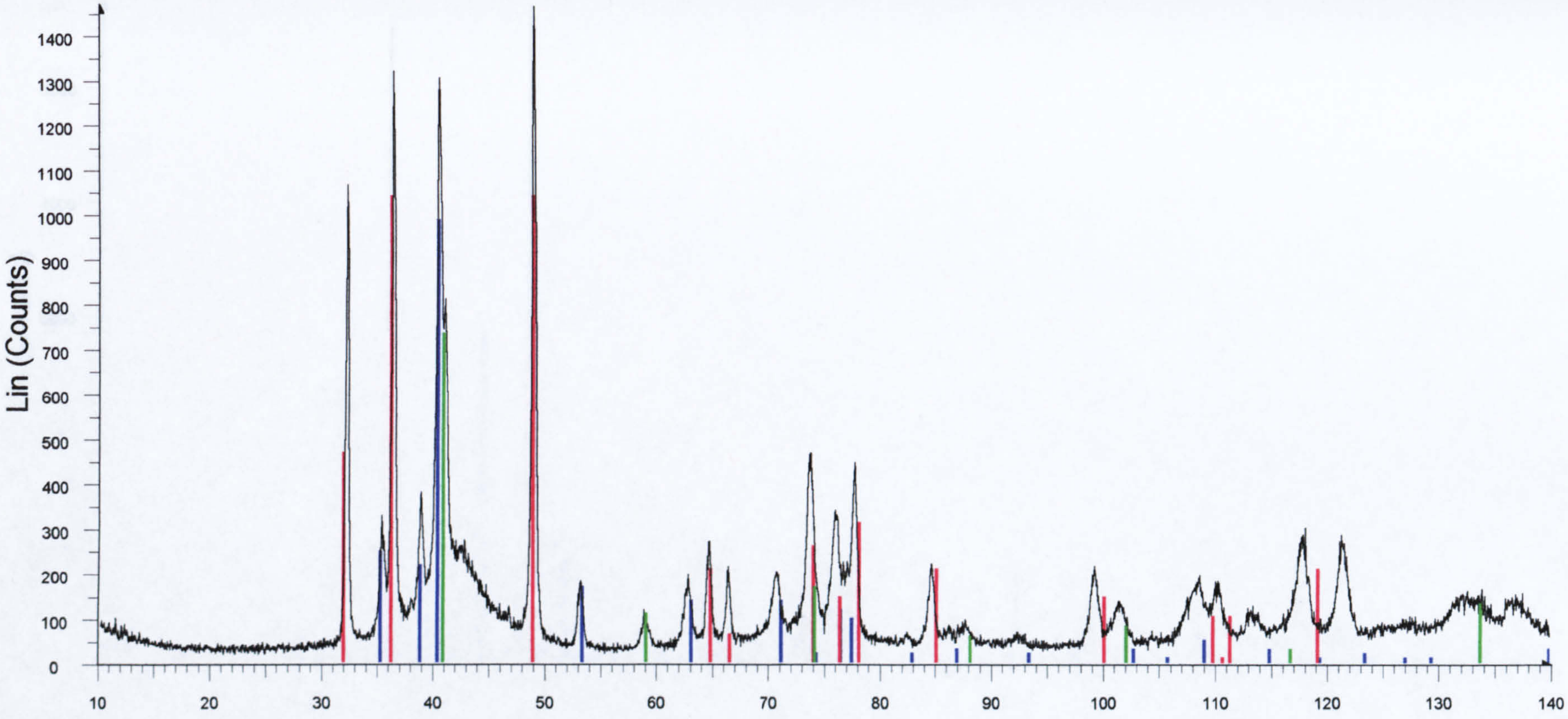

HVOGF sprayed nanoscale WC-12 wt% Co coating (Run 4)

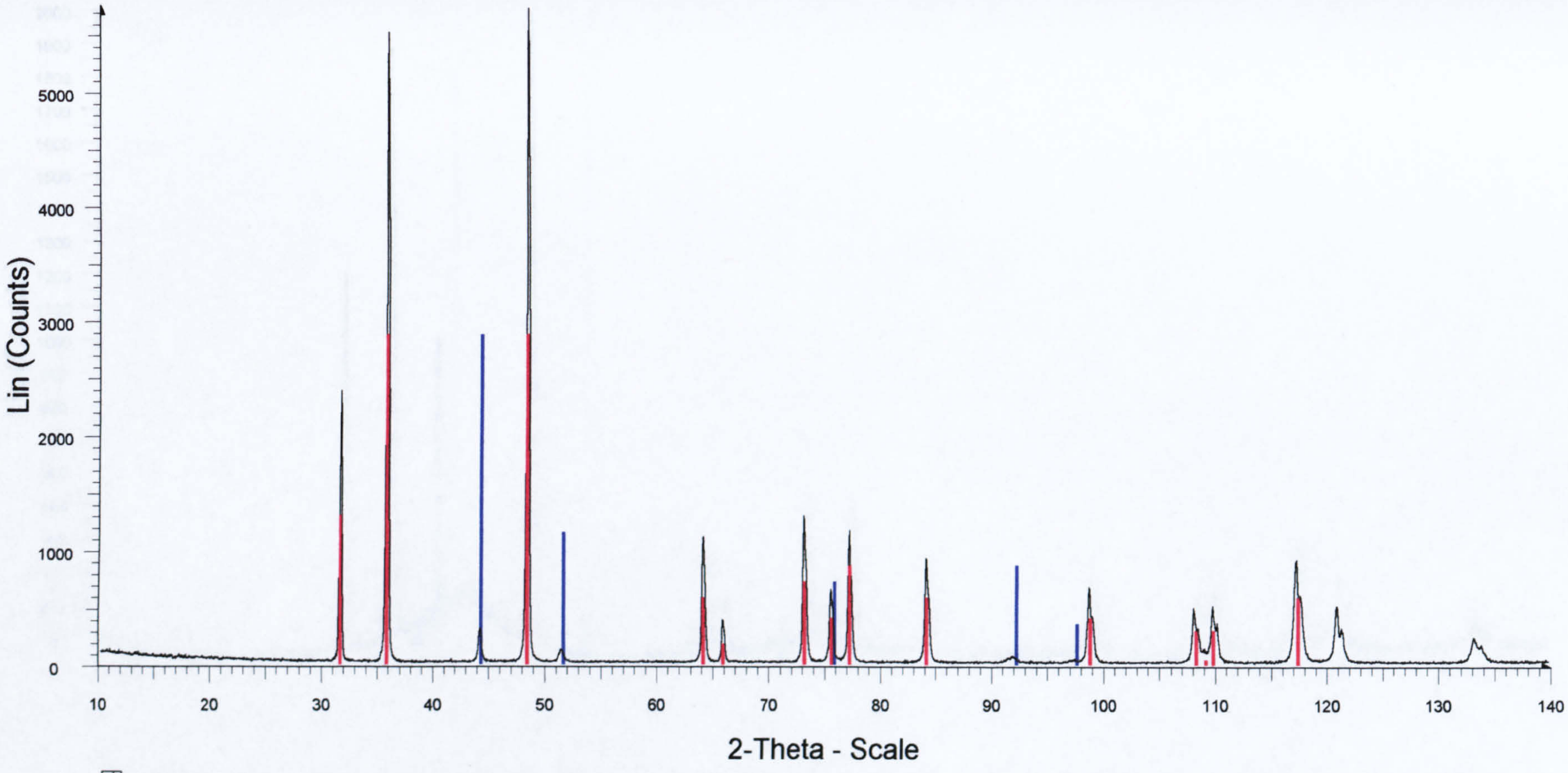

WC-17 wt% Co (M) powder

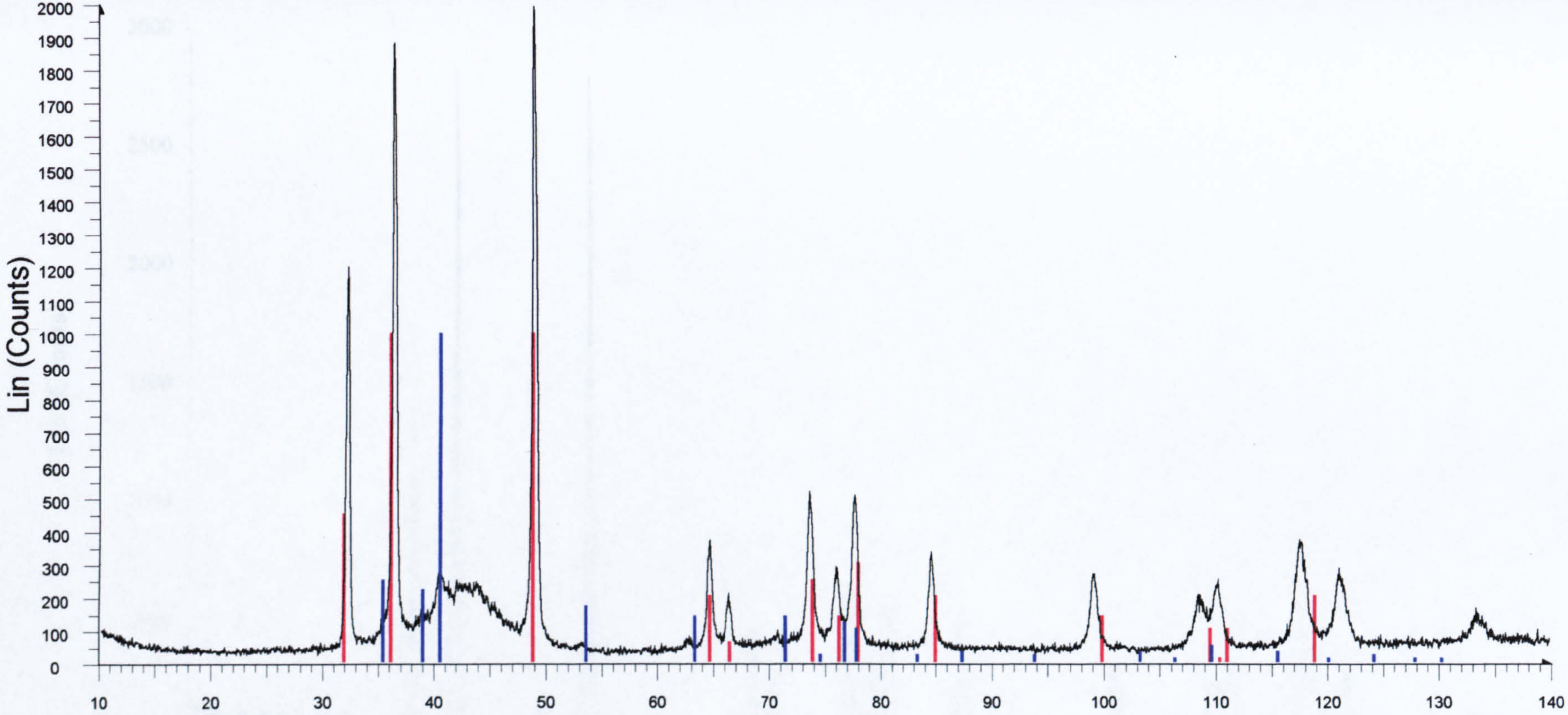

HVOLF sprayed WC-17 wt% Co (M) coating

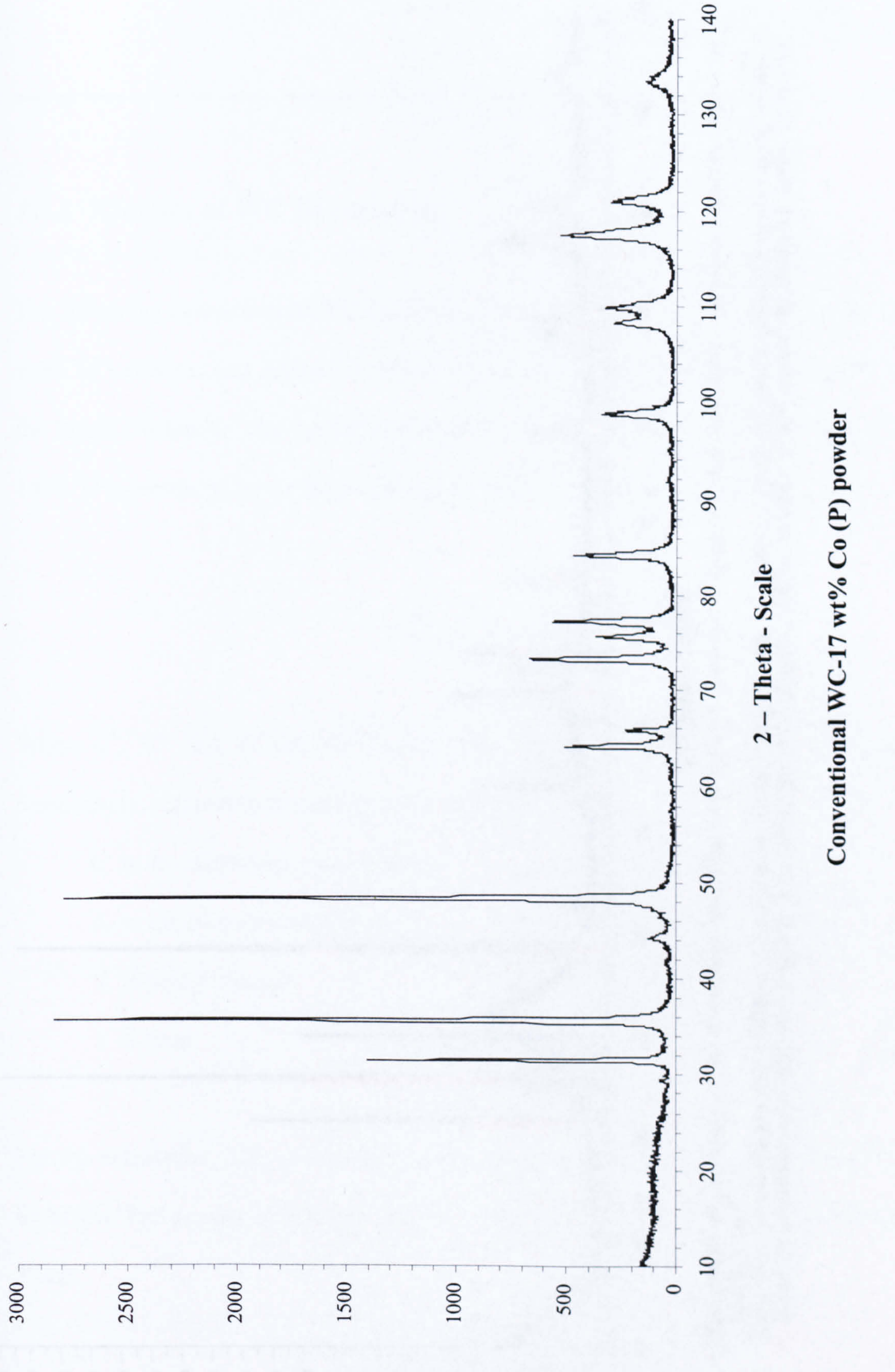
Conventional WC-17 wt% Co (P) powder
2 – Theta - Scale
Lin (Counts)
3000
2500
2000
1500
1000
500
0
10
20
30
40
50
60
70
80
90
100
110
120
130
140

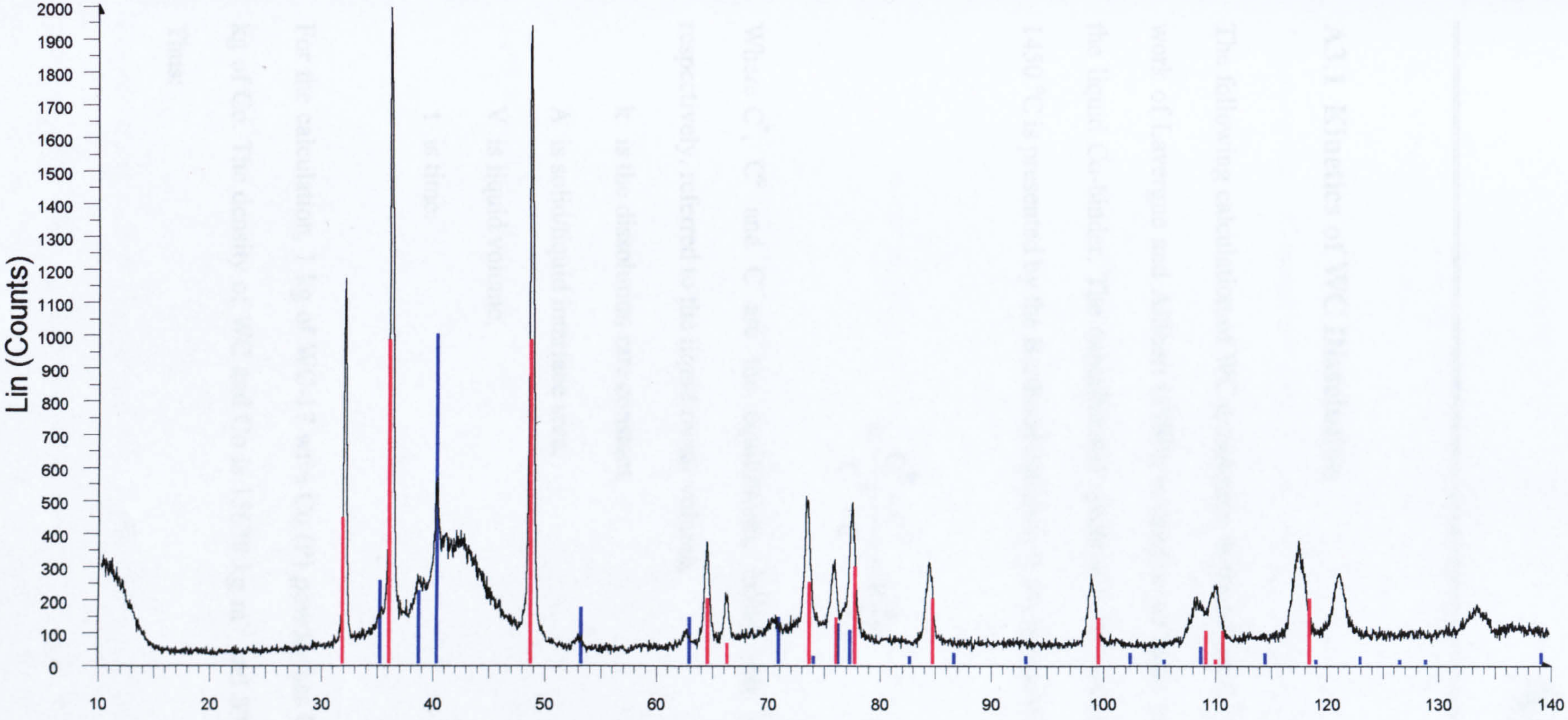

HVOGF sprayed WC-17 wt% Co (P) coating

Appendix 3

A3.1 Kinetics of WC Dissolution

The following calculation of WC dissolution in the liquid Co-binder, relating with the work of Lavergne and Allibert (1999), is used to estimate the solute content (W) in the liquid Co-binder. The experimental result of a WC block in liquid Co heated at 1450 °C is presented by the Berthoud equation (Lavergne and Allibert, 1999):

$$\ln\frac{C^{*}-C^{o}}{C^{*}-C}=k\frac{A}{V}t$$

Where C^{*}, C^{o} and C are the equilibrium, initial and instant solute contents, respectively, referred to the liquid molar volume,

k is the dissolution rate constant,

A is solid/liquid interface area,

V is liquid volume,

t is time.

For the calculation, 1 kg of WC-17 wt% Co (P) powder has 0.83 kg of WC and 0.17 kg of Co. The density of WC and Co is 15630 kg m^{-3} and 8920 kg m^{-3}, respectively. Thus:

$$\text{Volume of WC} = \frac{0.83}{15630} = 5.31 \times 10^{-5} \quad m^3$$

$$\text{Volume of Co} = \frac{0.17}{8920} = 1.91 \times 10^{-5} \quad m^3$$

Assuming the WC grains are spheres and average carbide grain size of WC (WC-17 wt% Co(P) powder, see Table 4.1) is 1 μm. Thus:

$$\text{Volume of each WC grain} = \frac{4}{3}\pi r^3 = \frac{4}{3}\pi \times (0.5\times10^{-6})^3 \ m^3$$

$$= 0.52 \times 10^{-18} \quad m^3$$

$$\therefore \text{ Number of WC grains in 1 kg} = \frac{5.31\times10^{-5}}{0.52\times10^{-18}} = 10.21 \times 10^{13} \ (N_{WC})$$

$$\text{Volume of Co associated with each WC grain (V)} = \frac{1.91\times10^{-5}}{10.21\times10^{13}} \ m^3$$

$$= 0.187 \times 10^{-18} m^3$$

$$\text{Area of each WC grain (A)} = 4\pi r^2 = 4\pi(0.5\times10^{-6})^2 = 3.14 \times 10^{-12} \ m^2$$

$$\therefore \quad \frac{A}{V} = \frac{3.14\times10^{-12}}{0.187\times10^{-18}} = 16.8\times10^6 \quad m^{-1}$$

In general, $$\frac{A}{V} = \frac{8.34}{r} \quad m^{-1}$$

Dissolution rate of W (k_W) obtained from the Berthoud equation is 5.0×10^{-5} m s^{-1} (Lavergne and Allibert, 1999) and t is assumed to be 2 ms. Therefore,

$$\ln\frac{C^* - C^o}{C^* - C} = (5.0 \times 10^{-5}) \times (16.8 \times 10^{6}) \times (2 \times 10^{-3})$$

$C^o = 0$ at the initial state,

$$\ln\frac{C^*}{C^* - C} = 1.65$$

$$\frac{C^*}{C^* - C} = e^{1.65}$$

$$1 - \frac{C}{C^*} = e^{-1.65}$$

$$\frac{C}{C^*} = 0.81$$

Thus after 2 ms the solute content is 0.81 times its equilibrium value. The differences of WC grain size and the influence of the exposure time on the W content dissolving in the liquid Co-binder can be calculated.

Average WC grain radius (μm)	$\frac{A}{V} = \frac{8.34}{r}$ (m^{-1})	Exposure time (ms)	$\frac{C}{C^*}$
0.15	0.56×10^{8}	0.5	0.74
		1	0.93
		2	0.99
0.5	16.8×10^{6}	0.5	0.33
		1	0.56
		2	0.81

Average WC grain radius (μm)	$\frac{A}{V} = \frac{8.34}{r}$ (m^{-1})	Exposure time (ms)	$\frac{C}{C^*}$
1	8.38×10^6	0.5	0.19
		1	0.34
		2	0.56
2	4.19×10^6	0.5	0.10
		1	0.19
		2	0.34

The calculation shows that the extent of dissolution of WC depends on exposure time and size.

A3.2 Volume of WC Dissolved

Assume we can divide the entire powder particles into a number of "unit cells". A "unit cell" comprises a WC particle surrounded by Co-binder. So we can estimate the binder thickness as a function of the WC size prior to any dissolution. Assume that:

1. there is one WC grain in a "unit cell",
2. WC grain and powder particle are spherical.

Volume of Co associated with each WC grain = Volume of "unit cell" - Volume of WC grain

Diameter of WC grain = 1 μm ($\therefore r_{WC} = 0.5 \times 10^{-6}$ m),

Thus $$0.187 \times 10^{-18}\,m^3 = \frac{4}{3}\pi r_o^3 - \frac{4}{3}\pi(0.5\times10^{-6})^3 \qquad m^3$$

$$r_o = 5.5 \times 10^{-7} \qquad m$$

$$= 0.55 \qquad \mu m$$

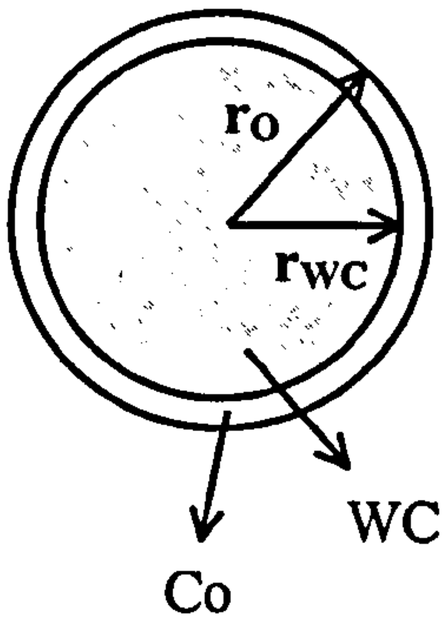

A3.2 Volume of WC Dissolved

Assume we can divide the entire powder particles into a number of "unit cells". A "unit cell" comprises a WC particle surrounded by Co-binder. So we can estimate the binder thickness as a function of the WC size prior to any dissolution. Assume that:

1. there is one WC grain in a "unit cell",
2. WC grain and powder particle are spherical.

Volume of Co associated with each WC grain = Volume of "unit cell" - Volume of WC grain

Diameter of WC grain = 1 μm ($\therefore r_{WC} = 0.5 \times 10^{-6}$ m),

Thus $$0.187 \times 10^{-18}\ m^3 = \frac{4}{3}\pi r_O^{\,3} - \frac{4}{3}\pi(0.5\times10^{-6})^3 \qquad m^3$$

$$r_O = 5.5 \times 10^{-7} \qquad m$$

$$= 0.55 \qquad \mu m$$

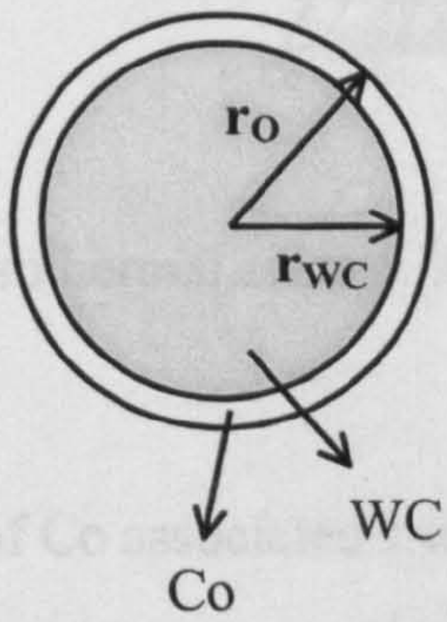

Radius of WC grain size (r_{WC} : μm)	Radius of "unit cell"(r_O : μm) ($r_O = 1.108\ r_{WC}$)
0.15	0.17
0.5	0.55
1	1.11
2	2.22

From the phase diagram, we can estimate the solute content of Co at equilibrium. This allows us to determine how much WC dissolved into the surrounding Co to achieve this concentration. As an example, this calculation will be performed for the 0.5 μm radius.

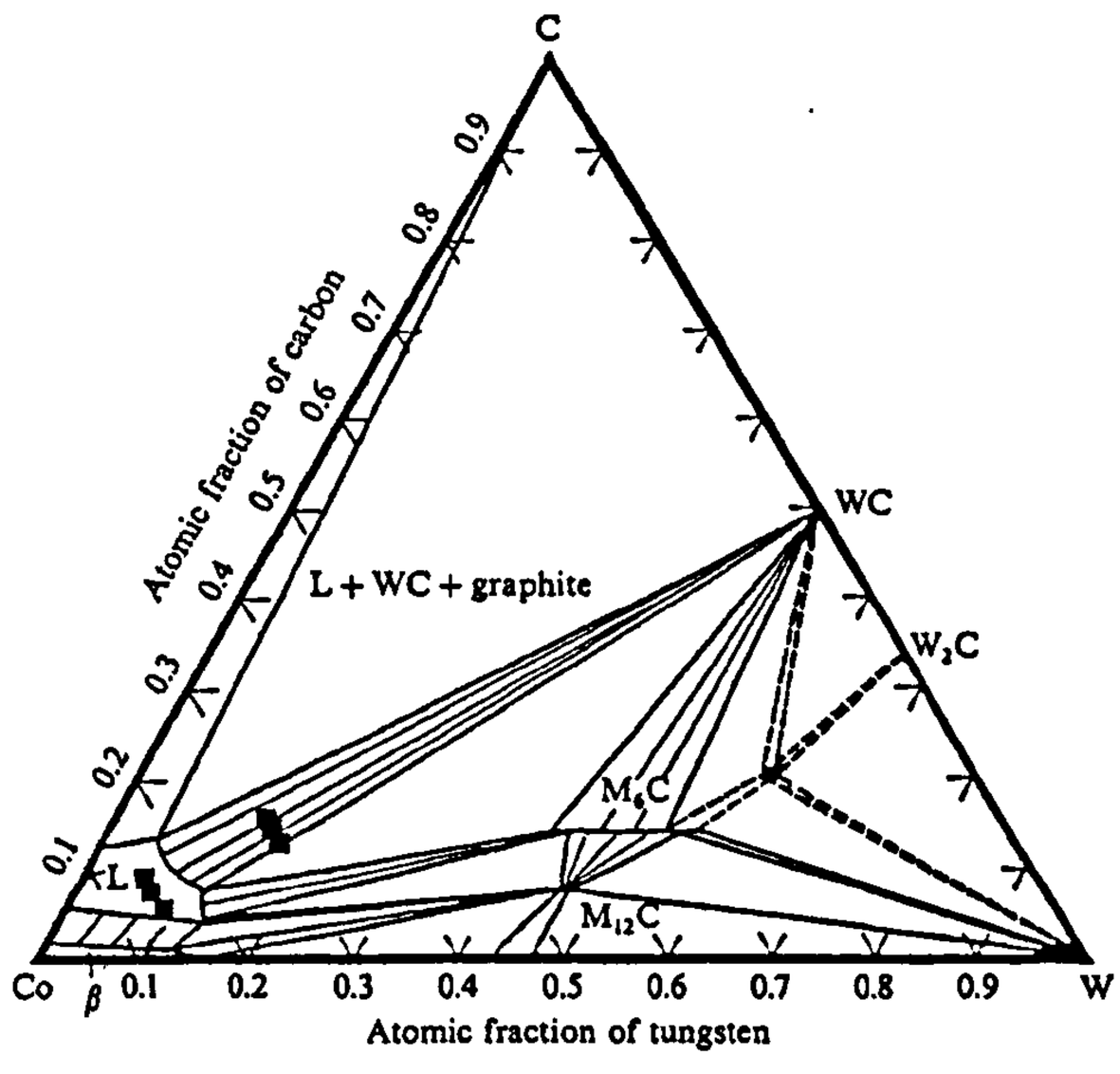

Isothermal section W-C-Co at 1425 °C (Lavergne and Allibert, 1999)

Volume of Co associated with each WC grain = 0.187×10^{-18} m^3

(for 1 μm diameter)

Volume of 1 unit cell of Co (FCC) $= a^3$ $(a = 3.5447 \times 10^{-10}\ m)$

$\therefore$ Volume of 1 unit cell of Co (FCC) $= 44.5 \times 10^{-30}\ m^3$

Thus, it can be calculated the number of unit cells in the volume of Co associated with WC grain.

The number of the unit cells in the volume of Co $= \dfrac{0.187 \times 10^{-18}}{44.5 \times 10^{-30}}$ unit cells

$= 4.2 \times 10^9$ unit cells

As is known, 1 unit cell of Co has 4 atoms. Therefore, 4.2×10^9 unit cells has 16.8×10^9 atoms.

From the phase diagram,

Equilibrium atom fraction of W $= 0.1$

$$\text{Equilibrium atom fraction of W} = \frac{\text{Number of atoms of W}}{\text{Number of atoms of (W + C + Co)}}$$

$$\frac{\text{Number of atoms of W}}{\text{Number of atoms of (W + C + Co)}} = 0.1$$

The number of dissolved W and C atoms was the same in the liquid Co at equilibrium (Lavergne and Allibert, 1999). As is known, the number of atoms of Co is 16.8×10^9 atom and it can be assumed that number of atom of W = x. Thus:

$$\frac{x}{2x+(16.8\times10^{9})} = 0.1 \qquad \text{atoms}$$

$$x = 2.1\times10^{9} \qquad \text{atoms}$$

$\therefore$ At equilibrium the number of dissolved W or C atoms in the liquid Co is 2.1×10^{9} atoms.

Volume of WC (hexagonal) in 1 unit cell $= 0.866\,a^2c$ ($a = 2.9062\times10^{-10}$ m, $c = 2.8378\times10^{-10}$ m)

$\therefore$ Volume of 1 unit cell of WC (hexagonal) $= 20.76\times10^{-30}$ m^3

One atom of W per unit cell. The amount of the dissolved W $= 2.1\times10^{9}$ atoms.

Hence,

Volume of WC lost $= 2.1\times10^{9}\times$ unit cell volume of WC m^3

$= (2.1\times10^{9})\times(20.76\times10^{-30})$

$= 43.6\times10^{-21}$ m^3

Starting volume of eachWC grain $= \frac{4}{3}\pi(0.5\times10^{-6})^3 = 5.2\times10^{-19}$ m^3

Hence, finishing volume of each WC grain $= (5.2\times10^{-19}) - (0.436\times10^{-19})$ m^3

$= 0.48\times10^{-18}$ m^3

The finishing volume of WC must equal to new volume of WC that is $\frac{4}{3}\pi(r^*)^3$.

Hence,

$$\frac{4}{3}\pi (r^*)^3 = 0.48 \times 10^{-18} \quad m^3$$

$$r^* = 0.485 \quad \mu m$$

It can be stated that WC grain size, which has the radius of 0.5 μm, has the "unit cell" radius of 0.55 μm. The total number of W atom lost is 43.6×10^{-21} m^3. Due to the dissolved W (assuming equilibrium is reached) the WC grain size is reduced to from 0.5 to 0.485 μm in radius.

References

Aakasawa, T. and Ai, K. (1998) Wear properties of WC-Co coatings with plasma and high velocity oxyfuel spraying. Proceedings of the 15th International Thermal Spray Conference, 25-29 May, Nice, France, 281-286

Ahmed, R. and Hadfield, M. (1997) Wear of high-velocity oxy-fuel (HVOF)-coated cones in rolling contact. Wear, 203-204, 98-106

Ahn, H.S. and Lee, C.H. (1998) A study on the wear characteristics of plasma sprayed NiCrSiB/WC-12Co mixed coating. Proceedings of the 15th International Thermal Spray Conference, 25-29 May, Nice, France, 175-180

Ajdelsztajn, L., Bastain, F.L., Skandan, G. and Lavernia, E.J. (2001) Synthesis and properties of Multimodal WC-12Co coatings. Proceedings of the International Thermal Spray Conference 2001, 28-30 May, Singapore, 353-359

Archard, J.F. (1953) Contact and rubbing of flat surfaces. Journal of Applied Physics, 24, 8, 981-988

Bahadur, S. and Yang, C.N. (1996) Friction and wear behavior of tungsten and titanium carbide coatings. Wear, 196, 156-163

Barin, I. (1995) Thermochemical data of pure substances. Third Ed., VCH

Barin, I., Knocke, O. and Kubaschewski, O. (1973) Thermochemical properties of inorganic substances, Springer-Verlag.

Berger, S., Porat, R., and Rosen, R. (1997) Nanocrystalline materials: A study of WC-based hard metals. Progress in Materials Science, 42, 311-320

Bhagat, R.B., Conway, J.C. Jr., Amateau, M.E. and Brezler III, R.A. (1996) Tribological performance evaluation of tungsten carbide-based cermets and development of a fracture wear model. Wear, 201, 233-243

Bjerregaard, L., Geels, K., Cttesen, B., and Rückert, M. (1996) Metalog guide. 2nd ed. Denmark:Struers A/S.

Brook,R.J. and MaCkenzie, R.A.D. (1993) Nanocomposite materials. Materials World, January, 27-30

Clare, J.H. and Crawmer, D.E. (1982) Thermal spray coatings. In: Metal Handbook Vol. 5, 9th ed., ASM International, Ohio, 361-374

Coulson, W. and Harris, S.J. (1997) The microstructure of WC-Co coatings produced by HVOF spraying with liquid fuel. Trans IMF, 75, 3, 108-112

DeHoff, R.T. and Rhines, F.N. (1968) Quantitative microscopy. The United States of America, McGraw-Hill.

Dent, A.H., Sampath, S. and Herman, H. (2001) The effect of powder processing method on the physical properties of nanocomposite WC-Co thermally sprayed coatings. Journal of Thermal Spray Technology, 10, 1 167-169

De Villiers Lovelock, H.L., Kinds, J. and Young, P.M. (1998) Characterisation of WC-12Co thermal spray powders and HPHVOF wear resistant coatings, Powder Metallurgy, 41, 4, 292-299

Dorfman, M.R., Kushner, B.A., Nerz, J. and Rotolico, A.J. (1989) A technical assessment of high velocity oxygen-fuel versus high energy plasma tungsten carbide coatings for wear resistance, Proceedings of the 12th International Thermal Spray Conference, The Welding Institute, London, 108

Eyre, T.S. (1978) The mechanism of wear. Tribology Internation, April, 91-96

Exner, H.E. and Gurland, J. (1970) A review of parameters influencing some mechanical properties of tungsten carbide-cobalt alloys. Powder Metallurgy, 13, 25, 13-31

Fauchais, P., Vardelle, A. and Dusscubs, B. Quo vadis thermal spraying?. Journal of Thermal Spray Coaing, 10(1), March 2001, 44-66

Fernández-Guillermet, A. (1989) Thermodynamic properties of the Co-W-C system. Metallurgical Transactions A, 20A, May, 935-956

Fincke, J.R., Swank, W.D. and Haggard, D.C. (1994) Comparison of the characteristics of HVOF and plasma thermal spray. Proceedings of the 7th National Thermal Spray Conference, 20-24 June, Boston, Massachusetts, 325-330

Gärtner, F., Bormann, R., Klassen, T., Kreye, H. and Mitra, N. (2000) Nanocrystalline composites for thermal spray applications. Materials Science Forum, 343-346, 933-940

Gee, M.G., Roebuck, B., Lindahl, P. and Andren, H.O. (1996) Constituent phase nanoindentation of WC/Co and Ti(C,N) hard metals. Materials Science and Engineering A - Structural, 209, 1-2, 128-136

Gell, M. (1994) Applying nanostructured materials to future gas turbine engines. JOM, 30-34

Golden, J. and Rowe, G.W. (1958) Transfer of tungsten carbide to soft metals during single-traverse and reciprocating sliding. British Journal of Applied Physics, 9, March, 120-121

Gu, S. (2000) Numerical simulations of a high velocity oxy-fuel thermal spraying system. PhD Thesis, The University of Nottingham, Nottingham, UK

Gu, S. (2001) Thermal spray of water treatment components. CRAFT Project BRST.CT98.5393, Not published

Guilemany, J.M. and De Paco, J.M. (1996) Structure/properties relationship of WC+Co coatings obtained by HVOF spraying using starting powders with different content in metallic matrix, Proceedings of the Thermal Spray Conference 96, Düsseldrof, Germany, 390-393

Guilemany, J.M. and De Paco, J.M. (1998) Variation of friction coefficient with percentage of metallic matrix in WC-Co coatings sprayed by HVOF. Surface Engineering, 14, 2, 129-132

Guilemany, J.M. and De Paco, J.M. (1999 a) Study and characterisation of the W_2C-phase transformation during the HVOF spraying of WC+12% CO powders. United Thermal Spray Conference'99, Düsseldrof, Germany, 765-770

Guilemany, J.M., De Paco, J.M., Nutting, J. and Miguel, J.R. (1999 b) Characterization of the W_2C phase formed during the high velocity oxygen fuel spraying of a WC+12 pct Co powder. Metallurgical and Materials Transactions A-Physical Metallurgy and Materials Science, 30, 8, 1913-1921

Haller, M.N. (1998) Metallography and microstructures. In: Metal Handbook Vol. 9, 9th ed., ASM International, Ohio, 273-278

Harvey, D. (1996) The tough truth-wear-resistant coatings using high velocity oxyfuel. Industrial Lubrication and Tribilogy, 48, 2, 11-16

Harvey, M.D.F., Sturgeon, A.J., Blunt, F.J. and Dunkerton, S.B. (1995) Investigation into the relationship between fuel gas selection, wear performance and microstructure of HVOF sprayed WC-Co coatings. Proceedings of the 14th International Thermal Spray Conference, vol. 1, 22-26 May, Kobe, Japan, 471-476

He, J.H., Ice, M., Dallek, S. and Lavernia, E. J. (2000) Synthesis of nanostructured WC-12 Pct Co coating using mechanical milling and high velocity oxygen fuel thermal spraying. Metallurgical and Materials Transactions A, 21A, 541-553

He, J.H., Liu, Y.R., Qiao, Y.F., Fischer, T.E. and Lavernia, E.J. (2002) Near-nanostructured WC-18 Pct Co coatings with low amounts of non-WC carbide phase: Part 1 Synthesis and characterization. Metallurgical and Materials Transactions A, 33, 1, 145-157

Herman, H. (1998) Plasma-sprayed coatings. Scientific American, 256, 9, September, 112-117

Hewitt, A.D., (1972) Technology of oxy-fuel gas processes Part 2: Comparative combustion properties of fuel gases. Welding and Metal Fabrication, November, 382-389

Hirst, W and Lancaster, J.K. (1956) Surface film formation and metallic wear. J. Appl. Phys. 27, 1057-1065

Huddleston, J.B. (1990) Powder production methods, size and powder morphology and how it affects the user. Thermal Spray Research and Applications, Proceedings of the 3rd National Thermal Spray Conference, Long Beach, CA, 20-25 May, 321-324

Hutchings, I.M., (1992) Tribology: fracture and wear of engineering materials. London : Edward Arnold

Irving, B. (2000) HVIF process improves densities of many thermal sprayed coatings. Welding Journal, 42-44

Jacobs, L., Hyland, M.M. and De Bonte, M. (1998) Comparative study of WC-cermet coatings sprayed via the HVOF and the HVAF process. Journal of Thermal Spray Technology, 7, 2, 213-218

Jacobs, L., Hyland, M.M. and De Bonte, M. (1998) Wear behaviour of HVOF and HVAF sprayed WC-cermet coatings. Proceedings of the 15th International Thermal Spray Conference, 25-29 May, Nice, France, 169-174

Jacobs, L., Hyland, M.M. and De Bonte, M. (1999) Study of the influence of microstructural properties on the sliding-wear behavior of HVOF and HVAF sprayed WC-cermet coatings. Journal of Thermal Spray Technology, 8, 1, 125-132

Jacobs, L., Hyland, M.M. and Gutleber, J. and Sampath, S. (1999) Study of the carburisation reactions and phase transformations of a WC-Co powder. United Thermal Spray Conference, 17-19 March, Düsseldrof, Germany, 439-445

Jarosinski, W.J., Gruninger, M.F. and Londry, C.H. (1993) Characterization of tuugsten carbide cobalt powders and HVOF coatings. Proceedings of the 7th National Thermal Spray Conference, 7-11 June, Anaheim, CA, 153-157

Jia, K. and Fischer, T.E. (1996) Abrasion resistance of nanostructured and conventional cemented carbides. Wear, 200, 206-214

Jia, K. and Fischer, T.E. (1997 a) Microstructure, mechanical properties and wear resistance of WC-Co nanocomposites. Mat. Res. Soc. Symp. Proc., 457, 303-308

Jia, K. and Fischer, T.E. (1997 b) Sliding wear conventional and nanostructured cemented carbides, Wear, 203-204, 310-318

Jia, K., Fischer, T.E and Gallois, B. (1998) Microstructure, hardness and toughness of nanostructured and conventional WC-Co composites. NanoStructured Materials, 10, 5, 875-891

Jin, Y.S. and Yang, Y.Y. (1996) Tribological behavior of various plasma-sprayed ceramic coatings. Surface and Coating Technology, 88, 248-254

Karimi, A. Verdon, C. and Barbezat, G. (1993) Microstructure and hydroabrasive wear behaviour of high velocity oxy-fuel thermally sprayed WC-Co(Cr) coatings. Surface and Coatings Technology, 57, 81-89

Karthikeyan, J., Kay, C.M., Lindemann, J., Lima, R.S. and Berndt, C.C. (2001) Cold sprayed nanostructured WC-Co. Proceeding of the International of Thermal Spray Conference, 28-30 May, Singapore, 383-387

Kayaba, T. and Kato, K. (1979) The analysis of adhesive wear mechanism by successive observations of the wear process in SEM. Wear of Materials, The International Conference on Wear of Materials, 16-18 April, Michigan, 45-55

Kear, B.H., Sadangi, R.K., Jain, M., Yao, R., Kalman, Z., Skandan, G. and Mayo, W.E. (2000) Thermal sprayed nanostructured WC/Co hardcoatings. Journal of Thermal Spray Technology, 9, 3, 399-406

Kear, B.H. and Skandan, G. (1997) Conference report: Thermal processing of nanoscale materials. NanoStructured Materials, 8, 6, 765-769

Keller, N., Bertrand, G., Comas, B. and Coddet, C. (2001) On the tailoring of spray dried thermal spray powders. Thermal Spray 2001: New Surfaces for a New Millennium, Proceedings of the International Thermal Spray Conference, 28-30 May, Singapore, 285-295

Khan, M.S.A. and Clyne, T.W. (1996) Microstructure and abrasion resistance of plasma sprayed cermet coatings. Thermal Spray: Practical Solutions for Engineering Problems, Proceedings of the 9th National Thermal Spray Conference, 7-11 October, Cincinnati, Ohio, 113-122

Khan, M.S.A., Clyne, T.W. and Sturgeon, A.J. (1997) Microstructure and abrasive resistance of WC-Co coatings produced by high velocity oxy-fuel spraying. Proceedings of the United Thermal Spray Conference, 15-18 September, Indianapolis, Indiana, 681-690

Kim, B.H. and Suhr, D.S. (2001) Characteristics of spray-dried WC-17 mass% Co composite powder part 1: Effect of heating. Materials Transactions, 42, 3, 491-495

Knight, R., Smith, R.W., Xiao, Z. and Hoffman, T.T. (1994) Particle velocity measurments in HVOF and APS systems. Proceedings of the 7th National Thermal Spray Conference, 20-24 June, Boston, Massachusetts, 331-336

Korpiola, K., Hirvonen, J.-P., Jalkanen, H., Laas, L. and Rossi, F. (1995) Oxygen partial pressure measurement in the HVOF gun tail flame. Proceedings of the 8th National Thermal Spray Conference, 11-15 September, Texas, 181-185

Korpiola, K. and Vuoristo, P. (1996) Effect of HVOF gas velocity and fuel to oxygen ratio on the wear properties of tungsten carbide coating. Proceedings of the 9th National Thermal Spray Conference, 7-11 October, Cincinati, 177-184

Kreye, H., Schwetzke, R. and Zimmermann, S. (1996) High velocity oxy-fuel flame spraying process and coating characteristics, Proceedings of the 9th National Thermal Spray Conference, 7-11 October, Cincinati, 451-456

Larsen-Basse, J. (1985) Binder extrusion in sliding wear of WC-Co alloys. Wear, 105, 247-256

Lavergne, O. and Allibert C.H. (1999) Dissolution mechanism of tungsten carbide in cobalt-based liquids. High Temperature-High Pressures, 31, 347-355

Li, C.H., Ohmori, A. and Harada, Y. (1996) Effect powder structure on the structure of thermally sprayed WC-Co coatings. Journal of Materials Science, 31, 785-794

Lim. S.C., Ashby, M.F. and Brunton, J.H. (1987) Wear rate transition and their relationship to wear mechanisms. Acta Metall., 35, 6, 1343-1348

Liu, B., Zhang, Y. and Ouyang, S. (2000) Study on the relation between structural parameters and fracture strength of WC-Co cemented carbides. Materials Chemistry and Physics, 62, 35-43

Liu, Y.P., Qiao, Y.F., He, J.H., Lavernia, E.J. and Fischer, T.E. (2002) Near-nanostructured WC-18 %Co coating with low amounts of non-WC carbide phase: Part II Hardness and resistance to sliding and abrasive wear. Metallurgical and Materials Transactions A, 33, 1, 159-164

Marple, B.R., Arsenault, B. and Voyer, J. (1997) Performance of WC-based, HVOF-processed coatings in sliding wear. Thermal Spray: A united Forum for Scientific and Technological Advances. Proceedings of the 9th National Thermal Spray Conference, 5-18 September, Indianapolis, Indiana, 73-81

Marple, B.R., Voyer, J., Bisson, J.-F. and Moreau, C. (2001) Processing and characterisation of nanostructured cermet coatings. Proceedings of the International Thermal Spray Conference 2001, 28-30 May, Singapore, 343-352

McCandlish, L.E., Kear, B.H. and Bhatia, S. (1991) International Patent WO91/07244

McCandlish, L.E., Kear, B.H. and Kim, B.K. (1990) Chemical-processing of nanophase WC-Co composite powders. Materials Science and Technology, 6, 953-957

McCandlish, L.E., Kear, B.H., Kim, B.K. and Wu, L.W. (1990) Low pressure plasma-sprayed coatings of nanophase WC-Co in protective coatings: Processing and characterisation. In: The Minerals, Metals & Materials Society, Yazici, R.M. (ed), 113-119

McCandlish, L. E., Kevorkian, V., Jia, K. and Fischer, T.E. (1994) Nanostructured WC-Co composited powders advanced. In: Chaman, L and Albert, J (ed.) Powder Metallurgy & Particulate Material, vol. 5, APMI International, 329-337

McIntyre, R. (1996) Plasma sprayed coatings versus high velocity oxy fuel processes. Materials World, 4, 8, 455-457

Metallisation Ltd., Met-Jet II HVOF spray system, Brochure.

Milman, Y.V., Luyckx, S. and Northrop, I.T. (1999) Influence of temperature, grain size and cobalt content on the hardness of WC-Co alloy. International Journal of Refractory Metals & Hard Materials, 17, 39-44

Mohan, K. and Strtt, P.R. (1996 a) Observation of Co nanoparticle dispersions in WC nanograins in WC-Co cermets consolidated from chemically synthesized powders. NanoStructured Materials, 7, 5, 547-555

Mohan, K. and Strtt, P.R. (1996 b) Microstructure of spray converted nanostructured tungsten carbide-cobalt composite. Materials Science and Engineering A, 209, 237-242

Musada, M., Kuroshima, Y. and Chujo, Y. (1993) Failure of tungsten carbide-cobalt alloy tools in machining of carbon materials. Wear, 169, 135-140

Nerz, J.E., Kaufold, R., Kushner, B.A., Jr. and Rotolico, A.J. (1991) Reduction of solid particle erosion by using HVOF and HEP coating deposition methods. Thermal Spray Coatings: Properties, Processes and Applications, Proceedings of the 4th national Thermal spray Conference, 4-10 May, Pittsburgh, PA, 67-74

Nerz, J.E., Kushner, B.A., Jr. and Rotolico, A.J. (1991) Microstructural evaluation of tungsten carbide-cobalt coatings. Thermal Spray Coatings: Properties, Processes and Applications, Proceedings of the 4th national Thermal spray Conference, 4-10 May, Pittsburgh, PA, 115-120

Nicoletto, G., Tucci, A. and Esposito, L. (1993) Comparative any wear behavior of hard coatings. Wear, 162-164, 925-929

O'Quigley, D.G.F., Luyckx, S. and James, M.N. (1996) New results on the relationship between hardness and fracture toughness of WC-Co hardmetal, Materials Science and Engineering A209, 228-230

Pawlowski, L. (1995) The science and engineering of thermal spray coatings, Chichester: John Wiley & Sons

Poorman, R.M., Sargent, H.B. and Lamprey, H. (1955) Method and apparatus utilizing detonation waves for spraying and other purposes. US Patent 2 714 553

Praxair Surface Technologies, INC. (2001) HVOF equipment solutions

Praxair Surface Technologies, INC. (1997) Thermal spray products: HV-2000, Reversion June 1

Qiao, Y.F., Liu, Y.R. and Fischer, T.E. (2001) Sliding and abrasive wear resistance of thermal-sprayed WC-Co coatings. Journal of Thermal Spray Technology, 10, 1, 118-125

Ramnath, V. and Jayaraman, N. (1989) Characterisation and wear performance of plasma sprayed WC-Co coatings. Materials Science and Technology, 5, 382-388

Schwarzkopf, P., Kieffer, R., Leszynski, W. and Benesovsky, F. (1960) Cemented carbide. New York, The Macmillian Company

Sasada, T., Norose, S. and Mishina, H. (1979) The behaviour of adhered fragments interposed between sliding surfaces and the formation process of wear particles. Wear of Materials, The International Conference on Wear of Materials, 16-18 April, Michigan, 72-80

Schwetzke, R. and Kreye, H. (1998) Microstructure and properties of tungsten carbide coating sprayed with various HVOF systems. Proceedings of the 15th International Thermal Spray Conference, 25-29 May, Nice, France, 187-192

Schwetzke, R. and Kreye, H. (1999) Microstructure and properties of tungsten carbide coatings sprayed with various high velocity oxygen fuel spray system, Journal of Thermal Spray Technology, 8, 3, 433-439

Scussel, H.J. (1992) Friction and wear of cemented carbides, In: ASM Handbook Vol. 18, 10th ed., ASM International, Ohio, 795-800

Seegopaul, P, McCandlish, L.E. and Shinneman, F.M. (1997) Production capability and powder processing methods for nanostructured WC-Co powder, Int. J. of Refractory Metals & Hard Materials, 15, 133-138

Sheikh-Ahmad, J.Y. and Bailey, J.A. (1999) The wear characteristics of some cemented tungsten carbides in machining particleboard. Wear, 225-229, 256-266

Shipway, P.H. (1999) The role of test conditions on the microabrasive wear behaviour of soda-lime glass. Wear, 233-235,191-199

Skandan, G., Yao, R., Kear, B.H., Qiao Y.F., Liu, L. and Fischer, T.E. (2001) Multimodal powders: A new class of feedstock material for thermal spraying of hard coatings. Scripta MATERIALIA, 44, 1699-1702

Slavin, T.P. and Nerz, J. (1990) Material characteristics performance of WC-Co wear-resistant coatings. Proceedings of the 3rd International Thermal Spray Conference, 20-25 May, Long Beach, CA, 159-164

Smithells, C.J. (1992) Hardmetals. In: Smithells metals reference book, 7th ed, Brandes, E.A. and Brook, G.B. (ed), 23.3-23.4

Smith, R.W. and Knight, R. (1995) Thermal spraying I: Powder consolidation-from coating to forming. JOM, 47, 32-39

Smith, R.W. and Novak, R. (1991) Advance and applications in United States thermal spray technology 1: Technology and materials. Powder Metallurgy International, 23, 3, 147-155

Sobolev, V.V. and Guilemany, J.M. (1996) Dynamic processes during high velocity oxyfuel spraying, Int. Mater. Rev., 41, 32-39

Stewart, D.A. (1998) Studies on the abrasive wear behaviour of HVOF WC-Co coatings. PhD Thesis, The University of Nottingham, Nottingham, UK

Stewart, D.A, Shipway, P.H. and McCartney, D.G. (1999) Abrasive wear behaviour of conventional and nanocomposite HVOF-sprayed WC-Co coatings. Wear, 225-229, 789-798

Stewart, D.A, Shipway, P.H. and McCartney, D.G. (2000) Microstructural evolution in thermally sprayed WC-Co coatings: Comparison between nanocomposite and conventional starting powder. Acta Materialia, 48, 1593-1604

Stoica, V. and Ahmed, R. (2002) Wear of hot isostatically pressed (HIPed) thermal spray cermet coatings. Proceedings of the International Thermal Spray Conference 2002, 4-6 March, Essen, Germany, 930-937

Sturgeon, A.J. (1992) High velocity oxyfuel spraying promises better coatings. Metals and Materials, 8, 10, 547-548

Sturgeon, A.J. (1993) Thermal spray technology. Materials World, 351-354

Strutt, P.R. (1998) Thermal spray processing of nanoscale materials by HVOF/HVIF. Journal of Thermal Spray Technology, 7, 3, 413-415

Su, Y.L. and Lin, J.S. (1993) Friction and wear behavior of a number of ceramic-coated steels matched as sliding pairs to various surface-treated steels. Wear, 166, 27-35

Sudaprasert, T., McCartney, D.G. and Shipway, P.H. (2002) Role of spray system and powder feedstock on the sliding wear behaviour of WC-Co HVOF spryaed coatings, Proceedings of the International Thermal Spray Conference 2002, Essen, Germany, 4-6 March, 494-499

Suh, N.P. (1973) The delamination theory of wear, Wear, 25, 111-124

Sundararajan, G., Prasad, K.U.M., Sao, D.S. and Joshi, S.V. (1998) A comparative study of tribological behavior of plasma and D-gun sprayed coatings under different wear modes. Journal of Materials Engineering and Performance, 7, 3, 343-351

Thorpe, M.L. and Richter, H.J. (1992) A pragmatic analysis and comparison of HVOF processes. Journal of Thermal Spray Technology, 1, 2, 161-170

Tomita, T., Takatani, Y., Kobayashi Y., Harada, Y. and Nakahira, H. (1993) Durability of WC/Co Sprayed Coatings in Molten pure zinc. ISIJ International, 33, 9, 982-988

Tucker, R.C. Jr. (1994) Thermal spray coatings. In: Sufarce Engineering, ASM handbook, Vol. 5, Ohio, ASM International, 497-509

Usmani, S., Sampath, S., Houck, D.L. and Lee, D. (1997) Effect of carbide grain size on the sliding and abrasive wear behavior of thermally sprayed WC-Co coatings, Tribology Transactions, 40, 3, 470-478

Vander Voort, G.F. (1999) Metallography Principles and Practice. Ohio: ASM International

Verdon, C., Karimi, A. and Martin, J.-L. (1998) A study of high velocity oxy-fuel thermally sprayed tungsten carbide based coatings Part 1: Microstructures. Material Science and Engineering A, 246, 11-24

Vinayo, M.E., Kassabji, F., Guyonnet, J. and Fauchais, P. (1985) Plasma sprayed WC-Co coatings: Influence of spray conditions (atomospheric and low pressure plasma spraying) on the crystal structure, porosity and hardness, J. Vac. Sci., Technol. A, 3, 6, 2483-2489

Voyer, J. and Marple, B.R. (1999) Sliding wear behavior of high velocity oxy-fuel and high powder plasma spray-processed tungsten carbide-based cermet coatings. Wear, 225-229, 135-145

Voyer, J. and Marple, B.R. (2000) Thermal spray processing of WC-Co Nanomaterials. Proceedings of the 1st International Thermal Spray Conference, 8-11 May, Montréal, Québac, Canada, 895-904

Wang, Y.S. and Hsu, S.M. (1996) Wear and wear transitions of ceramics. Wear, 195, 112-122

Zhu, Y.T. and Manthiram, A. (1994) A new route for the synthesis of tungsten carbide-cobalt nanocomposites, J. Am. Ceram. Soc, 77, 10, 2777-2778